

AD-A310 434

AIR FORCE INST OF TECH WRIGHT-PATTERSON AFB OH
PERFORMANCE OF FABRIC REINFORCED AGGREGATE-SOIL SYSTEMS UNDER R--ETC(U)
DEC 81 W SCHAUZ
AFIT-CI-81-690

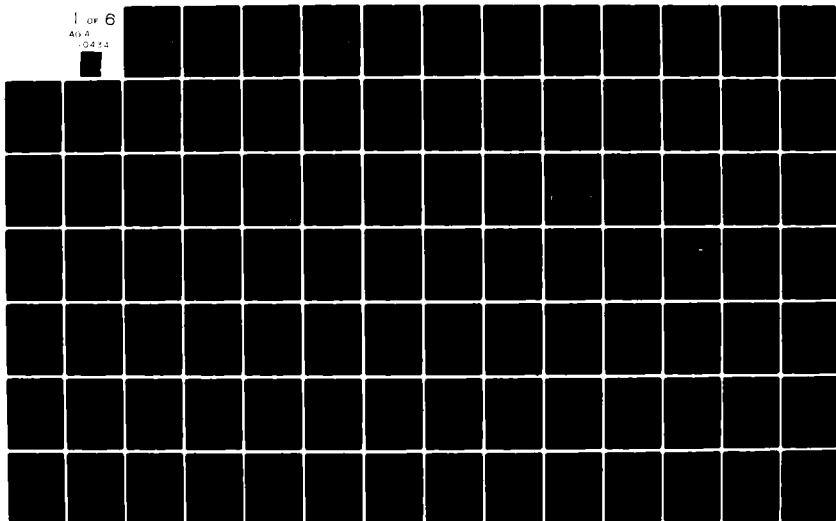
F/6 13/2

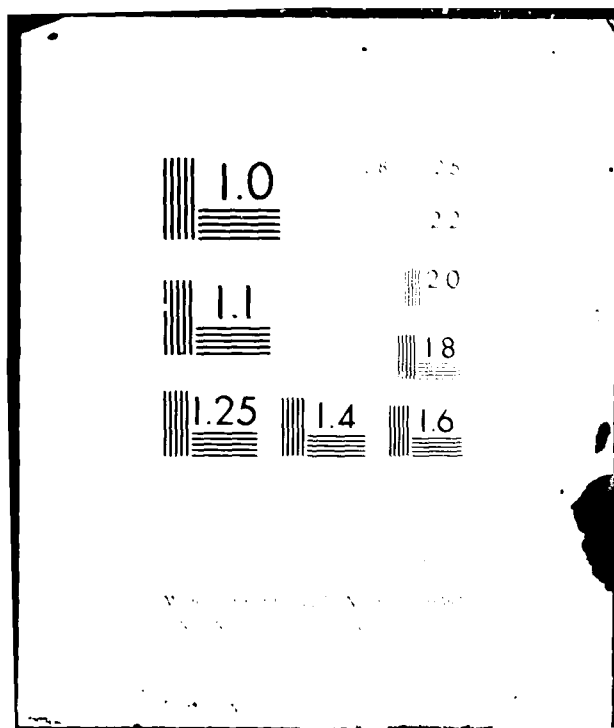
UNCLASSIFIED

NL

1 OF 6

AD-A
104 10





UNCLASS

SECURITY CLASSIFICATION OF THIS PAGE (When Data Entered)

REPORT DOCUMENTATION PAGE		READ INSTRUCTIONS BEFORE COMPLETING FORM	
1. REPORT NUMBER 81-69D	2. GOVT ACCESSION NO. AD-A110434	3. RECIPIENT'S CATALOG NUMBER	
4. TITLE (and Subtitle) Performance of Fabric Reinforced Aggregate-Soil Systems under Repeated Loading		5. TYPE OF REPORT & PERIOD COVERED THESIS/DISSERTATION	
7. AUTHOR(s) William Schauz		6. PERFORMING ORG. REPORT NUMBER	
9. PERFORMING ORGANIZATION NAME AND ADDRESS AFIT STUDENT AT: Georgia Institute of Technology		8. CONTRACT OR GRANT NUMBER(s)	
11. CONTROLLING OFFICE NAME AND ADDRESS AFIT/NR WPAFB OH 45433		10. PROGRAM ELEMENT PROJECT, TASK AREA & WORK UNIT NUMBERS	
14. MONITORING AGENCY NAME & ADDRESS (if different from Controlling Office)		12. REPORT DATE Dec 1981	
LEVEL II		13. NUMBER OF PAGES 482	
		15. SECURITY CLASS. (of this report) UNCLASS	
16. DISTRIBUTION STATEMENT (of this Report) APPROVED FOR PUBLIC RELEASE; DISTRIBUTION UNLIMITED		15a. DECLASSIFICATION/DOWNGRADING SCHEDULE	
17. DISTRIBUTION STATEMENT (of the abstract entered in Block 20, if different from Report)			
22 JAN 1982			
18. SUPPLEMENTARY NOTES APPROVED FOR PUBLIC RELEASE: IAW AFR 190-17		DTIC ELECTED FEB 2 1982 H	
19. KEY WORDS (Continue on reverse side if necessary and identify by block number)		FREDDIE CLAYTON, Major, USAF Director of Public Affairs Air Force Institute of Technology (AFIT) Dayton, Ohio, OH 45433	
20. ABSTRACT (Continue on reverse side if necessary and identify by block number)			
ATTACHED xxvii			
82 02 01 088			

DD FORM 1473 EDITION OF 1 NOV 65 IS OBSOLETE

UNCLASS

SECURITY CLASSIFICATION OF THIS PAGE (When Data Entered)

82 02 01 088

AD A110434

DTIC FILE COPY

PERFORMANCE OF FABRIC REINFORCED AGGREGATE-SOIL
SYSTEMS UNDER REPEATED LOADING

A THESIS

Presented to

The Faculty of the Division of Graduate Studies

By

William Schauz

In Partial Fulfillment
of the Requirements for the Degree
Doctor of Philosophy
in the School of Civil Engineering

Georgia Institute of Technology

December, 1981

AFIT RESEARCH ASSESSMENT

81-69D

The purpose of this questionnaire is to ascertain the value and/or contribution of research accomplished by students or faculty of the Air Force Institute of Technology (AFIT). It would be greatly appreciated if you would complete the following questionnaire and return it to:

AFIT/NR
Wright-Patterson AFB OH 45433

RESEARCH TITLE: Performance of Fabric Reinforced Aggregate-Soil System under Repeated Loading

AUTHOR: William Schauz

RESEARCH ASSESSMENT QUESTIONS:

1. Did this research contribute to a current Air Force project?
☐ a. YES ☐ b. NO
2. Do you believe this research topic is significant enough that it would have been researched (or contracted) by your organization or another agency if AFIT had not?
☐ a. YES ☐ b. NO
3. The benefits of AFIT research can often be expressed by the equivalent value that your agency achieved/received by virtue of AFIT performing the research. Can you estimate what this research would have cost if it had been accomplished under contract or if it had been done in-house in terms of manpower and/or dollars?
☐ a. MAN-YEARS ☐ b. \$
4. Often it is not possible to attach equivalent dollar values to research, although the results of the research may, in fact, be important. Whether or not you were able to establish an equivalent value for this research (3. above), what is your estimate of its significance?
☐ a. HIGHLY SIGNIFICANT ☐ b. SIGNIFICANT ☐ c. SLIGHTLY SIGNIFICANT ☐ d. OF NO SIGNIFICANCE
5. AFIT welcomes any further comments you may have on the above questions, or any additional details concerning the current application, future potential, or other value of this research. Please use the bottom part of this questionnaire for your statement(s).

NAME _____ GRADE _____ POSITION _____

ORGANIZATION _____ LOCATION _____

STATEMENT(s):

FOLD DOWN ON OUTSIDE - SEAL WITH TAPE

AFIT/NR
WRIGHT-PATTERSON AFB OH 45433
OFFICIAL BUSINESS
PENALTY FOR PRIVATE USE, \$300



NO POSTAGE
NECESSARY
IF MAILED
IN THE
UNITED STATES

BUSINESS REPLY MAIL

FIRST CLASS PERMIT NO. 73236 WASHINGTON D.C.

POSTAGE WILL BE PAID BY ADDRESSEE

AFIT/ DAA
Wright-Patterson AFB OH 45433



FOLD IN

PERFORMANCE OF FABRIC REINFORCED AGGREGATE-SOIL
SYSTEMS UNDER REPEATED LOADING

APPROVED:

Quentin L. Robnett

Q. L. Robnett

R. D. Barksdale

R. D. Barksdale

R. C. Bachus

R. C. Bachus

Date Approved by Chairman: Nov. 24, 1981

TABLE OF CONTENTS

	Page
ACKNOWLEDGMENTS.	v
LIST OF TABLES	vi
LIST OF ILLUSTRATIONS.	xv
SUMMARY.	xxvii
Chapter	
I. INTRODUCTION	1
Statement of the Problem	
Objectives of Study	
Research Approach	
II. REVIEW OF THE LITERATURE	8
Fabric Types	
Fabric Properties	
Design Methodologies	
Rut Depth Prediction	
Review of Previous Work	
III. MATERIAL SELECTION, PROCUREMENT AND PROPERTIES	48
Crushed Stone	
Subgrade Soil	
Sand	
Fabrics	
IV. MODEL TEST EQUIPMENT, INSTRUMENTATION AND TESTING PROCEDURES	74
Load Frame and Test Pit	
Loading System	
Subgrade Soil Preparation and Instrumentation	
Fabric	
Sand	
Crushed Stone	
Surface Instrumentation	
Test Procedure	
Excavation	

Chapter	Page
V. MODEL TEST PROGRAM RESULTS.	92
VI. DISCUSSION OF TEST RESULTS.	109
Rutting Component Deformations Pressure Cell Data	
VII. RUTTING RESPONSE PREDICTIVE MODELS.	155
Prediction of Rutting Response	
VIII. INTERPRETATION OF RESULTS	245
Mechanisms Alteration of Stress, Strain, and Deformation Factors Affecting System Responses Rut Depth Prediction	
IX. CONCLUSIONS	258
X. RECOMMENDATIONS FOR FURTHER STUDY	260
Appendix	
A. REPEATED LOAD TRIAXIAL TEST SAMPLE PREPARATION, EQUIPMENT, INSTRUMENTATION AND PROCEDURES.	262
Sample Preparation Loading Equipment Instrumentation Test Procedure	
B. MATERIAL PROPERTIES DATA.	268
C. SOIL STRAIN SENSORS	295
D. STRESS CELLS.	304
Limitations Theoretical Considerations	
E. MODEL TEST PROGRAM DEFORMATION DATA	314
F. MODEL TEST PROGRAM SUBGRADE SOIL SURFACE PROFILE CHANGE DATA.	393

Appendix	Page
G. MODEL TEST PROGRAM STRAIN SENSOR DATA	402
H. MODEL TEST PROGRAM FABRIC DEFORMATION DATA.	411
I. MODEL TEST PROGRAM STRESS CELL DATA	429
J. STRESS RATIO-CUMULATIVE PERMANENT DEFORMATION-LOAD CYCLE RELATIONSHIPS FOR MODEL TEST PROGRAM.	451
K. BEARING CAPACITY ANALYSES	483
BIBLIOGRAPHY.	486

ACKNOWLEDGMENTS

I wish to thank the following people for their assistance in this research effort:

Dr. Q. L. Robnett for serving as thesis advisor, for his assistance in obtaining required equipment and materials, and for his guidance throughout the project.

Dr. R. D. Barksdale for serving as a reader and as a member of the examining committee, and for his suggestions concerning data analysis.

Dr. R. C. Bachus for serving as a reader and as a member of the examining committee.

Dr. J. S. Lai for his inputs on geotextile properties and data analysis.

Regents Professor G. F. Sowers, Dr. B. B. Mazanti, and Dr. W. D. Freeston for serving as members of the examining committee.

Family and friends for their aid and moral support throughout.

LIST OF TABLES

Table	Page
3-1. Soil Properties	53
3-2. Summary of Repeated Load Triaxial Test Program.	54
3-3. Repeated Load Triaxial Test Results for Crushed Stone . . .	55
3-4. Repeated Load Triaxial Test Results for Subgrade Soil . . .	66
3-5. Repeated Load Triaxial Test Results for Subgrade Soil . . .	67
3-6. Repeated Load Triaxial Test Results for Subgrade Soil . . .	68
3-7. Fabric Properties	73
5-1. Summary of Model Test Program	94
5-2. Summary of Pertinent Material Properties, Test Group I. . .	95
5-3. Summary of Pertinent Material Properties, Test Group II (Stone Thickness = 4.5 in.)	96
5-4. Summary of Pertinent Material Properties, Test Group II (Stone Thickness = 7.0 in.)	97
5-5. Summary of Pertinent Material Properties, Test Group II (Stone Thickness = 10.0 in.)	98
5-6. Summary of Pertinent Material Properties, Test Group II (Stone Thickness = 13.0 in.)	99
5-7. Summary of Pertinent Material Properties, Test Group III. .	100
5-8. Summary of Pertinent Material Properties, Test Group IV . .	101
5-9. Summary of Selected Model Test Program Results, Test Group I	102
5-10. Summary of Selected Model Test Program Results, Test Group II (Stone Thickness = 4.5 in.)	103
5-11. Summary of Selected Model Test Program Results, Test Group II (Stone Thickness = 7.0 in.)	104

Table	Page
5-12. Summary of Selected Model Test Program Results, Test Group II (Stone Thickness = 10.0 in.).	105
5-13. Summary of Selected Model Test Program Results, Test Group II (Stone Thickness = 13.0 in.).	106
5-14. Summary of Selected Model Test Program Results, Test Group III.	107
5-15. Summary of Selected Model Test Program Results, Test Group IV	108
7-1. Summary of Method 1 Predictions of Model Test Program Rutting Responses.	157
7-2. Method 1 Stress Ratio-Rut Depth-Load Cycle Relationships for Full-Scale Loading	162
7-3. Summary of Selected Results from Full-Scale Tests. . .	164
7-4. Summary of Method 1 Predictions of Rutting Responses for Full-Scale Tests	168
7-5. Summary of Method 2 Predictions of Model Test Program Rutting Responses.	173
7-6. Summary of Method 2 Predictions of Rutting Responses for Full-Scale Tests	176
7-7. Summary of Method 3 Predictions of Model Test Program Rutting Responses.	181
7-8. Summary of Method 3 Predictions of Rutting Responses for Full-Scale Tests	185
7-9. Summary of Method 4 Predictions of Model Test Program Rutting Responses.	192
7-10. Summary of Method 4 Predictions of Rutting Responses for Full-Scale Tests	193
7-11. Summary of Method 5 Predictions of Model Test Program Rutting Responses.	200
7-12. Summary of Method 5 Predictions of Rutting Responses for Full-Scale Tests	202
7-13. Example Calculation for Method 5 Prediction of Rutting Response	205

Table	Page
7-14. Summary of Selected Transient Elastic Deformation per Cycle Data.	210
7-15. Aggregate Centerline Vertical Permanent Strains at Selected Load Cycles (Bison Strain Sensor Pair 1-2) . . .	211
7-16. Subgrade Centerline Vertical Permanent Strains at Selected Load Cycles (Bison Strain Sensor Pair 2-3) . . .	212
7-17. Subgrade Centerline Vertical Permanent Strains at Selected Load Cycles (Bison Strain Sensor Pair 3-4) . . .	213
7-18. Summary of Method 6 Predictions of Model Test Program Rutting Responses Based Upon Stress State Determined at $N = i$ Load Cycles.	215
7-19. Example Calculation for Method 6 Prediction of Rutting Response.	218
7-20. Summary of Method 6 Predictions of Model Test Program Rutting Responses Based Upon Stress State Determined with Correlated Aggregate Resilient Moduli	221
7-21. Summary of Method 6 Predictions of Component Permanent Deformation Ratios.	225
7-22. Summary of Method 7 Predictions of Model Test Program Rutting Responses Based Upon Load Induced Stress State Determined at $N = i$ Load Cycles	228
7-23. Summary of Method 7 Predictions of Model Test Program Rutting Responses Based Upon Stress State Determined at $N = i$ Load Cycles, with Gravity Stress Confinement Considered.	230
7-24. Summary of Method 7 Predictions of Component Permanent Deformation Ratios.	233
7-25. Summary of Method 8 Predictions of Model Test Program Rutting Responses	238
7-26. Summary of Method 8 Predictions of Component Permanent Deformation Ratios.	243
7-27. Summary of Method 8 Predictions of Elastic Transient Surface Deformation per Cycle at $N = 100$	244
E-1. Load Cycle-Deformation Relationships, Test No. 1B (6.0 in. Stone/None/Unsoaked CBR = 0.38)	315

Table	Page
E-2. Load Cycle-Deformation Relationships, Test No. 2B (6.0 in. Stone/T-3401/Unsoaked CBR = 0.39)	317
E-3. Load Cycle-Deformation Relationships, Test No. 3B (7.5 in. Stone/None/Unsoaked CBR = 0.43)	319
E-4. Load Cycle-Deformation Relationships, Test No. 4B (7.5 in. Stone/T-3401/Unsoaked CBR = 0.41)	321
E-5. Load Cycle-Deformation Relationships, Test No. 5B (9.0 in. Stone/None/Unsoaked CBR = 0.40)	323
E-6. Load Cycle-Deformation Relationships, Test No. 6B (9.0 in. Stone/T-3401/Unsoaked CBR = 0.41)	325
E-7. Load Cycle-Deformation Relationships, Test No. 7A (4.5 in. Stone/None/Unsoaked CBR = 0.88)	327
E-8. Load Cycle-Deformation Relationships, Test No. 7B (4.5 in. Stone/None/Unsoaked CBR = 0.91)	329
E-9. Load Cycle-Deformation Relationships, Test No. 8A (4.5 in. Stone/Sand/Unsoaked CBR = 0.97)	331
E-10. Load Cycle-Deformation Relationships, Test No. 9A (4.5 in. Stone/T-3401/Unsoaked CBR = 0.86)	333
E-11. Load Cycle-Deformation Relationships, Test No. 9B (4.5 in. Stone/T-3401/Unsoaked CBR = 0.89)	335
E-12. Load Cycle-Deformation Relationships, Test No. 10A (4.5 in. Stone/T-3401/Unsoaked CBR = 0.85)	337
E-13. Load Cycle-Deformation Relationships, Test No. 11A (4.5 in. Stone/M-140/Unsoaked CBR = 0.75)	339
E-14. Load Cycle-Deformation Relationships, Test No. 12A (4.5 in. Stone/B-C22/Unsoaked CBR = 0.78)	341
E-15. Load Cycle-Deformation Relationships, Test No. 13A (7.0 in. Stone/None/Unsoaked CBR = 0.82)	343
E-16. Load Cycle-Deformation Relationships, Test No. 13B (7.0 in. Stone/None/Unsoaked CBR = 0.81)	345
E-17. Load Cycle-Deformation Relationships, Test No. 14A (7.0 in. Stone/Sand/Unsoaked CBR = 0.81)	347

Table	Page
E-18. Load Cycle-Deformation Relationships, Test No. 15A (7.0 in. Stone/T-3401/Unsoaked CBR = 0.94)	349
E-19. Load Cycle-Deformation Relationships, Test No. 15B (7.0 in. Stone/T-3401/Unsoaked CBR = 0.78)	351
E-20. Load Cycle-Deformation Relationships, Test No. 16A (7.0 in. Stone/T-3601/Unsoaked CBR = 0.74)	353
E-21. Load Cycle-Deformation Relationships, Test No. 17A (7.0 in. Stone/M-140/Unsoaked CBR = 0.82)	355
E-22. Load Cycle-Deformation Relationships, Test No. 18A (7.0 in. Stone/B-C22/Unsoaked CBR = 0.83)	357
E-23. Load Cycle-Deformation Relationships, Test No. 19A (10.0 in. Stone/None/Unsoaked CBR = 0.90)	359
E-24. Load Cycle-Deformation Relationships, Test No. 19B (10.0 in. Stone/None/Unsoaked CBR = 0.93)	361
E-25. Load Cycle-Deformation Relationships, Test No. 20A (10.0 in. Stone/T-3401/Unsoaked CBR = 0.87)	363
E-26. Load Cycle-Deformation Relationships, Test No. 20B (10.0 in. Stone/T-3401/Unsoaked CBR = 0.96)	365
E-27. Load Cycle-Deformation Relationships, Test No. 21A (10.0 in. Stone/T-3601/Unsoaked CBR = 0.78)	367
E-28. Load Cycle-Deformation Relationships, Test No. 22A (13.0 in. Stone/None/Unsoaked CBR = 0.99)	369
E-29. Load Cycle-Deformation Relationships, Test No. 23A (13.0 in. Stone/T-3401/Unsoaked CBR = 0.97)	371
E-30. Load Cycle-Deformation Relationships, Test No. 24A (13.0 in. Stone/M-140/Unsoaked CBR = 0.84)	373
E-31. Load Cycle-Deformation Relationships, Test No. 25A (13.0 in. Stone/B-C22/Unsoaked CBR = 0.84)	375
E-32. Load Cycle-Deformation Relationships, Test No. 26B (3.0 in. Stone/None/Unsoaked CBR = 1.55)	377
E-33. Load Cycle-Deformation Relationships, Test No. 27B (3.0 in. Stone/T-3401/Unsoaked CBR = 1.56)	379

Table	Page
E-34. Load Cycle-Deformation Relationships, Test No. 28B (4.5 in. Stone/None/Unsoaked CBR = 1.59).	381
E-35. Load Cycle-Deformation Relationships, Test No. 29B (4.5 in. Stone/T-3401/Unsoaked CBR = 1.61).	383
E-36. Load Cycle-Deformation Relationships, Test No. 30B (6.0 in. Stone/None/Unsoaked CBR = 1.72).	385
E-37. Load Cycle-Deformation Relationships, Test No. 31B (6.0 in. Stone/T-3401/Unsoaked CBR = 1.44).	387
E-38. Load Cycle-Deformation Relationships, Test No. 32B (3.0 in. Stone/None/Unsoaked CBR = 2.43).	389
E-39. Load Cycle-Deformation Relationships, Test No. 33B (3.0 in. Stone/T-3401/Unsoaked CBR = 2.39).	391
F-1. Subgrade Soil Surface Profile Changes, Test Group I. . .	395
F-2. Subgrade Soil Surface Profile Changes, Test Group II (Stone Thickness = 4.5 in.).	396
F-3. Subgrade Soil Surface Profile Changes, Test Group II (Stone Thickness = 7.0 in.).	397
F-4. Subgrade Soil Surface Profile Changes, Test Group II (Stone Thickness = 10.0 in.).	398
F-5. Subgrade Soil Surface Profile Changes, Test Group II (Stone Thickness = 13.0 in.).	399
F-6. Subgrade Soil Surface Profile Changes, Test Group III. .	400
F-7. Subgrade Soil Surface Profile Changes, Test Group IV . .	401
G-1. Strain Sensor Relative Movements, Test Group I	404
G-2. Strain Sensor Relative Movements, Test Group II (Stone Thickness = 4.5 in.).	405
G-3. Strain Sensor Relative Movements, Test Group II (Stone Thickness = 7.0 in.).	406
G-4. Strain Sensor Relative Movements, Test Group II (Stone Thickness = 10.0 in.).	407
G-5. Strain Sensor Relative Movements, Test Group II (Stone Thickness = 13.0 in.).	408

Table	Page
G-6. Strain Sensor Relative Movements, Test Group III.	409
G-7. Strain Sensor Relative Movements, Test Group IV	410
H-1. Fabric Segment Deformations, Test No. 2B (6.0 in. Stone/T-3401/Unsoaked CBR = 0.39)	412
H-2. Fabric Segment Deformations, Test No. 4B (7.5 in. Stone/T-3401/Unsoaked CBR = 0.41)	413
H-3. Fabric Segment Deformations, Test No. 6B (9.0 in. Stone/T-3401/Unsoaked CBR = 0.41)	414
H-4. Fabric Segment Deformations, Test No. 9A (4.5 in. Stone/T-3401/Unsoaked CBR = 0.86)	415
H-5. Fabric Segment Deformations, Test No. 9B (4.5 in. Stone/T-3401/Unsoaked CBR = 0.89)	416
H-6. Fabric Segment Deformations, Test No. 10A (4.5 in. Stone/T-3601/Unsoaked CBR = 0.85)	417
H-7. Fabric Segment Deformations, Test No. 15A (7.0 in. Stone/T-3401/Unsoaked CBR = 0.94)	418
H-8. Fabric Segment Deformations, Test No. 15B (7.0 in. Stone/T-3401/Unsoaked CBR = 0.78)	419
H-9. Fabric Segment Deformations, Test No. 16A (7.0 in. Stone/T-3601/Unsoaked CBR = 0.74)	420
H-10. Fabric Segment Deformations, Test No. 20A (10.0 in. Stone/T-3401/Unsoaked CBR = 0.87)	421
H-11. Fabric Segment Deformations, Test No. 20B (10.0 in. Stone/T-3401/Unsoaked CBR = 0.96)	422
H-12. Fabric Segment Deformations, Test No. 21A (10.0 in. Stone/T-3601/Unsoaked CBR = 0.78)	423
H-13. Fabric Segment Deformations, Test No. 23A (13.0 in. Stone/T-3401/Unsoaked CBR = 0.97)	424
H-14. Fabric Segment Deformations, Test No. 27B (3.0 in. Stone/T-3401/Unsoaked CBR = 1.56)	425
H-15. Fabric Segment Deformations, Test No. 29B (4.5 in. Stone/T-3401/Unsoaked CBR = 1.61)	426

Table	Page
H-16. Fabric Segment Deformations, Test No. 31B (6.0 in. Stone/T-3401/Unsoaked CBR = 1.44)	427
H-17. Fabric Segment Deformations, Test No. 33B (3.0 in. Stone/T-3401/Unsoaked CBR = 2.39)	428
I-1. Pressure Cell Readings, Test No. 1B (6.0 in. Stone/None/Unsoaked CBR = 0.38)	431
I-2. Pressure Cell Readings, Test No. 2B (6.0 in. Stone/T-3401/Unsoaked CBR = 0.39)	432
I-3. Pressure Cell Readings, Test No. 3B (7.5 in. Stone/None/Unsoaked CBR = 0.43)	433
I-4. Pressure Cell Readings, Test No. 4B (7.5 in. Stone/T-3401/Unsoaked CBR = 0.41)	434
I-5. Pressure Cell Readings, Test No. 5B (9.0 in. Stone/None/Unsoaked CBR = 0.40)	435
I-6. Pressure Cell Readings, Test No. 6B (9.0 in. Stone/T-3401/Unsoaked CBR = 0.41)	436
I-7. Pressure Cell Readings, Test No. 7B (4.5 in. Stone/None/Unsoaked CBR = 0.91)	437
I-8. Pressure Cell Readings, Test No. 9B (4.5 in. Stone/T-3401/Unsoaked CBR = 0.89)	438
I-9. Pressure Cell Readings, Test No. 13B (7.0 in. Stone/None/Unsoaked CBR = 0.81)	439
I-10. Pressure Cell Readings, Test No. 15B (7.0 in. Stone/T-3401/Unsoaked CBR = 0.78)	440
I-11. Pressure Cell Readings, Test No. 19B (10.0 in. Stone/None/Unsoaked CBR = 0.93)	441
I-12. Pressure Cell Readings, Test No. 20B (10.0 in. Stone/T-3401/Unsoaked CBR = 0.96)	442
I-13. Pressure Cell Readings, Test No. 26B (3.0 in. Stone/None/Unsoaked CBR = 1.55)	443
I-14. Pressure Cell Readings, Test No. 27B (3.0 in. Stone/T-3401/Unsoaked CBR = 1.56)	444
I-15. Pressure Cell Readings, Test No. 28B (4.5 in. Stone/None/Unsoaked CBR = 1.59)	445

Table	Page
I-16. Pressure Cell Readings, Test No. 29B (4.5 in. Stone/ T-3401/Unsoaked CBR = 1.61).	446
I-17. Pressure Cell Readings, Test No. 30B (6.0 in. Stone/None/ Unsoaked CBR = 1.72)	447
I-18. Pressure Cell Readings, Test No. 31B (6.0 in. Stone/ T-3401/Unsoaked CBR = 1.44).	448
I-19. Pressure Cell Readings, Test No. 32B (3.0 in. Stone/None/ Unsoaked CBR = 2.43)	449
I-20. Pressure Cell Readings, Test No. 33B (3.0 in. Stone/ T-3401/Unsoaked CBR = 2.39).	450
K-1. Bearing Capacity Values for Models and Prototypes.	485

LIST OF ILLUSTRATIONS

Figure		Page
1-1.	Schematic of Aggregate-Fabric-Subgrade System.	5
2-1.	Typical Design Curves for AS and AFS Systems Based Upon Limiting Subgrade Stress Method - 5 kip Wheel Load	19
2-2.	Typical Design Curves for AS and AFS Systems Based Upon Research by Celanese Fibers Marketing Company . .	21
2-3.	Typical Design Curves for AS and AFS Systems Based Upon Research by Law Engineering - 20 kip Axle Load and 10.00-20 Tires on Dual Wheels.	22
2-4.	Rutting Response Predicted by Hammitt Modification to U.S. Army Corps of Engineers Equation.	25
2-5.	Typical Design Curves for AS and AFS Systems Based Upon CBR Method - 5000 Load Repetitions and 100 psi Contact Pressure	27
2-6.	Typical Strain-Stress State Relationship for Soil. . .	33
2-7.	Typical Strain-Reciprocal of Secant Modulus Relation- ship for Soil.	34
2-8.	Typical Bulk Stress-Resilient Modulus Relationship for Granular Material.	40
2-9.	Typical Deviator Stress-Resilient Modulus Relation- ship for Fine-Grained Soil	41
3-1.	Crushed Stone Grain Size Distribution.	49
3-2.	Mohr Envelope for Crushed Stone.	52
3-3.	Subgrade Soil Grain Size Distribution.	56
3-4.	Subgrade Soil Strength Correlations.	61
3-5.	Mohr Envelope for Subgrade Soil.	62
3-6.	Mohr Envelope for Subgrade Soil.	63
3-7.	Mohr Envelope for Subgrade Soil.	64

Figure		Page
3-8.	Sand Grain Size Distribution.	69
4-1.	Load Frame and Test Pit Details	75
4-2.	Load System Pneumatic Schematic	77
4-3.	Load System Electrical-Mechanical Schematic	78
4-4.	Time-Pressure Relationships for Loading Types A and B .	80
4-5.	Bison Coil Designations and Initial Placement Configuration	83
6-1.	Influence of Subgrade Strength on Load Cycle-Cumulative Permanent Deformation Relationship in AS Systems (Tests 1B/30B)	110
6-2.	Influence of Subgrade Strength on Load Cycle-Cumulative Permanent Deformation Relationship in AS Systems (Tests 26B/32B).	111
6-3.	Influence of Subgrade Strength on Load Cycle-Cumulative Permanent Deformation Relationship in T-3401 Reinforced AFS Systems (Tests 2B/31B).	112
6-4.	Influence of Subgrade Strength on Load Cycle-Cumulative Permanent Deformation Relationship in T-3401 Reinforced AFS Systems (Tests 27B/33B)	113
6-5.	Influence of Crushed Stone Layer Thickness on Load Cycle-Cumulative Permanent Deformation Relationship in AS Systems (Tests 7B/13B/19B)	115
6-6.	Influence of Crushed Stone Layer Thickness on Load Cycle-Cumulative Permanent Deformation Relationship in T-3401 Reinforced AFS Systems (Tests 9B/15B/20B). . . .	116
6-7.	Stress Ratio-Rut Depth Relationships for AS and Typar 3401 Reinforced AFS Systems for 10 Load Cycles, Type B Loading	118
6-8.	Load Cycle-Stress Ratio Relationships for AS and Typar 3401 Reinforced AFS Systems for 2 in. Rut, Type B Loading	119
6-9.	Influence of Load Pulse Duration on Load Cycle- Cumulative Permanent Deformation Relationships in AS Systems (Tests 7A/7B; 13A/13B; 19A/19B)	121

Figure		Page
6-10.	Influence of Load Pulse Duration of Load Cycle-Cumulative Permanent Deformation Relationships in T-3401 Reinforced AFS Systems (Tests 9A/9B; 15A/15B; 20A/20B).	122
6-11.	Influence of T-3401 Membrane Inclusion on Load Cycle-Cumulative Permanent Deformation Relationships (Tests 7B/9B; 13B/15B; 19B/20B).	124
6-12.	Influence of Membrane Inclusion Type on Load Cycle-Cumulative Permanent Deformation Relationship (Tests 13A/14A/15A/16A/17A/18A).	125
6-13.	Comparison of Computer Rutting Relationship for AS Systems (Rutting Scale Factor of 1.0; N Corrected for Instrumentation) and Response Predicted by Hammitt Modification to U.S. Army Corps of Engineers Equation, Type B Loading.	132
6-14.	Comparison of Computed Rutting Relationship for AS Systems (Rutting Scale Factor of 2.0; N Corrected for Instrumentation) and Response Predicted by Hammitt Modification to U.S. Army Corps of Engineers Equation, Type B Loading.	133
6-15.	Comparison of Computed Rutting Relationship for AS Systems (Rutting Scale Factor of 1.7; N Corrected for Instrumentation) and Response Predicted by Hammitt Modification to U.S. Army Corps of Engineers Equation, Type B Loading.	134
6-16.	Influence of Crushed Stone Thickness on Centerline Vertical Plastic Strain Distribution in AS Systems (26B/28B/30B).	136
6-17.	Influence of Crushed Stone Thickness on Centerline Vertical Plastic Strain Distribution in T-3401 Reinforced AFS Systems (27B/29B/31B).	138
6-18.	Influence of Membrane Type on Centerline Vertical Plastic Strain Distribution (7A/8A/11A/12A).	140
6-19.	Influence of Membrane Type on Centerline Vertical Plastic Strain Distribution (7A/9A/10A).	141
6-20.	Bison Coil Designations and Typical Final Configuration.	142

Figure	Page
6-21. Influence of Crushed Stone Thickness on Subgrade Soil Profile Changes in AS and AFS Systems (9B/15B/20B) . . .	144
6-22. Influence of Membrane Type on Subgrade Soil Profile Changes (13A/14A/17A/18A)	145
6-23. Influence of Membrane Type on Subgrade Soil Profile Changes (13A/15A/16A)	146
6-24. Influence of Stress Ratio on T-3401 Fabric Strain Distribution (9B/15B/20B)	148
6-25. Initial Pressure Cell Readings for AS Systems, Type B Loading	150
6-26. Initial Pressure Cell Readings for T-3401 Reinforced AFS Systems, Type B Loading	151
6-27. Final Pressure Cell Readings for Groups I and IV AS Systems, Type B Loading	153
6-28. Final Pressure Cell Readings for Groups I and IV T-3401 Reinforced AFS Systems, Type B Loading	154
7-1. Load Cycle-Cumulative Permanent Deformation Relationship for Full-Scale Field Tests	165
7-2. Load Cycle-Cumulative Permanent Deformation Relationships for Full-Scale Model Tests.	166
7-3. Comparison of Actual and Method 1 Predictions of Rutting Response for Full-Scale Field Test (U.S. Army Corps of Engineers).	169
7-4. Comparison of Actual and Method 1 Predictions of Rutting Response for Full-Scale Model Tests (Georgia Institute of Technology).	170
7-5. Comparison of Actual and Method 2 Predictions of Rutting Response for Full-Scale Field Tests (U.S. Army Corps of Engineers).	177
7-6. Comparison of Actual and Method 2 Predictions of Rutting Response for Full-Scale Model Tests (Georgia Institute of Technology).	178
7-7. Comparison of Actual and Method 3 Predictions of Rutting Response for Full-Scale Field Tests (U.S. Army Corps of Engineers)	186

Figure		Page
7-8.	Comparison of Actual and Method 3 Predictions of Rutting Response for Full-Scale Model Tests (Georgia Institute of Technology).	187
7-9.	Method 4 Rutting Relationships for 3 in. Rut in AS Systems	189
7-10.	Method 4 Rutting Relationship for 3 in. Rut in T-3401 Reinforced AFS Systems.	191
7-11.	Single Layer Deflection Factors	199
7-12.	Comparison of Actual and Method 5 Predictions of Rutting Response for Full-Scale Field Tests (U.S. Army Corps of Engineers)	203
7-13.	Comparison of Actual and Method 5 Predictions of Rutting Response for Full-Scale Model Tests (Georgia Institute of Technology).	204
7-14.	Typical Aggregate Resilient Modulus-Transient Surface Deflection per Cycle and Aggregate Resilient Modulus-Stress Relationships from VESYS Analysis.	209
8-1.	Comparison of Actual and Methods 3/5 Composite Predictions of Rutting Response for Full-Scale Field Tests (U.S. Army Corps of Engineers).	254
8-2.	Comparison of Actual and Methods 3/5 Composite Predictions of Rutting Response for Full-Scale Methods Tests (Georgia Institute of Technology)	255
8-3.	Design Chart for Methods 3/5 for 1000 Load Cycles and a 3 in. Rut	257
B-1.	Crushed Stone Compaction Moisture-Density Relationship.	269
B-2.	Load Cycle-Plastic Strain Relationships for Crushed Stone, Type A Loading	270
B-3.	Load Cycle-Plastic Strain Relationships for Crushed Stone, Type B Loading	271
B-4.	Plastic Strain-Stress State Relationships for Crushed Stone at 10 Load Cycles, Type B Loading	272
B-5.	Bulk Stress-Resilient Modulus Relationship for Crushed Stone at 10 Load Cycles, Type B Loading	273

Figure		Page
B-6.	Subgrade Soil Compaction Moisture-Density Relationship.	274
B-7.	Subgrade Soil Compaction Moisture-Unsoaked CBR Relationship.	275
B-8.	Subgrade Soil Compaction Moisture-Penetration Resistance Relationship	276
B-9.	Subgrade Soil Compaction Moisture-Cone Load Relationship.	277
B-10.	Subgrade Soil Compaction Moisture-Cone Index Relationship.	278
B-11.	Subgrade Soil Compaction Moisture-Density Relationship.	279
B-12.	Subgrade Soil Compaction Moisture-Unsoaked CBR Relationship.	280
B-13.	Subgrade Soil Compaction Moisture-Penetration Resistance Relationship	281
B-14.	Subgrade Soil Compaction Moisture-Cone Load Relationship.	282
B-15.	Subgrade Soil Compaction Moisture-Cone Index Relationship.	283
B-16.	Subgrade Soil Compaction Moisture-Vane Shear Strength Relationship	284
B-17.	Subgrade Soil Penetration Resistance-Unsoaked CBR Correlation	285
B-18.	Subgrade Soil Penetration Resistance-Cone Load Correlation	286
B-19.	Subgrade Soil Penetration Resistance-Vane Shear Strength Correlation.	287
B-20.	Load Cycle-Plastic Strain Relationships for Subgrade Soil, Type B Loading.	288
B-21.	Load Cycle-Plastic Strain Relationships for Subgrade Soil, Type A Loading.	289

Figure		Page
B-22.	Load Cycle-Plastic Strain Relationships for Subgrade Soil, Type B Loading.	290
B-23.	Load Cycle-Plastic Strain Relationships for Subgrade Soil, Type B Loading.	291
B-24.	Plastic Strain-Stress State Relationships for Subgrade Soil at 1 Load Cycle, Type B Loading.	292
B-25.	Deviator Stress-Resilient Modulus Relationship for Subgrade Soil at 1 Load Cycle, Type B Loading	293
B-26.	Deviator Stress-Resilient Modulus Relationship for Subgrade Soil at 1 Load Cycle, Type B Loading	294
C-1.	United Kingdom Transport and Road Research Laboratory Strain Cell	296
C-2.	Bison Sensors and Plexiglas Calibration Mounting Fixture	299
C-3.	Amplitude Dial Reading-Sensor Separation Relationships for Coaxial Coils	301
C-4.	Amplitude Dial Reading-Sensor Separation Relationships for Coplanar Coils.	302
D-1.	Stress Cell Details	310
D-2.	Stress Cell Equipment Schematic	311
E-1.	Load Cycle-Cumulative Permanent Deformation Relationship, Test No. 1B (6.0 in. Stone/None/Unsoaked CBR = 0.38)	316
E-2.	Load Cycle-Cumulative Permanent Deformation Relationship, Test No. 2B (6.0 in. Stone/T-3401/Unsoaked CBR = 0.39)	318
E-3.	Load Cycle-Cumulative Permanent Deformation Relationship, Test No. 3B (7.5 in. Stone/None/Unsoaked CBR = 0.43)	320
E-4.	Load Cycle-Cumulative Permanent Deformation Relationship, Test No. 4B (7.5 in. Stone/T-3401/Unsoaked CBR = 0.41)	322
E-5.	Load Cycle-Cumulative Permanent Deformation Relationship, Test No. 5B (9.0 in. Stone/None/Unsoaked CBR = 0.40)	324

Figure		Page
E-6.	Load Cycle-Cumulative Permanent Deformation Relationship, Test No. 6B (9.0 in. Stone/T-3401/Unsoaked CBR = 0.41)	326
E-7.	Load Cycle-Cumulative Permanent Deformation Relationship, Test No. 7A (4.5 in. Stone/None/Unsoaked CBR = 0.88)	328
E-8.	Load Cycle-Cumulative Permanent Deformation Relationship, Test No. 7B (4.5 in. Stone/None/Unsoaked CBR = 0.91)	330
E-9.	Load Cycle-Cumulative Permanent Deformation Relationship, Test No. 8A (4.5 in. Stone/Sand/Unsoaked CBR = 0.97)	332
E-10.	Load Cycle-Cumulative Permanent Deformation Relationship, Test No. 9A (4.5 in. Stone/T-3401/Unsoaked CBR = 0.86)	334
E-11.	Load Cycle-Cumulative Permanent Deformation Relationship, Test No. 9B (4.5 in. Stone/T-3401/Unsoaked CBR = 0.89)	336
E-12.	Load Cycle-Cumulative Permanent Deformation Relationship, Test No. 10A (4.5 in. Stone/T-3601/Unsoaked CBR = 0.85)	338
E-13.	Load Cycle-Cumulative Permanent Deformation Relationship, Test No. 11A (4.5 in. Stone/M-140/Unsoaked CBR = 0.75)	340
E-14.	Load Cycle-Cumulative Permanent Deformation Relationship, Test No. 12A (4.5 in. Stone/B-C22/Unsoaked CBR = 0.78)	342
E-15.	Load Cycle-Cumulative Permanent Deformation Relationship, Test No. 13A (7.0 in. Stone/None/Unsoaked CBR = 0.82)	344
E-16.	Load Cycle-Cumulative Permanent Deformation Relationship, Test No. 13B (7.0 in. Stone/None/Unsoaked CBR = 0.81)	346
E-17.	Load Cycle-Cumulative Permanent Deformation Relationship, Test No. 14A (7.0 in. Stone/Sand/Unsoaked CBR = 0.81)	348

Figure		Page
E-18.	Load Cycle-Cumulative Permanent Deformation Relationship, Test No. 15A (7.0 in. Stone/T-3401/Unsoaked CBR = 0.94)	350
E-19.	Load Cycle-Cumulative Permanent Deformation Relationship, Test No. 15B (7.0 in. Stone/T-3401/Unsoaked CBR = 0.78)	352
E-20.	Load Cycle-Cumulative Permanent Deformation Relationship, Test No. 16A (7.0 in. Stone/T-3601/Unsoaked CBR = 0.74)	354
E-21.	Load Cycle-Cumulative Permanent Deformation Relationship, Test No. 17A (7.0 in. Stone/M-140/Unsoaked CBR = 0.82)	356
E-22.	Load Cycle-Cumulative Permanent Deformation Relationship, Test No. 18A (7.0 in. Stone/B-C22/Unsoaked CBR = 0.83)	358
E-23.	Load Cycle-Cumulative Permanent Deformation Relationship, Test No. 19A (10.0 in. Stone/None/Unsoaked CBR = 0.90)	360
E-24.	Load Cycle-Cumulative Permanent Deformation Relationship, Test No. 19B (10.0 in. Stone/None/Unsoaked CBR = 0.93)	362
E-25.	Load Cycle-Cumulative Permanent Deformation Relationship, Test No. 20A (10.0 in. Stone/T-3401/Unsoaked CBR = 0.87)	364
E-26.	Load Cycle-Cumulative Permanent Deformation Relationship, Test No. 20B (10.0 in. Stone/T-3401/Unsoaked CBR = 0.96)	366
E-27.	Load Cycle-Cumulative Permanent Deformation Relationship, Test No. 21A (10.0 in. Stone/T-3601/Unsoaked CBR = 0.78)	368
E-28.	Load Cycle-Cumulative Permanent Deformation Relationship, Test No. 22A (13.0 in. Stone/None/Unsoaked CBR = 0.99)	370
E-29.	Load Cycle-Cumulative Permanent Deformation Relationship, Test No. 23A (13.0 in. Stone/T-3401/Unsoaked CBR = 0.97)	372

Figure		Page
E-30.	Load Cycle-Cumulative Permanent Deformation Relationship, Test No. 24A (13.0 in. Stone/M-140/Unsoaked CBR = 0.84)	374
E-31.	Load Cycle-Cumulative Permanent Deformation Relationship, Test No. 25A (13.0 in. Stone/B-C22/Unsoaked CBR = 0.84)	376
E-32.	Load Cycle-Cumulative Permanent Deformation Relationship, Test No. 26B (3.0 in. Stone/None/Unsoaked CBR = 1.55)	378
E-33.	Load Cycle-Cumulative Permanent Deformation Relationship, Test No. 27B (3.0 in. Stone/T-3401/Unsoaked CBR = 1.56)	380
E-34.	Load Cycle-Cumulative Permanent Deformation Relationship, Test No. 28B (4.5 in. Stone/None/Unsoaked CBR = 1.59)	382
E-35.	Load Cycle-Cumulative Permanent Deformation Relationship, Test No. 29B (4.5 in. Stone/T-3401/Unsoaked CBR = 1.61)	384
E-36.	Load Cycle-Cumulative Permanent Deformation Relationship, Test No. 30B (6.0 in. Stone/None/Unsoaked CBR = 1.72)	386
E-37.	Load Cycle-Cumulative Permanent Deformation Relationship, Test No. 31B (6.0 in. Stone/T-3401/Unsoaked CBR = 1.44)	388
E-38.	Load Cycle-Cumulative Permanent Deformation Relationship, Test No. 32B (3.0 in. Stone/None/Unsoaked CBR = 2.43)	390
E-39.	Load Cycle-Cumulative Permanent Deformation Relationship, Test No. 33B (3.0 in. Stone/T-3401/Unsoaked CBR = 2.39)	392
G-1.	Bison Coil Designations and Initial Placement Configuration	403
J-1.	Stress Ratio-Rut Depth Relationships for 10 Load Cycles, Type A Loading.	453
J-2.	Stress Ratio-Rut Depth Relationships for 100 Load Cycles, Type A Loading.	454

Figure		Page
J-3.	Stress Ratio-Rut Depth Relationships for 1000 Load Cycles, Type A Loading.	455
J-4.	Load Cycle-Stress Ratio Relationships for 2 in. Rut, Type A Loading.	456
J-5.	Load Cycle-Stress Ratio Relationships for 3 in. Rut, Type A Loading.	457
J-6.	Load Cycle-Stress Ratio Relationships for 4 in. Rut, Type A Loading.	458
J-7.	Stress Ratio-Rut Depth Relationships for 10 Load Cycles, Type A Loading.	459
J-8.	Stress Ratio-Rut Depth Relationships for 100 Load Cycles, Type A Loading.	460
J-9.	Stress Ratio-Rut Depth Relationships for 1000 Load Cycles, Type A Loading.	461
J-10.	Load Cycle-Stress Ratio Relationships for 2 in. Rut, Type A Loading.	462
J-11.	Load Cycle-Stress Ratio Relationships for 3 in. Rut, Type A Loading.	463
J-12.	Load Cycle-Stress Ratio Relationships for 4 in. Rut, Type A Loading.	464
J-13.	Stress Ratio-Rut Depth Relationships for 10 Load Cycles, Type A Loading.	465
J-14.	Stress Ratio-Rut Depth Relationships for 100 Load Cycles, Type A Loading.	466
J-15.	Stress Ratio-Rut Depth Relationships for 1000 Load Cycles, Type A Loading.	467
J-16.	Load Cycle-Stress Ratio Relationships for 2 in. Rut, Type A Loading.	468
J-17.	Load Cycle-Stress Ratio Relationships for 3 in. Rut, Type A Loading.	469
J-18.	Load Cycle-Stress Ratio Relationships for 4 in. Rut, Type A Loading.	470
J-19.	Stress Ratio-Rut Depth Relationships for 10 Load Cycles, Type A Loading.	471

Figure		Page
J-20.	Stress Ratio-Rut Depth Relationships for 100 Load Cycles, Type A Loading.	472
J-21.	Stress Ratio-Rut Depth Relationships for 1000 Load Cycles, Type A Loading.	473
J-22.	Load Cycle-Stress Ratio Relationships for 2 in. Rut, Type A Loading.	474
J-23.	Load Cycle-Stress Ratio Relationships for 3 in. Rut, Type A Loading.	475
J-24.	Load Cycle-Stress Ratio Relationships for 4 in. Rut, Type A Loading.	476
J-25.	Stress Ratio-Rut Depth Relationships for 10 Load Cycles, Type B Loading.	477
J-26.	Stress Ratio-Rut Depth Relationships for 100 Load Cycles, Type B Loading.	478
J-27.	Stress Ratio-Rut Depth Relationships for 1000 Load Cycles, Type B Loading.	479
J-28.	Load Cycle-Stress Ratio Relationships for 2 in. Rut, Type B Loading.	480
J-29.	Load Cycle-Stress Ratio Relationships for 3 in. Rut, Type B Loading.	481
J-30.	Load Cycle-Stress Ratio Relationships for 4 in. Rut, Type B Loading.	482

SUMMARY

1

Key words: Geotextiles, fabric, pavements, aggregate, thickness design.

Accession For
NATIONAL ARCHIVES
U.S. DEPARTMENT OF THE ARMY
U.S. DEPARTMENT OF THE NAVY

DTIC COPY INSPECTED 2

CHAPTER I

INTRODUCTION

Geotextiles are defined by the American Society for Testing and Materials (ASTM) as:

"Any permeable textile used with geotechnical materials as an integral part of a man-made project, structure, or system."

The use of these products in Civil Engineering applications is in a state of rapid development. In recent years, geotextiles have become increasingly popular and proven commercially successful in a variety of applications, including: subgrade stabilization, reinforced earth construction, subsurface drainage, and control of reflection cracking, erosion and sediment runoff (17, 34, 47, 57, 66, 87, 100, 117, 118).

One of the most promising applications for these fabrics is subgrade stabilization, wherein the fabric is used in conjunction with crushed stone to provide strong and durable support layers in unsurfaced low volume roads. The use of fabrics has proven to be especially effective in improving the performance of aggregate layers placed on very soft subgrades. In this application, the fabric is placed between the aggregate and subgrade soil, creating an aggregate-fabric-subgrade (AFS) system.

The mechanisms by which the fabric affects the behavior and performance of AFS systems have never been well defined, but are generally believed (14, 17, 81, 100) to include the following:

- (1) Separation of the aggregate and subgrade soil.
- (2) Provision of a filter medium to facilitate drainage.
- (3) Confinement and reinforcement of the aggregate layer.
- (4) Alteration of the failure mechanism in the subgrade soil.

The separation mechanism prevents the aggregate and subgrade soil from intermixing, which would tend to reduce the effective depth and load distributing capability of the aggregate layer. Additionally, the aggregate voids may become clogged by subgrade soil particles, preventing free drainage of water, thereby reducing system stability and strength through a buildup of pore pressure. The fabric induces the formation of a natural filter in the subgrade soil. This process, termed bridging, is initiated with the migration of some soil particles through the fabric as a result of fluid flow. These soil particles, originally adjacent to the subgrade face of the fabric, leave voids which are filled or bridged over by other particles. Further migration and reorientation create an inverted filter and filter cake that become stable under the bridging action of the particles. Reversing flow conditions may destroy this bridging effect.

It has been shown (64) that thick non-woven fabrics generally provide the best performance, in single layer placements, under conditions of severe flow reversal. Creation of the subgrade filter depends upon the size and number of migrating particles and the hydraulic gradient of the flow. The latter may be influenced by the in-situ stress state of the fabric, where tensile and compressive stresses can alter the pore size distribution in the fabric. Maintaining the integrity of the fabric is critical to successful separation. Repeated dynamic

loading tends to cause the angular aggregate particles to puncture the fabric, creating openings through which intermixing may occur.

As previously described, the fabric induces the formation of an inverted natural filter in the subgrade soil. This maintains separation of the aggregate and subgrade soil, while permitting the free flow of water. Flow of water from the weak subgrade into the aggregate allows consolidation of the former material under loading, thereby stabilizing it and enhancing its strength.

Confinement and reinforcement of the aggregate layer apparently provide a tensile capacity along the bottom of that layer. Characteristically, granular materials have negligible tensile strength, thus when an aggregate-subgrade (AS) system is subjected to load, the load distributing effectiveness of the aggregate is limited by the shear stresses which develop at the system interface. A layer of fabric at this location can restrain interfacial aggregate movement from under the loaded area, thereby increasing the interfacial shear strength and corresponding load distributing effectiveness of the aggregate layer.

The presence of fabric tends to create a more even distribution of the load induced stresses, resulting in less abrupt deformation patterns. When the subgrade fails under applied loading, slip plane failure surfaces theoretically form. When fabric is placed along the aggregate-subgrade interface, tensile forces in the fabric and frictional/adhesive resistance along the fabric-subgrade interface tend to limit the plastic flow of the soil mass contained within these slip planes. The tensile forces in the fabric, in conjunction with curvature along the interface in a deformed system, induce a normal stress perpendicular to the plane

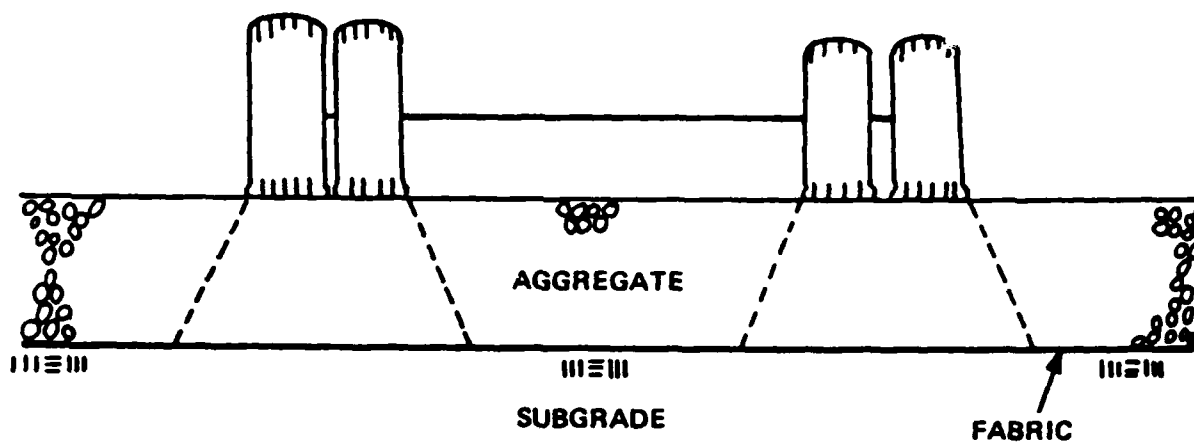
of the fabric. The magnitude of this stress depends upon the tensile stress developed in the membrane and the radius of curvature along the interface. In the wheel path, the net effect is a reduction in the stress imposed on the subgrade. Outside the wheel path, where reverse curvature of the membrane occurs, a resultant downward pressure or "apparent surcharge" is created, combining with the frictional/adhesive resistance to restrain upheaval of the soil mass within the slip planes. These actions, depicted schematically in Figure 1-1, tend to increase the load bearing capacity of the system.

Concentrated loading due to aggregate layer weight and/or imposed vehicular loading can cause a punching or localized bearing capacity failure at the contact points between aggregate and subgrade. A geotextile at this interface serves to distribute the load, reducing localized stresses and providing greater resistance to such failures.

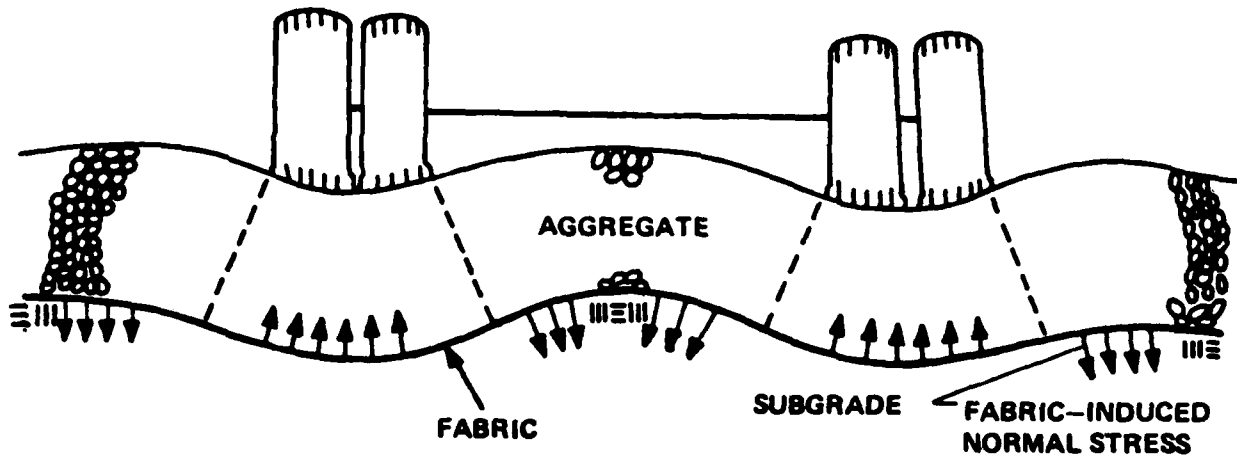
Statement of the Problem

Designs of AS and AFS pavement systems are currently accomplished by empirical based methods. The methods for AFS systems have generally been developed for use with specific fabrics, without fully predicting system response. Field verification of design adequacy is still required of all methodologies.

Prediction of rutting for conventional pavement systems may be accomplished by application of a hyperbolic plastic stress-strain law to the stress state within the system (9, 10, 70). Parameters for use of the hyperbolic curve fitting technique are obtained from laboratory triaxial testing, both static and dynamic, of material from each layer in the system. Non-linear soil properties and the inability of granular



(a) INITIAL STATE AFTER CONSTRUCTION



(b) STATE AFTER SUBSTANTIAL HEAVY TRAFFIC

Figure 1-1. Schematic of Aggregate-Fabric-Subgrade System (81).

materials to carry tensile forces may be modeled. Determination of the correct stress state remains a problem, especially for those systems experiencing large deformations. Inclusion of fabric in the system creates further problems in predicting the true stress state. The effects of a fabric inclusion vary with the deformation state (i.e., fabric elongation and contour, and interfacial slippage) within the system (56). The influences of specific fabric properties create additional uncertainties in the analysis.

The pressure of fabric is believed (14, 17, 81, 100) to impart a tensile capacity to the crushed stone layer in AFS systems and thereby alter the subgrade failure mechanism. If the degree of such capability can be ascertained for a particular fabric, the correct AFS system stress state might be approximated and the hyperbolic plastic stress-strain law applied to predict rutting. Empirical determination of the degree of such capability might be possible, by comparison of theoretically computed deformations and the deformations observed during a series of model tests. Such model tests would also provide an indication of the adequacy of the existing design techniques, perhaps permitting refinement of those methodologies or development of a single methodology suitable for use with a variety of fabrics and capable of fully predicting system response.

Objectives of Study

The general objective of this study is to examine the performance characteristics of AS and AFS systems subjected to repeated (i.e., transient) loading. Specific objectives of this study are as follows:

- (1) Evaluate the influence of subgrade strength on the perfor-

mance of AS and AFS systems.

(2) Evaluate the influence of aggregate layer thickness on the performance of AS and AFS systems.

(3) Evaluate the influence of load pulse duration on the performance of AS and AFS systems.

(4) Evaluate the influence of limited range of membrane types on the performance of AFS systems.

(5) Experimentally determine the states of stress and strain within the aggregate and subgrade materials of AS and AFS systems, at various stages of testing.

(6) Experimentally determine the in-plane deformations/strains of the geotextile membrane in AFS systems at the completion of testing.

(7) Analyze, refine, or develop methodologies for the analysis and prediction of the rutting response of AS and AFS systems.

Research Approach

The research approach for achieving the objectives of this study is as follows:

(1) Phase 1 - Conduct literature review.

(2) Phase 2 - Formulate model test program.

(3) Phase 3 - Conduct model test program.

(4) Phase 4 - Reduce data obtained during model test program.

(5) Phase 5 - Analyze influences of model test program variables on system responses.

(6) Phase 6 - Compare computed deformations with those observed in the model test program to analyze, refine, or develop methodologies for the analysis and prediction of rutting response in AS and AFS systems.

CHAPTER II

REVIEW OF THE LITERATURE

Fabric Types

Woven and non-woven fabrics, available for application in sub-grade stabilization, have been thoroughly discussed in the literature (16, 19, 57, 100). These materials may be constructed in various ways and consist of one or more synthetics, generally nylon, polyester, polypropylene, polyethylene and vinyl. The filament properties within any synthetic group can vary widely, but generally nylon and polyester have significantly higher strength properties than the other groups. All are combustible and, unless chemically stabilized, have a low resistance to exposure to ultraviolet light. Ultraviolet light can cause serious deterioration to occur in polypropylene, the most susceptible polymer, within four to eight weeks. Water absorption is minimal. All groups are considered to have high resistance to the pH levels likely to be encountered in soil.

Woven fabrics are made from either extruded filaments or split-film tapes. Monofilament fabrics are composed of strands of single polymer filaments. Multifilament fabrics are woven from yarns composed of many fine filaments. Extruded filaments are generally circular in cross-section and stronger and more expensive to produce than split-film tapes, which are flat in cross-section. Due to the parallel filament arrangement, woven fabrics are characterized by high strength and low breaking strain. Woven fabrics are usually anisotropic, being stiffer

along the warp direction (i.e., parallel to the long axis of the fabric) and more flexible along the bias (i.e., at a 45° angle from the warp). In the unstressed fabric, the individual fibers are straight in the warp and fill (i.e., parallel to the short axis of the fabric) directions, but curved in the plane of the fabric as they are woven over and under each other. When one set of fibers is stressed, it becomes straight in the plane of the fabric, while displacing the unstressed cross-fibers. This results in an apparent length increase with little applied stress. Additional straining requires an actual stressing of the fibers, with the stress-strain relationship of the fibers controlling the corresponding behavior of the fabric. The mechanical properties of a woven fabric may, therefore, be related to the mechanical properties of the polymer composing the fibers.

There are three major types of non-woven fabrics, distinguished from each other by their methods of construction, which give them differing physical properties. These fabric types are needle-punched, heat-bonded, and resin-bonded. The fabrics may be formed from either staple or continuous filaments. The staple filament fabrics are formed by arranging short fiber pieces on a supporting screen or belt in preparation for bonding. Continuous filament fabrics are formed by extruding the polymer from dies at high temperature. The filament is then cold drawn to form a thin continuous thread, which is arranged on a belt in preparation for bonding. Staple filaments are formed by chopping such a thread into pieces of the desired length. Filament arrangement is generally accomplished by means of air jets, although slurry placement is possible with staple filaments.

The needle-punched fabrics consist of filaments mechanically interlocked by a barbed needle-punching operation, carried out normal to the plane of the fabric, which physically entangles the filaments and produces a three-dimensional mat material. These fabrics are thick, compressible, and have very complex pore structures.

Heat-bonded fabrics consist of filaments calendered or rolled under heat and pressure to fuse the filaments at their crossover points. This process produces tough, compact fabrics and due to the more numerous fiber-to-fiber bondings, the process can achieve comparable strengths at lower weights than the needle-punching process. The pore structure is relatively discrete and simple. There are two types of heat-bonded fabrics. These are homofilament and heterofilament fabrics. The former utilizes single polymer filaments (homofilaments), with different filaments having varied melting point characteristics. The latter type utilizes both single polymer filaments and filaments of the same polymer sheathed in a second polymer, having a differing melting point (heterofilaments). Bonding is achieved by controlling temperature and pressure so as to fuse the lower melting point polymer.

The final type of non-woven fabric is resin bonded. These materials are characterized by spraying or impregnating acrylic resin into a fibrous web. The resin bonds the filaments, producing a fabric of intermediate weight.

In addition to woven and non-woven fabrics, knitted, special and combination fabrics are commercially available. These latter categories have yet to receive the extensive degree of utilization, in Civil Engineering applications, achieved by the former types. Knits are

composed of loops of fibers connected by straight segments. Knitted fabrics may be monofilament or multifilament and may stretch in one or both directions (double knits) without significantly stressing the fibers. Combination fabrics are produced by utilizing more than one of the various construction and bonding techniques previously discussed. Special fabrics are those which do not fit into any of the other categories, such as extruded plastic mesh.

Fabric Properties

In recent years, accompanying the increased usage of fabrics in Civil Engineering applications, many tests have been developed to assess the quality of the fabrics. Test methods are well documented in the literature (1, 5, 6, 16, 19, 57, 75, 92, 100, 112, 114). Several of the more commonly cited fabric characterizations are summarized in the following:

(1) Thickness (ASTM D-1777) is expressed in units of mils and generally reflects the construction process. Split-film tape woven fabrics and heat-bonded non-woven fabrics are typically 15 to 30 mils thick, while needle-punched fabrics range from 75 to 250 mils in thickness.

(2) Weight (ASTM D-1910) is expressed in units of oz/yd^2 . Heat-bonded fabrics generally weigh the least (i.e., $4\text{--}5 \text{ oz/yd}^2$) and needle-punched fabrics are the heaviest (i.e., $4\text{--}20 \text{ oz/yd}^2$).

(3) The specific gravity (ASTM D-792) of fabrics is controlled exclusively by the specific gravity of the polymers. Values range from 0.9 to 1.25, with nylon and polyester having specific gravities greater than one, and polypropylene and polyethylene below one.

(4) Equivalent Opening Size (U.S. Army Corps of Engineers CW-02215), or EOS, is expressed in terms of the U.S. standard sieve size (ASTM D-422). The EOS refers to the diameter of the uniformly sized glass beads, of designated EOS number, for which 95 percent by weight of the beads are retained on the fabric after vigorous shaking, carried out in accordance with a standardized test procedure. The EOS of non-woven fabrics is more variable and more subject to change under load than for woven fabrics. The EOS is a "retained on" measure and typically ranges between 30 and 200. This property is important to the separation mechanism in AFS systems. For filtration of soils with greater than 50 percent passing a No. 200 sieve, it has been recommended (57, 100) that the EOS have a value in the range of 60-100. In those cases with less than 50 percent passing a No. 200 sieve, the EOS, expressed in length units, should be no greater than the D_{85} (i.e., largest particle diameter of the finest 85 percent of the filtered soil) for well-graded material, and no greater than the D_{60} (i.e., largest particle diameter of the finest 60 percent of the filtered soil) for uniformly graded material.

(5) Grab tensile strength (ASTM D-1682) is expressed in pounds, as is strip tensile strength (ASTM D-1682). These tests report peak load. Additionally, stress-strain data may be collected during these tests and modulus and elongation at rupture values reported. The latter test calls for gripping the full sample width during testing, while in the former test, only a portion of the specimen is gripped.

(6) Burst strength (ASTM D-751) is the peak hydrostatic force, expressed in psi, required to rupture the fabric while it is clamped

in a standard test ring. This test involves a localized form of tensile failure. Higher strength polymers offer greater bursting resistance. As the stresses are applied in all directions, isotropic materials offer very high bursting resistance.

(7) Impact strength (ASTM D-1424), or dynamic tear strength, is expressed in pounds and is the resistance against the propagation or enlargement of a hole or rip in the fabric after initial tearing or breaking of the fibers. The tear resistance is related to anisotropy in the fabric and bonding.

(8) Water permeability is expressed in cm/sec. It is not presently measured by a formally adopted testing method, but rather through a variety of procedures developed primarily by individual fabric manufacturers. Both constant head and variable head testing procedures are utilized, generally following standard soil testing practices. Values are typically greater than 10^{-2} cm/sec (i.e., corresponding to a clean, medium-to-fine sand). For woven fabrics, permeability decreases as the tightness of the weave is increased. For non-woven fabrics, needle-punched fabrics tend to have the highest permeabilities and resin-bonded fabrics the lowest.

While the above properties are readily available for most fabrics, their importance in relation to the behavior of AFS systems remains uncertain. EOS is an important characteristic for the drainage and separation mechanisms. Burst strength testing may provide an indication of the imposed deformation a fabric may withstand prior to rupture, by the height of the dome created prior to failure (92). Dynamic tear strength provides an indication of the damage a fabric would experience

once a tear has been initiated by, for instance, a sharp stone (92). Such failures will adversely influence all behavior mechanisms of the AFS system. Properties determined from uniaxial tensile tests may be quite inappropriate when used to predict the response of the fabric under a bi-axial stress state, as experienced in AFS systems. The plane strain, CBR, and OSU ring testing methods may provide more realistic tensile strength and elastic properties data for the study of sub-grade stabilization. Several additional properties are believed (17) to be important in relation to system behavior, including the creep, stress relaxation, and fatigue characteristics of the fabric and the frictional interaction of the fabric and soils. The availability of suitable data remains limited at this time.

Creep is the continual straining of a fabric while maintained under constant stress and is strongly stress dependent. Stress relaxation is related to creep and is the stress reduction experienced when a material is maintained at a constant strain level. The reinforcement and restraint mechanisms may be influenced by the creep and stress relaxation properties of the fabric under cycled stress and strain levels.

The fatigue resistance of the fabric refers to a loss in strength due to the application of a repetitive load of lower magnitude than the normal failure load in the same mode of loading. Available information (16, 56) is for non-woven fabrics, with needle-punched fabrics having a higher resistance than the bonded fabrics. The maximum allowable strip tensile load for an infinite number of load applications appears to range from 30 to 60 percent of the single load strength. Fatigue resis-

tance is pertinent to understanding the reinforcement and restraint mechanisms.

The reinforcement and restraint mechanisms greatly depend upon the friction/adhesion developed at the fabric-soil interfaces. Fabric construction, soil type, and normal stress are controlling factors. High frictional/adhesive resistance enhances the AFS system behavior, while low resistance may result in loss of anchorage and sliding of the fabric toward the rut center under loading. In the latter case, the development of fabric tension is retarded, further minimizing the beneficial effects of the fabric.

Design Methodologies

Several attempts have been made to develop design procedures for fabric application in subgrade stabilization. Generally, the methods have been proposed for use with a particular fabric, often with little or no field confirmation of results. At the present time, a general theory does not exist, which will allow calculation of the effects of specific fabric properties on the performance of AFS pavement systems.

Barenberg, et al. (14, 17) conducted both two and three-dimensional model tests of AS and AFS systems, utilizing single layers of either Mirafi 140 or Mirafi 280, or double layers of Mirafi 140 fabric. The aggregate used during testing was an open graded crushed limestone, while the tested subgrade soils were a silty clay and a silt of low strengths (i.e., CBR less than one). The aggregate gradation was outside the range generally recommended for use on fabric stabilized subgrades (30, 31). Subgrade strength was measured by cone penetrometer

and vane shear testing. Both static and dynamic loading tests were conducted, with the latter utilizing a one second load duration, applied at a frequency of six cycles per minute. The loading magnitudes in the three-dimensional tests were such that the vertical stresses transmitted to the subgrade surface, through the granular layer, were generally less than 10 psi, a level much lower than might be anticipated in the field. Conclusions drawn from the tests (14, 17) included the following:

(1) Fabrics are effective in preventing intrusion of the subgrade soil into the aggregate layer.

(2) Inclusion of fabric tends to stabilize the entire system and prevent the uncontrolled permanent rutting which was apparent in the heavily loaded AS systems. Thus, the fabric can provide an effective safety factor against complete failure of underdesigned or occasionally overloaded AFS systems.

(3) Use of fabrics generally reduces the amount of aggregate required in road construction by approximately one-third and reduces the subsequent maintenance needed to compensate for rutting.

(4) Fabrics have a significant effect on the performance and behavior of low type, unsurfaced pavement systems, resulting in a lower rate of permanent deformation development under repeated loading or allowing a higher stress to be transmitted to the subgrade soil without significantly increasing permanent rutting, as compared to AS systems with identical soil layer properties.

(5) Design of AS and AFS systems may be accomplished by a quasi-rational approach to system performance, taking subgrade strength, load configuration, and load magnitude into account.

(6) Fabric properties may have a significant effect on system behavior, thus, AFS systems utilizing different fabrics must be individually evaluated when developing design procedures.

A design procedure for AS and AFS systems reinforced with Mirafi 140 non-woven fabric was proposed (14, 17, 29, 30, 100) utilizing the model test results, Boussinesq stress distribution theory (20, 35, 65, 77, 122), and an AS system design model proposed by Rodin (82). Boussinesq theory is the best known of the stress distribution theories utilized in geotechnical engineering. While intended for single layer homogeneous, isotropic, linear elastic systems, the theory has been shown (46, 67, 113) to yield reasonable results for the subgrade vertical stress distribution caused by loads applied through a granular layer. The presence of fabric tensile reinforcement and plastic deformations in the system are limiting factors, although this is also true of other available stress distribution models, such as Westergaard theory (119), elastic layered system theory (26), shear layer theory (12), the transformed section concept (14), and most finite element models. Rodin proposed that the limiting stress on the subgrade soil in an AS system, for an allowable rut depth of two inches, could be expressed as:

$$q = 5c \quad (2-1)$$

where q = limiting vertical stress in subgrade soil, due to surface loading, computed by Boussinesq theory, psi

c = subgrade soil shear strength expressed as cohesion, psi.

The value falls between the limits of the bearing capacity of a soil in undrained conditions (i.e., $\phi = 0$) for the cases of general and local

shear failures (i.e., 6.2c and 3.8c respectively). On the basis of the model testing program, it was proposed that for AS systems, the limiting subgrade stress be taken as 3.3c. This value is very near to the value of πc proposed by Rodin as the stress level at which localized plastic strains are initiated, and somewhat below the theoretical stress level of 3.8c required to cause a local bearing capacity failure in the subgrade. For AFS systems, utilizing Mirafi 140 non-woven fabric, a limiting subgrade stress level of 6.0c was recommended by Barenberg (14, 17). This is greater than the value of 5.0c proposed by Rodin for unreinforced systems, and slightly lower than the theoretical stress level of 6.2c required to cause a general bearing capacity failure of the subgrade. Design curves were developed for both AS and AFS systems, based upon in-situ subgrade soil strength (i.e., vane shear or cone penetrometer determinations), total wheel load, and tire contact pressure. A typical design chart is provided in Figure 2-1. An increase of 10 percent in the thickness of the aggregate layer is recommended (14) when more than 10^4 load applications are expected, or when poorly graded aggregates with rounded particles are utilized. It is believed (100) that use of these limiting stress values will result in a rut depth of approximately four inches within 10^2 load cycles. It has been recommended (100) that design values of 2.8c and 5.0c be utilized for AS and AFS systems respectively, to limit rutting to two inches after 10^3 load repetitions. No published data relative to field confirmation of the design method are available. The design method does not predict system response (i.e., the load cycle-rut depth relationship) and the method is proposed for use only with Mirafi 140 fabric.

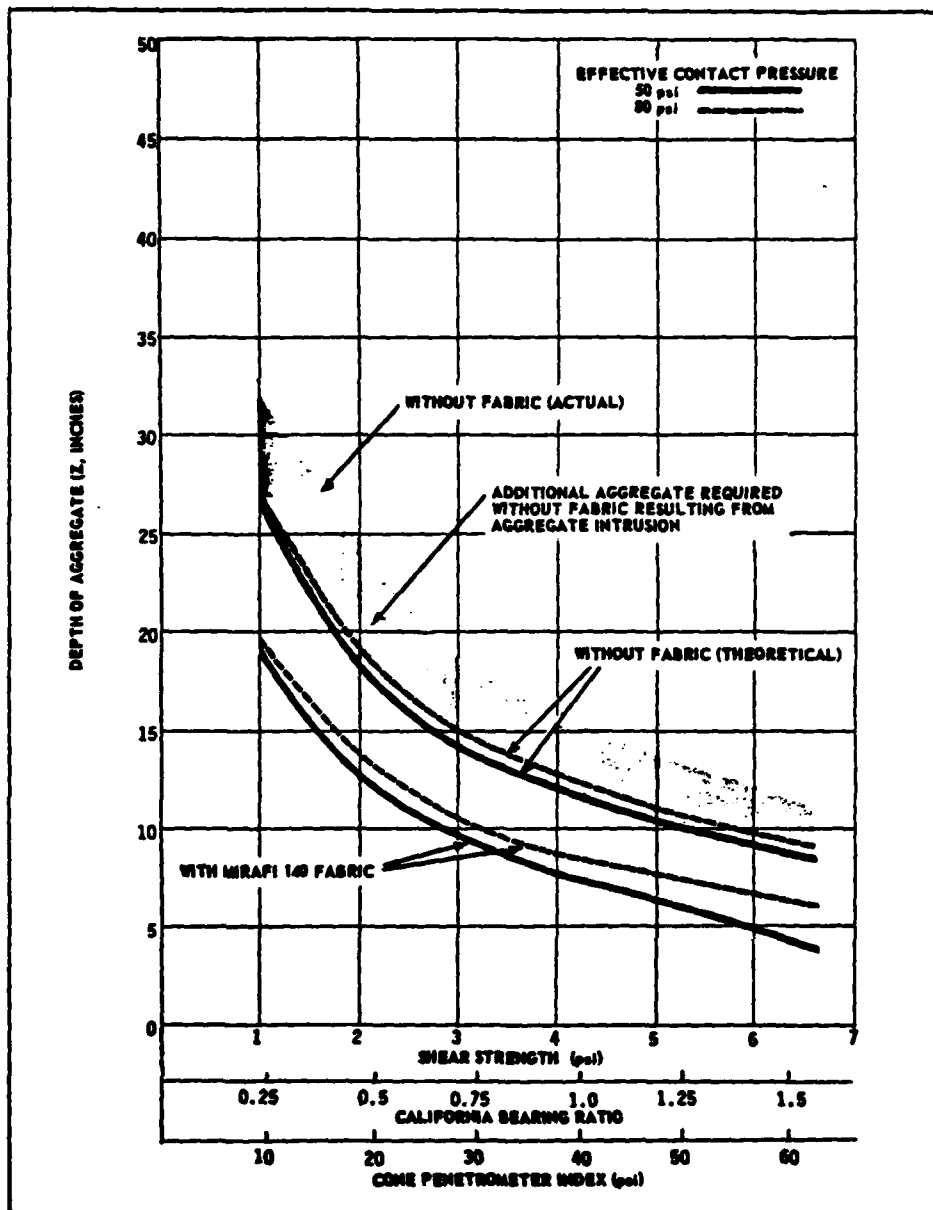


Figure 2-1. Typical Design Curves for AS and AFS Systems Based Upon Limiting Subgrade Stress Method - 5 kip Wheel Load (14, 17).

Celanese (31) has also presented design curves for AS systems and AFS systems reinforced with Mirafi 500X fabric. A typical design chart is presented in Figure 2-2. The basis of the design is not described, although it appears that the charts are based upon the limiting subgrade stress method, utilizing the stress ratio (i.e., vertical stress on load centerline at subgrade soil surface computed from Boussinesq theory, divided by subgrade soil vane shear strength) limits proposed by Barenberg (14, 17). As with the charts developed for Mirafi 140 fabric, system response is not predicted and field confirmation of results is lacking.

Kinney (56) recently proposed a means of predicting the reduction in the total vertical load transmitted to the subgrade soil, resulting from the presence of fabric at the aggregate-subgrade soil interface. This method is based upon two-dimensional model tests (i.e., plane strain), with the load reduction being a function of the deformed shape of the aggregate-subgrade soil interface, the tension in the fabric, the strain energy stored in the fabric, and the interfacial shear stresses. Utilizing the reduced load, as computed from this model, the system may be designed to limit the vertical stress on the subgrade soil surface to any desired level, such as 3.3c. This approach is a refinement to the limiting subgrade stress method, although system response is again not fully predicted and field confirmation of results is required.

Monsanto (71) has presented design curves for AS systems and AFS systems reinforced with Bidim fabrics. A typical design chart is presented in Figure 2-3. The curves are based upon research conducted by Law Engineering, Marietta, Georgia. Details of the testing program are

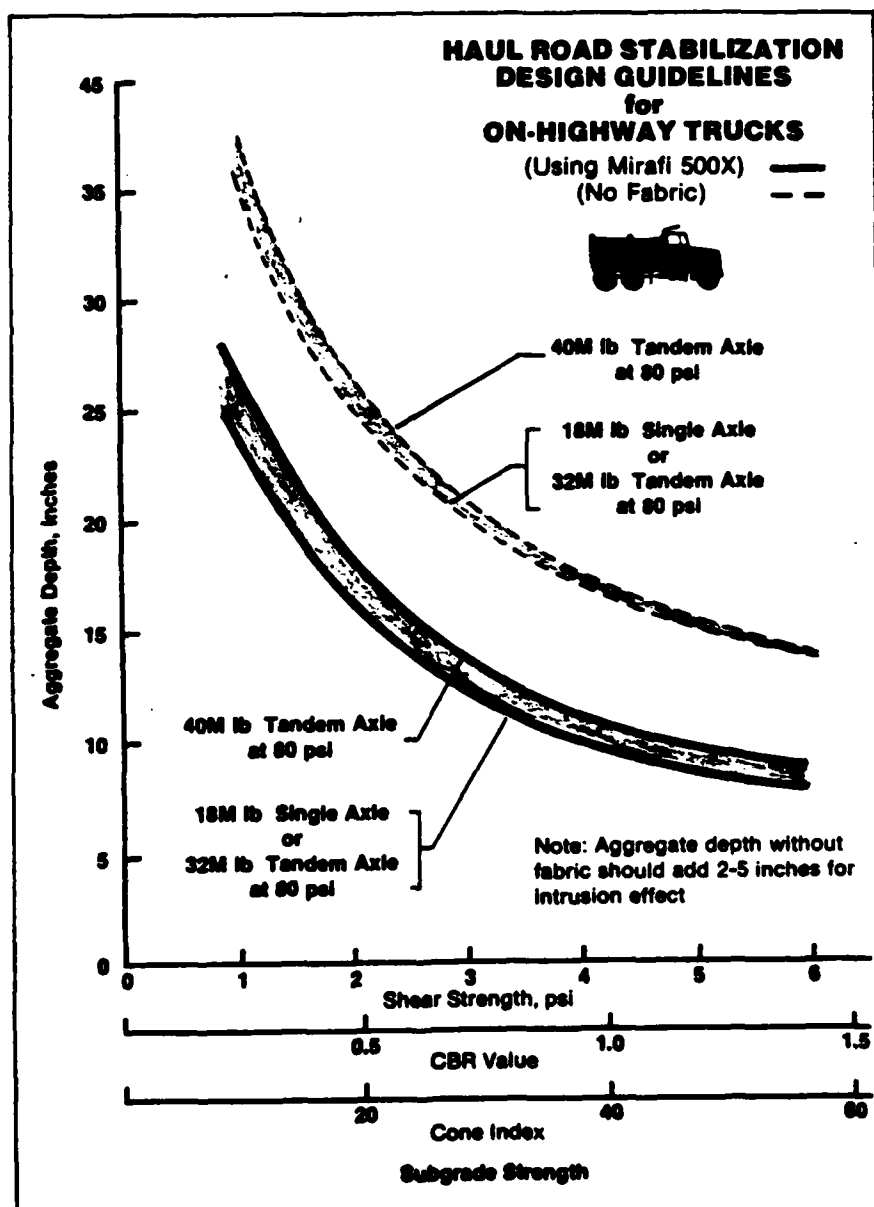


Figure 2-2. Typical Design Curves for AS and AFS Systems Based Upon Research by Celanese Fibers Marketing Company (31).

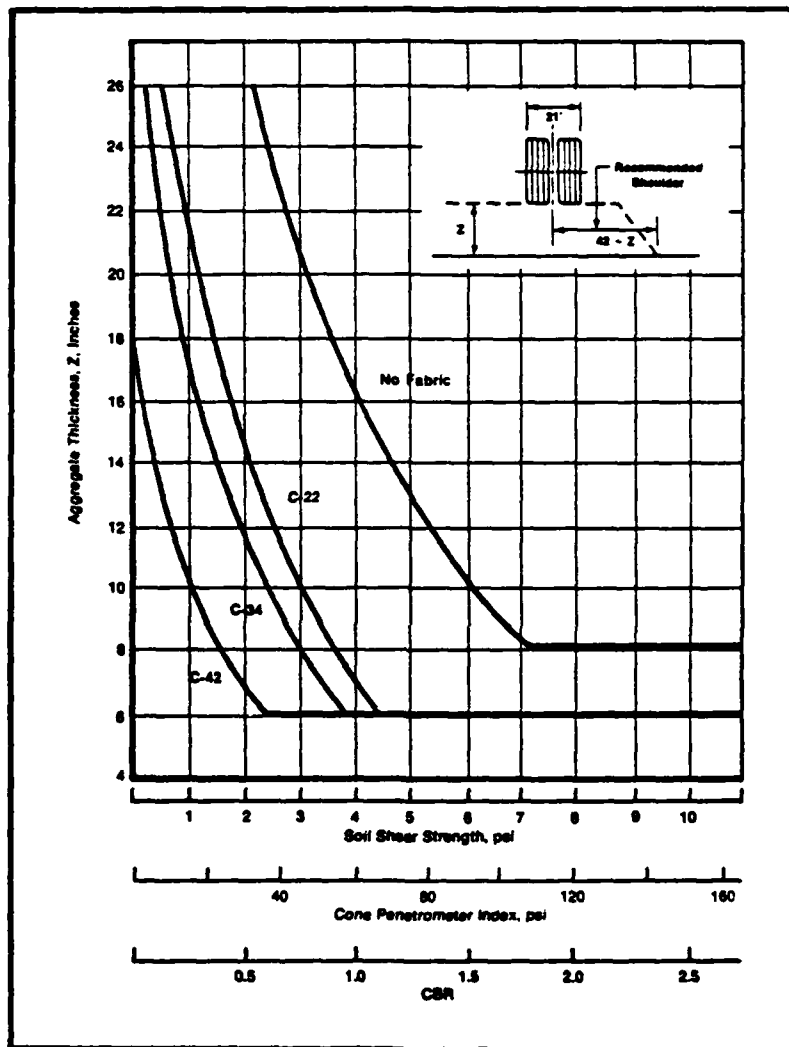


Figure 2-3. Typical Design Curves for AS and AFS Systems Based Upon Research by Law Engineering - 20 kip Axle Load and 10.00-20 Tires on Dual Wheels (71).

not provided, although the manufacturer's literature indicates that full-scale repeated load tests were conducted, utilizing a very weak subgrade. For the curves shown in Figure 2-3, assuming a 90 psi contact pressure, the maximum subgrade stress for the AS system, as computed by Boussinesq theory, is approximately four times the subgrade shear strength, while for the AFS system reinforced with Bidim C22 fabric, this ratio approaches nine. Higher ratios are permitted for AFS systems reinforced with heavier fabric weights, but having identical subgrade strengths. Higher ratios are also indicated for AFS systems reinforced with a given fabric weight as subgrade strength decreases.

According to Steward, et al. (100), a high degree of deformation within a few load cycles (i.e., greater than four inches of rutting within 10^2 load repetitions) might be anticipated for systems utilizing these stress ratios. The analysis procedures used in developing the charts are not revealed. Thus, it remains unclear as to why higher stress ratios are permitted by this method, especially for AFS systems, than by previously discussed design methodologies. Field confirmation of design results have not been published and system response is not predicted.

The U.S. Army Corps of Engineers (44, 45, 103) proposed a design method for flexible pavement systems, based upon analysis of full-scale pavement sections, which were tested under a range of subgrade strengths, tire pressures, wheel loads and service lives. The original design procedure was based upon limiting the shear stresses in the underlying material. The design thickness of a flexible layer may be expressed by the following equation:

$$t = F \left(P \left(\frac{1}{8.1 \text{ CBR}} - \frac{1}{p\pi} \right) \right)^{0.5} \quad (2-2)$$

where t = required layer thickness, inches

$$F = 0.231 \log N + 0.144$$

N = number of load repetitions during design period

P = total wheel load, pounds

CBR = California Bearing Ratio of underlying layer of material

p = tire contact pressure, psi.

The design procedure was developed for conventional flexible pavement systems (i.e., asphalt cement concrete surface plus aggregate base course), with surface deflection limitations incorporated during and subsequent to the original formulation, which may be somewhat unrealistic for haul roads or construction sites. For unsurfaced pavement systems, based upon failure criteria of a rut depth of three inches or an elastic deformation of 1.5 inches, Hammitt (44) proposed that the F factor in Equation (2-2) be modified to:

$$F' = 0.176 \log N + 0.120. \quad (2-3)$$

Equation (2-3) and the data from which it was developed are depicted in Figure 2-4.

For AFS systems reinforced with Typar 3401 fabric, it has been proposed (109) that the required aggregate thickness be computed using Equation (2-2), but using a CBR value increased four units to account for the presence of the fabric. The recommended value for the fabric induced CBR increase was determined (109) from laboratory investigations using CBR equipment, full-scale test roads, and experience, although the

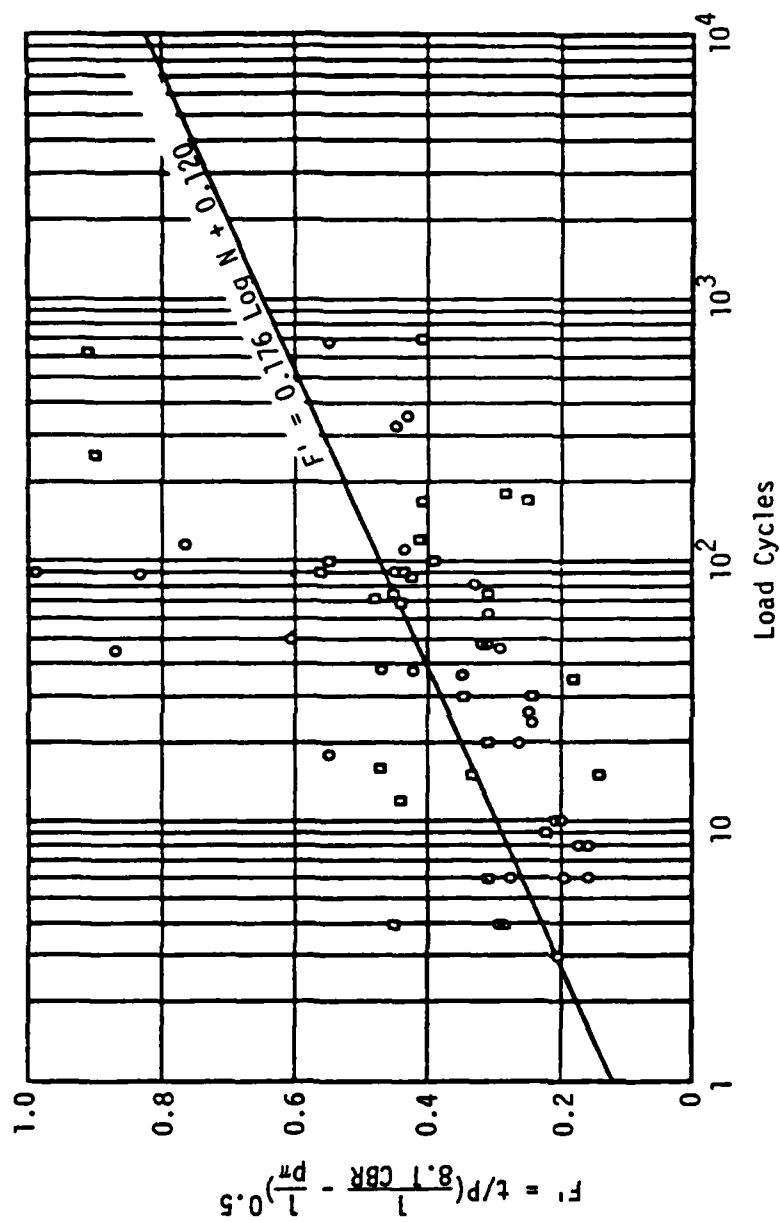


Figure 2-4. Rutting Response Predicted by Hammett Modification to U.S. Army Corps of Engineers Equation (44).

exact laboratory test procedure and test road results have not been revealed. One possible laboratory approach would be to test two identical soil samples, with one specimen having a piece of fabric placed between the soil and the CBR test head, then comparing the resulting CBR values. The validity of using such a technique to model system behavior in the field would appear highly questionable. The CBR method enables design accomplishment for an anticipated number of load repetitions, removing some of the uncertainty involved in the previously discussed procedures. A typical design chart is provided in Figure 2-5. The modified CBR equation proposed by DuPont applies only to Typar 3401 fabric, does not predict system response, and requires field verification of results.

Use of any of the manufacturer published design charts generally indicates a reduction of one-third to one-half in the required aggregate thickness when fabric is utilized at the interface of the soil layers. A comparison between various designs would be valid only if the loadings and load cycle-rut depth criteria used to develop the charts were identical and these generally are not. The design loadings vary and the load cycle-rut depth criteria are not provided by the manufacturers.

Giroud and Noiray (41) have recently proposed a general design methodology, based upon a combination of previously cited works (14, 44, 45, 56, 117, 118). The method is derived for axle loads carried by dual tires and recommended for use only when the number of load repetitions does not exceed 10^4 . Design of AS systems is accomplished utilizing the following equation:

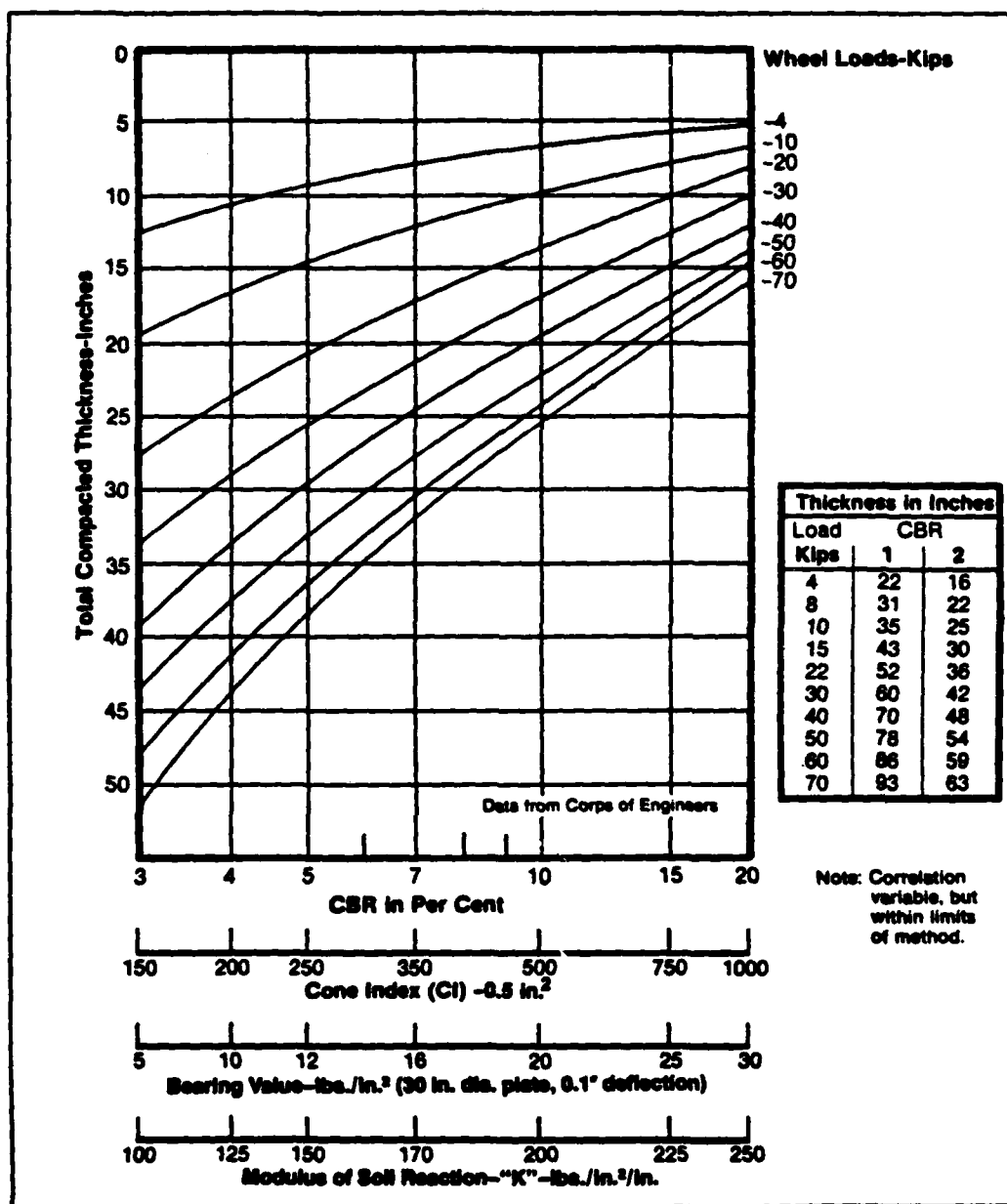


Figure 2-5. Typical Design Curves for AS and AFS Systems Based Upon CBR Method - 5000 Load Repetitions and 100 psi Contact Pressure (109).

$$h = \frac{17.92 \log N + 70.78 \log P}{c_u^{0.63}} = 1.06 r - 297.40 \quad (2-4)$$

where h = aggregate layer thickness, inches

N = load cycles

P = single axle load, pounds

r = rut depth, inches

c_u = subgrade soil undrained shear strength, psi.

Equation (2-4) was derived by first establishing an equation in agreement with a plot of experimental data presented by Webster and Alford (118), which related load cycles, subgrade soil CBR, and aggregate layer thickness, for a single axle load of 18 kips and a rut depth of three inches. This equation was modified to account for repetitions of single axle loads other than 18 kips, by use of procedures generally accepted for analyzing traffic on paved roads (122). On the basis of data presented by Webster and Watkins (117), the equation was then empirically extended for use at rut depths other than three inches, and c_u substituted for CBR (i.e., $c_u = 4.35 \text{ CBR}$), thus achieving the presented form of the expression.

Once a rut depth is established, a system may be designed (i.e., required aggregate layer thickness determined) to achieve a given number of load cycles, or an established system may be analyzed for the allowable number of load cycles. To design for AFS systems, two bi-dimensional static bearing capacity analyses of the subgrade are conducted. The load applied to the surface of the system, by dual tires, is assumed to act over a rectangular area (i.e., 2.83 times the contact area of a single tire) and is considered to be dissipated in the system

by a truncated pyramidal pressure distribution, until reaching the surface of the subgrade. The width of the rectangular area equals 0.5 (i.e., off-highway trucks) or 0.71 (i.e., on-highway trucks) times its length. Each side of the truncated pyramidal pressure distribution is considered to make an acute angle of 59° with the horizontal. Without fabric, the allowable bearing capacity of the subgrade is taken as equal to πc , in solving for the required thickness of aggregate utilizing the expression:

$$\pi c = \frac{P}{2(B + 2h_0 \tan \theta)(L + 2h_0 \tan \theta)} \quad (2-5)$$

where c = subgrade soil undrained shear strength, psi

P = single axle load, pounds

B = width of rectangular load contact area, inches

L = length of rectangular load contact area, inches

h_0 = aggregate layer thickness, inches

$\theta = 31^\circ$.

With a fabric inclusion, it is assumed that the allowable bearing capacity of the subgrade increases to $(\pi + 2)c$, while the vertical pressure reaching the subgrade surface decreases due to the influence of the vertical component of the fabric tensile force. The resulting expression for the required thickness of the aggregate layer becomes:

$$(\pi + 2)c + \frac{K_e}{a \sqrt{1 + \left(\frac{a}{2s}\right)^2}} = \frac{P}{2(B + 2h \tan \theta)(L + 2h \tan \theta)} \quad (2-6)$$

where c = subgrade soil undrained shear strength, psi

K = fabric tensile secant modulus, lbs/in
 ϵ = fabric strain, in/in
 a = subgrade depression half-width, inches
 s = subgrade depression, inches
 P = single axle load, pounds
 B = width of rectangular load contact area, inches
 L = length of rectangular load contact area, inches
 h = aggregate layer thickness, inches
 $\theta = 31^\circ$.

The deformed shape of the aggregate-subgrade interface is assumed to consist of parabolic segments, with the segment characteristics (i.e., a , s , and ϵ) dependent upon the values of B , h , and r . Aggregate stability and aggregate-fabric friction are considered sufficient to limit aggregate deformations to negligible levels. Fabric strain is considered constant throughout the fabric length. Although not described as such by Giroud and Noiray, the solution of Equation (2-6) must be accomplished by iteration. A value of h is first assumed to establish values of a , s , and ϵ , then Equation (2-6) solved for h utilizing these values. The procedure is repeated until agreement between the h value used to establish a , s , and ϵ , and the computed value is obtained. The difference between the values of the aggregate layer thicknesses computed by Equations (2-5) and (2-6) (i.e., $\Delta h = h_0 - h$) represents the improvement produced by a fabric inclusion. The value of ϵ used to determine h must be less than the strain exhibited by the fabric at failure. While based upon static analyses, equal improvement is assumed for dynamic loadings. For design of AFS systems,

Equation (2-4) is solved for h , which is then reduced by Δh . For analysis of AFS systems, the actual aggregate layer thickness is increased by Δh and Equation (2-4) solved for the allowable number of load repetitions. The method may be utilized to fully predict system response, however field verification of results is required.

Rut Depth Prediction

Procedures are available for estimating the amount of rutting to be expected in a pavement system due to repeated traffic loading (7, 9, 10, 36, 39, 70, 80). The effect of a fabric inclusion on system rutting performance remains uncertain, due to the need to determine the stress state changes created by the fabric presence. As previously mentioned, theoretical solutions to this problem are limited at the present time. The procedures for rutting prediction may be divided into two categories. One utilizes an elastic stress-strain analysis in modeling the system, with materials characterized from either creep tests or repeated load triaxial tests. The second approach utilizes a viscoelastic layered system to represent the pavement structure, with materials characterized by creep tests. The former approach is better documented at this time.

Hyperbolic Plastic Stress-Strain Law

Kondner (58) was the first to propose that the stress-strain curve of a soil, under a constant confining pressure, could be approximated by a hyperbolic equation of the form:

$$\sigma_d = \frac{\epsilon_a}{a + b\epsilon_a} \quad (2-7)$$

where σ_d = deviator stress, psi

ϵ_a = axial strain, in/in

a, b = experimental constants.

The constant a is the reciprocal of the initial tangent modulus and the constant b is the reciprocal of the asymptotic stress level from a stress-strain plot (Figure 2-6). These constants may be readily evaluated by plotting the axial strain versus the reciprocal of the corresponding secant modulus for that strain level, as depicted in Figure 2-7. The values of a and b are obtained as the intercept and slope respectively of the best fit straight line. Duncan and Chang (38) extended this work to include a correction factor for the asymptotic nature of the hyperbolic curve, the relation between the initial tangent modulus and confining pressure, and the Mohr failure criterion. The resulting general hyperbolic expression may be written as:

$$\epsilon_a = \frac{\sigma_d / K \sigma_3^n}{1 - \frac{\sigma_d R_f (1 - \sin \phi)}{2(c \cos \phi + \sigma_3 \sin \phi)}} \quad (2-8)$$

where ϵ_a = axial strain, in/in

σ_d = deviator stress, psi

σ_3 = confining stress, psi

K, n = intercept ($\sigma_3 = 1$) and slope respectively, for best straight line from log-log plot of σ_3 versus initial tangent modulus

R_f = ratio of measured failure strength to ultimate hyperbolic strength

c = cohesion, psi

ϕ = angle of internal friction.

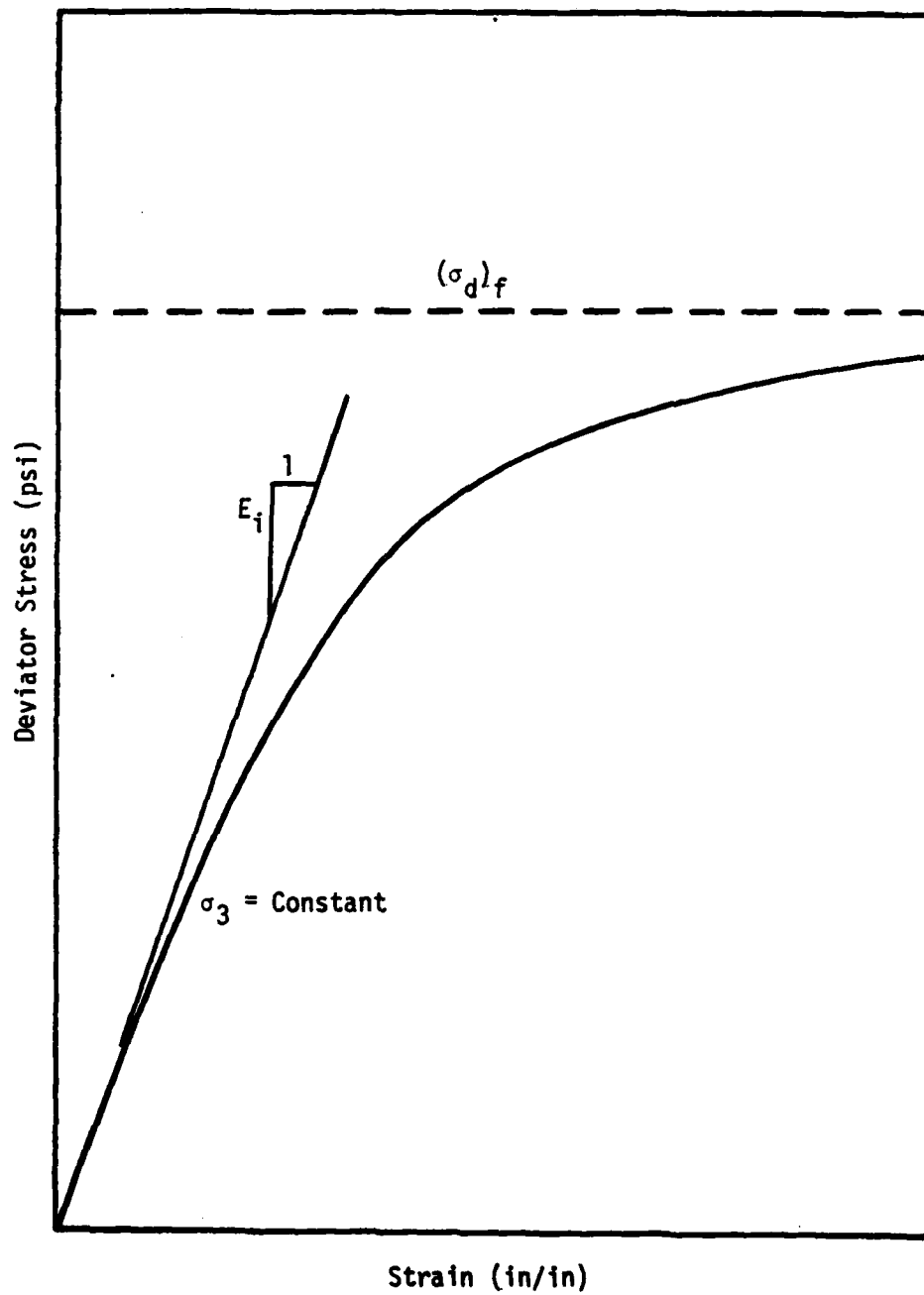


Figure 2-6. Typical Strain-Stress State Relationship for Soil.

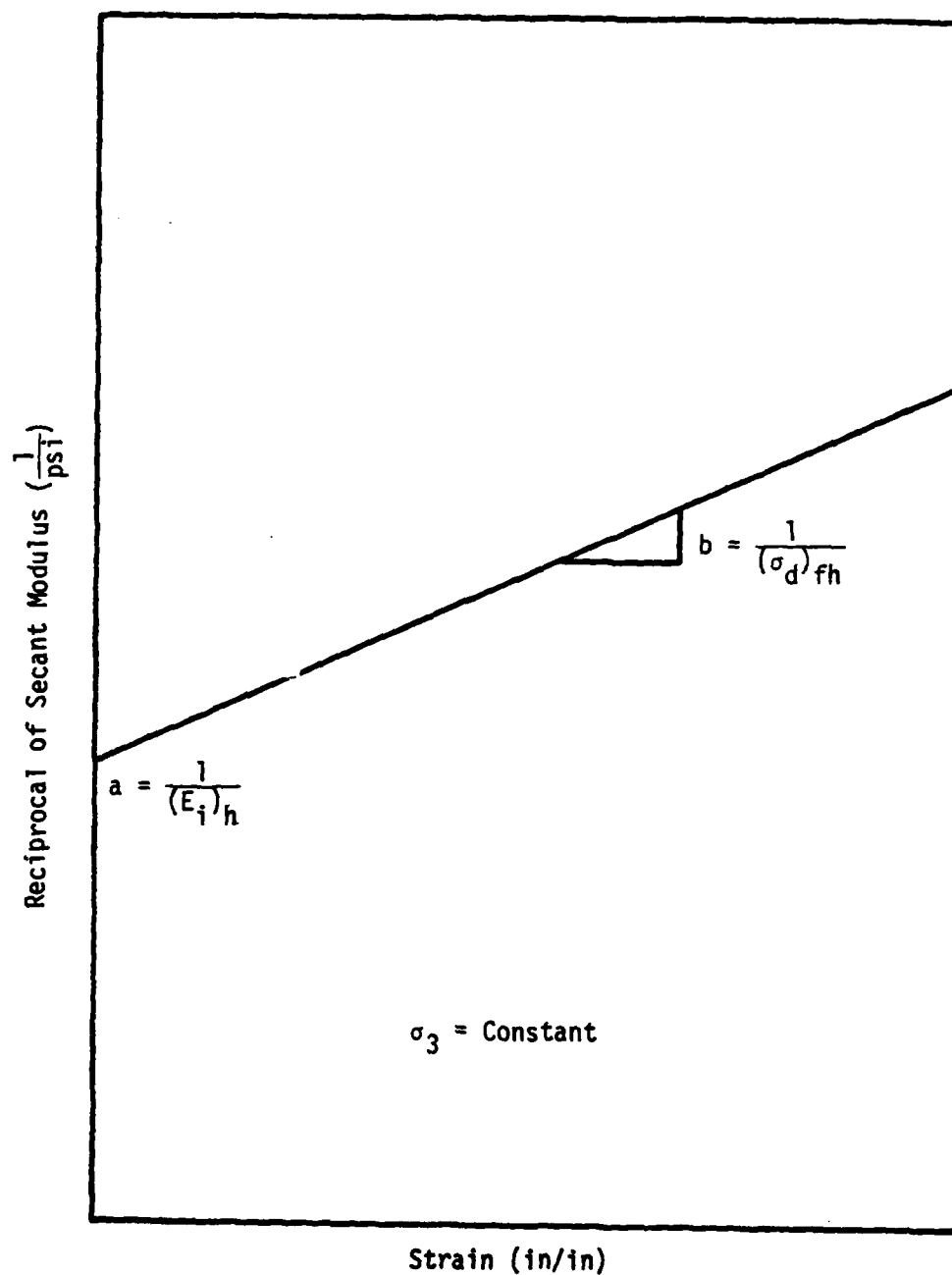


Figure 2-7. Typical Strain-Reciprocal of Secant Modulus Relationship for Soil.

The value of R_f will vary somewhat with confining pressure, with an average value typically utilized in constructing the theoretical hyperbolic curves. For a given material, analysis of two or three experimentally derived curves yields results which may then be extended to cover a wide range of stress states.

While originally developed for use with conventional static triaxial tests, the method can be adapted to the analysis of data from repeated load tests. Provided the stress state in the system can be properly modeled, the development of rutting with traffic applications may then be estimated.

The data for plastic strain and cyclic deviator stress are analyzed at various points during the loading histories of the triaxial specimens. Values of K , n , and R_f may be determined at a specific number of load cycles and Equation (2-8) then extended (10, 70) for use at any other number of load repetitions by including the following expression on the right-hand side of the equation:

$$\left(\frac{N}{N_0}\right)^m$$

where N = load cycles at which the axial plastic strains are being evaluated

N_0 = load cycles at which K , n , and R_f were determined

m = experimentally derived constant.

An alternate approach is to determine values of K , n , and R_f at each specific number of load repetitions for which the pavement system is to be analyzed, utilizing the appropriate values as Equation (2-8) is

applied to evaluate the load cycle-axial plastic strain relationships.

Rut Depth Analysis

To permit prediction of rutting, the data from repeated load triaxial tests is analyzed by the previously discussed procedures. The pavement system is next divided into several sublayers, sufficient in number to adequately define the variations in stress and strain with depth. The major principal stress, σ_1 , and the average confining pressure, σ_3 , are then determined at the center of each sublayer, utilizing an appropriate theoretical solution. The plastic strains for each sublayer may then be calculated by the hyperbolic stress-strain law, utilizing the appropriate parameters. The rut depth after a given number of load applications may be found by summing the plastic strains within the system. This last step may be represented as:

$$d = \sum_{i=1}^n \epsilon_{ai} h_i \quad (2-9)$$

where d = rut depth, inches

n = total number of sublayers

ϵ_{ai} = average plastic strain in i^{th} sublayer, in/in

h_i = thickness of i^{th} sublayer, inches.

Stress State Analysis

Classical solutions for the stress state within a pavement system are readily available. These include Boussinesq, Westergaard, and layered (linear and non-linear) theories. The VESYS G computer program (48, 59) provides a solution for an N-layered viscoelastic system. A constant modulus and a tensile capacity are assumed for each layer.

Barksdale (10, 11) has recommended that a non-linear analysis be utilized in predicting the system stress state. One computer solution which utilizes a simplified non-linear approach is the University of Illinois axisymmetric finite element program (110). This program permits use of a constant modulus value, or an appropriate stress dependent modulus model, for each material. For the subgrade material, the resilient modulus may be input as a function of the deviator stress. A failure modulus is specified for use in the event that the shear strength of the material is anywhere exceeded. The resilient modulus for a granular material may be input as a function of the bulk stress. Additionally, for granular materials, a failure modulus is specified for use in those cases exceeding a maximum ratio of σ_1/σ_3 (i.e., shear failure) and/or a minimum value of σ_3 (i.e., tensile failure). Solution is accomplished by an iterative procedure, until convergence of stress state and modulus criteria is achieved.

Although not available during the time period when the major portion of this research was conducted, two refinements, which offer improved solutions, have been recently described. Raad and Figueroa (78) present an axisymmetric finite element program in which stress dependent moduli values may be input for each material, as with the University of Illinois program. However, the new program does not assign arbitrary moduli values when established stress state criteria are not satisfied. In this approach, the computed stress state for each element is compared to the Mohr-Coulomb failure criteria for the material. Stress states are modified as necessary to comply with these criteria, then new moduli values computed for each element. The

iterative solution procedure is continued until convergence of stress state and Mohr-Coulomb failure criteria. While the University of Illinois program minimizes the tensile stresses in unbound granular materials, this method provides a better model by totally eliminating such stresses.

Zeevaert (123) has presented an axisymmetric finite element program which includes the moduli characterization capabilities of the previously discussed models and the iterative stress state solution developed by Raad and Figueroa (78). Additionally, this model incorporates fabric and interface elements, which permit modeling AFS systems, including slippage along the interface. Interface elements, capable of transmitting normal and shearing stresses, are placed along each side of the fabric elements. The fabric elements are two-dimensional and are capable of carrying tensile stresses in the radial and tangential directions, but possess no resistance to compression and bending. An option for evaluating large displacement problems is also available with this program.

Resilient Modulus Analysis

The resilient modulus of a material may be defined as the repeated axial deviator stress applied to repeated load test triaxial specimens, divided by the elastic or recoverable strain associated with the repeated load. The recoverable strain is the axial unit deformation which occurs when the repeated axial deviator stress on the sample is removed. For granular materials, it has been shown (10) that the resilient modulus is dependent upon the bulk stress. This relationship may be expressed as:

$$M_R = K\theta^{\bar{n}} \quad (2-10)$$

where M_R = resilient modulus, psi

θ = bulk stress, psi

K, n = intercept ($\theta = 1$ psi) and slope respectively, for best-fit straight line from a log-log plot of θ versus M_R .

The resilient modulus of fine-grained subgrade soils is a function of the deviator stress. The modulus normally decreases as the deviator stress increases. In some instances, at higher deviator stress values, the resilient modulus has been observed to become constant or actually increase very slightly. Depending upon the rate of change in the resilient modulus with variations of the deviator stress, the deviator stress-resilient modulus relationship may be linearized through use of either an arithmetic-log or a log-log plot of the data. The stress state-resilient modulus relationships may be analyzed after any number of load cycles of interest. Typical relationships for granular and fine-grained soils are depicted in Figures 2-8 and 2-9 respectively.

Review of Previous Work

A number of laboratory and field studies have been conducted on AS and AFS systems. The research indicates that the inclusion of fabric does indeed improve the ability of a system to resist permanent deformations. The most improvement is displayed in systems which experience high deformations. With greater aggregate depths and/or stiffer subgrade materials, these high deformations are not experienced and the results indicate minimal benefit. Results, especially for static load tests, are discussed only in generalized terms. For dynamic load tests,

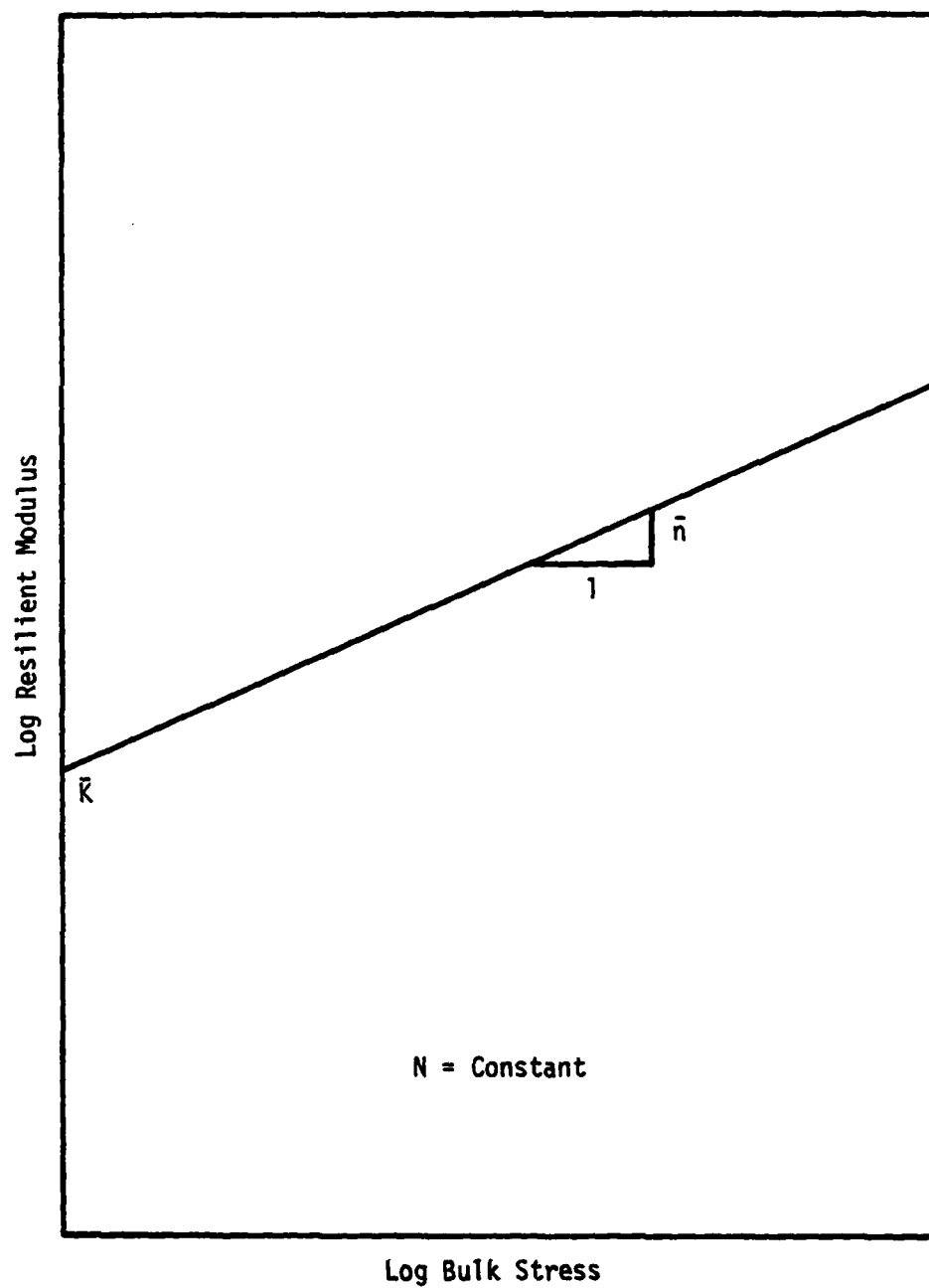


Figure 2-8. Typical Bulk Stress-Resilient Modulus Relationship for Granular Material.

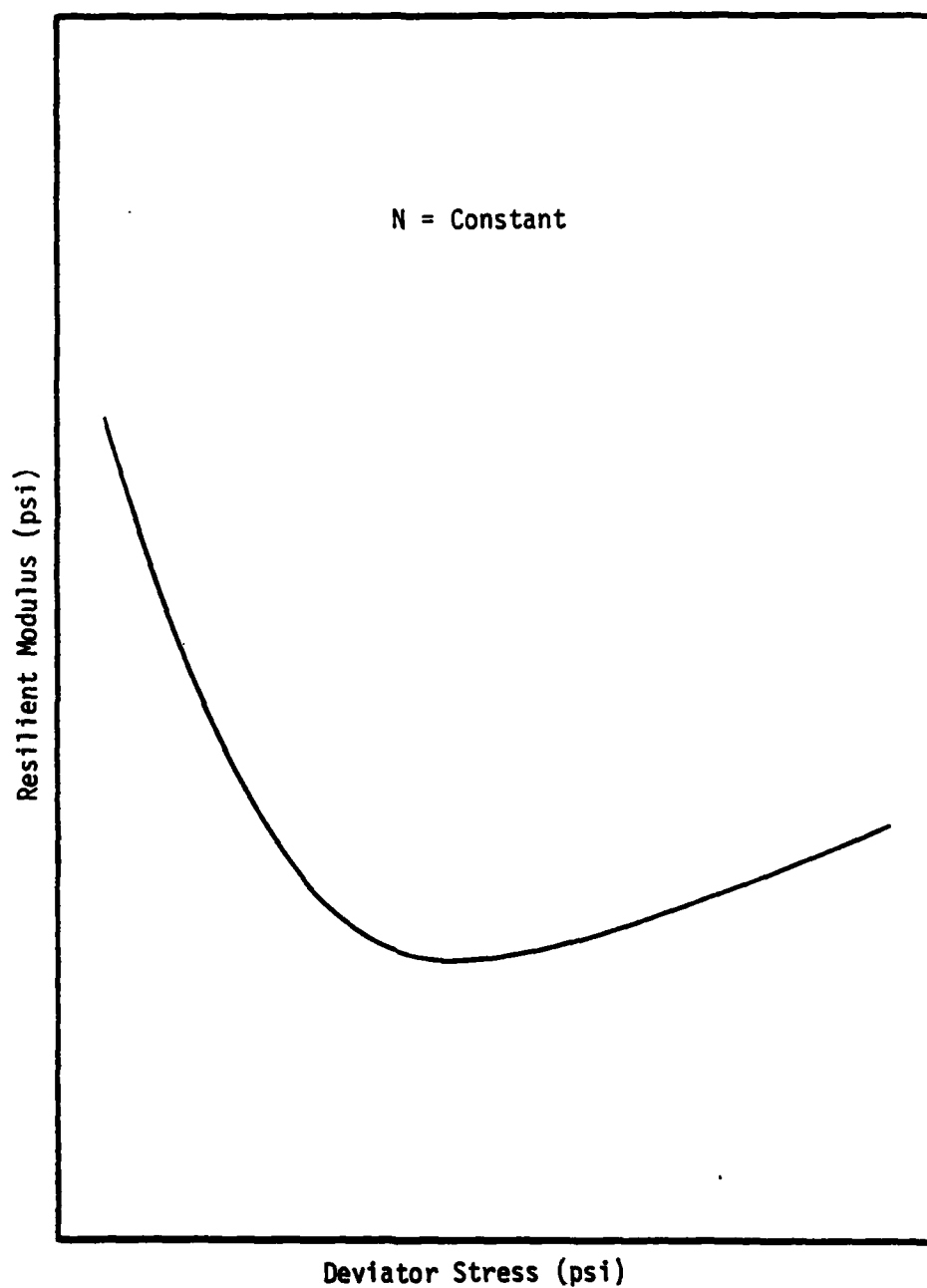


Figure 2-9. Typical Deviator Stress-Resilient Modulus Relationship for Fine-Grained Soil.

system response is partially predicted (i.e., a relationship between load cycles and total rut depth at a single point during the life of the system) at best. The findings of some of the published studies are briefly described below.

Barenberg, Dowland, and Hales

Barenberg, et al. (14, 17) conducted both two- and three-dimensional model tests (i.e., plane strain and axisymmetric respectively) of AS and AFS systems, utilizing single layers of either Mirafi 140 or Mirafi 280, or double layers of Mirafi 140 fabric. The aggregate used during the testing was an open graded crushed limestone, while the tested subgrade materials were a silty clay and a silt of low strengths (i.e., CBR less than one). Both static and dynamic loading tests were conducted, with the latter utilizing a one second load duration, applied at a frequency of six cycles per minute. The tests showed a significant improvement in the permanent deformation characteristics of systems with a fabric inclusion at the interface of the soil layers. The test results were utilized to develop a quasi-rational design methodology recommended by Celanese for AS systems and those AFS systems reinforced with Mirafi fabric. The methodology limits the vertical stress at the subgrade soil surface, and has its roots in bearing capacity theory and the work of Rodin (83), as previously discussed.

Jessberger

Jessberger (52) conducted plate bearing tests on both AS and AFS systems. The aggregate was a poorly graded gravel, while the subgrade was a silt of low plasticity. A non-woven fabric, Terram 280, was utilized in the AFS systems. Anisotropic axisymmetric finite element

analyses were conducted to verify the field results. The fabric improved the permanent deformation characteristics of the reinforced systems, with the greatest improvement shown in high deformation systems. The FEM analyses greatly underestimated the beneficial influence of a fabric inclusion. Theory predicted a 2-5 percent bearing capacity improvement, as contrasted to observed improvements reaching 30 percent.

Jarrett, Lee, and Ridell

Jarrett, et al. (51) conducted plate bearing tests on AS and AFS systems. Several thicknesses of granular base were tested, with the subgrade in all cases being a peat deposit. Four fabrics were utilized: Mirafi 140 and 280; and Terrafix 300N and 1000N. A fabric inclusion was found to improve stability in those systems experiencing high deformations. The greatest benefits were achieved with stiffer fabrics.

Barvashov, Budanov, Famin, Perkov, and Pushkin

Barvashov, et al. (15) conducted plate bearing tests on a Bidim reinforced medium sand. The load carrying capacity and settlement characteristics were improved by the fabric inclusion in the higher deformation systems. Pretensioning and anchoring of the fabric further improved system behavior.

McGown and Andrawes

McGown and Andrawes (66) conducted plane strain tests on samples of sand reinforced with a non-woven fabric inclusion, and plane strain model footing tests on a variety of materials, utilizing several grades of non-woven Terram fabric in both single and multiple layer placements. In those tests involving the unit cell of sand, the fabric was placed at various angles with respect to the major principal stress. The greatest

strength improvement was observed when the fabrics were placed normal to the major principal plane. When the fabrics were inclined at angles close to the failure plane, the system was weakened. For the model footing tests, fabrics improved the permanent deformation characteristics, with stiffer fabrics and multiple layers producing the greatest benefits. The model footing tests also established a dependence between system response and the relative depth of the inclusion(s). The greatest improvement was created when fabric was placed at that depth at which the observed strains were a maximum in the corresponding unreinforced system.

Andersson

Andersson (2) conducted cyclic plate bearing tests, on both AS and Terram reinforced AFS systems, at low deformation levels. No significant differences were noted between the response behaviors of the AS and AFS systems so tested.

Sørli

Sørli (95) performed plate bearing tests on AS and AFS systems. The AFS systems utilized Fibertex S170 fabric. Various gravel thicknesses were utilized over three different subgrades: an expanded clay, bark, and a very soft clay (i.e., vane shear strength = 1.5 psi). Only with the very soft clay material did the fabric inclusion produce any consistent trend of improvements in the bearing capacity results. Even with that material, the differences in bearing capacity, with and without the fabric inclusion, were insignificant.

Kinney

Kinney (56) conducted a variety of two-dimensional (i.e., plane

strain) model tests on both AS and AFS systems, utilizing incremental, constant repetitive, and variable repetitive loadings. Mirafi 40 and a stiffer fabric, W2, were tested in the AFS systems. A fabric inclusion was found to improve stability in high deformation systems. Based upon the test results, a means of predicting the reduction in the total vertical load transmitted to the subgrade soil, resulting from a fabric inclusion, was proposed. This reduction is a function of the deformed shape of the aggregate-subgrade soil interface, the tension in the fabric, the strain energy stored in the fabric, and the interfacial shear stresses.

Steward, Williamson and Mahoney

Steward, et al. (100) presented results of field tests conducted by the U.S. Forest Service. A variety of fabrics were tested, each being installed over a weak clay subgrade (i.e., CBR less than one). The test sections were constructed in accordance with the Forest Service's design procedure, which utilizes the limiting subgrade stress concept. Design values of 3.3c and 6.0c are utilized for AS and AFS systems respectively, when rutting of approximately four inches can be tolerated within 10^2 load cycles. To limit rutting to two inches after 10^3 load repetitions, corresponding design values of 2.8c and 5.0c are recommended. The test road sections were narrow, with normal traffic wander permitted. Rutting occurred rapidly and was up to six inches in depth. Complete data was not presented. Based upon preliminary results, the design procedures were deemed satisfactory, as measured rutting was generally within anticipated limits. Further testing and refinement of the design parameters was considered necessary.

Morel, Quibel, Puiatt, and Puig

Morel, et al. (72) presented the results of field tests on AS and AFS systems underlain with a weak clay subgrade. Loading was applied to the test sections by a 26 kip axle load, each section being constructed with one of three possible aggregates (i.e., one ballast and two gravels) and aggregate thicknesses, and the AFS systems containing one of three fabrics (i.e., Bidim C34 or C44, or Stabilenka N99). Traffic wander was permitted during the tests. No significant improvements in rutting characteristics were noted in systems with the fabric inclusions and in some instances, it was thought that the fabric may have actually accelerated the rate of rut formation.

Webster and Watkins

Webster and Watkins (117) presented the results of tests conducted by the U.S. Army Corps of Engineers Waterways Experiment Station. An AS control section and two AFS sections were constructed, the latter utilizing either Bidim C38 or a stiffer, neoprene coated, woven nylon fabric, Reeves T-16. A soft clay subgrade (i.e., CBR = 1.0) and 14 inches of crushed stone were used in all cases. Loading was applied by a loaded dump truck, with vehicle wander minimized. The AFS systems displayed less permanent deformation than did the AS section, after an equal number of load repetitions. The amount of relative improvement increased with continued rutting. The Reeves T-16 fabric produced the greater beneficial effects in regard to reducing rutting and spreading out the shear deformations observed in the subgrade material.

Webster and Alford

Webster and Alford (118) reported on a Waterways Experiment

Station study, which was a follow-up to that discussed previously. Two AFS test sections were constructed: one consisting of Reeves T-16 fabric placed over a relatively weak clay subgrade (i.e., CBR = 1.0) and covered with six inches of crushed stone, while the second section was constructed over a weaker subgrade (i.e., CBR = 1.0) and covered with 14 inches of crushed stone. In the latter system, heavy wire mesh was utilized in conjunction with Bidim C38 fabric, being placed above the fabric in one wheel path and below the fabric in the other. Load was applied by a loaded dump truck, with vehicle wander minimized. For the Reeves T-16 fabric section, a two inch rut developed after 15,000 load repetitions. Utilizing a theoretical prediction for rutting in a geometrically identical AS system, it was concluded that the fabric significantly reduced rut development. In the second test section, placement of the mesh above the fabric provided the greater rut depth reduction. When placed below the fabric, the mesh penetrated into the subgrade material in the rut area, while when placed above the fabric, the mesh conformed to the deformed shape along the interface of the soil layers.

CHAPTER III

MATERIAL SELECTION, PROCUREMENT AND PROPERTIES

Crushed Stone

The crushed stone used for the surface layer in the model testing program was a Biotite Granite Gneiss, obtained from the Vulcan Materials Company Quarry at Norcross, Georgia. The material was received as standard gradations (115) Nos. 67 and 89 (ASTM D-448) and 1.0-1.5 inches crushed stone base. The material was spread in lifts of 1-2 inches depth on the floor of an area protected from the elements and allowed to become sufficiently dry for sieving. When dry, the material was separated into various particle size ranges using a Gilson Mechanical Testing Screen, manufactured by The Gilson Screen Company, Malinta, Ohio. The segregated material was stored by particle size in covered barrels. When sufficient amounts of all desired particle sizes were obtained, the material was mixed in known quantities, each weighed out on a Model 31-0850-FH scale, with a capacity of 100 pounds, marked in 0.1 pound gradations, manufactured by the Toledo Scale Company, Toledo, Ohio, to produce the desired gradation (Figure 3-1). This gradation follows the form:

$$P = \left(\frac{d}{D}\right)^n \quad (3-1)$$

where P = percent of particles smaller than d in diameter

d = sieve size in question, inches

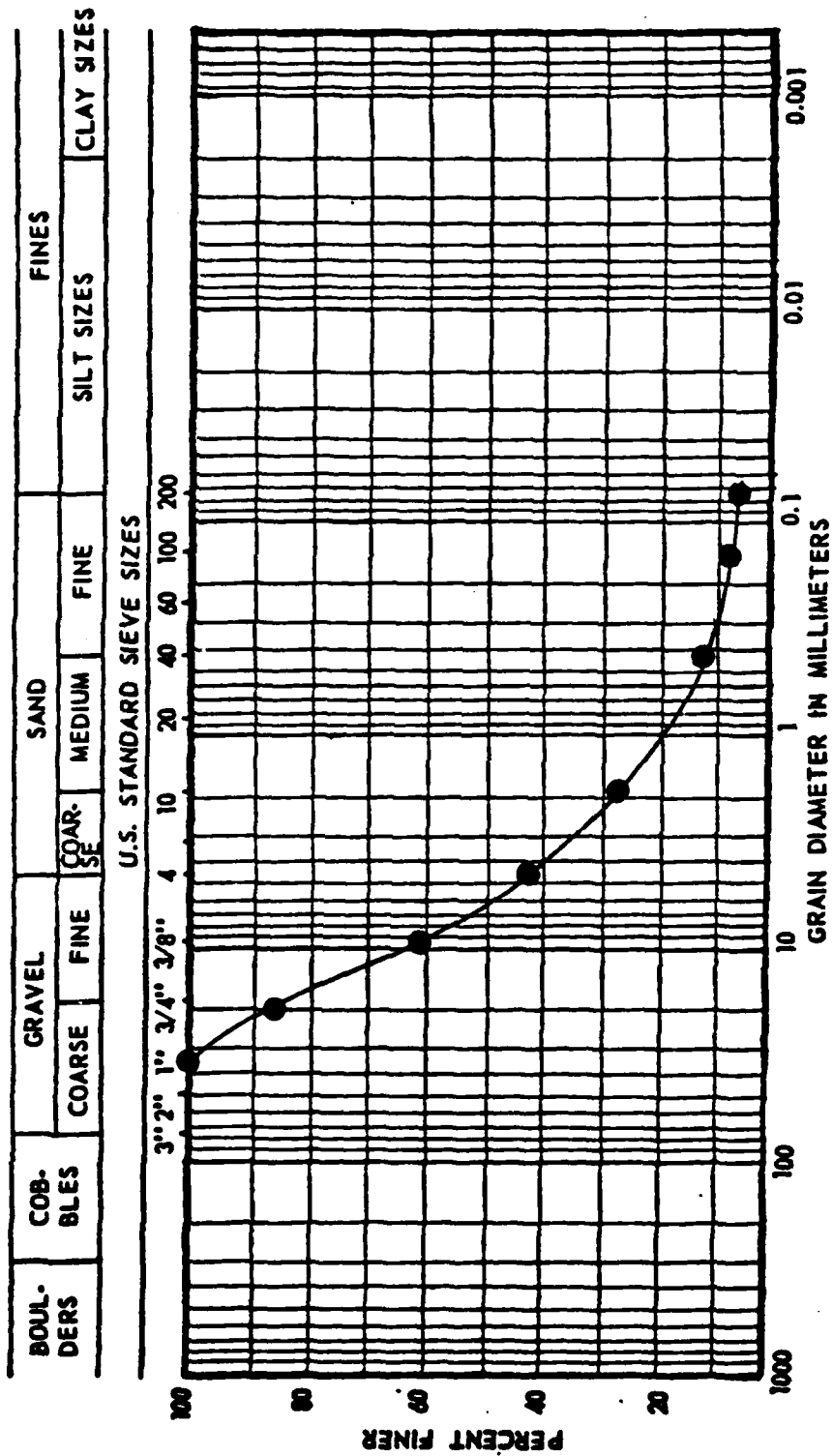


Figure 3-1. Crushed Stone Grain Size Distribution.

D = maximum particle size, inches

n = gradient coefficient.

Such a gradation, with n ranging from 0.33 to 0.5, has been shown to produce maximum density and good compactibility (49, 122). For this case, D was taken as one inch and n as 0.5. The resulting gradation falls near the middle of the range generally recommended for use on fabric stabilized subgrades (30, 31). The Unified Classification (ASTM D-2487) for this gradation is GW, while the corresponding AASHTO Classification (AASHTO M-145) is A-1-a.

The compaction moisture-density relationships of the crushed stone were determined by Method C of ASTM D-698. Mixing of aggregate and water was accomplished manually, in a large bowl, and moisture contents were determined in accordance with ASTM D-2216. The maximum dry density was found to be 139.1 pcf at a corresponding optimum moisture content of 6.3 percent.

Triaxial shear tests were conducted on laboratory compacted specimens of the crushed stone. Both static and repeated load tests were conducted. Details of the sample preparation procedure are given in Appendix A, as is a description of the equipment used in the repeated load triaxial tests. The samples were six inches in diameter and 12 inches high. The dry density of the samples was 132.1 pcf, which was the anticipated density of the crushed stone during the model testing program. For the conventional tests, a 20 kip capacity, screw-type loading machine, manufactured by the Tinius-Olsen Testing Machine Co., Willow Grove, Pennsylvania, was used to load the sample at the rate of 0.02 inch per minute. Deformation was measured with a Model E81S

dial gage, manufactured by Federal, Providence, Rhode Island. This dial gage has divisions of 0.001 inch and a range of six inches.

The crushed aggregate exhibits no cohesion, but considerable friction, with the Mohr envelope (Figure 3-2) having a friction angle of 48° . Basic aggregate properties are summarized in Table 3-1, with additional data available in Appendix B.

A summary of the repeated load triaxial test program is provided in Table 3-2. The specimens were loaded axially by a pneumatic system which matched the load pulse durations and frequencies to be used in the model test program. Deformations were monitored by L.V.D.T.'s. The ranges for the confining and axial stresses were estimated using Boussinesq theory and the geometry of the test pit. The data were analyzed by the procedures described in Chapter II, to determine the appropriate relationships between resilient modulus, plastic strain, and stress state, for 10 , 10^2 , 10^3 , and 10^4 load cycles. The pertinent dynamic test results are summarized in Table 3-3, with additional data available in Appendix B.

Subgrade Soil

The subgrade material used for this study was Dry Mill Fire Clay, purchased from A. P. Green Refractories, Morris, Illinois. The material was received in sacks, each containing 100 pounds of soil. The specific gravity of solids (ASTM D-854) was determined in two separate tests, with the average value being 2.67. Two particle size tests (ASTM D-422) were conducted. The average gradation curve is shown in Figure 3-3. Two series of tests were conducted to determine the Liquid Limit (ASTM

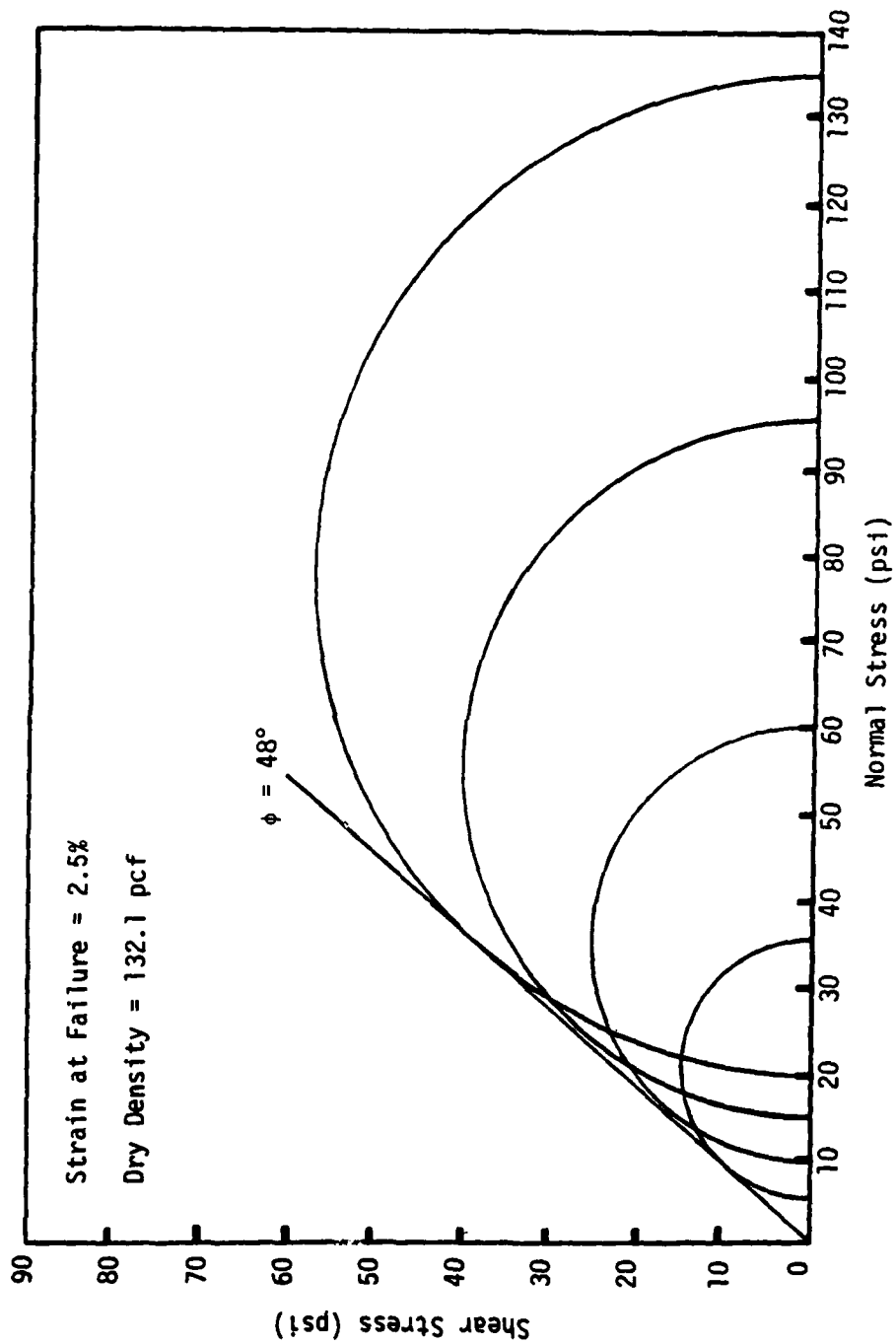


Figure 3-2. Mohr Envelope for Crushed Stone.

Table 3-1. Soil Properties.

Crushed Stone

Aggregate Description	Biotite Granite Gneiss
Maximum Particle Size (ASTM D-422)	1.0 inch
Unified Classification (ASTM D-2487)	GW
Maximum Dry Density (ASTM D-698)	139.1 pcf
Optimum Moisture Content (ASTM D-698)	6.3 %
Angle of Internal Friction ($\gamma_d = 132.1$ pcf)	48°

Subgrade Soil

Liquid Limit (ASTM D-423)	27.2 %
Plastic Limit (ASTM D-424)	12.0 %
Plasticity Index (ASTM D-424)	15.2 %
Specific Gravity of Solids (ASTM D-854)	2.67
Unified Classification (ASTM D-2487)	CL
Maximum Dry Density (ASTM D-698)	118.2 pcf
Optimum Moisture Content (ASTM D-698)	12.7 %
Unsoaked CBR at w_{opt}	21.4
Penetration Resistance at w_{opt} (ASTM D-1558)	471 psi
Cone Load at w_{opt}	331 lb.
Cone Index at w_{opt}	662

Strength Correlations

(ASTM D-698 Compactive Effort; $w = 18-24\%$)

Unsoaked CBR = 0.0401 (Penetration Resistance) - 0.1250

Cone Load = 0.7531 (Penetration Resistance) - 3.6903

Cone Index = 1.5062 (Penetration Resistance) - 7.3805

Vane Shear Strength = 0.1290 (Penetration Resistance) + 1.3176

Unconsolidated-Undrained Shear Strength (ASTM D-2850)

 $(w = 23.4 - 24.6\%; \gamma_d = 98.5 - 100.5 \text{ pcf})$ 3.3 psi $(w = 22.2 - 22.9\%; \gamma_d = 102.4 - 104.1 \text{ pcf})$ 4.6 psi $(w = 19.3 - 20.4\%; \gamma_d = 104.9 - 106.2 \text{ pcf})$ 6.7 psiSand

Unified Classification (ASTM D-2487)	SP
Fineness Modulus	1.46

Table 3-3. Repeated Load Triaxial Test Results for Crushed Stone.
Dry Density = 132.1 pcf

Load Type	c (psi)	ϕ	Load Cycles	$K^{(a)}$	$n^{(a)}$	Avg. $R_f^{(a)}$	$\bar{K}^{(b)}$	$\frac{1}{n}^{(b)}$	$r^2^{(b)}$
A 3.0 sec pulse 10 cpm	0	48	10	11545	0.341	0.50	1242	0.762	0.987
			10^2	7677	0.425	0.61	1406	0.735	0.989
			10^3	7311	0.405	0.81	1218	0.785	0.981
			10^4	6421	0.395	0.79	1142	0.798	0.985
B 0.2 sec pulse 20 cpm	0	48	10	12616	0.335	0.63	1854	0.659	0.889
			10^2	9766	0.360	0.49	1510	0.715	0.923
			10^3	6733	0.428	0.53	1815	0.672	0.903
			10^4	5881	0.428	0.42	1669	0.697	0.879

(a) Constants for Hyperbolic Plastic Stress-Strain Law (Equation 2-8).

(b) Constants and Coefficients of Determination for Bulk Stress-Resilient Modulus Relationships (Equation 2-10).

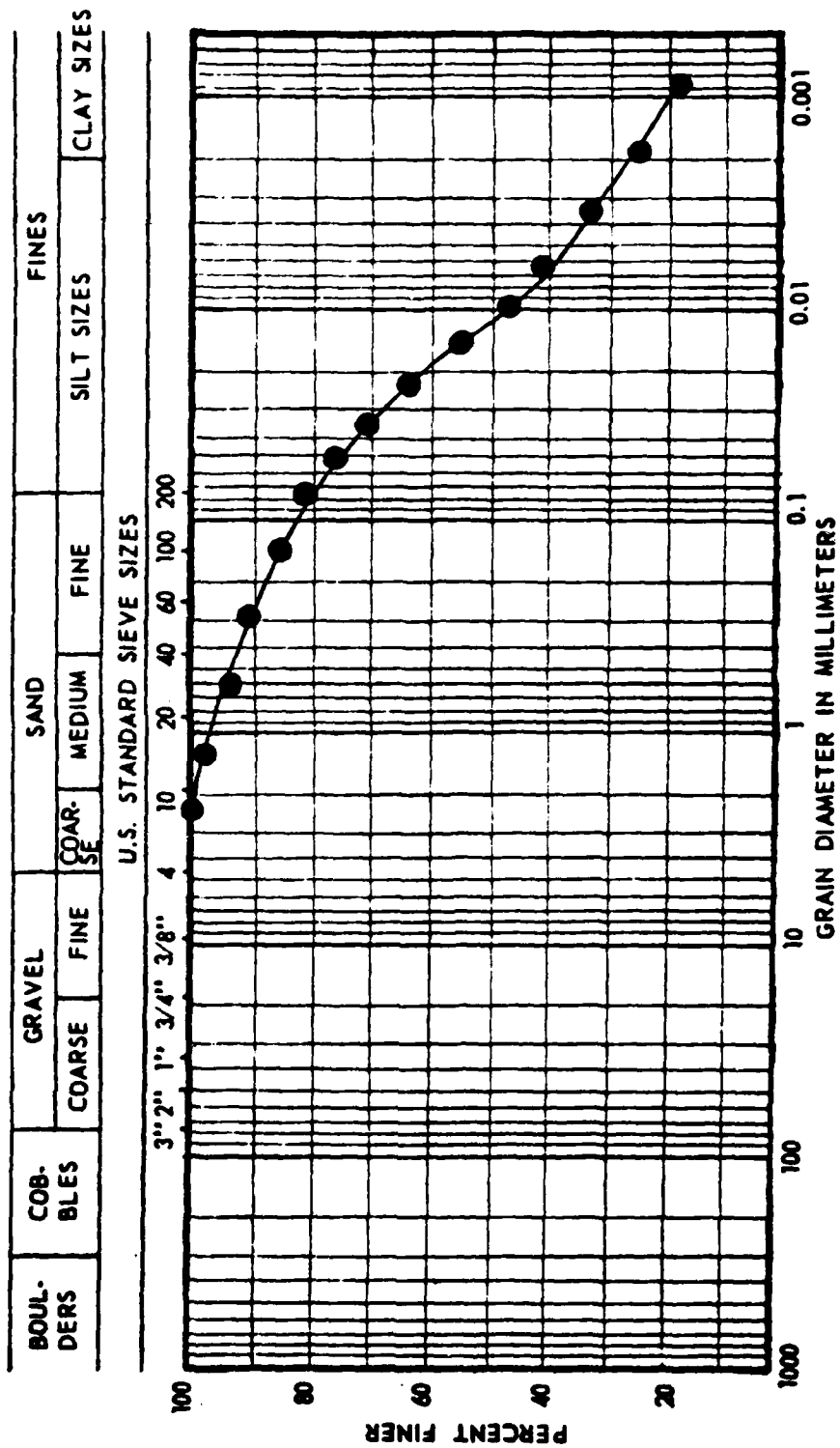


Figure 3-3. Subgrade Soil Grain Size Distribution.

D-423), Plastic Limit (ASTM D-424), and Plasticity Index (ASTM D-424) of the material as received. The average Liquid Limit was determined as 27.2 percent, while the average Plastic Limit was determined as 12.0 percent. The resulting Plasticity Index was 15.2 percent. The Unified Classification (ASTM D-2487) for the subgrade material is CL. The AASHTO Classification (AASHTO M-145) for the material is A-6. Basic soil properties are summarized in Table 3-1, with additional data available in Appendix B.

The compaction moisture-density relationships of the subgrade material were determined by Method A of ASTM D-698. The soil and water were mixed thoroughly in a Type PC Lancaster Counter Current Batch Mixer, manufactured by Posey Iron Works, Inc., Lancaster, Pennsylvania. Moisture contents were determined in accordance with ASTM D-2216. Two series of compaction tests were conducted. The average maximum dry density was found to be 118.2 pcf, with a corresponding optimum moisture content of 12.7 percent. An unsoaked California Bearing Ratio (CBR) test was made on each compaction specimen. The CBR (ASTM D-1883) is a comparison measure, expressed as a percentage, of the penetration resistance of the material being tested to the resistance of a high quality crushed stone to the same penetration. The standard resistance is usually taken as 1000 psi at a penetration of 0.1 inch. The specimens were loaded in the 20 kip capacity Timms-Olsen Testing Machine, with penetration made by a CBR test head. Penetration was carried to a depth of 0.1 inch and was measured with a dial gage. The standard test procedure (3, 122) utilizes six inch diameter specimens, which have been soaked in water for a period of four days prior to testing, and have

surcharge weights applied during both soaking and penetration of the test head. Thus, the test procedure utilized varied somewhat from the recommended procedure. The average value of unsoaked CBR at the optimum moisture content of the subgrade was determined to be 21.4. At different moisture contents the unsoaked CBR values ranged from 47.2 to 4.4 for the various specimens.

A moisture-penetration resistance relationship (ASTM D-1558) for the specimens was determined for each test series. This test utilizes a spring dynamometer with a load indicating scale on the stem of the handle. The penetration resistance is calculated as the maximum penetration load divided by the end area of the penetration needle head. The penetration was carried to a depth of 0.3 inch, rather than the recommended minimum depth of three inches. The shallow penetration depth was utilized to facilitate use of the penetrometer and established strength-density-moisture correlations during the model testing program, when numerous deep penetrations into the compacted lifts would have resulted in greater soil disturbance than considered desirable. The average value of penetration resistance at the optimum moisture content was 471 psi, with values ranging from 1044 to 74 psi at other moisture contents.

Finally, each specimen was penetrated with a cone, having an enclosed tip angle of 30° and a projected base area of 0.5 square inch, at the rate of four inches per minute. The U.S. Army Corps of Engineers uses a cone with these same dimensions in determining the Cone Index (28) of fine-grained soils. The standard Cone Index (CI) test utilizes the cone, attached to one end of a 0.625 inch diameter rod, three feet

in length, equipped with a proving ring, dial gage, and handle at the opposite end. The cone is forced into the soil at the rate of approximately six feet per minute. The deflection of the proving ring results in movement of the dial gage, from which the CI value is read directly. The CI is reported as a dimensionless number, although being a function of the maximum penetration load divided by the projected base area of the cone. At the time of this study, only the cone, without the related equipment, was available. For these tests, penetration was accomplished using the 20 kip capacity Tinius-Olsen Testing Machine. The load was read when penetration to the base of the cone was achieved. This load corresponded to twice the CI value, for the projected base area of the cone utilized. The average CI value at the optimum moisture content of the subgrade was 662, with values ranging from 1670 to 120 at other moisture contents.

A third series of compaction tests was conducted on the subgrade, utilizing Method A of ASTM D-698, while varying the compaction moisture content between 18 and 24 percent. Unsoaked CBR, penetration resistance, and cone penetration tests were conducted on all the specimens of this test series. Additionally, vane shear strength tests were made on each sample, using a vane one inch in diameter by two inches in height. Torque was applied with, and determined by, a Model TQ-12-B Torqometer, manufactured by the Snap-On Tools Corp., Kenosha, Wisconsin. This instrument has a capacity of 50 inch-pounds and is marked in divisions of five inch-pounds.

Correlations of penetration resistance with unsoaked CBR, cone penetration, and vane shear strength were made utilizing a linear curve

fit method. Pertinent strength correlations are summarized in Table 3-1 and Figure 3-4, while additional compaction test data appear in Appendix B.

Triaxial shear tests were conducted on laboratory compacted specimens of the subgrade. Conventional unconsolidated-undrained (UU) tests (ASTM D-2850) and repeated load tests were made. Details of the sample preparation procedure and the repeated load test equipment are provided in Appendix A. The samples were 2.8 inches in diameter by 5.6 inches in height.

The conventional triaxial tests were conducted using the 20 kip capacity, Tinius-Olsen Testing Machine, loading the samples at the rate of 0.1 inch per minute, with deflections measured by a Federal, Model E81S, dial gage. Three soil strengths were tested, corresponding to the range anticipated for use in the model testing program. The soil exhibited a failure by slow progressive bulging. For establishing the Mohr envelopes (Figures 3-5 through 3-7), the failure stress state was taken as that corresponding to 20 percent axial strain. The shear strengths obtained from the UU tests varied slightly from the vane shear strengths computed on the basis of the correlation with the penetration resistance values obtained from all triaxial test samples. Some variation was expected since the undrained strength of a soil is sensitive to test conditions, with variations of ± 20 percent not being unusual (61). Observed variations were within this range. Results from the UU tests are summarized in Table 3-1.

A summary of the repeated load triaxial test program is provided in Table 3-2. The specimens were loaded axially by a pneumatic system

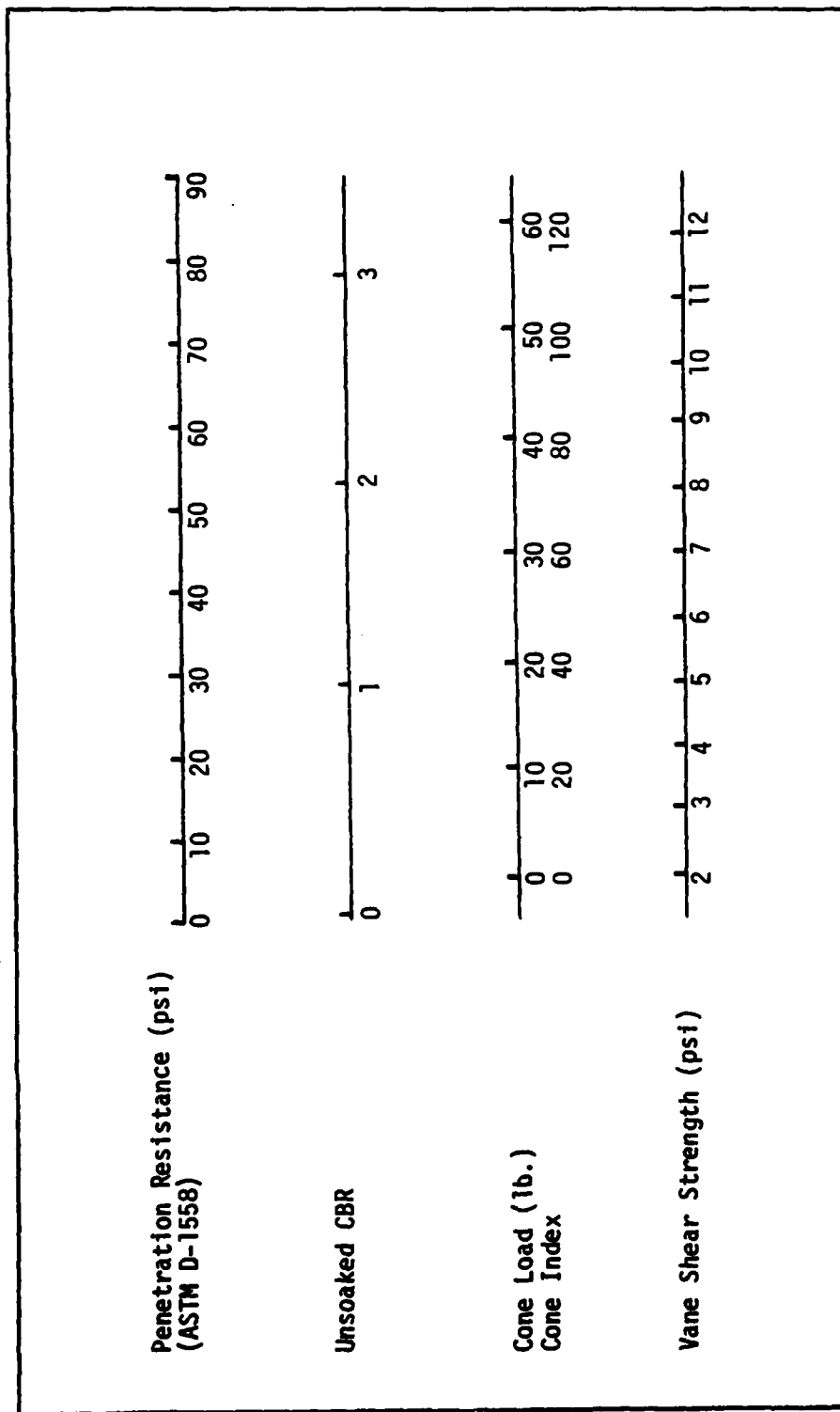


Figure 3-4. Subgrade Soil Strength Correlations.

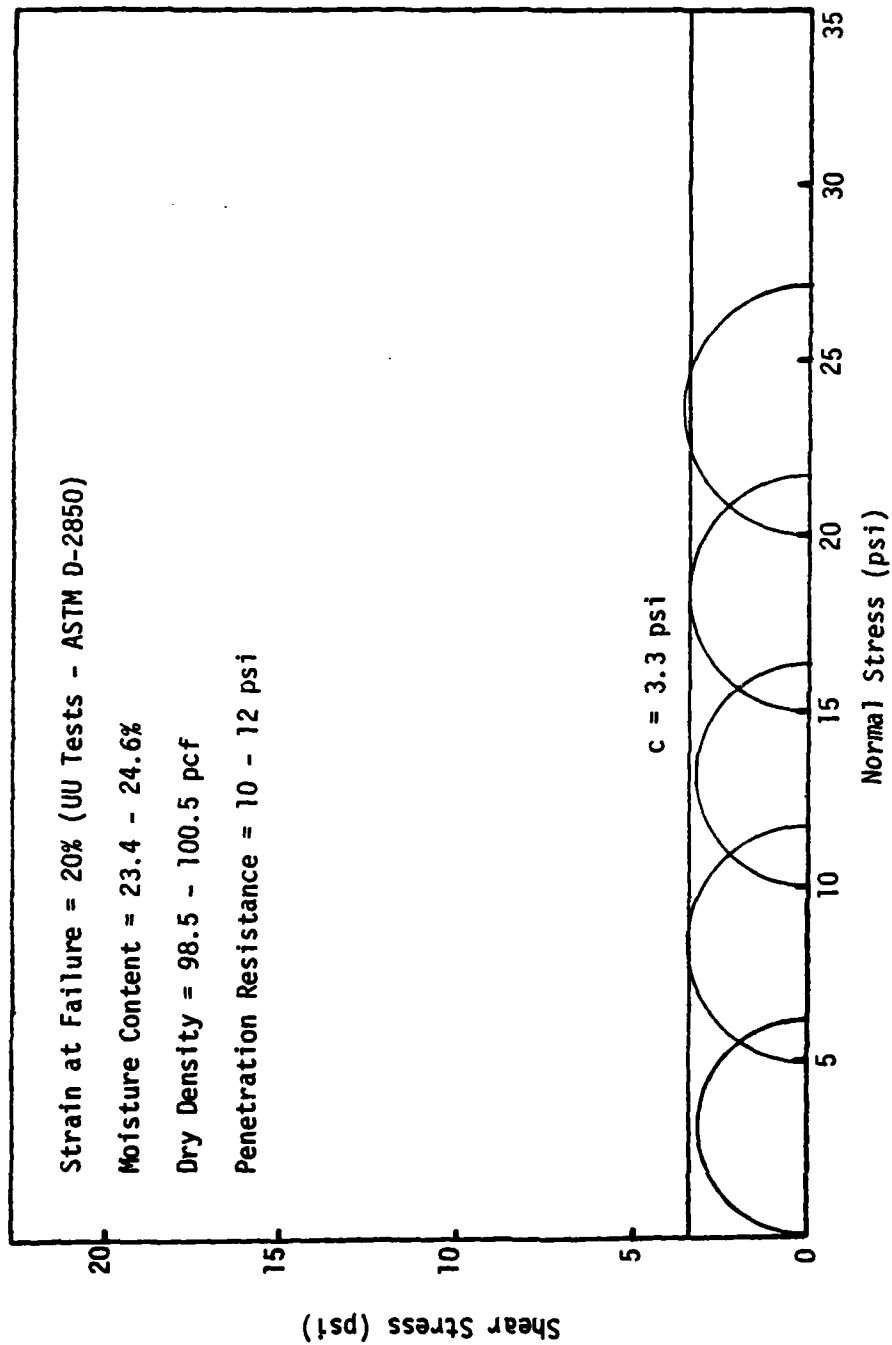


Figure 3-5. Mohr Envelope for Subgrade Soil.

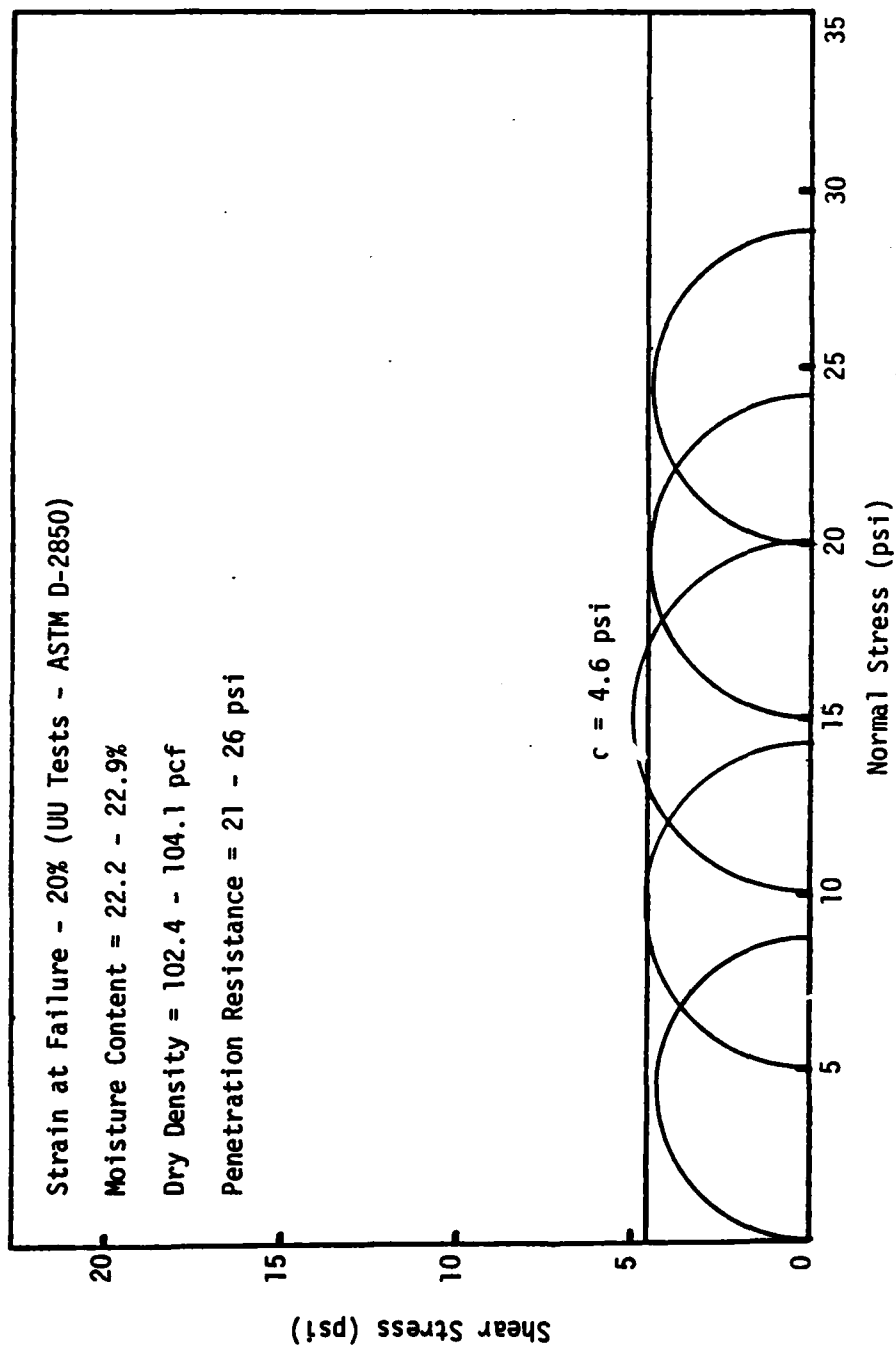


Figure 3-6. Mohr Envelope for Subgrade Soil.

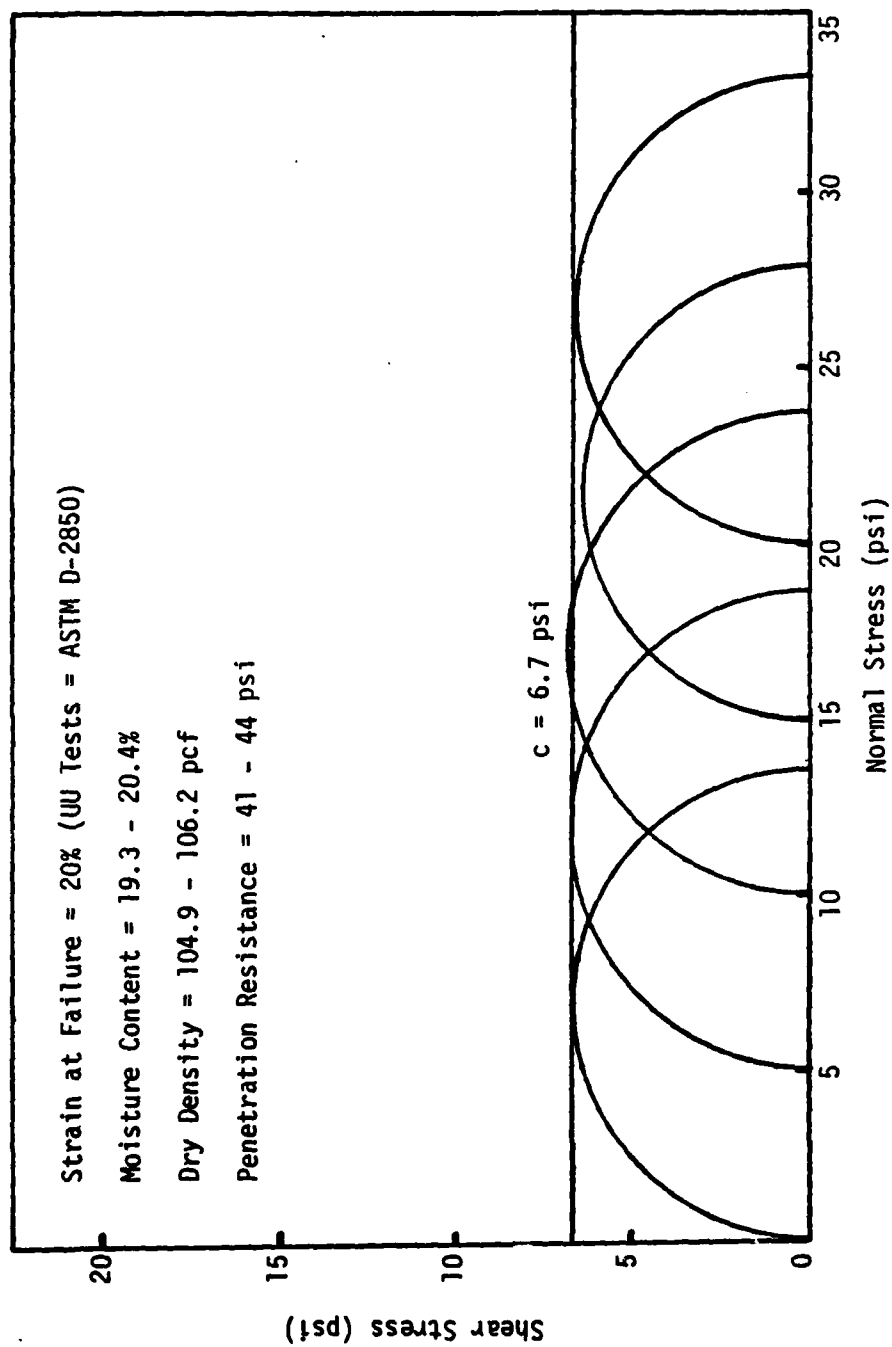


Figure 3-7. Mohr Envelope for Subgrade Soil.

which matched the load pulse durations and frequencies to be used in the model test program. Deformations were monitored by L.V.D.T.'s. The ranges for confining and axial stresses were estimated using Boussinesq theory and the geometry of the test pit. The appropriate relationships between resilient modulus, plastic strain, and stress state were determined by the procedures set forth in Chapter II, for 1, 10, 10^2 , 10^3 , and 10^4 load cycles. The pertinent dynamic test results are provided in Tables 3-4 through 3-6. Additional data are presented in Appendix B.

Sand

The Chattahoochee River sand utilized in the model testing program was available from the Civil Engineering Materials Laboratory at the Georgia Institute of Technology. The grain size distribution (ASTM D-422) was determined and is presented in Figure 3-8. The Unified Classification (ASTM D-2487) for this material is SP, while the AASHTO Classification (AASHTO M-145) is A-3. The Fineness Modulus of the sand was determined as 1.46. The sand was utilized as a separator or filter layer between the subgrade soil and crushed stone in a portion of the model testing program, to study the influence of blocking the migration of fines from the subgrade into the crushed stone on rutting. To restrain soil particles from migrating, it is generally required (35, 97, 121) that:

$$D_{15} (\text{Filter}) \leq 5 D_{85} (\text{Soil}) \quad (3-2)$$

where $D_{15} (\text{Filter})$ = largest particle diameter of the finest 15 percent

AD-A110 434

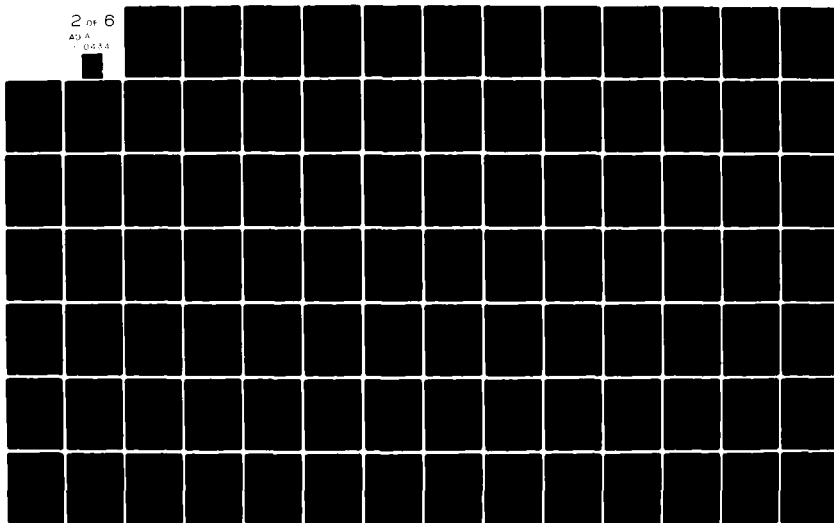
AIR FORCE INST OF TECH WRIGHT-PATTERSON AFB OH F/G 13/2
PERFORMANCE OF FABRIC REINFORCED AGGREGATE-SOIL SYSTEMS UNDER R--ETC(U)
DEC 81 W SCHAUZ
AFIT-CI-81-69D

UNCLASSIFIED

NL

2 OF 6

AD-A
1 0634



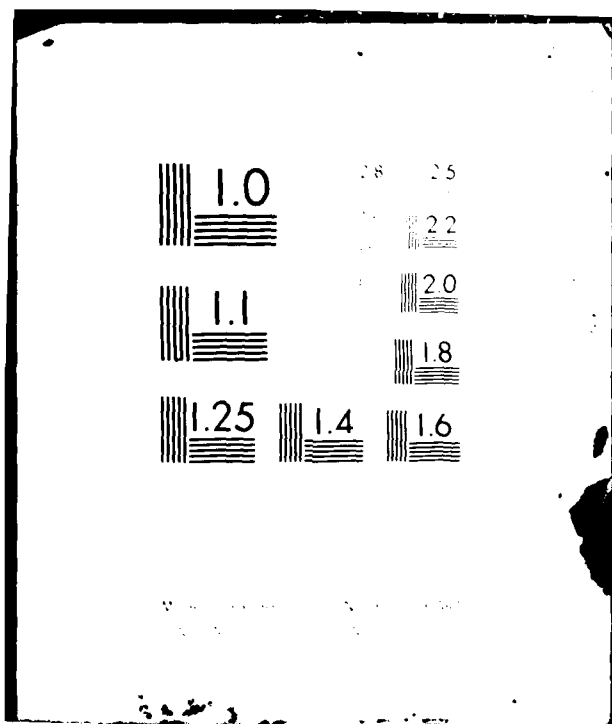


Table 3-4. Repeated Load Triaxial Test Results for Subgrade Soil.

Moisture Content = 23.1 - 24.9%

Dry Density = 100.6 - 101.7 pcf

Penetration Resistance = 10 - 13 psi

Load Type	c (psi)	ϕ	Load Cycles	K ^(a)	n ^(a)	Avg. R_f ^(a)	Log M_R ^(b) (psi)	r^2 ^(b)
B	3.3	0	1	89	0.245	0.65	2.64192 - 0.03405 σ_d	0.506
0.2 sec pulse			10	39	0.317	0.68	2.61790 - 0.04394 σ_d	0.846
20 cpm			10 ²	18	0.430	0.69	2.65403 - 0.07909 σ_d	0.704
			10 ³	15	0.297	0.94	2.66681 - 0.08079 σ_d	0.958

(a) Constants for Hyperbolic Plastic Stress-Strain Law (Equation 2-8).

(b) Deviator Stress-Resilient Modulus Relationships and Coefficients of Determination.

Table 3-5. Repeated Load Triaxial Test Results for Subgrade Soil.

Moisture Content = 21.8 - 23.2%

Dry Density = 101.9 - 104.5 pcf

Penetration Resistance = 22 - 27 psi

Load Type	c (psi)	ϕ	Load Cycles	$k(a)$	$n(a)$	Avg. R_f (a)	Log M_R (b) (psi)	$r^2(b)$
A 3.0 sec pulse 10 cpm	4.6	0	1	123	0.397	0.68	2.76849 - 0.01406 σ_d	0.427
			10	65	0.438	0.75	2.74829 - 0.01317 σ_d	0.563
			10 ²	38	0.464	0.88	2.77232 - 0.02780 σ_d	0.901
			10 ³	27	0.378	0.93	2.75524 - 0.01972 σ_d	0.638
			10 ⁴	20	0.288	0.95	2.77238 - 0.02655 σ_d	0.862

Moisture Content = 22.1 - 23.0%

Dry Density = 102.2 - 104.7 pcf

Penetration Resistance = 22 - 26 psi

Load Type	c (psi)	ϕ	Load Cycles	$k(a)$	$n(a)$	Avg. R_f (a)	Log M_R (b) (psi)	$r^2(b)$
B 0.2 sec pulse 20 cpm	4.6	0	1	237	0.519	0.90	2.89106 - 0.04440 σ_d	0.861
			10	82	0.453	0.76	2.72238 - 0.02065 σ_d	0.699
			10 ²	40	0.474	0.80	2.73863 - 0.02895 σ_d	0.635
			10 ³	27	0.263	0.80	2.70187 - 0.03279 σ_d	0.641
			10 ⁴	22	0.249	0.69	2.67493 - 0.03053 σ_d	0.582

(a) Constants for Hyperbolic Plastic Stress-Strain Law (Equation 2-8).

(b) Deviator Stress-Resilient Modulus Relationships and Coefficients of Determination.

Table 3-6. Repeated Load Triaxial Test Results for Subgrade Soil.

Moisture Content = 19.9 - 21.0%

Dry Density = 105.4 - 107.5 pcf

Penetration Resistance = 40 - 45 psi

Load Type	c (psi)	ϕ	Load Cycles	K(a)	n(a)	Avg. R_f (a)	Log M_R (b) (psi)	r^2 (b)
B	6.7	0	1	548	0.197	0.76	2.95052 - 0.01408 σ_d	0.719
0.2 sec pulse			10	306	0.140	0.86	2.86611 - 0.01111 σ_d	0.394
20 cpm			10^2	147	0.287	0.92	2.89322 - 0.01910 σ_d	0.551
			10^3	81	0.196	0.91	2.84685 - 0.01183 σ_d	0.436
			10^4	45	0.158	0.72	2.83176 - 0.01445 σ_d	0.597

(a) Constants for Hysteretic Plastic Stress-Strain Law (Equation 2-8).

(b) Deviator Stress-Strain Relationship and Coefficients of Determination.

Figure 3-8. Sand Grain Size Distribution.

of filter material, inches

$D_{85} \text{ (Soil)}$ = largest particle diameter of the finest 85 percent
of filter soil, inches

and

$$D_{50} \text{ (Filter)} \leq 25 D_{50} \text{ (Soil)} \quad (3-3)$$

where $D_{50} \text{ (Filter)}$ = largest particle diameter of the finest 50 percent
of filter material, inches

$D_{50} \text{ (Soil)}$ = largest particle diameter of the finest 50 percent
of filtered soil, inches.

To retain sufficient permeability characteristics in the system, it is
necessary (35, 121) that:

$$D_{15} \text{ (Filter)} \geq 4 D_{15} \text{ (Soil)} \quad (3-4)$$

where $D_{15} \text{ (Filter)}$ = largest particle diameter of the finest 15 percent
of filter material, inches

$D_{15} \text{ (Soil)}$ = largest particle diameter of the finest 15 percent
of filtered soil, inches.

For the sand-subgrade system:

$$\frac{D_{15} \text{ (Sand)}}{D_{85} \text{ (Subgrade)}} = 1.07 < 5$$

$$\frac{D_{50} \text{ (Sand)}}{D_{50} \text{ (Subgrade)}} = 24.3 < 25$$

and

$$\frac{D_{15} \text{ (Sand)}}{D_{15} \text{ (Subgrade)}} = 320.0 \gg 4.$$

For the crushed stone-sand system:

$$\frac{D_{15} \text{ (Stone)}}{D_{85} \text{ (Sand)}} = 1.24 < 5$$

$$\frac{D_{50} \text{ (Stone)}}{D_{50} \text{ (Sand)}} = 21.8 < 25$$

and

$$\frac{D_{15} \text{ (Stone)}}{D_{15} \text{ (Sand)}} = 3.88 < 4.$$

The particle migration criteria are satisfied for both systems, while the permeability criterion is satisfied for the sand-subgrade system. For the crushed stone-sand system, the gradation mix is slightly unacceptable with regard to the permeability criterion. As the system is so close to meeting this criterion (i.e., 3.88 versus 4), it was decided to proceed with use of the sand. Ideally, a less uniformly graded sand should have been used to best meet the filter criteria.

Fabrics

Four fabrics were utilized during the model testing program. These included: two grades of Tytar, a heat-bonded polypropylene homofilament fabric, manufactured by E. I. DuPont, Wilmington, Delaware; one grade of Bidim, a needle-punched polyester fabric manufactured by the Monsanto Textiles Co., St. Louis, Missouri; and a non-

woven (heat-bonded polypropylene/nylon heterofilament fabric) form of Mirafi, manufactured by the Celanese Fibers Marketing Co., New York, New York. The physical and mechanical properties of these materials, as stated in the literature (16, 19, 29, 57, 71, 100, 108), are summarized in Table 3-7.

Table 3-7. Fabric Properties (16, 19, 29, 57, 71, 100, 108).

Fabric Name	Mirafi 140	Bidim C22	Typar 3401	Typar 3601
Construction	Heat-bonded Polypropylene/ Nylon Sheathed Heterofilaments	Needle-punched Polyester	Heat-bonded Polypropylene Homofilaments	Heat-bonded Polypropylene Homofilaments
Thickness (mils) (ASTM D-1777)	30	60	15	19
Weight (oz./yd. ²) (ASTM D-1910)	4.0	4.5	4.0	6.0
Equivalent Opening Size (U.S. Standard Sieve) (ASTM D-422)	100	80	70-100	140-170
Grab Tensile Strength (lb.) (ASTM D-1682)	140	115	130	225
Burst Strength (lb.) (ASTM D-751)	125	225	170	263

CHAPTER IV

MODEL TEST EQUIPMENT, INSTRUMENTATION AND TESTING PROCEDURES

To investigate the beneficial effects of fabrics in reducing rutting induced by repeated load applications, scale model tests were conducted on pavement systems composed of compacted crushed stone over soft subgrades. A number of aggregate-subgrade systems, varied in subgrade strength and/or crushed stone thickness, were tested. Identical systems were then tested with fabric placed at the interface of the soil layers. Additionally, several duplicate systems were tested at varied load pulse durations and frequencies to determine the influence of these variables on system performance. The following equipment, instrumentation and procedures were used during this study.

Load Frame and Test Pit

A frame for supporting a test pit and loading system was constructed from steel sections. Rollers were installed to provide for frame mobility. Aluminum sheeting was bolted to the frame base to serve as a solid floor for the test pit. The test pit was a piece of steel pipe, 30 inches in length, with an inside diameter of three feet and a wall thickness of 0.3 inch. The pipe was placed on end on the aluminum sheeting and centered under the midpoint of the frame reaction beam. The load frame and test pit are depicted in Figure 4-1.

Loading System

A laminated plexiglas footing, six inches in diameter and two

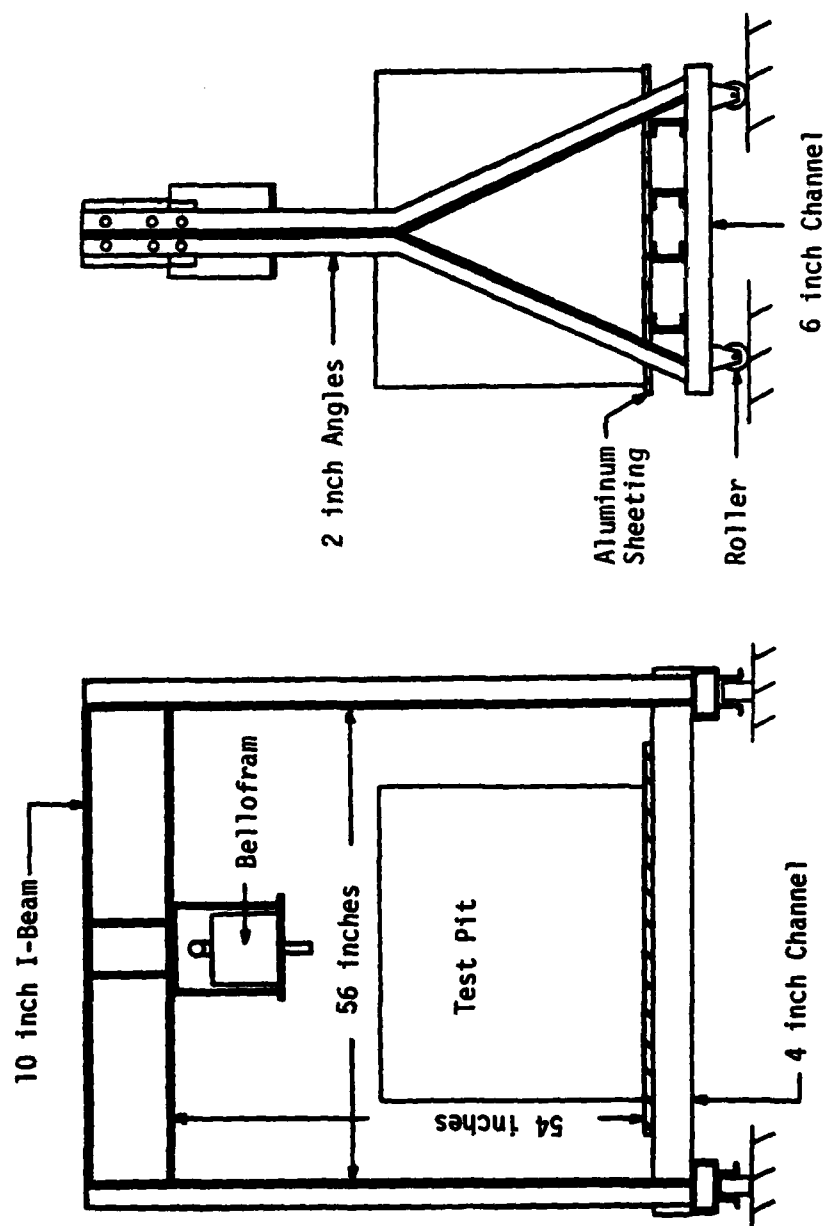


Figure 4-1. Load Frame and Test Pit Details.

inches thick, was used to transmit the load to the soil. The footing was loaded by a pneumatic system (10), with the load transferred to the footing by a Type S Size 36 diaphragm air cylinder, manufactured by the Bellofram Products Co., Burlington, Massachusetts. The Bellofram unit was housed in a steel box section, 9.5 inches in length and width and 12 inches high, bolted to the lower flange of the frame reaction beam. A 15 gallon steel tank, manufactured by Karcord Industries Inc., Marinette, Wisconsin, was used as a surge to minimize pressure fluctuations of the air delivered to the Bellofram unit. Tank air pressure was controlled by a Conoflow pressure regulator and monitored by an Ashcroft pressure gage. The frequency and duration of the flow of air from the tank to the Bellofram unit was controlled by a main valve, driven by two Model 225-111C solenoid valves, all manufactured by Mac, Wixom, Michigan. Air pressure to the pilot valves was controlled by a Conoflow pressure regulator and monitored by an Ashcroft pressure gage. The pilot valves were activated by a micro-switch and cam device operated by a Model 2T60-18 variable speed reversible motor, manufactured by the Gerald K. Heller Co., Las Vegas, Nevada. The number of load pulses was monitored by a Model PCC 6 counter, produced by Eagle Signal, Davenport, Iowa. Schematics of the pneumatic and electrical-mechanical portions of the loading system are provided in Figures 4-2 and 4-3 respectively.

The magnitude, frequency and duration of the applied load vary with surge tank and pilot valve pressures, the volume of air entering the Bellofram unit (i.e., a function of piston position), the operating speed of the motor, and the size of the cam used to trip the micro-

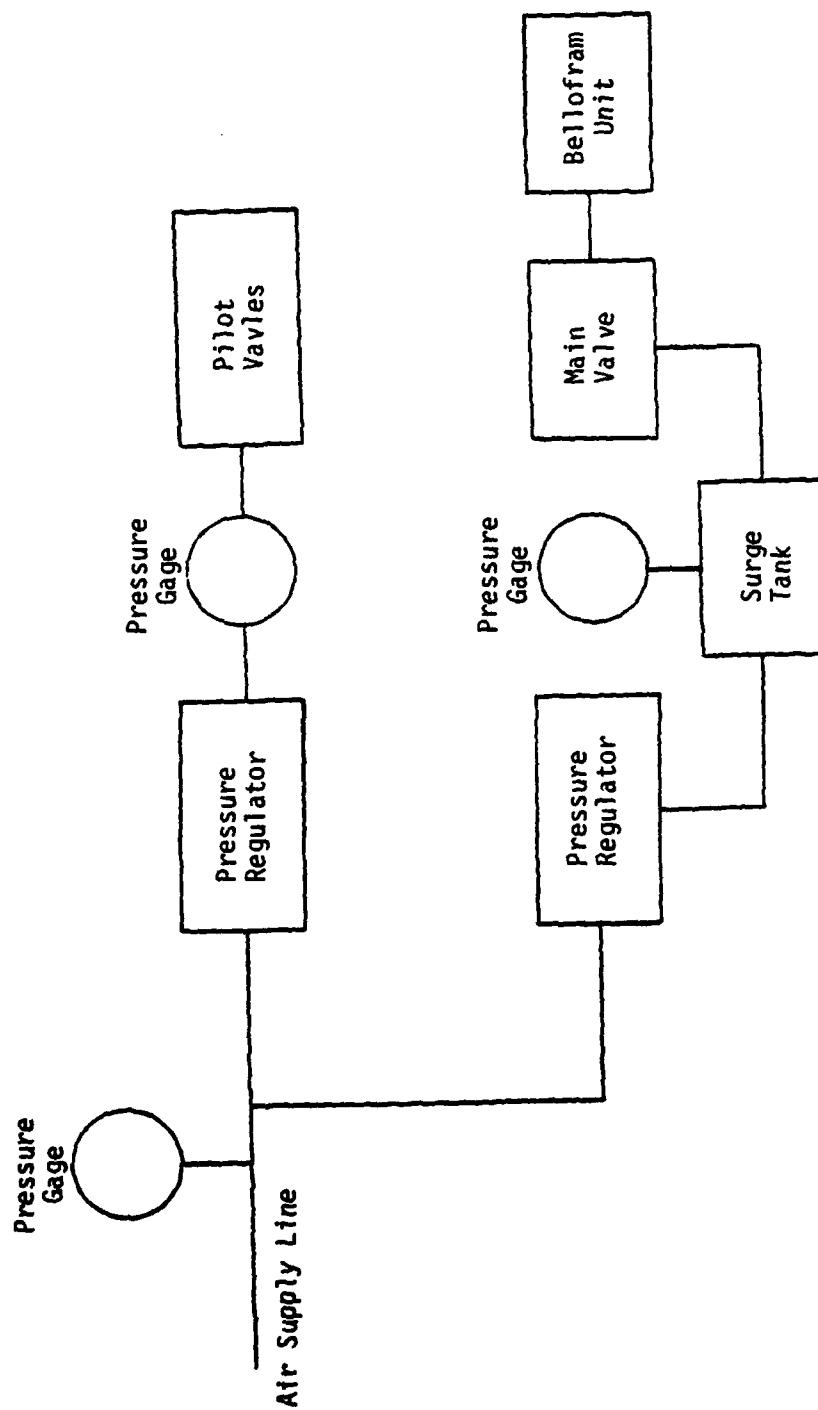


Figure 4-2. Load System Pneumatic Schematic.

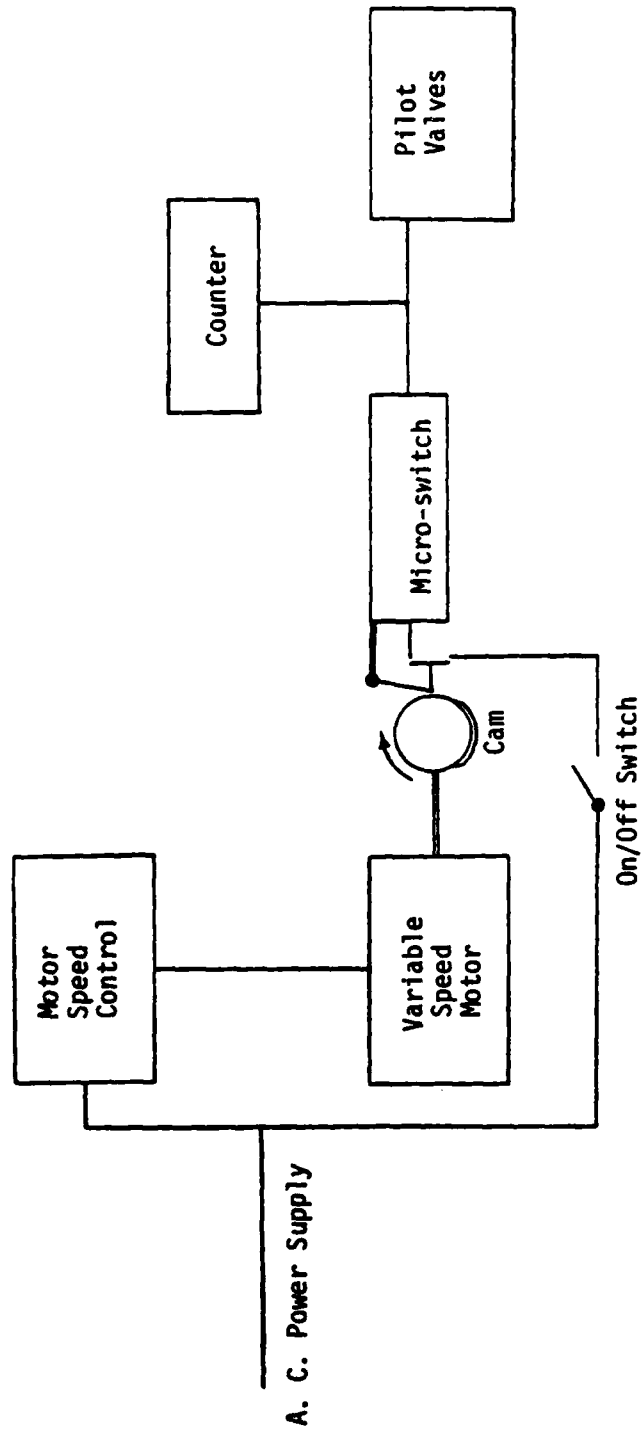


Figure 4-3. Load System Electrical-Mechanical Schematic.

switch. A 10 kip capacity universal flat load cell manufactured by Strainert, Bryn Mawr, Pennsylvania, was calibrated statically in a 20 kip capacity screw-type Tinius-Olsen loading machine. Load cell output was monitored on a Type 564 display storage oscilloscope manufactured by Tektronix, Inc., Portland, Oregon. The load cell and oscilloscope were then used to calibrate the dynamic loading system. To reduce the number of variables involved, the pilot valve pressure was set at 60 psi, any fluctuation in the volume of air entering the Bellofram unit was minimized by maintaining the piston position to within ± 0.5 inch of a selected reference point by inserting spacers between the piston and footing, and by utilizing either of two cam sizes. Thus, the calibration procedure considered only surge tank pressure and motor speed as variables, for a given cam size.

Two loadings were chosen for the model testing program, each with an essentially triangular load pulse which delivered a peak plate pressure of 70 psi. The first loading type, designated Type A, had a pulse length of 3.0 seconds, with the peak reached at 2.25 seconds, and a frequency of 10 applications per minute. The second type loading, designated Type B, had a pulse length of 0.2 second, reaching a peak at 0.07 second, and a frequency of 20 applications per minute. Figure 4-4 shows a sketch of the approximate time-pressure curves for the two loading types.

Subgrade Soil Preparation and Instrumentation

The subgrade soil (Dry Mill Fire Clay) was blended with the appropriate amount of water in a Type 30DP Lancaster Counter Current Batch Mixer, manufactured by Posey Iron Works, Inc., Lancaster,

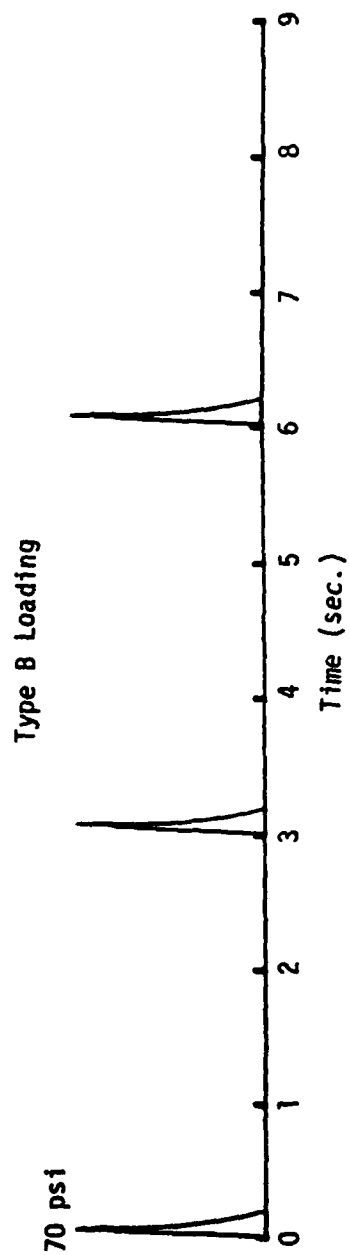
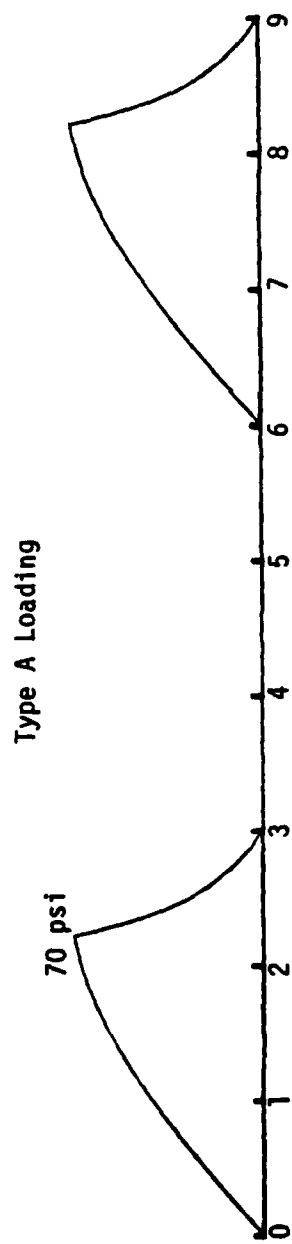


Figure 4-4. Time-Pressure Relationships for Loading Types A and B.

Pennsylvania. This mixer has a capacity of 300 pounds and uses scraping blades and a heavy roller to mix the soil and water in a circular steel container having a diameter of 2.5 feet and a height of one foot. Each batch contained 100 pounds of dry soil.

The material was placed in the test pit in clumps, 1.0-2.5 inches in diameter, to produce an uncompacted lift of 1.5-2.0 inches in height. The material was manually tamped using a two inch diameter steel plate attached to a rod, two feet in length, which served as a handle. Three to four coverages were made with this tamper, then the lift was further compacted with two to three coverages of a pneumatic tamper, having a base diameter of six inches.

The average moisture content of each compacted lift was determined in accordance with ASTM D-2216, sampling a minimum of five locations per lift. For each compacted lift, twenty penetration resistance (ASTM D-1558) determinations were made and the average value recorded. Penetration with the spring dynamometer was carried to a depth of 0.3 inch, rather than the recommended minimum depth of three inches. The shallow penetration resulted in minimum soil disturbance. The penetration resistance was used to estimate the unsoaked CBR, cone load, cone index, and vane shear strength of the subgrade utilizing the strength-density-moisture correlations developed by tests on compacted laboratory samples of the same soil, as described in Chapter III. The maximum ranges in average moisture content and penetration resistance for the lifts of any single model test were 2.3 percent (average value of 22.3 percent) and 5.8 psi (average value of 42.7 psi) respectively. The average density was determined by the drive cylinder method (ASTM

D-2937), making three tests during the construction process. The subgrade was constructed to produce a completed layer depth of 15.0 inches. The surface of the final lift was finished by a process of rolling (using a piece of aluminum stock six inches in diameter and 12 inches in length), scraping and troweling, to produce a smooth level surface. A reference beam was placed across the top of the test pit and the distance between the subgrade soil and this beam measured at intervals of two inches across the diameter of the pit to determine the initial surface profile.

Strain Sensors

The development of inductance strain sensors (89, 90) has made it possible to measure, quite accurately, a change in gage length between any two points in a soil mass. To determine the vertical and horizontal strains within the subgrade, Bison strain sensors, manufactured by Bison Instruments, Inc., Minneapolis, Minnesota, were placed at predetermined locations (Figure 4-5) in the soil mass. The sensors are disc-shaped coils of insulated wire coated with waterproof plastic. The coils are operated in pairs, with their separation related to the electromagnetic coupling between the two. When an electric current is passed through one coil, a magnetic flux field is formed in its vicinity, inducing a current in the second coil. As the coil spacing changes, the amplitude of the induced current also changes. A Bison Model 4101A instrument package was used to input current to one coil and measure the amplitude of the induction. Changes in amplitude reading were directly related to displacements between a coil pair by a simple calibration procedure. Appendix C provides a complete descrip-

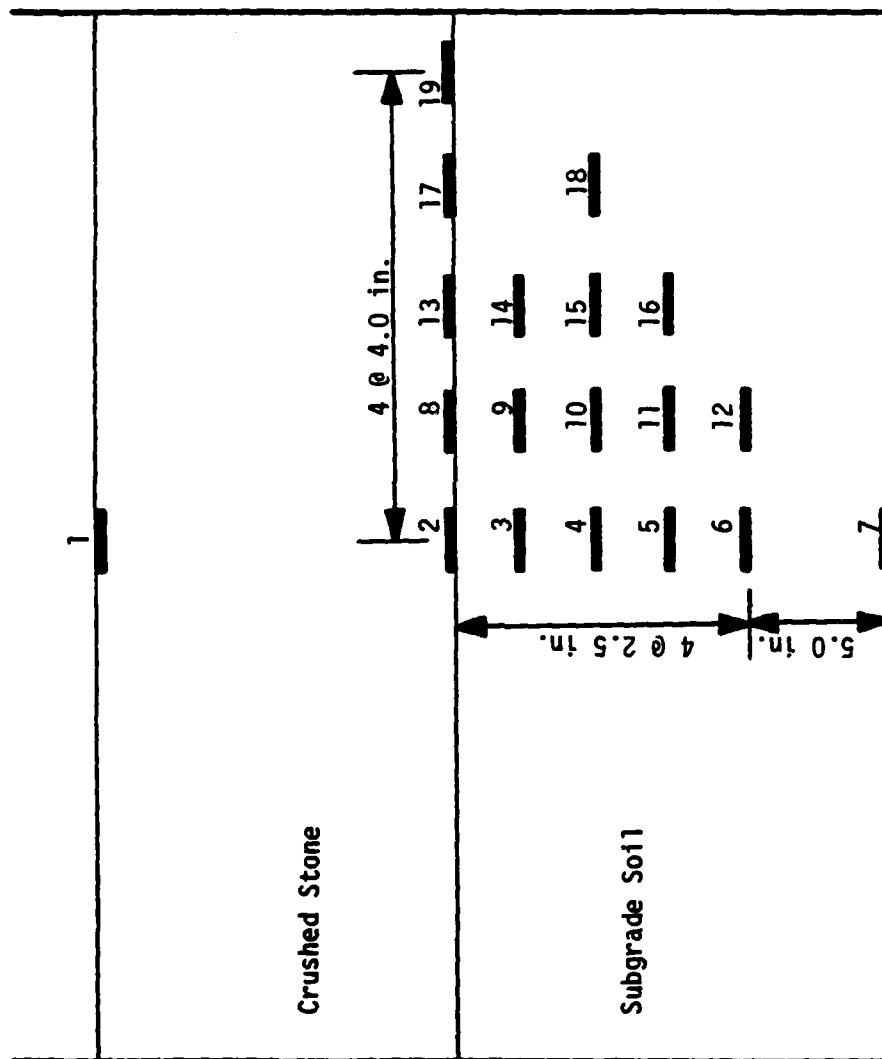


Figure 4-5. Bison Coil Designations and Initial Placement Configuration.

tion of the sensors and instrument package and the procedures for coil pair calibration and operation.

For sensor placement, the compacted subgrade lifts were completed to a height of approximately one inch above the desired coil location. A trench was then carefully excavated to the desired placement depth, wide enough to accommodate the sensors and their cable leads. All coils were carefully labeled and tagged for identification. A reference beam was placed across the top of the test pit. Radial distances were marked on this beam and a small plumb bob suspended at any desired radial coil location. The sensor was centered under the plumb bob and the vertical placement checked by measurement from the reference beam to the coil. A small hand level was used to insure no initial tilting of the coil from a horizontal plane, as "out-of-plane" rotations have been shown to adversely influence results (18, 90). The sensors were covered with the same material as previously removed, which was replaced carefully by hand and compacted to the same strength as the surrounding area. This was verified by making two or three penetration resistance determinations on the backfilled trench. The sensors were checked for proper operation prior to proceeding with construction of the next lift. The uppermost row of sensors was placed with the lower sides resting directly on the subgrade surface or fabric, as appropriate to the particular test. When placed on fabric, the sensors were epoxied into the desired positions.

Stress Cells

Deflecting diaphragm type pressure cells, having one active diaphragm, were used to monitor pressures within the subgrade soil

during a portion of the model testing program. These cells were designed and constructed by Intrapasart (50). The pressure was related, by a simple calibration procedure, to diaphragm deflection or strain, as measured by an etched foil electrical resistance diaphragm strain gage. Design considerations, cell details, and procedures for calibration and operation are provided in Appendix D.

Five pressure cells were utilized, placed in a single stack, centered under the edge of the footing, and placed along the diametral radius from the strain sensors. The vertical placement resulted in installation of a stress cell near the midpoint of each initial gage length separation of the strain sensor pairs on the footing centerline. This placement was found to have no effect on strain sensor output, which may be adversely affected by any metal within the zone of influence of the electromagnetic field (about two sensor diameters) coupling the coil pair. The cell placement was accomplished with the same installation technique as described previously for the strain sensors. The cells were installed with the diaphragm up, as suggested by Brown (24).

Fabric

When fabric was to be utilized at the interface of the subgrade and crushed stone layers, a circular piece of fabric, having a diameter of 48 inches, was cut, taking care to mark the machine direction (MD). For the two grades of Typar fabric, a silk-screen process was used to place a spider web like pattern on the fabric. This pattern was composed of 24 radial lines, each connected to the two adjoining radials at intervals of one inch, proceeding outward from the center to a radial

distance of 10 inches. Initial pattern gage lengths were measured with a caliper along perpendicular diameters (i.e., MD and XD). The fabric was centered on the subgrade surface, with the XD diameter parallel to that of the stress and strain instrumentation. Excess fabric, approximately six inches around the test pit perimeter, was turned up at the pit wall and the fabric worked to produce a smooth taut surface across the subgrade. This placement minimized sliding or pulling in of the fabric toward the rut center under loading, thereby enhancing the reinforcing effects of interface friction/adhesion and fabric tension. The final row of strain sensors was positioned by the procedures previously described, with each coil epoxied into position on the fabric.

When the Typar fabrics were utilized, three aluminum discs, approximately 0.5 inch in diameter, were also epoxied to the fabric. These were placed at radial distances of 12, 14, and 16 inches from the center of the test pit. A thin rod was welded to each disc. These rods were run along the fabric surface and extended to outside the test pit wall through holes drilled specifically for that purpose. The rods were each attached to a Model 25-441 dial gage stem by means of a set-screw. These dial gages were bolted to the exterior of the test pit wall. The dial gages had a range of one inch, being marked in divisions of 0.001 inch. The dial gages permitted determination of both absolute movement of and relative movement between those points on the fabric to which the discs were fastened. Any influence of these rods on system stiffness was not evaluated.

Epoxied items were held in place by dead weight loading and allowed to cure for a minimum period of one hour prior to proceeding

with placement of the crushed stone.

Sand

When sand was utilized as a separator layer between the subgrade soil and crushed stone, a compacted lift depth of one inch was produced by three to four coverages with a pneumatic tamper.

Crushed Stone

The crushed stone was placed in loose lifts of two to three inches. The material was manually tamped using a two inch diameter steel plate attached to a rod, two feet in length, which served as a handle. After three to four coverages of manual tamping, a pneumatic tamper, having a base diameter of six inches, was used to further compact the material in four to five coverages. Density was determined with a nuclear meter (ASTM D-2922), using a Model 1401 nuclear surface gage, connected to a Model 1651 portable scaler, both manufactured by Troxler Laboratories, Raleigh, North Carolina. This surface gage utilizes a radium-beryllium source. The equipment was calibrated by filling a box of known volume with crushed stone placed at the anticipated test pit lift thicknesses and densified with varying compactive efforts. Scaler readings, of two minutes duration, were taken and then the crushed stone weighed to produce calibration curves of scaler reading versus density. Outputs for crushed stone thicknesses of less than six inches were found to be markedly influenced by the underlying subgrade soil layer. Therefore, calibration curves for crushed stone thicknesses of both 3.0 and 4.5 inches, overlying the subgrade soil, and for stone thicknesses of six inches or greater were developed.

A minimum of three readings were taken for each three inches of compacted stone depth. The average scaler reading was used to determine density to the nearest 0.25 pcf. A density of 94-96 percent of the maximum dry density, as determined by Method C of ASTM D-698, was used throughout the model testing program. When the crushed stone layer was brought to the desired thickness for a particular test, a small recess was made for a Bison strain sensor to be placed on the footing centerline, with the top of the coil flush with the soil surface. The central area of the surface was then smoothed, filling irregularities with crushed stone fines, and the footing centrally placed and leveled.

Surface Instrumentation

With the footing in place, a series of spacers were positioned between the upper footing surface and the Bellofram unit piston. The lowest spacer was composed of two steel plates (3.0 x 2.75 x 0.5 inches in size), connected by four 0.5 inch diameter steel rods, 7.5 inches in length, at the plate corners. The lower plate had a centrally located hole, one inch in diameter, drilled through it to permit an L.V.D.T. core to be aligned directly on the centerline of the footing surface. The remaining spacers were cut from aluminum rod, two inches in diameter, providing a variety of lengths ranging from 0.5-4.0 inches. The spacers were utilized to maintain the Bellofram unit piston to within ± 0.5 inch of that position for which the loading system was calibrated.

Two pieces of aluminum angle (leg lengths of 1.75 inches) were placed across the top of the test pit and secured to it by clamps.

These angles were placed in a parallel configuration, perpendicular to a pit diameter, with each at a distance of seven inches from the footing centerline. A Model SS207 L.V.D.T. was suspended inside the lowest spacer, being securely cantilevered from one angle section by a clamp and rod arrangement.

This L.V.D.T. was manufactured by the G. L. Collins Corp., Long Beach, California, and had a linear range of ± 1.0 inch. The L.V.D.T. was powered by a 24 volt D.C. output source and was connected to a Model 60-1300 Twin-Viso Strip Chart Recorder manufactured by the Sanborn Company, Cambridge, Massachusetts. This strip chart recorder is equipped with a Model 60-1600 control panel and a Model 64-300A D.C. amplifier.

The L.V.D.T. was calibrated using a plexiglas mounting fixture equipped with a micrometer to measure movements to the nearest 0.001 inch, with output recorded to an appropriate scale on the strip chart recorder. Both transient and permanent deflections could be monitored using the L.V.D.T. Three Model E81S dial gages were cantilevered from the aluminum angle and utilized to measure the permanent deflections of three equally spaced points on the footing perimeter. These dial gages were marked in divisions of 0.001 inch and had a range of six inches. The footing centerline deflection was determined as the average of the deflections indicated by these dial gages.

Test Procedure

Once all soil, equipment, and instrumentation were in place, initial determinations of strain sensor pair separations were made and

initial dial gage readings taken. The variable speed motor was set at the desired speed and pilot valve and surge tank pressures raised to the appropriate levels. Loading of the footing was then begun. To determine the load cycle-cumulative permanent deformation relationships, the loading was stopped and changes in surface dial gage readings determined at appropriate load cycle intervals.

Transient surface movement for any load cycle of interest was monitored by the L.V.D.T. Stress cell readings were taken of each cell for a period of two to three load cycles during the beginning stages of the test. The readings were taken beginning with the uppermost cell, proceeding in order to the lowest cell in the stack. This procedure was utilized to minimize any uncertainty concerning cell position due to cell translation and rotation under load application. For several tests, stress cell readings were also taken during the latter stages of the test. In such cases, final stress cell positions and orientations were carefully determined during excavation of the subgrade soil.

Model tests were carried to a maximum of 20,000 load cycles or a minimum surface deflection of 4.5 inches, whichever occurred first. When loading was completed, final dial gage readings were taken and final soil strain sensor pair separations determined. In some instances, especially on the footing centerline, individual vertical coil pairs moved so close together as to be out of range, thus prohibiting an amplitude reading for that pair. By a leapfrog procedure, working toward a sensor pair within range, it remained possible to determine the final pair separations in any column.

Excavation

Surface instrumentation and the footing were removed once all necessary final readings were taken. The crushed stone was scooped from the test pit and stored in covered barrels. Care was taken not to damage the fabric, nor disturb the subgrade soil surface during removal of the stone. Any epoxied instrumentation was freed from the fabric and the fabric then removed from the test pit. For the Typar fabrics, final gage lengths were measured with a caliper along the same diameters as were initially measured. These measurements, in conjunction with the changes in dial gage readings for the discs, permitted determination of the average fabric deformation at intervals between the load centerline and a radial distance of 16 inches. A reference beam was placed across the top of the test pit and the distance between the subgrade soil and this beam measured at intervals of two inches across the diameter of the pit to determine the final surface profile. The readings were taken along the same diameter for which the initial surface profile was determined. This procedure permitted determination of the changes in the subgrade soil surface profile caused by load application. The subgrade soil was excavated, broken into medium size clumps (i.e., 4-6 inches in diameter), placed in barrels, sprinkled lightly with water, and covered with plastic sheeting for storage between tests. All instrumentation was cleaned, checked for proper operation, and repaired or replaced as necessary to prepare for further testing.

CHAPTER V

MODEL TEST PROGRAM RESULTS

Scale model tests were conducted on a series of AS and AFS pavement systems, to investigate the beneficial effects of fabrics in reducing rutting caused by repeated load applications. A summary of the test program is provided in Table 5-1, indicating crushed stone depth, interfacial membrane type, the unsoaked CBR of the subgrade soil, and test number designation. The suffix A or B of the test number designation indicates use of the corresponding load type during a particular test (i.e., 3.0 seconds pulse duration at 10 cpm and 0.2 second pulse duration at 20 cpm respectively). Pertinent material properties for all tests are detailed in Tables 5-2 through 5-8.

Selected model test program results are summarized in Tables 5-9 through 5-15. These include: the stress ratio (i.e., vertical stress on load centerline at subgrade soil surface computed from Boussinesq theory, divided by subgrade soil vane shear strength); the numbers of load cycles to achieve total rut depths of two, three, and four inches; the number of load cycles at the end of the test (i.e., a maximum of 20,000 load cycles or at a point subsequent to achieving a minimum surface deflection of 4.5 inches, whichever occurred first); and the permanent vertical deformations (per layer and total) on the footing centerline at the end of the test. A full range of deformation data is presented in Appendices E through H. Pressure cell data, in tabular

form, are provided in Appendix I, while stress ratio-permanent deformation-load cycle relationships are presented in graphical form in Appendix J.

Table 5-2. Summary of Pertinent Material Properties, Test Group I.

Test No.	1B	2B	3B	4B	5B	6B
Membrane Type	None	T-3401	None	T-3401	None	T-3401
Crushed Stone Depth (in.)	6.0	6.0	7.5	7.5	9.0	9.0
Crushed Stone Density (pcf) (ASTM D-2922)	131.00	131.75	132.50	132.25	131.50	133.25
Subgrade Depth (in.)	15.0	15.0	15.0	15.0	15.0	15.0
Subgrade Dry Density (pcf) (ASTM D-2937)	100.14	99.78	100.81	100.46	100.63	99.48
Subgrade Moisture Content (%) (ASTM D-2216)	23.22	23.62	23.57	22.94	23.08	23.63
Penetration Resistance (psi) (ASTM D-1558)	12.64	12.73	13.92	13.30	12.97	13.32
*Unsoaked CBR	0.38	0.39	0.43	0.41	0.40	0.41
*Cone Load (lb.)	5.83	5.90	6.79	6.33	6.08	6.34
*Cone Index	11.66	11.79	13.59	12.65	12.15	12.68
*Vane Shear Strength (psi)	2.95	2.96	3.11	3.03	2.99	3.04

*Estimated from Strength Correlations (Ref. Table 3-1).

Table 5-4. Summary of Pertinent Material Properties, Test Group II
(Stone Thickness = 7.0 in.).

Test No.	13A	13B	14A	15A	15B	16A	17A	18A
Membrane Type	None	None	Sand	T-3401	T-3401	T-3601	M-140	B-C22
Crushed Stone Depth (in.)	7.0	7.0	7.0	7.0	7.0	7.0	7.0	7.0
Crushed Stone Density (pcf) (ASTM D-2922)	130.75	133.50	130.75	133.50	130.75	131.25	131.00	130.75
Subgrade Depth (in.)	15.0	15.0	15.0	15.0	15.0	15.0	15.0	15.0
Subgrade Dry Density (pcf) (ASTM D-2937)	102.95	101.96	102.12	103.82	101.92	102.16	102.63	103.76
Subgrade Moisture Content (%) (ASTM D-2216)	21.35	22.29	21.74	22.05	22.31	21.91	21.46	21.53
Penetration Resistance (psi) (ASTM D-1558)	23.67	23.35	23.25	26.68	22.55	21.58	23.50	23.83
*Unsoaked CBR	0.82	0.81	0.81	0.94	0.78	0.74	0.82	0.83
*Cone Load (lb.)	14.14	13.89	13.82	16.40	13.29	12.56	14.01	14.26
*Cone Index	28.27	27.79	27.64	32.80	26.58	25.12	28.02	28.51
*Vane Shear Strength (psi)	4.37	4.33	4.32	4.76	4.23	4.10	4.35	4.39

*Estimated from Strength Correlations (Ref. Table 3-1).

Table 5-5. Summary of Pertinent Material Properties, Test Group II
(Stone Thickness = 10.0 in.).

Test No.	19A	19B	20A	20B	21A
Membrane Type	None	None	T-3401	T-3401	T-3601
Crushed Stone Depth (in.)	10.0	10.0	10.0	10.0	10.0
Crushed Stone Density (pcf) (ASTM D-2922)	133.50	131.00	133.00	131.75	132.75
Subgrade Depth (in.)	15.0	15.0	15.0	15.0	15.0
Subgrade Dry Density (pcf) (ASTM D-2937)	103.15	102.83	101.92	103.76	102.37
Subgrade Moisture Content (%) (ASTM D-2216)	20.36	21.89	22.56	21.66	22.57
Penetration Resistance (psi) (ASTM D-1558)	25.66	26.20	24.78	27.04	22.67
*Unsoaked CBR	0.90	0.93	0.87	0.96	0.78
*Cone Load (lb.)	15.63	16.04	14.97	16.67	13.38
*Cone Index	31.27	32.08	29.94	33.35	26.77
*Vane Shear Strength (psi)	4.63	4.70	4.51	4.81	4.24

*Estimated from Strength Correlations (Ref. Table 3-1).

Table 5-6. Summary of Pertinent Material Properties, Test Group II
(Stone Thickness = 13.0 in.).

Test No.	22A	23A	24A	25A
Membrane Type	None	T-3401	M-140	B-C22
Crushed Stone Depth (in.)	13.0	13.0	13.0	13.0
Crushed Stone Density (pcf) (ASTM D-2922)	131.00	133.50	130.75	131.75
Subgrade Depth (in.)	15.0	15.0	15.0	15.0
Subgrade Dry Density (pcf) (ASTM D-2937)	103.39	104.14	102.39	103.85
Subgrade Moisture Content (%) (ASTM D-2216)	20.70	21.74	20.89	21.53
Penetration Resistance (psi) (ASTM D-1558)	27.75	27.42	24.00	24.00
*Unsoaked CBR	0.99	0.97	0.84	0.84
*Cone Load (1b.)	17.21	16.96	14.38	14.38
*Cone Index	34.42	33.92	28.77	28.77
*Vane Shear Strength (psi)	4.90	4.85	4.41	4.41

*Estimated from Strength Correlations (Ref. Table 3-1).

Table 5-7. Summary of Pertinent Material Properties, Test Group III.

Test No.	26B	27B	28B	29B	30B	31B
Membrane Type	None	T-3401	None	T-3401	None	T-3401
Crushed Stone Depth (in.)	3.0	3.0	4.5	4.5	6.0	6.0
Crushed Stone Density (pcf) (ASTM D-2922)	133.25	132.75	131.25	133.00	132.75	132.25
Subgrade Depth (in.)	15.0	15.0	15.0	15.0	15.0	15.0
Subgrade Dry Density (pcf) (ASTM D-2937)	104.72	105.15	105.49	105.37	106.23	104.16
Subgrade Moisture Content (%) (ASTM D-2216)	19.68	20.15	19.68	20.49	19.95	20.33
Penetration Resistance (psi) (ASTM D-1558)	41.76	42.10	42.72	43.28	45.97	39.10
*Unsoaked CBR	1.55	1.56	1.59	1.61	1.72	1.44
*Cone Load (lb.)	27.76	28.02	28.48	28.90	30.93	25.76
*Cone Index	55.52	56.03	56.96	57.81	61.86	51.51
*Vane Shear Strength (psi)	6.70	6.75	6.83	6.90	7.25	6.36

*Estimated from Strength Correlations (Ref. Table 3-1).

Table 5-8. Summary of Pertinent Material Properties,
Test Group IV.

Test No.	32B	33B
Membrane Type	None	T-3401
Crushed Stone Depth (in.)	3.0	3.0
Crushed Stone Density (pcf) (ASTM D-2922)	131.25	130.75
Subgrade Depth (in.)	15.0	15.0
Subgrade Dry Density (pcf) (ASTM D-2937)	108.72	108.21
Subgrade Moisture Content (%) (ASTM D-2216)	18.43	18.62
Penetration Resistance (psi) (ASTM D-1558)	63.81	62.71
*Unsoaked CBR	2.43	2.39
*Cone Load (lb.)	44.36	43.54
*Cone Index	88.73	87.07
*Vane Shear Strength (psi)	9.55	9.41

*Estimated from Strength Correlations (Ref.
Table 3-1).

Table 5-9. Summary of Selected Model Test Program Results, Test Group ..

Test No.	Membrane Type	Depth of Stone (in.)		Vane Shear Strength (psi)		Stress Ratio	Load Repetitions (c)				Permanent Deformations (c)	
							N ₂	N ₃	N ₄	N _f	Stone (in.)	Subgrade (in.)
1B	None	6.0	2.95	2.95	6.75	6.75	20	40	68	100	0.62	4.30
2B	T-3401	6.0	2.96	2.96	6.72	6.72	46	140	320	700	1.91	3.06
3B	None	7.5	3.11	3.11	4.50	4.50	48	140	310	600	1.20	3.61
4B	T-3401	7.5	3.03	3.03	4.62	4.62	120	290	875	3000	2.28	2.42
5B	None	9.0	2.99	2.99	3.38	3.38	170	480	1100	2000	1.80	2.99
6B	T-3401	9.0	3.04	3.04	3.32	3.32	850	4500	--	20000	1.94	1.82
												3.76

(a) Estimated from Strength Correlations (Ref. Table 3-1).

(b) Ref. Page 92 for Definition.

(c) N₂, N₃, N₄ = Number of Load Repetitions to 2, 3, and 4 inches of Total Cumulative Permanent Deformation. N_f = Number of Load Repetitions at Test Termination.(d) At N_f.

Table 5-10. Summary of Selected Model Test Program Results, Test Group II
(Stone Thickness = 4.5 in.).

Test No.	Membrane Type	Depth of Stone (in.)	(a) Vane Shear Strength (psi)		(b) Stress Ratio	(c) Load Repetitions				(c) Cumulative Permanent Deformations		
						N ₂	N ₃	N ₄	N _f	Stone (in.)	Subgrade (in.)	Total (in.)
7A	None	4.5	4.54	6.55		2	4	6	10	0.73	4.00	4.73
7B	None	4.5	4.63	6.41		13	20	60	100	0.76	4.03	4.79
8A	Sand	4.5	4.83	6.14		2	4	7	12	0.51	4.24	4.75
9A	T-3401	4.5	4.48	6.62		19	76	200	300	2.04	2.99	5.03
9B	T-3401	4.5	4.59	6.46		50	220	500	700	2.00	2.96	4.96
10A	T-3601	4.5	4.45	6.67		22	76	220	600	1.28	3.47	4.75
11A	M-140	4.5	4.12	7.20		5	16	39	80	0.67	4.12	4.79
12A	B-C22	4.5	4.23	7.01		7	20	44	80	0.83	3.92	4.75

(a) Estimated from Strength Correlations (Ref. Table 3-1).

(b) Ref. Page 92 for Definition.

(c) N₂, N₃, N₄ = Number of Load Repetitions to 2, 3, and 4 inches of Total Cumulative Permanent Deformation. N_f = Number of Load Repetitions at Test Termination.

(d) At N_f.

Table 5-11. Summary of Selected Model Test Program Results, Test Group II
(Stone Thickness = 7.0 in.).

Test No.	Membrane Type	Depth of Stone (in.)	Vane Shear Strength (psi)	Stress Ratio (b)	Load Repetitions (c)				Cumulative Permanent Deformations (d)	
					N ₂	N ₃	N ₄	N _f	Stone (in.)	Total (in.)
13A	None	7.0	4.37	3.59	9	14	18	20	1.29	4.70
13B	None	7.0	4.37	3.63	140	300	570	900	1.37	4.68
14A	Sand	7.0	4.32	3.63	11	29	62	100	1.13	4.75
15A	T-3401	7.0	4.76	3.30	80	330	1300	4000	2.28	4.73
15B	T-3401	7.0	4.23	3.71	260	610	1700	6000	2.45	4.74
16A	T-3601	7.0	4.10	3.83	90	540	2500	7000	1.82	4.79
17A	M-140	7.0	4.35	3.61	27	90	250	400	1.46	4.78
18A	B-C22	7.0	4.39	3.58	28	60	160	600	1.48	4.75

(a) Estimated from Strength Correlations (Ref. Table 3-1).

(b) Ref. Page 92 for Definition.

(c) N₂, N₃, N₄ = Number of Load Repetitions to 2, 3, and 4 inches of Total Cumulative Permanent Deformation. N_f = Number of Load Repetitions at Test Termination.

(d) At N_f.

Table 5-12. Summary of Selected Model Test Program Results, Test Group II
(Stone Thickness = 10.0 in.).

Test No.	Membrane Type	(a)		Stress Ratio (b)	(c)				(d)	
		Depth of Stone (in.)	Vane Shear Strength (psi)		N ₂	N ₃	N ₄	N _f	Stone (in.)	Cumulative Permanent Deformations Subgrade (in.) Total (in.)
19A	None	10.0	4.63	1.83	1700	--	--	20000	1.75	0.82 2.57
19B	None	10.0	4.70	1.81	2800	--	--	20000	1.65	0.88 2.53
20A	T-3401	10.0	4.51	1.88	7000	--	--	20000	1.25	0.90 2.15
20B	T-3401	10.0	4.81	1.77	--	--	--	20000	1.07	0.64 1.71
21A	T-3601	10.0	4.24	2.00	12000	--	--	20000	1.27	0.78 2.05

(a) Estimated from Strength Correlations (Ref. Table 3-1).

(b) Ref. Page 92 for Definition.

(c) N₂, N₃, N₄ = Number of Load Repetitions to 2, 3, and 4 inches of Total Cumulative Permanent Deformation. N_f = Number of Load Repetitions at Test Termination.

(d) At N_f.

Table 5-13. Summary of Selected Model Test Program Results, Test Group II
(Stone Thickness = 13.0 in.).

Test No.	Membrane Type	(a)		(b)	(c)			(d)	
		Depth of Stone (in.)	Vane Shear Strength (psi)		Stress Ratio	N ₂	N ₃ N ₄ N _f	Permanent Stone Deformations (in.)	Cumulative Subgrade Total Deformations (in.)
22A	None	13.0	4.90	1.06	9500	--	-- 20000	1.65	0.49 2.14
23A	T-3401	13.0	4.85	1.07	--	--	-- 20000	1.00	0.59 1.59
24A	M-140	13.0	4.41	1.18	--	--	-- 20000	1.32	0.53 1.85
25A	B-C22	13.0	4.41	1.18	--	--	-- 20000	1.49	0.30 1.79

(a) Estimated from Strength Correlations (Ref. Table 3-1).

(b) Ref. Page 92 for Definition.

(c) N₂, N₃, N₄ = Number of Load Repetitions to 2, 3, and 4 inches of Total Cumulative Permanent Deformation. N_f = Number of Load Repetitions at Test Termination.

(d) At N_f.

Table 5-14. Summary of Selected Model Test Program Results, Test Group III.

Test No.	Membrane Type	(a)		(b)				(c)				(d)	
		Depth of Stone (in.)	Vane Shear Strength (psi)	Stress Ratio	N_2	N_3	N_4	N_f	Permanent Stone (in.)	Subgrade (in.)	Total (in.)		
268	None	3.0	6.70	6.76	16	31	52	80	0.39	4.65	5.04		
278	T-3401	3.0	6.75	6.71	59	110	170	200	1.38	3.28	4.66		
288	None	4.5	6.83	4.34	68	180	380	600	0.90	3.74	4.64		
298	T-3401	4.5	6.90	4.30	360	1150	2150	3000	1.84	2.87	4.71		
308	None	6.0	7.25	2.74	280	770	2500	10000	1.61	3.11	4.72		
318	T-3401	6.0	6.36	3.13	175	600	2250	7000	2.33	2.38	4.71		

(a) Estimated from Strength Correlations (Ref. Table 3-1).

(b) Ref. Page 92 for Definition.

(c) N_2 , N_3 , N_4 = Number of Load Repetitions to 2, 3, and 4 inches of Total Cumulative Permanent Deformation. N_f = Number of Load Repetitions at Test Termination.(d) At N_f .

Table 5-15. Summary of Selected Model Test Program Results, Test Group IV.

Test No.	Membrane Type	Depth of Stone (in.)		Vane Shear Strength (psi)	Stress Ratio (b)	Load Repetitions (c)				Cumulative Permanent Deformations (d)	
						N ₂	N ₃	N ₄	N _f	Stone (in.)	Subgrade Total (in.)
32B	None	3.0	3.0	9.55	4.74	25	60	120	200	0.49	4.25
33B	T-3401	3.0	3.0	9.41	4.81	58	150	280	400	1.03	3.78
											4.81

(a) Estimated from Strength Correlations (Ref. Table 3-1).

(b) Ref. Page 92 for Definition.

(c) N₂, N₃, N₄ = Number of Load Repetitions to 2, 3, and 4 inches of Total Cumulative Permanent Deformation. N_f = Number of Load Repetitions at Test Termination.(d) At N_f.

CHAPTER VI

DISCUSSION OF TEST RESULTS

Rutting

The model test results showed rutting to be influenced, to some extent, by each of the test program variables. These variables included: subgrade soil strength, thickness of the crushed stone layer, load pulse duration, placement of a membrane at the aggregate-subgrade interface and the type of membrane thus utilized. Although not tested, variables such as aggregate gradation and strength, anchorage of the membrane ends, and variations in the load pulse frequency, shape, and/or magnitude might also be expected to influence system response.

Subgrade Strength Influence

The rutting within all sets of test systems, with the tests of a given set identical except for subgrade strength, was observed to decrease as subgrade strength increased. There were six sets of tests, three of both AS and AFS systems, in which strength was the independent variable. Figures 6-1 through 6-4 depict the influence of subgrade strength on rutting in selected test sets. For comparable reference values of subgrade strength and increases thereto, the sets of AS system tests displayed greater relative improvements in permanent deformation characteristics than the corresponding sets of AFS system tests. The improvements displayed by both AS and AFS systems were greater when the subgrade strength increases were made from weaker reference systems.

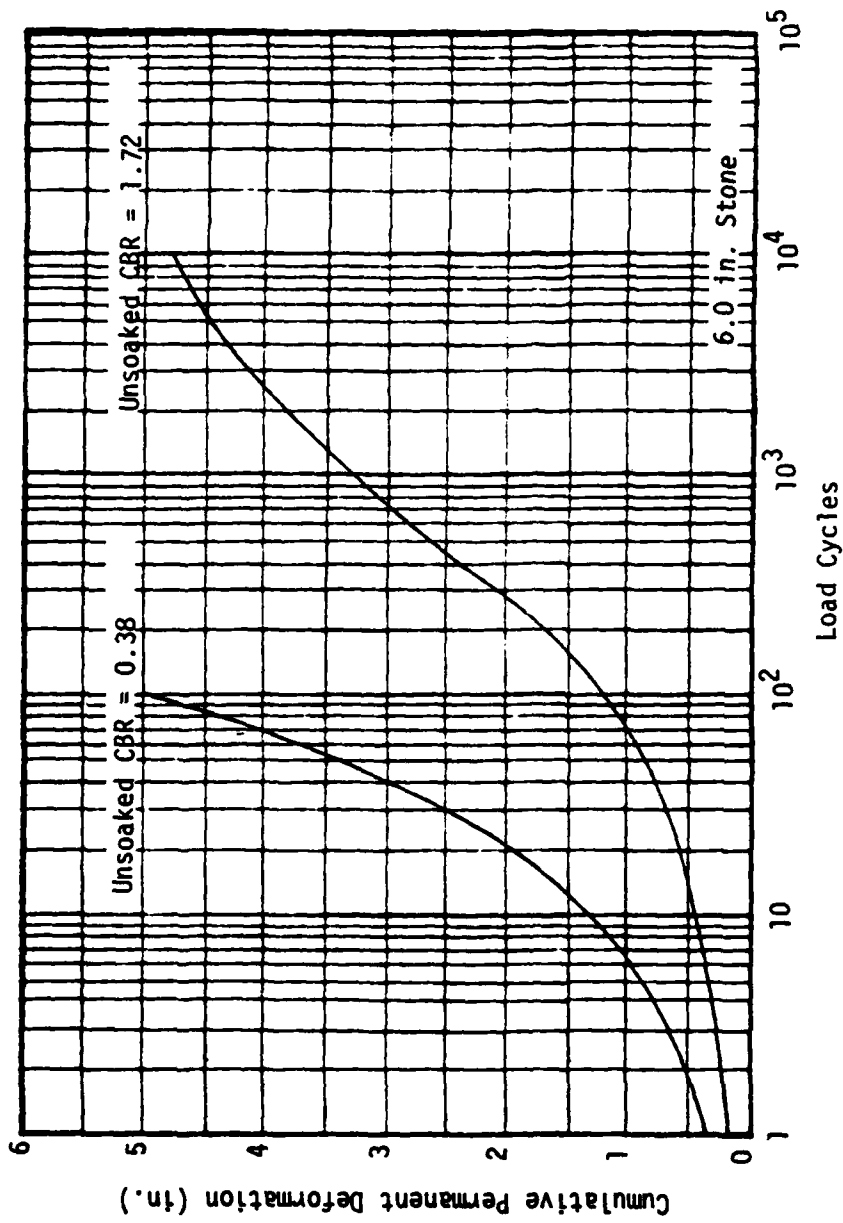


Figure 6-1. Influence of Subgrade Strength on Load Cycle-Cumulative Permanent Deformation Relationship in AS Systems (Tests 1B/30B).

Note: Data points omitted to avoid clutter - refer to Appendix E for data and individual test plots.

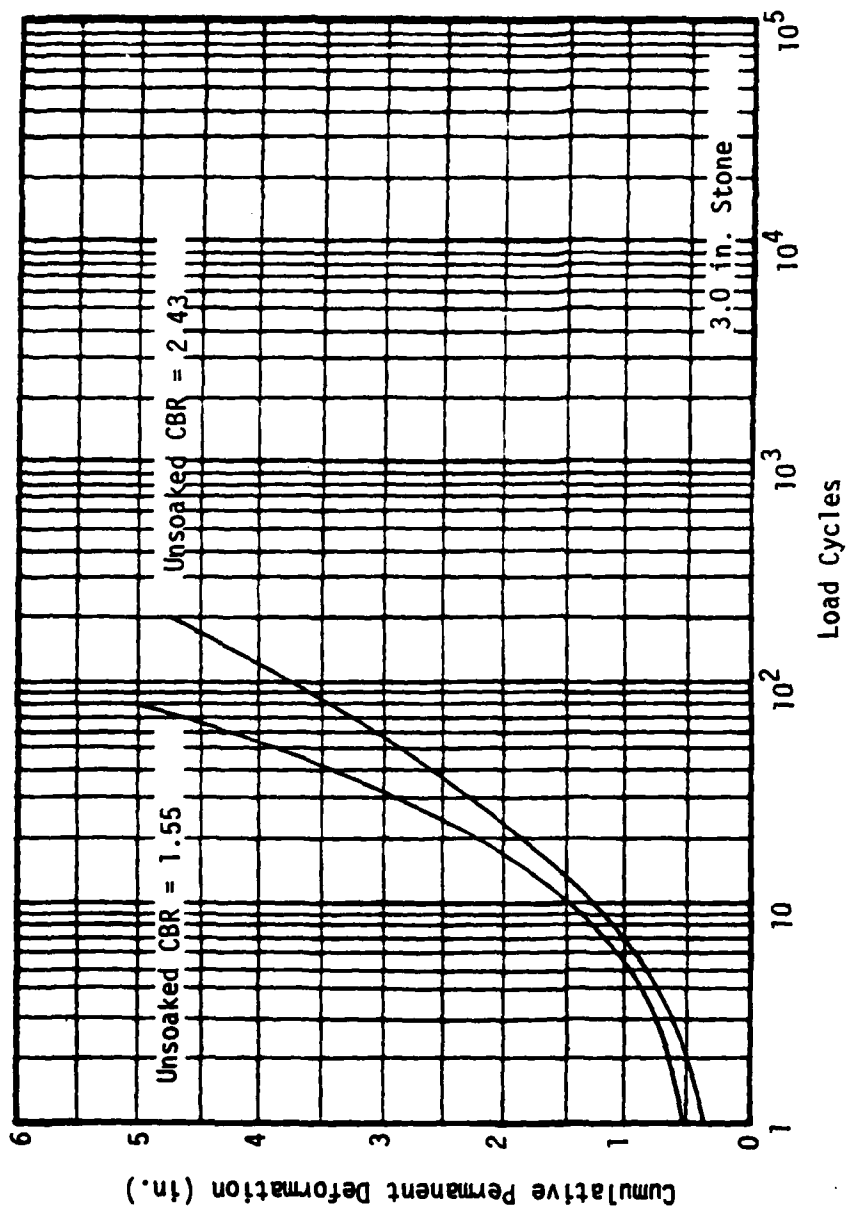


Figure 6-2. Influence of Subgrade Strength on Load Cycle-Cumulative Permanent Deformation Relationship in AS Systems (Tests 26B/32B).

Note: Data points omitted to avoid clutter - refer to Appendix E for data and individual test plots.

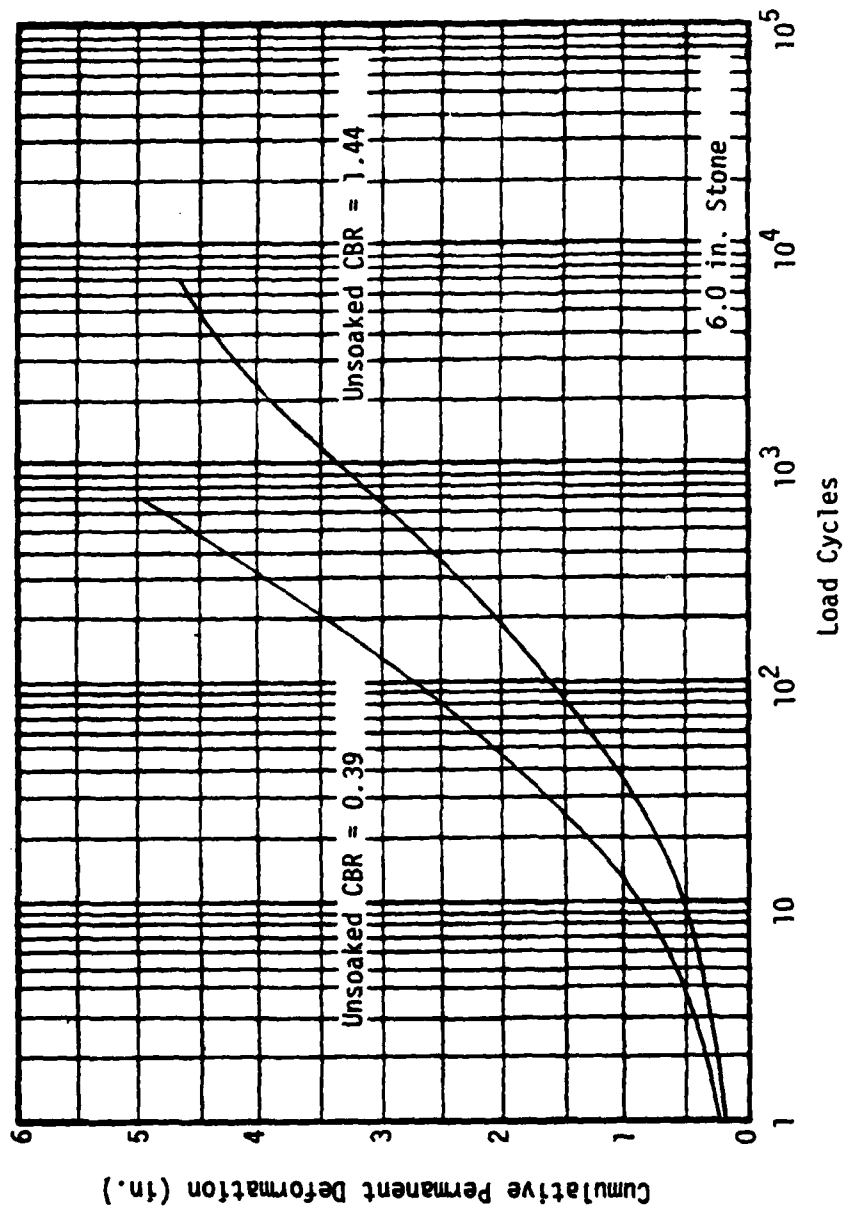


Figure 6-3. Influence of Subgrade Strength on Load Cycle-Cumulative Permanent Deformation Relationship in T-3401 Reinforced AFS Systems (Tests 2B/31B).

Note: Data points omitted to avoid clutter - refer to Appendix E for data and individual test plots.

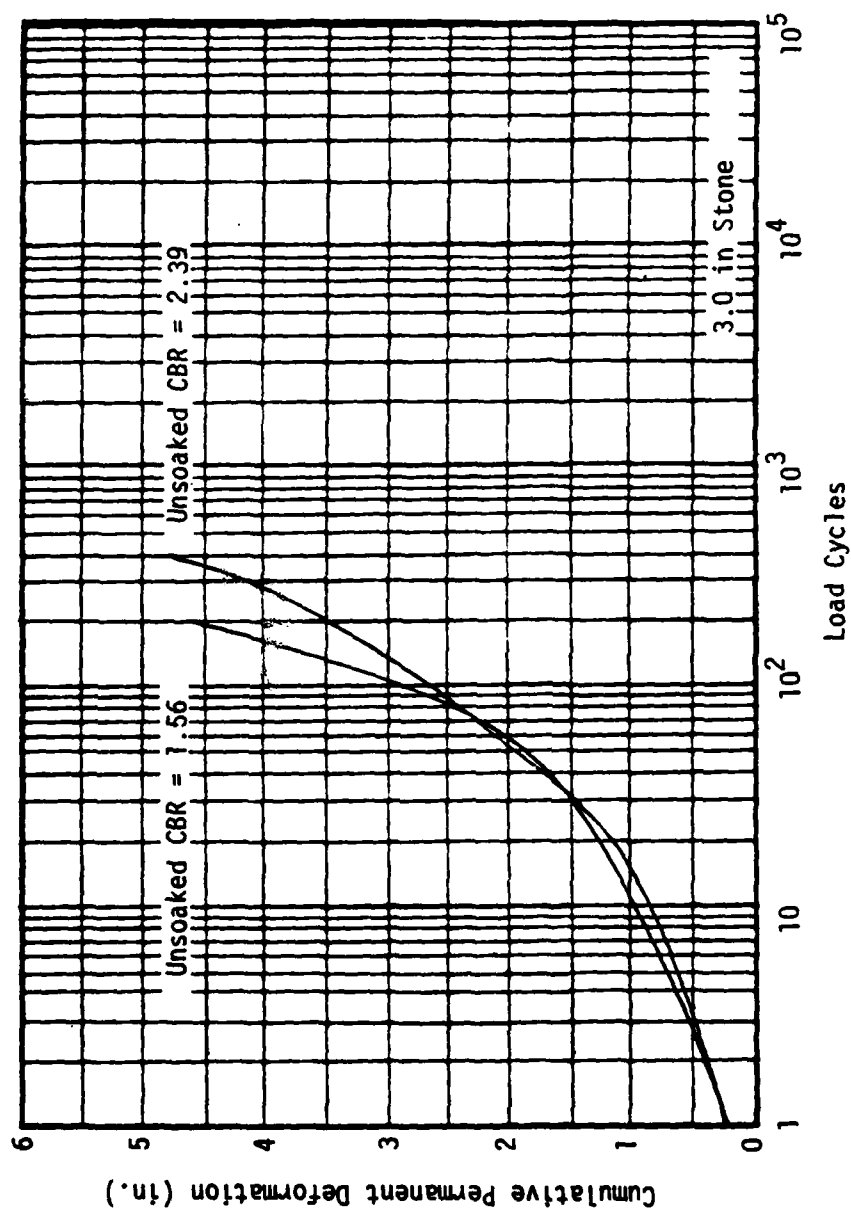


Figure 6-4. Influence of Subgrade Strength on Load Cycle-Cumulative Permanent Deformation Relationship in T-3401 Reinforced AFS Systems (Tests 27B/33B).

Note: Data points omitted to avoid clutter - refer to Appendix E for data and individual test plots.

The relative improvements in rutting response were taken as the percentage increases in load repetitions required to achieve rut depths of two, three, and four inches. Within any given test set, improvements were more pronounced at higher deformation levels. Corresponding AS and AFS systems were those model tests in which the strengths and thicknesses of the soil layers were identical, with only a membrane at the soil layer interface differentiating the systems.

Crushed Stone Layer Thickness Influence

For all sets of test systems in which the thickness of the crushed stone layer was the independent variable, rutting decreased as the aggregate thickness increased. There were 12 such test sets in the model test program: seven sets of AFS systems, four sets of AS systems, and one set with a one inch thick layer of sand at the aggregate-subgrade interface. The influence of crushed stone thickness on rutting is depicted in Figure 6-5 for a representative set of AS system tests and in Figure 6-6 for the corresponding set of AFS system tests. The relative improvements in rutting resistance were comparable in all corresponding test sets, for identical increases in aggregate thickness, with no clear distinction evident between the improvements displayed by AS and AFS systems. Within any given test set, the relative improvements in rutting characteristics were more pronounced at higher deformation levels.

Subgrade Strength and Crushed Stone Layer Thickness Combined Influence

A convenient means of reducing the number variables involved when analyzing their influences on system rutting response, is through the use of the stress ratio concept (i.e., vertical stress on the load

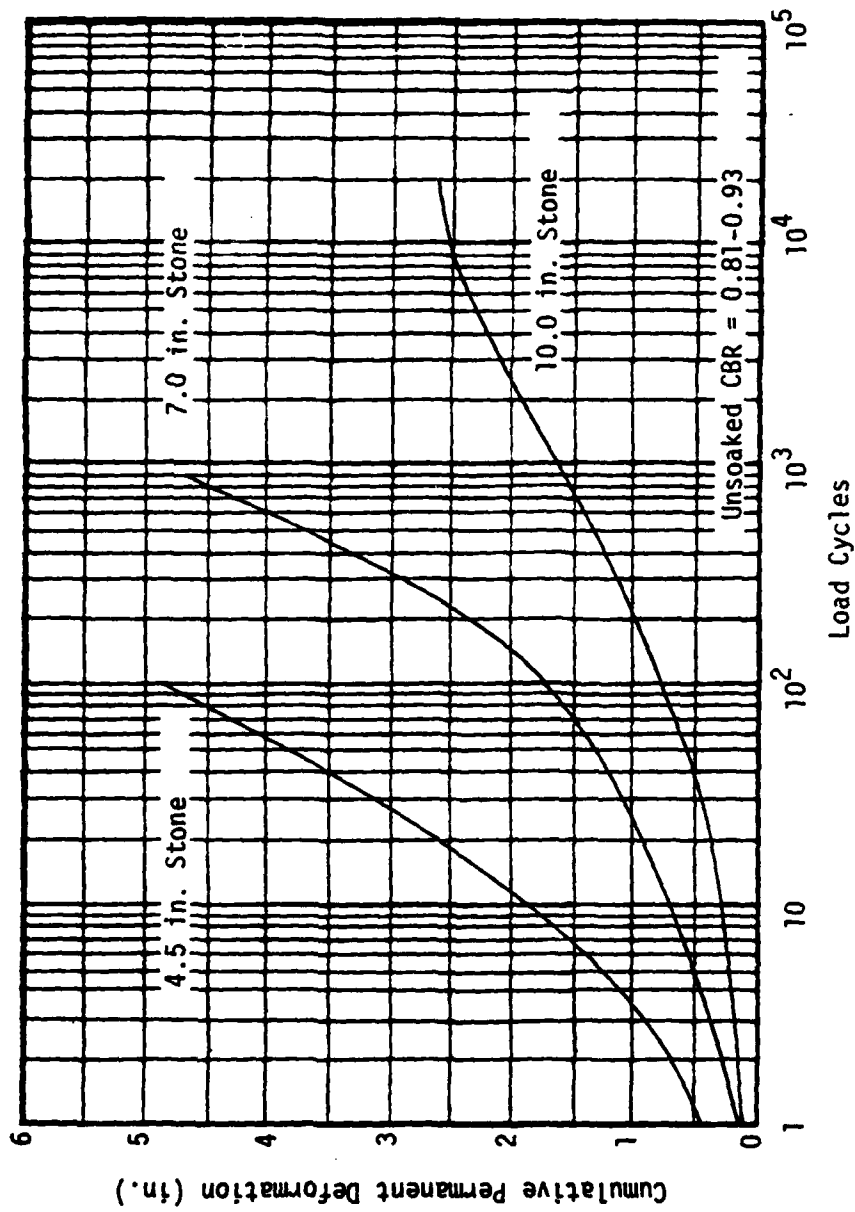


Figure 6-5. Influence of Crushed Stone Layer Thickness on Load Cycle-Cumulative Permanent Deformation Relationship in AS Systems (Tests 7B/13B/19B).

Note: Data points omitted to avoid clutter - refer to Appendix E for data and individual test plots.

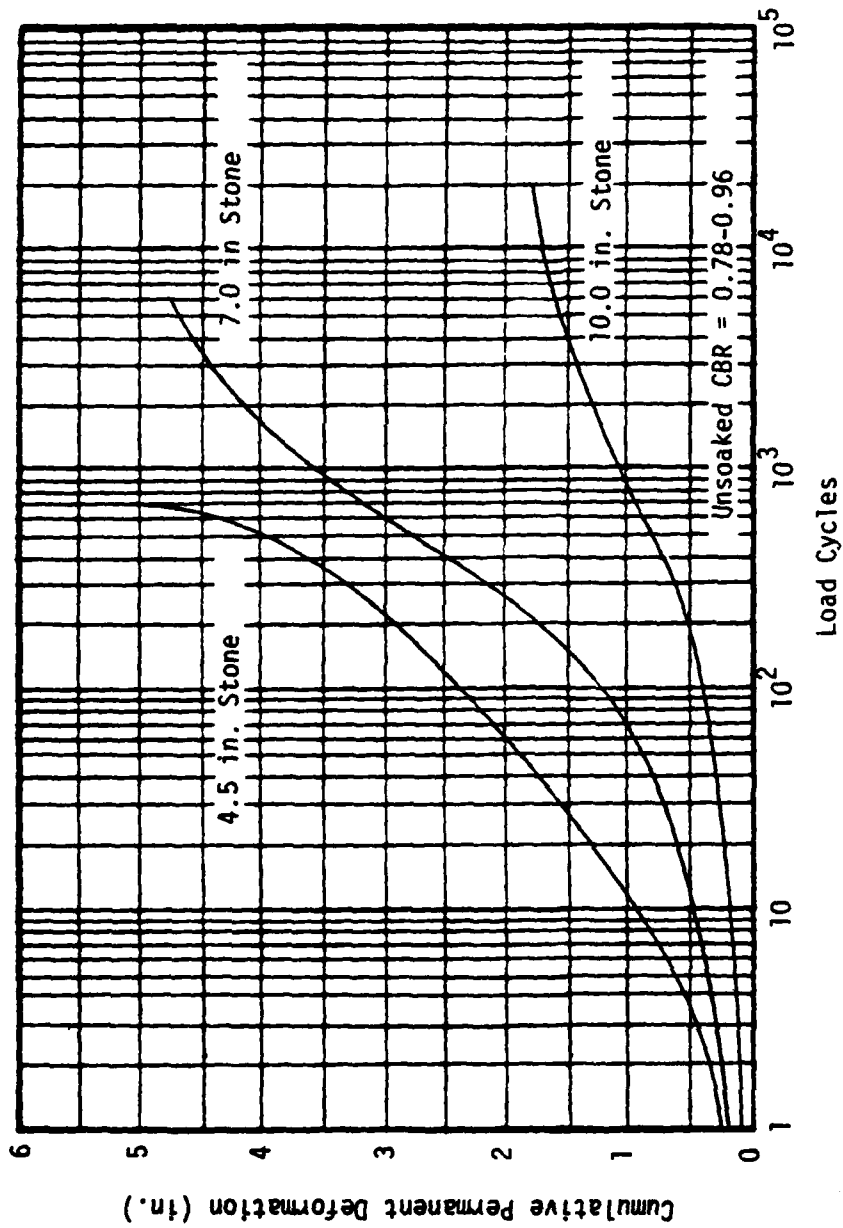


Figure 6-6. Influence of Crushed Stone Layer Thickness on Load Cycle-Cumulative Permanent Deformation Relationship in T-3401 Reinforced AFS Systems (Tests 9B/15B/20B).

Note: Data points omitted to avoid clutter - refer to Appendix E for data and individual test plots.

centerline at the subgrade surface computed by Boussinesq theory, divided by the vane shear strength of the subgrade soil). The stress ratio thus combines, for a given loading condition, the influence of subgrade strength (i.e., vane shear strength) and that of the crushed stone layer thickness (i.e., Boussinesq vertical stress at base of aggregate layer). For a given load pulse and membrane type, relationships were developed between stress ratio, cumulative permanent deformation and load cycles, with these relationships having the following forms:

At a given load cycle:

$$RD = C_1 (SR)^{C_2} \quad (6-1)$$

At a given rut depth:

$$\text{Log } N = C_3 (SR)^{C_4} \quad (6-2)$$

where RD = rut depth, inches

SR = stress ratio at subgrade surface

N = load cycles

C_1 = regression analysis constants.

Plots of stress ratio versus rut depth after 10 , 10^2 , and 10^3 load cycles, and load cycles versus stress ratio, for rut depths of two, three, and four inches, are presented in Appendix J. Typical plots of each type relationship are provided in Figures 6-7 and 6-8 respectively. Stress ratio relationships, after a certain number of load cycles or at a given rut depth, provide a simple means of comparing, at a given instant, the influence of membrane type for a given load pulse or the

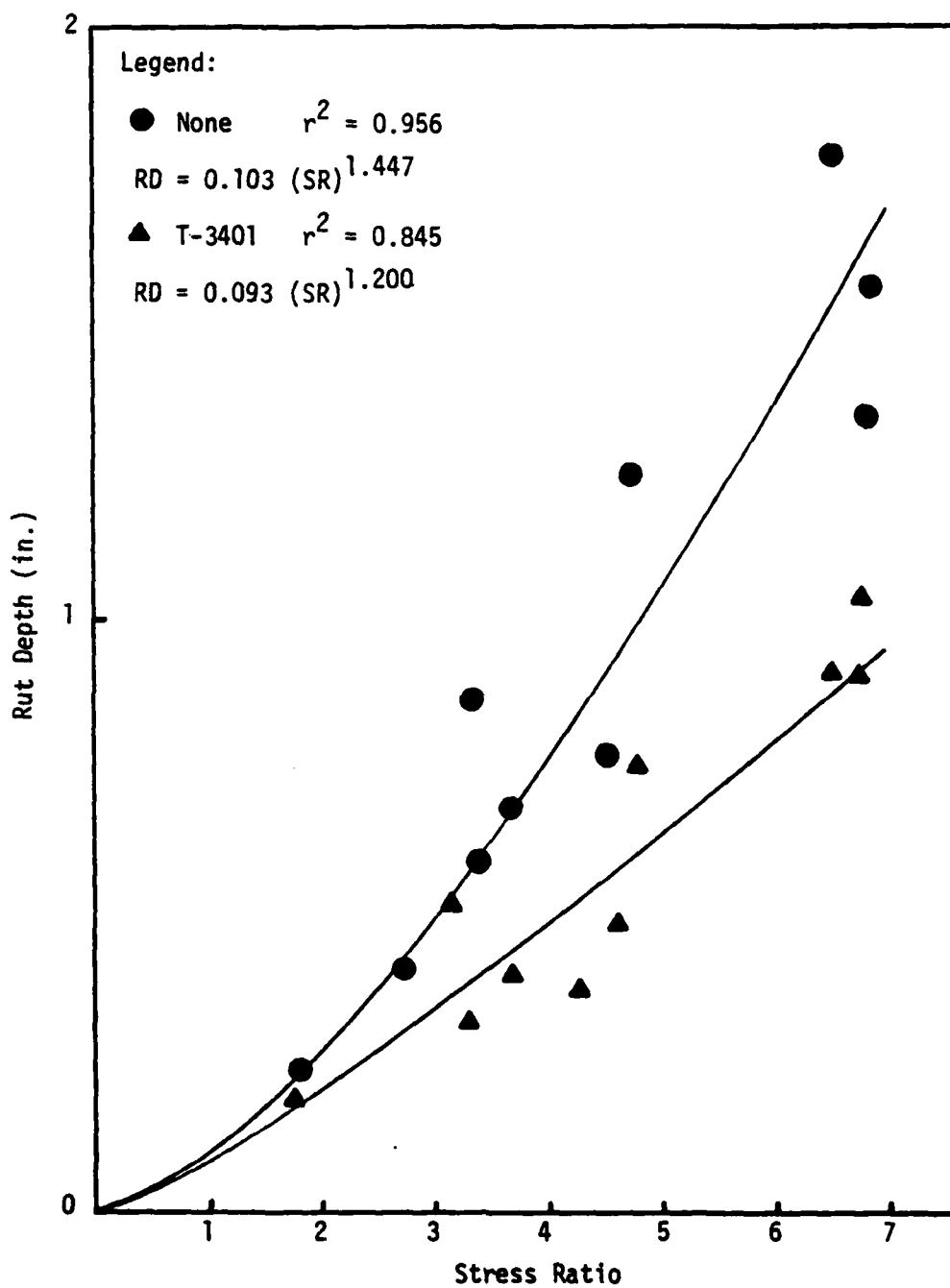


Figure 6-7. Stress Ratio-Rut Depth Relationships for AS and Typar 3401 Reinforced AFS Systems for 10 Load Cycles, Type B Loading.

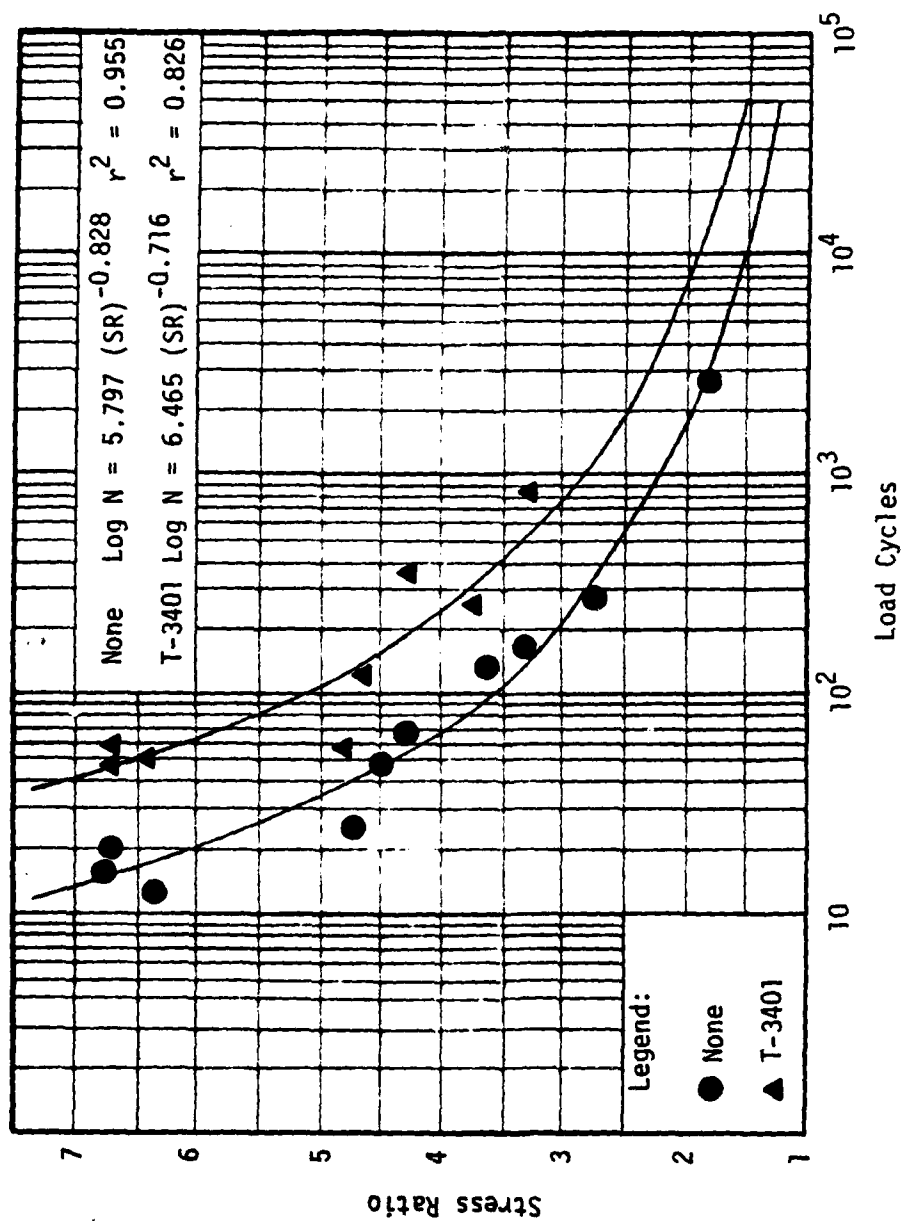


Figure 6-8. Load Cycle-Stress Ratio Relationships for AS and Typar 3401 Reinforced AFS Systems for 2 in. Rut, Type B Loading.

influence of load pulse on a given membrane type.

Load Pulse Duration Influence

Load pulse duration was the independent variable in three test sets of both AS and AFS systems. In all cases, for a given number of load repetitions, rutting decreased as the load pulse duration decreased. This trend was to be expected on the basis of viscoelastic considerations. The influence of load pulse duration on rutting response is depicted in Figure 6-9 for three sets of AS systems and in Figure 6-10 for the corresponding sets of AFS systems. The relative improvements in rutting characteristics were generally greater in the test sets of AS systems, than in the corresponding sets of AFS systems. In low deformation systems, the differences between AS and AFS system tests were less distinct. Within given test sets of AS systems, the relative improvements in permanent deformation characteristics were more pronounced at higher deformation levels, while the reverse was true within sets of AFS systems.

Membrane Inclusion and Type Influence

Inclusion of a membrane at the aggregate-subgrade interface improved rutting resistance within all sets of test systems in which such an inclusion was the independent variable. There were 25 pairs of tests within which the tests were differentiated by a membrane inclusion. The relative improvements in rutting characteristics produced by the membrane were greater at high deformation levels. This trend was anticipated in that higher deformations are more effective in producing fabric straining and the resultant development of fabric tensile stresses required by the mechanisms of confinement/reinforcement and alteration

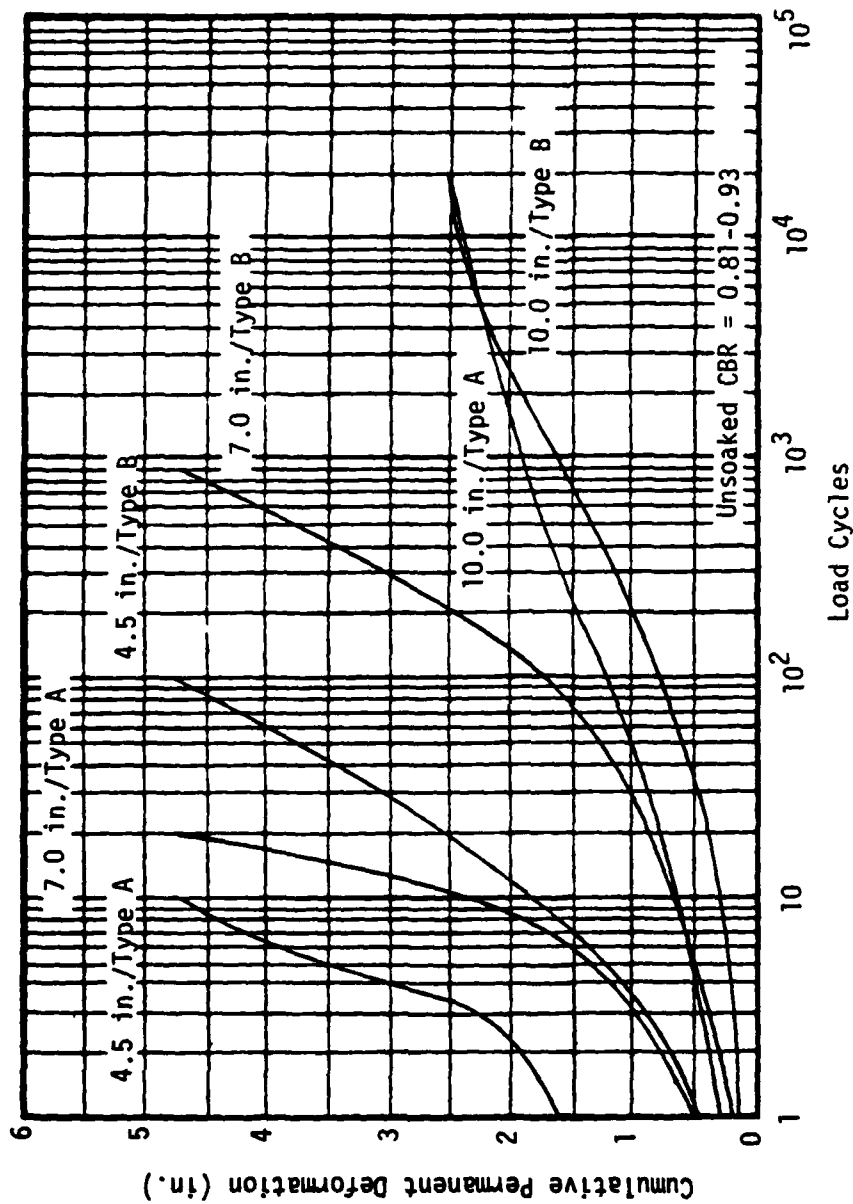


Figure 6-9. Influence of Load Pulse Duration on Load Cycle-Cumulative Permanent Deformation Relationships in AS Systems (Tests 7A/7B; 13A/13B; 19A/19B).

Note: Data points omitted to avoid clutter - refer to Appendix E for data and individual test plots.

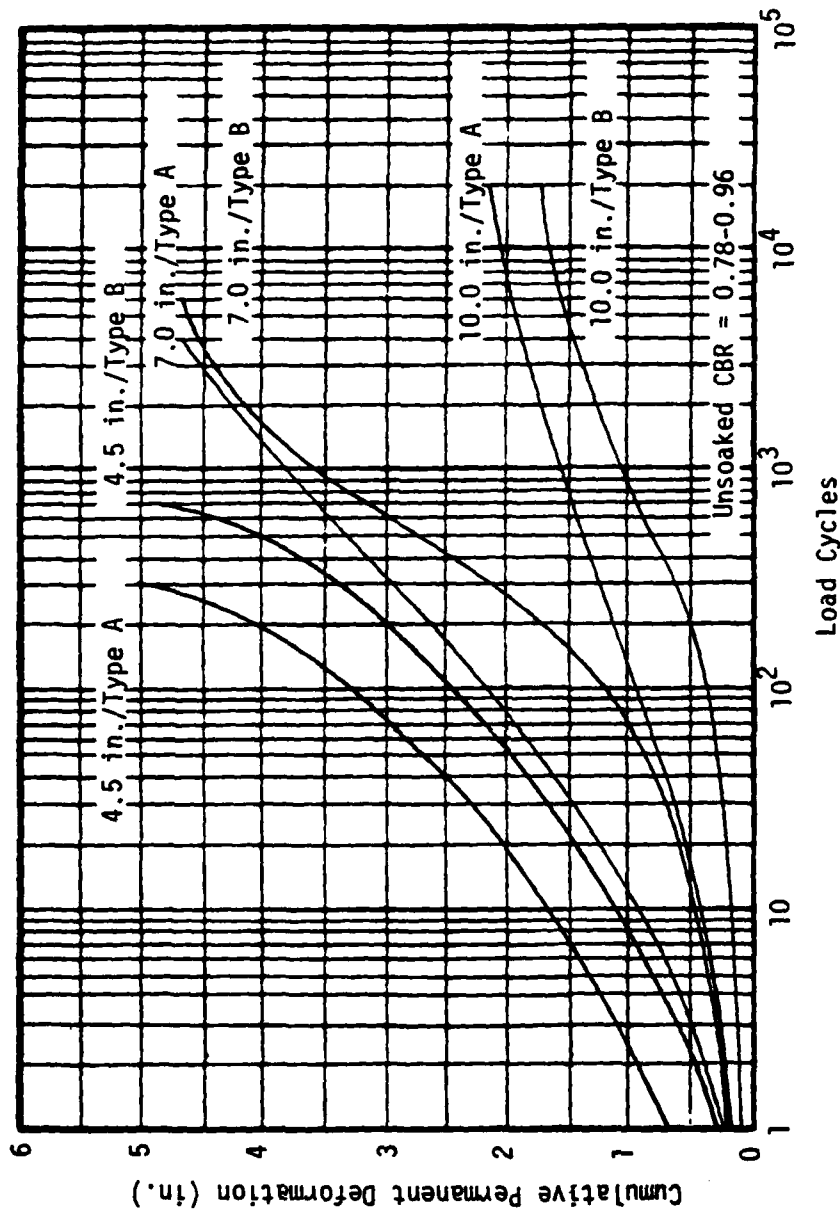


Figure 6-10. Influence of Load Pulse Duration on Load Cycle-Cumulative Permanent Deformation Relationships in T-3401 Reinforced AFS Systems (Tests 9A/9B; 15A/15B; 20A/20B).

Note: Data points omitted to avoid clutter - refer to Appendix E for data and individual test plots.

of the subgrade failure mode. The influence of a membrane inclusion is depicted in Figure 6-11 for three pairs of tests, with the AFS systems utilizing Typar 3401 fabric. There were four sets of tests within which the tests were identical except for the type of membrane utilized. The influence of membrane type is depicted in Figure 6-12 for a representative test set. In analyzing the effectiveness of the membrane types, the tests within each set were compared on the basis of the relative improvements in permanent deformation characteristics achieved by each of the various membranes, versus rutting in the corresponding AS system. The least effective interlayer was a one inch layer of sand. The sand layer would not serve to reinforce the aggregate layer as would a fabric membrane, the primary advantages of a sand layer being to promote separation of the aggregate and subgrade soil and to facilitate drainage. That inclusion of sand layer did not produce a significant improvement in the rutting resistance is understandable upon study of the crushed stone and subgrade soil gradations and the filter criteria of Equations (3-2) through (3-4) (i.e., two particle migration and one permeability criterion respectively). For the crushed stone-subgrade soil:

Particle Migration:

$$\frac{D_{15}(\text{Stone})}{D_{85}(\text{Subgrade})} = 4.13 < 5 \quad (3-2)$$

$$\frac{D_{50}(\text{Stone})}{D_{50}(\text{Subgrade})} = 530.4 \gg 25 \quad (3-3)$$

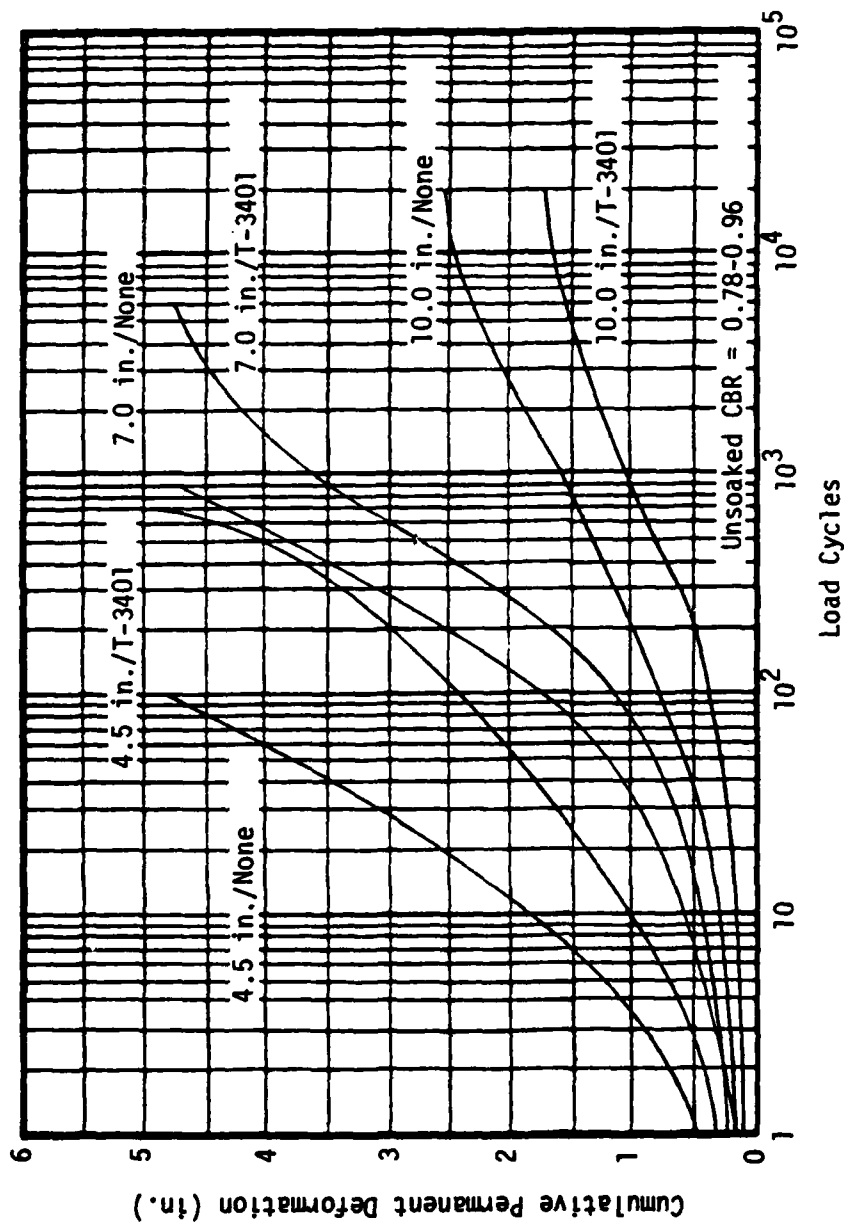


Figure 6-11. Influence of T-3401 Membrane Inclusion on Load Cycle-Cumulative Permanent Deformation Relationships (Tests 7B/9B; 13B/15B; 19B/20B).

Note: Data points omitted to avoid clutter - refer to Appendix E for data and individual test plots.

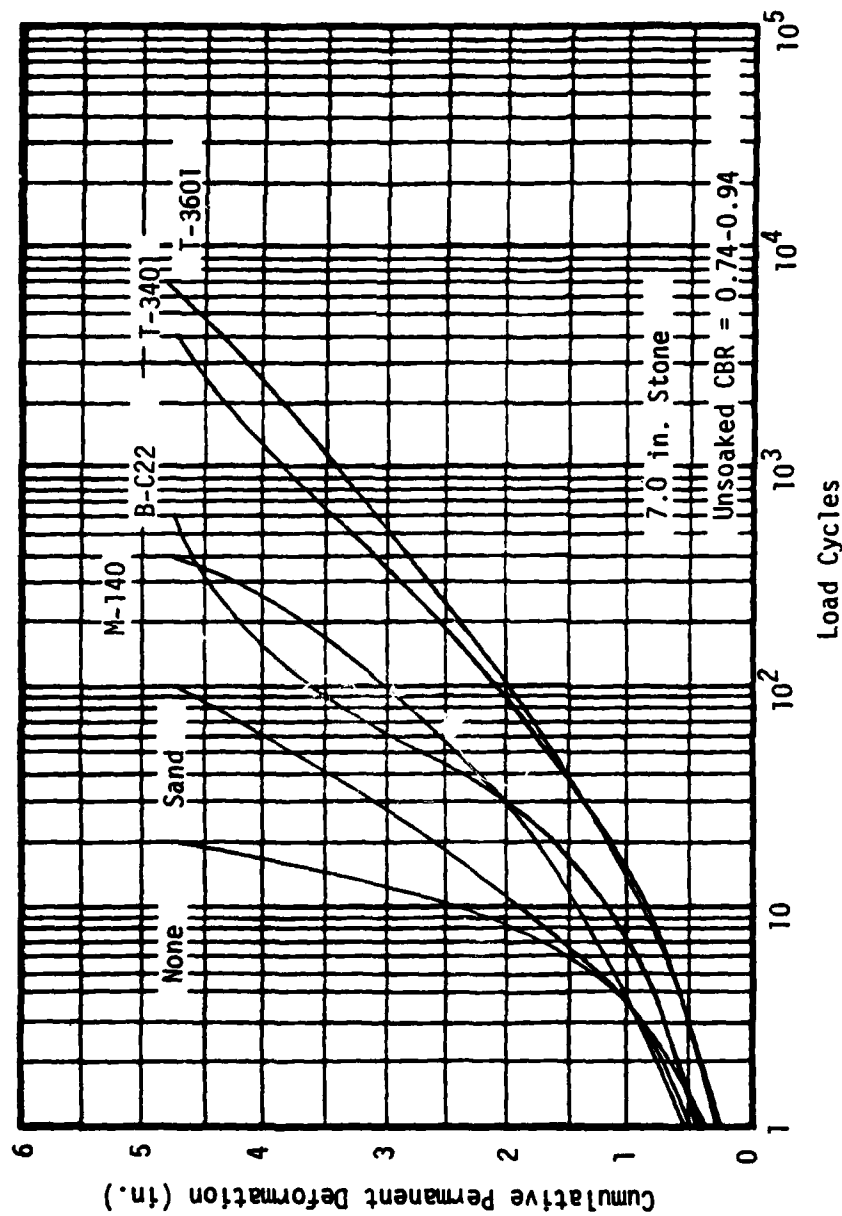


Figure 6-12. Influence of Membrane Inclusion Type on Load Cycle-Cumulative Permanent Deformation Relationship (Tests 13A/14A/15A/16A/17A/18A).

Note: Data points omitted to avoid clutter - refer to Appendix E for data and individual test plots.

Permeability:

$$\frac{D_{15}(\text{Stone})}{D_{15}(\text{Subgrade})} = 1550.0 \gg 4 \quad (3-4).$$

The first of the two particle migration criteria is satisfied, as is the permeability criterion. The gradation of the stone is unacceptable with regard to the second particle migration criterion (i.e., 530.4 versus 25); however, meeting the first particle migration criterion is more critical. It has been proposed (97) that an adequate filter material need only satisfy the first particle migration criterion and the permeability criterion. Therefore, the crushed stone itself was an adequate filter for the subgrade soil and hence the minimal benefits observed due to the sand layer inclusion were not unexpected. A sand filter might be expected to produce greater benefits when used in a system with an open graded aggregate, which would not, by itself, serve to filter the subgrade.

The Typar 3601 fabric consistently produced slightly better rutting resistance than did the Typar 3401 fabric. Mirafi 140 and Bidim C22 fabrics produced virtually identical rutting resistance, both products being less effective than either weight of Typar fabric. The relative effectiveness of the various membrane types may also be noted by comparison of the stress ratio-cumulative permanent deformation-load cycle relationships of Appendix J.

Observed Rutting Versus Anticipated Response

Rutting in excess of four inches, within 10^2 load cycles, is anticipated (100) for stress ratios of 3.3c and 6.0c in AS and AFS

systems respectively. Corresponding stress ratio values of 2.8c and 5.0c are believed to limit rutting to two inches after 10^3 load cycles.

Three considerations must be made in comparing the model test program results to these anticipated field responses. First, the load pulse durations must be comparable; second, the influence of subsurface instrumentation (i.e., Bison strain sensors and pressure cells) on rutting response must be accounted for; and third, the model scaling influence must be considered.

The Type A loading (i.e., pulse length of 3.0 seconds) corresponds to a vehicle velocity of less than one mile per hour (10), while the Type B loading (i.e., pulse length of 0.2 second) corresponds to a vehicle velocity of 10-15 miles per hour. Thus, the Type B loading provided a better representation of probable field conditions.

To determine the influence of instrumentation on rutting response, two test sets were conducted (82), within which tests were identical except for the presence of subsurface instrumentation in one-half of the tests. The approximate stress ratios of the test sets were 3.5 and 6.0, with the sets comprised of seven and four tests respectively. Rutting was carried to a minimum depth of five inches. A comparison was then made, between the instrumented and non-instrumented tests of each set, of the load cycles required to achieve one, two, three, four, and five inches of rutting. The instrumented tests consistently took longer to achieve a given rut depth, with the average ratio of load cycle values between instrumented and non-instrumented tests being 2.4.

To initially estimate the range of model scaling influence, elastic and plastic theory solutions, as well as experimental results, were

viewed, keeping in mind that the actual systems were typically experiencing large deformations. The model test program approximated a half-scale radius of typical field tire contact areas. The contact pressure utilized in the model test program (i.e., 70 psi) was comparable to common field values.

For constant contact pressures, geometrically similar systems, and identical soil properties, elastic theory (26, 65, 77, 121, 122) indicates static load deformations in the prototype, compared to those in the model, will be in direct proportion to the corresponding ratio of loaded area dimensions.

Utilizing a bearing capacity analysis for layered systems (i.e., dense sand on soft clay) presented by Meyerhof (68), for geometrically similar systems and identical soil properties, the bearing capacities of the prototypes would average 1.43 times those of the half-scale models of this study, with a range of 1.07-2.0 (Appendix K). For equal contact pressures and assuming similar relationships between load and settlement (expressed as a percentage of footing diameter), deformations in the prototypes will be less than twice those in the models.

From tests of square footings, relationships have been proposed (102, 121) for extrapolating settlements between load tests on a one foot square plate and a full size footing. For cohesive soils, the following relationship has been proposed:

$$S = S_1 B \quad (6-3)$$

where S = settlement of square footing, inches

S_1 = settlement of one foot square plate, inches

B = width of square footing ($B > 0$), feet.

Thus, this result agrees with elastic theory. For cohesionless soils, the following relationship has been proposed:

$$S = S_1 \left(\frac{2B}{B+1} \right)^2 \quad (6-4)$$

where S = settlement of square footing, inches

S_1 = settlement of one foot square plate, inches

B = width of square footing ($B \geq 1$), feet.

This relationship, most accurate for footing widths less than 4-5 feet, indicates that on cohesionless soils, settlement increases at a rate less than that predicted by elastic theory. Additionally, tests on smaller footings founded on cohesionless soils indicated that settlements were essentially identical for plates with widths of 0.5-1.0 foot.

In static penetration tests on cohesive soil, using similar plates, Schuring (84) showed that the ratio of penetration and plate width remained constant for the prototype and the model, provided that the total load ratio varied as the square of the scale factor. That is, for a half-scale model, the total load on the prototype must equal four times the load on the model to achieve the same ratio of penetration to plate width in each case. This may be achieved by maintaining an identical contact pressure for the model and the prototype and agrees with elastic theory. For static penetration tests on cohesionless material, Schuring showed that the ratio of penetration to plate width remained constant for the prototype and any similar model, provided that the total load ratio varied as the cube of the scale factor. In this

instance, the total load on the prototype must be eight times that on a half-scale model to achieve the identical penetration to plate width ratio. This requires a change in contact pressure between model and prototype. For constant contact pressures, rutting in the prototype will be less than in direct proportion to the scale factor of plate widths. In both materials, Schuring's tests dealt with large deflections.

If dynamic influences on the scaling influence are minimal, for the half-scale model used in this program, with equal contact pressures in the model and the prototype, the field rutting under load, after any given number of load cycles, should fall between one and two times the corresponding model test rut, depending upon the relative influences of the aggregate and subgrade materials. One might empirically determine the scaling influence on rutting by comparing the model test program results with the rutting response relationship determined from tests on full-scale systems.

A rut depth of three inches is anticipated, in vehicle trafficked unsurfaced AS systems, at the number of load cycles computed on the basis of the U.S. Army Corps of Engineers (44, 45, 103) equation (i.e., Equation (2-2)), as modified (i.e., Equation (2-3)) by Hammitt (44). The resulting expression may be written as:

$$t = F(P(\frac{1}{8.1 \text{ CBR}} - \frac{1}{p\pi}))^{0.5} \quad (6-5)$$

where t = required layer thickness, inches

$$F = 0.176 \text{ Log } N + 0.120$$

N = number of load repetitions during design period

P = total wheel load, pounds

CBR = California Bearing Ratio of underlying layer of material

p = tire contact pressure, psi.

Equation (6-5) may be linearized on a semi-log plot after dividing both sides of the equation by the radical expression. The expression is plotted in Figure 6-13, along with appropriate model test data, corrected for instrumentation, and the calculated regression equation to these data, assuming a scale factor of one for rutting. In Figure 6-14, the expression is plotted, along with model test data, corrected for instrumentation, and the regression equation to these data, assuming a scale factor of two for rutting. As would be expected, a scale factor of one proves unconservative, while a scale factor of two proves conservative when compared to Equation (6-5). By a trial and error procedure, varying the scale factor for rutting in increments of 0.1 within the anticipated range of 1.0-2.0, a rutting scale factor of 1.7 (i.e., prototype rut equal to 1.7 times the model rut) was found to most closely approximate Equation (6-5). The data for a rutting scale factor of 1.7, corrected for instrumentation, and the calculated regression equation to these data, are plotted in Figure 6-15 along with Equation (6-5). Only Type B loading data were analyzed, as being more representative of field conditions.

For a full-scale wheel load and a contact pressure equal to that used in the model test program, correcting for instrumentation (i.e., model test load cycle data reduced by a factor of 2.4) and scaling (i.e., model test rut depths increased by a factor of 1.7), the stress

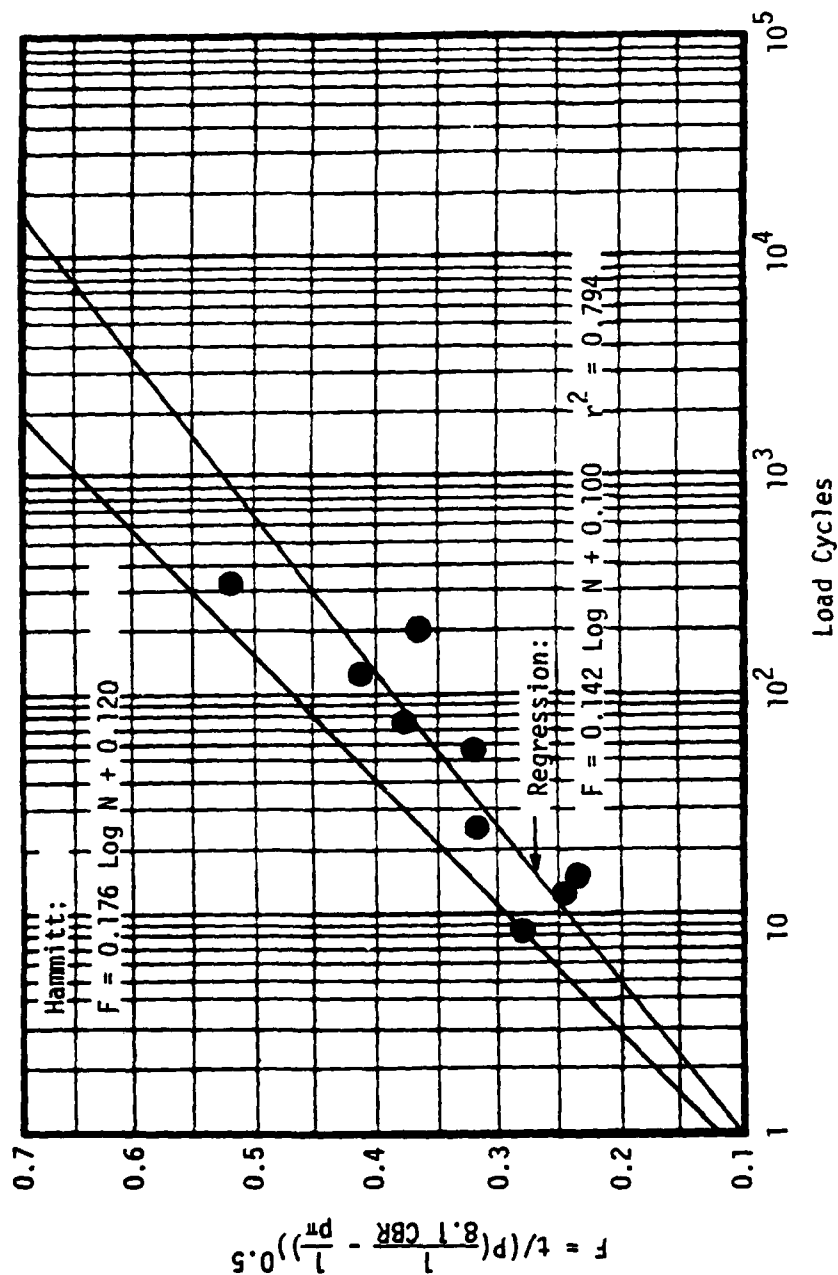


Figure 6-13. Comparison of Computed Rutting Relationship for AS Systems (Rutting Scale Factor of 1.0; N Corrected for Instrumentation) and Response Predicted by Hammitt Modification to U.S. Army Corps of Engineers Equation, Type B Loading.

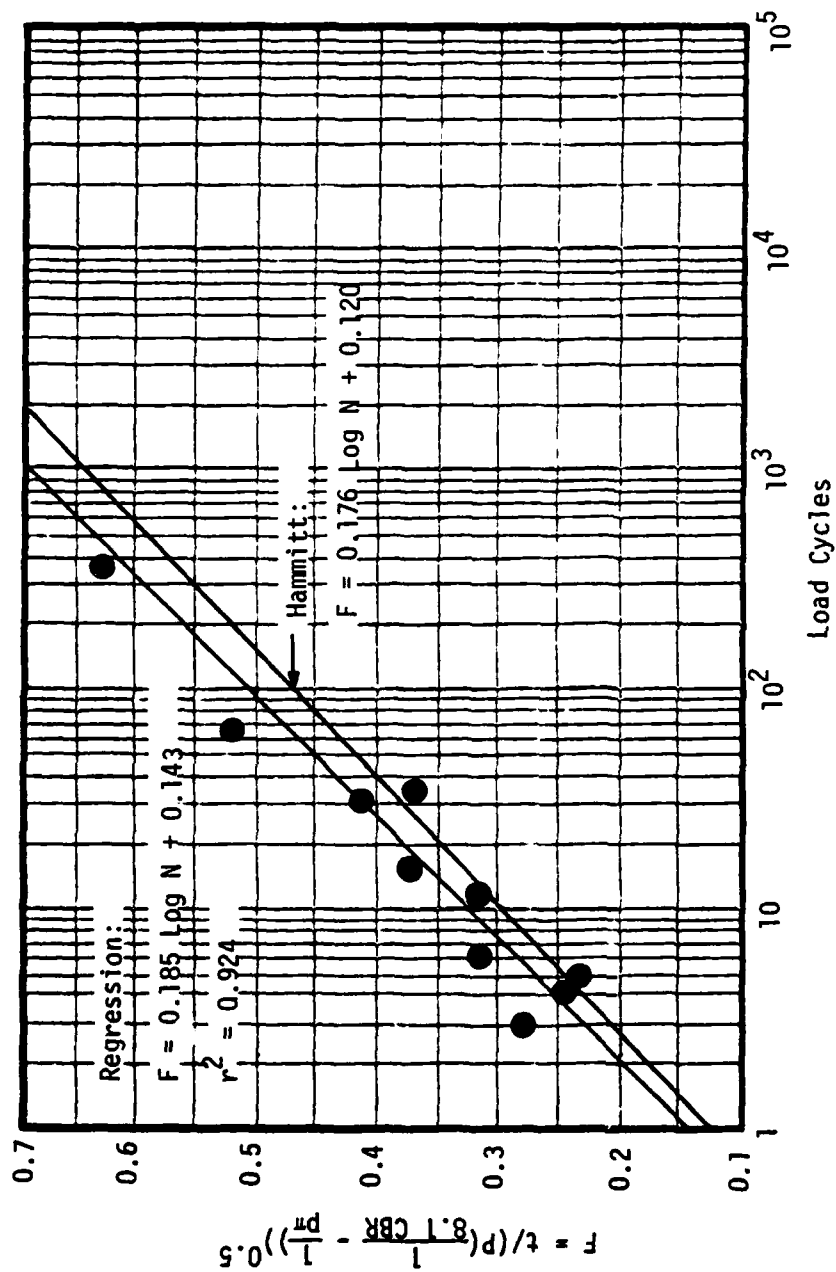


Figure 6-14. Comparison of Computed Rutting Relationship for AS Systems (Rutting Scale Factor of 2.0; N Corrected for Instrumentation) and Response Predicted by Hammitt Modification to U.S. Army Corps of Engineers Equation, Type B Loading.

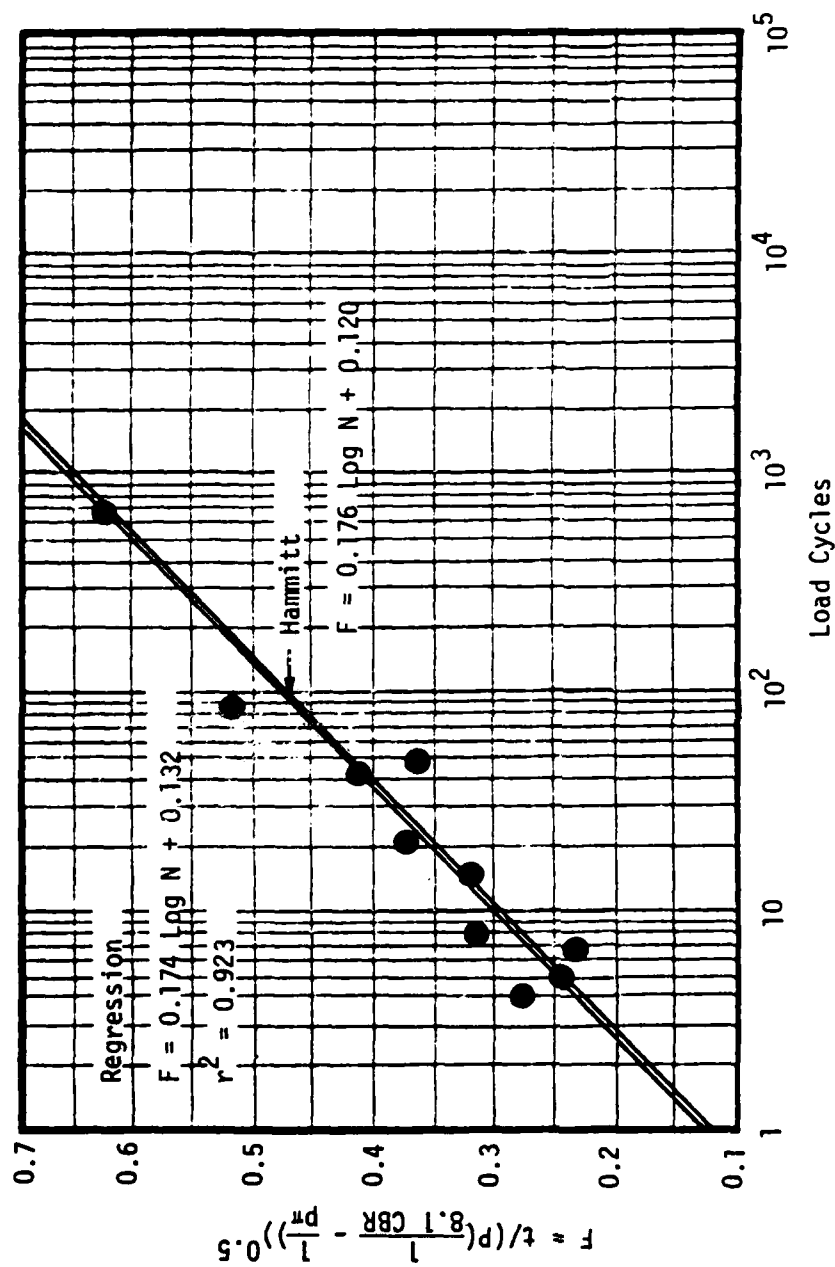


Figure 6-15. Comparison of Computed Rutting Relationship for AS Systems (Rutting Scale Factor of 1.7; N Corrected for Instrumentation) and Response Predicted by Hamitt Modification to U.S. Army Corps of Engineers Equation, Type B Loading.

ratio-cumulative permanent deformation-load cycle relationships indicate rut depths of 4.1 and 6.2 inches at 10^2 load cycles, for stress ratios of 3.3c and 6.0c in AS and AFS systems respectively. For a four inch rut at 10^2 load cycles, corresponding stress ratios of 3.2c and 4.4c would be required. At 10^3 load cycles, rut depths of 6.7 and 9.4 inches are indicated for stress ratios of 2.8c and 5.0c in AS and AFS systems. To limit rutting to two inches at 10^3 load cycles, AS and AFS system stress ratios of 1.3c and 1.5c would be required. The indicated responses at 10^2 load cycles approximate the anticipated level (i.e., greater than four inches), however, the responses of 10^3 load cycles greatly exceed the anticipated level (i.e., less than two inches).

Component Deformations

A fabric interlayer was observed to alter both the plastic strain magnitudes exhibited by the aggregate and subgrade materials, and the deformed shape of the soil layer interface. Strain sensor data are presented in Appendix G, while data on the deformed shape of the interface are provided in Appendix F.

For AS systems, the greatest vertical plastic strains were experienced along the load centerline, in the upper one-third of the subgrade layer, reaching levels as great as 69 percent. For a given subgrade strength, the subgrade strains decreased as the thickness of the overlying aggregate layer increased, with the most dramatic changes experienced in the upper portion of the layer. The aggregate layer centerline vertical strains varied only slightly for all tests, displaying a mild tendency to increase as the layer thickness was increased above a given subgrade material. Figure 6-16 depicts the centerline vertical

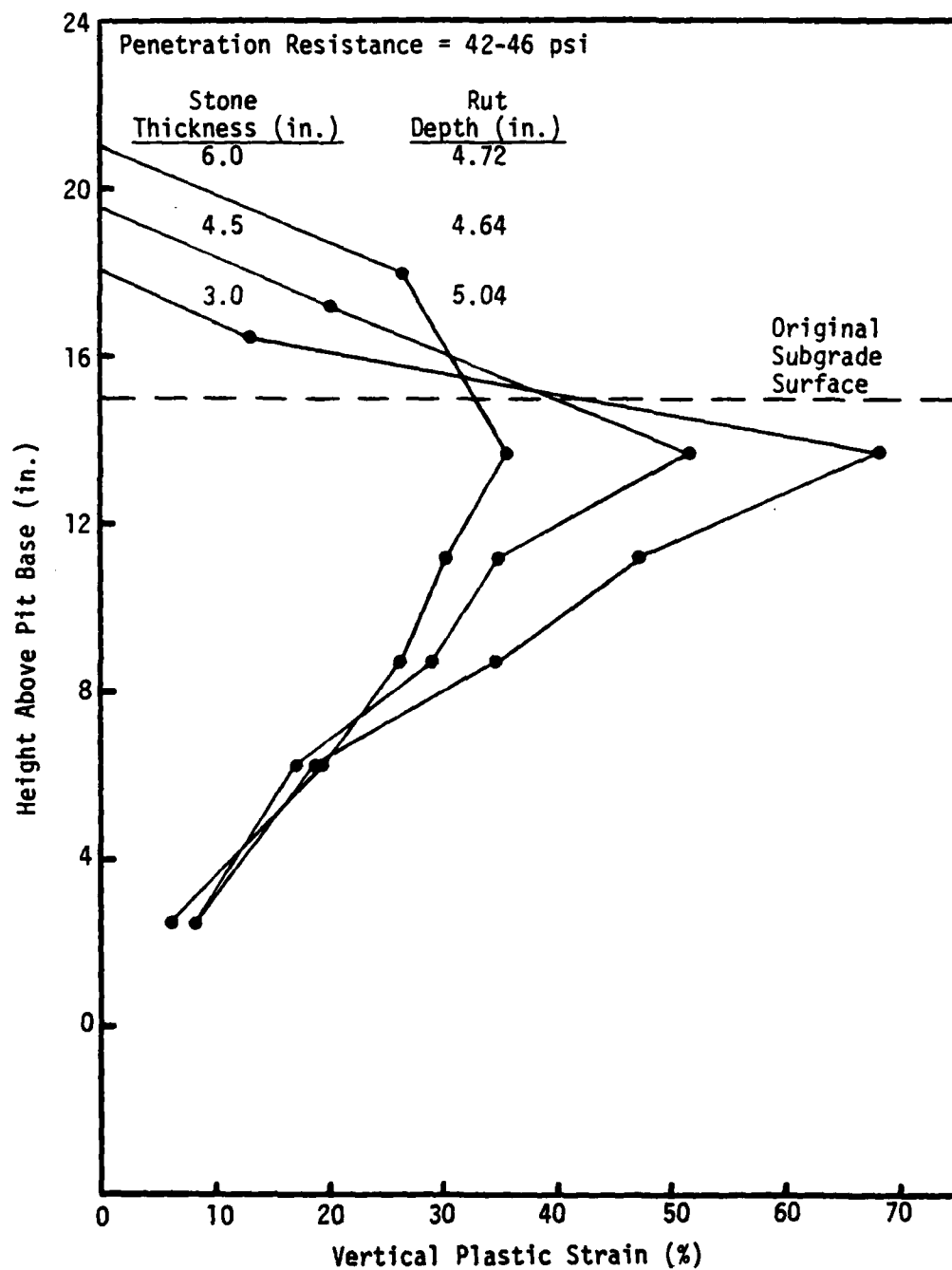


Figure 6-16. Influence of Crushed Stone Thickness on Centerline Vertical Plastic Strain Distribution in AS Systems (26B/28B/30B).

strains for a typical test set of AS systems, with the independent variable being aggregate layer thickness. Strain magnitudes are plotted at the midpoints of the appropriate soil sublayers.

For AFS systems containing Typar 3401 fabric, the greatest centerline vertical strains were experienced along the load centerline, but in the aggregate layer rather than in the subgrade. The aggregate layer strains ranged up to three times those of the corresponding AS systems. This phenomenon was also observed by Johnson (53), in a limited series of two-dimensional model tests utilizing the same materials and conducted in conjunction with this study. For a given subgrade strength, both aggregate and subgrade strains decreased as the aggregate layer thickness increased. In AS systems, the greatest centerline vertical strains occurred in the uppermost subgrade sublayer. The Typar 3401 reinforced AFS system results indicated that the centerline vertical strains were similar in the two upper subgrade sublayers, with the greater value most frequently occurring in the second sublayer below the aggregate subgrade interface. This would indicate that the Typar 3401 inclusions did alter the subgrade stress states as compared to those of the corresponding AS systems. Figure 6-17 depicts the centerline vertical strains for a typical test set of AFS systems, with the independent variable being the aggregate layer thickness.

For either AS or AFS systems varying only in load pulse duration, with the corresponding tests terminated at approximately the same total surface rut depth, the centerline vertical strain distributions were comparable. While these trends were found for each strength of subgrade material tested, no distinct patterns were discerned which

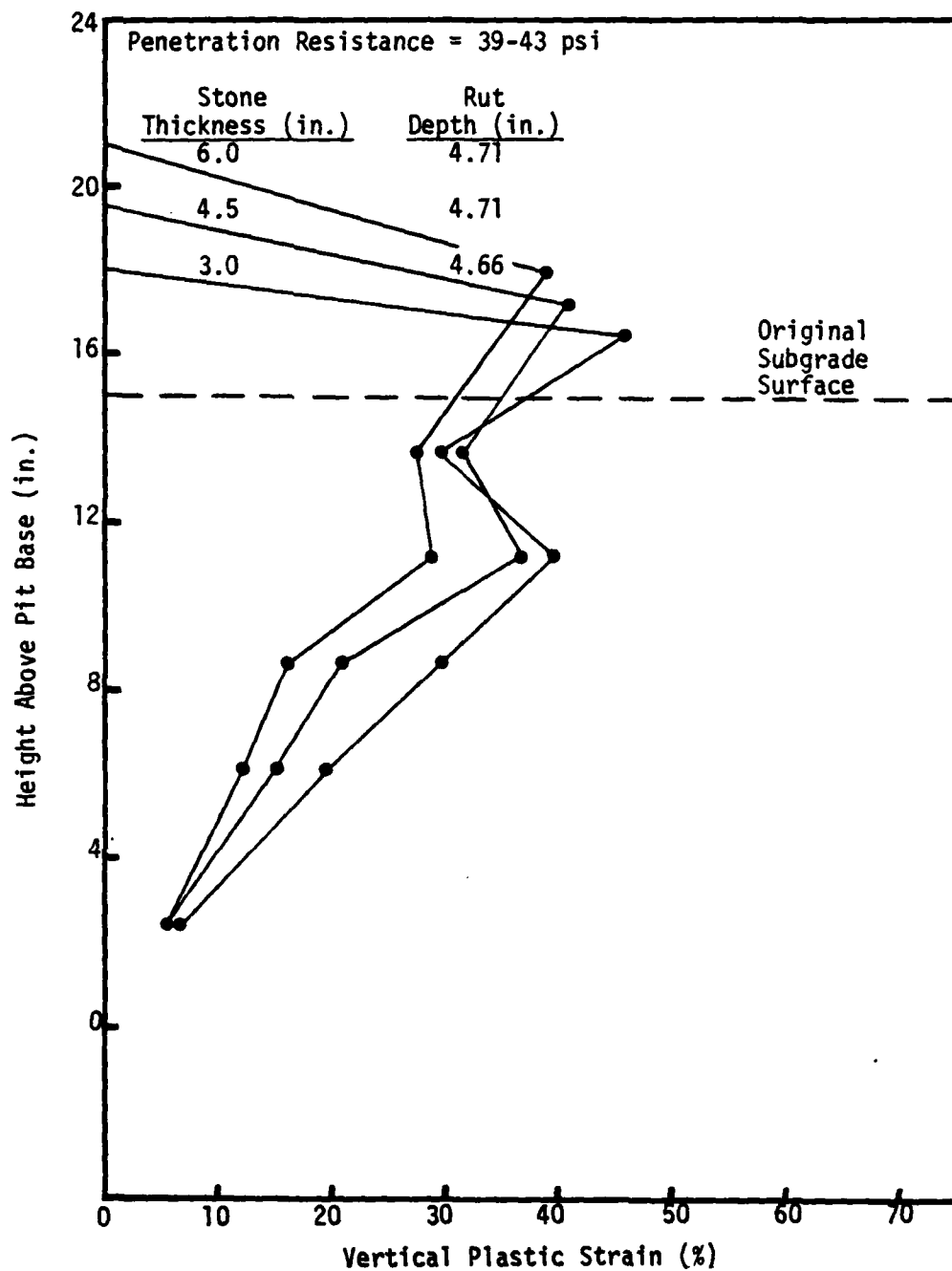


Figure 6-17. Influence of Crushed Stone Thickness on Centerline Vertical Plastic Strain Distribution in T-3401 Reinforced AFS Systems (27B/29B/31B).

encompassed all of the subgrade strength groupings, such as a pattern based upon stress ratio.

In AFS systems which differed only in the type of interlayer utilized, a one inch layer of sand and Mirafi 140 or Bidim C22 fabrics resulted in centerline vertical strain distributions comparable to those of the corresponding AS systems. Typar 3601 fabric produced centerline vertical strain distributions with shapes similar to those of the corresponding AS systems, although slightly lower subgrade sublayer strains and slightly greater aggregate layer strains were evident. The influence of membrane type is depicted in Figures 6-18 and 6-19 for tests from a representative set.

Summation of the centerline vertical deformations, as measured with the Bison coils, was found to be in excellent agreement with the total surface rutting as measured by the three dial gages, for all tests. Deformations as observed within the aggregate layer are in contrast to the design models proposed by Kinney (56) and Giroud (41), wherein a stable, rigid aggregate wedge is assumed to exist beneath the loaded area. Due to "out-of-plane" rotations of some coils and movements between coil pairs perpendicular to the direction of interest, the deformation data cannot be considered accurate in terms of absolute deformation measurement. These data do, however, provide an indication of the relative deformation pattern within the subgrade material for each model test. A typical deformed pattern is depicted in Figure 6-20.

The deformed shape of the subgrade soil surface profile conformed to that for a general shear failure, displaying a rutted portion, centered below the footing, and a radially offset bulge or heave. The

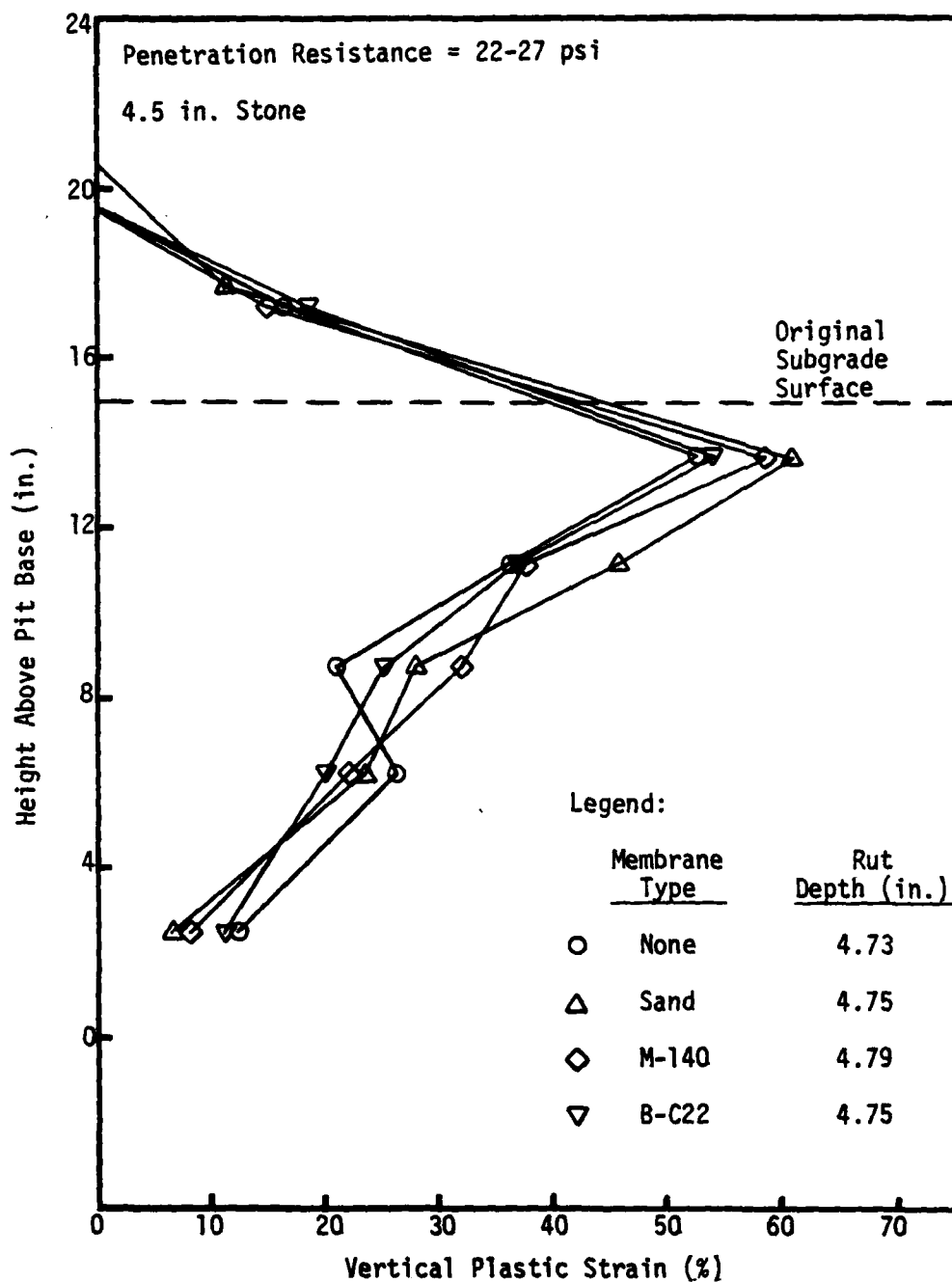


Figure 6-18. Influence of Membrane Type on Centerline Vertical Plastic Strain Distribution (7A/8A/11A/12A).

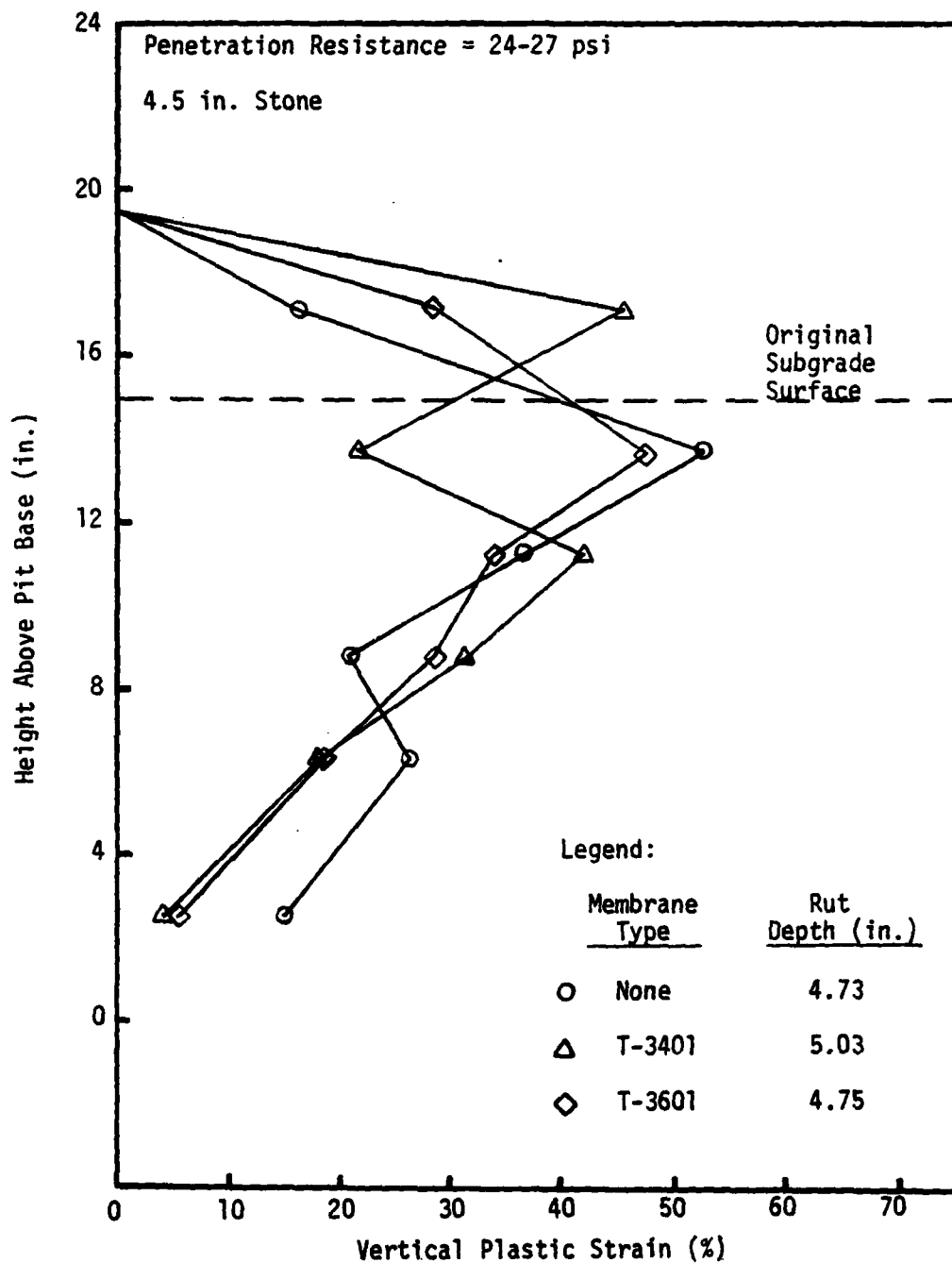


Figure 6-19. Influence of Membrane Type on Centerline Vertical Plastic Strain Distribution (7A/9A/10A).

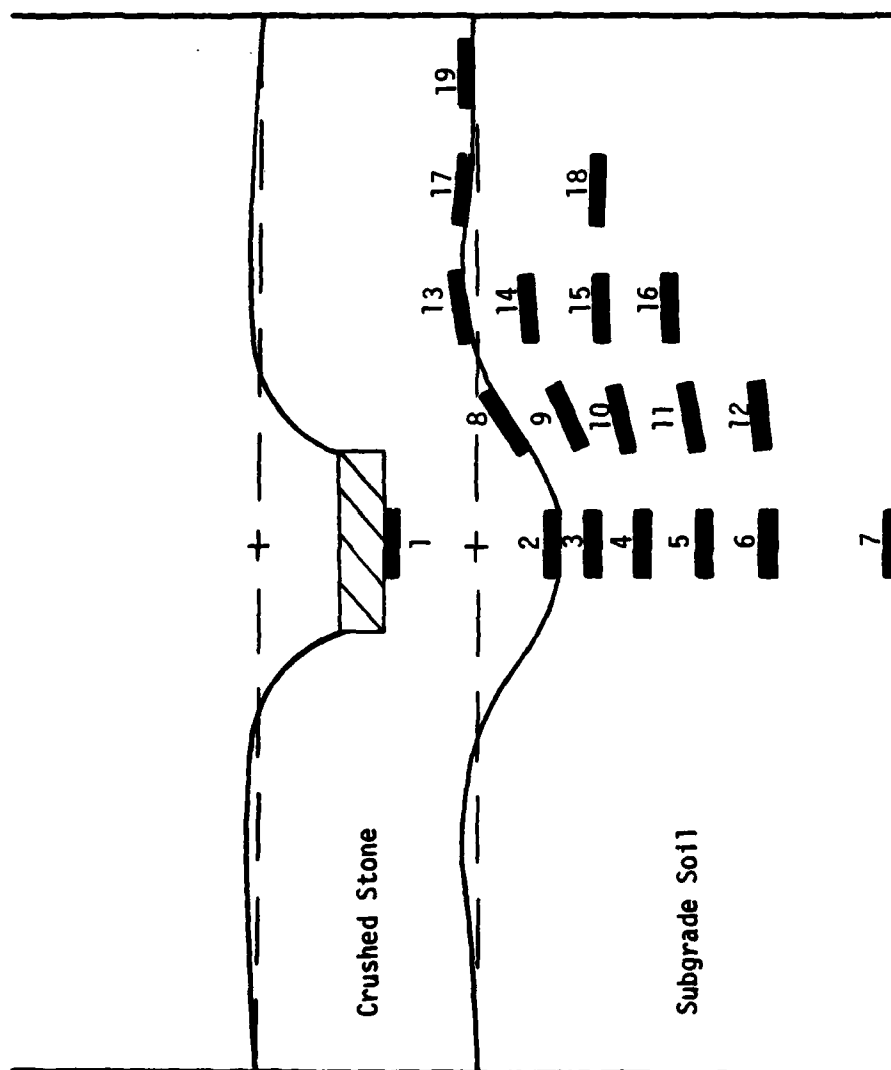


Figure 6-20. Bison Coil Designations and Typical Final Configuration.

deformed shape of the profile, for a given subgrade strength, was influenced by the aggregate layer thickness in both AS and AFS systems. As the thickness of the aggregate layer increased, the depth of the subgrade rutting decreased, the height of the heave decreased, and the width of the subgrade rut increased. The influence of aggregate layer thickness on the deformed shape of the interface is depicted in Figure 6-21 for a typical set of tests. A fabric inclusion generally decreased the depth of the subgrade rut, decreased the height of the heave, and increased the width of the rut, as compared to the deformed interface shape in the correspondence AS system. Tensile stresses in the fabric would be expected to decrease the stress imposed on the subgrade within the wheel path and hence the subgrade rut, while outside the wheel path an "apparent surcharge" is created by the reverse curvature of the membrane, and upheaval is restrained. The most dramatic beneficial changes (i.e., greatest reduction in subgrade rut depth compared to the corresponding AS system) resulted with a membrane of Typar 3401 fabric. The use of a one inch layer of sand, and Mirafi 140 and Bidim C22 fabrics, produced the least changes from the results of the corresponding AS systems. Typar 3601 fabric inclusions resulted in deformed interface shapes bounded by those of corresponding AS systems and Typar 3401 reinforced AFS systems. The influence of membrane type on the deformed interface shape is depicted in Figures 6-22 and 6-23 for tests from a representative set. For a given subgrade material, the influence of the interfacial membrane type decreased as the thickness of the overlying aggregate layer increased.

The percentage of the subgrade rut volume taken in shear (i.e.,

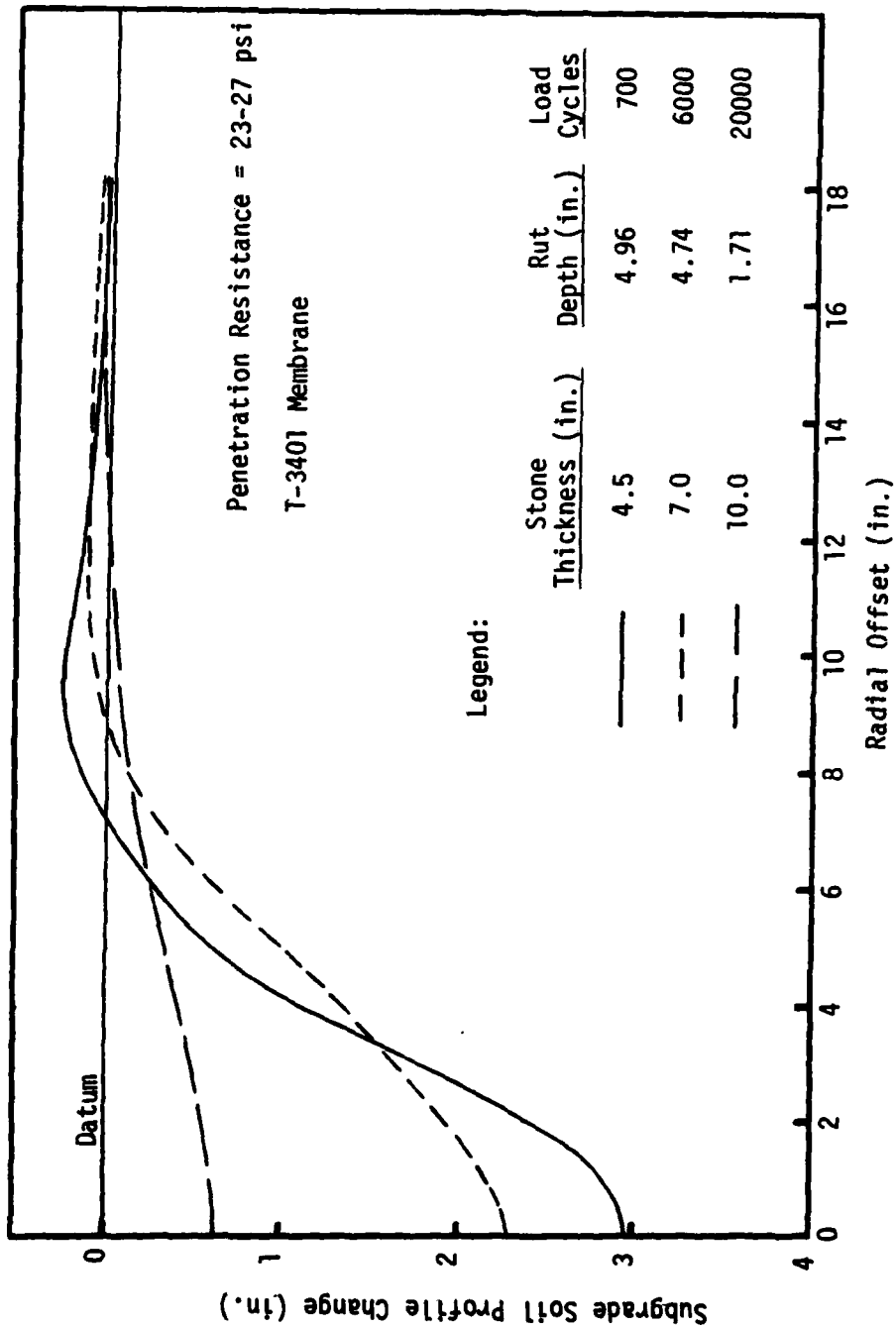


Figure 6-21. Influence of Crushed Stone Thickness on Subgrade Soil Profile Changes in AS and AFS Systems (9B/15B/20B).

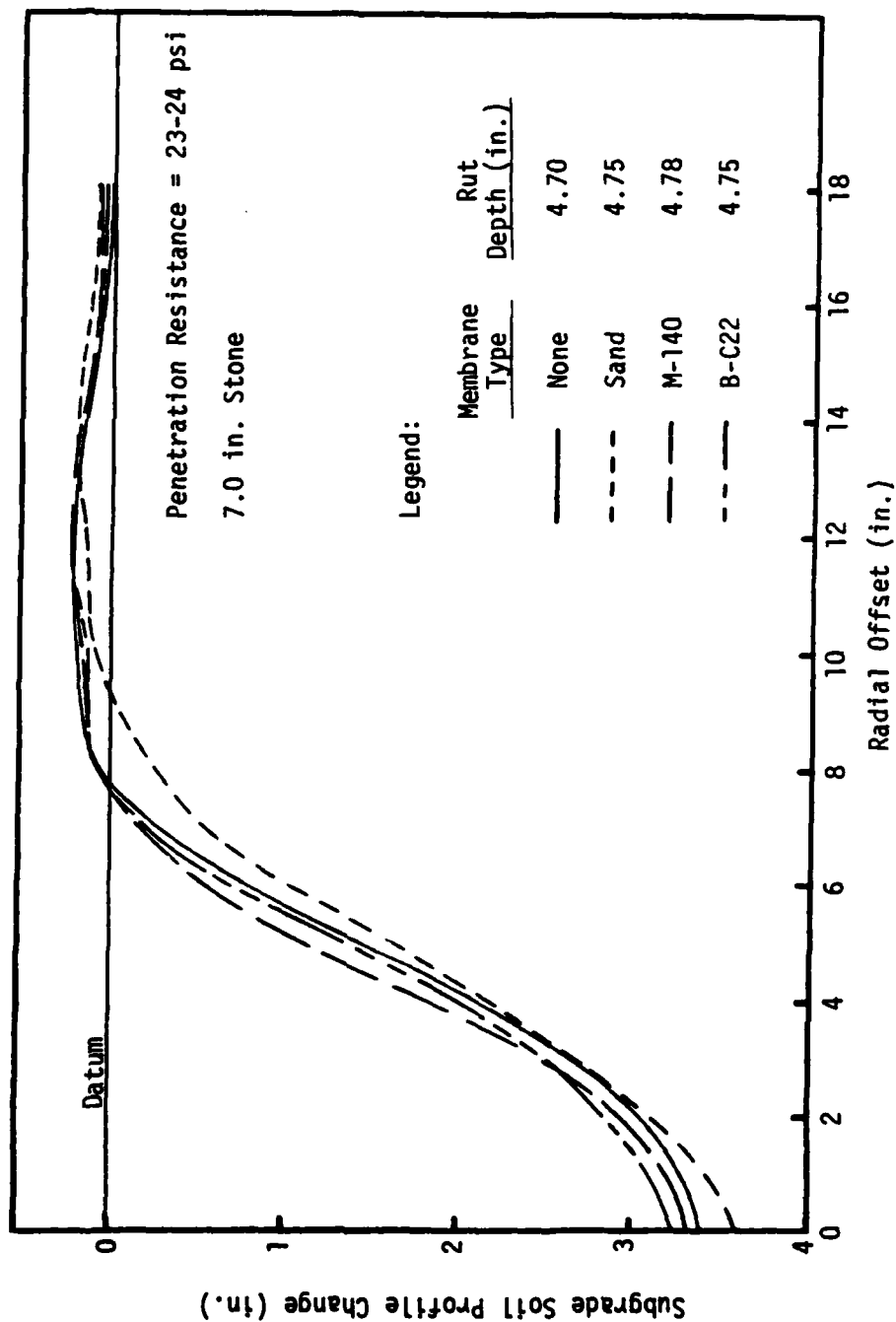


Figure 6-22. Influence of Membrane Type on Subgrade Soil Profile Changes (13A/14A/17A/18A).

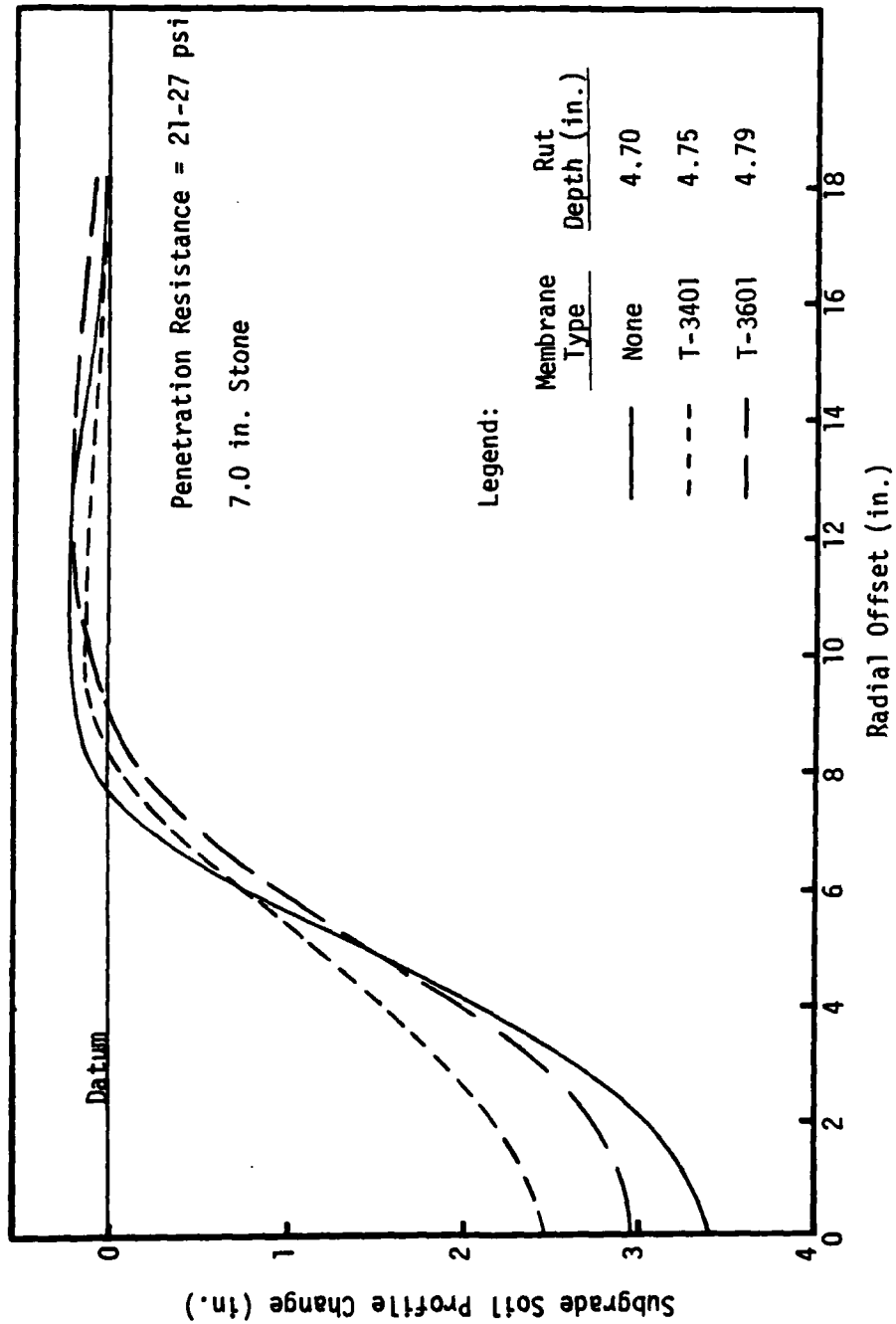


Figure 6-23. Influence of Membrane Type on Subgrade Soil Profile Changes (13A/15A/16A).

due to change in shape, not volume), computed by the procedure described in Appendix F, was less in AFS systems than in the corresponding AS systems. Data scatter was too great to discern any trends in this area, even within the test grouping for a given subgrade strength.

The in-plane permanent strains, as measured by the procedure described in Appendix H, exhibited by the Typar 3401 fabric inclusions were generally greatest in magnitude in a zone between the load centerline and an offset of one radius, decreasing with further radial offset. Strain magnitudes decreased as the stress ratios of the systems decreased. Tearing of the fabric was observed in three of the 14 tests which utilized Typar 3401 fabric, with the tears initiating at a distance of 0.5-1.5 offset radii from the load centerline. The tearing propagated in a circular pattern within this offset zone. The phenomenon was only observed in AFS systems utilizing stiffer subgrade materials (i.e., Groups III and IV - CBR greater than 1.5) and appears to be a function of subgrade strength rather than stress ratio. While 75 percent of the tests of AFS systems conducted with the stiffer subgrade materials displayed tearing of the fabric, none of the tests conducted on the weaker subgrades, but within the same range of stress ratio values (i.e., 4.30-6.71), exhibited fabric tearing. Typar 3401 fabric strain distributions are depicted in Figure 6-24 for selected tests.

Pressure Cell Data

Pressure cell data, taken at the beginning of all Type B load tests, are plotted versus both the Boussinesq and Westergaard theoreti-

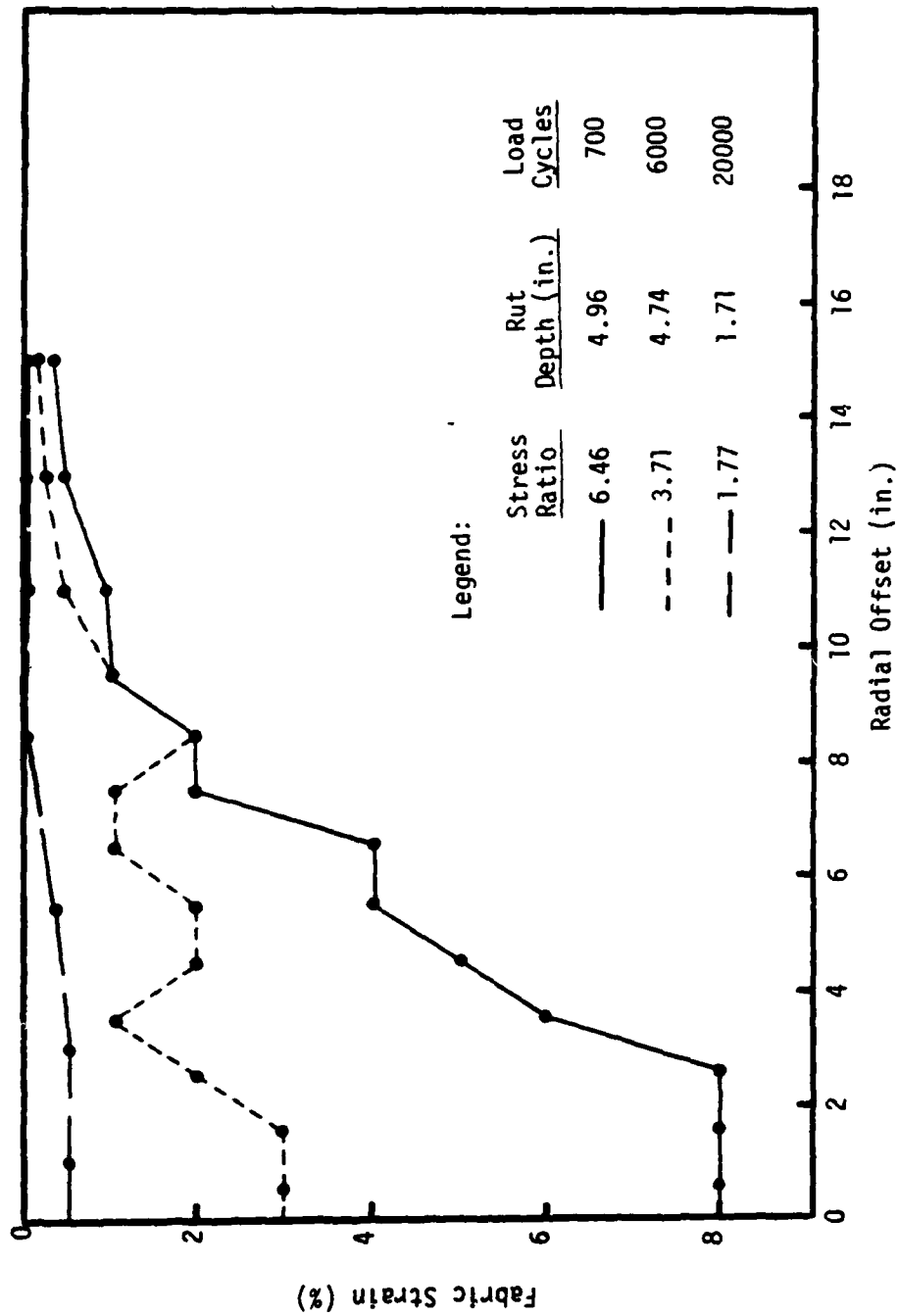


Figure 6-24. Influence of Stress Ratio on T-3401 Fabric Strain Distribution (9B/15B/20B).

cal stress distributions in Figures 6-25 and 6-26 for AS and Typar 3401 reinforced AFS systems respectively. The Boussinesq solution provided a significantly closer approximation to the measured stresses than did the Westergaard solution, for both AS and AFS systems. In AS systems, the data averaged 91 percent of the stresses predicted by Boussinesq theory, with a range of 77-112 percent, and 136 percent of the stresses predicted by the Westergaard solution, with a range of 107-168 percent. The data averaged 90 percent of the stresses predicted by Boussinesq theory for the Typar 3401 reinforced AFS systems, with a range of 57-111 percent. These data averaged 135 percent of the Westergaard theory stresses, with a range of 76-172 percent. During the initial stages of the model tests, the data indicated only minor differences (i.e., less than two percent) between the stress states of corresponding AS and Typar 3401 reinforced AFS systems.

Pressure cell data from the final stages of the model tests of Groups I and IV (Table 5-1) indicate that some changes in the stress distributions occurred during the courses of the tests. In the AS systems, the final data averaged 88 percent of the stresses predicted by Boussinesq theory, with a range of 74-98 percent. For the Typar 3401 reinforced AFS systems, the final data averaged 83 percent of the stresses computed from the Boussinesq solution, with a range of 67-95 percent. The data from the final stages of these model tests indicate a noticeable difference (i.e., greater than five percent) between the stress states of corresponding AS and Typar 3401 reinforced AFS systems. Some stress reduction, within the wheel path, is anticipated due to the action of tensile stresses in the fabric in conjunction with curvature

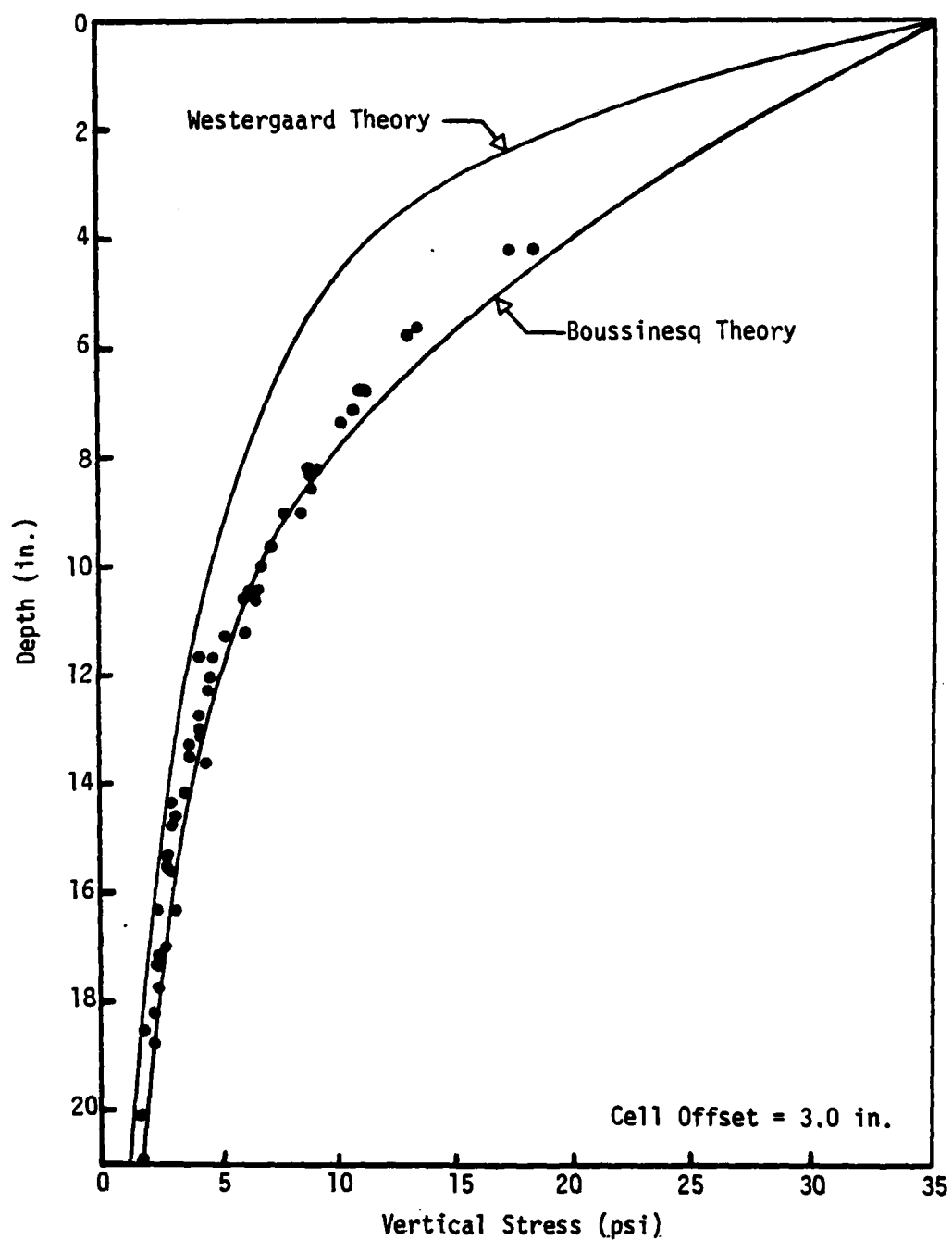


Figure 6-25. Initial Pressure Cell Readings for AS Systems, Type B Loading.

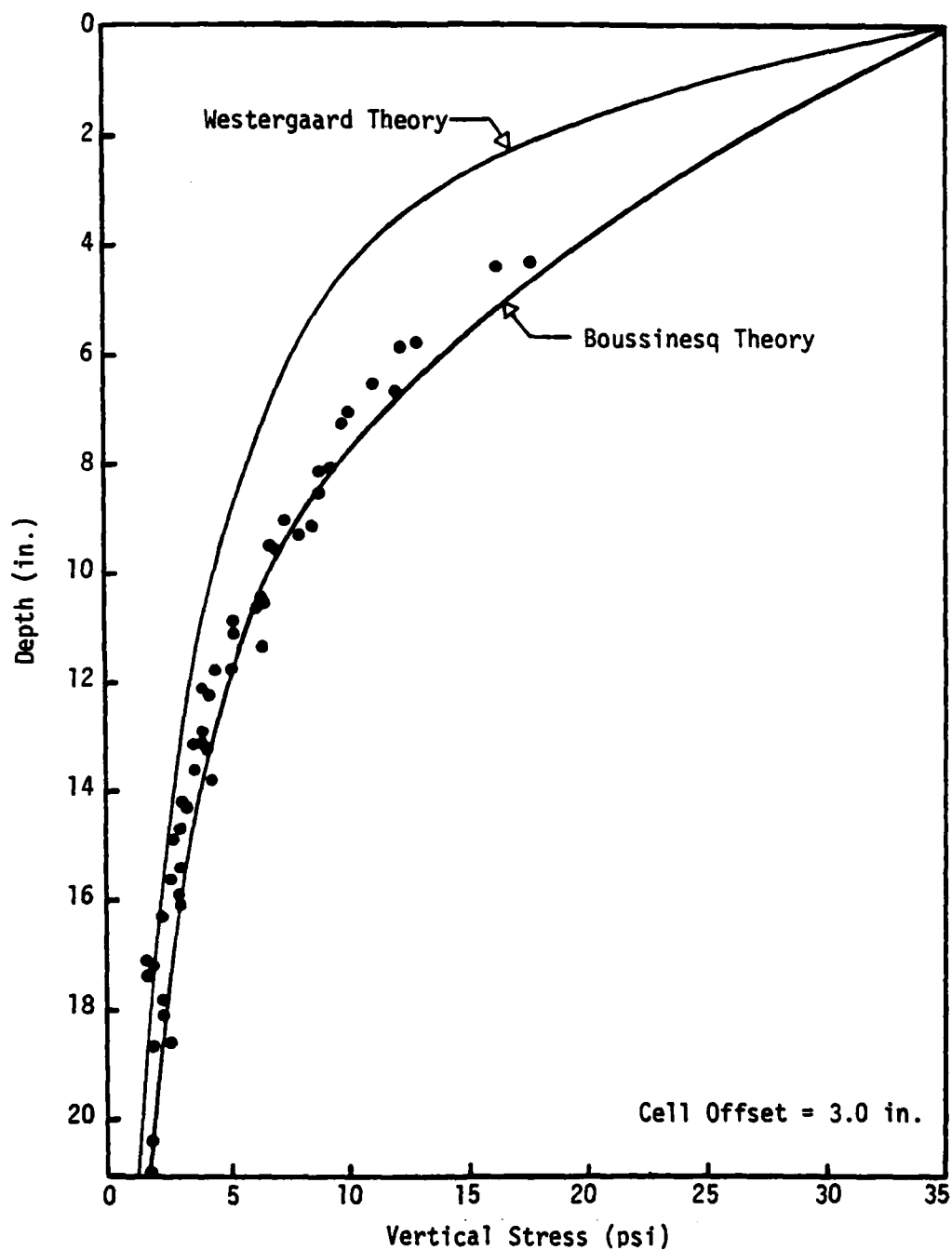


Figure 6-26. Initial Pressure Cell Readings for T-3401 Reinforced AFS Systems, Type B Loading.

along the interface in the deformed system. Such a difference was also expected in view of the reduced centerline vertical strains exhibited by the subgrade sublayers of the Typar 3401 reinforced AFS system, as compared to these sublayer strains in the corresponding AS systems. Final pressure cell data are plotted versus the Boussinesq stresses, normal to the plane of the final cell orientation, in Figures 6-27 and 6-28 for AS and Typar 3401 reinforced AFS systems respectively. Final cell locations and orientations were determined during excavation of the subgrade, upon test completion, as discussed in Chapter IV. In computing the Boussinesq stresses, the influence chart solutions prepared by Foster and Ahlvin (40), based upon a Poisson's ratio of 0.5, were utilized. These charts yield the vertical, radial, and shear stresses at a point, which may then be utilized to compute the normal stress for any desired orientation from Mohr's circle or from the following equation:

$$\sigma_n = \frac{\sigma_z + \sigma_r}{2} + \frac{\sigma_z - \sigma_r}{2} \cos 2\theta + \tau_{zr} \sin 2\theta \quad (6-6)$$

where σ_n = stress normal to plane of interest, psi

σ_z = vertical stress, psi

σ_r = radial stress, psi

τ_{zr} = shear stress, psi

θ = angle from horizontal to plane of interest.

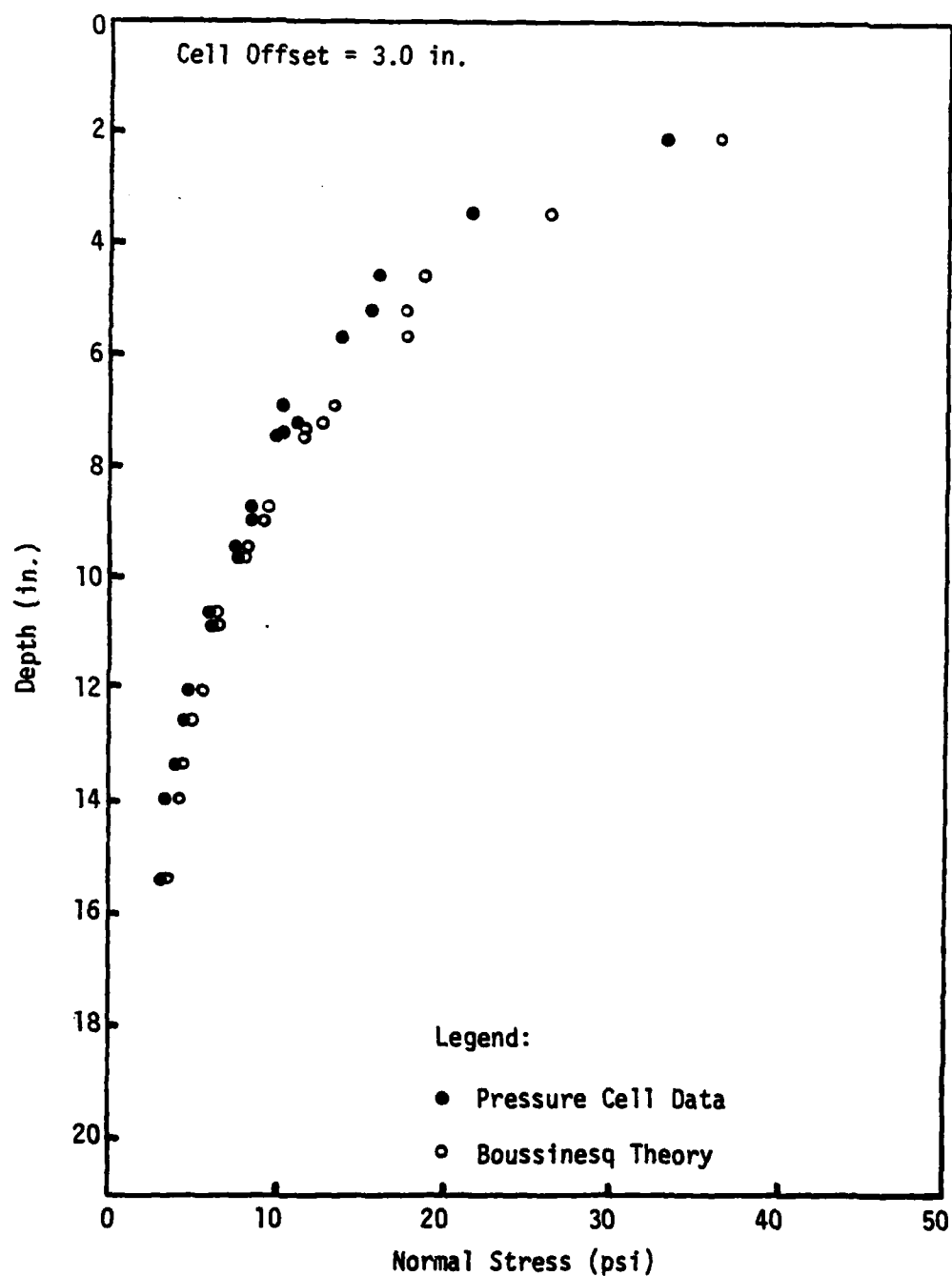


Figure 6-27. Final Pressure Cell Readings for Groups I and IV AS Systems, Type B Loading.

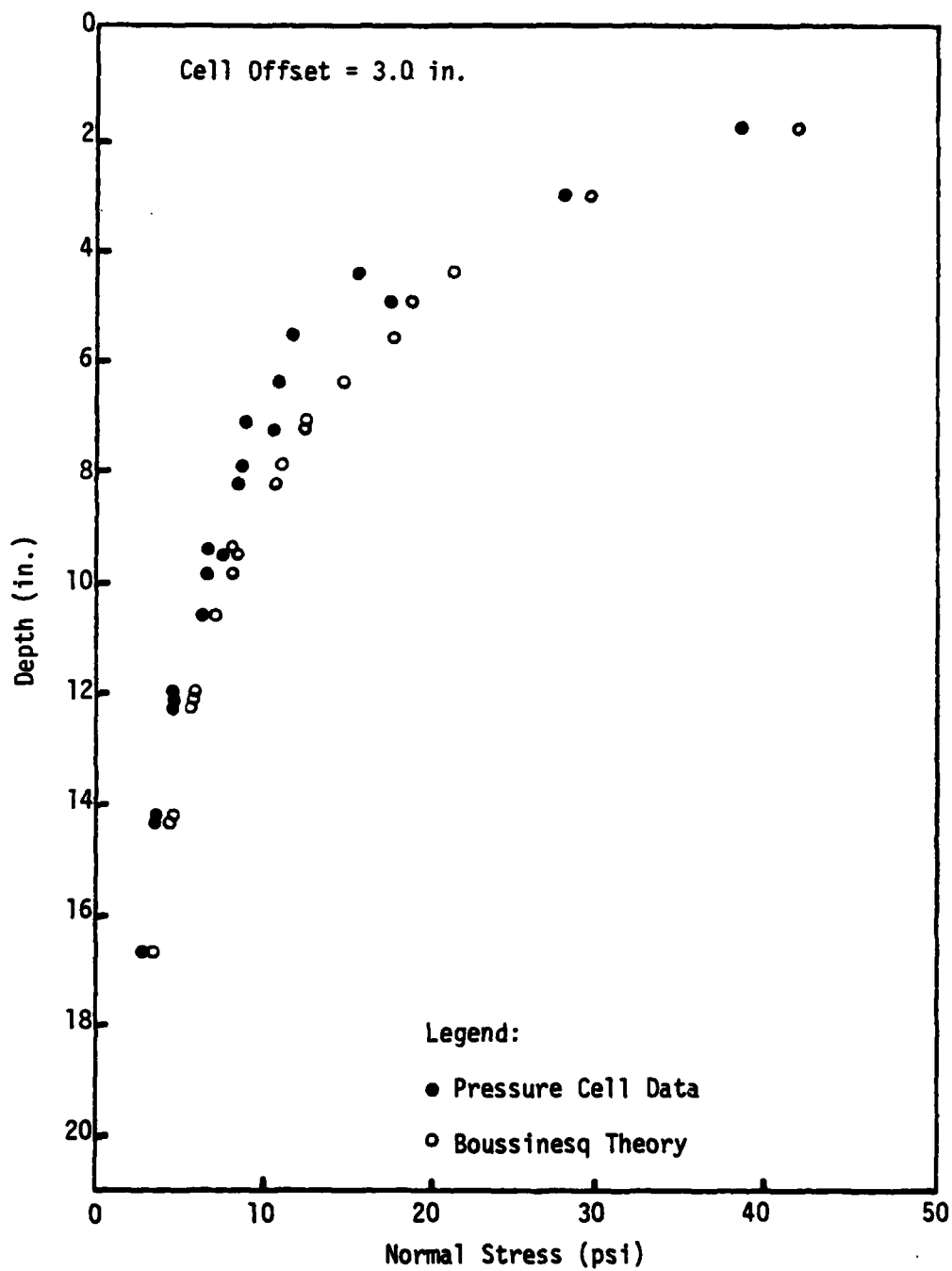


Figure 6-28. Final Pressure Cell Readings for Groups I and IV T-3401 Reinforced AFS Systems, Type B Loading.

CHAPTER VII

RUTTING RESPONSE PREDICTIVE MODELS

Prediction of Rutting Response

Rutting response was predicted for all AS systems, and for those AFS systems utilizing Typar 3401 fabric, by several of eight possible models. All predictive methods were initially used to estimate the rutting of the tests of subgrade Group II (i.e., unsoaked CBR = 0.74-0.99), then used for the remaining tests if initial results appeared promising. Three models utilized correlations between the stress ratio at the subgrade surface, rut depth, and load cycles. A fourth model utilized the U.S. Army Corps of Engineers design method equation (44, 45, 103) and modifications thereto. A fifth model utilized the design approach recommended by Giroud and Noiray (41). The remaining three models involved prediction of the stress state within the system and subsequent application of the hyperbolic plastic stress-strain law.

Method 1

The results of the model test program were analyzed to provide correlations between stress ratio and rut depth after a given number of load cycles (i.e., 10, 10^2 , and 10^3) and between load cycles and stress ratio at a given rut depth (i.e., two, three, and four inches) for both AS and AFS systems. These regression equations are of the following forms:

At a given load cycle:

$$RD = C_1 (SR)^{C_2} \quad (7-1)$$

At a given rut depth:

$$\text{Log } N = C_3 (SR)^{C_4} \quad (7-2)$$

where RD = rut depth, inches

SR = stress ratio at subgrade surface

N = load cycles

C_i = regression analysis constants.

These stress ratio-permanent deformation-load cycle relationships are presented in Appendix J.

Once the stress ratio of a system is determined, the rutting response may be predicted by applying the appropriate correlations. A minimum of three values (i.e., rut depth at 10 , 10^2 , and 10^3 load cycles, or load cycles at two, three, and four inches of rut depth) or a maximum of six values (i.e., rut depth at 10 , 10^2 , and 10^3 load cycles and load cycles at two, three, and four inches of rut depth) for the load cycle-cumulative permanent deformation relationship can thus be computed and plotted for any system.

The results of this method, as applied to the model test program, are presented in Table 7-1. Rutting predictions after a given number of load cycles were in excellent agreement with measured values for both AS and AFS systems, with either Type A or B loading. For AS systems with Type A loading, computed rut depths averaged 111 percent of the observed

Table 7-1. Summary of Method 1 Predictions of Model Test Program Rutting Responses.

Depth of Stone Stress (a)				Rut at Given N			Load Cycles to Given Rut			
Test No.	Membrane Type	Stone (in.)	Stress Ratio	Method	$N = 10^2$ $\frac{N}{\Delta(\text{in.})} \Delta(\text{in.})$	$N = 10^3$ $\frac{N}{\Delta(\text{in.})} \Delta(\text{in.})$	$N = 10^4$ $\frac{N}{\Delta(\text{in.})} \Delta(\text{in.})$	$\Delta = 2 \text{ in.}$ N	$\Delta = 3 \text{ in.}$ N	$\Delta = 4 \text{ in.}$ N
18	None	6.0	6.75	Actual Pred.	1.35 1.63	4.92 5.10	-- --	20 16	40 29	68 56
38	None	7.5	4.50	Actual Pred.	0.78 0.91	2.76 2.77	5.57* 5.98	-- --	48 47	140 109
58	None	9.0	3.38	Actual Pred.	0.60 0.60	1.62 1.79	3.93 4.04	-- --	170 130	480 378
7A	None	4.5	6.55	Actual Pred.	4.73 4.90	-- --	-- --	2 2	4 4	6 6
7B	None	4.5	6.41	Actual Pred.	1.79 1.51	4.79 4.72	-- --	13 18	20 33	60 66
13A	None	7.0	3.59	Actual Pred.	2.56 2.14	-- --	-- --	9 7	14 14	18 18
13B	None	7.0	3.63	Actual Pred.	0.68 0.67	1.75 2.00	4.97* 4.45	-- --	140 98	300 269
19A	None	10.0	1.83	Actual Pred.	0.63 0.85	1.20 1.75	1.86 2.70	2.37 --	1700 210	-- --
19B	None	10.0	1.81	Actual Pred.	0.24 0.24	0.82 0.70	1.61 1.71	2.42 --	2800 3523	-- --

(a) Ref. Page 92 for Definition
* Extrapolated Data Point

Table 7-1. (Continued).

Test No.	Membrane Type	Depth of Stone (in.)	Stress Ratio	(a) Method	Rut at Given N				Load Cycles to Given Rut		
					N = 10	N = 10 ²	N = 10 ³	N = 10 ⁴	Δ = 2 in. Δ = 3 in. Δ = 4 in.		
					$\frac{\Delta(\text{in.})}{\Delta}$	$\frac{\Delta(\text{in.})}{\Delta}$	$\frac{\Delta(\text{in.})}{\Delta}$	$\frac{\Delta(\text{in.})}{\Delta}$	N	N	N
22A	None	13.0	1.06	Actual Pred.	0.46 0.40	0.81 0.80	1.36 1.21	2.01 --	9500 152777	-- --	-- --
26B	None	3.0	6.76	Actual Pred.	1.57 1.64	5.53* 5.12	-- --	-- --	16 16	31 29	52 56
28B	None	4.5	4.34	Actual Pred.	0.88 0.86	2.40 2.62	5.50* 5.69	-- --	68 52	180 125	380 278
30B	None	6.0	2.74	Actual Pred.	0.42 0.44	1.18 1.31	3.30 3.03	4.72 --	280 328	770 1158	2500 2897
32B	None	3.0	4.74	Actual Pred.	1.25 0.98	3.72 2.99	-- --	-- --	25 40	60 89	120 193
2B	T-3401	6.0	6.72	Actual Pred.	0.91 0.91	2.71 3.02	5.50* 6.05	-- --	46 45	140 121	320 218
4B	T-3401	7.5	4.62	Actual Pred.	0.49 0.58	1.83 1.78	4.12 3.87	-- --	120 145	290 435	875 1185
6B	T-3401	9.0	3.32	Actual Pred.	0.32 0.39	1.08 1.11	2.08 2.61	3.50 --	850 547	4500 1781	50000* 8148
9A	T-3401	4.5	6.62	Actual Pred.	1.64 1.64	3.28 3.53	-- --	-- --	19 16	76 76	200 200

(a) Ref. Page 92 for Definition

* Extrapolated Data Point

Table 7-1. (Continued).

Test Membrane No. Type		Depth of Stone (in.)	Stress Ratio	(a) Method	Rut at Given N				Load Cycles at Given Rut							
					$N = 10^1$				$\Delta = 2 \text{ in.}$				$\Delta = 3 \text{ in.}$		$\Delta = 4 \text{ in.}$	
					$\frac{\Delta (\text{in.})}{\Delta (\text{in.})}$	$N = 10^2$	$N = 10^3$	$N = 10^4$	N	N	N	N				
98	T-3401	4.5	6.46	Actual Pred.	0.92 0.87	2.46 2.86	-- --	-- --	50 50	220 137	500 255					
15A	T-3401	7.0	3.30	Actual Pred.	0.86 0.82	2.16 1.84	3.79 3.44	-- --	80 155	330 330	1300 1300					
15B	T-3401	7.0	3.71	Actual Pred.	0.40 0.45	1.28 1.30	3.72 2.98	4.97* --	260 338	610 1073	1700 4044					
20A	T-3401	10.0	1.88	Actual Pred.	0.43 0.47	0.99 1.08	1.59 1.93	2.01 --	7000 3610	-- --	-- --					
20B	T-3401	10.0	1.77	Actual Pred.	0.19 0.18	0.36 0.46	1.07 1.24	1.63 --	-- --	-- --	-- --					
23A	T-3401	13.0	1.07	Actual Pred.	0.28 0.27	0.64 0.64	1.19 1.08	1.59 --	-- --	-- --	-- --					
27B	T-3401	3.0	6.71	Actual Pred.	1.04 0.91	2.96 3.02	-- --	-- --	59 45	110 122	170 220					
29B	T-3401	4.5	4.30	Actual Pred.	0.38 0.54	1.24 1.61	2.97 3.56	-- --	360 188	1150 577	2150 1734					
31B	T-3401	6.0	3.13	Actual Pred.	0.53 0.37	1.67 1.02	3.49 2.44	4.94* --	175 718	600 2364	2250 12099					

(a) Ref. Page 92 for Definition

* Extrapolated Data Point

Table 7-1. (Continued).

Test Membrane No.	Type	Depth of Stone Stress (in.)	Ratio (a)	Method	Rut at Given N			Load Cycles at Given Rut		
					$N = 10^2$ $\frac{N}{\Delta(\text{in.})}$	$N = 10^3$ $\frac{N}{\Delta(\text{in.})}$	$N = 10^4$ $\frac{N}{\Delta(\text{in.})}$	$\Delta = 2 \text{ in.}$ $\frac{\Delta}{N}$	$\Delta = 3 \text{ in.}$ $\frac{\Delta}{N}$	$\Delta = 4 \text{ in.}$ $\frac{\Delta}{N}$
338	T-3401	3.0	4.81	Actual Pred.	0.76 0.61	2.63 1.88	-- --	58 126	150 374	280 966

(a) Ref. Page 92 for Definition

* Extrapolated Data Point

rut depths, with a range of 84-116 percent. For Type B loading, this average was 100 percent, with a range of 78-121 percent. For AFS systems reinforced with Typar 3401 fabric, the computed rut depths averaged 100 percent of the actual rut depths, with a range of 85-121 percent, for Type A loading. For Type B loading, this average was 102 percent, with a range of 61-142 percent.

To extend this method for use with a full-scale loading, corrections must be applied to the model test program results for instrumentation (i.e., model test load cycle data reduced by a factor of 2.4) and scaling (i.e., model test rut depths increased by a factor of 1.7) as discussed in Chapter VI. Utilizing these correction factors, correlations were developed for use with full-scale systems, with the resulting regression equations presented in Table 7-2.

Only limited full-scale load test results are available, with which the response predicted by the equations presented in Table 7-2 might be compared. Webster and Watkins (117) presented the results of tests conducted by the U.S. Army Corps of Engineers Waterways Experiment Station. Test sections included an AS control section and a corresponding AFS section utilizing Bidim C38 fabric. Load was applied by a dump truck, with rutting response presented in terms of coverages by an 18 kip single axle having dual tires (i.e., Equivalent Single Wheel Load of 8.46 kips, on a tire with a contact area of 85 square inches inflated to a pressure of 100 psi). Direct comparison for the Bidim C38 reinforced system is not valid, in that the developed correlations are for Typar 3401 fabric. However, from the model test program, it is known that an inclusion of Bidim C22 fabric produced

AD-A210 434

AIR FORCE INST OF TECH WRIGHT-PATTERSON AFB OH
PERFORMANCE OF FABRIC REINFORCED AGGREGATE-SOIL SYSTEMS UNDER R--ETC(U)
DEC 81 W SCHAUZ
AFIT-CI-81-690

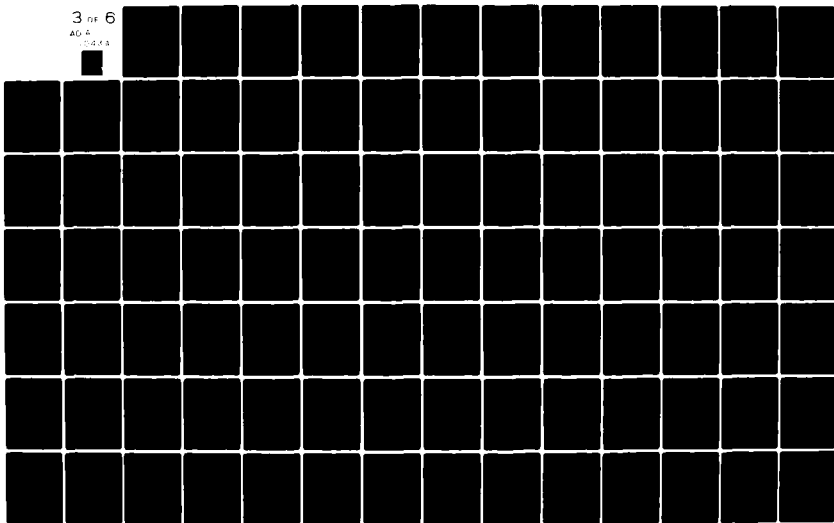
F/6 13/2

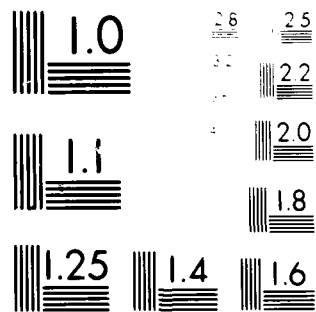
UNCLASSIFIED

NL

3 OF 6

AD-A
100000





W. R. C. C. F. Y. R. E. S. O. L. U. T. I. O. N. T. E. S. T. C. H. A. R. T.
M. I. T. M. A. S. S. A. C. H. U. S. E. T. S.

Table 7-2. Method 1 Stress Ratio-Rut Depth-Load Cycle Relationships for Full-Scale Loading.

Application	Point During Test	Membrane Type	Relationship	r^2
Rut at a Given N	N = 10	None	RD = 0.283 (SR) ^{1.430}	0.954
	N = 10 ²	None	RD = 0.812 (SR) ^{1.359}	0.901
	N = 10 ³	None	RD = 1.318 (SR) ^{1.582}	0.994
	N = 10	T-3401	RD = 0.233 (SR) ^{1.251}	0.864
	N = 10 ²	T-3401	RD = 0.506 (SR) ^{1.402}	0.841
	N = 10 ³	T-3401	RD = 1.186 (SR) ^{1.288}	0.857
	RD = 2 in.	None	Log N = 6.140 (SR) ^{-1.390}	0.860
	RD = 3 in.	None	Log N = 6.037 (SR) ^{-1.117}	0.929
	RD = 4 in.	None	Log N = 6.622 (SR) ^{-1.028}	0.959
Load Cycles at a Given Rut	RD = 6 in.	None	Log N = 7.161 (SR) ^{-0.908}	0.957
	RD = 2 in.	T-3401	Log N = 5.200 (SR) ^{-0.955}	0.915
	RD = 3 in.	T-3401	Log N = 6.728 (SR) ^{-0.930}	0.846
	RD = 4 in.	T-3401	Log N = 6.652 (SR) ^{-0.800}	0.785
	RD = 6 in.	T-3401	Log N = 7.523 (SR) ^{-0.736}	0.724

rutting responses falling between those of corresponding AS and Typar 3401 reinforced AFS systems (i.e., Figures J-19 through J-24). The heavier grade of Bidim fabric utilized in the field tests could reasonably be expected to produce a response approximating that of the Typar 3401 reinforced systems.

A pair of full-scale model tests was conducted at the Georgia Institute of Technology (60, 81), involving an AS system and the corresponding Typar 3401 reinforced AFS system. These tests were conducted in a circular pit, having a diameter of eight feet. The subgrade and crushed stone materials were the same ones utilized in the model test program. Thirty inches of subgrade material was utilized during each of these tests. Repeated loading was applied through a 12 inch diameter footing, having a contact pressure of 70 psi.

Pertinent material properties and selected results for the full-scale tests are presented in Table 7-3, while the load cycle-cumulative permanent deformation relationships are presented in Figures 7-1 and 7-2. The large scale tests display lower initial rates of rutting than those observed in the model test program. This trend is especially evident in the full-scale model tests conducted at the Georgia Institute of Technology. A possible cause for this change in rutting response might be thixotropic strengthening effects in the full-scale tests due to increased construction times. Repeated load testing (85, 86) of highly saturated compacted clay specimens has shown such effects to be most severe at lower deformation (i.e., less than five percent strain) and load cycle (i.e., 10^2 to 10^3) levels (i.e., initial rates of rutting). During the half-scale model test program, sections were constructed

Table 7-3. Summary of Selected Results from Full-Scale Tests.

Test No.	1(c)	2(c)	3(d)	4(d)
Membrane Type	None	B-C38	None	T-3401
Crushed Stone Depth (in.)	14.0	14.0	14.7	14.8
Subgrade Soil:				
Unsoaked CBR	0.90	1.15	0.73(e)	0.73(e)
Vane Shear Strength	4.61(e)	5.42(e)	4.05(e)	4.05(e)
Stress Ratio (a)	3.82	3.25	3.58	3.51
Load Repetitions: (b)				
N ₂	31	125	25	220
N ₃	68	260	37	305
N ₄	89	415	48	400
N ₆	130	830	65	540

(a) Ref. Page 92 for Definition

(b) N_i = Number of Load Repetitions to 1 inches of Total Cumulative Permanent Deformation

(c) U.S. Army Corps of Engineers Tests

(d) Georgia Institute of Technology Tests

(e) Estimated from Strength Correlations (Ref. Table 3-1)

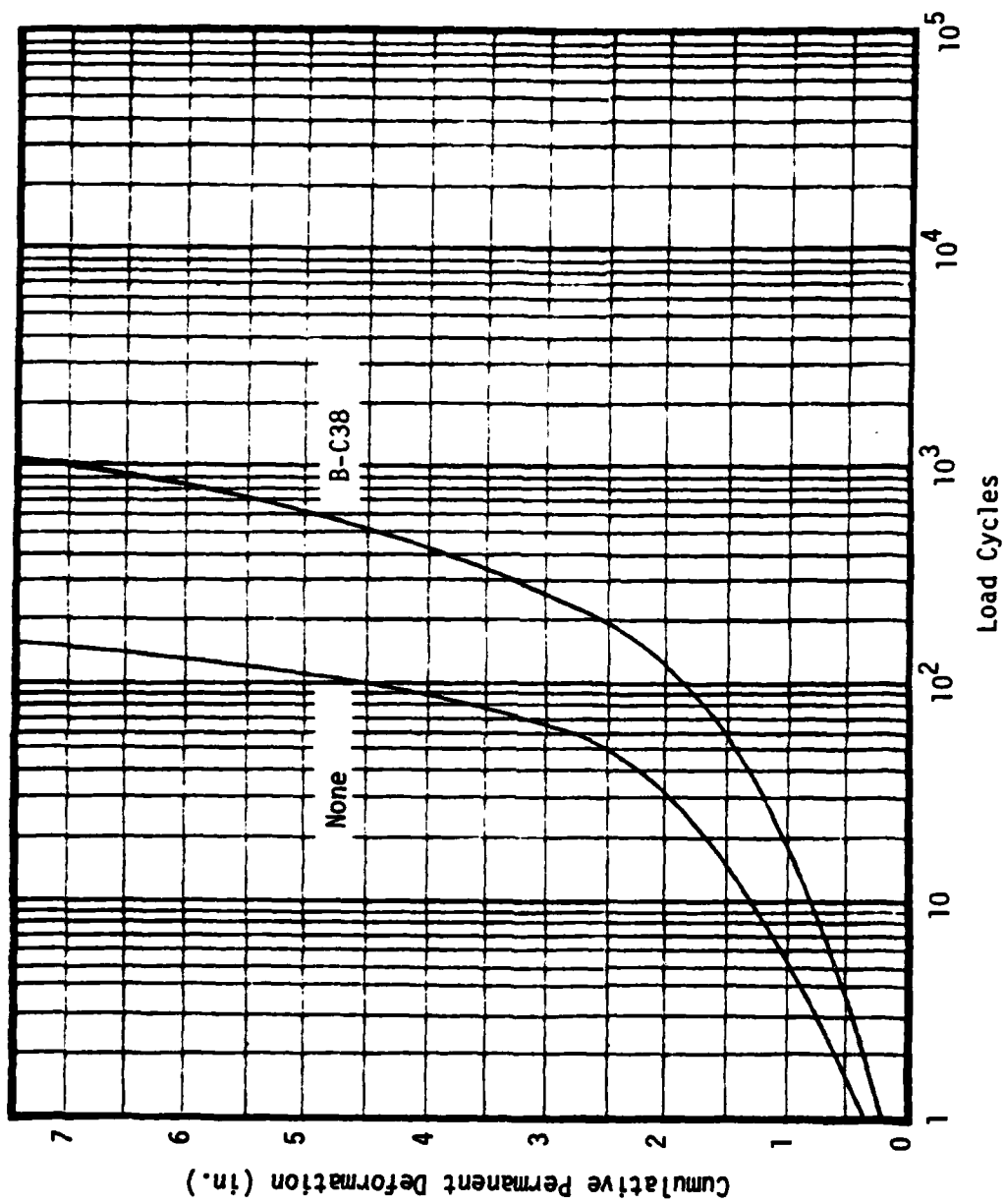


Figure 7-1. Load Cycle Cumulative Permanent Deformation Relationships for Full-Scale Field Tests (Ref. Table 7-3 for Pertinent Test Data).

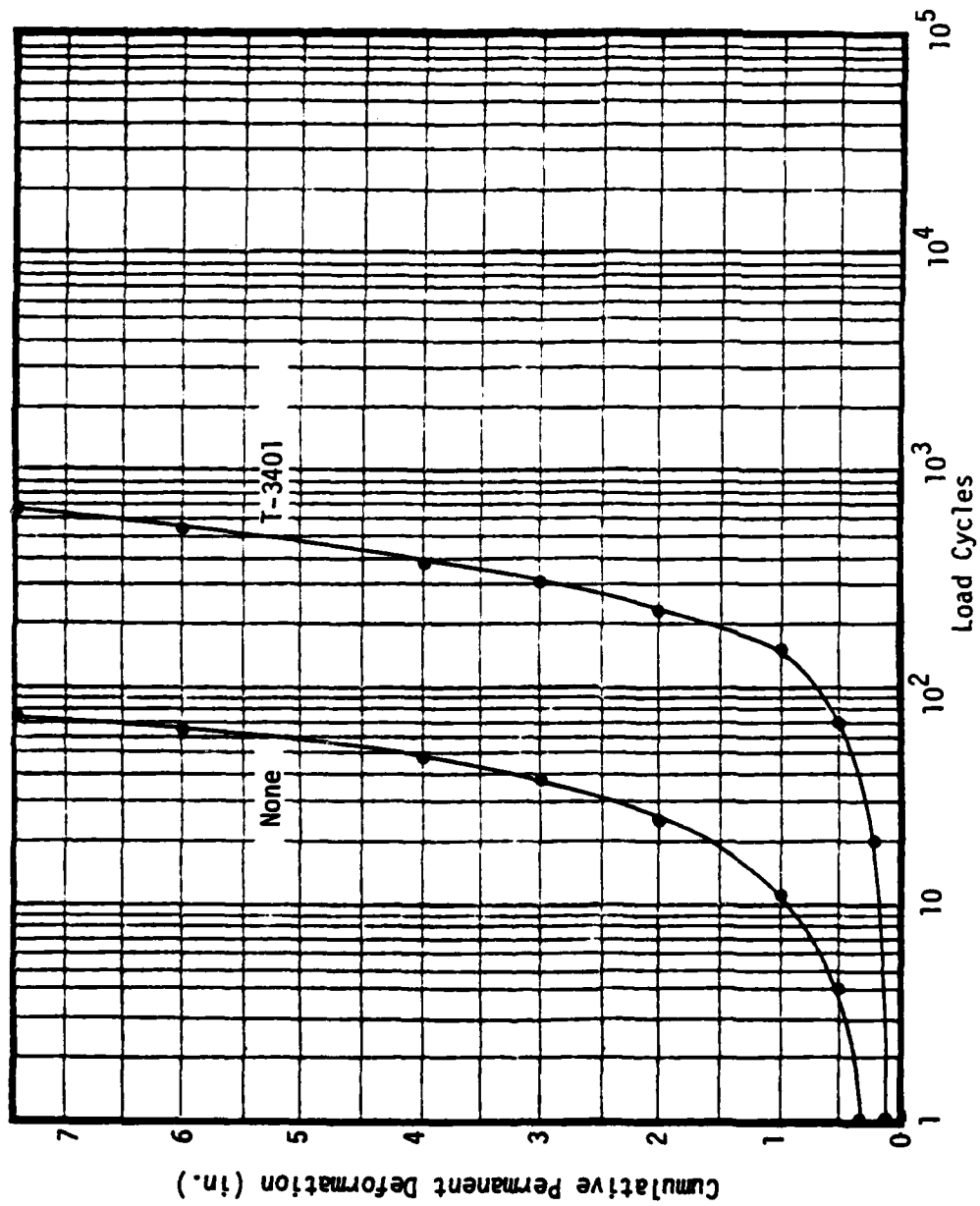


Figure 7-2. Load Cycle-Cumulative Permanent Deformation Relationships for Full-Scale Model Tests (Ref. Table 7-3 for Pertinent Test Data).

within an 8-10 hour period and testing initiated immediately thereafter. Preparation of the full-scale model tests required in excess of two weeks (62). While not studied extensively, limited testing (82) did show the subgrade material to display thixotropic strengthening characteristics which could have altered the initial rutting responses in the observed manner. Construction time for the full-scale field test sections was 2-3 days. The thixotropic characteristics of the subgrade material used in these tests is not known.

The equations presented in Table 7-2 were applied to the full-scale tests, with the results summarized in Table 7-4. The actual and predicted rutting responses are presented in Figures 7-3 and 7-4. The predicted responses are conservative at rut depths of less than approximately 4.5 inches, but somewhat unconservative at higher rut depths, where the full-scale tests displayed an extremely high rate of rutting. As mentioned previously, the conservative predictions at lower deformation levels may be due to thixotropic strengthening effects altering the initial rates of rutting in the full-scale tests.

Method 2

The results of the model test program were analyzed, for Type B loading, to provide correlations of stress ratio, rut depth, and load cycles, having the form:

$$SR^{0.65} = C_1 + C_2 \frac{\sqrt{RD}}{\log N} \quad (7-3)$$

where SR = stress ratio at subgrade surface

RD = rut depth, inches

N = load cycles

Table 7-4. Summary of Method 1 Predictions of Rutting Responses for Full-Scale Tests.

Test No.	Membrane Type	Depth of Stone Stress (a) (in.) Ratio	Method	Rut at Given N		Load Cycles to Given Rut					
				N = 10 ²		N = 10 ³		Δ = 2 in.		Δ = 3 in.	
				Δ (in.)	Δ (in.)	Δ (in.)	Δ (in.)	N	N	N	N
1(b)	None	14.0	3.82	Actual	1.30	4.50	--	31	68	89	130
				Pred.	1.92	5.02	10.98	9	22	47	132
2(b)	B-C38	14.0	3.25	Actual	0.80	1.80	7.10	125	260	415	830
				Pred.	1.02	2.64	5.41	49	177	390	1444
3(c)	None	14.7	3.58	Actual	0.95	--	--	25	37	48	65
				Pred.	1.75	4.60	9.91	11	28	61	178
4(c)	T-3401	14.8	3.51	Actual	0.15	0.70	--	220	305	400	540
				Pred.	1.12	2.94	5.98	37	124	273	968

(a) Ref. Page 92 for Definition
 (b) U.S. Army Corps of Engineers Tests
 (c) Georgia Institute of Technology Tests

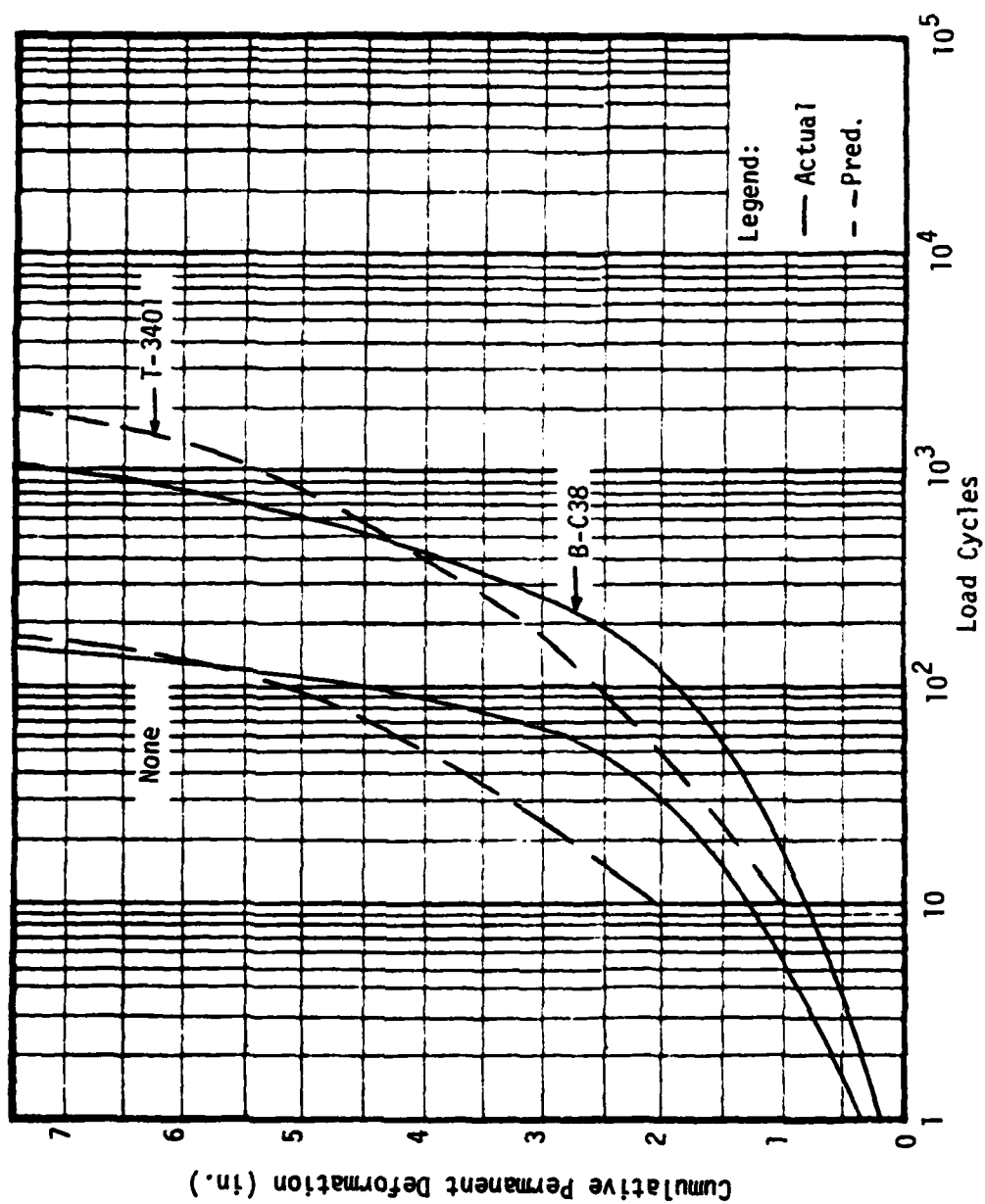


Figure 7-3. Comparison of Actual and Method 1 Predictions of Rutting Response for Full-Scale Field Tests (U.S. Army Corps of Engineers).

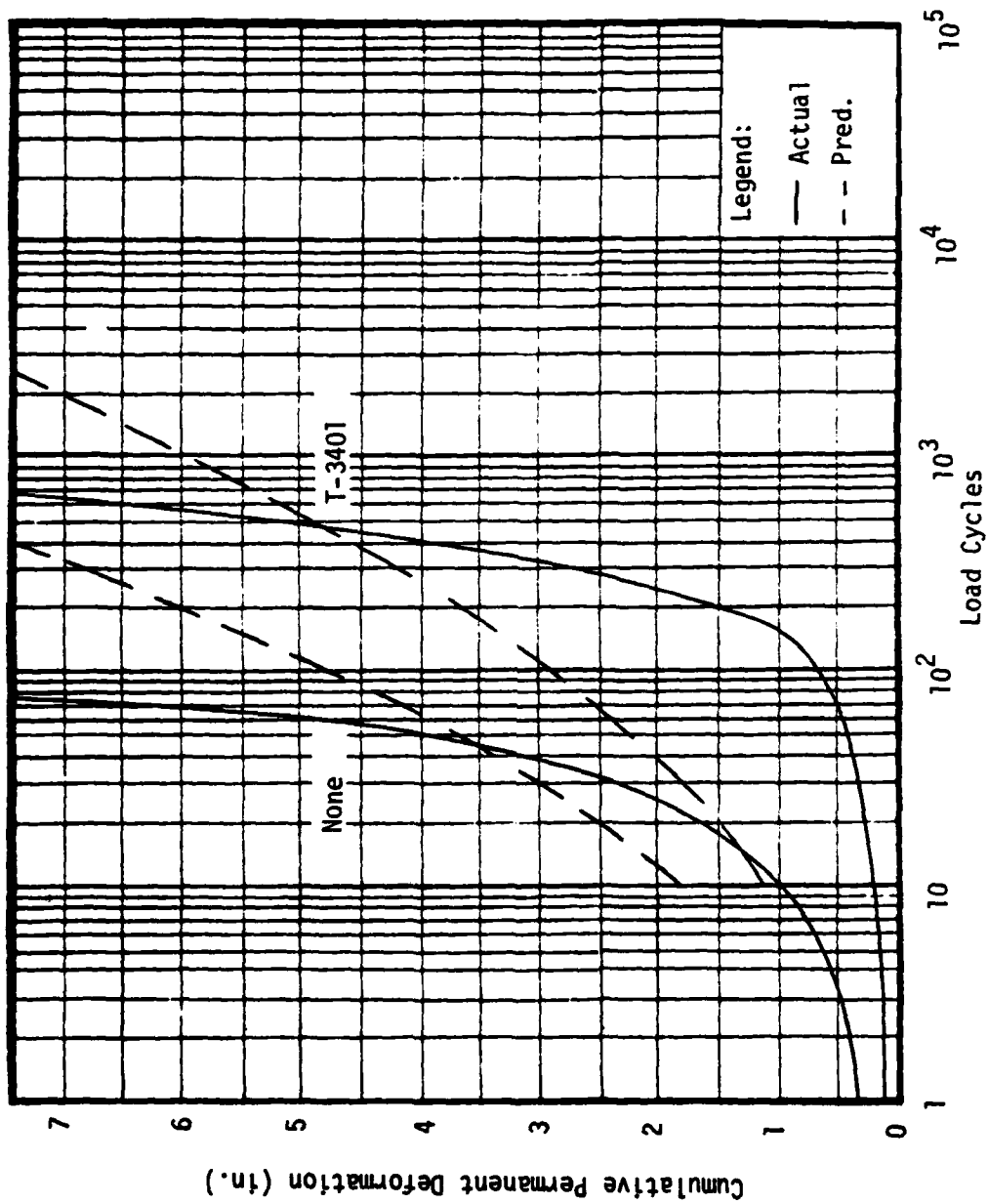


Figure 7-4. Comparison of Actual and Method 1 Predictions of Rutting Response for Full-Scale Model Tests (Georgia Institute of Technology).

C_i = regression analysis constants.

Relationships were developed for both AS and Typar 3401 reinforced AFS systems, utilizing techniques available in the Biomedical Computer Program, P-series (37). Data input included stress ratio and the load cycle-cumulative permanent deformation data presented in tabular form in Appendix E. The power to which the stress ratio is raised in Equation (7-3) was chosen on the basis of the correlations developed for Method 1 (i.e., Equations (7-1) and (7-2)) and presented in Appendix J. If those expressions are solved for stress ratio in terms of the square root of rut depth or the reciprocal of the log of the number of load cycles, the power to which the stress ratio is raised varies from 0.60-0.83. Preliminary calculations with the tests of subgrade Group I, varying the exponent by increments of 0.05 within this range, indicated 0.65 to provide the best data fit. The resulting expressions are as follows:

AS systems:

$$SR^{0.65} = 0.596 + 2.328 \frac{\sqrt{RD}}{\log N} \quad (7-4)$$

Typar 3401 reinforced AFS systems:

$$SR^{0.65} = 0.576 + 3.022 \frac{\sqrt{RD}}{\log N} \quad (7-5)$$

The coefficients of determination (i.e., r^2) for these relationships are 0.880 and 0.715 respectively.

While Method 1 results in the fit of a power curve to a semi-log plot of load cycles and rut depth, Method 2 results in the fit of a

parabolic curve. The results of this method, as applied to the model test program, are presented in Table 7-5. For AS systems, with Type B loading, computed rut depths averaged 99 percent of the observed rut depths, with a range of 58-127 percent. For Typar 3401 reinforced AFS systems, the computed rut depths averaged 98 percent of the actual rut depths, with a range of 42-148 percent. The average values were comparable to those of Method 1, while the ranges were slightly greater. While the predictions of the methods were not significantly different, Method 2 offers the major advantage of predicting rutting response at any point during a test, while Method 1 is limited in application to selected points.

If the corrections for instrumentation and scaling are applied, for extension of the method to full-scale tests, the following expressions result:

AS systems:

$$SR^{0.65} = 0.596 + 1.785 \frac{\sqrt{RD}}{\text{Log } (2.4N)} \quad (7-6)$$

Typar 3401 reinforced AFS systems:

$$SR^{0.65} = 0.576 + 2.318 \frac{\sqrt{RD}}{\text{Log } (2.4N)} \quad (7-7)$$

Equations (7-6) and (7-7) were applied to the full-scale tests, with the results presented in Table 7-6. The actual and predicted rutting responses are presented in Figures 7-5 and 7-6. As with Method 1, the predicted responses are conservative at rut depths of less than approximately 4.5 inches, but unconservative at higher rut depths. No

Table 7-5. Summary of Method 2 Predictions of Model Test Program Rutting Responses.

Test Membrane Stone Stress (a) No.	Type	Depth of (in.)	Ratio	Method	Rut at Given N			Load Cycles at Given Rut		
					N = 10			$\Delta = 2$ in. $\Delta = 3$ in. $\Delta = 4$ in.		
					$\frac{N}{\Delta} \left(\frac{\text{in.}}{\text{in.}} \right)$	$\frac{N}{\Delta} \left(\frac{\text{in.}}{\text{in.}} \right)$	$\frac{N}{\Delta} \left(\frac{\text{in.}}{\text{in.}} \right)$	N	N	N
1B	None	6.0	6.75	Actual Pred.	1.35 1.51	4.92 6.05	-- --	20 14	40 26	68 42
3B	None	7.5	4.50	Actual Pred.	0.78 0.78	2.76 3.14	5.57* 7.06	48 39	140 90	310 181
5B	None	9.0	3.38	Actual Pred.	0.60 0.48	1.62 1.92	3.93 4.31	170 111	480 318	1100 776
7B	None	4.5	6.41	Actual Pred.	1.79 1.39	4.79 5.58	-- --	13 16	20 29	60 49
13B	None	7.0	3.63	Actual Pred.	0.68 0.54	1.75 2.17	4.97* 4.89	140 83	300 224	570 517
19B	None	10.0	1.81	Actual Pred.	0.24 0.14	0.82 0.56	1.61 1.27	2800 5812	-- --	-- --
26B	None	3.0	6.76	Actual Pred.	1.57 1.52	5.53* 6.07	-- --	16 14	31 25	52 42
28B	None	4.5	4.34	Actual Pred.	0.88 0.74	2.40 2.95	5.50* 6.65	68 44	180 104	380 213
30B	None	6.0	2.74	Actual Pred.	0.42 0.33	1.18 1.30	3.30 2.94	280 299	770 1079	2500 3177

(a) Ref. Page 92 for Definition
* Extrapolated Data Point

Table 7-5. (Continued).

Test Membrane No.	Type	Depth of Stone (in.)	Stress Ratio	Method	Rut at Given N				Load Cycles to Given Rut		
					$N = 10^2$				$\Delta = 2 \text{ in.}$		
					$\frac{N}{\Delta} \left(\frac{\text{in.}}{\text{in.}} \right)$	$\frac{N}{\Delta} \left(\frac{\text{in.}}{\text{in.}} \right)$	$\frac{N}{\Delta} \left(\frac{\text{in.}}{\text{in.}} \right)$	$\frac{N}{\Delta} \left(\frac{\text{in.}}{\text{in.}} \right)$	N	N	N
32B	None	3.0	4.74	Actual Pred.	1.25 0.86	3.72 3.42	-- --	-- --	25 34	60 75	120 145
2B	T-3401	6.0	6.72	Actual Pred.	0.91 0.90	2.71 3.62	5.50* 8.14	-- --	46 31	140 66	320 127
4B	T-3401	7.5	4.62	Actual Pred.	0.49 0.50	1.83 1.98	4.12 4.46	-- --	120 102	290 288	875 692
6B	T-3401	9.0	3.32	Actual Pred.	0.32 0.28	1.08 1.13	2.08 2.54	3.50 4.52	850 459	4500 1821	50000* 5818
9B	T-3401	4.5	6.46	Actual Pred.	0.92 0.85	2.46 3.40	-- --	-- --	50 34	220 76	500 148
15B	T-3401	7.0	3.71	Actual Pred.	0.40 0.34	1.28 1.37	3.72 3.08	4.97* 5.48	260 261	610 911	1700 2613
20B	T-3401	10.0	1.77	Actual Pred.	0.19 0.08	0.36 0.33	1.07 0.75	1.63 1.34	-- --	-- --	-- --
27B	T-3401	3.0	6.71	Actual Pred.	1.04 0.90	2.96 3.61	-- --	-- --	59 31	110 67	170 128
29B	T-3401	4.5	4.30	Actual Pred.	0.38 0.44	1.24 1.76	2.97 3.96	-- --	360 135	1150 408	2150 1035

(a) Ref. Page 92 for Definition
* Extrapolated Data Point

Table 7-5. (Continued).

Test Membrane No.	Type	Depth of Stone (in.)	Stress Ratio (a)	Method	Rut at Given N				Load Cycles to Given Rut		
					$N = 10$	$N = 10^2$	$N = 10^3$	$N = 10^4$	$\Delta = 2$ in.	$\Delta = 3$ in.	$\Delta = 4$ in.
					$\frac{\Delta(\text{in.})}{\Delta(\text{in.})}$	$\frac{\Delta(\text{in.})}{\Delta(\text{in.})}$	$\frac{\Delta(\text{in.})}{\Delta(\text{in.})}$	$\frac{\Delta(\text{in.})}{\Delta(\text{in.})}$	N	N	N
318	T-3401	6.0	3.13	Actual Pred.	0.53 0.25	1.67 1.02	3.49 2.29	4.94* 4.07	175 639	600 2728	2250 9278
338	T-3401	3.0	4.81	Actual Pred.	0.76 0.53	2.63 2.12	-- --	-- --	58 88	150 240	280 559

(a) Ref. Page 92 for Definition

* Extrapolated Data Point

Table 7-6. Summary of Method 2 Predictions of Rutting Responses for Full-Scale Tests.

Test Membrane No.	Type	Depth of Stone (in.)	Stress Ratio (a)	Method	Rut at Given N		Load Cycles to Given Rut									
					$N = 10^2$		$N = 10^3$		$\Delta = 2$ in.		$\Delta = 3$ in.		$\Delta = 4$ in.		$\Delta = 6$ in.	
					$\frac{\Delta(\text{in.})}{N}$	$\frac{\Delta(\text{in.})}{N}$	$\frac{\Delta(\text{in.})}{N}$	$\frac{\Delta(\text{in.})}{N}$	N	N	N	N	N	N	N	N
1(b)	None	14.0	3.82	Actual Pred.	1.30 1.92	4.50 5.72	-- 11.54	-- 11.54	31 11	68 22	89 41	130 114				
2(b)	B-C38	14.0	3.25	Actual Pred.	0.80 0.88	1.80 2.62	7.10 5.28	7.10 5.28	125 50	260 147	415 365	830 1675				
3(c)	None	14.7	3.58	Actual Pred.	0.95 1.72	-- 5.11	-- 10.30	-- 10.30	25 13	37 28	48 53	65 158				
4(c)	T-3401	14.8	3.51	Actual Pred.	0.15 1.01	0.70 3.00	-- 6.04	-- 6.04	220 37	305 100	400 234	540 972				

(a) Ref. Page 92 for Definition
 (b) U.S. Army Corps of Engineers Tests
 (c) Georgia Institute of Technology Tests

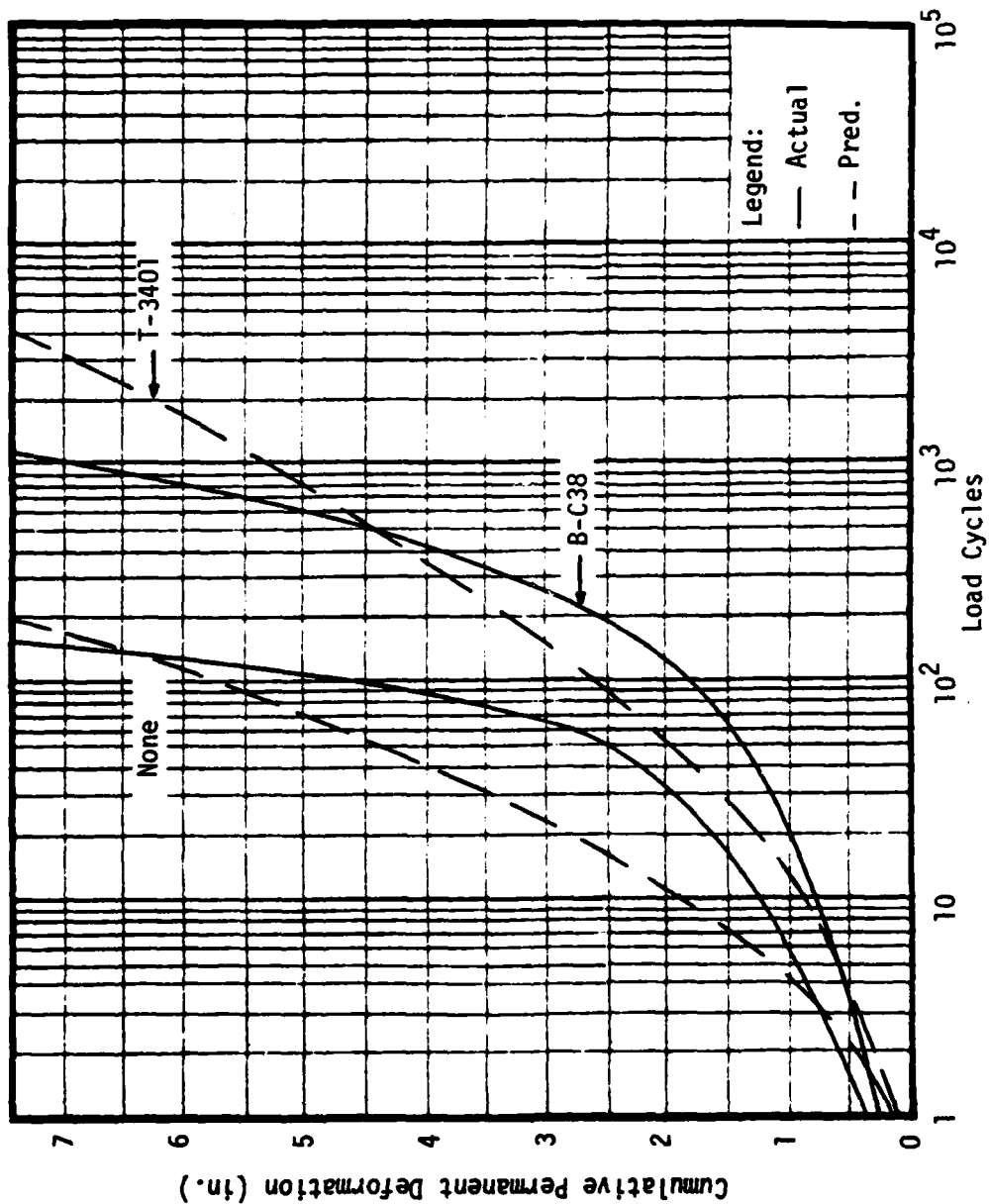


Figure 7-5. Comparison of Actual and Method 2 Predictions of Rutting Response for Full-Scale Field Tests (U.S. Army Corps of Engineers).

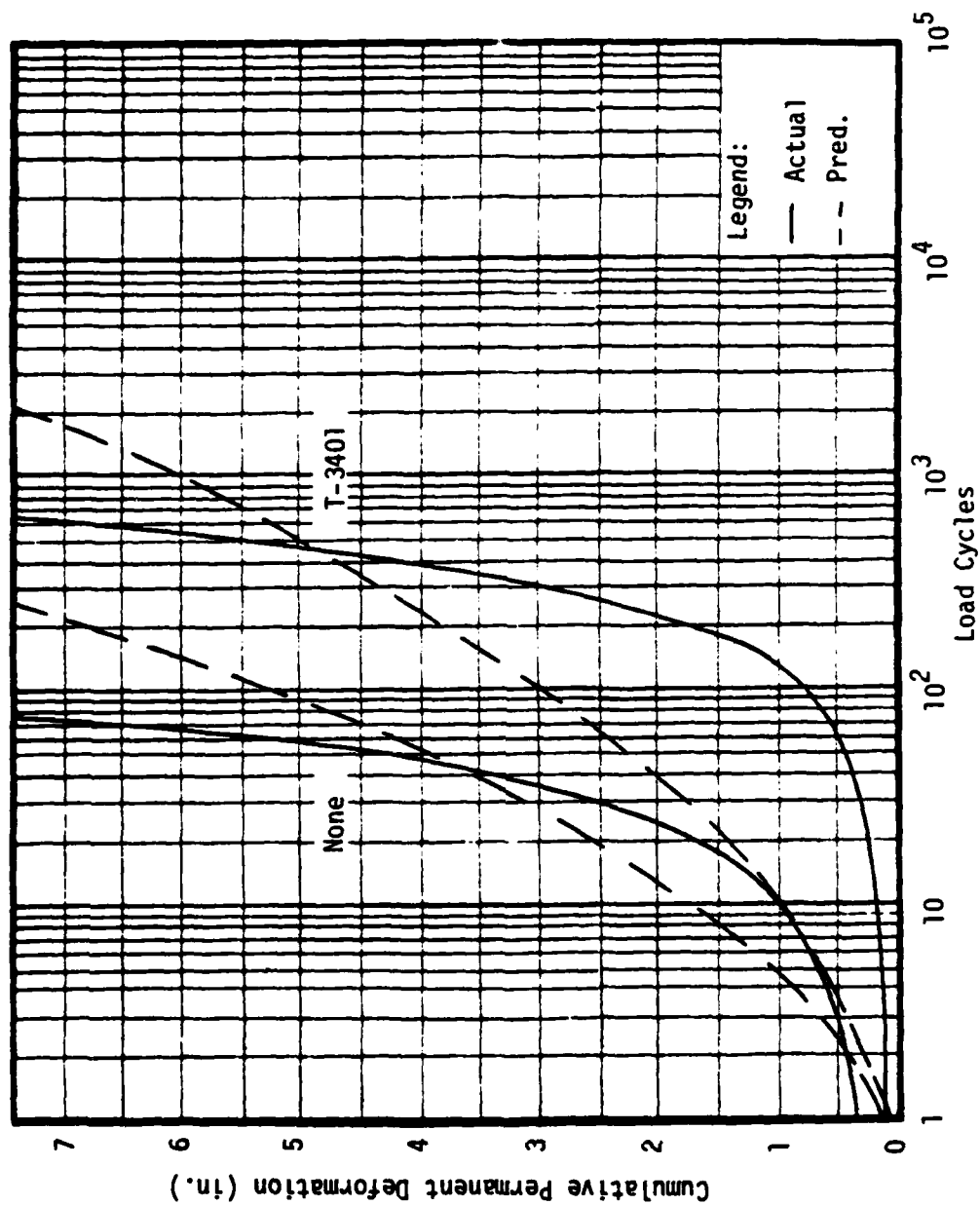


Figure 7-6. Comparison of Actual and Method 2 Predictions of Rutting Response for Full-Scale Model Tests (Georgia Institute of Technology).

major improvement was evident, as compared to the calculated responses of Method 1.

Method 3

The results of the model test program were analyzed, for Type B loading, to provide correlations of rut depth and load cycles for each test having the form:

$$\text{Log } N = \frac{\text{RD}}{C_1 + C_2 \text{ RD}} \quad (7-8)$$

where N = load cycles

RD = rut depth, inches

C_1 = regression analysis constants.

Data input for each test included the load cycle-cumulative permanent deformation data presented in tabular form in Appendix E.

The curve fitting constants for AS system tests were then evaluated in terms of the corresponding system stress ratios, to provide a correlation of stress ratio, rut depth, and load cycles. The procedure was then repeated with the curve fitting constants of the Typar 3401 reinforced AFS systems. The resulting expressions are as follows:

AS systems:

$$\text{Log } N = \frac{\text{RD}}{(0.117(\text{SR})^{1.198}) + \left(\frac{\text{SR}}{6.696 + 2.732 \text{ SR}}\right) (\text{RD})} \quad (7-9)$$

Typar 3401 reinforced AFS systems:

$$\text{Log } N = \frac{\text{RD}}{(0.088(\text{SR})^{1.113}) + \left(\frac{\text{SR}}{4.023 + 3.900 \text{ SR}}\right) (\text{RD})} \quad (7-10)$$

where N = load cycles

RD = rut depth, inches

SR = stress ratio at subgrade surface.

The above expressions fit a hyperbolic curve to a semi-log plot of load cycles and rut depth. The results of this method, as applied to the model test program, are presented in Table 7-7. For AS systems, with Type B loading, computed rut depths averaged 103 percent of the observed rut depths, with a range of 78-146 percent. For Typar 3401 reinforced AFS systems, the computed rut depths averaged 106 percent of the actual rut depths, with a range of 61-177 percent. The average values were slightly greater than those of Methods 1 or 2, and the ranges were greater than those of Method 1 and comparable to those of Method 2. As with Method 2, this approach predicts rutting response at any point during a test, a major advantage over the selected point predictions of Method 1.

If the corrections for instrumentation and scaling are applied, for extension of the method to full-scale tests, the following expressions result:

AS systems:

$$\text{Log } (2.4N) = \frac{RD}{(0.199 (SR)^{1.198}) + \left(\frac{SR}{6.696 + 2.732 SR}\right) (RD)} \quad (7-11)$$

Typar 3401 reinforced AFS systems:

$$\text{Log } (2.4N) = \frac{RD}{(0.150 (SR)^{1.113}) + \left(\frac{SR}{4.023 + 3.900 SR}\right) (RD)} \quad (7-12)$$

Table 7-7. Summary of Method 3 Predictions of Model Test Program Rutting Responses.

Test Membrane No.	Type	Depth of Stone Stress (in.)	Ratio	Method	Rut at Given N			Load Cycles to Given Rut		
					$N = 10$	$N = 10^2$	$N = 10^3$	$\Delta = 2$ in.	$\Delta = 3$ in.	$\Delta = 4$ in.
					$\frac{\Delta(\text{in.})}{\Delta(\text{in.})}$	$\frac{\Delta(\text{in.})}{\Delta(\text{in.})}$	$\frac{\Delta(\text{in.})}{\Delta(\text{in.})}$	N	N	N
1B	None	6.0	6.75	Actual Pred.	1.35 1.58	4.92 4.98	-- --	20 15	40 34	68 63
3B	None	7.5	4.50	Actual Pred.	0.78 0.93	2.76 2.70	5.57* 7.36	48 49	140 130	310 260
5B	None	9.0	3.38	Actual Pred.	0.60 0.64	1.62 1.75	3.93 4.15	170 143	480 429	1100 910
7B	None	4.5	6.41	Actual Pred.	1.79 1.47	4.79 4.60	-- --	13 17	20 40	60 74
13B	None	7.0	3.63	Actual Pred.	0.68 0.70	1.75 1.95	4.97* 4.77	140 107	300 311	570 650
19B	None	10.0	1.81	Actual Pred.	0.24 0.28	0.82 0.69	1.61 1.34	2800 4395	-- --	-- --
26B	None	3.0	6.76	Actual Pred.	1.57 1.58	5.53* 4.99	-- --	16 15	31 34	52 62
28B	None	4.5	4.34	Actual Pred.	0.88 0.89	2.40 2.55	5.50* 6.83	68 56	180 149	380 301
30B	None	6.0	2.74	Actual Pred.	0.42 0.48	1.18 1.27	3.30 2.79	280 374	770 1232	2500 2734

(a) Ref. Page 92 for Definition
* Extrapolated Data Point

Table 7-7. (Continued).

Depth of Stone Stress (a)				Rut at Given N				Load Cycles to Given Rut				
Test No.	Membrane Type	Stone (in.)	Ratio	Method	N = 10		N = 10 ²		N = 10 ³		N = 10 ⁴	
					$\frac{\Delta(\text{in.})}{N}$	$\frac{\Delta(\text{in.})}{\Delta(\text{in.})}$	$\frac{\Delta(\text{in.})}{N}$	$\frac{\Delta(\text{in.})}{\Delta(\text{in.})}$	$\frac{\Delta(\text{in.})}{N}$	$\frac{\Delta(\text{in.})}{\Delta(\text{in.})}$	$\frac{\Delta(\text{in.})}{N}$	$\frac{\Delta(\text{in.})}{\Delta(\text{in.})}$
32B	None	3.0	4.74	Actual Pred.	1.25	3.72	--	--	25	60	120	
					0.99	2.92	--	--	41	107	212	
2B	T-3401	6.0	6.72	Actual Pred.	0.91	2.71	5.50*	--	46	140	320	
					0.95	2.65	6.63	--	49	137	289	
4B	T-3401	7.5	4.62	Actual Pred.	0.49	1.83	4.12	--	120	290	875	
					0.61	1.67	3.92	--	163	493	1052	
6B	T-3401	9.0	3.32	Actual Pred.	0.32	1.08	2.08	3.50	850	4500	50000*	
					0.42	1.10	2.44	6.19	562	1779	3763	
9B	T-3401	4.5	6.46	Actual Pred.	0.92	2.46	--	--	50	220	500	
					0.90	2.53	--	--	55	156	329	
15B	T-3401	7.0	3.71	Actual Pred.	0.40	1.28	3.72	4.97*	260	610	1700	
					0.48	1.27	2.87	7.71	403	1133	2407	
20B	T-3401	10.0	1.77	Actual Pred.	0.19	0.36	1.07	1.63	--	--	--	
					0.20	0.49	0.97	1.89	--	--	--	
27B	T-3401	3.0	6.71	Actual Pred.	1.04	2.96	--	--	59	110	170	
					0.95	2.65	--	--	50	138	290	
29B	T-3401	4.5	4.30	Actual Pred.	0.38	1.24	2.97	--	360	1150	2150	
					0.56	1.53	3.54	--	210	643	1370	

(a) Ref. Page 92 for Definition
* Extrapolated Data Point

Table 7-7. (Continued).

Test Membrane No.	Type	Depth of Stone (in.)	Stress Ratio	(a) Method	Rut at Given N				Load Cycles to Given N		
					$N = 10$	$N = 10^2$	$N = 10^3$	$N = 10^4$	$\Delta = 2$ in.	$\Delta = 3$ in.	$\Delta = 4$ in.
					$\frac{N}{\Delta(\text{in.})}$	$\frac{N}{\Delta(\text{in.})}$	$\frac{N}{\Delta(\text{in.})}$	$\frac{N}{\Delta(\text{in.})}$	N	N	N
31B	T-3401	6.0	3.13	Actual Pred.	0.53 0.39	1.67 1.02	3.49 2.24	4.94* 5.51	175 717	600 2282	2250 4815
33B	T-3401	3.0	4.81	Actual Pred.	0.76 0.64	2.63 1.76	-- --	-- --	58 142	150 426	280 910

(a) Ref. Page 92 for Definition

* Extrapolated Data Point

Equations (7-11) and (7-12) were applied to the full-scale tests, with the results presented in Table 7-8. The actual and predicted rutting responses are presented in Figures 7-7 and 7-8. As with Methods 1 and 2, the predicted responses are conservative at rut depths of less than approximately 4.5 inches, but somewhat unconservative at higher rut depths. The calculated responses for the full-scale tests represent a slight improvement over those of the previously described methods. Additionally, the type of rutting response curve for this method (i.e., hyperbolic) more nearly approximates the high rate of rutting observed in the full-scale tests at deformation levels greater than three inches, than do the curve types of Methods 1 and 2 (i.e., power curve and parabolic curve respectively).

Method 4

Response may be predicted, for AS systems, by utilizing the U.S. Army Corps of Engineers (44, 45, 103) equation (i.e., Equation (2-2)) as modified (i.e., Equation (2-3)) by Hammitt (44). A rut depth of three inches, in vehicle trafficked unsurfaced AS systems, is anticipated at the number of load cycles computed on the basis of the resulting relationship (i.e., Equation 6-5)), which is expressed as:

$$t = F(P(\frac{1}{8.1 \text{ CBR}} - \frac{1}{p\pi}))^{0.5} \quad (6-5)$$

where t = required layer thickness, inches

$F = 0.176 \text{ Log } N + 0.120$

N = number of load repetitions during design period

P = total wheel load, pounds

CBR = California Bearing Ratio of underlying layer of material

Table 7-8. Summary of Method 3 Predictions of Rutting Responses for Full-Scale Tests.

Test Membrane No. Type		Depth of Stone Stress (in.)	Ratio	Method	Rut at Given N		Load Cycles to Given Run								
					$N = 10^2$		$N = 10^3$		$\Delta = 2$ in.		$\Delta = 3$ in.		$\Delta = 4$ in.		$\Delta = 6$ in.
				$\frac{N}{\Delta \text{ (in.)}}$		$\frac{N}{\Delta \text{ (in.)}}$		N		N		N		N	
1(b)	None	14.0	3.82	Actual Pred.	1.30 1.97	4.50 5.02	-- 13.59	31 10	68 27	89 56	130 157				
2(b)	B-C38	14.0	3.25	Actual Pred.	0.80 1.05	1.80 2.47	7.10 5.51	125 54	260 177	415 410	830 1249				
3(c)	None	14.7	3.58	Actual Pred.	0.95 1.81	-- 4.52	-- 11.66	25 13	37 34	48 72	65 210				
4(c)	T-3401	14.8	3.51	Actual Pred.	0.15 1.15	0.70 2.74	-- 6.22	220 41	305 130	400 299	540 910				

(a) Ref. Page 92 for Definition
 (b) U.S. Army Corps of Engineers Tests
 (c) Georgia Institute of Technology Tests

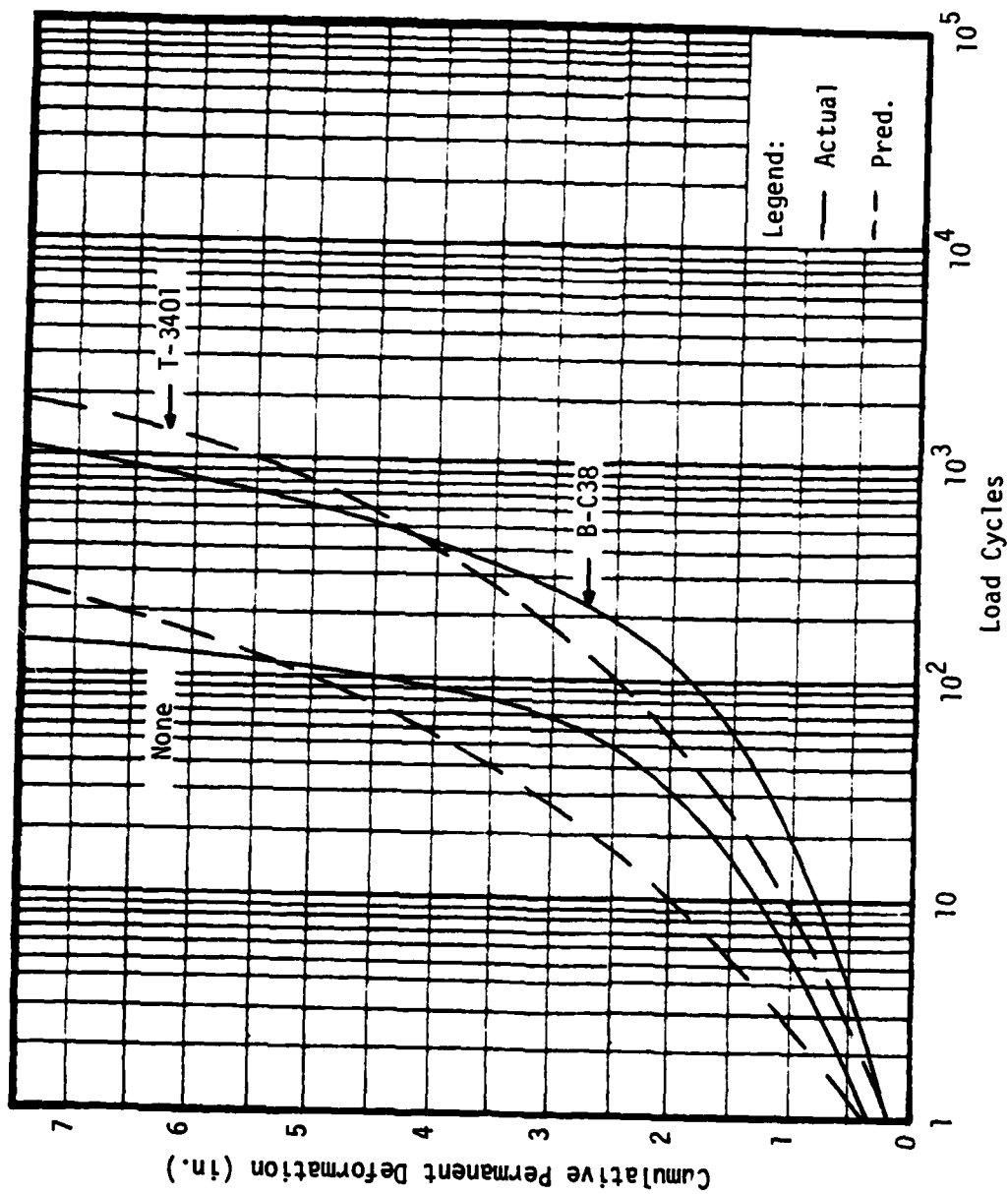


Figure 7-7. Comparison of Actual and Method 3 Predictions of Rutting Response for Full-Scale Field Tests (U.S. Army Corps of Engineers).

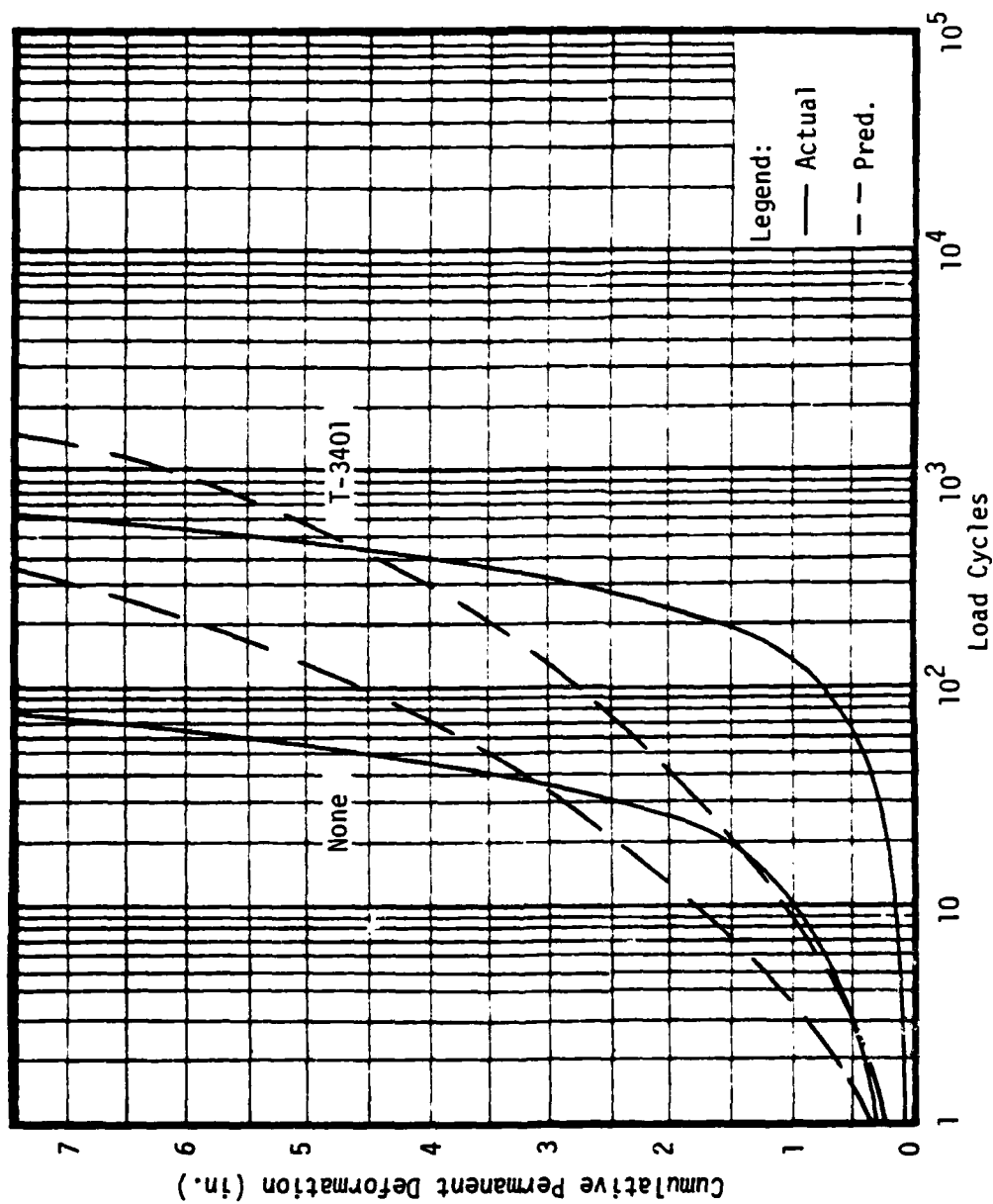


Figure 7-8. Comparison of Actual and Method 3 Predictions of Rutting Response for Full-Scale Model Tests (Georgia Institute of Technology).

p = tire contact pressure, psi.

Equation (6-5) may be linearized on a semi-log plot after dividing both sides of the equation by the radical expression.

Application of this method to the model test program requires correcting the model test data for instrumentation (i.e., model test load cycle data reduced by a factor of 2.4) and scaling (i.e., model test rut depths increased by a scale factor). As discussed in Chapter VI, applying a scale factor of 1.7 results in reasonable agreement with the responses predicted by Equation (6-5). Corrected model test data is plotted in Figure 7-9, along with Equation (6-5). Only Type B loading data are shown, as being more representative of field conditions. The regression equation to these data is also plotted in Figure 7-9. This regression equation may be expressed in the form:

$$t = F \left(P \left(\frac{1}{8.1 \text{ CBR}} - \frac{1}{p\pi} \right) \right)^{0.5} \quad (7-13)$$

where t = required layer thickness, inches

$F = 0.174 \text{ Log } N + 0.132$

N = number of load repetitions during design period

P = total wheel load, pounds

CBR = California Bearing Ratio of underlying layer of material

p = tire contact pressure, psi.

Equations (6-5) and (7-13) differ only in the value of F , with the latter equation predicting that a lower number of load applications (i.e., a reduction of approximately 10-15 percent) will produce a three inch rut.

A relationship of the above form was then developed for pre-

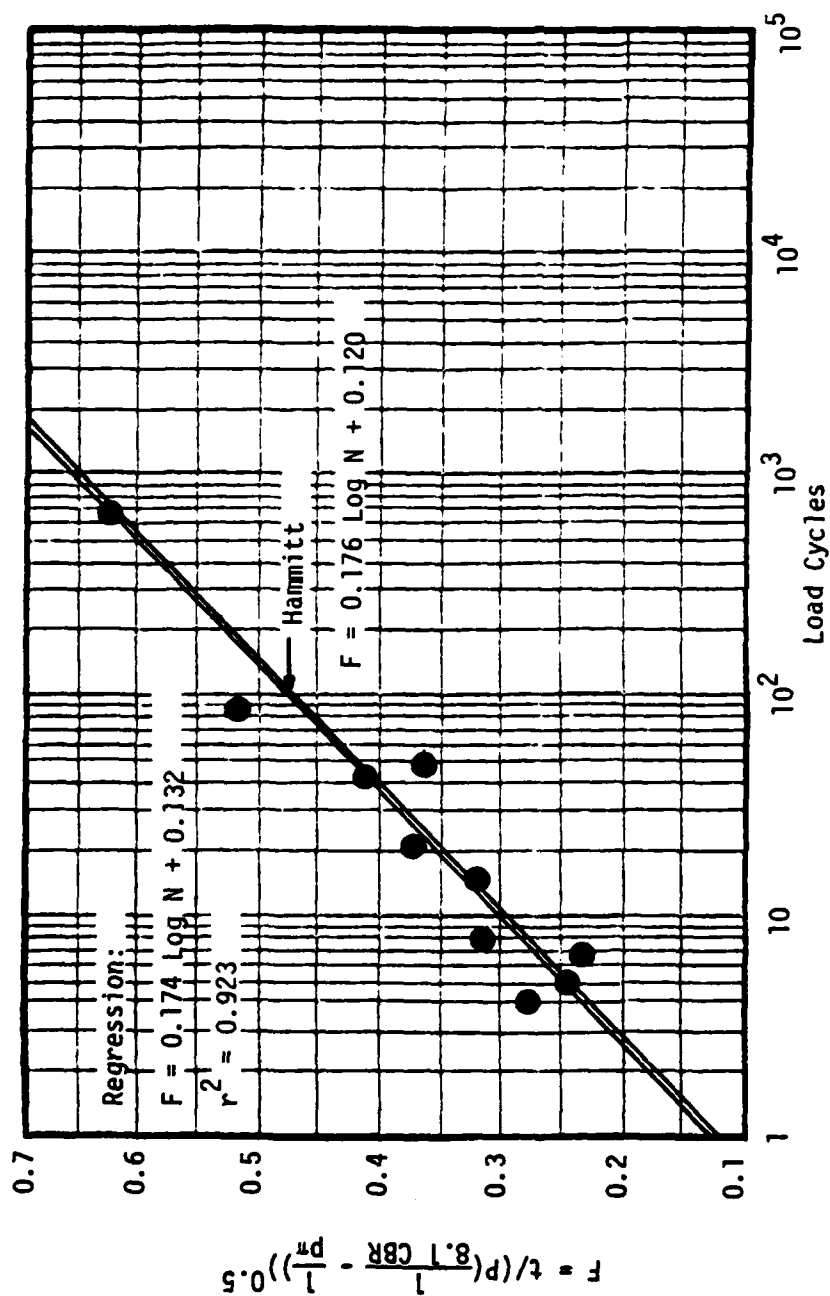


Figure 7-9. Method 4 Rutting Relationships for 3 in. Rut in AS System.

dicting the number of load cycles resulting in a three inch rut in vehicle trafficked unsurfaced AFS systems reinforced with Typar 3401 fabric. Model test data, corrected for instrumentation and scaling, for Typar 3401 reinforced AFS systems under Type B loading, is plotted in Figure 7-10, along with the regression equation to these data. This regression equation may be expressed as:

$$t = F(P(\frac{1}{8.1 \text{ CBR}} - \frac{1}{p\pi}))^{0.5} \quad (7-14)$$

where t = required layer thickness, inches

$F = 0.119 \text{ Log } N + 0.128$

N = number of load repetitions during design period

P = total wheel load, pounds

CBR = California Bearing Ratio of underlying layer of material

p = tire contact pressure, psi.

The results of this method as applied to the model test program are presented in Table 7-9, while Table 7-10 presents application of the method to the full-scale tests. The full-scale test prediction points for both AS systems and for the Typar 3401 reinforced AFS systems were more accurate than those of the three previously discussed methods. Only with the Bidim C38 reinforced AFS system was the predicted response point less accurate. For all full-scale tests, the corresponding prediction points of Methods 1-3 were more conservative, thus the comparatively increased inaccuracies noted in these predictions were safe in nature. Method 4 is the most limited of those presented thus far, predicting only one rutting response point during a given test.

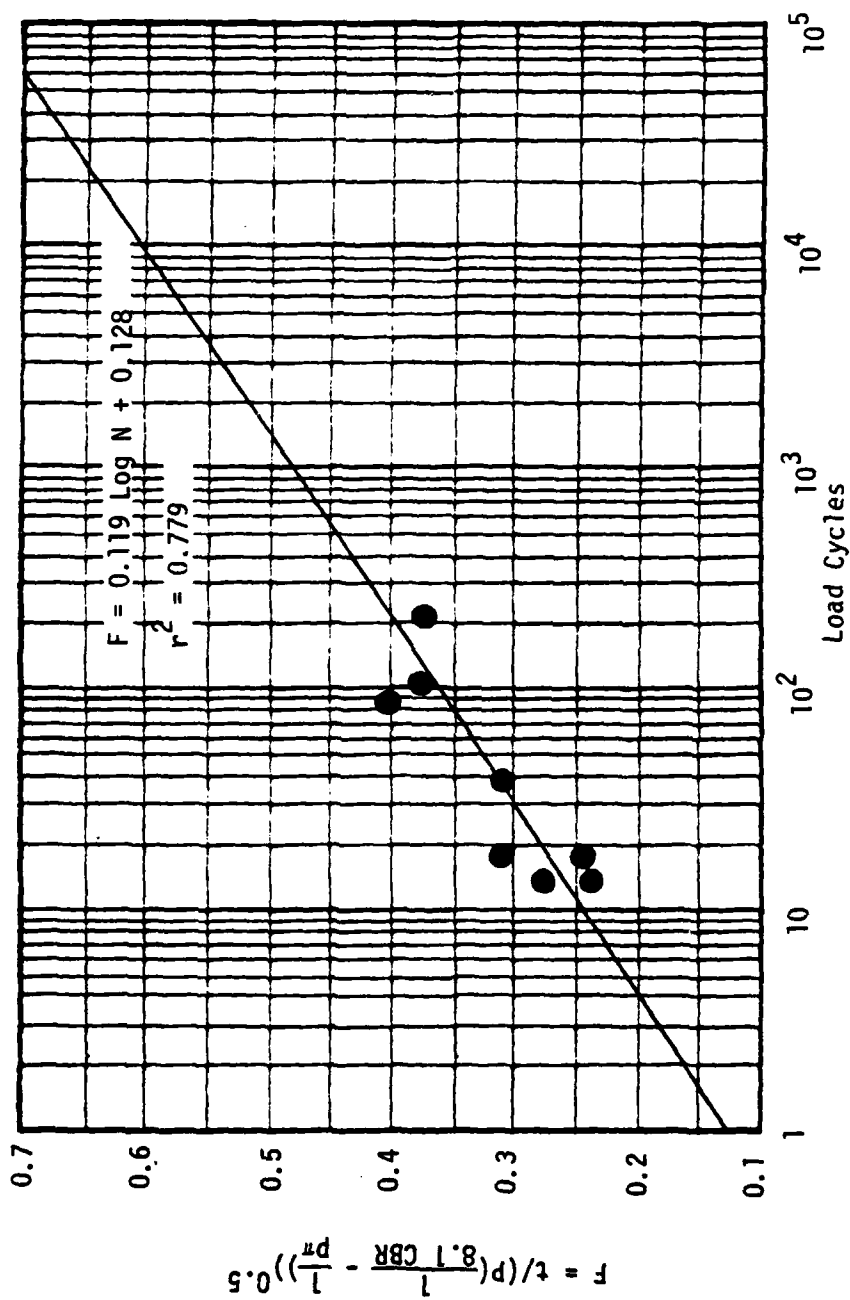


Figure 7-10. Method 4 Rutting Relationship for 3 in. Rut in T-3401 Reinforced AFS Systems.

Table 7-9. Summary of Method 4 Predictions of Model Test Program Rutting Responses.

Test No.	Membrane Type	Depth of Stone (in.)	Unsoaked CBR	Load Cycles to 3 in. Rut		
				N(a)	N(b)	N(c)
1B	None	6.0	0.38	7	5	4
3B	None	7.5	0.43	15	13	12
5B	None	9.0	0.40	48	25	22
7B	None	4.5	0.91	4	8	7
13B	None	7.0	0.81	42	44	39
19B	None	10.0	0.93	667	767	707
26B	None	3.0	1.55	5	5	5
28B	None	4.5	1.59	21	28	25
30B	None	6.0	1.72	85	188	170
32B	None	3.0	2.43	8	13	11
<hr/>						
2B	T-3401	6.0	0.39	14	--	9
4B	T-3401	7.5	0.41	38	--	34
6B	T-3401	9.0	0.41	208	--	111
9B	T-3401	4.5	0.89	15	--	18
15B	T-3401	7.0	0.78	85	--	198
20B	T-3401	10.0	0.96	>20000	--	19382
27B	T-3401	3.0	1.56	18	--	10
29B	T-3401	4.5	1.61	102	--	123
31B	T-3401	6.0	1.44	48	--	797
33B	T-3401	3.0	2.39	18	--	34

(a) Model Test Results Corrected for Instrumentation and Scale

(b) Prediction by Equation (6-5)

(c) Prediction by Equation (7-15) or (7-14) as Applicable

Table 7-10. Summary of Method 4 Predictions of Rutting Responses for Full-Scale Tests.

Test No.	Membrane Type	Depth of Stone (in.)	Unsoaked CBR	Load Cycles to 3 in. Rut		
				N ^(a)	N ^(b)	N ^(c)
1 ^(d)	None	14.0	0.90	68	48	43
2 ^(d)	B-C38	14.0	1.15	260	--	772
3 ^(e)	None	14.7	0.73	37	43	38
4 ^(e)	T-3401	14.8	0.73	305	--	234

(a) Actual

(b) Prediction by Equation (6-15)

(c) Prediction by Equation (7-13) or (7-14) as Applicable

(d) U.S. Army Corps of Engineers Tests

(e) Georgia Institute of Technology Tests

Method 5

The method proposed by Giroud and Noiray (41) may be utilized to predict the rutting responses of both AS and AFS systems. The method, based upon a combination of previously cited works (14, 44, 45, 56, 117, 118) is derived for axle loads carried by dual tires and recommended for use only when the number of load repetitions does not exceed 10^4 . Analysis of AS systems is accomplished utilizing Equation (2-4), which is expressed as:

$$h = \frac{17.92 \log N + 70.78 \log P - 1.06 r - 297.40}{c_u^{0.63}} \quad (2-4)$$

where h = aggregate layer thickness, inches

N = load cycles

P = single axle load, pounds

r = rut depth, inches

c_u = subgrade soil undrained shear strength, psi.

Equation (2-4) was derived by first establishing an equation in agreement with a plot of experimental data presented by Webster and Alford (118), which related load cycles, subgrade soil CBR, and aggregate layer thickness, for a single axle load of 18 kips and a rut depth of three inches. This equation was modified to account for repetitions of single axle loads other than 18 kips, by use of procedures generally accepted for analyzing traffic on paved roads (122). On the basis of data presented by Webster and Watkins (117) the equation was then empirically extended for use at rut depths other than three inches. This extension was based upon the observation that the load cycle-rut

depth relationships in these full-scale tests were essentially linear at rut depths greater than three inches. For any given system (i.e., h , c_u , and P constant) Equation (2-4) reduces to a linear relationship between log of load cycles and rut depth (i.e., 17.92 inches of rutting per each ten-fold increase in load cycles), to thereby model the observed response. Finally, c_u was substituted for CBR (i.e., $c_u = 4.35$ CBR), thus achieving the presented form of the expression.

Once a failure rut depth is established, a system may be designed (i.e., required aggregate layer thickness determined) to achieve a given number of load cycles, or an established system may be analyzed for the allowable number of load cycles. For AFS systems, two bi-dimensional static bearing capacity analyses of the subgrade are conducted. The load applied to the surface of the system, by dual tires, is assumed to act over a rectangular area (i.e., 2.83 times the contact area of a single tire) and is considered to be dissipated in the system by a truncated pyramidal pressure distribution, until reaching the surface of the subgrade. The width of the rectangular area equals 0.5 (i.e., off-highway trucks) or 0.71 (i.e., on-highway trucks) times its length. Each side of the truncated pyramidal pressure distribution is considered to make an acute angle of 59° with the horizontal. Without fabric, the allowable bearing capacity of the subgrade is taken as equal to πc , in solving for the required thickness of aggregate utilizing Equation (2-5), which is expressed as:

$$\pi c = \frac{P}{2(B + 2h_o \tan \theta)(L + 2h_o \tan \theta)} \quad (2-5)$$

where c = subgrade soil undrained shear strength, psi

P = single axle load, pounds

B = width of rectangular load contact area, inches

L = length of rectangular load contact area, inches

h_0 = aggregate layer thickness, inches

$\theta = 31^\circ$

With a fabric inclusion, it is assumed that the allowable bearing capacity of the subgrade increases to $(\pi + 2)c$, while the vertical pressure reaching the subgrade surface decreases due to the influence of the vertical component of the fabric tensile force. The resulting expression (i.e., Equation (2-6)) for the required thickness of the aggregate layer becomes:

$$(\pi + 2)c + \frac{K\epsilon}{a\sqrt{1 + \left(\frac{a}{2s}\right)^2}} = \frac{P}{2(B + 2h \tan \theta)(L + 2h \tan \theta)} \quad (2-6)$$

where c = subgrade soil undrained shear strength, psi

K = fabric tensile secant modulus, lbs/in

ϵ = fabric strain, in/in

a = subgrade depression half-width, inches

s = subgrade depression, inches

P = single axle load, pounds

B = width of rectangular load contact area, inches

L = length of rectangular load contact area, inches

h = aggregate layer thickness, inches

$\theta = 31^\circ$.

The deformed shape of the aggregate-subgrade interface is assumed to consist of parabolic segments, with the segment characteristics (i.e.,

a, s, and ϵ) dependent upon the values of B, h, and r. Aggregate stability and aggregate-fabric friction are considered sufficient to limit aggregate deformations to negligible levels. Fabric strain is considered constant throughout the fabric length. Although not described as such by Giroud and Noiray, solution of Equation (2-6) should be accomplished by iteration. A value of h is first assumed to establish values of a, s, and ϵ , then Equation (2-6) solved for h utilizing these values. The procedure is repeated until agreement between the h value used to establish a, s, and ϵ , and the computed value is obtained. The difference between the values of the aggregate layer thicknesses computed by Equations (2-5) and (2-6) (i.e., $\Delta h = h_0 - h$) represents the improvement produced by a fabric inclusion. The value of ϵ used to determine h must be less than the strain exhibited by the fabric at failure. While based upon static analyses, equal improvement is assumed for dynamic loadings. For design of AFS systems, Equation (2-4) is solved for h, which is then reduced by Δh . For analysis of AFS systems, the actual aggregate layer thickness is increased by Δh and Equation (2-4) solved for the allowable number of load repetitions. Due to its derivation, this method is best suited for application at rut depths of three or more inches.

As with Method 4, application of this method to the model test program requires correcting the model test data for instrumentation and scaling. An additional modification is required, in that this method was developed for a dual tire axle loading. The full-scale load to which the model test load corresponded, is a 12 inch diameter area with contact pressure of 70 psi. This full-scale load may be converted to a dual tire load utilizing the expression (122):

$$P_k = \frac{P_e F_e}{2F_k} \quad (7-15)$$

where P_k = load carried by one wheel of the dual tire equivalent for the applied single wheel load, pounds

P_e = applied single wheel load, pounds

F_e = factor for subgrade surface centerline deflection due to the applied single wheel load

F_k = factor for subgrade surface deflection, beneath the wheel configuration midpoint, due to one wheel of the dual tire equivalent for the applied single wheel load.

Equation (7-15) assumes all wheels to have the same contact area. The wheels of each dual tire pair were taken as spaced at 15 inches (i.e., 2.5 radii), with the dual tire groups spaced at 72 inches on center. The load was assumed to represent off-highway trucks. The deflection factors were obtained from Figure 7-11 (122). Use of two-layer deflection factors would have been somewhat more correct, but such application would require determination of the effective modular ratio for each system and these values were not accurately known. Basing Equation (7-15) on the deflection at the subgrade surface is consistent with the derivation of Method 5, which assumes only negligible deformations in the aggregate layer.

The results of this method as applied to the model test program are presented in Table 7-11. The method provides reasonable agreement for rutting responses in the range studied. At three inches of rutting, results are comparable to those of Method 4. Due to the high rate of rutting calculated for all systems by this method, predictions at

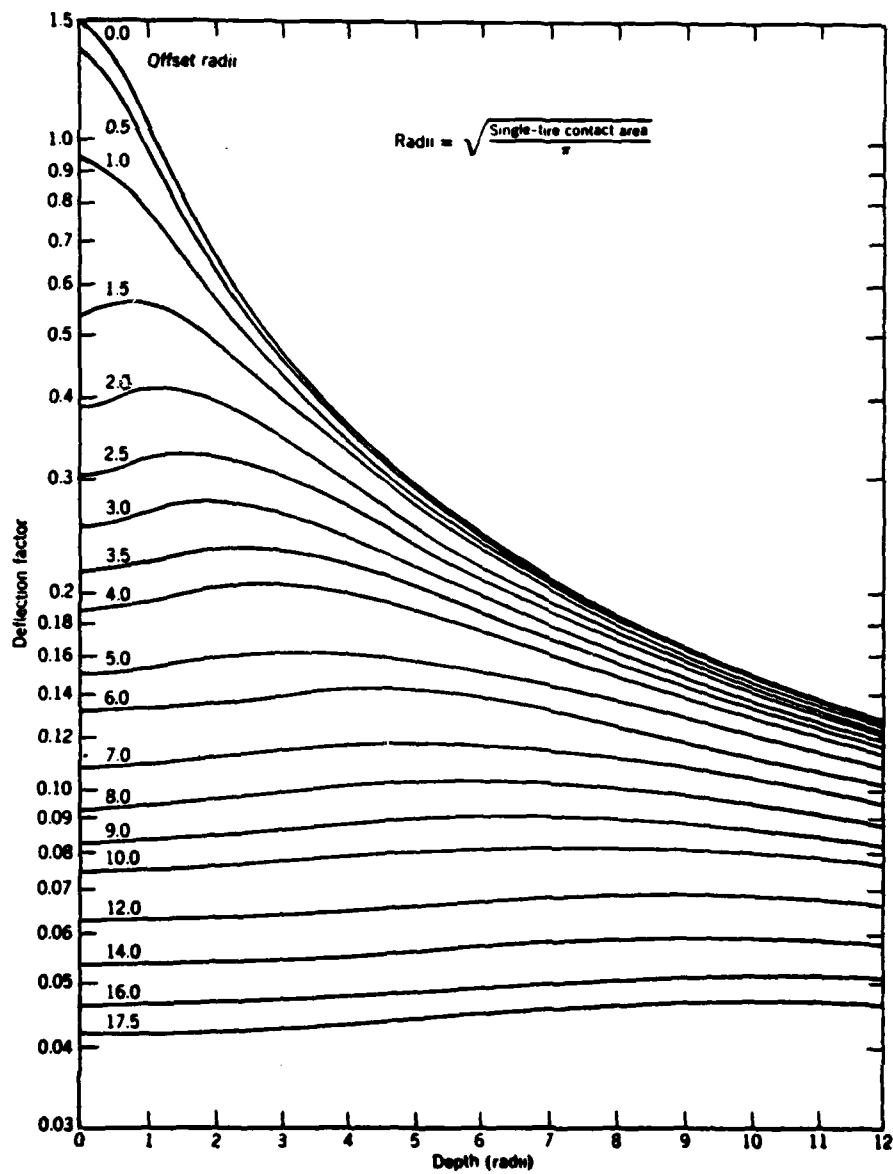


Figure 7-11. Single Layer Deflection Factors (122).

Table 7-11. Summary of Method 5 Predictions of Model Test Program Rutting Responses.

Test No.	Membrane Type	Depth of Stone (in.)	Shear Strength (psi)	Axle Load (lbs.)	Load Cycles to Given Rut			
					$\Delta = 3$ in.		$\Delta = 4$ in.	
					$\frac{N(d)}{N}$	$\frac{N(e)}{N}$	$\frac{N(d)}{N}$	$\frac{N(e)}{N}$
1B	None	12.0	1.65	20016	7	5	11	6
3B	None	15.0	1.87	18866	15	13	30	15
5B	None	18.0	1.74	17917	48	25	104	30
7B	None	9.0	3.96	22274	4	6	7	7
13B	None	14.0	3.52	19462	42	36	75	42
19B	None	20.0	4.05	17719	667	486	3333	533
26B	None	6.0	6.74	24682	5	4	8	4
28B	None	9.0	6.92	22274	21	20	41	23
30B	None	12.0	7.48	20016	85	146	162	167
32B	None	6.0	10.57	24682	8	8	14	9
<hr/>								
2B	T-3401	12.0	1.70	20016	14	22	30	26
4B	T-3401	15.0	1.78	18866	38	52	69	59
6B	T-3401	18.0	1.78	17917	208	105	667	120
9B	T-3401	9.0	3.87	22274	15	35	37	40
15B	T-3401	14.0	3.39	19462	85	165	150	189
20B	T-3401	20.0	4.18	17719	>20000	2766	>20000	3170
27B	T-3401	6.0	6.79	24682	18	27	32	31
29B	T-3401	9.0	7.00	22274	102	135	242	154
31B	T-3401	12.0	6.26	20016	48	471	112	539
33B	T-3401	6.0	10.40	24682	18	18	33	21

(a) Twice Model Test Depth

(b) 4.35 CBR

(c) Equation (7-15)

(d) Model Test Results Corrected for Instrumentation and Scale

(e) Prediction

greater rut depths are increasingly conservative, as none of the model tests displayed a similarly high rutting rate.

The results of Method 5 as applied to the full-scale tests are summarized in Table 7-12, with the actual and predicted rutting responses presented in Figures 7-12 and 7-13. An example calculation is presented in Table 7-13. The calculated responses for the full-scale tests represent a slight improvement over those of the previously described methods, with the calculated rutting rate most closely matching the observed response at higher deformation levels. Derived on the basis of the rutting rate at deformations in excess of three inches, such accuracy was anticipated. Of the previously discussed methods, only the Method 3 rutting response curve (i.e., hyperbolic) approaches a similarly high rutting rate, but generally not until rutting exceeds five inches.

Method 6

The load induced stresses in each system were computed utilizing the VESYS program (32, 48, 69) described in Chapter II. The subgrade was divided into three sublayers, with the resilient modulus of each sublayer estimated from the results of the repeated load triaxial tests (Ref. Tables 3-5 through 3-7) and the anticipated deviator stresses as estimated from Boussinesq theory. Several program runs were made for each aggregate layer thickness and subgrade strength combination, varying only the resilient modulus value of the aggregate layer. For each combination, plots were made of aggregate resilient modulus versus the elastic surface deflection per cycle on the load centerline, and of aggregate resilient modulus versus both vertical and radial centerline stresses at various depths. A typical form of each relationship is

Table 7-12. Summary of Method 5 Predictions of Rutting Responses for Full-Scale Tests.

Test No.	Membrane Type	Depth of Stone (in.)	Shear (a) Strength (psi)	Axle Load (lbs.)	Method	Load Cycles to Given Rut			
						$\Delta = 2$ in.	$\Delta = 3$ in.	$\Delta = 4$ in.	$\Delta = 6$ in.
						N	N	N	N
1(b)	None	14.0	3.92	18000	Actual Pred.	31 57	68 65	89 75	130 98
2(b)	B-C38	14.0	5.00	18000	Actual Pred.	125 586	260 672	415 783	830 1047
3(c)	None	14.7	3.18	19202(d)	Actual Pred.	25 31	37 36	48 41	65 53
4(c)	T-3401	14.8	3.18	18865(d)	Actual Pred.	220 166	305 190	400 218	540 294

(a) 4.35 CBR

(b) U.S. Army Corps of Engineers Tests

(c) Georgia Institute of Technology Tests

(d) Equation (7-15)

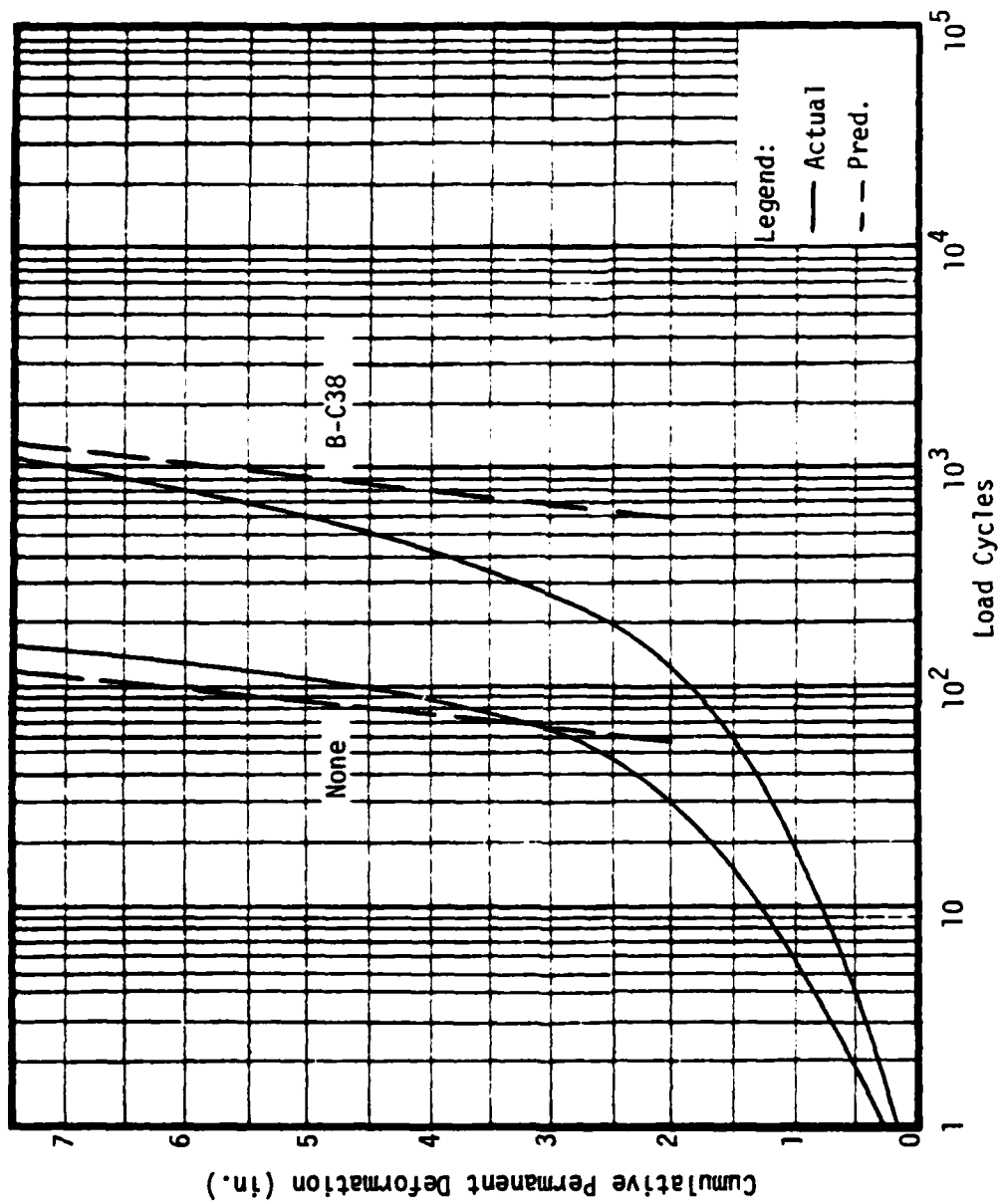


Figure 7-12. Comparison of Actual and Method 5 Predictions of Rutting Response for Full-Scale Field Tests (U.S. Army Corps of Engineers).

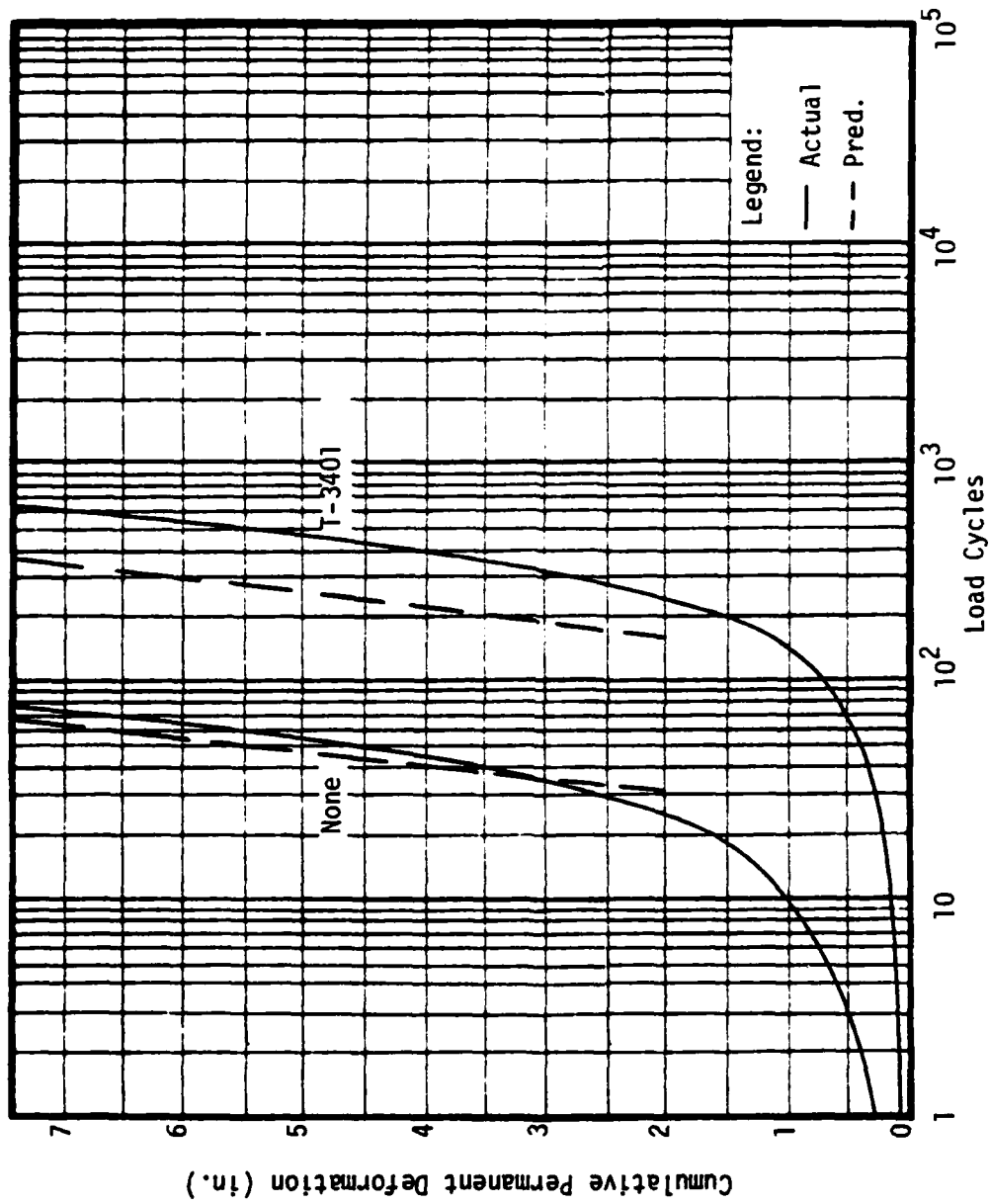


Figure 7-13. Comparison of Actual and Method 5 Predictions of Rutting Response for Full-Scale Model Tests (Georgia Institute of Technology).

Table 7-13. Example Calculation for Method 5 Prediction of Rutting Response.

Given:

Full-Scale Model Test 4

Depth of Stone = 14.8 in.

$$c_u = 4.35 \text{ CBR} = 4.35(0.73) = 3.18 \text{ psi}$$

$$P_e = 7916.8 \text{ lbs.}$$

$$A_e = 113.1 \text{ in}^2.$$

Calculations with $r = 6$ inches:

$$(1) \quad P_k = \frac{P_e F_e}{2 F_k} = \frac{(7916.8)(0.56)}{(2)(0.47)} = 4716.3 \text{ lbs.}$$

$$(2) \quad P = 4P_k = 4(4716.3) = 18865 \text{ lbs.}$$

$$(3) \quad B = 2.83 \sqrt{A_e} = 2.83 \sqrt{113.1} = 25.3 \text{ in.}$$

$$(4) \quad L = 0.5B = 0.5(25.3) = 12.6 \text{ in.}$$

(5) AS System:

$$\pi c = \frac{P}{2(B + 2h_o \tan \theta)(L + 2h_o \tan \theta)}$$

$$(3.14)(3.18) = \frac{18865}{2(25.3 + 2h_o (\tan 31^\circ))(12.6 + 2h_o (\tan 31^\circ))}$$

$$h_o = 11.5 \text{ in.}$$

(6) AFS System:

Assume $h = 5.5$ in.

$$(a) \quad 2a = B + 2h \tan \theta = 25.3 + 2(5.5)(\tan 31^\circ)$$

$$a = 15.95 \text{ in.}$$

Table 7-13. (Continued).

$$(b) \quad 2a' = e - 2a = 72 - 2(15.95)$$

$$a' = 20.05 \text{ in.}$$

Note: e = center-to-center spacing of dual tire pairs, inches.

$$(c) \quad s = \frac{ra}{a + a'} = \frac{6(15.95)}{15.95 + 20.05} = 2.66 \text{ in.}$$

$$(d) \quad \frac{b}{a} - 1 = \frac{1}{2} \left(\sqrt{1 + \left(\frac{2s}{a}\right)^2} + \frac{a}{2s} \ln\left(\frac{2s}{a} + \sqrt{1 + \left(\frac{2s}{a}\right)^2}\right) - 2 \right)$$

$$\frac{b}{15.95} - 1 = \frac{1}{2} \left(\sqrt{1 + \left(\frac{2(6)}{15.95}\right)^2} + \frac{15.95}{2(6)} \ln\left(\frac{2(6)}{15.95} + \sqrt{1 + \left(\frac{2(6)}{15.95}\right)^2}\right) - 2 \right)$$

$$b = 16.24 \text{ in.}$$

$$(e) \quad \frac{b'}{a'} - 1 = \frac{1}{2} \left(\sqrt{1 + \left(\frac{2(r-s)}{a'}\right)^2} + \frac{a'}{2(r-s)} \ln\left(\frac{2(r-s)}{a'} + \sqrt{1 + \left(\frac{2(r-s)}{a'}\right)^2}\right) - 2 \right)$$

$$\frac{b'}{20.05} - 1 = \frac{1}{2} \left(\sqrt{1 + \left(\frac{2(6 - 2.66)}{20.05}\right)^2} + \frac{20.05}{2(6 - 2.66)} \ln\left(\frac{2(6 - 2.66)}{20.05} + \sqrt{1 + \left(\frac{2(6 - 2.66)}{20.05}\right)^2}\right) - 2 \right)$$

$$b' = 20.41 \text{ in.}$$

$$(f) \quad \epsilon = \frac{b + b'}{a + a'} - 1 = \frac{16.24 + 20.41}{15.95 + 20.05} - 1 = 0.0181 \text{ in/in.}$$

Table 7-13. (Continued).

$$(g) \quad (\pi + 2)c + \frac{K\varepsilon}{a\sqrt{1 + \left(\frac{a}{2s}\right)^2}} = \frac{P}{2(B + 2h\tan \theta)(L + 2h\tan \theta)}$$

$$(3.14 + 2)(3.18) + \frac{600(0.0181)}{15.95\sqrt{1 + \left(\frac{15.95}{2(2.66)}\right)^2}} =$$

$$\frac{18865}{2(25.3 + 2h(\tan 31^\circ))(12.6 + 2h(\tan 31^\circ))}$$

$$h = 5.5 \text{ in.} - \text{Checks}$$

$$(7) \quad \Delta h = h_0 - h = 11.5 - 5.5 = 6.0 \text{ in.}$$

$$(8) \quad h = \frac{17.92 \log N + 70.78 \log P - 1.06 r - 297.40}{c_u^{0.63}}$$

$$(14.8 + 6.0) = \frac{17.92 \log N + 70.78 \log (18865) - 1.06(6) - 297.40}{(3.18)^{0.63}}$$

$$N = 294$$

depicted in Figure 7-14, with the curve types superimposed on a single plot. The viscoelastic analysis was not utilized, being considered unsuitable, as the aggregate deformations are not time dependent and due to the large deformations experienced in the model tests.

From the model test program results, the actual transient elastic deformation per cycle of the footing, on its centerline, was known at various times during most tests. Selected data are summarized in Table 7-14. Utilizing these actual deflection values, the equivalent aggregate resilient moduli and corresponding load induced stress states for the systems were determined from the plots of VESYS program output for any load cycles of interest. The hyperbolic plastic stress-strain law (i.e., Equation (2-8)) was applied to the resulting load induced stress states to predict rutting (i.e., Equation (2-9)) after the corresponding numbers of load cycles.

This approach could not be used in those sublayers where the calculated stress state produced a ratio of σ_1/σ_3 which exceeded the shear strength and/or predicted a σ_3 value which was equal to or less than zero (i.e., tensile failure). For the VESYS analyses, this situation arose in the lower aggregate sublayers of all systems and the upper subgrade sublayers in the weakest systems (i.e., stress ratios greater than four). In such instances, the vertical sublayer strains were determined on the basis of the Bison strain sensor measurements for the appropriate depths. Strain data for selected tests and sublayers are presented in Tables 7-15 through 7-17. This approach was also utilized with the other predictive models (i.e., Method 7 and 8) based upon the hyperbolic plastic stress-strain law.

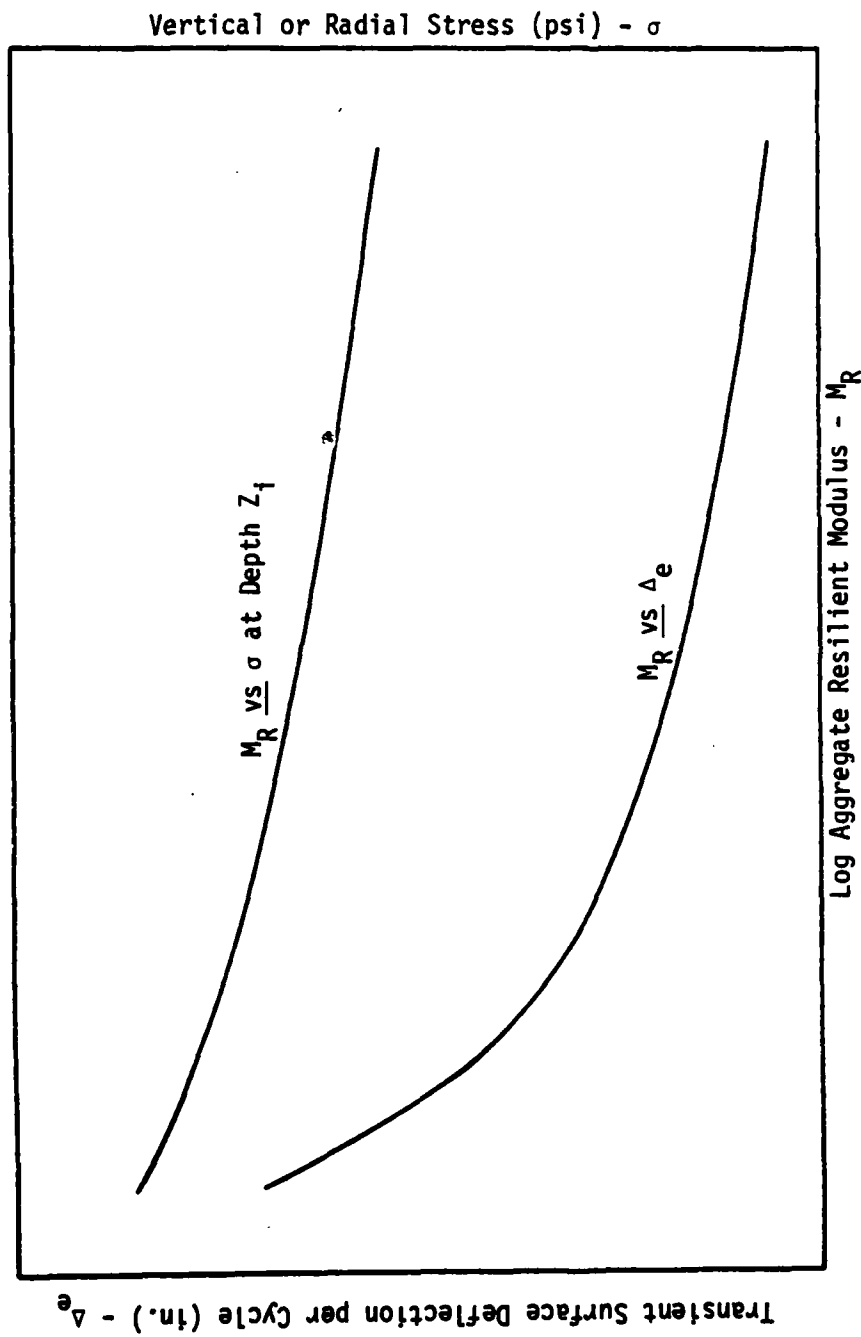


Figure 7-14. Typical Aggregate Resilient Modulus-Stress-Transient Surface Deflection per Cycle and Aggregate Resilient Modulus-Stress Relationships from VESYS Analysis.

Table 7-14. Summary of Selected Transient Elastic Deformation per Cycle Data.

Test No.	Membrane Type	Deformation at Given N			
		N = 10	N = 10 ²	N = 10 ³	N = 10 ⁴
		Deformation per Cycle (in.)			
1B	None	0.24	0.44	--	--
3B	None	0.20	0.20	--	--
5B	None	0.19	0.15	0.19	--
13B	None	0.15	0.17	--	--
19A	None	0.11	0.09	0.07	0.07
19B	None	0.10	0.09	0.07	0.07
22A	None	0.09	0.08	0.07	0.06
28B	None	0.20	0.23	--	--
30B	None	0.15	0.13	0.13	0.11
32B	None	0.31	0.40	--	--
2B	T-3401	0.30	0.36	--	--
4B	T-3401	0.20	0.21	0.23	--
6B	T-3401	0.16	0.15	0.12	0.13
9A	T-3401	0.33	0.35	--	--
9B	T-3401	0.36	0.31	--	--
15A	T-3401	0.20	0.17	0.17	--
15B	T-3401	0.21	0.15	0.14	--
20A	T-3401	0.10	0.09	0.08	0.07
20B	T-3401	0.08	0.08	0.08	0.07
23A	T-3401	0.08	0.08	0.07	0.05
27B	T-3401	0.30	0.54	--	--
29B	T-3401	0.21	0.22	0.27	--
31B	T-3401	0.18	0.17	0.14	--
33B	T-3401	0.30	0.29	--	--

Table 7-15. Aggregate Centerline Vertical Permanent Strains at Selected Load Cycles (Bison Strain Sensor Pair 1-2).

Test No.	Membrane Type	Strain at Given N			
		N = 10	N = 10 ²	N = 10 ³	N = 10 ⁴
		Vertical Permanent Strain (in/in)			
1B	None	0.0283	0.1033	--	--
3B	None	0.0258	0.0919	--	--
5B	None	0.0250	0.0678	0.1641	--
7A	None	0.1622	--	--	--
7B	None	0.0633	0.1689	--	--
13A	None	0.1004	--	--	--
13B	None	0.0285	0.0731	--	--
19A	None	0.0431	0.0820	0.1267	0.1615
19B	None	0.0159	0.0535	0.1053	0.1579
22A	None	0.0272	0.0478	0.0804	0.1188
26B	None	0.0405	--	--	--
28B	None	0.0377	0.1033	--	--
30B	None	0.0238	0.0673	0.1872	0.2683
32B	None	0.0432	0.1281	--	--
2B	T-3401	0.0585	0.1734	--	--
4B	T-3401	0.0315	0.1187	0.2667	--
6B	T-3401	0.0184	0.0618	0.1196	0.2010
9A	T-3401	0.0839	0.2253	--	--
9B	T-3401	0.0822	0.2209	--	--
15A	T-3401	0.0595	0.1490	0.2607	--
15B	T-3401	0.0297	0.0945	0.2745	--
20A	T-3401	0.0249	0.0576	0.0926	0.1166
20B	T-3401	0.0121	0.0222	0.0671	0.1021
23A	T-3401	0.0137	0.0309	0.0574	0.0726
27B	T-3401	0.1031	0.2926	--	--
29B	T-3401	0.0334	0.1082	0.2584	--
31B	T-3401	0.0440	0.1376	0.2877	--
33B	T-3401	0.0546	0.1876	--	--

Table 7-16. Subgrade Centerline Vertical Permanent Strains at Selected Load Cycles (Bison Strain Sensor Pair 2-3).

Test No.	Membrane Type	Strain at Given N			
		N = 10	N = 10 ²	N = 10 ³	N = 10 ⁴
		Vertical Permanent Strain (in/in)			
1B	None	0.1734	0.6320	--	--
3B	None	0.1037	0.3700	--	--
5B	None	0.0535	0.1451	0.3512	--
7A	None	0.5240	--	--	--
7B	None	0.2142	0.5720	--	--
13A	None	0.2573	--	--	--
13B	None	0.0595	0.1524	--	--
19A	None	0.0217	0.0412	0.0637	0.0812
19B	None	0.0100	0.0377	0.0664	0.0995
22A	None	0.0103	0.0181	0.0304	0.0449
26B	None	0.2132	--	--	--
28B	None	0.0974	0.2665	--	--
30B	None	0.0316	0.0893	0.2484	0.3560
32B	None	0.1829	0.5427	--	--
2B	T-3401	0.0684	0.2026	--	--
4B	T-3401	0.0240	0.0906	0.2035	--
6B	T-3401	0.0161	0.0539	0.1043	0.1753
9A	T-3401	0.0691	0.1382	--	--
9B	T-3401	0.0525	0.1411	--	--
15A	T-3401	0.0548	0.1372	0.2402	--
15B	T-3401	0.0180	0.0572	0.1663	--
20A	T-3401	0.0152	0.0350	0.0563	0.0709
20B	T-3401	0.0068	0.0125	0.0376	0.0573
23A	T-3401	0.0179	0.0402	0.0747	0.0945
27B	T-3401	0.0663	0.1883	--	--
29B	T-3401	0.0255	0.0826	0.1972	--
31B	T-3401	0.0308	0.0964	0.2015	--
33B	T-3401	0.1012	0.3475	--	--

Table 7-17. Subgrade Centerline Vertical Permanent Strains at Selected Load Cycles (Bison Strain Sensor Pair 3-4).

Test No.	Membrane Type	Strain at Given N			
		N = 10	N = 10 ²	N = 10 ³	N = 10 ⁴
		Vertical Permanent Strain (in/in)			
1B	None	0.1273	0.4640	--	--
3B	None	0.0580	0.2069	--	--
5B	None	0.0390	0.0954	0.2309	--
7A	None	0.3600	--	--	--
7B	None	0.1483	0.3960	--	--
13A	None	0.1831	--	--	--
13B	None	0.0426	0.1091	--	--
19A	None	0.0148	0.0281	0.0434	0.0554
19B	None	0.0073	0.0246	0.0485	0.0727
22A	None	0.0086	0.0151	0.0253	0.0374
26B	None	0.1471	--	--	--
28B	None	0.0657	0.1797	--	--
30B	None	0.0270	0.0763	0.2121	0.3040
32B	None	0.1099	0.3262	--	--
2B	T-3401	0.0603	0.1786	--	--
4B	T-3401	0.0286	0.1078	0.2422	--
6B	T-3401	0.0150	0.0505	0.0976	0.1641
9A	T-3401	0.1356	0.2712	--	--
9B	T-3401	0.0666	0.1789	--	--
15A	T-3401	0.0489	0.1226	0.2145	--
15B	T-3401	0.0193	0.0616	0.1788	--
20A	T-3401	0.0128	0.0295	0.0474	0.0597
20B	T-3401	0.0063	0.0116	0.0351	0.0534
23A	T-3401	0.0071	0.0161	0.0299	0.0378
27B	T-3401	0.0887	0.2519	--	--
29B	T-3401	0.0300	0.0974	0.2326	--
31B	T-3401	0.0326	0.1021	0.2134	--
33B	T-3401	0.0541	0.1858	--	--

The results of the method as applied to the model test program, utilizing the aggregate resilient modulus and corresponding stress state for the load cycle of interest, are summarized in Table 7-18. An example calculation is presented in Table 7-19. For AS systems with Type A loading, the calculated rut depths averaged 88 percent of the observed values, with a range of 62-122 percent. For Type B loading, this average was 109 percent, with a range of 39-246 percent. For AFS systems reinforced with Typar 3401 fabric, the computed rut depths averaged 105 percent of the actual rut depths, with a range of 57-173 percent, for Type A loading. For Type B loading, this average was 153 percent, with a range of 48-338 percent. This method was less accurate than all of the previous methods in terms of both the average prediction and the range of predictions. The predictions were most conservative during the early stages of loading, becoming increasingly unconservative with additional load repetitions. This trend is due to somewhat different material deformation responses in the repeated load triaxial tests and the model tests, and due to variations between the stress state computed on the basis of elastic theory and the actual stress state in a system experiencing large deformations.

In an attempt to improve accuracy, a modified approach was tried, with the elastic transient surface deflection per cycle, aggregate resilient modulus, and stress state values for a specific load cycle used to predict rutting response at all load cycles for the given test. Utilizing the data for the Type B load tests, a trial and error approach showed the overall results to be improved, with the results for AS and Typar 3401 reinforced AFS systems more in agreement in terms of average

Table 7-18. Summary of Method 6 Predictions of Model Test Program Rutting Responses Based Upon Stress State Determined at $N = i$ Load Cycles.

Test No.	Membrane Type	Depth of Stone (in.)	Stress Ratio (a)	Method	Rut at Given N			
					$N = 10$ $\frac{\Delta (\text{in.})}{\Delta (\text{in.})}$	$N = 10^2$ $\frac{\Delta (\text{in.})}{\Delta (\text{in.})}$	$N = 10^3$ $\frac{\Delta (\text{in.})}{\Delta (\text{in.})}$	$N = 10^4$ $\frac{\Delta (\text{in.})}{\Delta (\text{in.})}$
1B	None	6.0	6.75	Actual Pred.	1.35 1.88	4.92 6.24	-- --	-- --
3B	None	7.5	4.50	Actual Pred.	0.78 1.02	2.76 2.37	5.57* --	-- --
5B	None	9.0	3.38	Actual Pred.	0.60 1.20	1.62 2.46	3.93 3.93	-- --
13B	None	7.0	3.63	Actual Pred.	0.68 0.79	1.75 1.92	4.97* --	-- --
19A	None	10.0	1.83	Actual Pred.	0.63 0.77	1.20 1.31	1.86 1.69	2.37 2.14
19B	None	10.0	1.81	Actual Pred.	0.24 0.59	0.82 1.12	1.61 1.54	2.42 1.93
22A	None	13.0	1.06	Actual Pred.	0.46 0.38	0.81 0.65	1.36 0.94	2.01 1.25
28B	None	4.5	4.34	Actual Pred.	0.88 0.50	2.40 1.66	5.50* --	-- --
30B	None	6.0	2.74	Actual Pred.	0.42 0.33	1.18 0.72	3.30 1.34	4.72 1.82

(a) Ref. Page 92 for Definition
* Extrapolated Data Point

Table 7-18. (Continued).

Test No.	Membrane Type	Depth of Stone (in.)	Stress Ratio (a)	Method	$N = 10 \frac{\Delta(\text{in.})}{\Delta}$	Rut at Given N		
						$N = 10^2 \frac{\Delta(\text{in.})}{\Delta}$	$N = 10^3 \frac{\Delta(\text{in.})}{\Delta}$	$N = 10^4 \frac{\Delta(\text{in.})}{\Delta}$
2B	T-3401	6.0	6.72	Actual Pred.	0.91 1.65	2.71 4.16	5.50* --	-- --
4B	T-3401	7.5	4.62	Actual Pred.	0.49 0.93	1.83 2.41	4.12 3.70	-- --
6B	T-3401	9.0	3.32	Actual Pred.	0.32 1.08	1.08 2.23	2.08 2.27	3.50 --
9A	T-3401	4.5	6.62	Actual Pred.	1.64 1.75	3.28 4.05	-- --	-- --
9B	T-3401	4.5	6.46	Actual Pred.	0.92 2.46	2.46 4.22	-- --	-- --
15A	T-3401	7.0	3.30	Actual Pred.	0.86 1.49	2.16 2.31	3.79 3.21	-- --
15B	T-3401	7.0	3.71	Actual Pred.	0.40 1.23	1.28 2.00	3.72 3.32	4.97* --
20A	T-3401	10.0	1.88	Actual Pred.	0.43 0.66	0.99 1.21	1.59 1.58	2.01 1.87
20B	T-3401	10.0	1.77	Actual Pred.	0.19 0.42	0.36 0.86	1.07 1.23	1.63 1.60

(a) Ref. Page 92 for Definition
* Extrapolated Data Point

Table 7-18. (Continued).

Test No.	Membrane Type	Depth of Stone (in.)	Stress (a) Ratio	Method	Rut at Given N			
					$N = 10$ $\frac{\Delta(\text{in.})}{\Delta}$	$N = 10^2$ $\frac{\Delta(\text{in.})}{\Delta}$	$N = 10^3$ $\frac{\Delta(\text{in.})}{\Delta}$	$N = 10^4$ $\frac{\Delta(\text{in.})}{\Delta}$
23A	T-3401	13.0	1.07	Actual Pred.	0.28 0.28	0.64 0.53	1.19 0.81	1.59 0.91
27B	T-3401	3.0	6.71	Actual Pred.	1.04 1.26	2.96 3.39	-- --	-- --
29B	T-3401	4.5	4.30	Actual Pred.	0.38 0.54	1.24 1.27	2.97 2.73	-- --
31B	T-3401	6.0	3.13	Actual Pred.	0.53 0.41	1.67 1.00	3.49 1.66	4.94* --

(a) Ref. Page 92 for Definition

* Extrapolated Data Point

Table 7-19. Example Calculation for Method 6 Prediction of Rutting Response.

Given:

Model Test 138
 Depth of Stone = 7.0 in.
 Vane Shear Strength = 4.32 psi
 Calculations for $N = 100$:

Sublayer No.	Sublayer Height (in.)	Load Induced Stresses at (a)		Sublayer (b) Plastic Strains (in/in)	Sublayer (c) Plastic Deformations (in.)
		σ_v	σ_r		
1	2.0	65.3	57.0	0.0002	0.0004
2	2.0	52.4	6.5	0.0059	0.0119
3	2.0	17.5	<0.0	0.0731*	0.1462
4	1.0	8.4	<0.0	0.0731*	0.0731
5	2.0	5.9	1.3	0.1766	0.3532
6	2.0	4.5	3.5	0.1293	0.2586
7	2.0	3.7	0.9	0.0922	0.1985
8	2.0	3.0	0.5	0.1129	0.2258
9	2.0	2.5	0.3	0.1222	0.2443
10	2.0	2.1	0.25	0.1076	0.2152
11	3.0	1.3	0.2	0.0656	0.1969
					1.9241

(a) VESYS Analysis (Transient Surface Deflection per Cycle = 0.166 in.)

(b) Equation (2-8) (Ref. Tables 3-3 and 3-5 for Constants)

(c) Equation (2-9)

* Estimated from Bison Strain Sensor Measurements (Ref. Table 7-15)

prediction and range of prediction, when rutting calculations were based upon conditions at 10^2 and 10^4 load cycles respectively. The following correlations were then developed between stress ratio and aggregate resilient modulus:

AS systems:

$$M_R = 6770 - 846 (SR) \quad (7-16)$$

Typar 3401 reinforced AFS systems:

$$M_R = 10781 - 1289 (SR) \quad (7-17)$$

where M_R = aggregate resilient modulus, psi

SR = stress ratio at subgrade surface.

The value of aggregate resilient modulus computed from the appropriate correlation may be used as input to the VESYS program in determining the load induced stress state for a given system. The minimum resilient modulus value utilized for the aggregate layer should be no less than that of the subgrade material. Use of these correlations permits extension of the method to those model tests for which data on the transient surface deformation per cycle was not obtained, such as tests 7B and 26B. Equations (7-16) and (7-17) indicate that the effective aggregate moduli in AFS systems are greater than in the corresponding AS systems, which is consistent with the proposed confinement and reinforcement mechanism of fabric influence on system behavior. These increased moduli values result in lower calculated vertical stresses in the subgrade material of the AFS systems, which is consistent with the proposed stress alteration mechanism.

Results of this modified approach as applied to the model test program are presented in Table 7-20. Although the correlations were formulated from Type B load test data, Table 7-20 includes their application to Type A load tests. Theory predicts elastic response to loading to be independent of load duration. This is generally confirmed by the model test data (Ref. Table 7-14), thus application of the correlations to tests of varied load pulse duration would appear valid. For AS systems, with Type A loading, the calculated rut depths averaged 85 percent of the observed values, with a range of 55-113 percent. For Type B loading, the average was 102 percent, with a range of 39-204 percent. In AFS systems reinforced with Typar 3401 fabric, the computed rut depths averaged 93 percent of the actual rut depths, with a range of 58-130 percent, for Type A loading. For Type B loading, this average was 116 percent, with a range of 42-219 percent. These results are an improvement over the corresponding predictions based upon the stress state computed for the load cycle of interest. However, the results remain less accurate than those of all previously described methods.

A comparison between computed and observed values of the percentage of the total rutting exhibited by the subgrade was made for all tests, utilizing end-of-test data for the actual values and calculated values from the load cycle nearest to the actual end of test. Although introducing some error by comparing values from different load cycles, this procedure was utilized due to the greater completeness of end-of-test deformation data. The modified approach overestimated that portion of the total rutting exhibited by the subgrade, averaging 120 percent of the measured values for AS systems and 130 percent for AFS systems

Table 7-20. Summary of Method 6 Predictions of Model Test Program Rutting Responses Based Upon Stress State Determined with Correlated Aggregate Resilient Moduli.

Test No.	Membrane Type	Depth of Stone (in.)	Stress Ratio (a)	Method	Rut at Given N			
					N = 10 $\frac{\Delta(\text{in.})}{\Delta(\text{in.})}$	N = 10 ² $\frac{\Delta(\text{in.})}{\Delta(\text{in.})}$	N = 10 ³ $\frac{\Delta(\text{in.})}{\Delta(\text{in.})}$	N = 10 ⁴ $\frac{\Delta(\text{in.})}{\Delta(\text{in.})}$
1B	None	6.0	6.75	Actual Pred.	1.35 2.51	4.92 6.65	-- --	-- --
3B	None	7.5	4.50	Actual Pred.	0.78 1.07	2.76 2.56	5.57* 3.58	-- --
5B	None	9.0	3.38	Actual Pred.	0.60 1.05	1.62 2.48	3.93 3.50	-- --
7A	None	4.5	6.55	Actual Pred.	4.75 3.41	-- --	-- --	-- --
7B	None	4.5	6.41	Actual Pred.	1.79 2.62	4.79 4.99	-- --	-- --
13A	None	7.0	3.59	Actual Pred.	2.56 1.42	-- --	-- --	-- --
13B	None	7.0	3.63	Actual Pred.	0.68 0.81	1.75 1.72	4.97* 2.62	-- --
19A	None	10.0	1.83	Actual Pred.	0.63 0.71	1.20 1.35	1.86 1.97	2.37 2.50
19B	None	10.0	1.81	Actual Pred.	0.24 0.49	0.82 1.15	1.61 1.68	2.42 2.20

(a) Ref. Page 92 for Definition
* Extrapolated Data Point

Table 7-20. (Continued).

Test No.	Membrane Type	Depth of Stone (in.)	Stress Ratio (a)	Method	Rut at Given N			
					$N = 10$ $\frac{\Delta(\text{in.})}{\Delta}$	$N = 10^2$ $\frac{\Delta(\text{in.})}{\Delta}$	$N = 10^3$ $\frac{\Delta(\text{in.})}{\Delta}$	$N = 10^4$ $\frac{\Delta(\text{in.})}{\Delta}$
22A	None	13.0	1.06	Actual Pred.	0.46 0.36	0.81 0.63	1.36 0.93	2.01 1.33
26B	None	3.0	6.76	Actual Pred.	1.57 1.51	5.53* 4.74	-- --	-- --
28B	None	4.5	4.34	Actual Pred.	0.88 0.55	2.40 1.27	5.50* 2.37	-- --
30B	None	6.0	2.74	Actual Pred.	0.42 0.28	1.18 0.68	3.30 1.30	4.72 2.06
2B	T-3401	6.0	6.72	Actual Pred.	0.91 1.65	2.71 4.14	5.50* 5.64	-- --
4B	T-3401	7.5	4.62	Actual Pred.	0.49 0.84	1.83 2.10	4.12 3.17	-- --
6B	T-3401	9.0	3.32	Actual Pred.	0.32 0.53	1.08 1.35	2.08 1.85	3.50 --
9A	T-3401	4.5	6.62	Actual Pred.	1.64 1.84	3.28 3.93	-- --	-- --
9B	T-3401	4.5	6.46	Actual Pred.	0.92 1.49	2.46 3.34	-- --	-- --

(a) Ref. Page 92 for Definition

* Extrapolated Data Point

Table 7-20. (Continued).

Test No.	Membrane Type	Depth of Stone (in.)	Stress Ratio (a)	Method	Rut at Given N			
					$N = 10$ $\frac{\Delta(\text{in.})}{\Delta}$	$N = 10^2$ $\frac{\Delta(\text{in.})}{\Delta}$	$N = 10^3$ $\frac{\Delta(\text{in.})}{\Delta}$	$N = 10^4$ $\frac{\Delta(\text{in.})}{\Delta}$
15A	T-3401	7.0	3.30	Actual Pred.	0.86 0.97	2.16 1.85	3.79 2.69	-- --
15B	T-3401	7.0	3.71	Actual Pred.	0.40 0.79	1.28 1.83	3.72 3.15	4.97* 3.91
20A	T-3401	10.0	1.88	Actual Pred.	0.43 0.56	0.99 1.12	1.59 1.52	2.01 1.67
20B	T-3401	10.0	1.77	Actual Pred.	0.19 0.38	0.36 0.79	1.07 1.23	1.63 1.60
23A	T-3401	13.0	1.07	Actual Pred.	0.28 0.23	0.64 0.45	1.19 0.72	1.59 0.92
27B	T-3401	3.0	6.71	Actual Pred.	1.04 1.08	2.96 2.82	-- --	-- --
29B	T-3401	4.5	4.30	Actual Pred.	0.38 0.41	1.24 0.97	2.97 1.86	-- --
31B	T-3401	6.0	3.13	Actual Pred.	0.53 0.31	1.67 0.78	3.49 1.46	4.94* 2.23

(a) Ref. Page 92 for Definition
* Extrapolated Data Point

reinforced with Typar 3401 fabric. These data are summarized in Table 7-21.

The VESYS vertical stresses, determined utilizing the modified approach, were compared to the measured subgrade stresses for the corresponding model tests and stress cell locations. For AS systems, the VESYS stress data averaged 81 percent of actual, with a range of 39-150 percent. For Typar 3401 reinforced AFS systems, the VESYS stress data averaged 83 percent of actual, with a range of 36-178 percent. Underestimation of measured stress levels was greatest in the upper portion of the subgrade; overestimation in the lower portion. Raad and Figueroa (78) reported general underestimation of actual vertical stresses utilizing elastic layered theory.

As the results of this method were less accurate than those of all previously described methods, especially with regard to underestimation of deformations as the tests progress, the method was not applied to the full-scale tests. Such application would require correction for instrumentation, but not for scaling, provided that the VESYS program input is in terms of the full-scale system geometry. In such a case, corresponding sublayer mid-height stress states and plastic strains would be identical in the model and prototype, while computed deformations in the prototype would be increased by the geometric scale factor (Ref. Equation (2-9)).

Method 7

The load induced stress state was computed utilizing the University of Illinois axisymmetric finite element program (110) described in Chapter II. The resilient moduli for the aggregate and

Table 7-21. Summary of Method 6 Predictions of Component Permanent Deformation Ratios.

Test No.	Membrane Type	$\left(\frac{\Delta \text{ Subgrade}}{\Delta \text{ Total}}\right) \times 100\%$	
		Actual	Predicted ^(a)
1B	None	87.4	96.8
3B	None	75.1	76.7
5B	None	62.4	71.7
7A	None	84.6	90.4
7B	None	84.1	93.2
13A	None	72.6	64.6
13B	None	70.7	75.5
19A	None	31.9	59.3
19B	None	34.8	56.5
22A	None	22.9	35.5
26B	None	92.3	94.0
28B	None	80.6	79.9
30B	None	65.9	73.7
2B	T-3401	61.6	87.6
4B	T-3401	51.5	62.1
6B	T-3401	48.4	61.1
9A	T-3401	59.4	88.5
9B	T-3401	59.7	86.7
15A	T-3401	51.8	70.3
15B	T-3401	48.3	53.1
20A	T-3401	41.9	57.5
20B	T-3401	37.4	61.1
23A	T-3401	37.1	41.7
27B	T-3401	70.4	79.2
29B	T-3401	60.9	72.0
31B	T-3401	50.5	63.3

(a) Ref. Table 7-20 for Rutting Response Predictions

subgrade materials were modeled on the basis of the results from the repeated load triaxial tests (Ref. Tables 3-5 through 3-7). Several program runs were made for each aggregate layer thickness and subgrade strength combination, varying only the failure modulus for the aggregate layer. For each combination, plots were made of aggregate failure modulus versus the transient elastic surface deflection per cycle on the load centerline, and aggregate failure modulus versus both vertical and radial centerline stresses at various depths. The forms of these relationships are similar to those depicted in Figure 7-14, with aggregate failure modulus substituted for aggregate resilient modulus on the horizontal axis. Stress state output was provided for both the applied load and gravity contributions.

From the model test program results, the actual transient elastic deformation per cycle of the footing, on its centerline, was known at various times during most tests (Ref. Table 7-14). Utilizing these actual deflection values, the equivalent failure moduli for the aggregate layer and corresponding stress states for the systems were determined from the plots of FEM program output for any load cycles of interest. The hyperbolic plastic stress-strain law (i.e., Equation (2-8)) was applied to the resulting stress states to predict rutting (i.e., Equation (2-9)) after the corresponding numbers of load cycles.

As discussed under Method 6, in those sublayers for which the approach was not applicable (i.e., shear or tensile failure), vertical sublayer strains were determined on the basis of Bison strain sensor data (Ref. Tables 7-15 through 7-17). For the FEM analyses, this situation arose in the aggregate sublayers of all systems and in the

upper subgrade sublayers in the weakest systems (i.e., stress ratios greater than four). The calculated zone of centerline tensile failure in the aggregate is greater (i.e., approximately twice the depth) in the FEM analyses than in the corresponding VESYS analyses, which is consistent with the findings of Raad and Figueroa (78). Thus, greater reliance on the Bison strain sensor data was required for application of Method 7 than for application of Method 6, a major disadvantage with utilization of the former.

The results of the method as applied to a portion of the model test program, utilizing the aggregate failure modulus and corresponding load induced stress state for the load cycle of interest, are summarized in Table 7-22. For AS systems with Type A loading, the calculated rut depths averaged 134 percent of the observed values, with a range of 104-179 percent. For the Type B load tests of subgrade Group II (Ref. Table 5-1), this average was 173 percent, with a range of 120-292 percent. For AFS systems reinforced with Typar 3401 fabric, the computed rut depths averaged 140 percent of the actual rut depths, with a range of 96-219 percent, for Type A loading. For the Type B load tests of subgrade Group II, this average was 205 percent, with a range of 121-353 percent.

In an attempt to improve accuracy, by reducing the overestimation of observed rutting magnitudes, a modified approach was utilized, with the confining influence due to gravity stresses considered during rutting determination. Results of this modified approach are presented in Table 7-23. For AS systems with Type A loading, the calculated rut depths averaged 119 percent of actual, with a range of 91-154 percent.

Table 7-22. Summary of Method 7 Predictions of Model Test Program Rutting Responses Based Upon Load Induced Stress State Determined at $N = 1$ Load Cycles.

Test No.	Membrane Type	Depth of Stone (in.)	Stress Ratio (a)	Method	Rut at Given N			
					$N = 10$ Δ (in.)	$N = 10^2$ Δ (in.)	$N = 10^3$ Δ (in.)	$N = 10^4$ Δ (in.)
13B	None	7.0	3.63	Actual Pred.	0.68 0.98	1.75 2.12	4.97* --	-- --
19A	None	10.0	1.83	Actual Pred.	0.63 1.13	1.20 2.01	1.86 2.40	2.37 3.27
19B	None	10.0	1.81	Actual Pred.	0.24 0.70	0.82 1.57	1.61 2.72	2.42 2.90
22A	None	13.0	1.06	Actual Pred.	0.46 0.57	0.81 0.97	1.36 1.50	2.01 2.09
9A	T-3401	4.5	6.63	Actual Pred.	1.64 1.65	3.28 3.73	-- --	-- --
9B	T-3401	4.5	6.46	Actual Pred.	0.92 1.35	2.46 2.94	-- --	-- --
15A	T-3401	7.0	3.30	Actual Pred.	0.86 1.39	2.16 2.57	3.79 4.40	-- --
15B	T-3401	7.0	3.71	Actual Pred.	0.40 1.20	1.28 2.17	3.72 4.49	4.97* --
20A	T-3401	10.0	1.88	Actual Pred.	0.43 0.94	0.99 1.84	1.59 2.70	2.01 2.94

(a) Ref. Page 92 for Definition
* Extrapolated Data Point

Table 7-22. (Continued).

Test No.	Membrane Type	Depth of Stone (in.)	Stress (a) Ratio	Method	Rut at Given N		
					$N = 10$ $\frac{N}{\Delta \text{ (in.)}}$	$N = 10^2$ $\frac{N}{\Delta \text{ (in.)}}$	$N = 10^3$ $\frac{N}{\Delta \text{ (in.)}}$
20B	T-3401	10.0	1.77	Actual Pred.	0.19 0.63	0.36 1.27	1.07 1.79
23A	T-3401	13.0	1.07	Actual Pred.	0.28 0.46	0.64 0.79	1.19 1.25

(a) Ref. Page 92 for Definition
* Extrapolated Data Point

Table 7-23. Summary of Method 7 Predictions of Model Test Program Rutting Responses Based Upon Stress State Determined at $N = i$ Load Cycles, with Gravity Stress Confinement Considered.

Test No.	Membrane Type	Depth of Stone (in.)	Stress Ratio (a)	Method	Rut at Given N			
					$N = 10$ $\frac{N}{\Delta \text{ (in.)}}$	$N = 10^2$ $\frac{N}{\Delta \text{ (in.)}}$	$N = 10^3$ $\frac{N}{\Delta \text{ (in.)}}$	$N = 10^4$ $\frac{N}{\Delta \text{ (in.)}}$
13B	None	7.0	3.63	Actual Pred.	0.68 0.90	1.75 1.95	4.97* --	-- --
19A	None	10.0	1.83	Actual Pred.	0.63 0.97	1.20 1.73	1.86 2.16	2.37 3.01
19B	None	10.0	1.81	Actual Pred.	0.24 0.59	0.82 1.38	1.61 2.48	2.42 2.71
22A	None	13.0	1.06	Actual Pred.	0.46 0.51	0.81 0.87	1.36 1.39	2.01 1.97
9A	T-3401	4.5	6.62	Actual Pred.	1.64 1.52	3.28 3.37	-- --	-- --
9B	T-3401	4.5	6.46	Actual Pred.	0.92 1.15	2.46 2.53	-- --	-- --
15A	T-3401	7.0	3.30	Actual Pred.	0.86 1.19	2.16 2.29	3.79 3.92	-- --
15B	T-3401	7.0	3.71	Actual Pred.	0.40 1.06	1.28 1.97	3.72 3.84	4.97* --

(a) Ref. Page 92 for Definition
* Extrapolated Data Point

Table 7-23. (Continued).

Test No.	Membrane Type	Depth of Stone (in.)	Stress Ratio (a)	Method	Rut at Given N			
					$N = 10$ $\frac{\Delta \text{ (in.)}}{\Delta \text{ (in.)}}$	$N = 10^2$ $\frac{\Delta \text{ (in.)}}{\Delta \text{ (in.)}}$	$N = 10^3$ $\frac{\Delta \text{ (in.)}}{\Delta \text{ (in.)}}$	$N = 10^4$ $\frac{\Delta \text{ (in.)}}{\Delta \text{ (in.)}}$
20A	T-3401	10.0	1.88	Actual Pred.	0.43 0.79	0.99 1.55	1.59 2.36	2.01 2.67
20B	T-3401	10.0	1.77	Actual Pred.	0.19 0.52	0.36 1.03	1.07 1.65	1.63 2.06
23A	T-3401	13.0	1.07	Actual Pred.	0.28 0.41	0.64 0.69	1.19 1.12	1.59 1.41

(a) Ref. Page 92 for Definition
* Extrapolated Data Point

For the Type B load tests of subgrade Group II, this average was 154 percent, with a range of 111-246 percent. For AFS systems reinforced with Typar 3401 fabric, the computed rut depths averaged 123 percent of the observed values, with a range of 89-184 percent, for Type A loading. For the Type B load tests of subgrade Group II, this average was 177 percent, with a range of 103-286 percent. These results represent an improvement over those obtained without considering the confining influence of the gravity stresses.

As with Method 6, the predictions were most conservative during the early stages of loading. Unlike Method 6, which tended to underestimate rutting during the later stages of loading, Method 7 generally remained conservative in its estimations throughout the loading history. The rutting predictions, with gravity stress confinement effects considered, were comparable to those obtained initially utilizing the VESYS output (Ref. Table 7-18), being more accurate in 50 percent of the cases analyzed (i.e., 38 percent for AS systems and 57 percent for AFS systems). The results of the modified approach remain less accurate than those of all other methods.

A comparison between computed and observed values of the percentage of the total rutting exhibited by the subgrade was made for the tests as discussed under Method 6. That portion of the total rutting exhibited by the subgrade was overestimated (i.e., confining influence due to gravity stresses considered during rutting determination), averaging 151 percent of the measured values for AS systems and 153 percent for Typar 3401 reinforced AFS systems. These results are summarized in Table 7-24. Method 6 was more accurate for the corresponding tests

Table 7-24. Summary of Method 7 Predictions of Component Permanent Deformation Ratios.

Test No.	Membrane Type	$\left(\frac{\Delta \text{ Subgrade}}{\Delta \text{ Total}}\right) \times 100\%$	
		Actual	Predicted ^(a)
13B	None	70.7	88.4
19A	None	31.9	56.9
19B	None	34.8	53.3
22A	None	22.9	33.6
9A	T-3401	59.4	89.8
9B	T-3401	59.7	86.7
15A	T-3401	51.8	79.7
15B	T-3401	48.3	78.4
20A	T-3401	41.9	64.9
20B	T-3401	37.4	69.6
23A	T-3401	37.1	43.3

(a) Ref. Table 7-23 for Rutting Response Predictions

(Ref. Table 7-21).

The FEM load induced vertical stresses, determined on the basis of observed transient surface deflections per cycle at 10^2 load repetitions, were compared to the measured subgrade stresses for the corresponding model tests and stress cell locations. For AS systems, the FEM stress data averaged 134 percent of actual, with a range of 94-186 percent. For Typar 3401 reinforced AFS systems, the FEM stress data averaged 129 percent of actual, with a range of 89-219 percent. Overestimation was greatest in the lower portion of the subgrade; underestimation in the upper portion. Raad and Figueroa (78) reported general overestimation of actual vertical stresses utilizing this FEM program.

As calculations with the tests of subgrade Group II did not indicate significant improvement upon the corresponding Method 6 results (i.e., both methods based upon use of the hyperbolic plastic stress-strain law), it was not applied to the remaining model tests, nor to the full-scale tests. As discussed under Method 6, extension to full-scale tests would require correction for instrumentation, but not for scaling, provided that input is in terms of full-scale system geometry. During the period that this research was being conducted, an improved FEM program was being formulated by Zeevaert (123), which also negated to a large degree the need for further analysis utilizing the University of Illinois FEM program.

Method 8

The load induced vertical stresses in each system were shown by pressure cell readings (Ref. Figures 6-26 and 6-27) to be closely

approximated by Boussinesq theory. Application of the hyperbolic plastic stress-strain law (i.e., Equation (2-8)) to a stress state with Boussinesq theory vertical stresses was made in an attempt to predict rutting responses (i.e., Equation (2-9)). Initial rutting calculations utilized only the load induced stress state, with both vertical and radial stresses determined from chart solutions prepared by Foster and Ahlvin (40). These chart solutions assume a Poisson's ratio of 0.5. Preliminary calculations for the tests of subgrade Group II (Ref. Table 5-1) overestimated observed rutting magnitudes. The hyperbolic plastic stress-strain law was not directly applicable in a number of sublayers (i.e., shear or tensile failure), due to the rapid decrease, with depth, in centerline radial stress magnitudes predicted by Boussinesq theory (i.e., a decrease to an intensity of less than one percent of the applied contact pressure at a depth of 2.5 contact radii -- for the model tests this corresponds to a decrease in radial stress magnitude to less than 0.7 psi at a depth of 7.5 inches -- and to a value of zero at a depth of five contact radii). Adding the effects of gravity stress confinement to the Boussinesq stress state did not significantly improve the estimates of system responses.

To improve rutting predictions, an increase in the computed radial stress values was required, primarily for the upper sublayers of the subgrade. This was accomplished by determining the subgrade radial stresses utilizing a pseudo footing. The outer edge of this pseudo footing was taken as that point where a diagonal line extending downward and outward from the lower edge of the actual footing, and making an acute angle of 55° with the horizontal, cut the subgrade surface, based

upon the initial geometry of the system. The value of 55° was determined on the basis of the model test results, being an average value (to the nearest five degrees) of the angle, with the horizontal, made by a line connecting the lower edge of the actual footing and that point on the subgrade surface profile which experienced no measurable rutting or heave, again based upon initial system geometry. The pseudo footing load intensity, at the subgrade surface, was found by dividing the actual total applied load by the pseudo footing area. This approach is similar to an approximation sometimes used in foundation engineering (97) for estimating the dissipation of vertical stress beneath a footing and to an approximation used in the Giroud and Noiray (41) analyses of AS and AFS systems (Ref. Method 5). These approximations utilize truncated pyramidal pressure dissipations, with pyramid sides making acute angles of 63 and 59 degrees, respectively, with the horizontal compared to the truncated cone dissipation and 55 degree angle of this approach. Only subgrade radial stresses were determined on the basis of the pseudo footing, with all vertical stresses and the aggregate layer radial stresses determined on the basis of the actual footing. The hyperbolic plastic stress-strain law was applied to the resulting load induced stress state (i.e., gravity stress confinement neglected) to predict rutting.

Initial calculations (i.e., subgrade Group II) indicated reasonable agreement with the rutting observed in the model tests of AFS systems reinforced with Typar 3401 fabric, the results being more accurate than the corresponding results of Methods 6 and 7 (i.e., all methods based upon the hyperbolic plastic stress-strain law). For AS systems,

a modification to the stress state was required to model the increased rutting exhibited as compared to the corresponding AFS system responses. Such modification could take the form of increased vertical stresses, reduced radial stresses, or a combination thereof. Due to the close approximation between the Boussinesq theory vertical stresses and pressure cell measurements of actual stresses, it was decided to attempt modification of only the radial stresses (i.e., computed on the basis of the actual footing for the aggregate and psuedo footing for the subgrade). By a trial and error approach with the AS system tests of subgrade Group II, varying the radial stress values in increments of 10 percent, a reduction of 10 percent in the computed radial stresses in all sublayers was found to yield calculated rut depths which closely approximated the measured responses of AS systems. Prior to attempting any refinement of this method, application was made to the model tests of subgrade Groups I and III, to determine its suitability over a wider range of material strengths.

The results of the method as applied to the full model test program are summarized in Table 7-25. As with Methods 6 and 7, in those sublayers for which the approach was not applicable (i.e., shear or tensile failure), vertical sublayer strains were determined on the basis of Bison strain sensor data (Ref. Tables 7-15 through 7-17). This situation arose in aggregate sublayers at depths greater than approximately 4.5 inches and in the upper subgrade sublayers in the weakest systems (i.e., stress ratios greater than six). The frequency of this problem was comparable to that experienced in application of Methods 6 and 7. For AS systems with Type A loading, the calculated rut depths averaged 96

Table 7-25. Summary of Method 8 Predictions of Model Test Program Rutting Responses.

Test No.	Membrane Type	Depth of Stone (in.)	Stress Ratio (a)	Method	Rut at Given N			
					$N = 10$ $\frac{\Delta(\text{in.})}{\Delta(\text{in.})}$	$N = 10^2$ $\frac{\Delta(\text{in.})}{\Delta(\text{in.})}$	$N = 10^3$ $\frac{\Delta(\text{in.})}{\Delta(\text{in.})}$	$N = 10^4$ $\frac{\Delta(\text{in.})}{\Delta(\text{in.})}$
1B	None	6.0	6.75	Actual Pred.	1.35 2.34	4.92 5.72	-- --	-- --
3B	None	7.5	4.50	Actual Pred.	0.78 1.92	2.77 4.00	5.57* 6.26	-- --
5B	None	9.0	3.38	Actual Pred.	0.60 1.31	1.62 2.68	3.93 4.11	-- --
7A	None	4.5	6.55	Actual Pred.	4.73 2.61	-- --	-- --	-- --
7B	None	4.5	6.41	Actual Pred.	1.79 1.75	4.79 3.94	-- --	-- --
13A	None	7.0	3.59	Actual Pred.	2.56 1.24	-- --	-- --	-- --
13B	None	7.0	3.63	Actual Pred.	0.68 0.83	1.75 1.76	4.97* 3.01	-- --
19A	None	10.0	1.83	Actual Pred.	0.63 0.73	1.20 1.33	1.86 1.95	2.37 2.59
19B	None	10.0	1.81	Actual Pred.	0.24 0.47	0.82 1.10	1.61 1.79	2.42 2.33

(a) Ref. Page 92 for Definition
* Extrapolated Data Point

Table 7-25. (Continued) .

Test No.	Membrane Type	Depth of Stone (in.)	Stress Ratio (a)	Method	Rut at Given N			
					$N = 10$ $\frac{\Delta (in.)}{\Delta}$	$N = 10^2$ $\frac{\Delta (in.)}{\Delta}$	$N = 10^3$ $\frac{\Delta (in.)}{\Delta}$	$N = 10^4$ $\frac{\Delta (in.)}{\Delta}$
22A	None	13.0	1.06	Actual Pred.	0.46 0.50	0.81 0.88	1.36 1.35	2.01 1.91
26B	None	3.0	6.76	Actual Pred.	1.57 1.30	5.53* 3.69	-- --	-- --
28B	None	4.5	4.34	Actual Pred.	0.88 0.54	2.40 1.07	5.50* 2.09	-- --
30B	None	6.0	2.74	Actual Pred.	0.42 0.31	1.18 0.64	3.30 1.32	4.72 2.12
2B	T-3401	6.0	6.72	Actual Pred.	0.91 1.96	2.71 4.49	5.50* 7.51	-- --
4B	T-3401	7.5	4.62	Actual Pred.	0.49 1.63	1.83 3.56	4.12 5.97	-- --
6B	T-3401	9.0	3.32	Actual Pred.	0.32 1.06	1.08 2.31	2.08 3.35	3.50 --
9A	T-3401	4.5	6.62	Actual Pred.	1.64 1.69	3.28 3.43	-- --	-- --
9B	T-3401	4.5	6.46	Actual Pred.	0.92 1.33	2.46 2.87	-- --	-- --

(a) Ref. Page 92 for Definition
* Extrapolated Data Point

Table 7-25. (Continued).

Test No.	Membrane Type	Depth of Stone (in.)	Stress (a) Ratio	Method	Rut at Given N		
					$N = 10^2$ $\frac{\Delta (in.)}{\Delta (in.)}$	$N = 10^3$ $\frac{\Delta (in.)}{\Delta (in.)}$	$N = 10^4$ $\frac{\Delta (in.)}{\Delta (in.)}$
15A	T-3401	7.0	3.30	Actual Pred.	2.16 1.86	3.79 2.83	-- --
15B	T-3401	7.0	3.71	Actual Pred.	1.28 1.54	3.72 2.91	4.97* 3.53
20A	T-3401	10.0	1.88	Actual Pred.	0.99 1.07	1.59 1.58	2.01 2.10
20B	T-3401	10.0	1.77	Actual Pred.	0.36 0.80	1.07 1.40	1.63 1.81
23A	T-3401	13.0	1.07	Actual Pred.	0.64 0.65	1.19 0.98	1.59 1.34
27B	T-3401	3.0	6.71	Actual Pred.	2.96 1.90	-- --	-- --
29B	T-3401	4.5	4.30	Actual Pred.	1.24 0.81	2.97 1.58	-- --
31B	T-3401	6.0	3.13	Actual Pred.	1.67 0.74	3.49 1.45	4.94* 2.28

(a) Ref. Page 92 for Definition
* Extrapolated Data Point

percent of the observed values, with a range of 48-116 percent. For Type B loading, this average was 107 percent, with a range of 38-246 percent. For AFS systems reinforced with Typar 3401 fabric, the computed rut depths averaged 101 percent of the actual rut depths, with a range of 75-130 percent, for Type A loading. For Type B loading, this average was 138 percent, with a range of 42-333 percent.

As with Methods 6 and 7, the predictions were most conservative during the early stages of loading. The rutting predictions were more accurate than those obtained with the FEM output (Ref. Table 7-23), being more accurate in 72 percent of the cases analyzed (i.e., 86 percent for AS systems and 64 percent for AFS systems), and comparable to the results obtained with the VESYS output (Ref. Table 7-20), being more accurate in 49 percent of the cases analyzed (i.e., 53 percent for AS systems and 46 percent for AFS systems). The approach performed best with the tests of subgrade Group II (i.e., more accurate than Method 6 in 69 percent of the cases analyzed and more accurate than Method 7 in 72 percent of these cases), but provided poor results as applied to the tests of subgrade Groups I and III (i.e., more accurate than Method 6 in only 26 percent of the cases analyzed). This was not unexpected, as Method 8 computes the stress state based solely upon system geometry, whereas the VESYS and FEM programs utilized in Methods 6 and 7 account for both system geometry and material strengths. For example, Method 8 would indicate identical stress states for model tests 1B and 30B (i.e., six inches of crushed stone), while Methods 6 and 7 would indicate differing stress states in the two systems due to variations in subgrade strengths (i.e., vane shear strengths of 2.95 and 7.25 psi respectively).

Therefore it was to be expected that Method 8 would be less accurate over the full range of subgrade strengths than those other methods utilizing the hyperbolic plastic stress-strain law. This approach was also less accurate than Methods 1 through 5, both overall and within each subgrade group.

A comparison between computed and observed values of the percentage of the total rutting exhibited by the subgrade was made for the tests as discussed under Method 6. That portion of the total rutting exhibited by the subgrade was overestimated, averaging 131 percent of the measured values for AS systems and 155 percent for Typar 3401 reinforced AFS systems. These results are summarized in Table 7-26. Methods 6 and 7 were more accurate for the corresponding tests (Ref. Tables 7-21 and 7-24).

The elastic transient surface deflections per cycle, at 10^2 load repetitions, were computed and compared to the measured responses. For AS systems, the predictions averaged 84 percent of actual, with a range of 50-115 percent. For Typar 3401 reinforced AFS systems, the predictions averaged 72 percent of actual, with a range of 48-95 percent. These data are summarized in Table 7-27.

As calculations did not indicate significant potential for improvement upon the Method 6 results over the full range of model tests, (i.e., both methods based upon use of the hyperbolic plastic stress-strain law), further refinement was not attempted, nor was application made to the full-scale tests. As previously discussed, extension to full-scale tests would require correction for instrumentation, but not for scaling, provided that input is in terms of the full-scale system geometry.

Table 7-26. Summary of Method 8 Predictions of Component Permanent Deformation Ratios.

Test No.	Membrane Type	$(\frac{\Delta \text{ Subgrade}}{\Delta \text{ Total}}) \times 100\%$	
		Actual	Predicted ^(a)
1B	None	87.4	96.2
3B	None	75.1	92.2
5B	None	62.4	83.2
7A	None	84.6	99.2
7B	None	84.1	99.7
13A	None	72.6	74.3
13B	None	70.7	78.9
19A	None	31.9	61.8
19B	None	34.8	58.8
22A	None	22.9	42.8
26B	None	92.3	99.9
28B	None	80.6	99.1
30B	None	65.9	74.1
2B	T-3401	61.6	90.5
4B	T-3401	51.5	88.4
6B	T-3401	48.4	85.0
9A	T-3401	59.4	99.6
9B	T-3401	59.7	99.6
15A	T-3401	51.8	72.4
15B	T-3401	48.3	68.6
20A	T-3401	41.9	65.9
20B	T-3401	37.4	65.6
23A	T-3401	37.1	50.1
27B	T-3401	70.4	99.8
29B	T-3401	60.9	99.1
31B	T-3401	50.5	63.9

(a) Ref. Table 7-25 for Rutting Response Predictions

Table 7-27. Summary of Method 8 Predictions of Elastic Transient Surface Deformation per Cycle at N = 100.

Test No.	Membrane Type	Deformation per Cycle (in.)	
		Actual	Predicted ^(a)
1B	None	0.44	0.34
3B	None	0.20	0.21
5B	None	0.15	0.13
7A	None	--	0.26
7B	None	--	0.28
13A	None	--	0.11
13B	None	0.17	0.12
19A	None	0.09	0.07
19B	None	0.09	0.07
22A	None	0.08	0.04
26B	None	--	0.31
28B	None	0.23	0.22
30B	None	0.13	0.15
2B	T-3401	0.36	0.30
4B	T-3401	0.21	0.20
6B	T-3401	0.15	0.12
9A	T-3401	0.35	0.22
9B	T-3401	0.31	0.24
15A	T-3401	0.17	0.10
15B	T-3401	0.15	0.11
20A	T-3401	0.09	0.06
20B	T-3401	0.08	0.06
23A	T-3401	0.08	0.04
27B	T-3401	0.54	0.26
29B	T-3401	0.22	0.18
31B	T-3401	0.17	0.14

(a) Ref. Table 7-25 for Rutting Response Predictions

CHAPTER VIII

INTERPRETATION OF RESULTS

A model test program was conducted to experimentally examine the performance characteristics of AS and AFS systems subjected to repeated (i.e., transient) loading. Data on the subgrade stress state and on the deformations developed within the subgrade, aggregate and fabric have contributed to a better understanding of the mechanisms by which fabric affects the performance of AFS systems and of the influences of selected variables on system responses. The program has also permitted analysis and refinement of several design methodologies, with emphasis on the development of an approach for AS and Typar 3401 reinforced AFS systems that fully predicts rutting response (i.e., load cycle-rut depth relationship).

Mechanisms

Of the proposed mechanisms (i.e., separation, provision of filter medium to facilitate drainage, confinement and reinforcement of the aggregate, and alteration of the subgrade soil failure mode) by which a fabric inclusion influences the behavior of an AFS system, alteration of the failure mode within the subgrade soil appears to be of the greatest significance. Such is the case, whether the data are analyzed in terms of the total layer deformation experienced at test termination (i.e., disregarding any differences in load cycle values between corresponding AS and AFS systems) or the average layer deformation per load

cycle. While fabric does serve as a filter medium and prevents inter-mixing of the aggregate and subgrade soil in an AFS system, aggregate of the proper gradation (i.e., meeting filter and permeability criteria) in the corresponding AS system can provide these same benefits.

Based upon the systems and test method of this study, confinement and reinforcement of the aggregate layer does not appear to be a very significant mechanism, especially if the data are analyzed in terms of the total aggregate layer deformation experienced at the completion of each test. For AS systems with similar surface rutting, aggregate layer centerline vertical strains varied only slightly for all tests, displaying a mild tendency to increase as layer thickness was increased above a given subgrade strength. In Typar 3401 reinforced AFS systems, observed aggregate layer vertical strains ranged up to three times those in corresponding AS systems with similar surface rutting, with this trend most pronounced in the weakest systems. It should be noted, however, that a substantially greater number of loadings was required to reach the same surface rutting in the AFS systems. For a given subgrade strength, aggregate strains in AFS systems decreased as aggregate layer thickness increased. For both AS and AFS systems, exhibited aggregate strains were considerably greater than the levels assumed by the analysis models of Kinney (56) or Giroud and Noiray (41).

The observed variations in final aggregate layer deformations, between corresponding AS and AFS systems, are counter to the trends anticipated by the proposed confinement/reinforcement mechanism, which predicts reduced aggregate movement in AFS systems. However, when the data are analyzed in terms of the average aggregate layer deformation

per load cycle, the performances of AFS systems constructed on weaker subgrades (i.e., CBR less than 1.5) were superior, providing some support for this proposed mechanism. With weak subgrade soils, Typar 3401 reinforced AFS systems typically displayed deformation rates on the order of one-half those in the corresponding AS systems. No clear trends were evident in comparison of systems constructed with stronger subgrade materials.

Alteration of Stress, Strain, and Deformation

A fabric inclusion was observed to alter the states of stress and plastic strain in the subgrade soil as compared to those of the corresponding AS system. Pressure cell data from the beginning stages of loading were found to average 91 percent of the stresses predicted by Boussinesq theory for AS systems and 90 percent for Typar 3401 reinforced AFS systems. Pressure cell data collected during final stages of loading (rut depth = 4 to 5 inches) were found to average 88 percent of Boussinesq theory stresses for AS systems and 83 percent for AFS systems containing Typar 3401 fabric. The reduced stresses observed in deformed AFS systems, as compared to the corresponding AS systems, were anticipated on the basis of the proposed mechanism for alteration of the subgrade failure mode (e.g., in this case, a "membrane effect" as a result of induced stresses perpendicular to the fabric). The virtually identical stresses observed in corresponding AS and AFS systems at low deformation levels is also consistent with the operation of this mechanism.

For AS systems, the greatest vertical plastic strains were

experienced along the load centerline, in the upper one-third of the subgrade material, reaching levels as great as 69 percent. In Typar 3401 reinforced AFS systems, the greatest centerline vertical strains were experienced along the load centerline, but in the aggregate layer rather than in the subgrade. For a given subgrade strength, subgrade strains decreased in both AS and AFS systems as the thickness of the overlying aggregate layer increased. The reduced centerline vertical strains exhibited by the subgrade material in AFS systems, as opposed to AS systems, is consistent with the lower stress states measured in the former systems, when deformed, and with the proposed mechanism for subgrade failure mode alteration.

The deformed shape of the subgrade soil profile conformed to that for a shear failure, displaying a rutted portion, centered below the footing, and a radially offset bulge or heave. For a given subgrade strength, as the thickness of the aggregate layer increased, the depth of subgrade rutting decreased, the height of heave decreased, and the width of the rutted area increased. A fabric inclusion was observed to produce changes similar to those of increased aggregate layer thickness, as compared to the deformed interface shape in the corresponding AS systems. Such changes in the deformation pattern are consistent with those predicted by the subgrade failure mode alteration mechanism. The stress, plastic strain, and subgrade profile change data tend to confirm the design models of Barenberg, et al. (15, 24) and Giroud and Noiray (41), in which the capacity of AS systems is limited by localized shear failure criteria, while AFS systems are limited by general shear failure criteria.

The in-plane permanent strains exhibited by the Typar 3401 fabric inclusions were generally greatest in a zone between the load centerline and an offset of one radius, decreasing with further radial offset. Fabric tearing was observed in three of the 14 tests which utilized Typar 3401 fabric, with the tears initiating at a distance of 0.5-1.5 offset radii from the centerline and propagating in a circular pattern within this zone. This phenomenon was only observed in systems utilizing stiffer subgrade materials (i.e., unsoaked CBR greater than 1.5) and appears to be a function of subgrade strength rather than stress ratio. The analysis models of Kinney (56) or Giroud and Noiray (41) assume a constant strain level throughout the fabric, as compared to the more complex deformation patterns actually observed.

Factors Affecting System Responses

The model test program results showed rutting to be influenced, to some extent, by subgrade soil strength, thickness of the crushed stone layer, load pulse duration, placement of a membrane at the aggregate-subgrade interface and the type of membrane thus utilized.

For all sets of tests in which subgrade strength was the independent variable, the rate of rutting was observed to decrease as subgrade strength increased. For comparable reference values of subgrade strength and increases thereto, the sets of AS system tests displayed greater improvements (i.e., percentage increases in load repetitions required to achieve two, three, and four inches of rut depth) in response characteristics than did the corresponding sets of AFS system tests. Within any test set, improvements were greater at higher

deformation levels. For both AS and AFS systems, improvements were greater when comparable magnitudes of strength increases were made from weaker reference systems. This indicates that the benefit offered by fabric reinforcement decreases as the subgrade strength increases. It has been suggested (29, 30, 31, 57, 71, 109) that the use of geotextiles in unsurfaced pavement systems is not economically attractive when the subgrade CBR value is greater than three.

For all sets of tests in which the thickness of crushed stone was the independent variable, the rate of rutting decreased as the aggregate thickness increased. The improvements, for identical increases in aggregate thickness, were comparable in all corresponding test sets, with no clear distinction evident between the improvements displayed by AS and AFS systems. Within any test set, improvements were more pronounced at higher deformation levels.

For all sets of tests in which load pulse duration was the independent variable, the rate of rutting was observed to decrease as the load pulse duration decreased, a trend expected on the basis of visco-elastic considerations. The relative improvements in rutting response were generally greater in the test sets of AS systems, than in the corresponding sets of AFS systems. Within given test sets of AS systems, the relative improvements in permanent deformation characteristics were more pronounced at higher deformation levels, while the reverse was true within sets of AFS systems. These data suggest that AS and AFS systems subjected to slow moving loads will rut at faster rates than similar systems subjected to faster moving loads. To obtain the same rutting rates in two systems subjected to vehicles moving at different speed

limits, a greater thickness of crushed stone will be required for the system with the slower moving loads.

Inclusion of a membrane at the aggregate-subgrade interface improved rutting resistance within all sets of tests in which such an inclusion was the independent variable. The rutting response improvements produced by a membrane were greater at high deformation levels, which is consistent with the proposed performance influencing mechanism of alteration of the subgrade failure mode. The least effective interlayer was a one inch layer of sand. The most effective interlayer was Typar 3601 fabric, which produced slightly better rutting resistance than did Typar 3401 fabric. Mirafi 140 and Bidim C22 fabrics produced virtually identical rutting resistance, both products being less effective than either weight of Typar fabric. Effectiveness in reducing rutting appears dependent upon membrane strength and modulus characteristics, and friction/adhesion properties along the membrane/subgrade and membrane/aggregate interfaces, with high strength, modulus, and friction/adhesion characteristics being most desirable in improving system performance.

Rut Depth Prediction

Prediction of rutting response, with reasonable accuracy, is possible utilizing any of several models. Three models were studied, which utilize correlations between stress ratio, rut depth, and load cycles to fully estimate system response. These models are based upon exponential, parabolic, and hyperbolic curve-fit modeling of the relationship between load cycles and rut depth. The hyperbolic relationship provided greater predictive accuracy than the other two models

when applied to full-scale tests. On the basis of the application of these three models to full-scale tests, the proposed corrections of the model test data for instrumentation (i.e., model test load cycle data reduced by a factor of 2.4) and scaling (i.e., model test rut depth data increased by a factor of 1.7) appear valid. Successful application of these methods to the full-scale tests conducted by the U.S. Army Corps of Engineers also provides some validation of the model test program, where axisymmetric single point loading, with minimal recovery time between load cycles, was utilized to model an actual pavement system with its associated vehicle wander and varied recovery periods.

The U.S. Army Corps of Engineers method, and modifications thereto (43, 44, 99), provided accurate estimates of system response, but is the most limited of all the methods analyzed, in that only one response point (i.e., load cycles at a rut depth of three inches) is determined during a given test.

The model proposed by Giroud and Noiray (41) provided slightly more accurate estimates of rutting response for full-scale tests than all other methods studied, but has the disadvantage of being limited in application to rut depths in excess of three inches.

Three models were studied, which applied the hyperbolic plastic stress-strain law to a calculated stress state for prediction of rutting response. These models were the least accurate of all those analyzed. Within these three models, response calculations utilizing a stress state computed with the VESYS program (32, 48, 69) proved most accurate, with calculations utilizing a stress state determined with the University

of Illinois axisymmetric finite element program (110) being a bit less accurate, but more conservative. Response calculations utilizing a stress state computed on the basis of Boussinesq theory provided the least accurate overall response estimates within these models. Direct application of the hyperbolic plastic stress-strain law to sublayers of tensile or shear failure is not possible and presents a major problem in use and extension of this approach with the stress state solutions analyzed.

It appears that a combination of Methods 3 and 5 (i.e., hyperbolic curve-fit model of the load cycle-rut depth relationship, and the Giroud and Noiray predictive model respectively) might provide the most reasonable estimate of system rutting response. System response may be calculated with each method, then the more conservative (i.e., lower) value for the number of load cycles to reach a given rut depth utilized to generate a composite estimate of system response. This approach is depicted in Figures 8-1 and 8-2, as applied to the full-scale tests (Ref. Tables 7-8 and 7-12 for test data and separate rutting predictions).

Example Design Method Based on Study Results

For a given loading, if rut depth and load cycle failure criteria are established, design charts, similar to those presented in Chapter II, may be formulated. Such charts provide relationships between subgrade strength and required aggregate layer thickness. In preparing a chart, Methods 3 and 5 may both be utilized to determine the required aggregate layer thickness for the given conditions and criteria, then the more

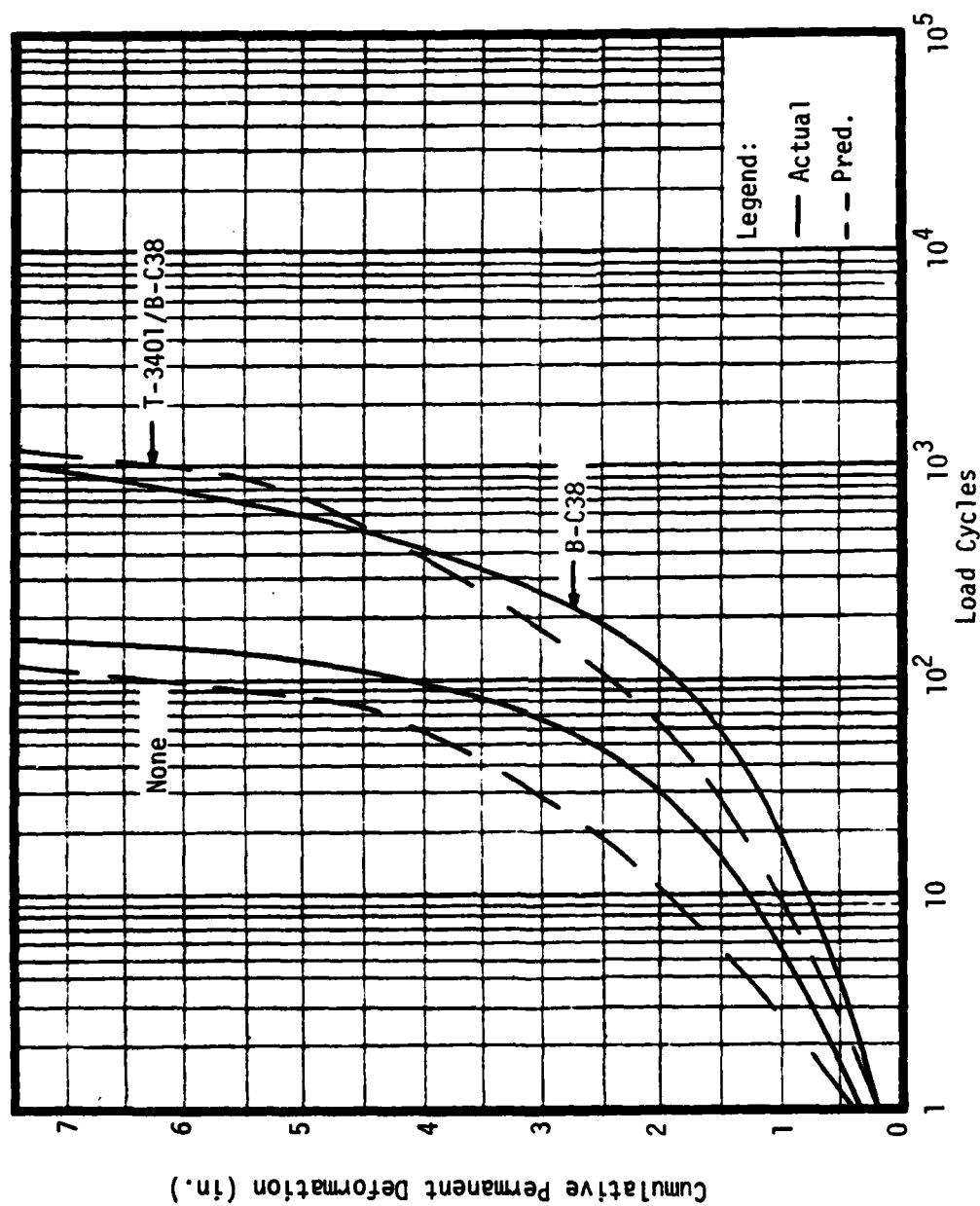


Figure 8-1. Comparison of Actual and Methods 3/5 Composite Predictions of Rutting Response for Full-Scale Field Tests (U.S. Army Corps of Engineers).

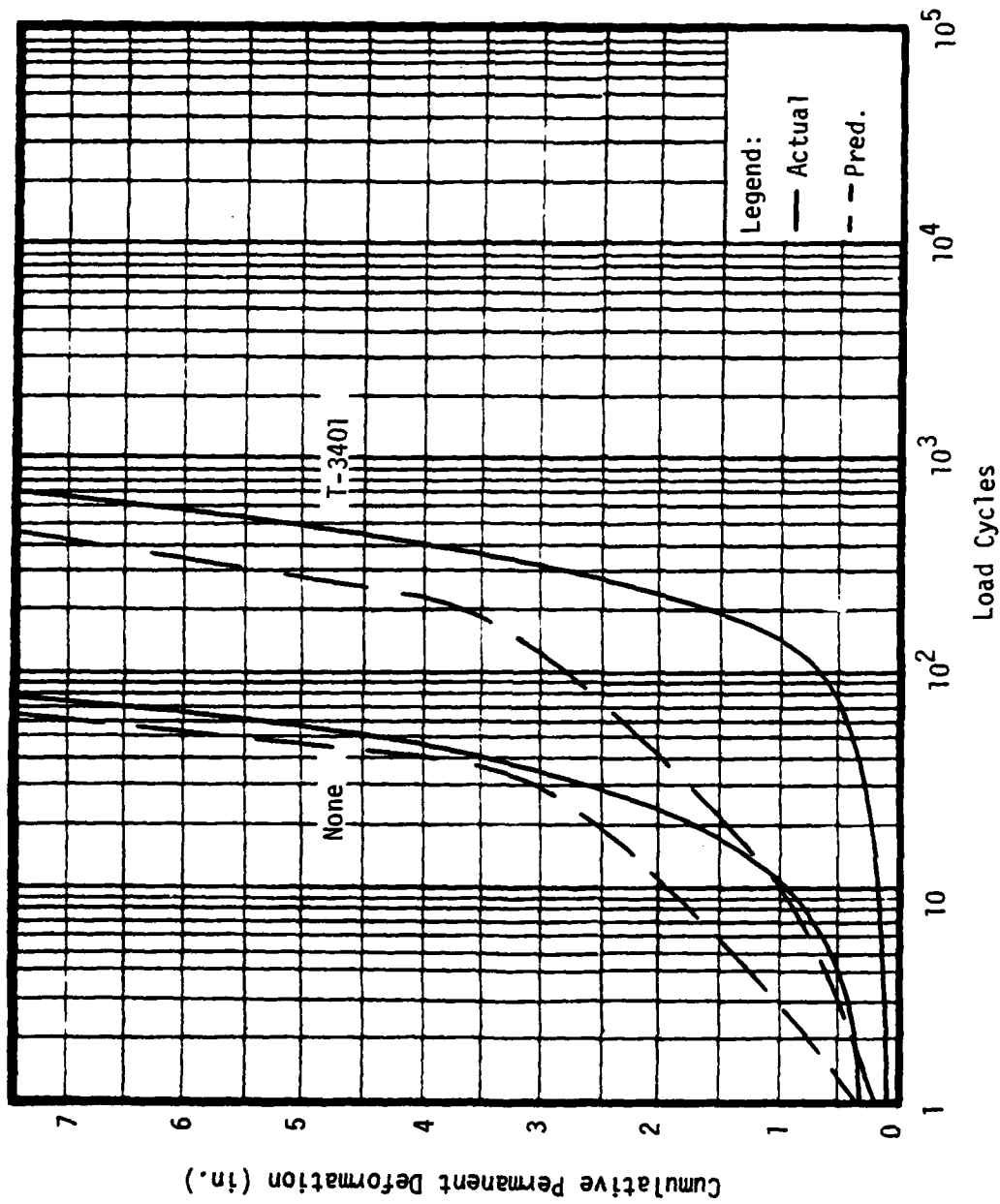


Figure 8-2. Comparison of Actual and Methods 3/5 Composite Predictions of Rutting Response for Full-Scale Model Tests (Georgia Institute of Technology).

conservative (i.e., greater) value depicted in the chart. An example of such a design chart is presented in Figure 8-3.

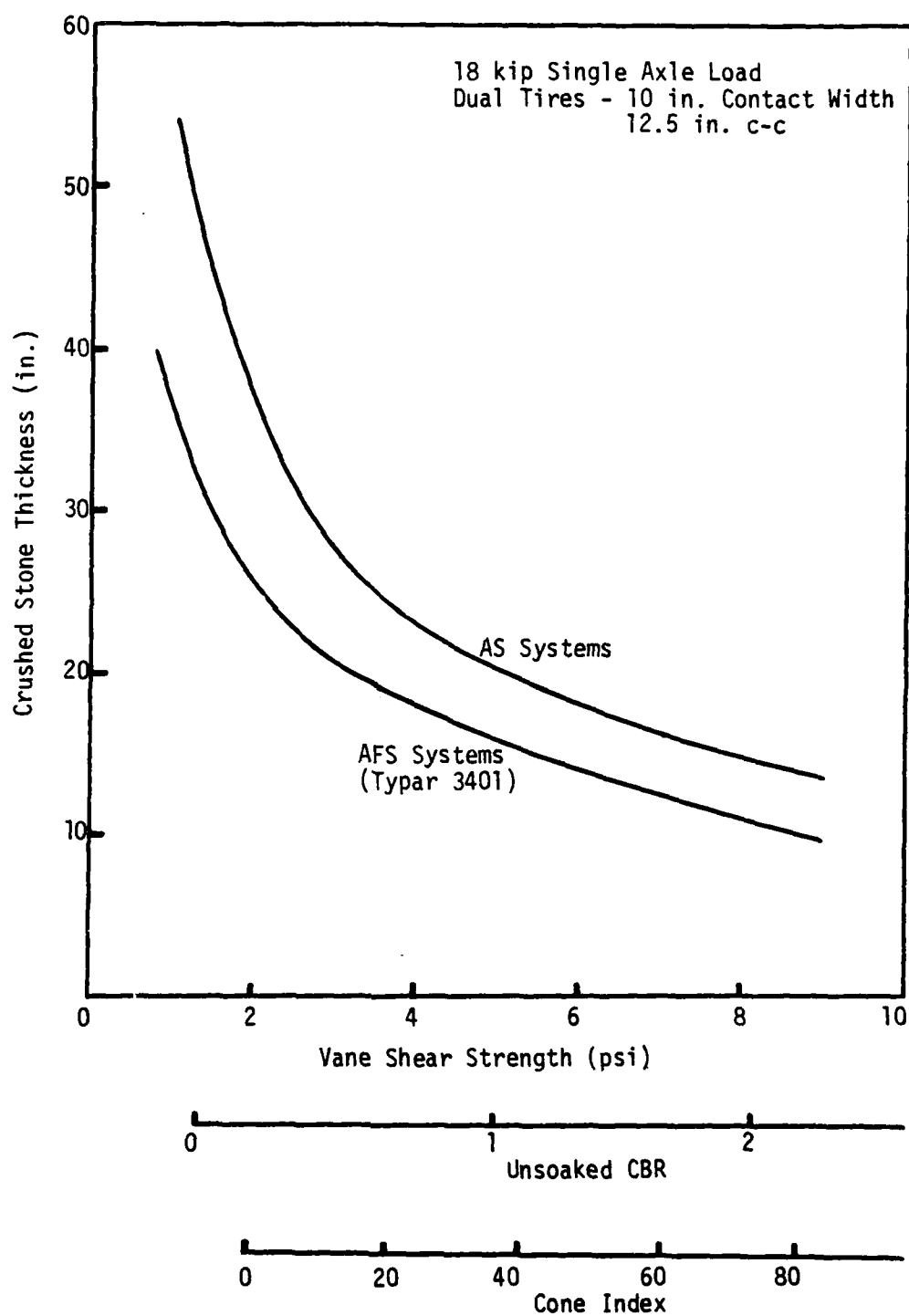


Figure 8-3. Design Chart for Methods 3/5 for 1000 Load Cycles and a 3 in. Rut.

AD-A110 434

AIR FORCE INST OF TECH WRIGHT-PATTERSON AFB OH
PERFORMANCE OF FABRIC REINFORCED AGGREGATE-SOIL SYSTEMS UNDER R--ETC(U)
DEC 81 W SCHAUZ
AFIT-CI-81-69D

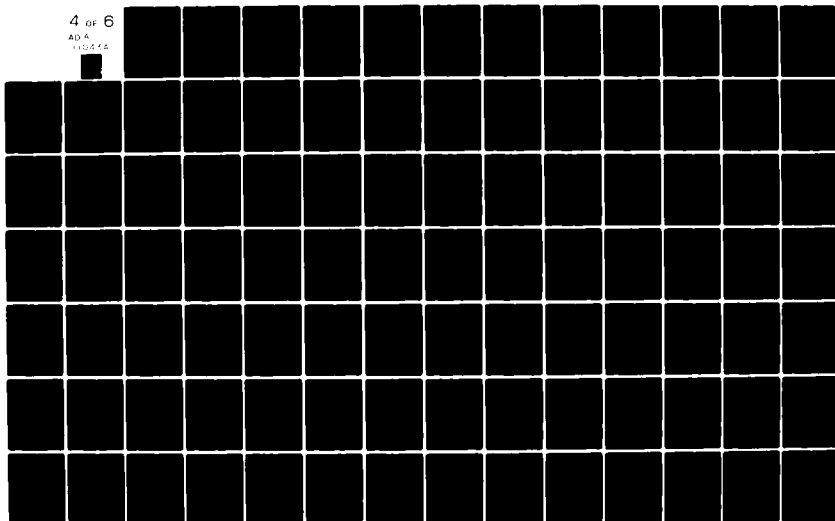
F/6 13/2

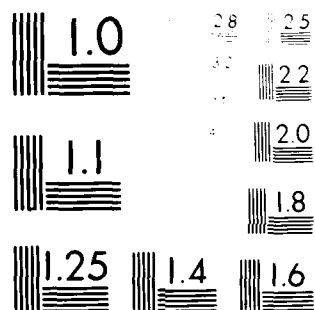
UNCLASSIFIED

NL

4 OF 6

AD-A
112544





MICROCOPY RESOLUTION TEST CHART
NBS 1010-A

CHAPTER IX

CONCLUSIONS

Based upon the results of the model test program, which experimentally examined the performance characteristics of AS and AFS systems subjected to repeated (i.e., transient) loading, the following conclusions can be made:

(1) Alteration of the failure mode within the subgrade soil is of the greatest significance of the proposed mechanisms by which a fabric influences the behavior of an AFS system.

(2) With subgrade strength as the independent variable, the rate of rutting decreases as subgrade strength increases. Improvements in system response are greatest at higher deformation levels, in AS systems as compared to the corresponding AFS systems, and/or when strength increases are made in weaker reference systems.

(3) With crushed stone layer thickness as the independent variable, the rate of rutting decreases as aggregate thickness increases. Improvements in system response are greatest at higher deformation levels, being comparable in corresponding AS and AFS systems.

(4) With load pulse duration as the independent variable, the rate of rutting decreases as the pulse duration decreases. Improvements in system response are greater in AS systems, than in the corresponding AFS systems.

(5) Inclusion of a membrane at the subgrade-aggregate interface

improves rutting resistance as compared to the corresponding AS system. Improvements in system response are greatest at higher deformation levels.

(6) Effectiveness in reducing rutting is enhanced by fabrics with high strength, high modulus, and high friction/adhesion characteristics.

(7) A membrane inclusion alters the states of stress and plastic strain as compared to those in the corresponding AS system. Subgrade stresses in deformed AFS systems are lower than those in the corresponding AS systems, while total plastic deformations, at identical points in the loading histories, are also considerably less in the AFS systems. Variations are most noticeable in high deformation systems.

(8) The aggregate layer in both AS and AFS systems undergoes considerable deformation, contrary to the analysis models of Kinney (56) or Giroud and Noiray (41).

(9) The in-plane permanent strains exhibited by the Typar 3401 fabric inclusions are greatest in a zone between the load centerline and an offset of one radius, decreasing with further offset. This deformation pattern is contrary to the analysis models of Kinney (56) or Giroud and Noiray (41), which assume constant strain throughout the fabric.

(10) Rutting response may be modeled with reasonable accuracy by use of a hyperbolic relationship between stress ratio, rut depth, and load cycles, in conjunction with the analysis model of Giroud and Noiray (41).

CHAPTER X

RECOMMENDATIONS FOR FURTHER STUDY

The experimental investigation on the behavior of AS and AFS systems under repeated loading, performed in this study, has indicated the need for additional investigation in the following areas:

(1) Model tests of both AS and Typar 3401 reinforced AFS systems, without subsurface instrumentation (i.e., strain sensors and pressure cells), should be conducted within the same range of subgrade strengths and stress ratios utilized in this study. Comparison of the rutting response results from these tests and response predictions from Methods 1-5 would permit verification/modification of the correlations presented in Methods 1-3, and of the factors proposed for use to account for instrumentation and scaling.

(2) Prediction of rutting response should be attempted utilizing the improved FEM programs described by Raad and Figueroa (78) and Zeevaert (123). It is expected that these models will provide much more accurate stress state estimates than those of the VESYS and earlier FEM programs. The stress states of these improved programs would eliminate the zone of aggregate tensile failure predicted by the earlier models, avoiding a major problem encountered in this study with application of the hyperbolic plastic stress-strain law in response prediction Methods 6 and 7. Additionally, the large displacement option of the FEM program described by Zeevaert (123) requires analysis in regard

to the direct estimation of rut depth.

(3) Full-scale tests of both AS and Typar 3401 reinforced AFS systems should be conducted. These tests should be conducted within the range of subgrade strengths and stress ratios utilized in this study. Analysis of these tests would aid in the verification/refinement of the response prediction models.

(4) Instrumented tests of both AS and AFS systems should be conducted to add to the fundamental understanding of the exact mechanisms influencing system response.

(5) A test program of AFS systems should be conducted, utilizing a variety of geotextiles, to determine the importance of various fabric properties (i.e., strength, modulus, friction/adhesion, and creep/stress relaxation) in influencing system response.

APPENDIX A

REPEATED LOAD TRIAXIAL TEST SAMPLE PREPARATION,
EQUIPMENT, INSTRUMENTATION AND PROCEDURES

Repeated load triaxial tests were conducted on laboratory compacted specimens of both the crushed stone and subgrade soil to enable characterization of their responses to dynamic loadings.

Sample PreparationCrushed Stone

Cylindrical samples six inches in diameter and 12 inches high were prepared directly on the base of the triaxial cell. One end of a cylindrical rubber membrane was secured to the bottom load platen of the triaxial cell. A steel mold, split into three equal segments, was then clamped over the bottom load platen and the membrane drawn up through the mold, doubled over the upper edge and fastened thereto. The membrane was drawn taut against the inside wall of the mold, by applying a vacuum to the interface through a hole in the wall of the mold. The correct amount of material for each sample was weighed out prior to sample preparation. All samples were prepared to a dry density of 132.1 pcf, which corresponded to 95 percent of the maximum dry density determined by Method C of ASTM D-698 and was the anticipated average density of the crushed stone layers during the model testing program. The material was compacted in the mold in six layers, each approximately two inches thick. Each lift was first tamped manually, making four to five

coverages with a steel plate, two inches in diameter, attached to a rod, two feet in length, serving as a handle. An eight pound steel plate, six inches in diameter, was then placed on the lift surface and vibrated for two to three seconds with a Model 25P electric hammer, manufactured by Pow-R-Tron, Inc., Home, Pennsylvania, to complete compaction of the lift. With all lifts in place, the top cap was placed on the sample and the rubber membrane undoubled from the mold and attached to this cap. A vacuum was drawn on the sample through the cell port connected to the base porous stone. The split mold was removed from the sample, which was then encased in a second rubber membrane. The use of a second membrane was found to be necessary to compensate for any holes created in the inner membrane during sample compaction and/or testing. The triaxial cell was assembled and secured about the sample and then centered under the reaction beam of the test frame. Confining pressure was applied to the sample and the vacuum removed, in preparation for specimen testing.

Subgrade Soil

Cylindrical samples 2.8 inches in diameter and 5.6 inches in height were prepared in a two segment split mold. The mold was equipped with a one inch extension collar. The material was mixed with water in a Type PC Lancaster Counter Current Batch Mixer. Placed in five layers, each lift of material was compacted by 12 blows from a hammer weighing four pounds, falling through a drop of 12 inches. The total compactive effort per unit volume of soil was equivalent to 97 percent of that of Method A of ASTM D-698. Sufficient material was compacted to fill the mold and extension collar to within 0.5 inch of their total combined

height. A single penetration resistance (ASTM D-1558) determination was made on each sample. The penetration resistance was used to estimate the soil strength utilizing the strength-density-moisture correlations developed from tests on compacted laboratory specimens of the same soil, as described in Chapter III. Three subgrade strength ranges were tested, corresponding to those used in the model testing program. The extension collar was removed from the mold and the sample trimmed to final height. The sample was removed from the mold by carefully sliding each mold segment along the side of the sample until detached. This process was facilitated by coating the mold interior with a silicon lubricant prior to sample preparation. The sample was encased in a rubber membrane utilizing a vacuum pump activated membrane stretcher. The sample was next placed on the triaxial cell bottom load platen, the top load cap positioned, and the membrane affixed to the cell base and top cap. The triaxial cell was assembled and secured about the sample and then centered under the reaction beam of the test frame. Confining pressure was applied to the specimen in preparation for testing.

Loading Equipment

Load was transferred to the sample through the triaxial cell piston, which was itself loaded by a pneumatic system. The pneumatic system applied load to the cell piston through a diaphragm air cylinder, manufactured by the Bellofram Products Co., Burlington, Massachusetts. The crushed stone was loaded through a Type S Size 30 unit, while the subgrade soil was loaded by a Type D Size 4 unit. The Bellofram units were bolted to steel section reaction beams, with the triaxial cells

centered, upon a fixed level surface, under the appropriate unit. For each system, a 15 gallon steel tank was used as a surge to minimize pressure fluctuations of the air delivered to the Bellofram unit. The frequency and duration of the air flow from the tank to the Bellofram unit was controlled by a main valve, driven by two Model 225-111C solenoid valves, all manufactured by Mac, Wixom, Michigan. Tank and pilot valve pressures were controlled by Conoflow pressure regulators and monitored by Ashcroft pressure gages. The pilot valves were activated by a micro-switch cam device operated by a Model 2T60-18 variable speed reversible motor, manufactured by the Gerald K. Heller Co., Las Vegas, Nevada. The number of load pulses was monitored by a Model PCC 6 counter, produced by Eagle Signal, Davenport, Iowa. The systems were identical in plan to that utilized during the model testing program. The schematics of the pneumatic and electrical-mechanical portions of that system, presented in Chapter IV (Figures 4-2 and 4-3, respectively), also apply to the systems utilized for the repeated load triaxial testing. A 2.5 kip capacity Strainert universal flat load cell was statically calibrated in a 20 kip capacity screw-type Tinius-Olsen loading machine. Load cell output was monitored, to an appropriate scale, on a Model 60-1300 Twin-Viso Strip Chart Recorder. This recorder is manufactured by the Sanborn Company, Cambridge, Massachusetts, and is equipped with a Model 60-1600 control panel, Model 64-500A strain gage amplifier and Model 64-300A D.C. amplifier. The load cell and recorder were then used to calibrate the dynamic loading systems. The magnitude, frequency, and duration of the applied load vary with surge tank and pilot valve pressures, the volume of air entering the Bellofram unit

(i.e., a function of piston position), the operating speed of the motor, and the size of the cam utilized to trip the micro-switch. To reduce the variables involved during calibration, pilot valve pressure was set at 60 psi, any fluctuation in the volume of air entering the Bellofram unit was minimized by maintaining the piston position to within ± 0.5 inch of a selected reference point by inserting spacers between the triaxial cell and Bellofram unit pistons, and by utilizing loading durations and frequencies corresponding to those chosen for the model testing program, as presented in Chapter IV (Figure 4-4). The calibration procedure had only to consider tank pressure as a variable for each Bellofram size and loading pattern.

Instrumentation

Total, permanent and resilient axial deformations of the samples were monitored by means of L.V.D.T.'s, all manufactured by the G. L. Collins Corp., Long Beach, California. Power was provided by a 24 volt D.C. output source. A horizontal plexiglas plate was affixed to the piston of each triaxial cell by a pair of setscrews. The cores of the L.V.D.T.'s were positioned vertically, with the tips resting on leveling screws located on the plates. The transducers were supported from the reaction frame by a clamp and rod arrangement. For the crushed stone, two Model SS203 units were utilized, while three Model SS205 units were used with the subgrade soil. These L.V.D.T.'s have linear ranges of ± 0.125 inch and ± 0.625 inch respectively. In each case, the electrical signals from the transducers were added together and the combined output recorded on a Sanborn Twin-Viso Strip Chart Recorder. The transducer-recorder systems were calibrated by simultaneously displacing

the electrically linked transducers through a range of known displacements, monitored by a micrometer with 0.001 inch divisions, while recording output to an appropriate scale.

Test Procedure

With the triaxial cell positioned beneath the Bellofram unit and sample confining pressure raised to the desired level, the transducers were properly positioned. The variable speed motor was set at the correct speed, in order to provide the desired load frequency and duration, and pilot valve and surge tank pressures raised to the appropriate levels. Loading of the sample was then begun. Elastic and plastic deformation readings were taken continuously for the first ten load repetitions and at appropriate load cycle intervals thereafter. Testing was carried to a maximum of 10^4 load cycles or a minimum strain of 20 percent, whichever occurred first. At the conclusion of testing, the samples of subgrade soil were weighed and moisture contents determined in accordance with ASTM D-2216. Data were analyzed by the procedures discussed in Chapter II, with pertinent results summarized in Chapter III (Tables 3-3 to 3-6). Additional data and typical plots of the relationships between plastic strain, stress state and resilient modulus are provided in Appendix B.

APPENDIX B

MATERIAL PROPERTIES DATA

Moisture-density relationships were determined for both the crushed stone and subgrade soil. For the latter material, a variety of strength tests were conducted on the compacted specimens. Testing equipment, instrumentation, and methodology are fully discussed in Chapter III, accompanied by a summary of pertinent test results (Table 3-1). Additional data are presented herein.

Repeated load triaxial tests were conducted on laboratory compacted specimens of the crushed stone and subgrade soil. Sample preparation and testing equipment, instrumentation and procedures are described in Appendix A. Pertinent test results are presented in Chapter III (Tables 3-3 through 3-6). Additional data are presented herein, accompanied by typical plots of the plastic strain-stress state and stress state-resilient modulus relationships for each material.

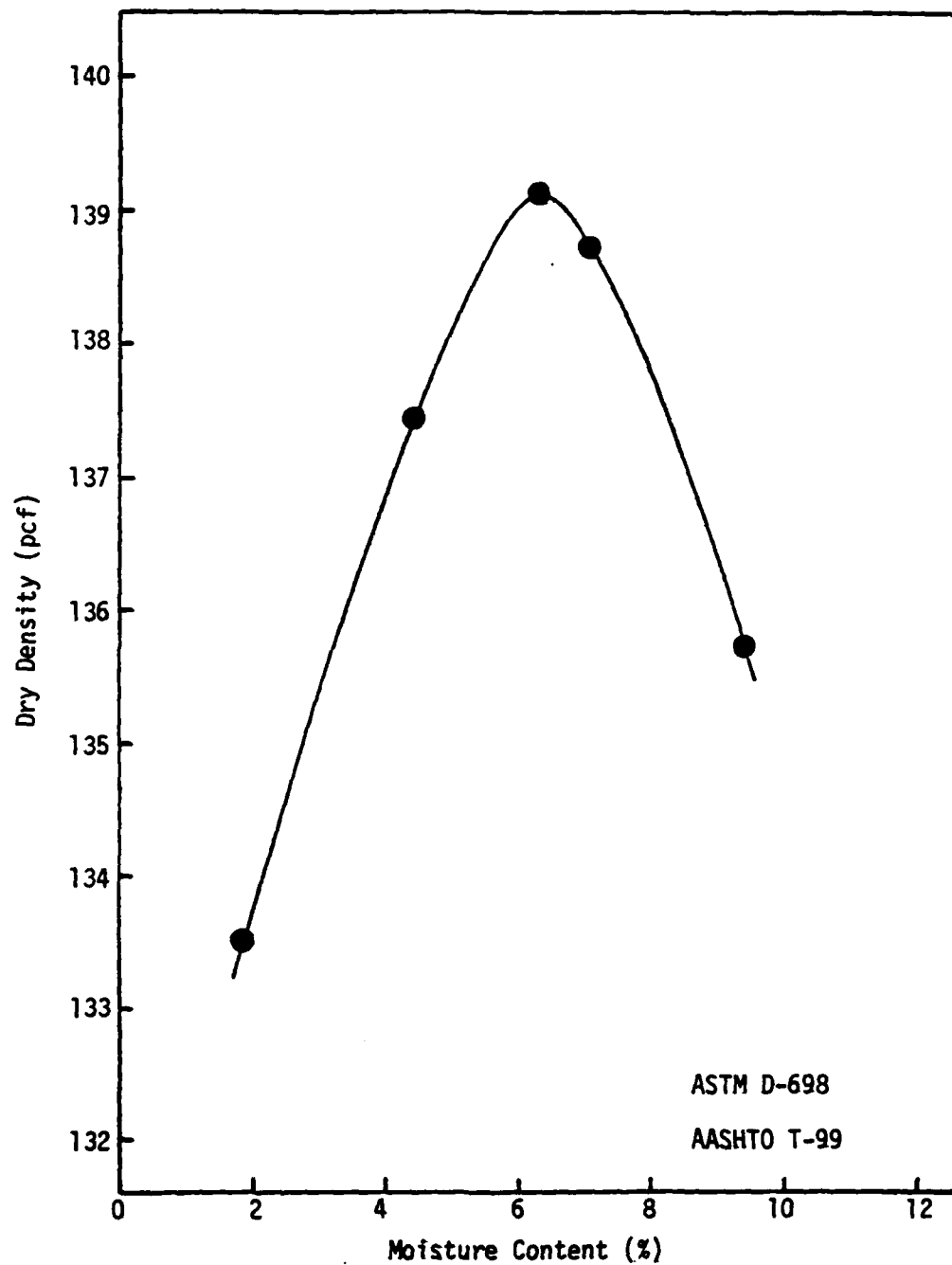


Figure B-1. Crushed Stone Compaction Moisture-Density Relationship.

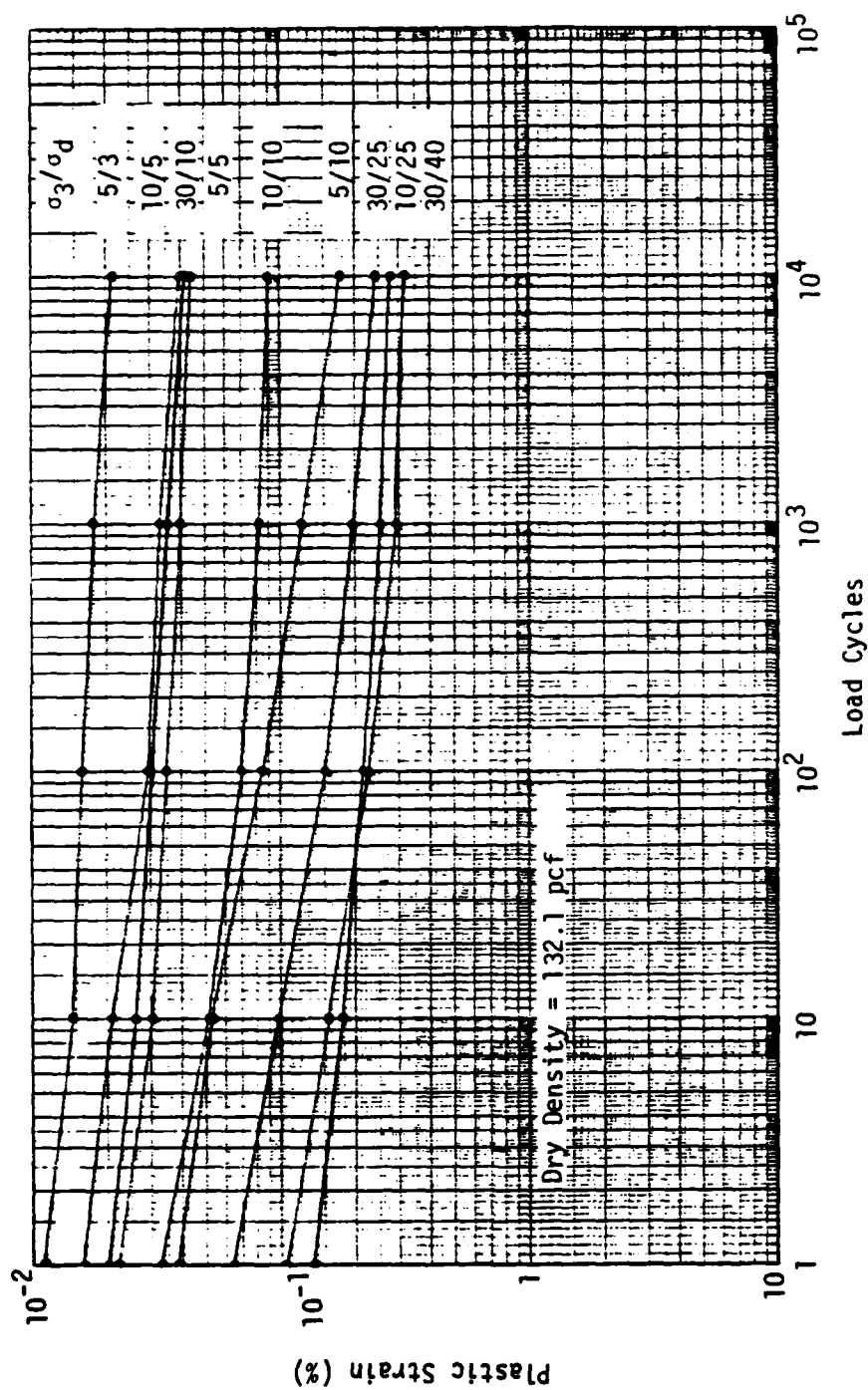


Figure B-2. Load Cycle-Plastic Strain Relationships for Crushed Stone, Type A Loading.

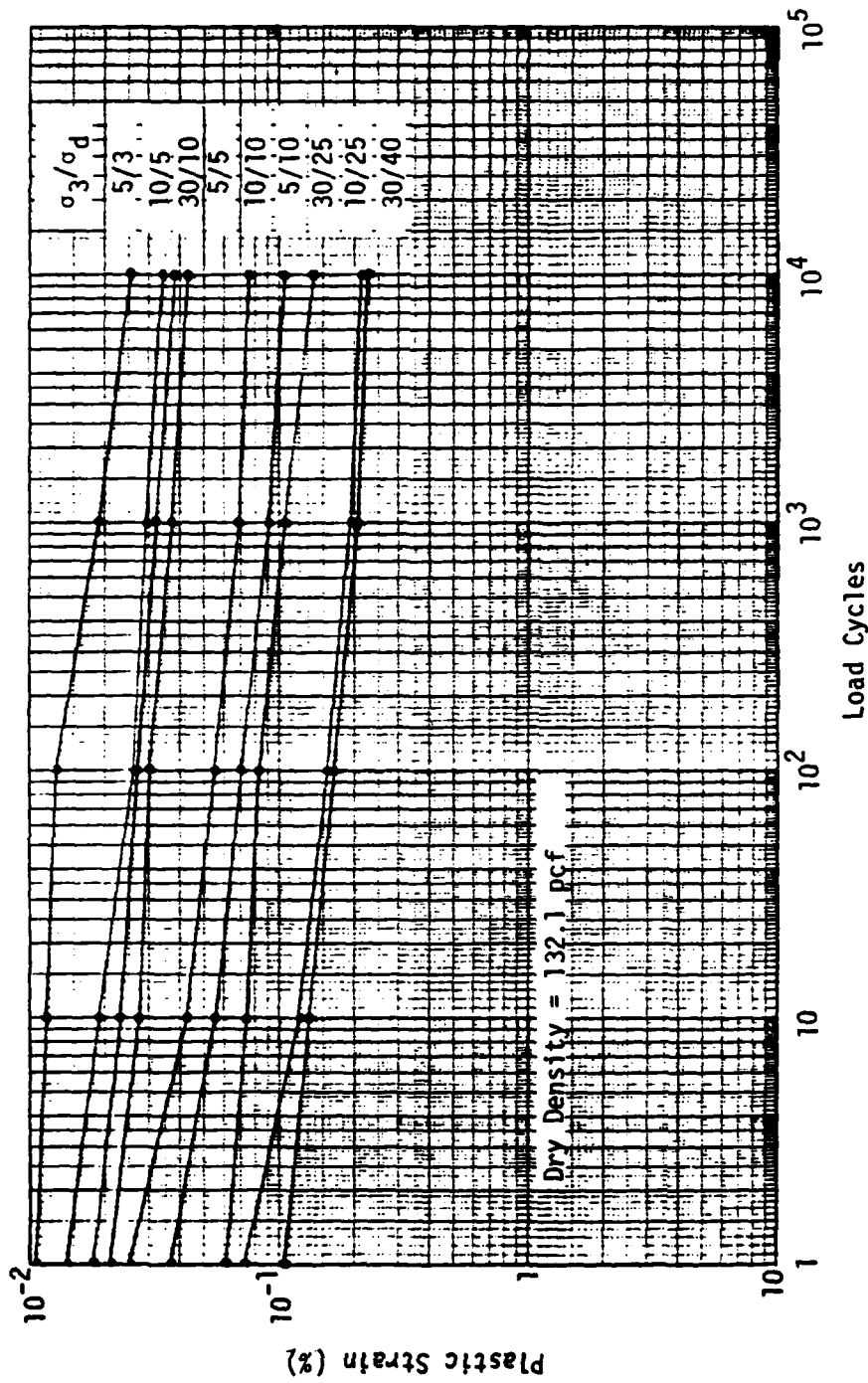


Figure B-3. Load Cycle-Plastic Strain Relationships for Crushed Stone, Type B Loading.

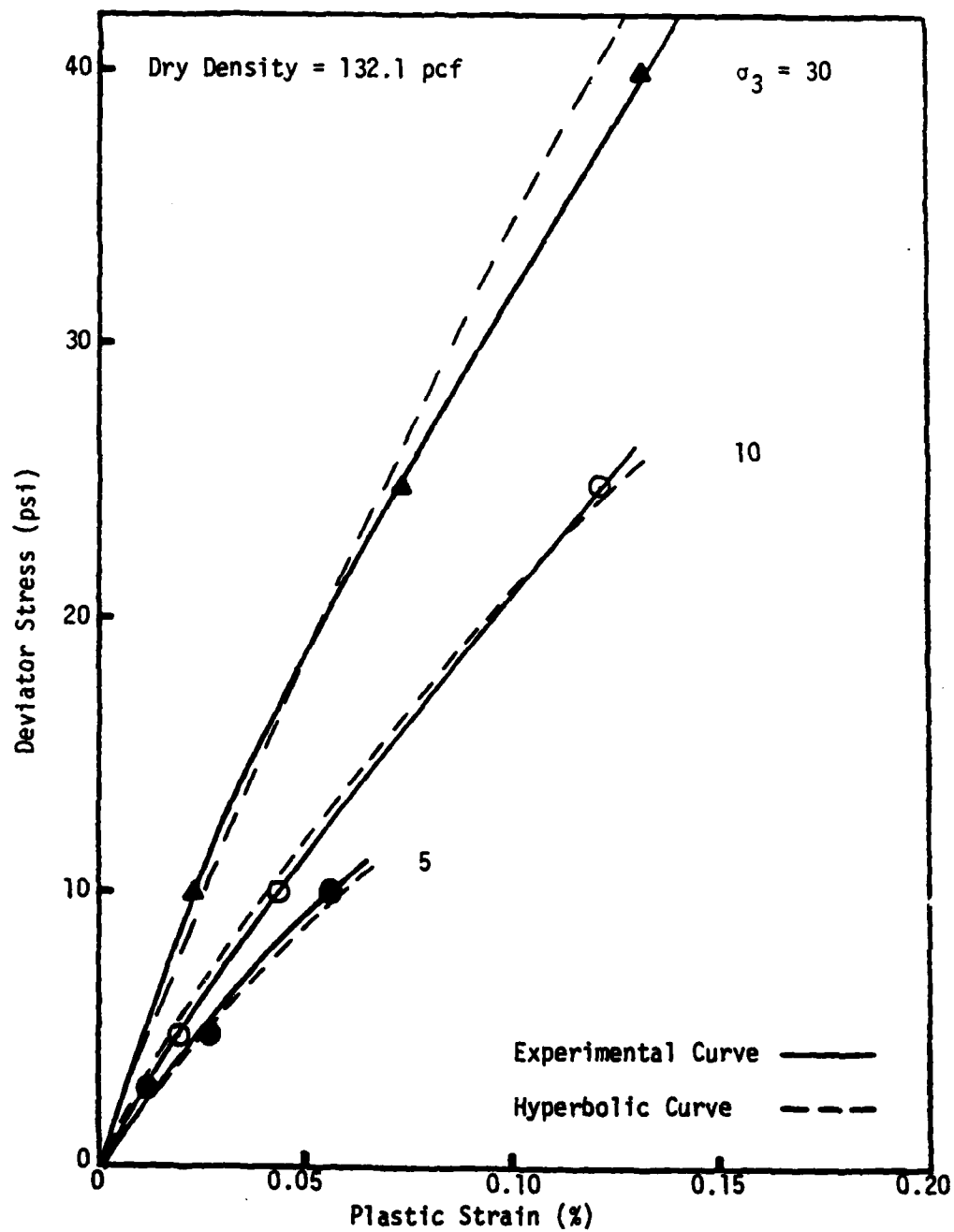


Figure B-4. Plastic Strain-Stress State Relationships for Crushed Stone at 10 Load Cycles, Type B Loading.

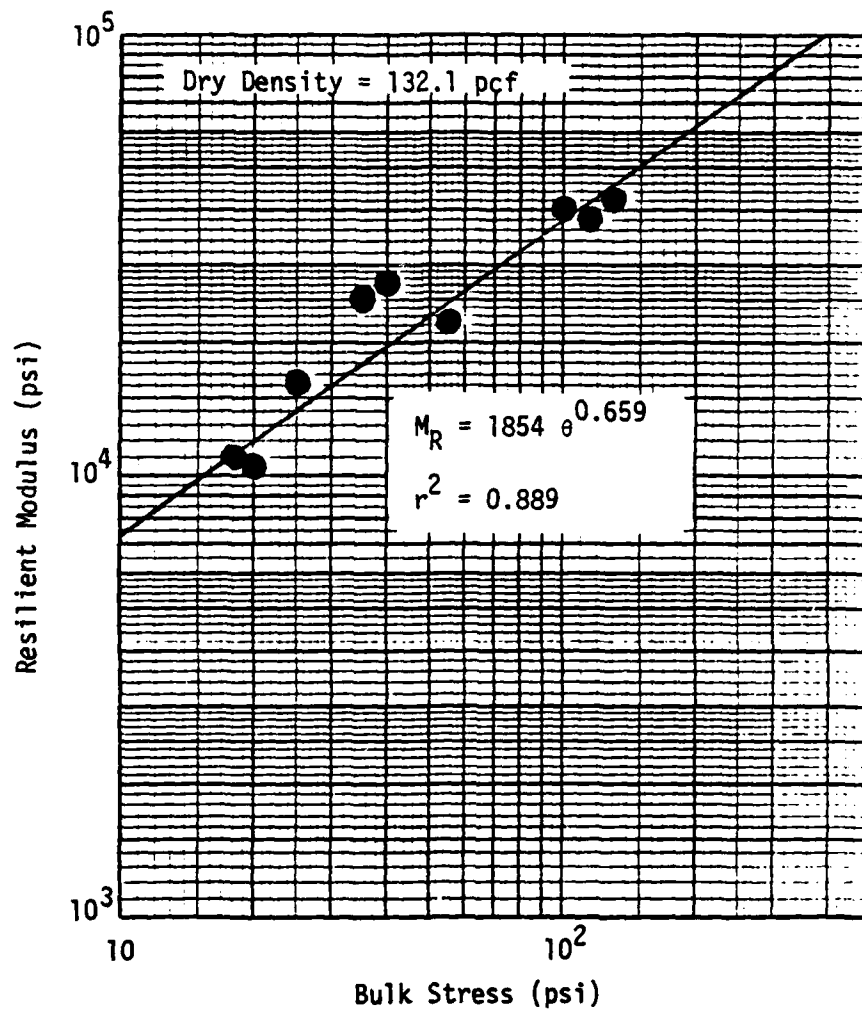


Figure B-5. Bulk Stress-Resilient Modulus Relationship for Crushed Stone at 10 Load Cycles, Type B Loading.

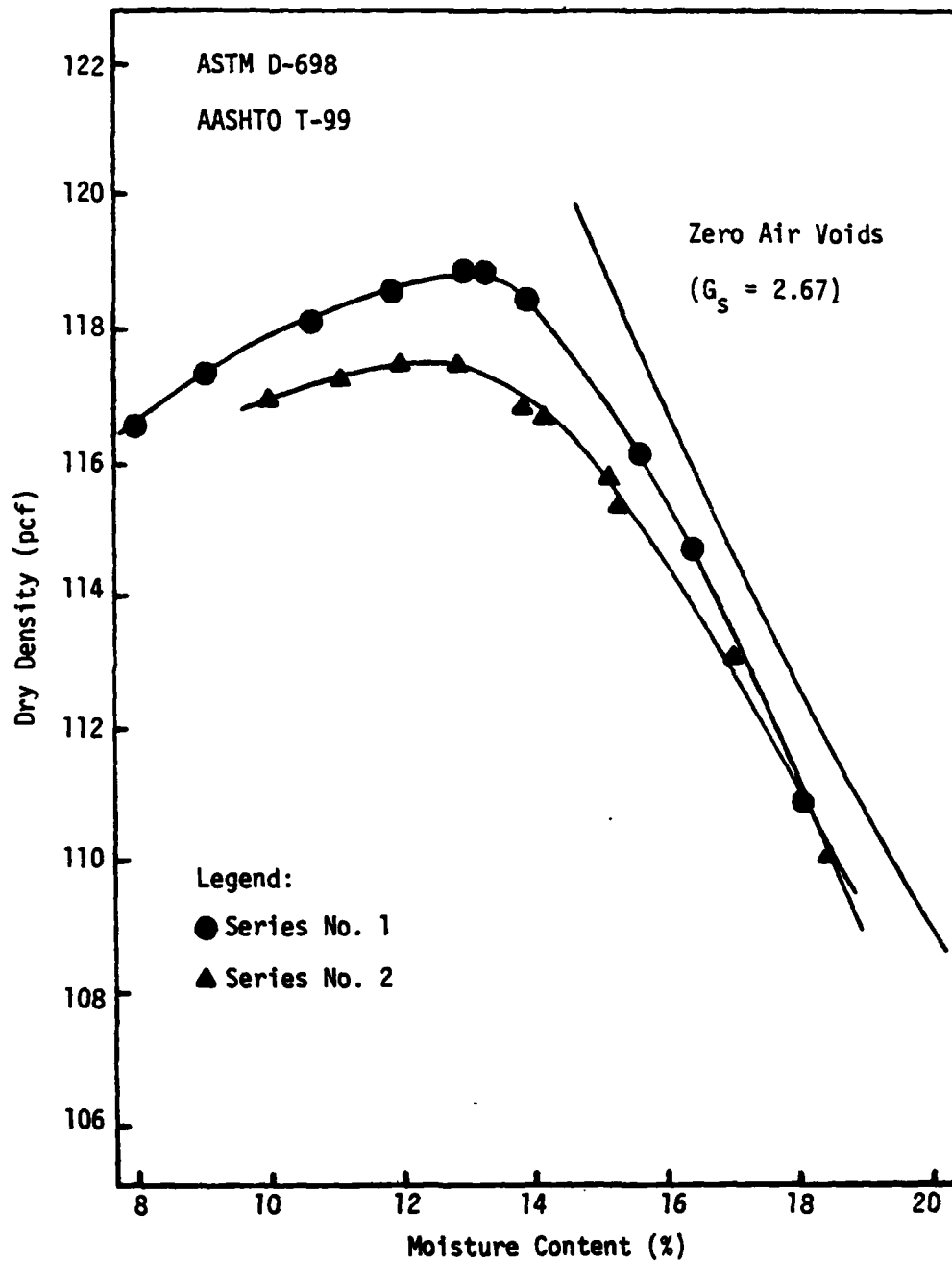


Figure B-6. Subgrade Soil Compaction Moisture-Density Relationship.

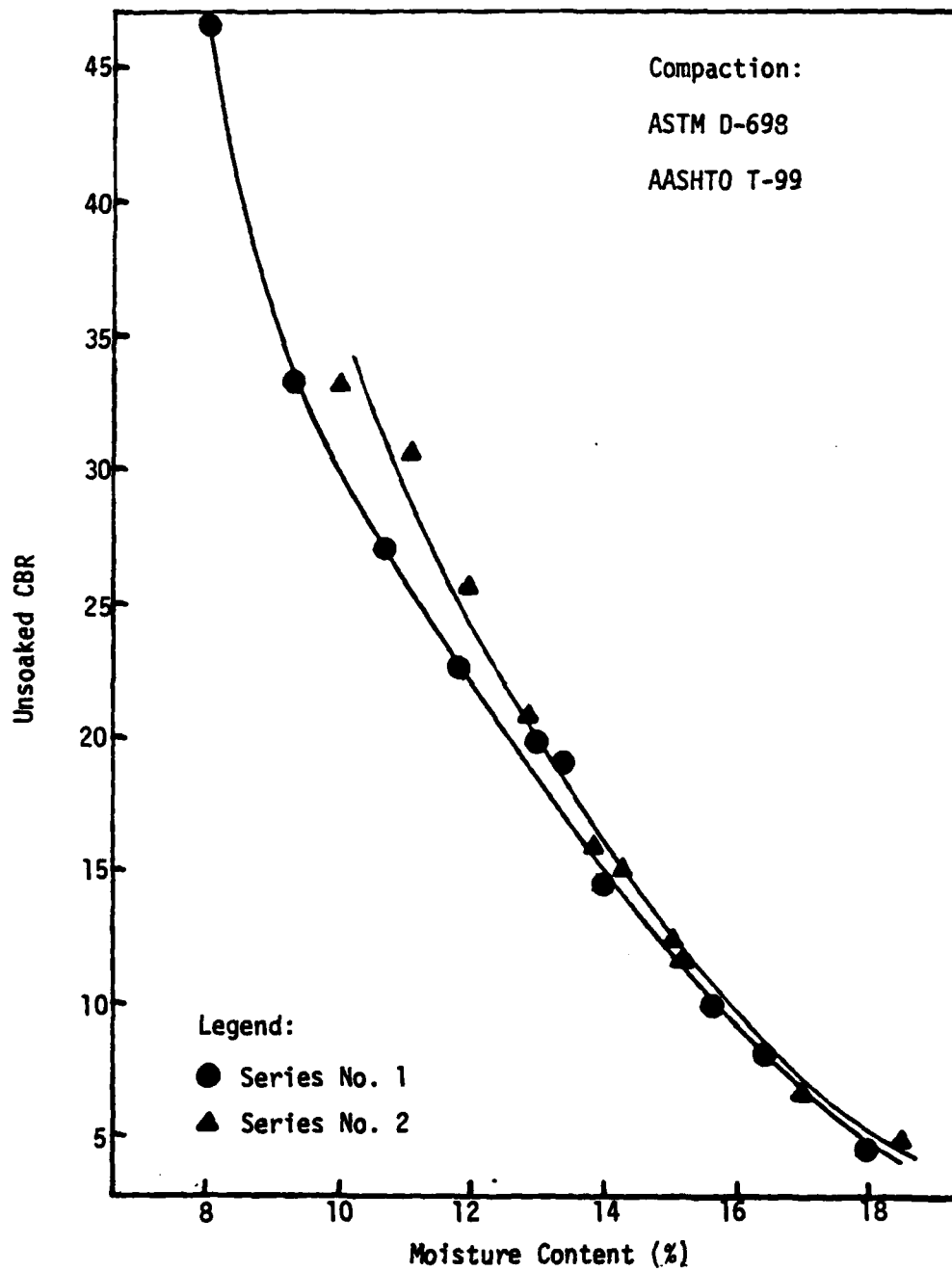


Figure B-7. Subgrade Soil Compaction Moisture-Unsoaked CBR Relationship.

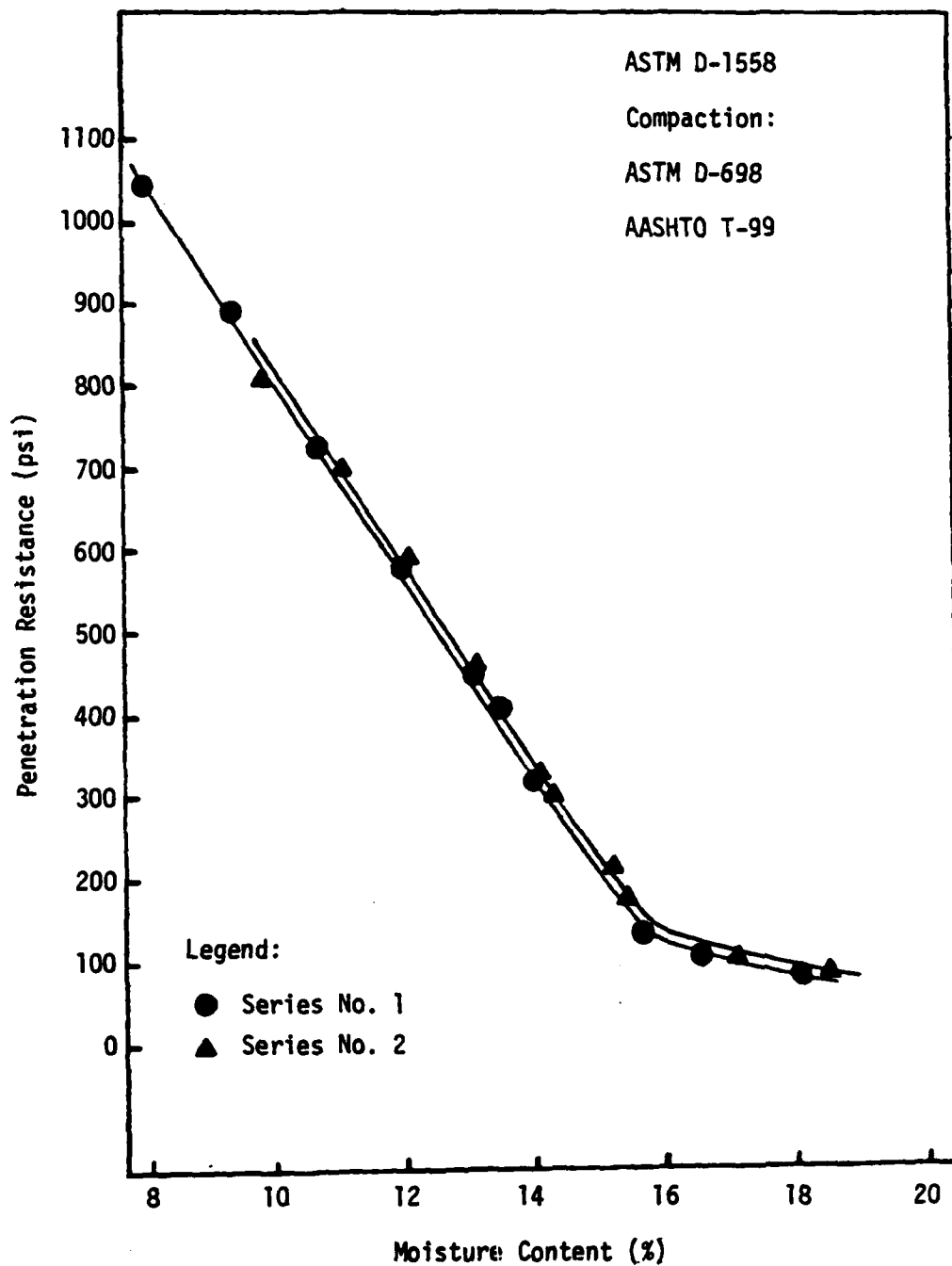


Figure B-8. Subgrade Soil Compaction Moisture-Penetration Resistance Relationship.

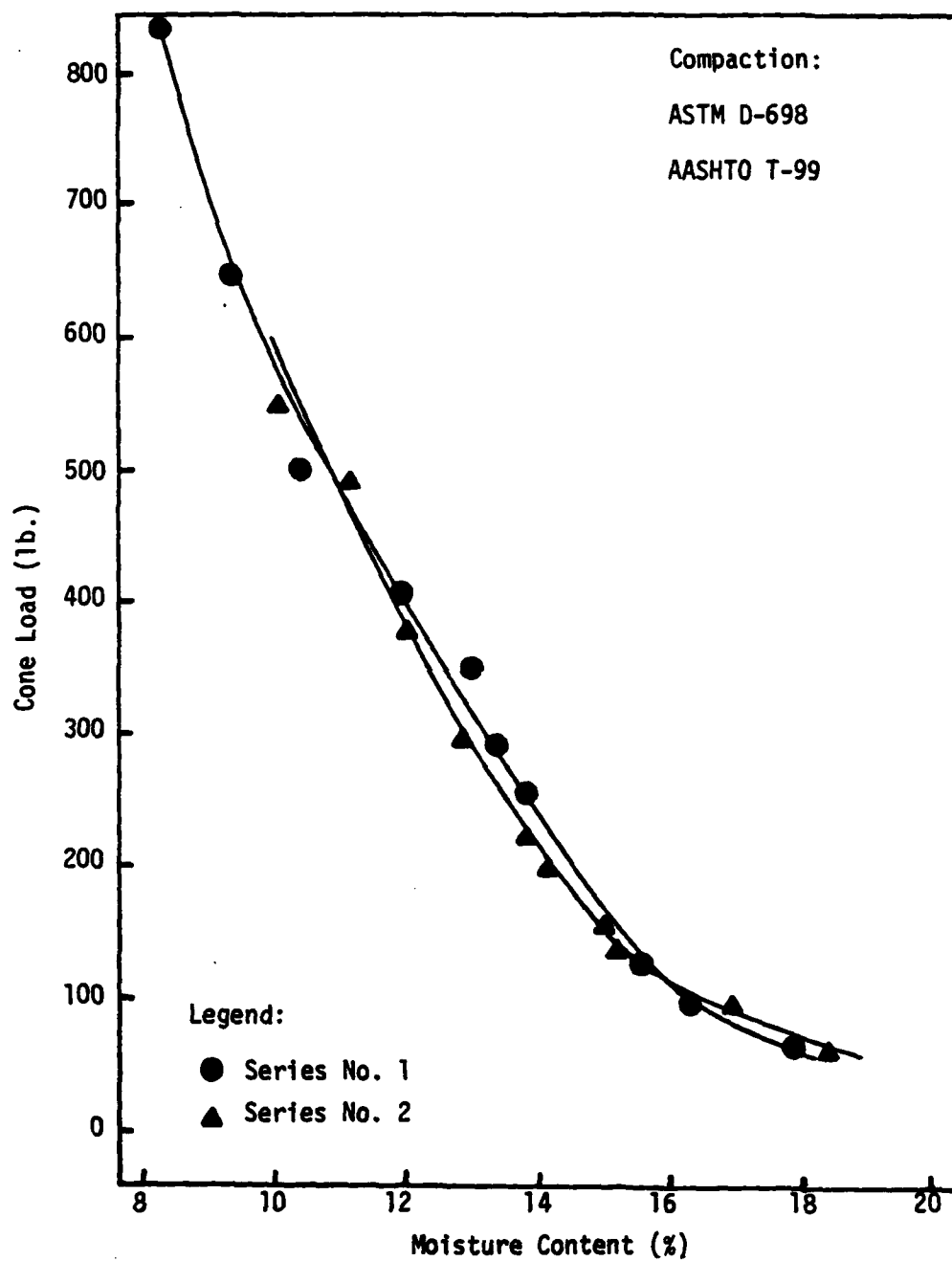


Figure B-9. Subgrade Soil Compaction Moisture-Cone Load Relationship.

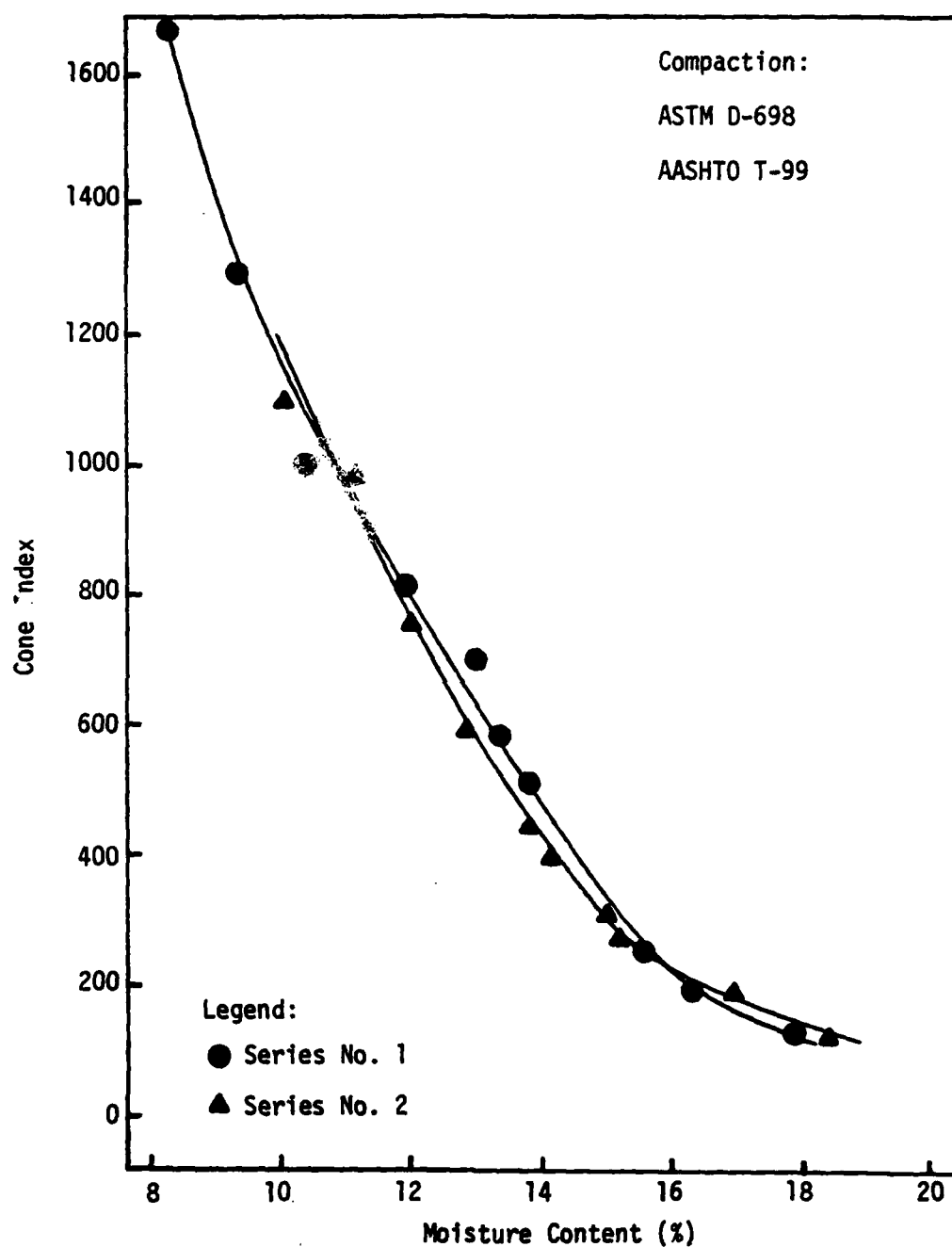


Figure B-10. Subgrade Soil Compaction Moisture-Cone Index Relationship.

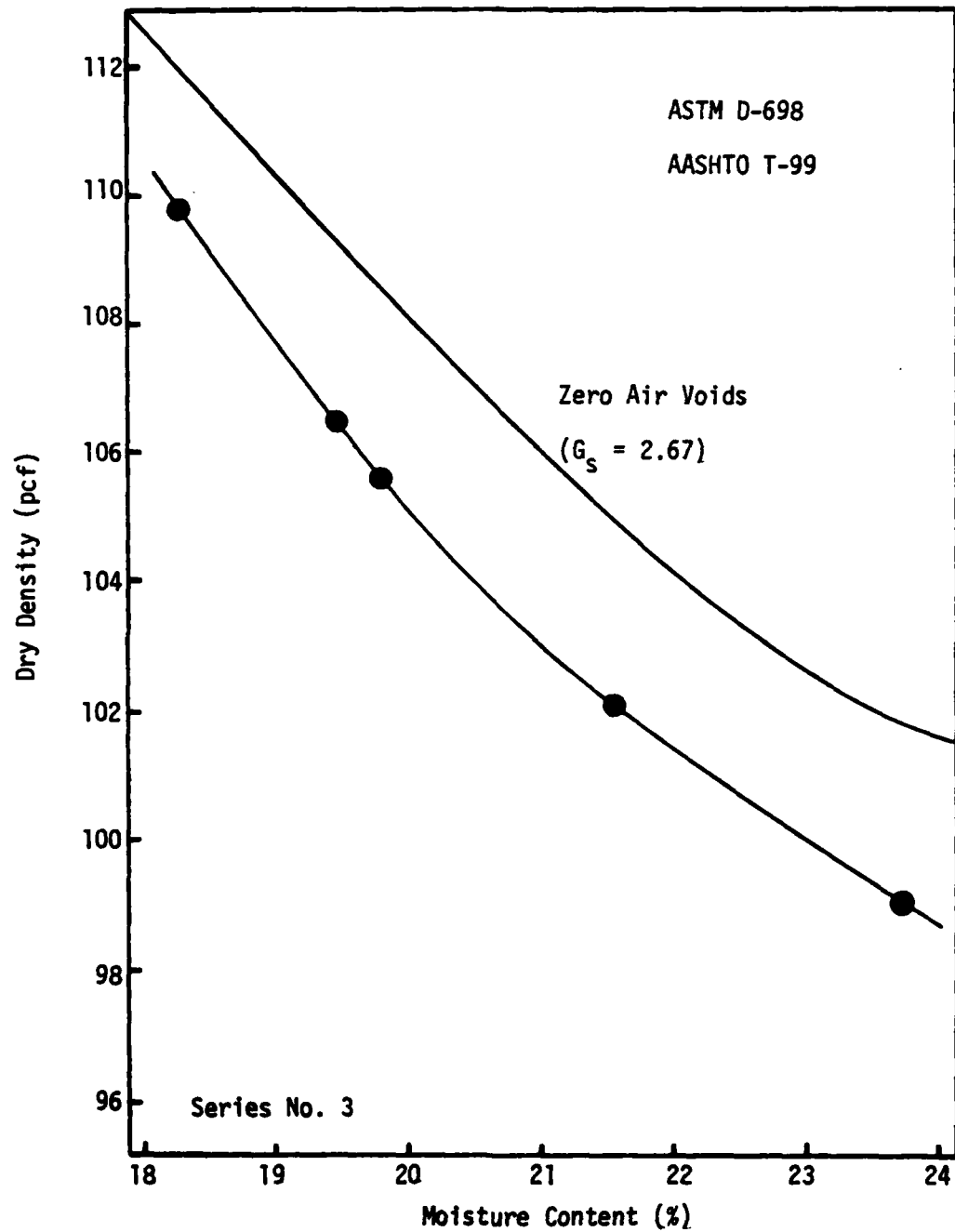


Figure B-11. Subgrade Soil Compaction Moisture-Density Relationship.

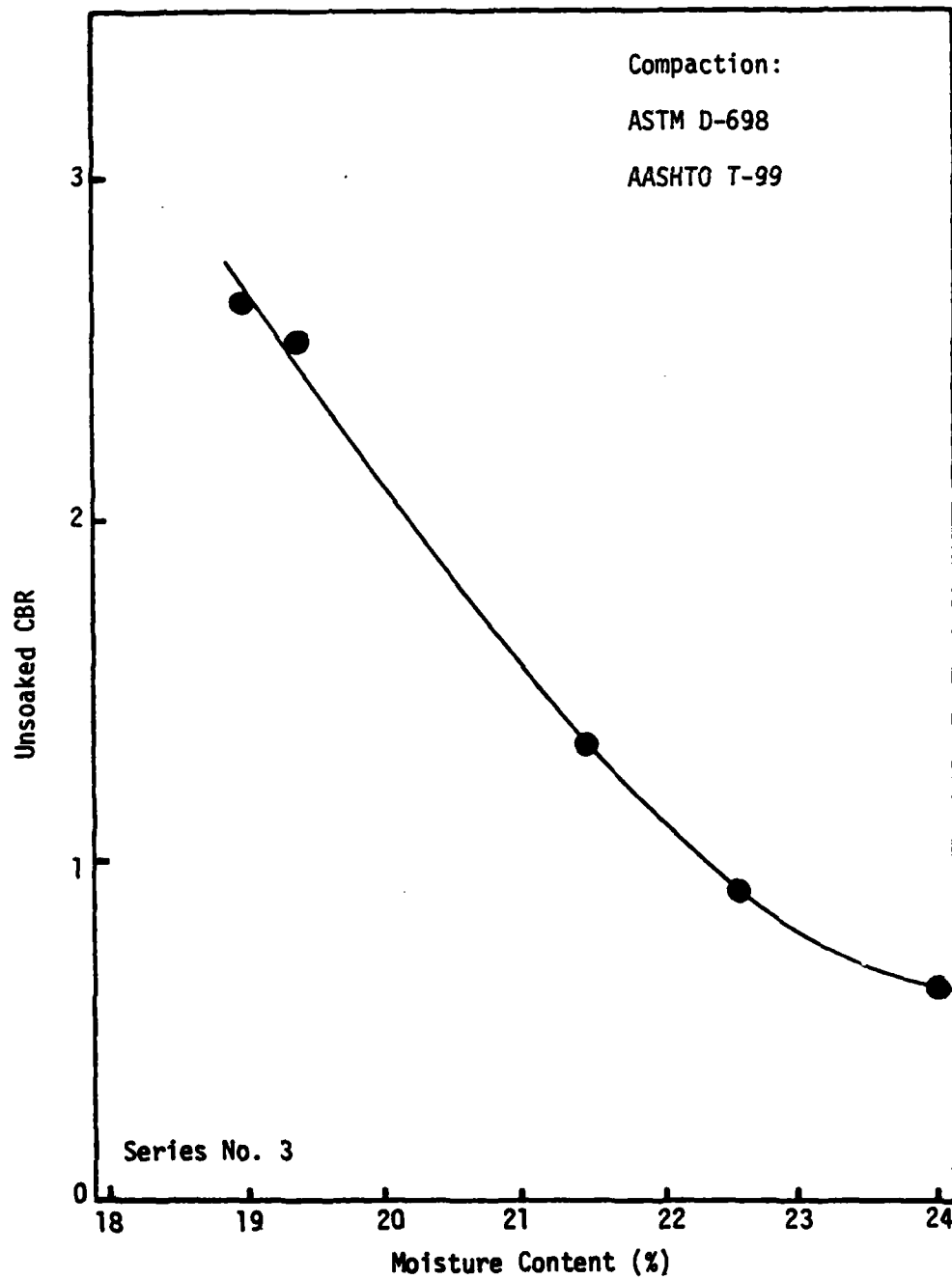


Figure B-12. Subgrade Soil Compaction Moisture-Unsoaked CBR Relationship.

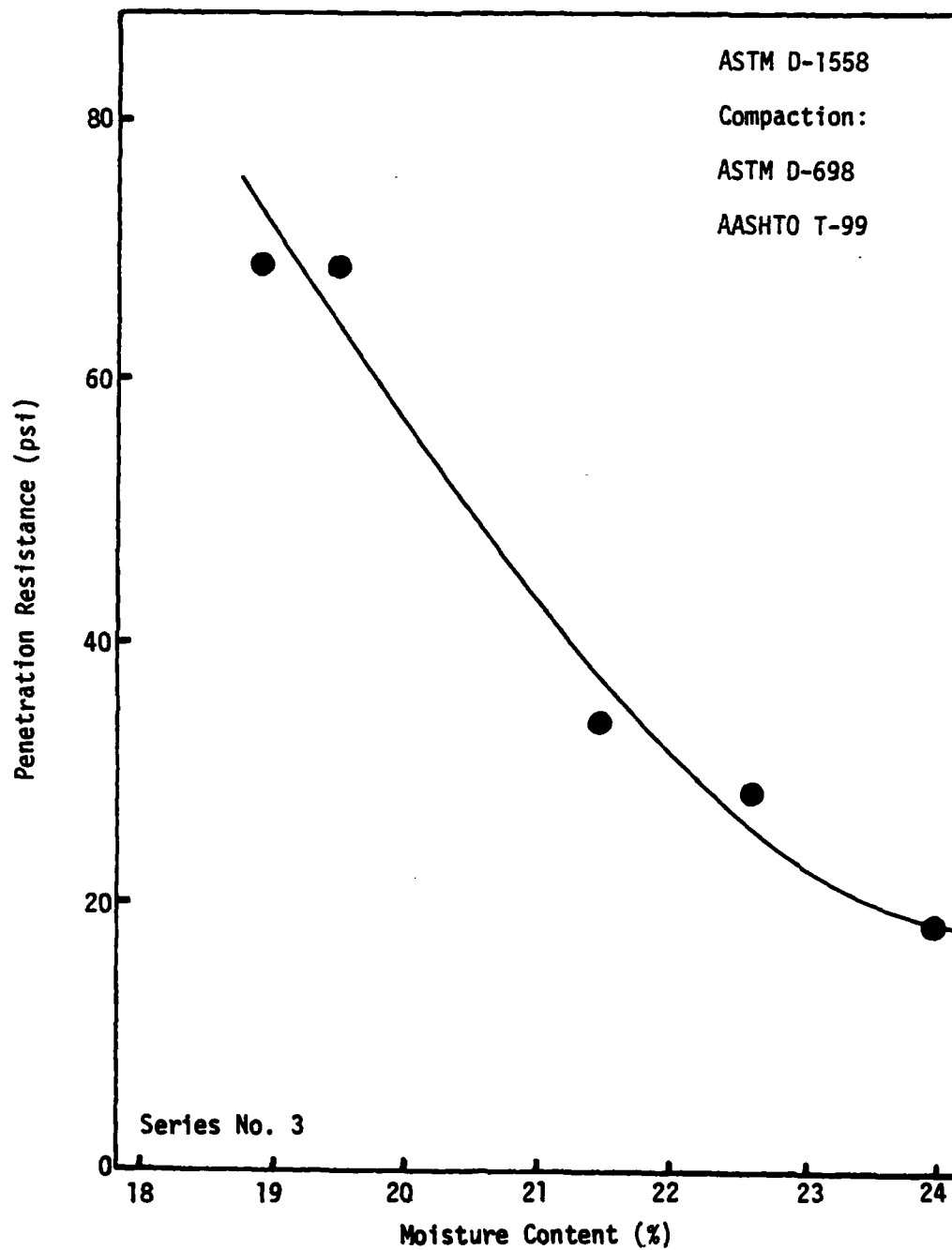


Figure B-13. Subgrade Soil Compaction Moisture-Penetration Resistance Relationship.

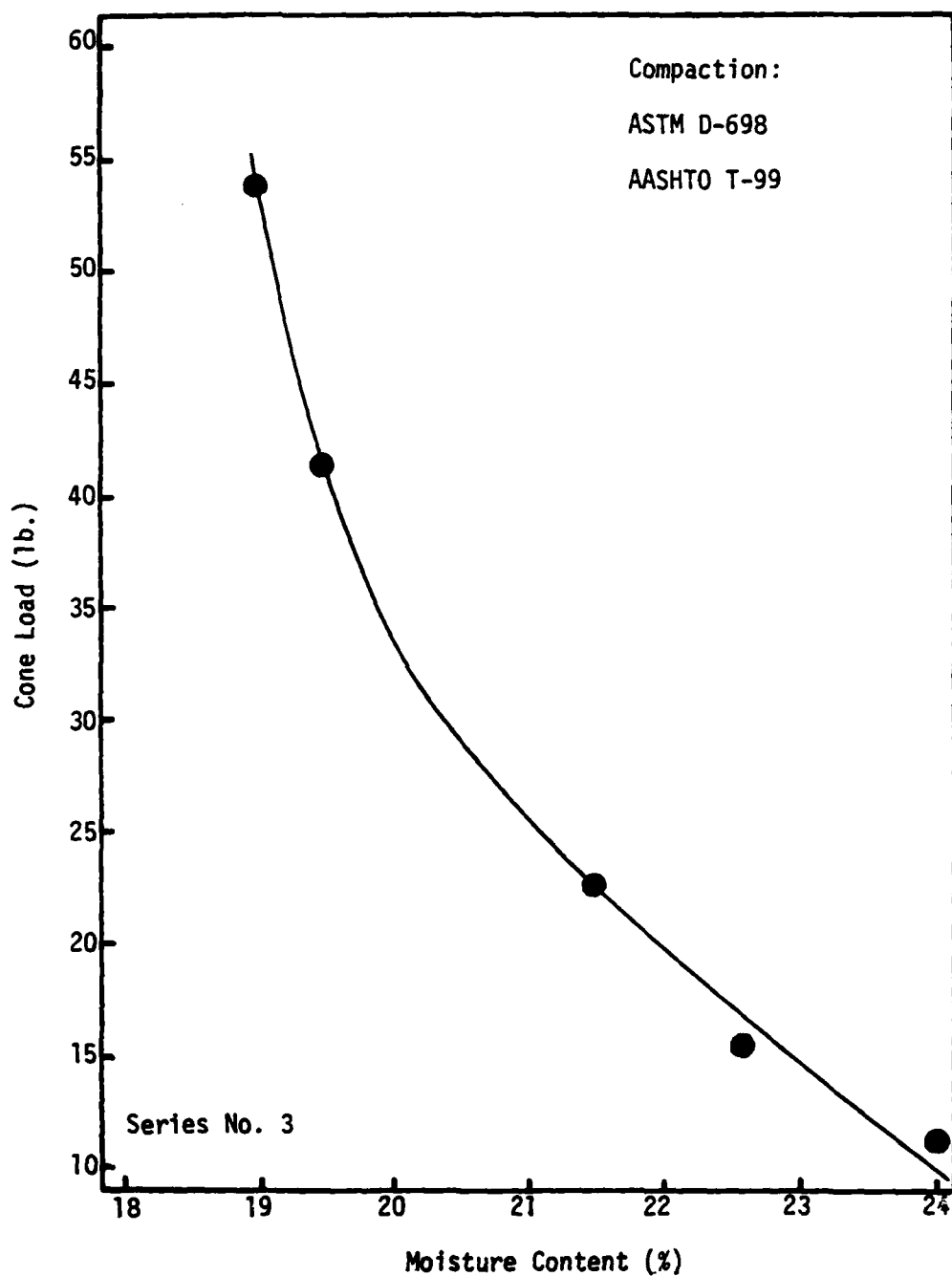


Figure B-14. Subgrade Soil Compaction Moisture-Cone Load Relationship.

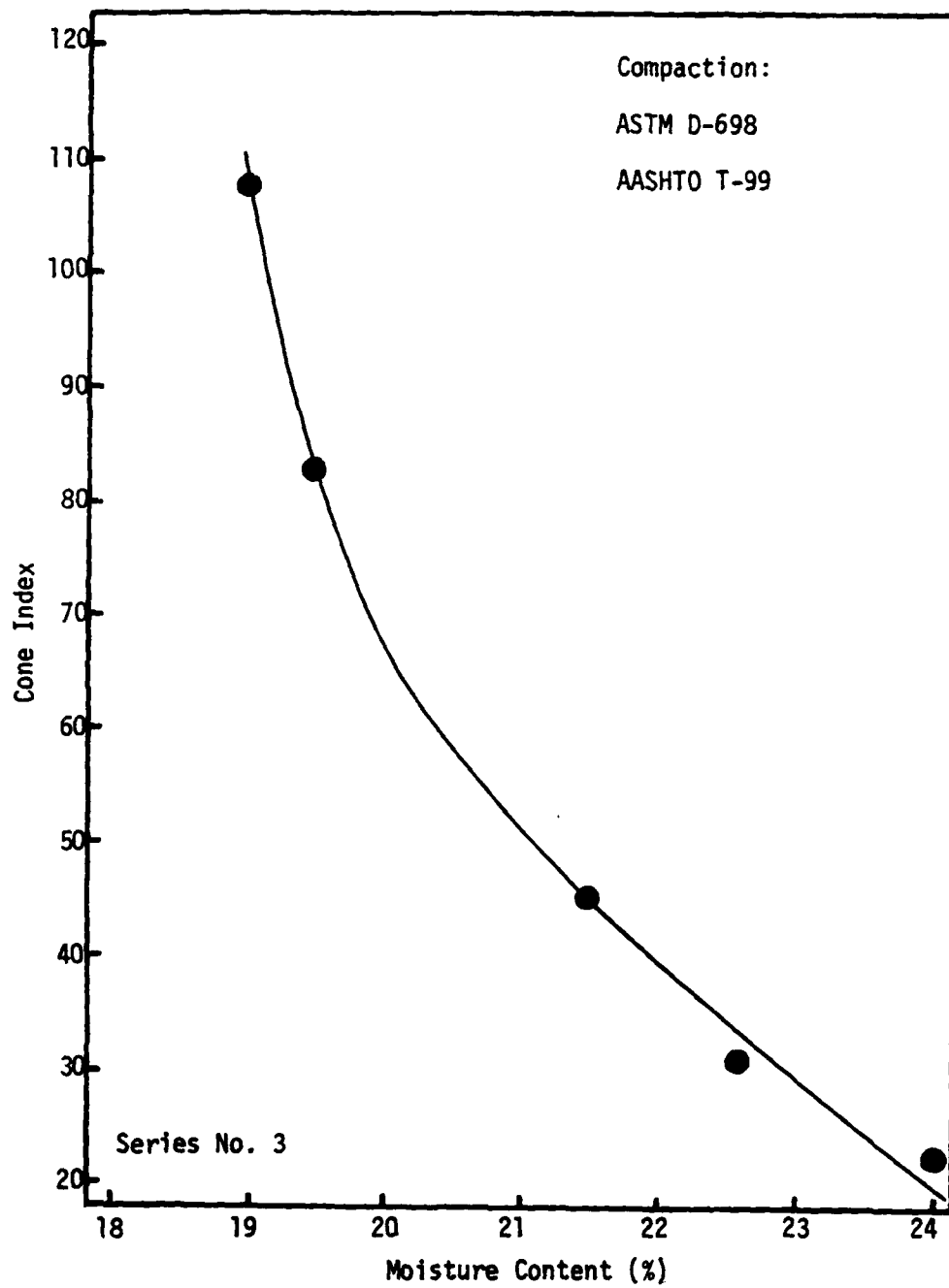


Figure B-15. Subgrade Soil Compaction Moisture-Cone Index Relationship.

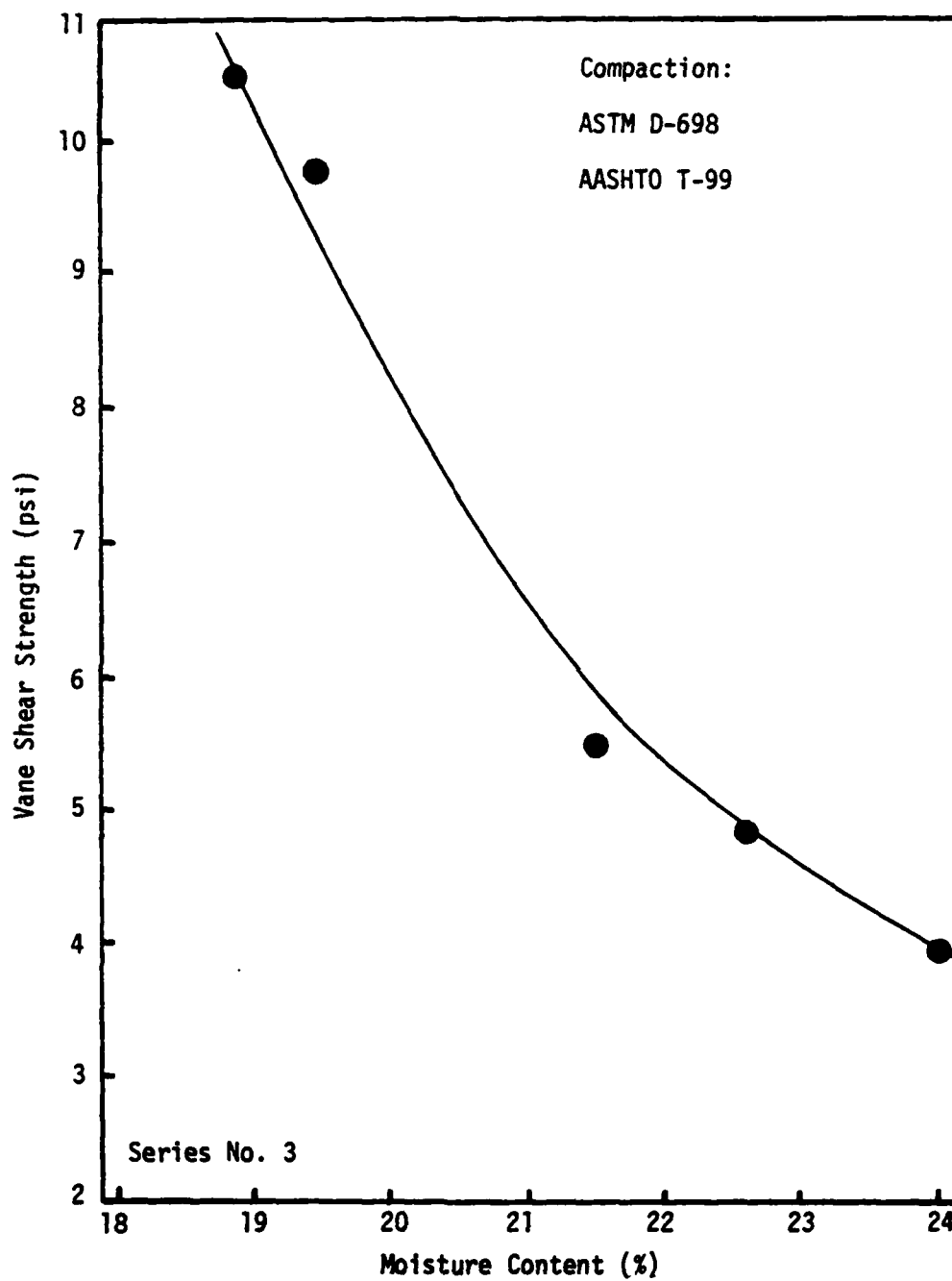


Figure B-16. Subgrade Soil Compaction Moisture-Vane Shear Strength Relationship.

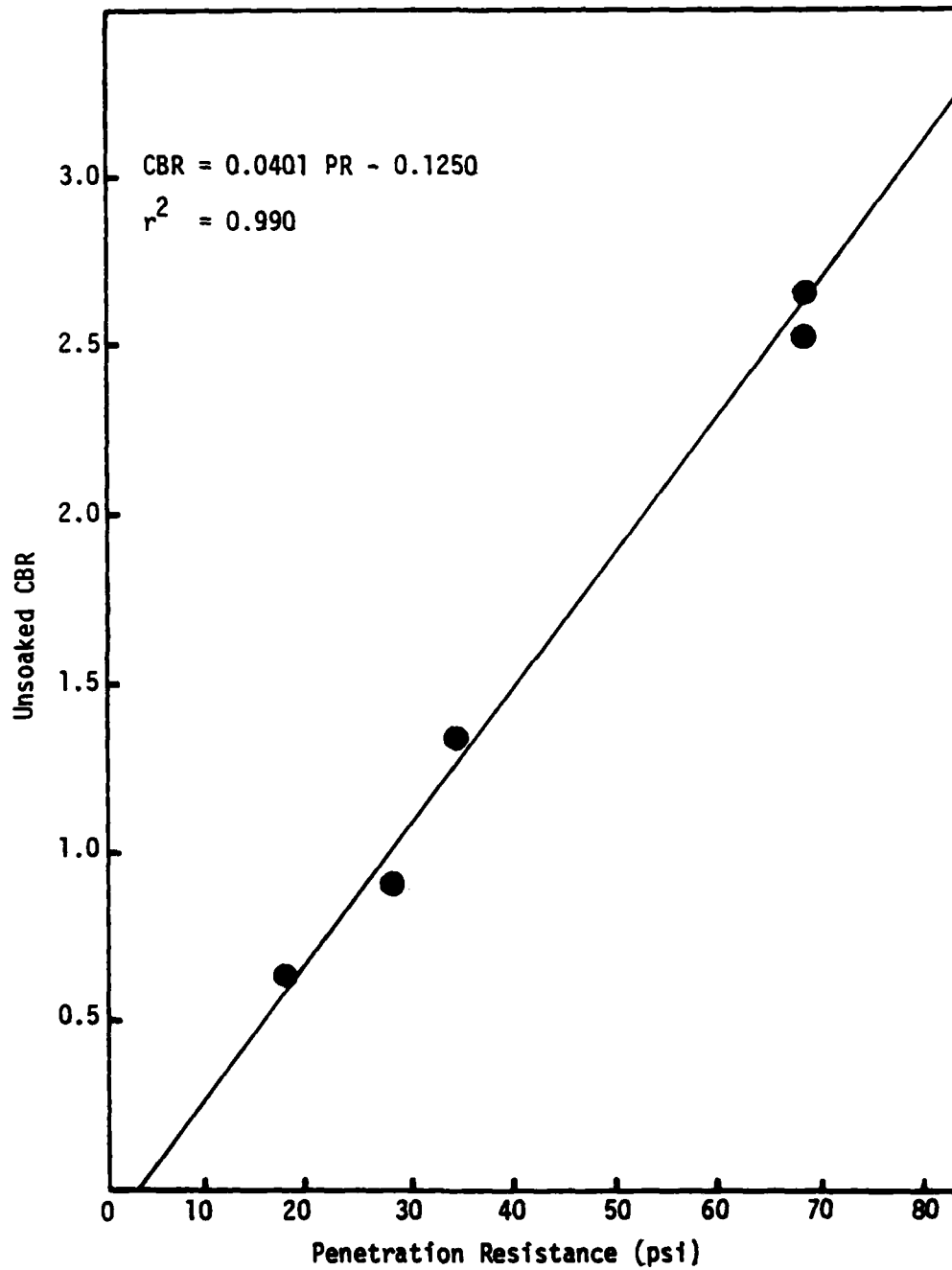


Figure B-17. Subgrade Soil Penetration Resistance-Unsoaked CBR Correlation.

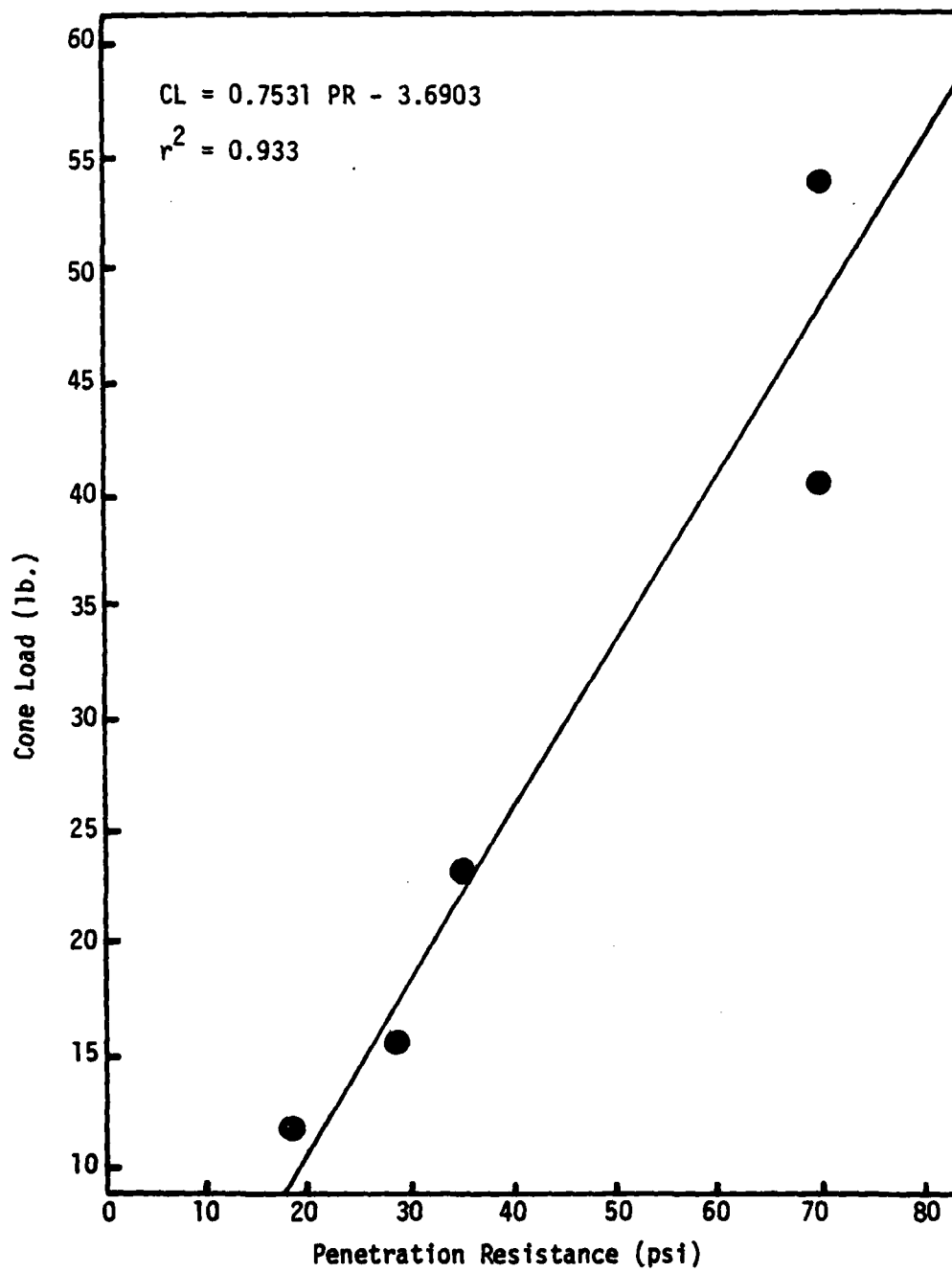


Figure B-18. Subgrade Soil Penetration Resistance-Cone Load Correlation.

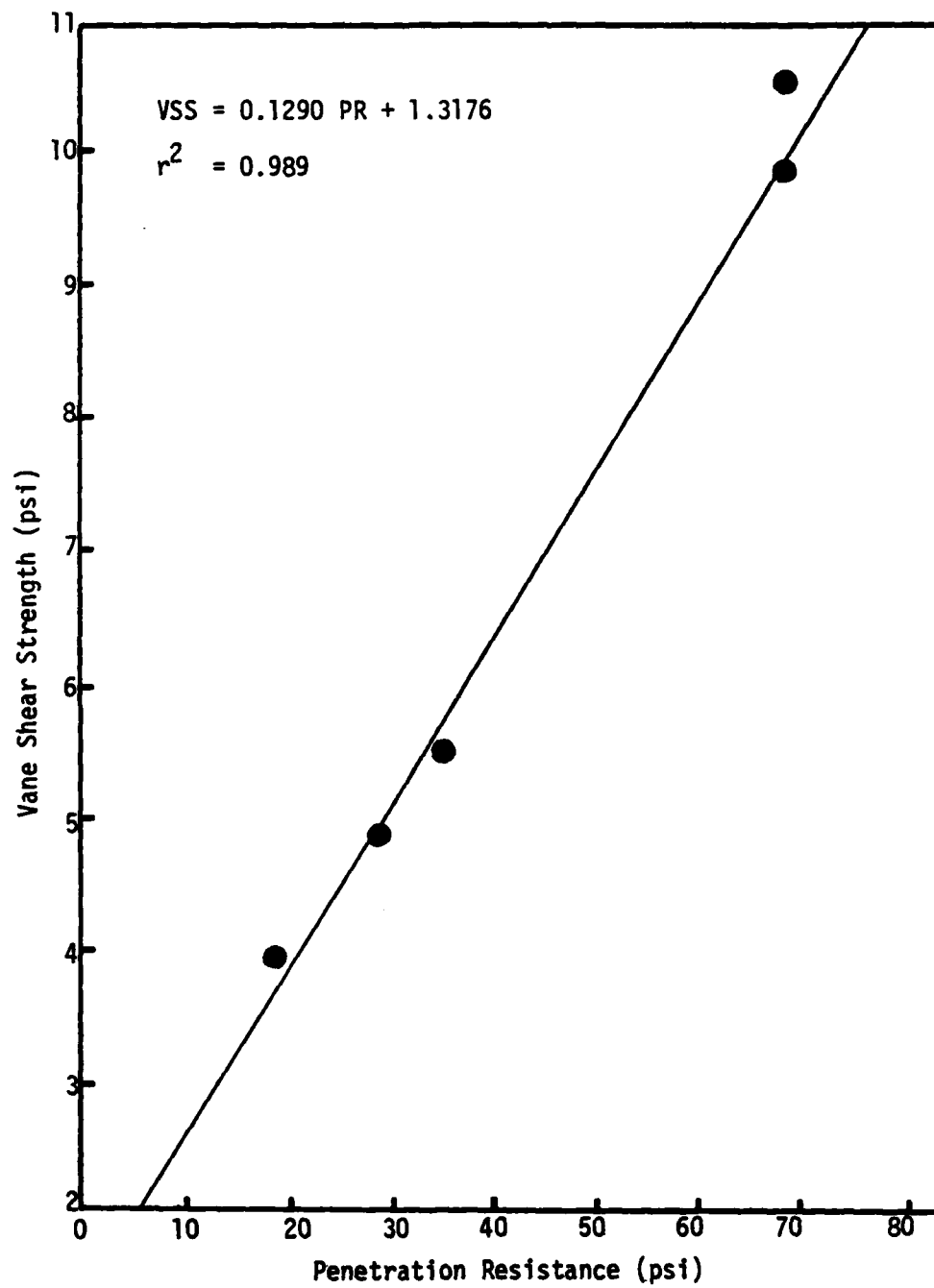


Figure B-19. Subgrade Soil Penetration Resistance-Vane Shear Strength Correlation.

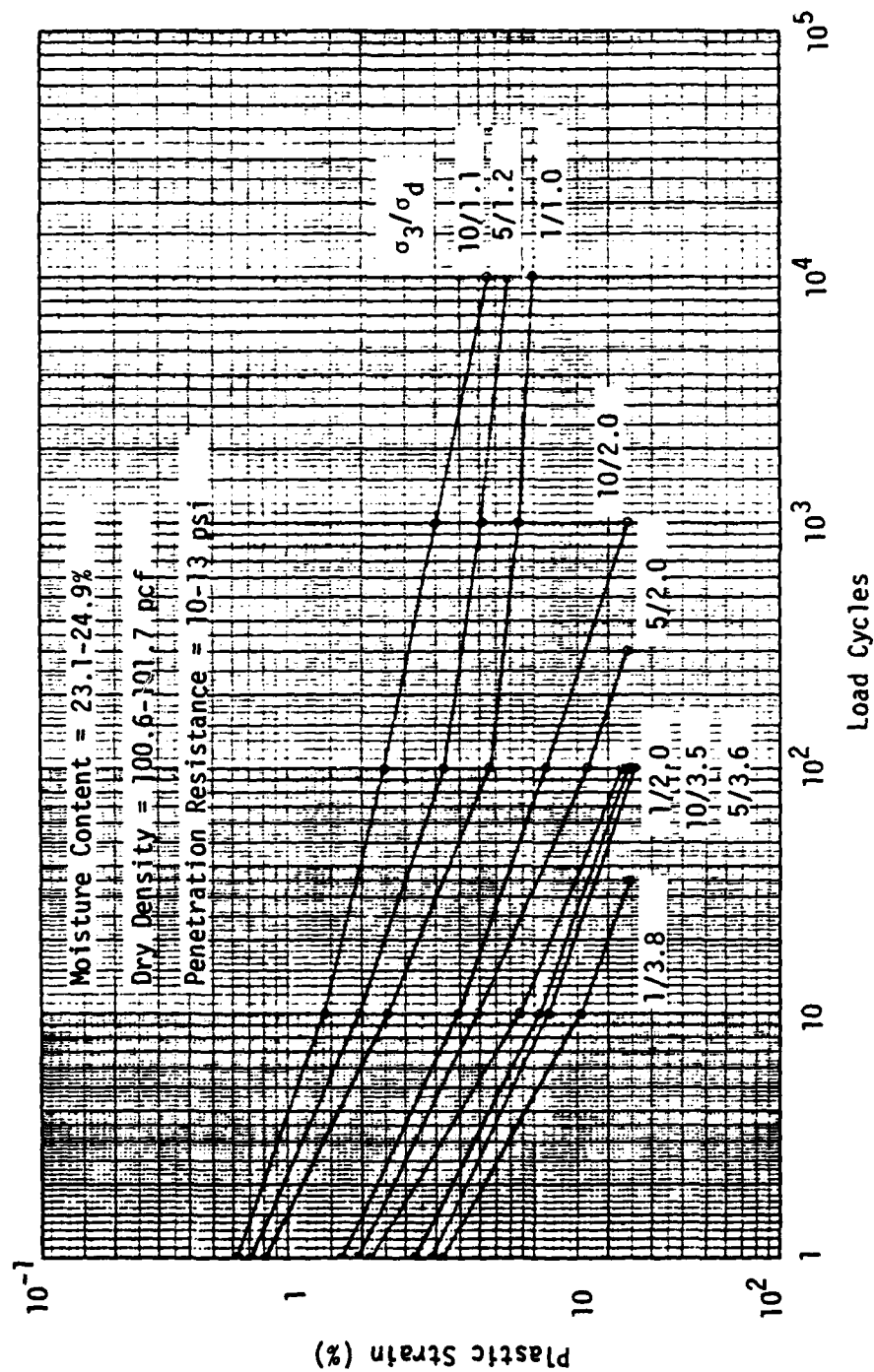


Figure B-20. Load Cycle-Plastic Strain Relationships for Subgrade Soil, Type B Loading.

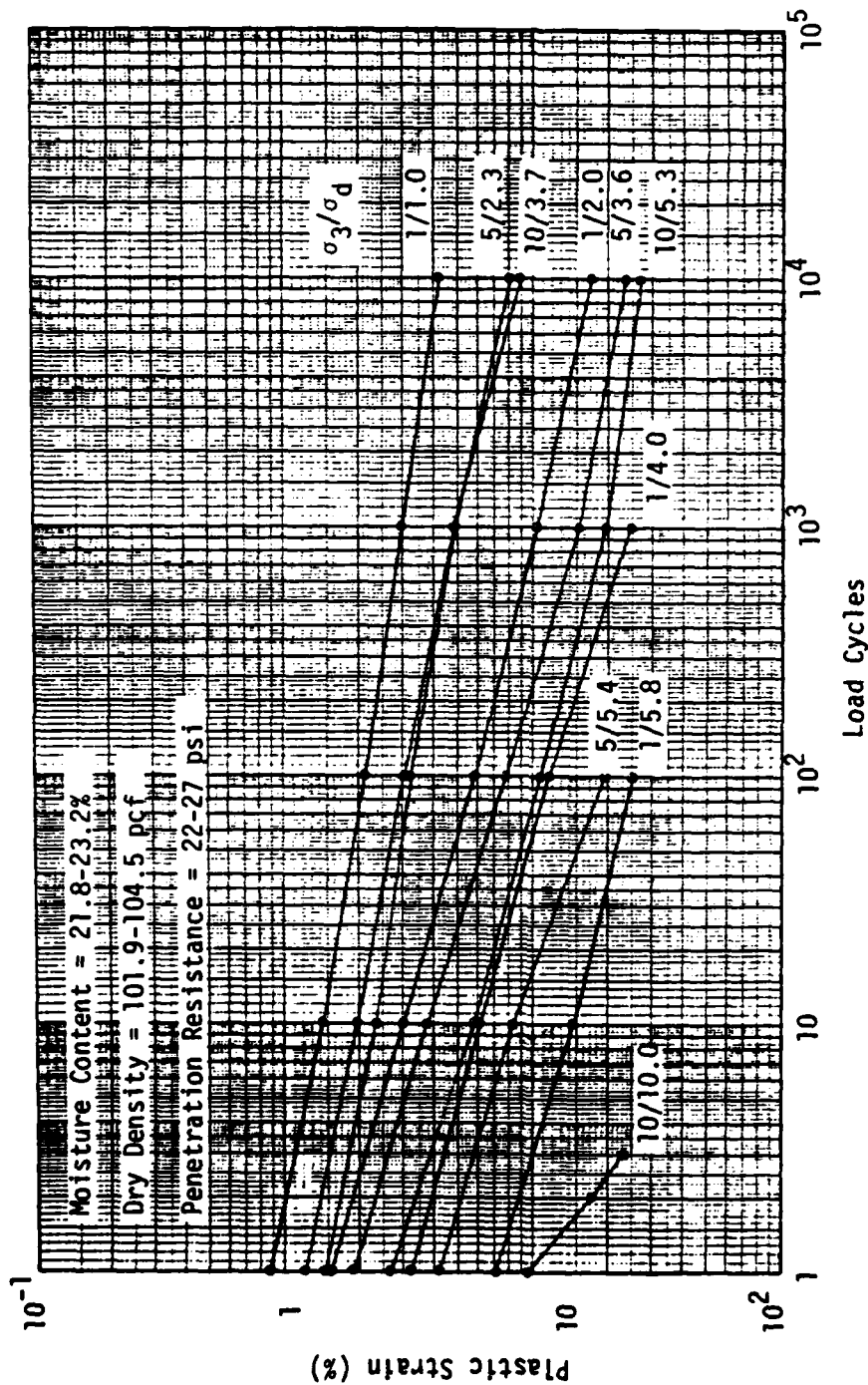


Figure B-21. Load Cycle-Plastic Strain Relationships for Subgrade Soil, Type A Loading.

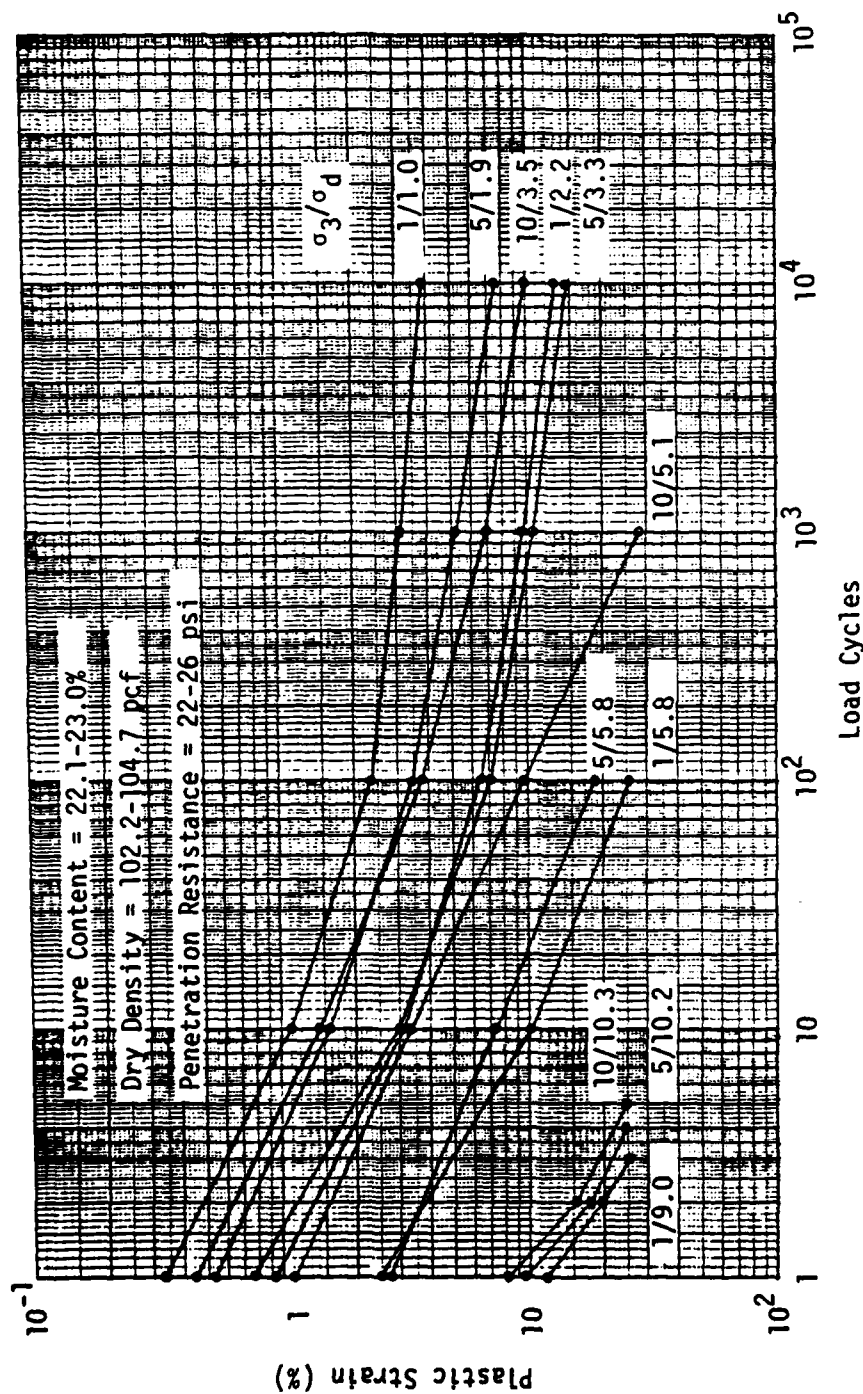


Figure B-22. Load Cycle-Plastic Strain Relationships for Subgrade Soil, Type B Loading.

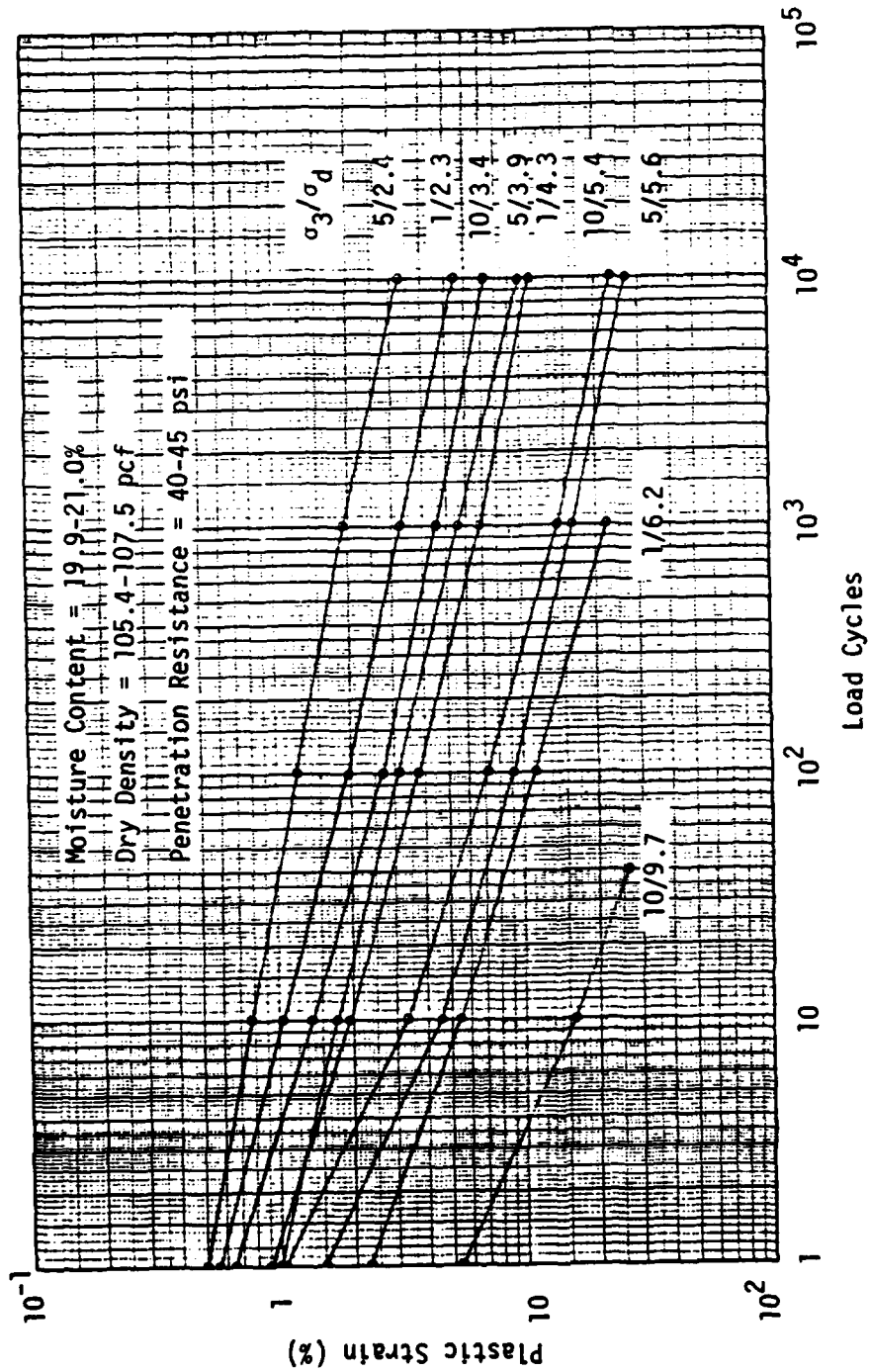


Figure B-23. Load Cycle-Plastic Strain Relationships for Subgrade Soil, Type B Loading.

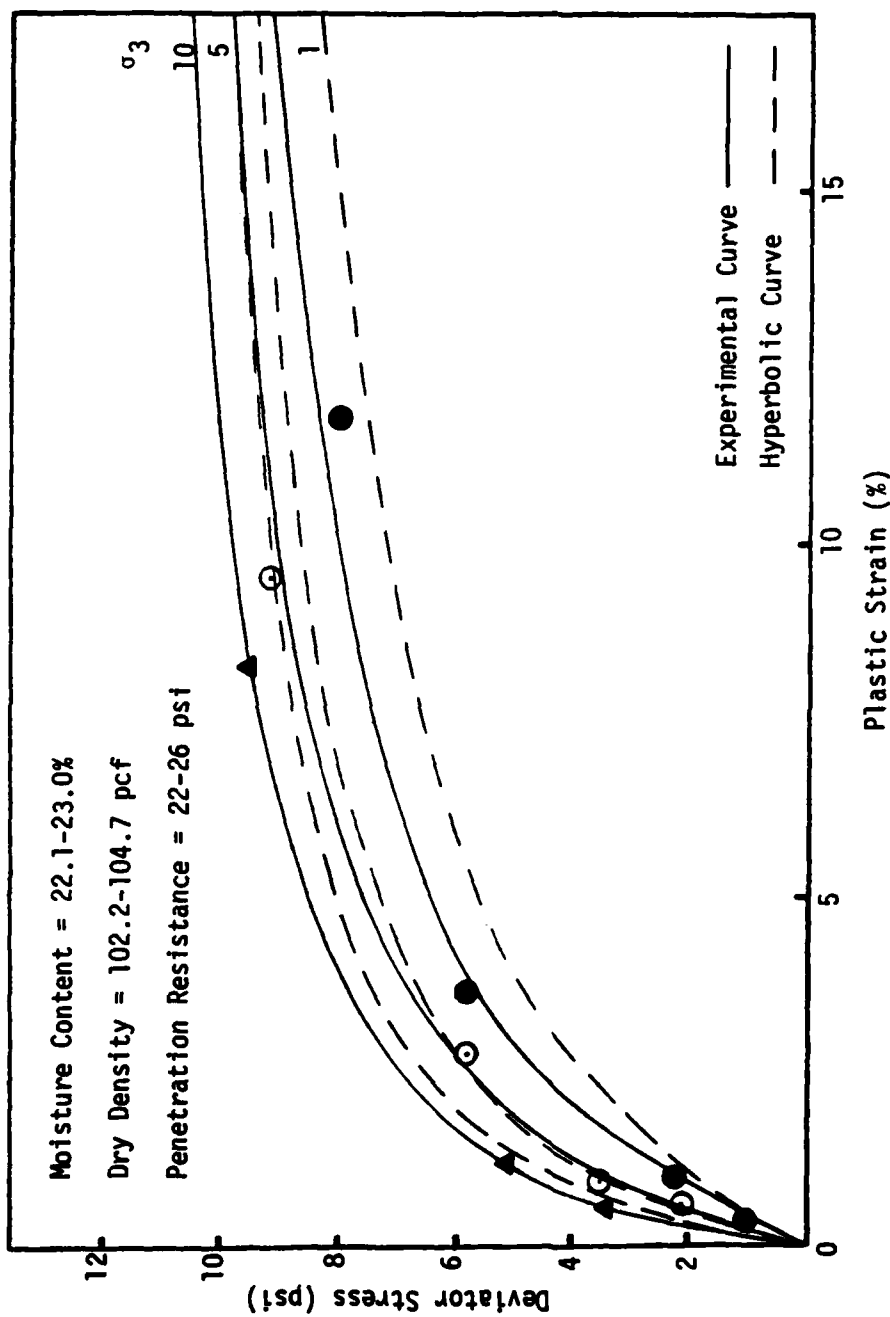


Figure B-24. Plastic Strain-Stress State Relationships for Subgrade Soil at 1 Load Cycle, Type B Loading.

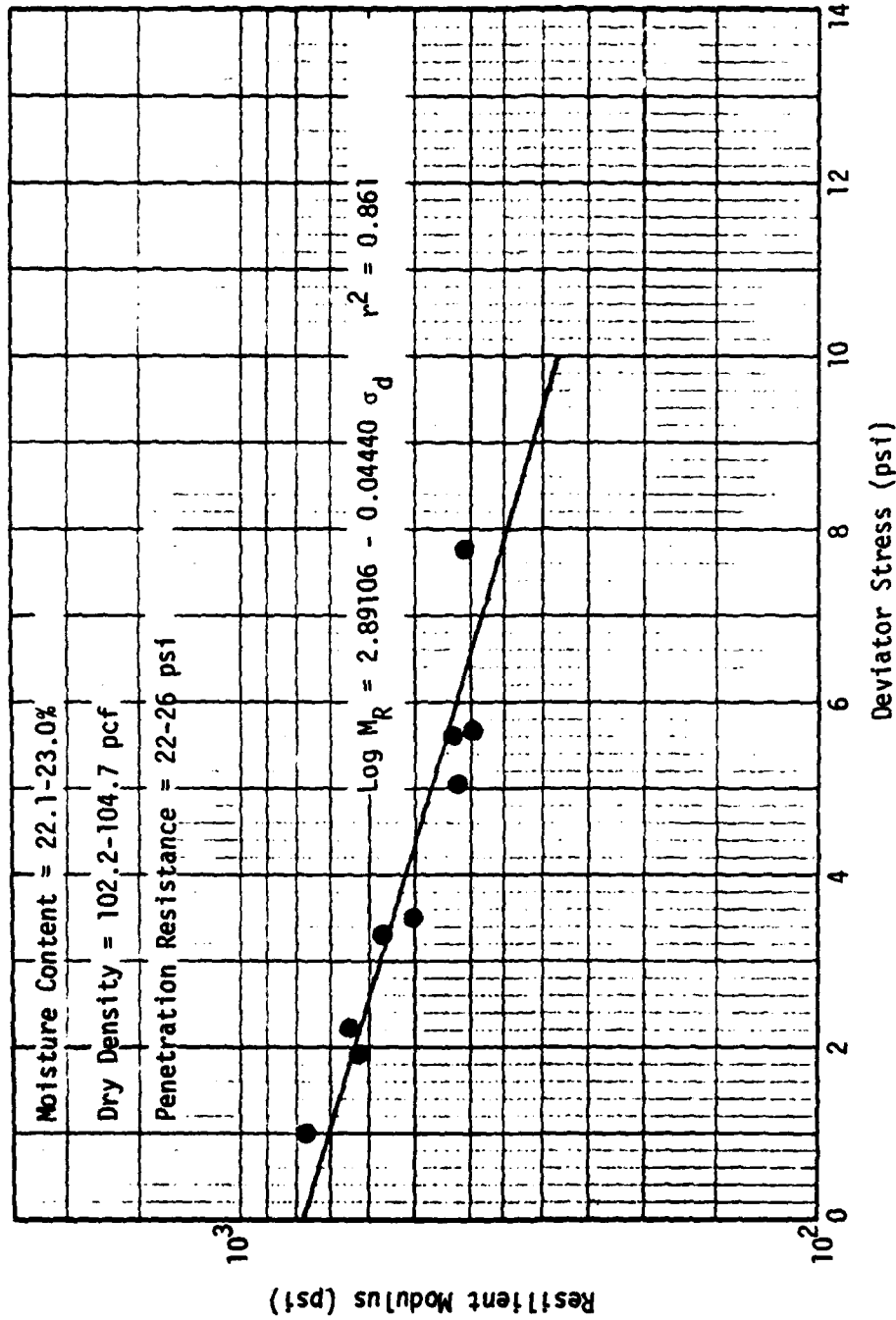


Figure B-25. Deviator Stress-Resilient Modulus Relationship for Subgrade Soil at 1 Load Cycle, Type B Loading.

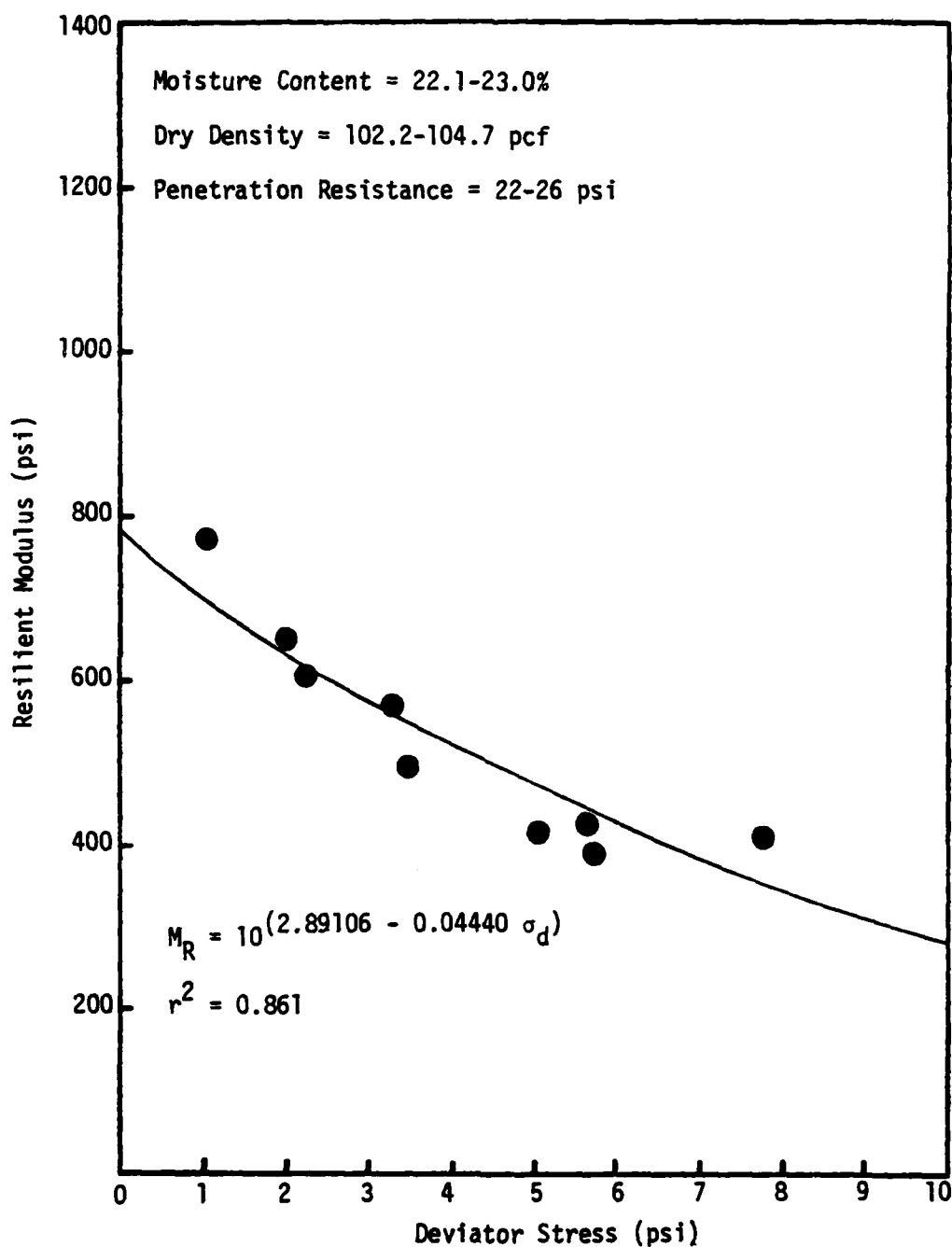


Figure B-26. Deviator Stress-Resilient Modulus Relationship for Subgrade Soil at 1 Load Cycle, Type B Loading.

APPENDIX C

SOIL STRAIN SENSORS

Strain measurements in a soil mass have received little attention in the past and only a few attempts to measure strain in soil have been reported (21, 90). There have been relatively few instruments for strain determination described in the literature.

To determine strain in a soil mass, deformation has to be measured over a known gage length. This implies that the instrument must determine the relative movement of two points in the mass. A strain measuring device (strain cell) should move freely within the soil mass in which it is placed, without reinforcing it in any way. There are several types of soil strain cells available, with two types receiving the majority of utilization. One consists of a L.V.D.T. connected to two end plates (24, 90), as shown in Figure C-1. The soil strain is measured as the relative displacement between the end plates. The main shortcoming of this type gage is the mechanical linkage between the plates. This results in implantation difficulties and friction, which inhibits free movement. The second type of soil strain instrumentation consists of a pair of wire wound inductance coils (89, 90) with cable leads. These coils are essentially free-floating in the soil mass, in coaxial, coplanar, or orthogonal configurations, providing minimum interference with the soil movement. The effects of changes in moisture, temperature, and cable length are generally negligible (18, 90).

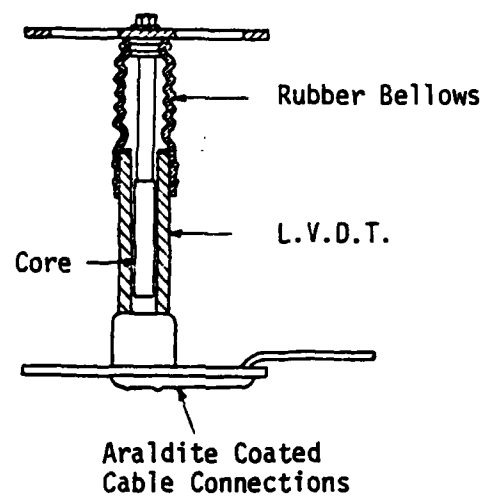


Figure C-1. United Kingdom Transport and Road Research Laboratory Strain Cell.

The sensors are relatively easy to install, durable, and fairly tolerant to changes in orientation due to misalignment and rotational placement errors or caused by movements in directions other than the one in which measurements are being taken (89, 90). Both laboratory and field measurements of dynamic and static strains have been made successfully (50, 63, 91, 101).

The strain sensors used in this study were of the second type and are commercially available from Bison Instruments, Inc., Minneapolis, Minnesota (18). Two different sizes of sensors were used in this study, with their dimensions being 2.125 inches in diameter by 0.25 inch thick and 4.125 inches in diameter by 0.25 inch thick. The sensors are machined linen phenolic base forms with electrical coils potted in epoxy for environmental stability. A Bison Model 4101A instrument package was used to excite the electronic sensors with a 20 KHz frequency signal with a peak to peak amplitude of 15 volts. In addition to the driving function, the instrument package contains the bridge balance controls, power supply, and amplification, readout, and calibration functions. According to the manufacturer (18), the maximum sensitivity of these sensors is 0.0004 inch of gage length movement per amplitude dial division on the indicator box. This is obtained with coils 1.125 inches in diameter, at a spacing of one to two times the sensor diameter. Resolution is limited to 0.04 percent strain on the amplitude dial.

The bridge balance in the readout unit is accomplished by means of phase and amplitude controls using a meter to indicate null. After a null condition of both phase and amplitude is obtained for a given sensor spacing, the amplitude dial reading (0 to 1000 divisions)

corresponds to the sensor separation. Changes in spacing are determined by re-nulling and noting the changes in the amplitude dial readings. The sensor separation selector on the readout unit is used to control the range over which the amplitude dial is effective. For sensor separations of one to two times the diameter of the sensors, two to three sensor diameters, and three to four sensor diameters, the coil separation selector was set at one, two, or three respectively. Some overlap exists between the ranges. Thus, by changing the sensor separation selector, the sensitivity of the readout unit remains approximately constant for any sensor spacing.

To establish the relationship between sensor separation and null amplitude and phase dial reading for each separation range, a calibration curve was developed for each sensor pair. The sensors were placed on a plexiglas mounting fixture, as shown in Figure C-2, equipped with a micrometer to measure the gage length to the nearest 0.001 inch. For each coil separation range, null amplitude and phase dial readings were taken at 0.25 inch incremental gage length changes over the full amplitude scale. The relationship between sensor separation and amplitude dial reading, for a given separation range, was thus established for each pair of coils of interest, for their respective field orientation and anticipated spacing. The calibration curves may be approximated by a polynomial curve fit method, using a fourth order curve (50). The typical relationship between sensor spacing and amplitude dial reading then takes the following form:

$$y = C_0 + C_1x + C_2x^2 + C_3x^3 + C_4x^4 \quad (C-1)$$

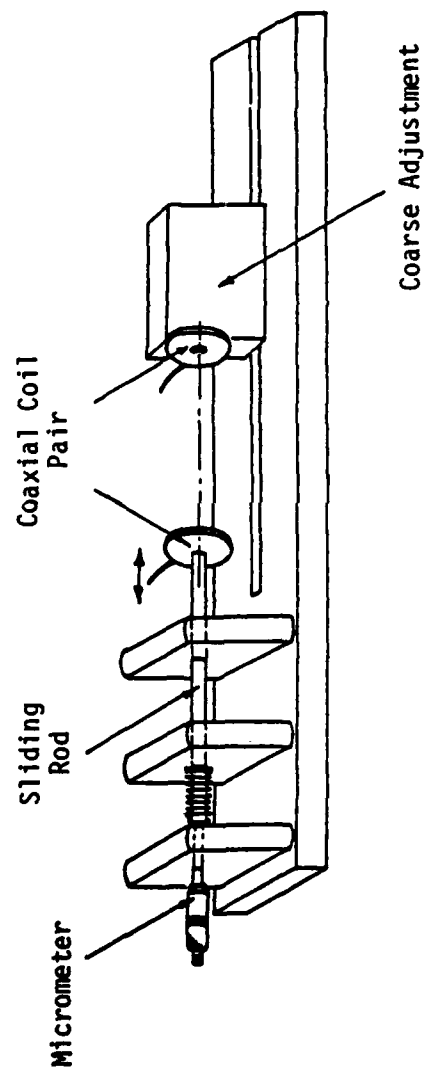


Figure C-2. Bison Sensors and Plexiglas Calibration Mounting Fixture.

where y = sensor spacing, inches

x = amplitude dial reading (null)

C_i = constants of curve fitting regression.

Typical curves for the 2.125 inches diameter coils, in both coaxial and coplanar configurations, are shown in Figures C-3 and C-4.

Vertical and horizontal motions within the soil mass may be easily monitored by vertical stacks of sensors in a coaxial configuration, with corresponding coils in adjacent columns being in a coplanar configuration. Sensor readings were facilitated using switching units of terminal strips. The sensitivity of the sensor movement may best be obtained if the sensor spacing is set so that the initial null amplitude dial reading is in the range of 0-400 for each coil separation because of the nonlinearities of the calibration curve. The actual sensitivity found ranged from 0.0015 to 0.0025 inch per unit change in amplitude. The typical initial null amplitude dial readings for the coil configurations of this study were in the range of 500-700. This was necessitated by the size and number of coils available, the maximum desired initial gage lengths, and the large movements experienced.

Two major problems were experienced with these coils. First, the lead wires of the sensor had to be shielded to reduce interference, to achieve consistent results, and to allow use of the maximum sensor spacing for each coil separation range as stated in the literature provided by the manufacturer (18, 50). Secondly, any metal in the zone of influence (about two sensor diameters) of the electromagnetic field coupling the sensors tends to affect the output. The effect is to move up or down the calibration curve, but not to change the shape of the

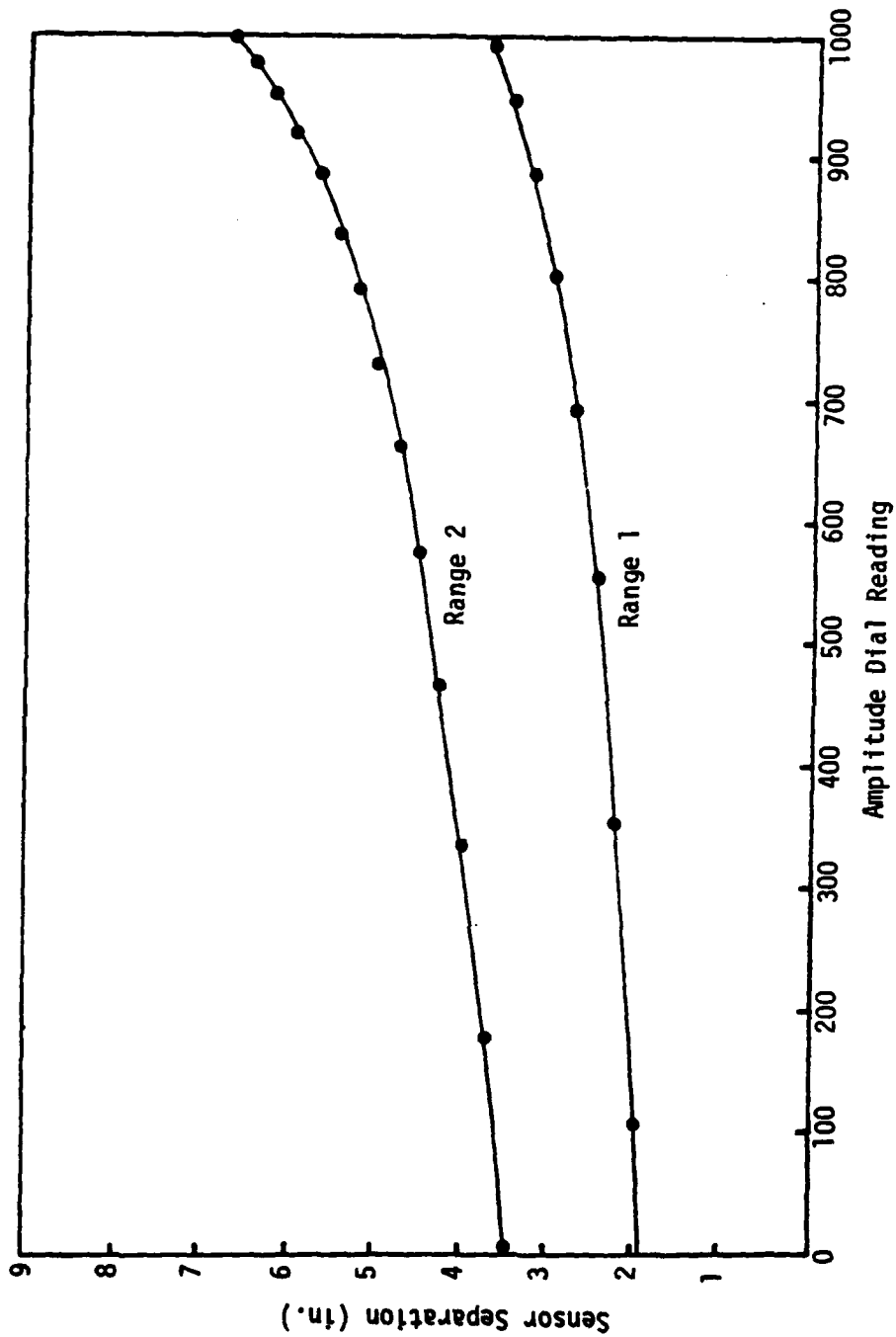


Figure C-3. Amplitude Dial Reading-Sensor Separation Relationships for Coaxial Coils.

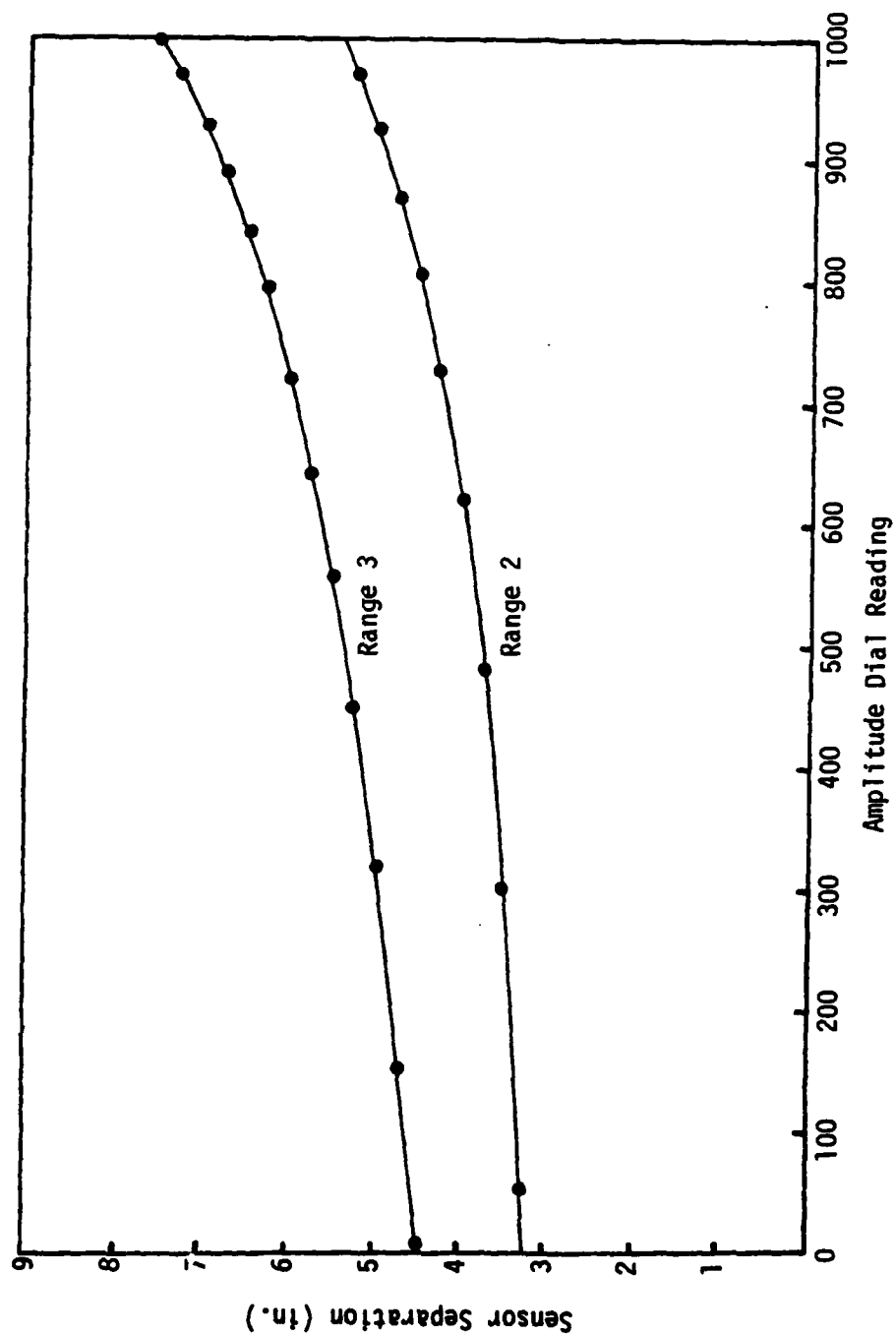


Figure C-4. Amplitude Dial Reading-Sensor Separation Relationships for Coplanar Coils.

curve. The stress cells (Appendix D), which were made of aluminum, were placed near the mid-points of the gage lengths of the strain sensor pairs on the vertical axis of the footing, offset by three inches (i.e., the stress cells were thus centered under the edge of the footing). This placement was found to have no effect on output. The steel wall of the test pit was not within the electromagnetic field of any of the coil pairs.

The coil separation indicated by the sensor readout is a result of movements in the direction of interest, as well as movements perpendicular to that direction and "out-of-plane" rotations of the coils, all of which influence the electromagnetic field generating the output. The misalignment and rotation effects are nonlinear, however, considerable distortion from the desired orientation is possible before serious errors result. For coaxial and coplanar sensors, an offset of not more than ten percent of the gage length and a rotation of 20° or less produce individual errors of approximately five percent (18, 90). The errors magnify rapidly for greater orientation distortions, of the types which were typically experienced during the model tests in the coaxial sensor pairs of column two and the coplanar sensor pairs of columns one and two and columns two and three.

APPENDIX D

STRESS CELLS

A variety of stress cells have been utilized to measure stresses in soil masses. Stress is usually measured indirectly, with a calibration curve being developed between applied pressure and the deflection of a thin diaphragm. The Nottingham Pressure Cell (22, 24) is a single diaphragm cell with deflection measured by a four-arm strain gage bridge. The United Kingdom Transport and Road Research Laboratory (24) has developed two double diaphragm cells, one measuring deflection with a small L.V.D.T. and the other utilizing four piezoelectric crystals. The Kyowa Cell and the Waterways Experiment Station Cell (22, 24) utilize a thin mercury filled cavity, situated between main and secondary diaphragms, with deflections measured by a strain gage bridge attached to the back of the secondary diaphragm. The United Research Service Cell (24) consists of an oil filled central cavity, between two diaphragms, with soil pressure calibrated against changes in fluid pressure as measured by a piezoresistive transducer. The Total Pressure Cell (94) utilizes two diaphragms, with a central cavity filled with antifreeze. Changes in soil pressure produce hydraulic pressure changes which are equilibrated pneumatically to determine stress. Diaphragm cells with bonded strain gage sensing elements are the most attractive cell type for reasons of simplicity and low production cost. The determination of in-situ stress remains a difficult

problem because the stress cannot be measured directly and must rely upon a measure of the deformation of the instrument, using an appropriate sensor. Due to the difficulties involved, accuracies much better than ± 20 percent cannot be expected (23, 43).

Limitations

When a stress cell is placed within a soil mass, the cell represents a rigid body which disturbs the stress distribution pattern in its vicinity. The result is a stress concentration around the cell, higher than the free field stress. The cell, therefore, has a natural tendency to indicate stresses that are higher than the true stresses in the soil mass. The ratio of measured stress to true stress is defined as cell registration. Over registration indicates that the measured stresses are higher than the actual stresses, while under registration indicates exactly the opposite case. For a stress cell to indicate true soil stresses, it should ideally have the same elastic properties as the surrounding soil. The possibility of producing such a cell is remote. A reasonable approach is to design a cell that will disturb the stress patterns as little as possible and therefore measure stresses very close to the true values. Theoretical analysis (107) indicates that a stress cell will yield more accurate results when the cell is stiffer, rather than softer, than the surrounding soil.

For laboratory soil stress measurements, Hadala (43) reported variations in over registration as large as 40 percent. These variations were attributed primarily to variations in placement techniques. It is important that the material around the cell be compacted to the

same density and stiffness as the soil mass.

Theoretical Considerations

Cell registration is affected by cell geometry and the stiffness of the diaphragm relative to the soil stiffness. The cell registration factor, C , is defined as:

$$C = \frac{\text{Measured Stress}}{\text{True Stress}} \quad (D-1)$$

The geometry is expressed in terms of the Aspect Ratio, which is defined as:

$$\text{Aspect Ratio} = \frac{\text{Cell Thickness}}{\text{Cell Diameter}} \quad (D-2)$$

The relative stiffness of the diaphragm is expressed by a Flexibility Factor, which is defined as:

$$\text{Flexibility Factor} = \frac{\text{Soil Stiffness}}{\text{Diaphragm Stiffness}} = \frac{E_s d^3}{E_c t^3} \quad (D-3)$$

where E_s = soil modulus of elasticity, psi

d = diaphragm diameter, inches

E_c = cell material modulus of elasticity, psi

t = diaphragm thickness, inches.

Brown (22, 24) presents a series of curves relating these variables.

Theoretically, the Flexibility Factor should be less than two and the Aspect Ratio should approach zero for the cell registration factor to equal one. In constructing a cell, cable entry requirements limit the Aspect Ratio to approximately 0.1, resulting in a theoretical cell

registration of 1.02.

Design Criteria

Practical criteria for diaphragm stress cells have been well summarized by Brown (24), Selig (88), and Triandafilidis (107). Important design criteria are as follows:

(1) The diaphragm diameter should be at least 50 times the largest soil particle dimension to prevent arching effects of the diaphragm (54, 120).

(2) The diaphragm area should be less than 45 percent of the total cell face area to keep the sensing area away from the cell edge, where stress concentration is greatest (76).

(3) The Aspect Ratio should be kept less than 0.1, with thickness for cable entry being the only limitation (8).

(4) The central deflection of the diaphragm should not exceed 1/2000 of its diameter under the anticipated field stress to avoid arching effects (111).

The diaphragm deflection may be calculated using the following relationship (42, 79) for a clamped plate:

$$y = \frac{3 p d^4 (1 - \nu^2)}{256 E_c t^3} \quad (D-4)$$

where y = diaphragm central deflection, inches

p = applied pressure, psi

d = diaphragm diameter, inches

ν = cell material Poisson's ratio

E_c = cell material modulus of elasticity, psi

t = diaphragm thickness, inches.

By keeping the diaphragm deflection to within this limit, the diaphragm thickness may be adjusted to assure a Flexibility Factor of less than two, subsequent to estimating E_s .

Stress Cells Used in Study

The stress cells used in this study were designed by Intrapasart (50) in accordance with the procedures described previously. The cells were originally designed and constructed for use in a micaceous clayey silt soil with a maximum particle dimension of approximately six millimeters. The required minimum diaphragm diameter for that soil was 1.18 inches. The minimum required diaphragm diameter for the subgrade material of this study was 0.46 inch, taking 2.38 millimeters as the maximum particle dimension.

The stress cells were machined from grade 2024 T-3 aluminum, which has a yield strength of 42 ksi, a Poisson's ratio of 0.35, and a modulus of elasticity of 10×10^6 psi. The stress cell has a diameter of two inches and a final diaphragm diameter of 1.25 inches. The ratio of diaphragm area to the total area for this cell is 39 percent, which is within the limit of the second design criterion. To provide for cable entry, the cell thickness was limited to a minimum of 0.25 inch. The cover plate thickness was 0.05 inch, for a total thickness of 0.3 inch. The Aspect Ratio of this stress cell is 0.15, which is slightly greater than the recommended value of 0.1. For an anticipated field stress of less than 30 psi, a diaphragm thickness of 0.05 inch was used to keep the central diaphragm deflection within the limit of the fourth criterion. The Flexibility Factor of the stress cell is

less than two for any soil modulus of elasticity below 1280 psi. The theoretical value of C for the cell is 1.05 for such a case (22), increasing to 1.08 for a Flexibility Factor of one or less.

A Model EA-06-11CJC-120 diaphragm strain gage, manufactured by Micro-Measurements, Inc., Romulus, Michigan, was used for each cell. This strain gage is designed to yield a maximum output by summing the absolute value of both tangential and radial strains developed in the diaphragm when subjected to pressure. The gages were connected to form a four-arm bridge capable of self temperature compensation. Stress cell details are shown in Figure D-1, while a full description of the cell construction process is given by Intraprasart (50).

Cell Calibration

Each of the stress cells was calibrated individually using a pressure chamber with a height of 6.75 inches and 18.0 inches in diameter. The chamber diameter meets the criterion given by Triandafilidis (107). The cells were connected to a Type PSBA 20-Model 3 switching and balancing unit manufactured by the Baldwin-Lima-Hamilton Corporation of Philadelphia, Pennsylvania, which was in turn connected to a Model 60-1300 Twin-Viso Strip Chart Recorder manufactured by the Sanborn Company, Cambridge, Massachusetts, as shown in Figure D-2. The strip chart recorder is equipped with a Model 60-1600 control panel and a Model 64-500A strain gage amplifier.

Hydrostatic Calibration. To determine the true registration of the stress cells, hydrostatic calibration tests were conducted for each cell. The cell was sandwiched between two rubber membranes in the center of the chamber which was filled with water. A rubber membrane was

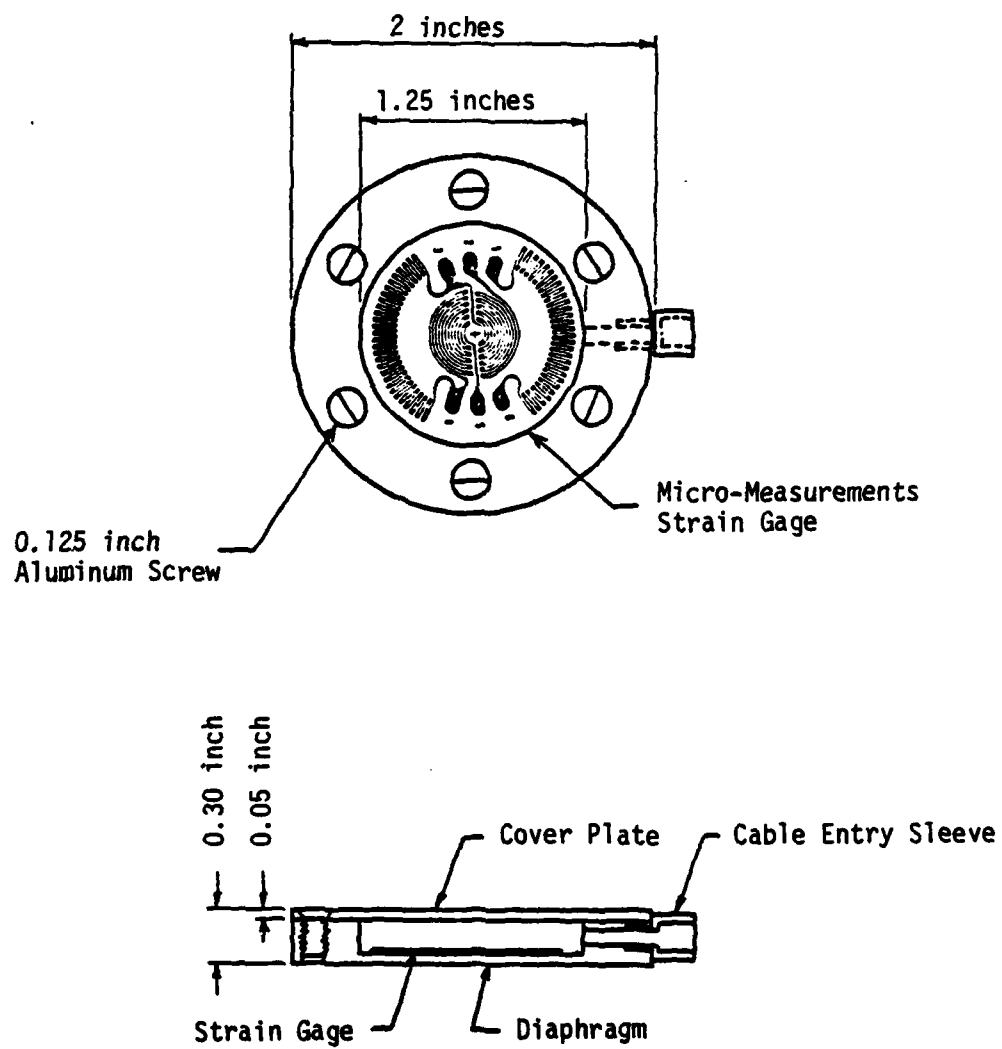


Figure D-1. Stress Cell Details.

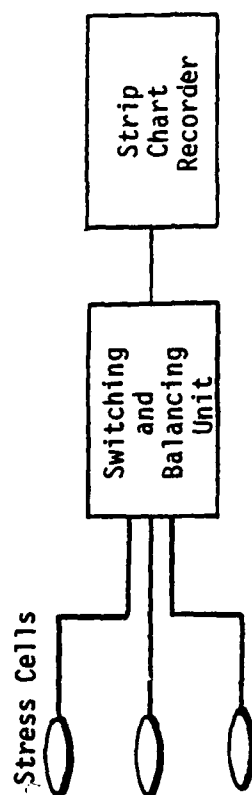


Figure D-2. Stress Cell Equipment Schematic.

used to seal the tank and apply pressure to the water. The top of the chamber was securely bolted down, prior to application of the pressure. An Ashcroft Pressure Gage, having a knife edge needle and reflecting mirror, was carefully calibrated using a dead weight tester and used to monitor the air pressure. During their original calibration (50), a pressure three to four times greater than the anticipated field stresses was first applied and cycled to relieve the metal of residual stresses caused during manufacture and to minimize hysteresis effects.

Soil Calibration. It is desirable to calibrate the stress cells under controlled laboratory conditions which correspond as closely as possible to the field situation. The stress cells were placed in the same soil in which they were to be used, with the soil compacted to the field density. Prior to placing the soil in the chamber, the interior wall was covered with rubber membranes, attached using silicone grease. The stress cells were positioned in the center of the tank using the same installation technique to be used in the test pit.

During both hydrostatic and soil calibrations, the pressure was incrementally increased to the design pressure and cycled twice to check the reproducibility of the output. Subsequent cell readings were found to differ only slightly from those of the first cycle. The outputs were recorded on the strip chart recorder, to an appropriate scale, and used to develop calibration curves for each cell. The calibration relationship was found to be linear within the design stress range. The experimental value of C was found to be 1.03, calculated by comparing the outputs for the calibrations in soil and water (reference or true stress). All of the cells were found to give over registration, although

the values were less than those indicated by a theoretical approach (22).

Tests by Brown and Brodrick (23) showed only small variations in average cell registration values were experienced between static and dynamic calibrations of diaphragm pressure cells installed in a silty clay soil, similar to the subgrade material of this study. Therefore, static calibration of the cells was deemed sufficiently accurate for measurement of the dynamic stresses in the subgrade during the model test program.

APPENDIX E

MODEL TEST PROGRAM DEFORMATION DATA

Cumulative permanent deformation was monitored during each model test. The centerline deflection was determined as the average of the cumulative changes in three dial gage readings. Federal, Model E81S, dial gages were utilized, being positioned at equally spaced points on the footing perimeter. Transient surface movement was monitored during the majority of tests, for any load cycle of interest, with a Model SS207 L.V.D.T., manufactured by the G. L. Collins Corporation. L.V.D.T. output was monitored, to an appropriate scale, on a strip chart recorder. Deformation data for all tests are presented herein, accompanied by plots of the load cycle-cumulative permanent deformation relationships. Crushed stone depth, interfacial membrane type, and the unsoaked CBR of the subgrade soil are provided with the deformation data for each test.

Table E-1. Load Cycle-Deformation Relationships, Test No. 1B (6.0 in. Stone/None/Unsoaked CBR = 0.38).

<u>Load Cycles</u>	<u>Total Deformation Per Cycle (in.)</u>	<u>Cumulative Permanent Deformation (in.)</u>
1	--	0.359
5	0.38	0.912
10	0.33	1.351
15	0.35	1.653
20	0.32	2.002
30	0.32	2.547
40	0.35	3.029
50	0.38	3.471
60	0.39	3.847
70	0.42	4.018
80	0.43	4.399
90	0.45	4.665
100	0.47	4.923

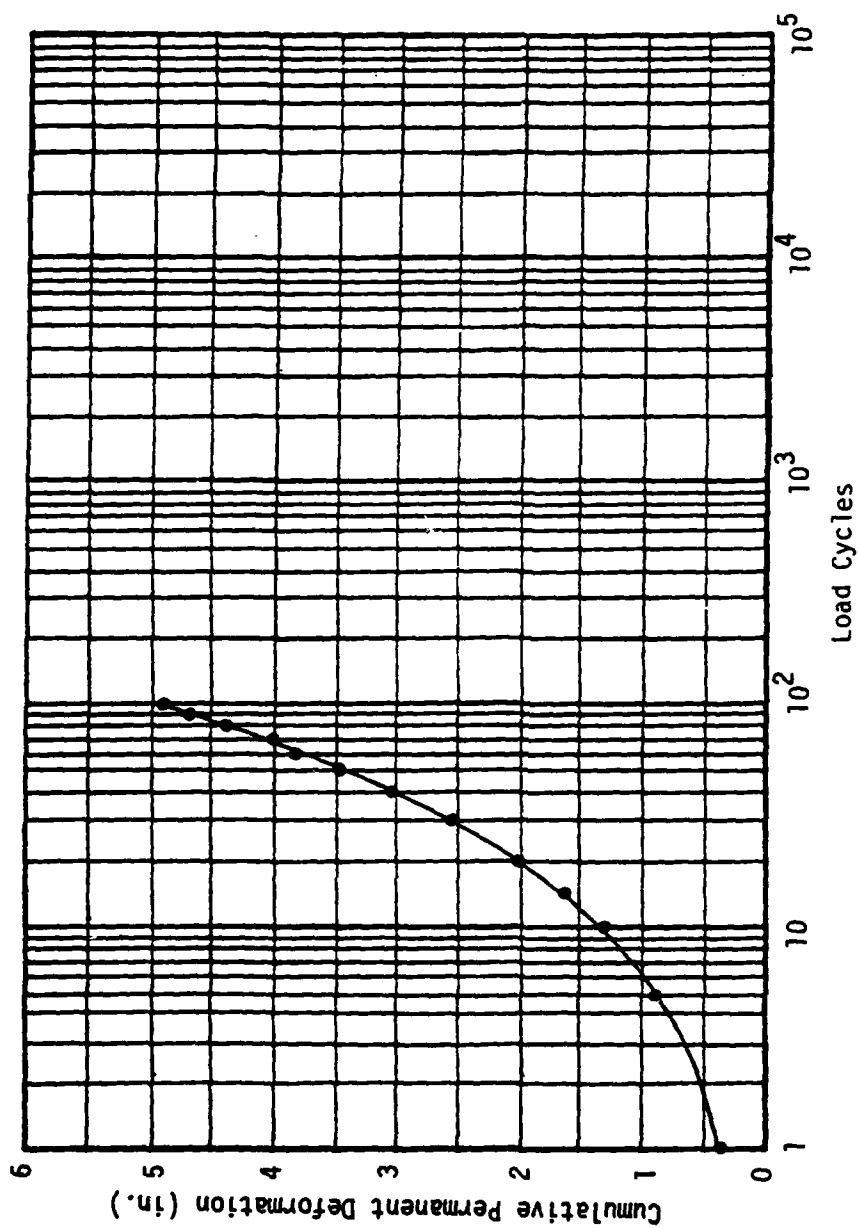


Figure E-1. Load Cycle-Cumulative Permanent Deformation Relationship, Test No. 1B (6.0 in. Stone/None/Unsoaked CBR = 0.38).

Table E-2. Load Cycle-Deformation Relationships, Test No. 2B (6.0 in. Stone/T-3401/Unsoaked CBR = 0.39).

<u>Load Cycles</u>	<u>Total Deformation Per Cycle (in.)</u>	<u>Cumulative Permanent Deformation (in.)</u>
1	--	0.246
5	0.42	0.533
10	0.38	0.914
15	0.36	1.089
20	0.34	1.287
30	0.34	1.591
40	0.35	1.886
50	0.32	2.061
60	0.30	2.194
70	0.32	2.329
80	0.34	2.493
90	0.38	2.606
100	0.37	2.708
200	0.34	3.424
300	0.32	3.976
400	0.32	4.175
500	0.36	4.502
600	0.38	4.681
700	0.39	4.972

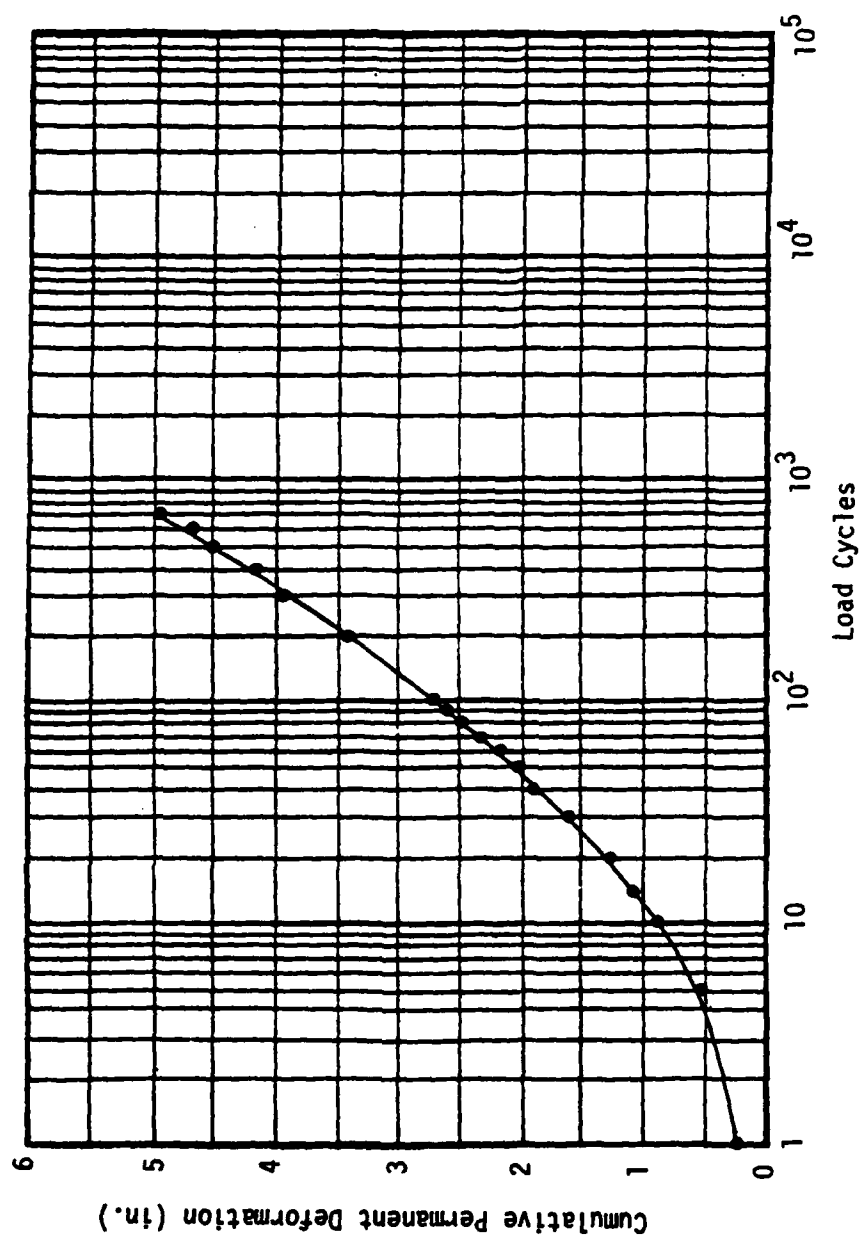


Figure E-2. Load Cycle-Cumulative Permanent Deformation Relationship, Test No. 2B (6.0 in. Stone/T-3401/Unsoaked CBR = 0.39).

Table E-3. Load Cycle-Deformation Relationships, Test No. 3B (7.5 in. Stone/None/Unsoaked CBR = 0.43).

<u>Load Cycles</u>	<u>Total Deformation Per Cycle (in.)</u>	<u>Cumulative Permanent Deformation (in.)</u>
1	--	0.231
5	0.25	0.565
10	0.24	0.775
15	0.24	0.997
20	0.25	1.247
30	0.24	1.524
40	0.23	1.801
50	0.24	2.005
60	0.24	2.184
70	0.22	2.346
80	0.23	2.449
90	0.22	2.618
100	0.21	2.765
200	0.20	3.441
300	0.19	3.921
400	0.20	4.289
500	0.21	4.576
600	0.22	4.812

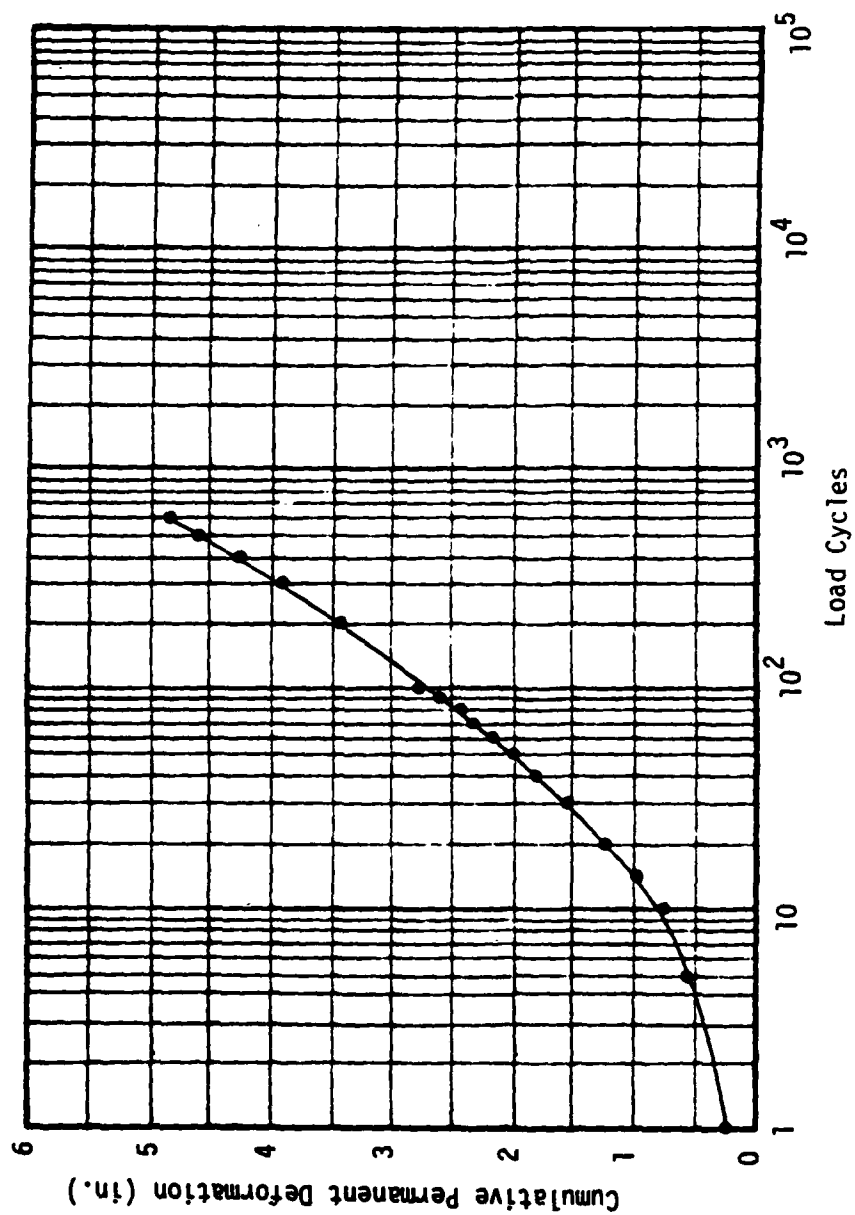


Figure E-3. Load Cycle-Cumulative Permanent Deformation Relationship, Test No. 3B (7.5 in. Stone/None/Unsoaked CBR = 0.43).

Table E-4. Load Cycle-Deformation Relationships, Test No. 4B (7.5 in. Stone/T-3401/Unsoaked CBR = 0.41).

<u>Load Cycles</u>	<u>Total Deformation Per Cycle (in.)</u>	<u>Cumulative Permanent Deformation (in.)</u>
1	--	0.159
5	0.28	0.350
10	0.23	0.486
15	0.25	0.581
20	0.24	0.722
30	0.23	0.899
40	0.24	1.094
50	0.26	1.317
60	0.23	1.401
70	0.24	1.582
80	0.24	1.634
90	0.23	1.735
100	0.22	1.834
200	0.21	2.562
300	0.22	3.072
400	0.23	3.370
500	0.24	3.520
600	0.22	3.665
700	0.21	3.810
800	0.20	3.962
900	0.22	4.049
1000	0.23	4.121
2000	0.21	4.497
3000	0.20	4.697

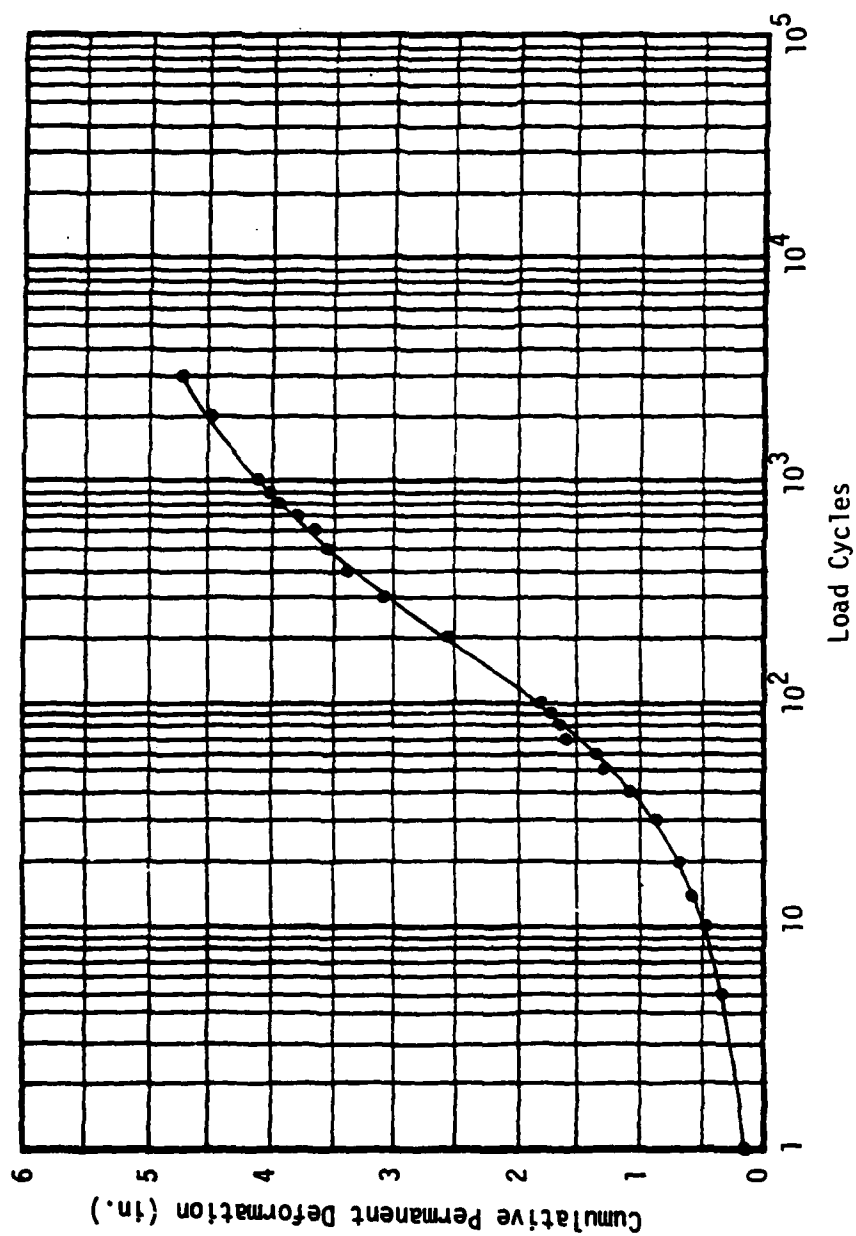


Figure E-4. Load Cycle-Cumulative Permanent Deformation Relationship, Test No. 4B (7.5 in. Stone/T-3401/Unsoaked CBR = 0.41).

Table E-5. Load Cycle-Deformation Relationships, Test No. 5B (9.0 in. Stone/None/Unsoaked CBR = 0.40).

<u>Load Cycles</u>	<u>Total Deformation Per Cycle (in.)</u>	<u>Cumulative Permanent Deformation (in.)</u>
1	--	0.157 ^
5	0.24	0.418
10	0.23	0.598
15	0.21	0.724
20	0.20	0.801
30	0.19	0.982
40	0.19	1.117
50	0.18	1.206
60	0.18	1.294
70	0.17	1.416
80	0.18	1.477
90	0.17	1.541
100	0.16	1.623
200	0.15	2.159
300	0.15	2.502
400	0.16	2.753
500	0.16	3.018
600	0.15	3.259
700	0.17	3.486
800	0.17	3.264
900	0.18	3.741
1000	0.19	3.929
2000	0.19	4.788

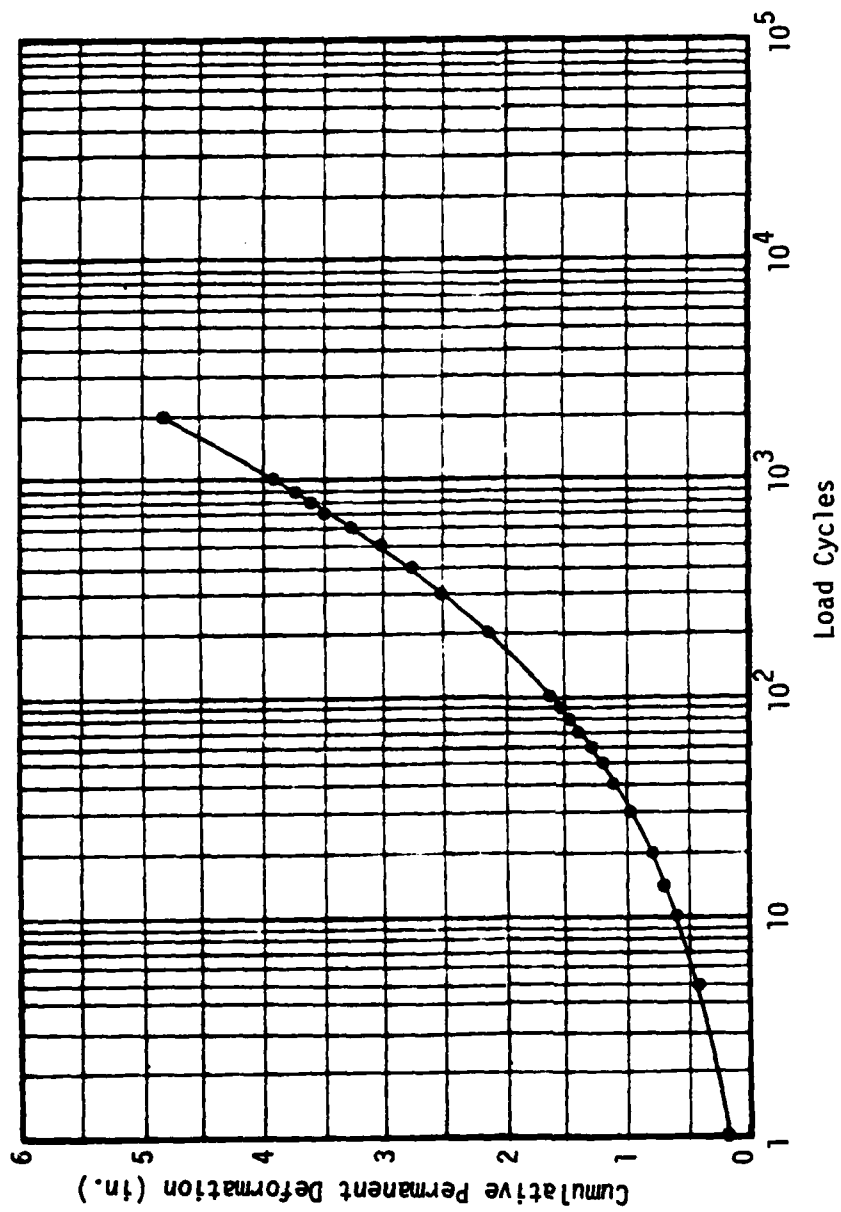


Figure E-5. Load Cycle-Cumulative Permanent Deformation Relationship, Test No. 5B (9.0 in. Stone/None/Unsoaked CBR = 0.40).

Table E-6. Load Cycle-Deformation Relationships, Test No. 6B (9.0 in. Stone/T-3401/Unsoaked CBR = 0.41).

<u>Load Cycles</u>	<u>Total Deformation Per Cycle (in.)</u>	<u>Cumulative Permanent Deformation (in.)</u>
1	--	0.133
5	0.20	0.275
10	0.17	0.321
15	0.18	0.364
20	0.17	0.456
30	0.17	0.643
40	0.17	0.731
50	0.16	0.771
60	0.17	0.855
70	0.16	0.926
80	0.16	0.983
90	0.15	1.040
100	0.15	1.077
200	0.14	1.313
300	0.13	1.502
400	0.12	1.654
500	0.13	1.765
600	0.13	1.835
700	0.11	1.875
800	0.12	1.969
900	0.12	2.034
1000	0.12	2.083
2000	0.12	2.501
3000	0.11	2.637
4000	0.13	2.777
5000	0.14	2.978
10000	0.13	3.502
15000	0.11	3.653
20000	0.10	3.756

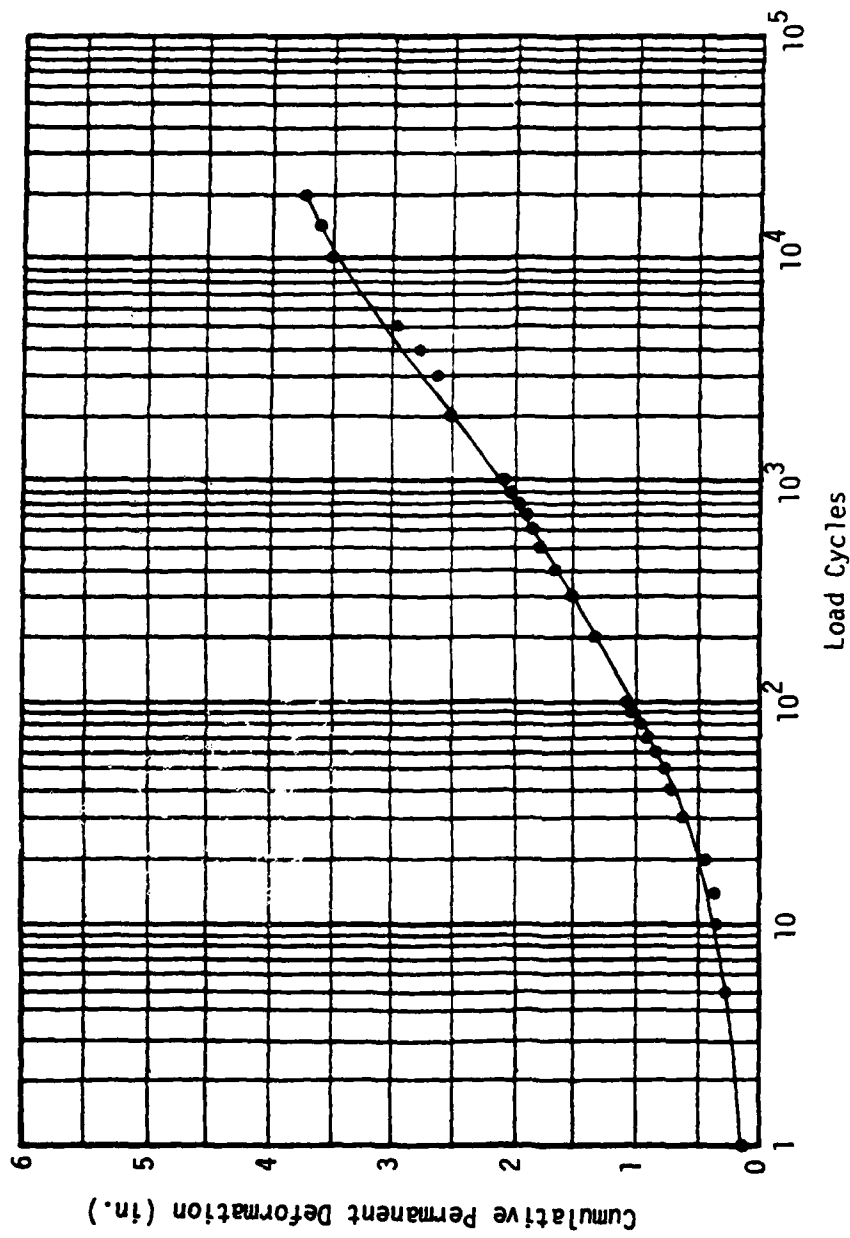


Figure E-6. Load Cycle-Cumulative Permanent Deformation Relationship, Test No. 6B (9.0 in. Stone/T-3401/Unsoaked CBR = 0.41).

Table E-7. Load Cycle-Deformation Relationships, Test No. 7A (4.5 in. Stone/None/Unsoaked CBR = 0.88).

<u>Load Cycles</u>	<u>Total Deformation Per Cycle (in.)</u>	<u>Cumulative Permanent Deformation (in.)</u>
1	--	1.595
2	--	1.996
3	--	2.214
4	--	2.940
5	--	3.544
6	--	3.858
7	--	4.092
8	--	4.374
9	--	4.586
10	--	4.731

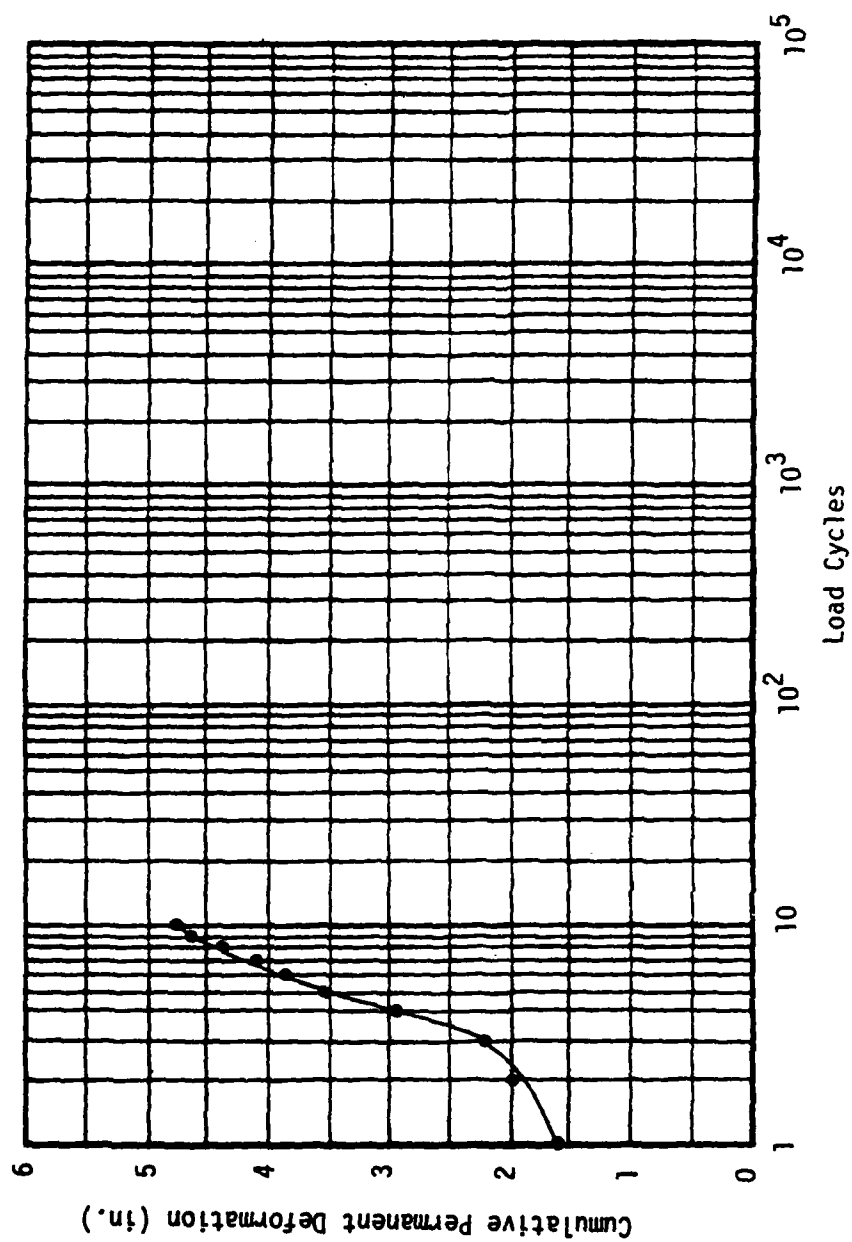


Figure E-7. Load Cycle-Cumulative Permanent Deformation Relationship, Test No. 7A (4.5 in. Stone/None/Unsoaked CBR = 0.88).

Table E-8. Load Cycle-Deformation Relationships, Test No. 7B (4.5 in. Stone/None/Unsoaked CBR = 0.91).

<u>Load Cycles</u>	<u>Total Deformation Per Cycle (in.)</u>	<u>Cumulative Permanent Deformation (in.)</u>
1	--	0.481
5	--	1.188
10	--	1.794
15	--	2.147
20	--	2.493
30	--	3.059
40	--	3.432
50	--	3.768
60	--	4.118
70	--	4.324
80	--	4.467
90	--	4.634
100	--	4.790

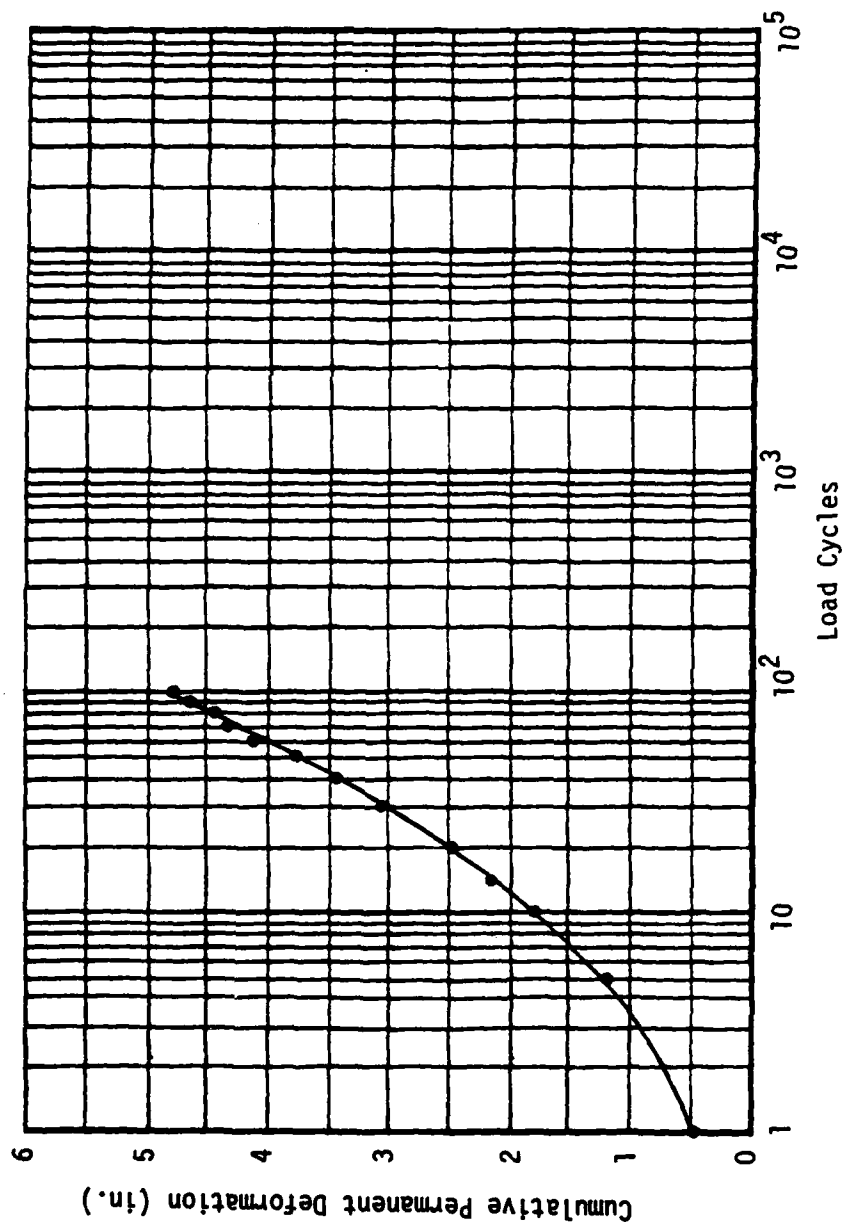


Figure E-8. Load Cycle-Cumulative Permanent Deformation Relationship, Test No. 7B (4.5 in. Stone/None/Unsoaked CBR ≈ 0.91).

Table E-9. Load Cycle-Deformation Relationships, Test No. 8A (4.5 in. Stone/Sand/Unsoaked CBR = 0.97).

<u>Load Cycles</u>	<u>Total Deformation Per Cycle (in.)</u>	<u>Cumulative Permanent Deformation (in.)</u>
1	--	1.266
2	0.97	1.676
3	0.88	2.459
4	0.73	2.975
5	0.64	3.269
6	0.62	3.773
7	0.55	4.092
8	0.51	4.297
9	0.48	4.451
10	0.45	4.575
11	0.45	4.662
12	0.42	4.749

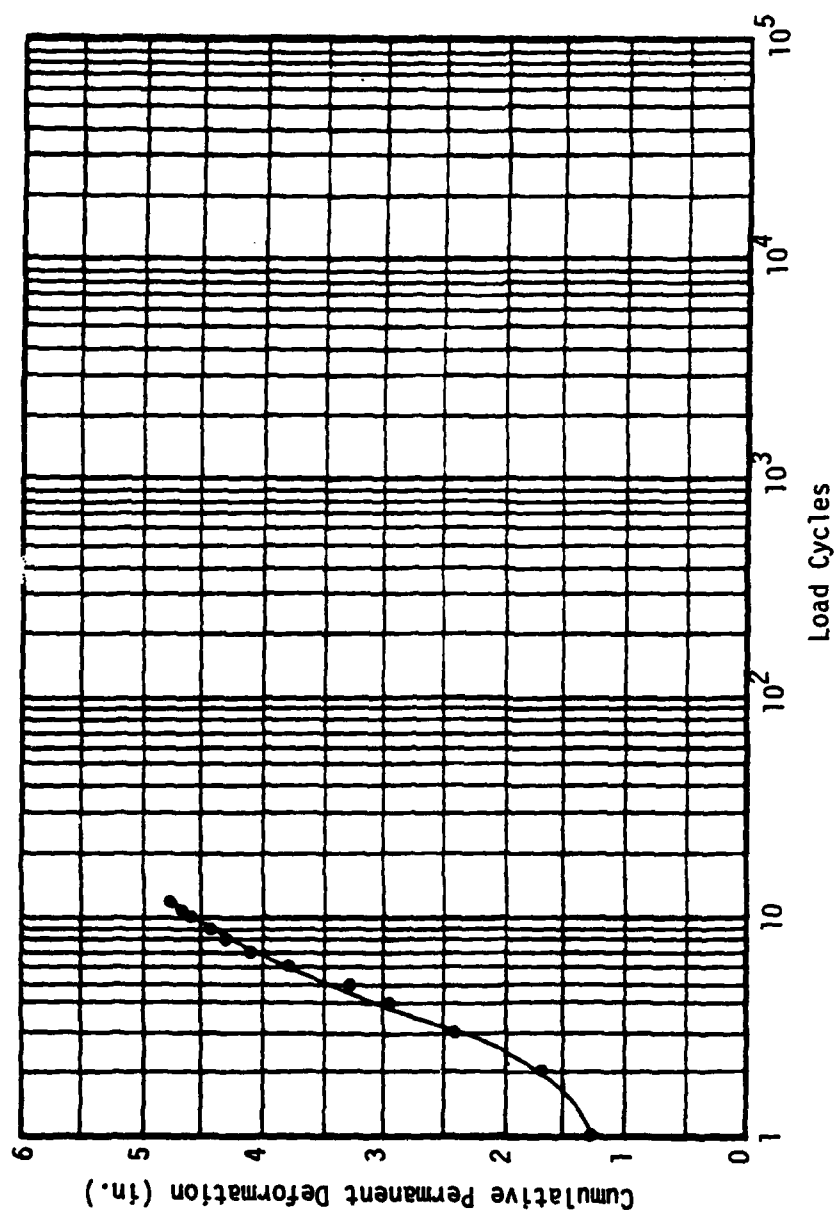


Figure E-9. Load Cycle-Cumulative Permanent Deformation Relationship, Test No. 8A (4.5 in. Stone/Sand/Unsoaked CBR = 0.97).

Table E-10. Load Cycle-Deformation Relationships, Test No. 9A (4.5 in. Stone/T-3401/Unsoaked CBR = 0.86).

<u>Load Cycles</u>	<u>Total Deformation Per Cycle (in.)</u>	<u>Cumulative Permanent Deformation (in.)</u>
1	--	0.601
5	0.48	1.365
10	0.38	1.639
15	0.36	1.778
20	0.36	2.000
30	0.38	2.311
40	0.40	2.432
50	0.43	2.668
60	0.39	2.842
70	0.36	2.989
80	0.36	3.102
90	0.36	3.195
100	0.36	3.278
200	0.35	4.021
300	0.41	5.029

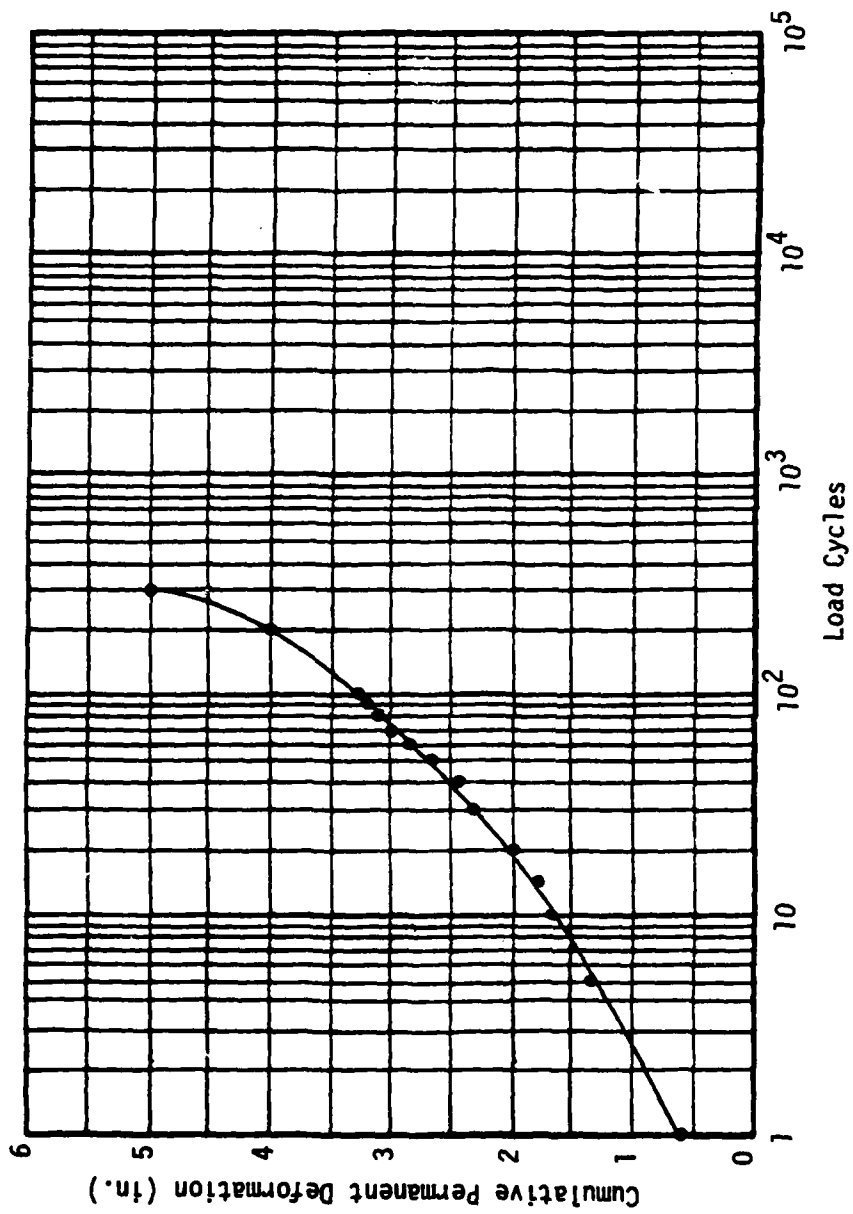


Figure E-10. Load Cycle-Cumulative Permanent Deformation Relationship, Test No. 9A (4.5 in. Stone/T-3401/Unsoaked CBR = 0.86).

Table E-11. Load Cycle-Deformation Relationships, Test No. 9B (4.5 in. Stone/T-3401/Unsoaked CBR = 0.89).

<u>Load Cycles</u>	<u>Total Deformation Per Cycle (in.)</u>	<u>Cumulative Permanent Deformation (in.)</u>
1	--	0.288
5	0.42	0.726
10	0.40	0.917
15	0.38	1.191
20	0.35	1.422
30	0.35	1.619
40	0.34	1.748
50	0.32	1.970
60	0.32	2.112
70	0.30	2.225
80	0.28	2.310
90	0.31	2.405
100	0.32	2.463
200	0.32	2.976
300	0.34	3.399
400	0.35	3.741
500	0.35	3.956
600	0.35	4.366
700	0.36	4.956

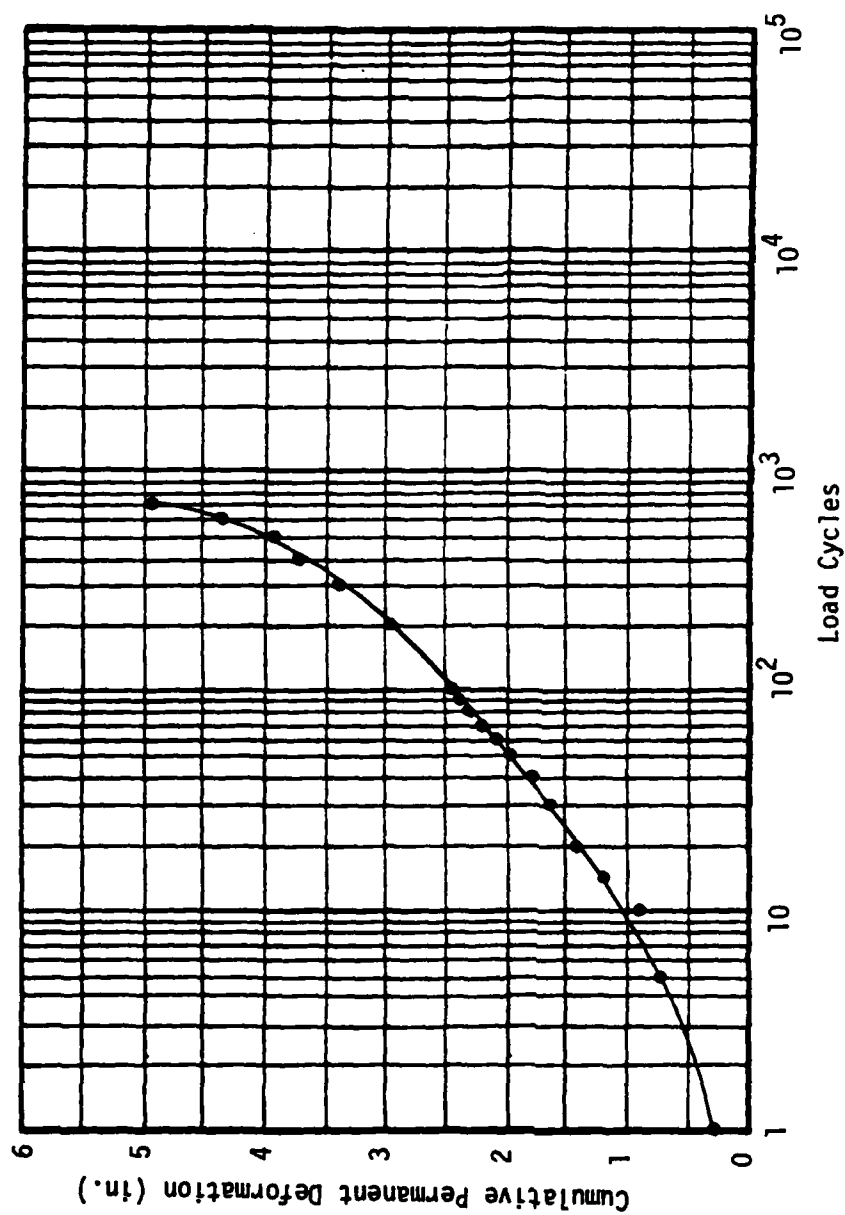


Figure E-11. Load Cycle-Cumulative Permanent Deformation Relationship, Test No. 9B (4.5 in. Stone/T-3401/Unsoaked CBR = 0.89).

Table E-12. Load Cycle-Deformation Relationships, Test No. 10A (4.5 in Stone/T-3601/Unsoaked CBR = 0.85).

<u>Load Cycles</u>	<u>Total Deformation Per Cycle (in.)</u>	<u>Cumulative Permanent Deformation (in.)</u>
1	--	0.513
5	0.47	1.062
10	0.44	1.430
15	0.41	1.696
20	0.39	1.833
30	0.38	2.058
40	0.41	2.307
50	0.38	2.638
60	0.36	2.874
70	0.36	3.012
80	0.38	3.126
90	0.39	3.240
100	0.38	3.325
200	0.38	3.893
300	0.41	4.182
400	0.43	4.384
500	0.41	4.644
600	0.39	4.753

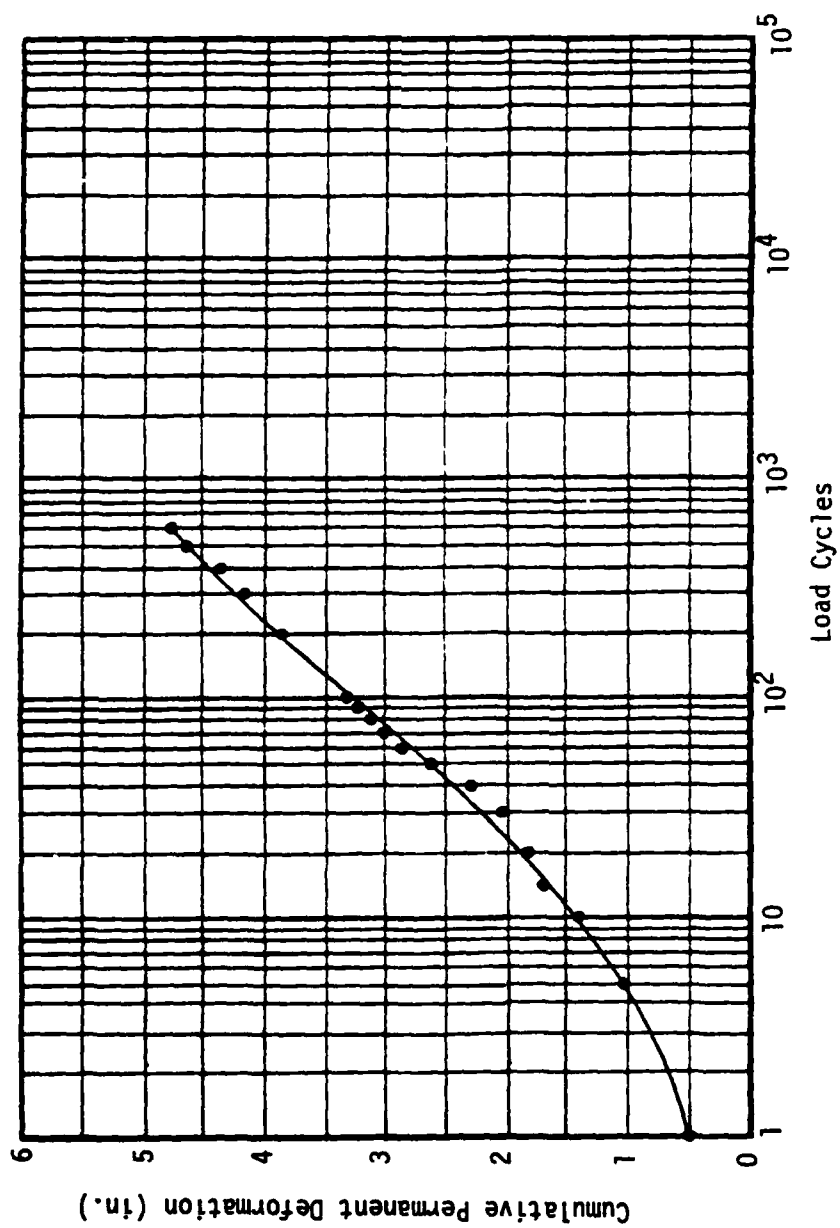


Figure E-12. Load Cycle-Cumulative Permanent Deformation Relationship, Test No. 10A (4.5 in. Stone/T-3601/Unsoaked CBR = 0.85).

Table E-13. Load Cycle-Deformation Relationships, Test No. 11A (4.5 in. Stone/M-140/Unsoaked CBR = 0.75).

<u>Load Cycles</u>	<u>Total Deformation Per Cycle (in.)</u>	<u>Cumulative Permanent Deformation (in.)</u>
1	--	0.898
5	0.67	1.953
10	0.54	2.574
15	0.54	3.002
20	0.51	3.371
30	0.48	3.717
40	0.50	4.054
50	0.53	4.326
60	0.55	4.474
70	0.48	4.613
80	0.51	4.793

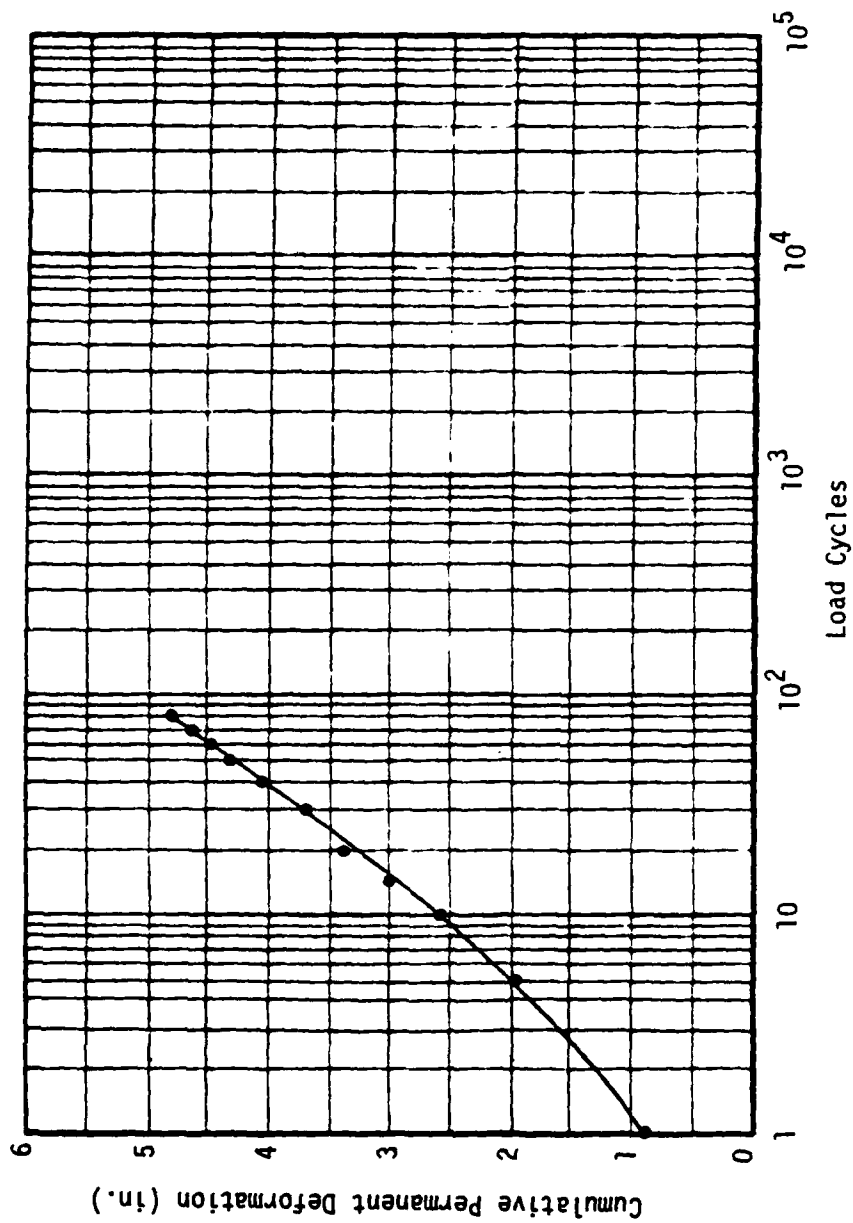


Figure E-13. Load Cycle-Cumulative Permanent Deformation Relationship, Test No. 11A (4.5 in. Stone/M-140/Unsoaked CBR = 0.75).

Table E-14. Load Cycle-Deformation Relationships, Test No. 12A (4.5 in. Stone/B-C22/Unsoaked CBR = 0.78).

<u>Load Cycles</u>	<u>Total Deformation Per Cycle (in.)</u>	<u>Cumulative Permanent Deformation (in.)</u>
1	--	0.677
5	0.58	1.689
10	0.54	2.408
15	0.48	2.682
20	0.46	2.985
30	0.42	3.502
40	0.48	3.823
50	0.51	4.106
60	0.49	4.398
70	0.47	4.553
80	0.45	4.753

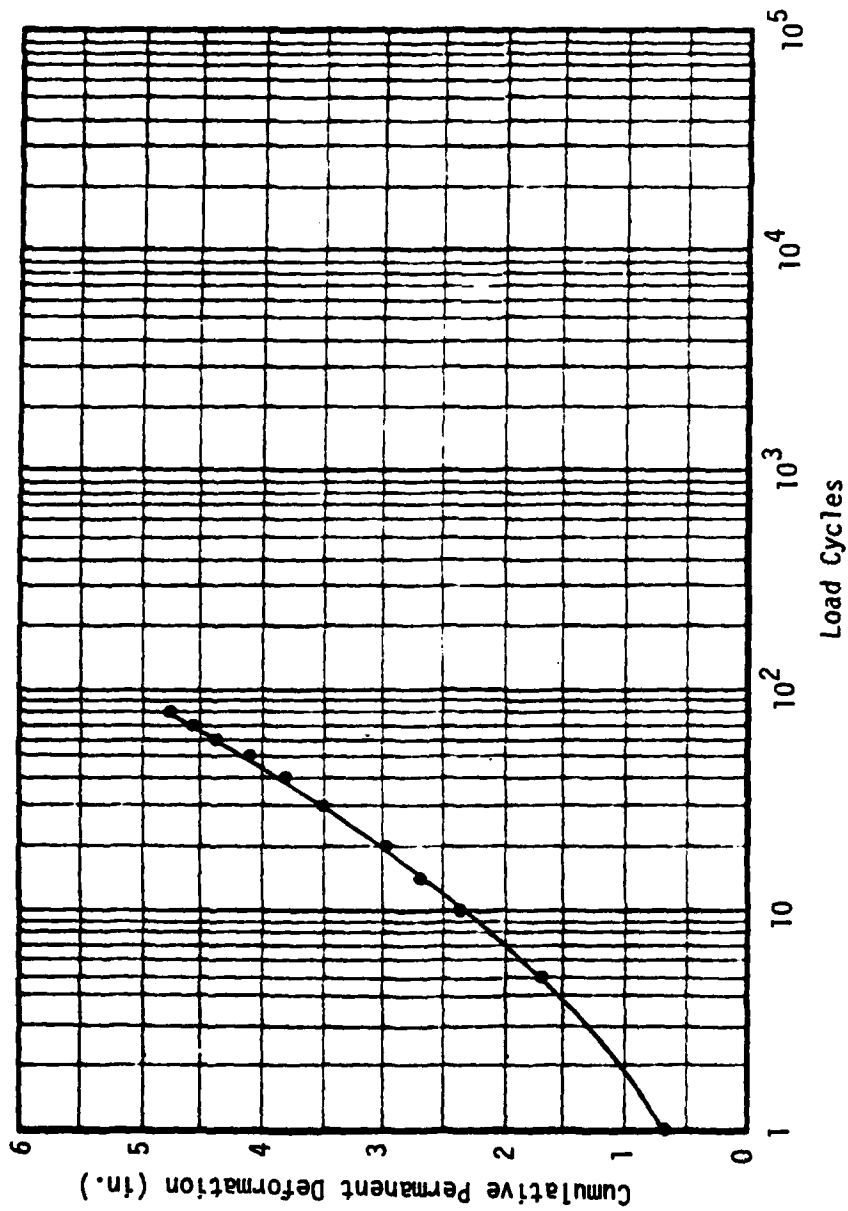


Figure E-14. Load Cycle-Cumulative Permanent Deformation Relationship, Test No. 12A (4.5 in. Stone/B-C22/Unsoaked CBR = 0.78).

Table E-15. Load Cycle-Deformation Relationships, Test No. 13A (7.0 in. Stone/None/Unsoaked CBR = 0.82).

<u>Load Cycles</u>	<u>Total Deformation Per Cycle (in.)</u>	<u>Cumulative Permanent Deformation (in.)</u>
1	--	0.495
5	--	1.401
10	--	2.560
15	--	3.407
20	--	4.697

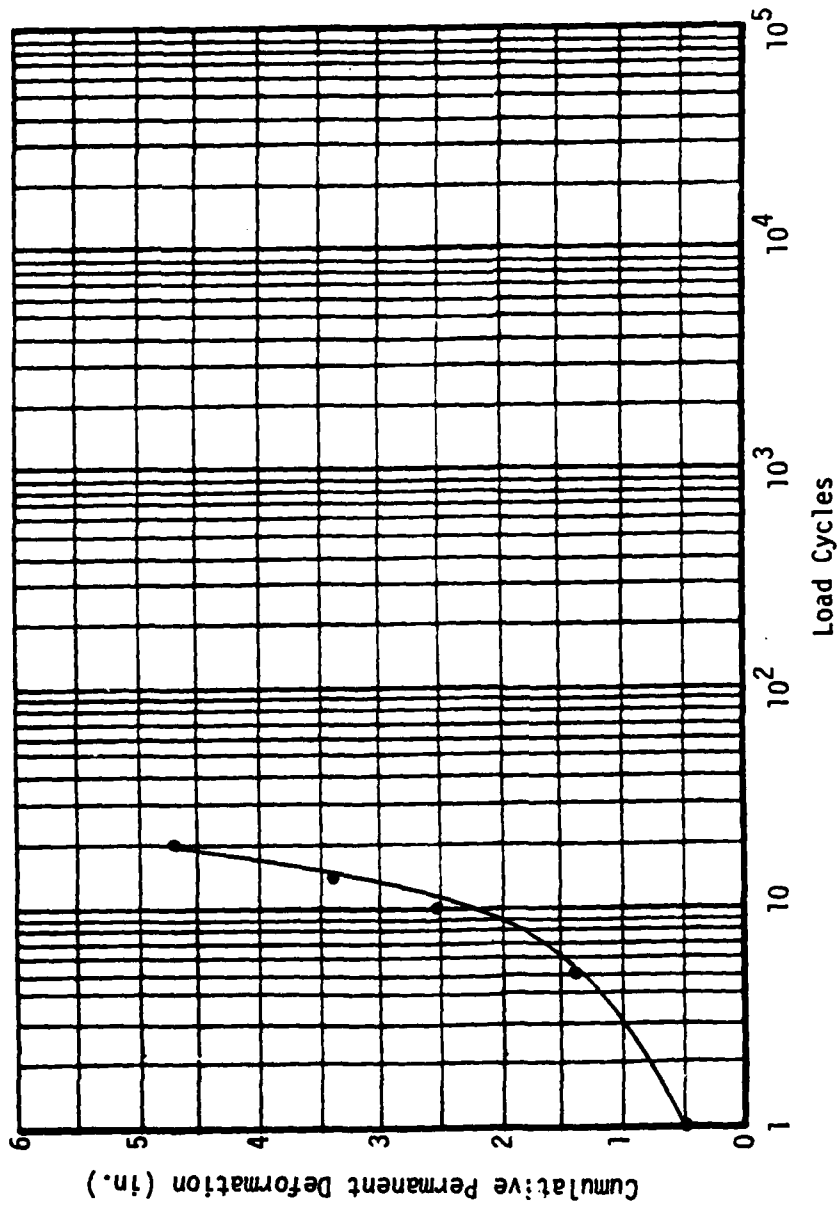


Figure E-15. Load Cycle-Cumulative Permanent Deformation Relationship, Test No. 13A (7.0 in. Stone/None/Unsoaked CBR = 0.82).

Table E-16. Load Cycle-Deformation Relationships, Test No. 13B (7.0 in. Stone/None/Unsoaked CBR = 0.81).

<u>Load Cycles</u>	<u>Total Deformation Per Cycle (in.)</u>	<u>Cumulative Permanent Deformation (in.)</u>
1	--	0.169
5	0.23	0.383
10	0.21	0.682
15	0.20	0.828
20	0.18	0.982
30	0.19	1.123
40	0.17	1.199
50	0.17	1.301
60	0.16	1.375
70	0.16	1.432
80	0.17	1.529
90	0.17	1.605
100	0.18	1.748
200	0.20	2.578
300	0.18	3.117
400	0.19	3.461
500	0.18	3.746
600	0.21	4.072
700	0.19	4.387
800	0.19	4.502
900	0.19	4.679

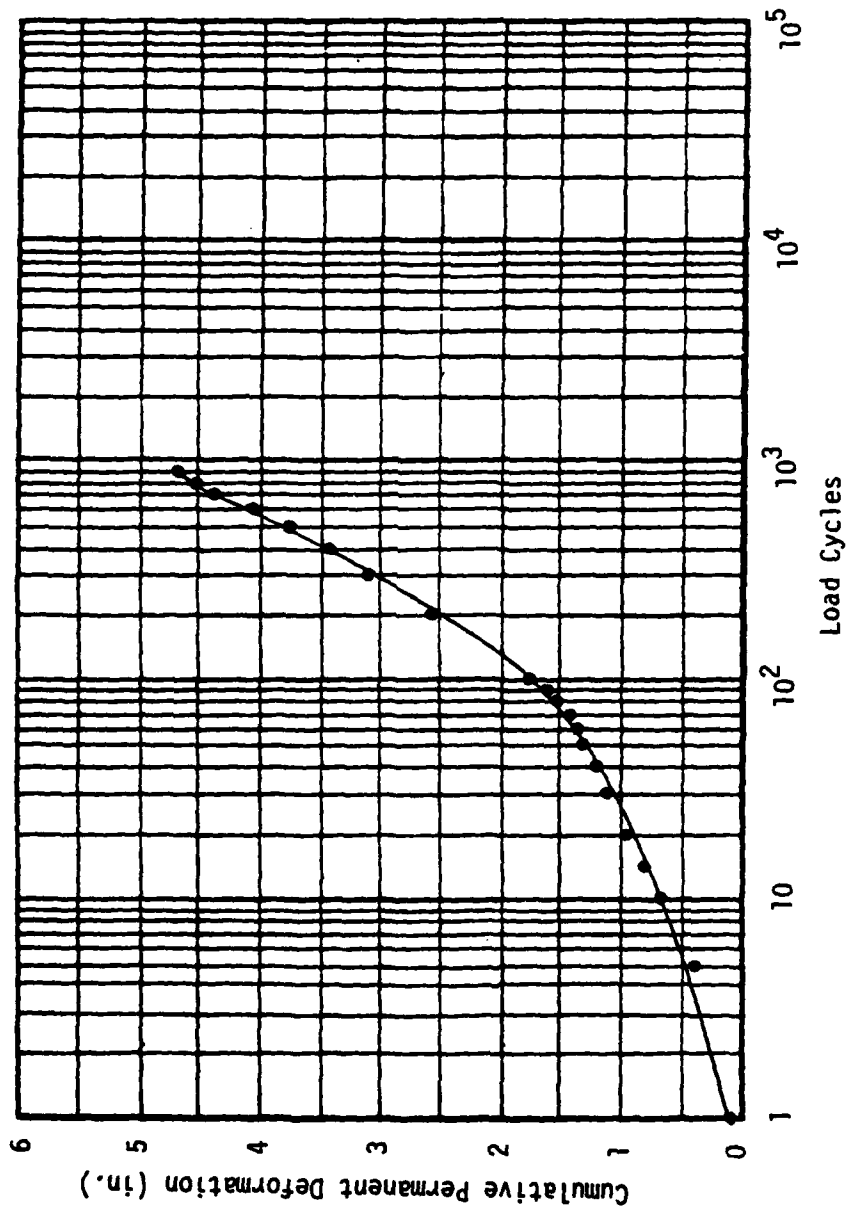


Figure E-16. Load Cycle-Cumulative Permanent Deformation Relationship, Test No. 138 (7.0 in. Stone/None/Unsoaked CBR = 0.81).

Table E-17. Load Cycle-Deformation Relationships, Test No. 14A (7.0 in. Stone/Sand/Unsoaked CBR = 0.81).

<u>Load Cycles</u>	<u>Total Deformation Per Cycle (in.)</u>	<u>Cumulative Permanent Deformation (in.)</u>
1	--	0.387
5	--	1.277
10	--	1.958
15	--	2.176
20	--	2.553
30	--	3.211
40	--	3.453
50	--	3.712
60	--	4.017
70	--	4.295
80	--	4.433
90	--	4.616
100	--	4.753

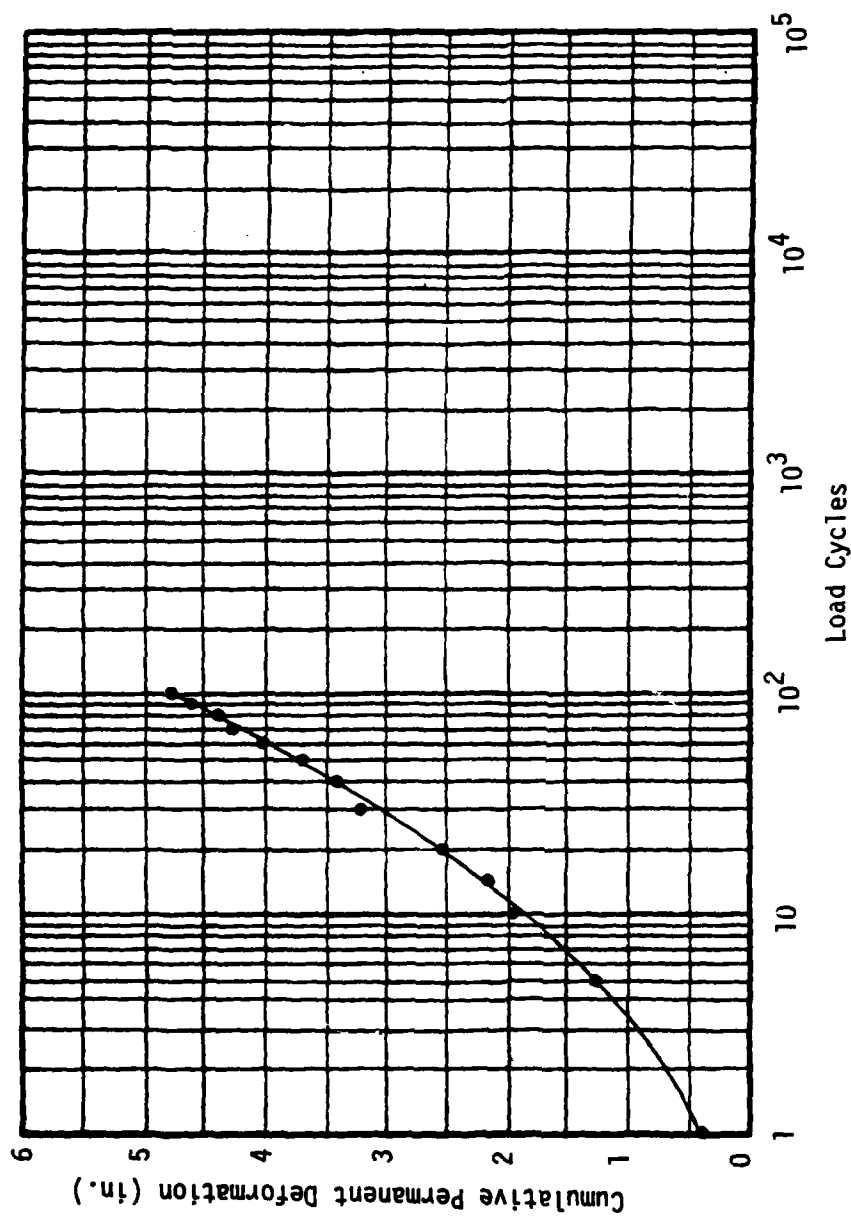


Figure E-17. Load Cycle-Cumulative Permanent Deformation Relationship, Test No. 14A (7.0 in. Stone/Sand/Unsoaked CBR = 0.81).

Table E-18. Load Cycle-Deformation Relationships, Test No. 15A (7.0 in. Stone/T-3401/Unsoaked CBR = 0.94).

<u>Load Cycles</u>	<u>Total Deformation Per Cycle (in.)</u>	<u>Cumulative Permanent Deformation (in.)</u>
1	--	0.257
5	0.27	0.676
10	0.24	0.864
15	0.23	0.998
20	0.22	1.176
30	0.20	1.429
40	0.19	1.551
50	0.20	1.706
60	0.19	1.794
70	0.18	1.912
80	0.19	2.026
90	0.19	2.106
100	0.18	2.165
200	0.17	2.618
300	0.17	3.021
400	0.18	3.212
500	0.17	3.361
600	0.17	3.448
700	0.18	3.583
800	0.17	3.672
900	0.17	3.739
1000	0.17	3.789
2000	0.17	4.139
3000	0.17	4.462
4000	0.16	4.733

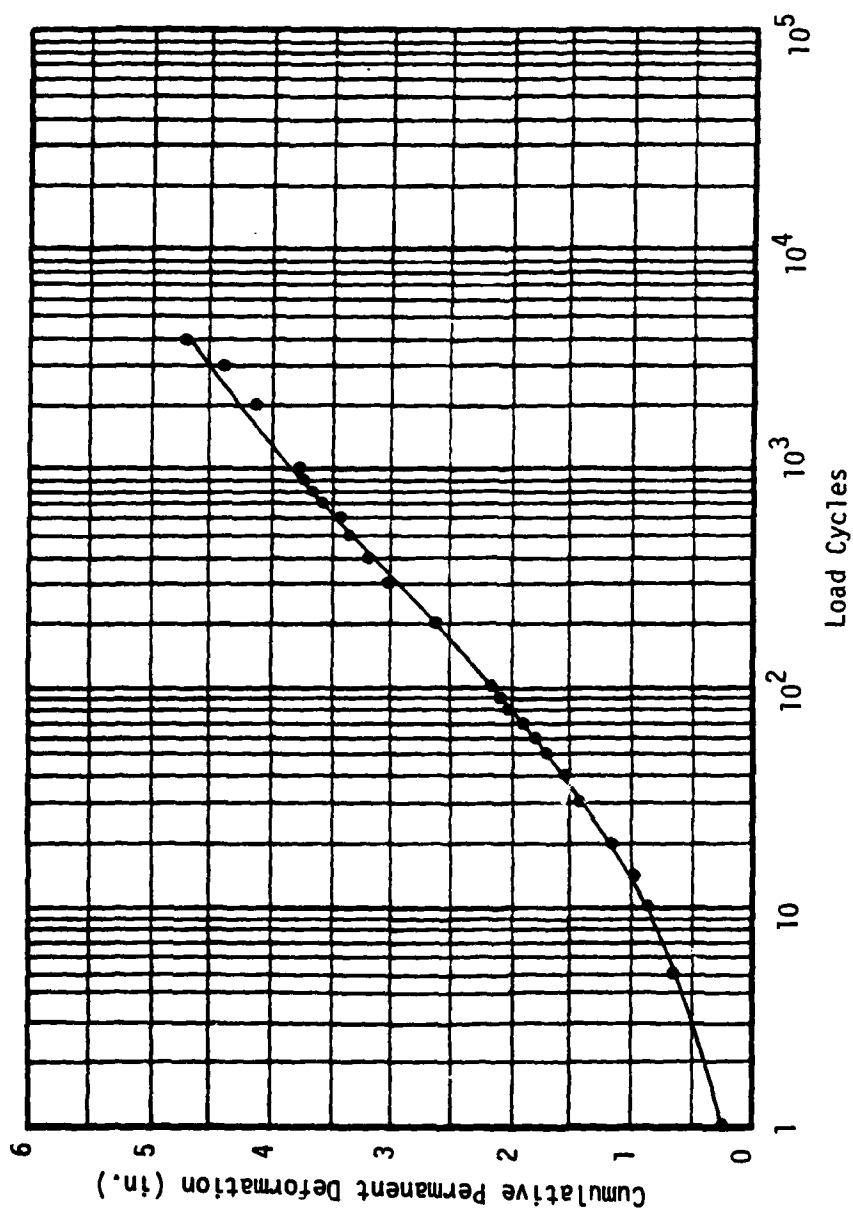


Figure E-18. Load Cycle-Cumulative Permanent Deformation Relationship, Test No. 15A (7.0 in. Stone/T-3401/Unsoaked CBR = 0.94).

Table E-19. Load Cycle-Deformation Relationships, Test No. 15B (7.0 in. Stone/T-3401/Unsoaked CBR = 0.78).

<u>Load Cycles</u>	<u>Total Deformation Per Cycle (in.)</u>	<u>Cumulative Permanent Deformation (in.)</u>
1	--	0.196
5	0.24	0.364
10	0.22	0.402
15	0.21	0.501
20	0.21	0.576
30	0.19	0.681
40	0.18	0.744
50	0.16	0.912
60	0.16	0.948
70	0.16	1.046
80	0.17	1.088
90	0.16	1.176
100	0.16	1.279
200	0.14	1.705
300	0.12	2.188
400	0.14	2.474
500	0.15	2.782
600	0.13	2.901
700	0.13	3.245
800	0.12	3.294
900	0.13	3.471
1000	0.14	3.715
2000	0.13	4.147
3000	0.12	4.315
4000	0.11	4.504
5000	0.11	4.639
6000	0.11	4.737

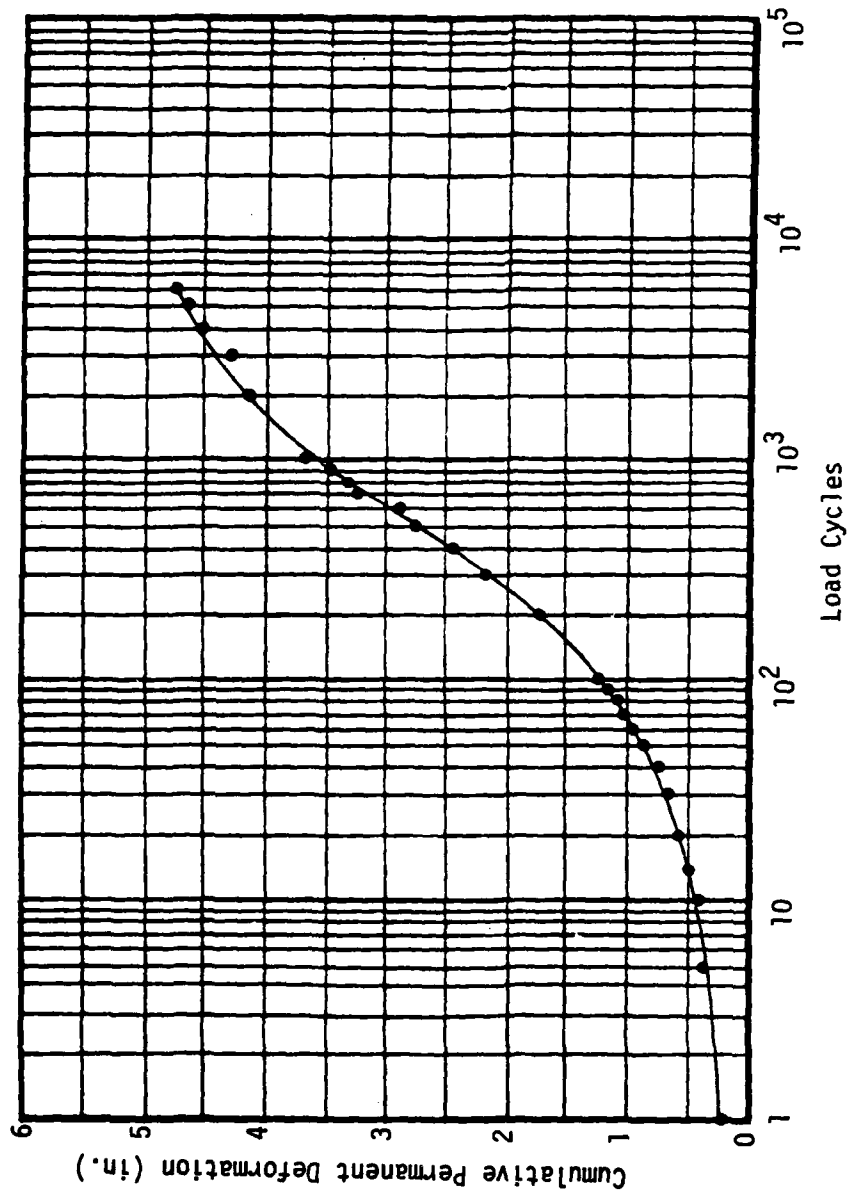


Figure E-19. Load Cycle-Cumulative Permanent Deformation Relationship, Test No. 15B (7.0 in. Stone/T-3401/Unsoaked CBR = 0.78).

Table E-20. Load Cycle-Deformation Relationships, Test No. 16A (7.0 in. Stone/T-3601/Unsoaked CBR = 0.74).

<u>Load Cycles</u>	<u>Total Deformation Per Cycle (in.)</u>	<u>Cumulative Permanent Deformation (in.)</u>
1	--	0.269
5	0.32	0.715
10	0.30	0.902
15	0.26	1.062
20	0.26	1.215
30	0.25	1.478
40	0.24	1.523
50	0.22	1.599
60	0.21	1.716
70	0.19	1.806
80	0.21	1.923
90	0.22	2.017
100	0.19	2.088
200	0.19	2.414
300	0.18	2.642
400	0.19	2.805
500	0.21	2.960
600	0.19	3.061
700	0.20	3.136
800	0.19	3.202
900	0.18	3.253
1000	0.18	3.346
2000	0.18	3.805
3000	0.19	4.141
4000	0.18	4.362
5000	0.19	4.547
6000	0.18	4.665
7000	0.17	4.788

AD-A110 434

AIR FORCE INST OF TECH WRIGHT-PATTERSON AFB OH
PERFORMANCE OF FABRIC REINFORCED AGGREGATE-SOIL SYSTEMS UNDER R--ETC(U)
DEC 81 W SCHAUZ
AFIT-CI-81-69D

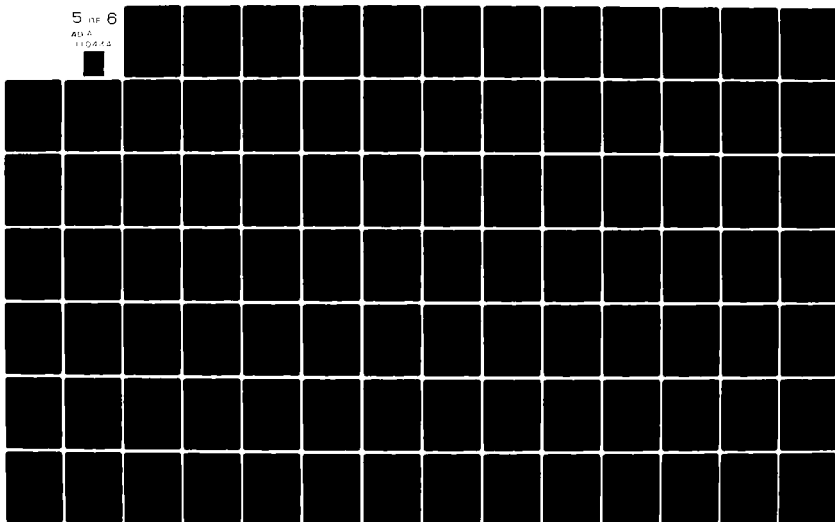
F/6 13/2

UNCLASSIFIED

NL

5 11F 6

AD-A
110614



1.0

1.8

2.5

2.2

1.1

2.0

1.8

1.25

1.4

1.6

MICROCOPY RESOLUTION TEST CHART
NATIONAL BUREAU OF STANDARDS-1963-A

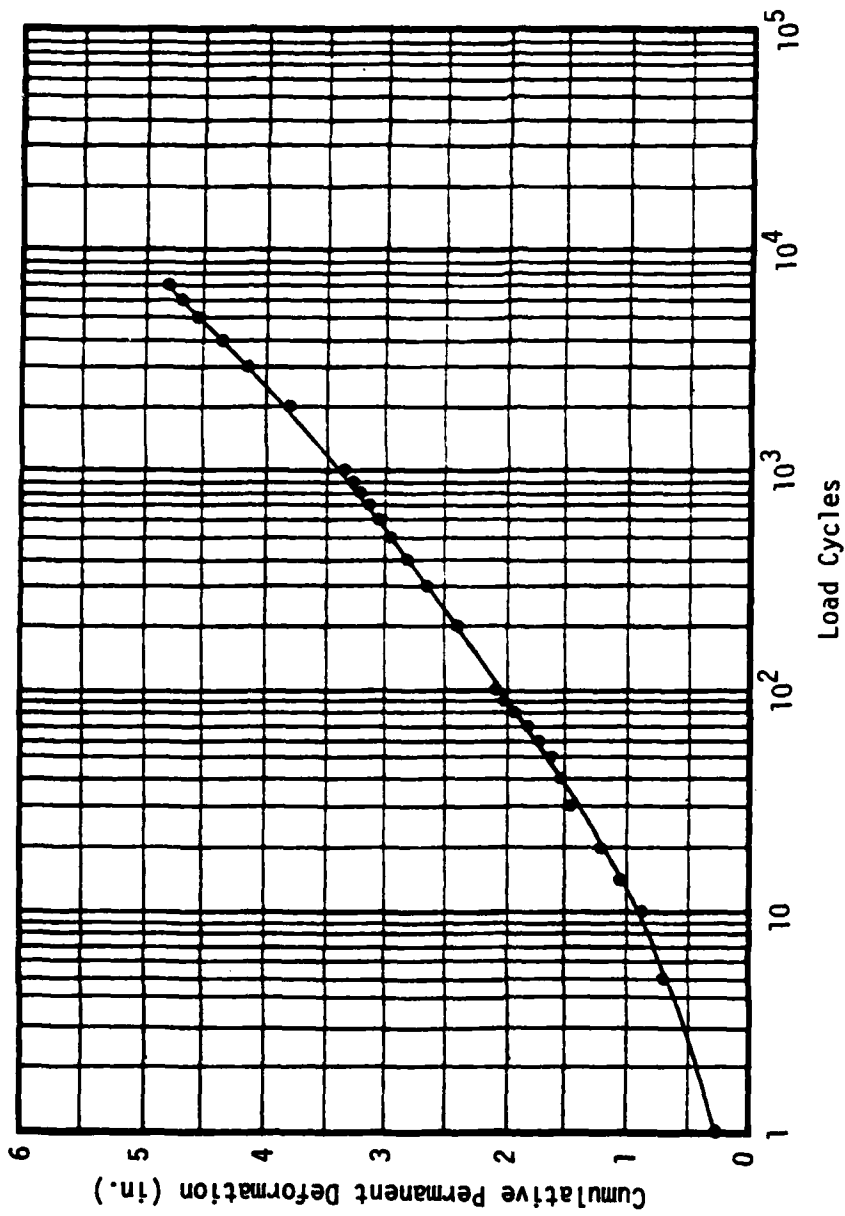


Figure E-20. Load Cycle-Cumulative Permanent Deformation Relationship, Test No. 16A (7.0 in. Stone/T-3601/Unsoaked CBR = 0.74).

Table E-21. Load Cycle-Deformation Relationships, Test No. 17A (7.0 in. Stone/M-140/Unsoaked CBR = 0.82).

<u>Load Cycles</u>	<u>Total Deformation Per Cycle (in.)</u>	<u>Cumulative Permanent Deformation (in.)</u>
1	--	0.519
5	0.32	1.136
10	0.32	1.429
15	0.29	1.618
20	0.27	1.765
30	0.24	2.069
40	0.22	2.336
50	0.21	2.496
60	0.23	2.602
70	0.23	2.706
80	0.23	2.908
90	0.22	3.062
100	0.23	3.123
200	0.24	3.657
300	0.26	4.258
400	0.28	4.780

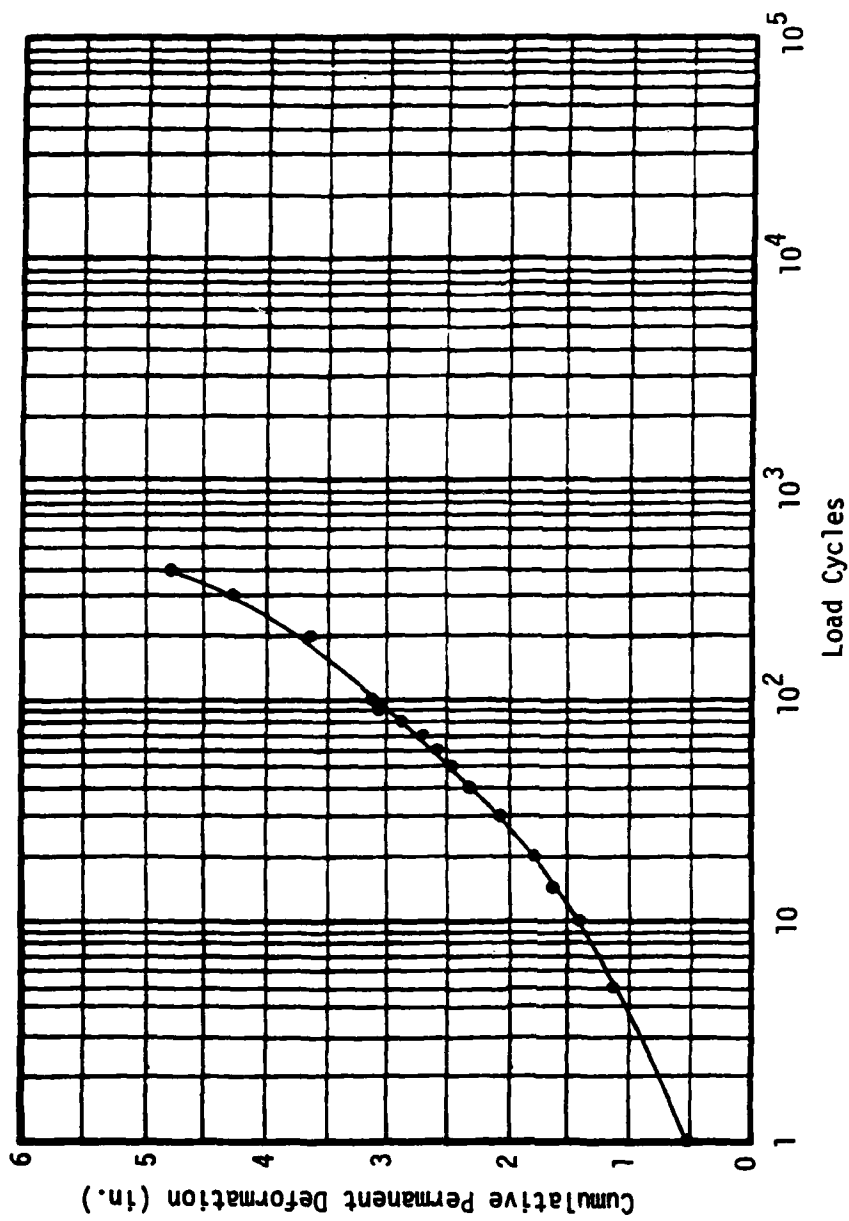


Figure E-21. Logarithmic-Cumulative Permanent Deformation Relationship, Test No. 17A (7.0 in. Stone/M-140/Unsoaked CBR = 0.82).

Table E-22. Load Cycle-Deformation Relationships, Test No. 18A (7.0 in. Stone/B-C22/Unsoaked CBR = 0.83).

<u>Load Cycles</u>	<u>Total Deformation Per Cycle (in.)</u>	<u>Cumulative Permanent Deformation (in.)</u>
1	--	0.459
5	0.32	0.899
10	0.29	1.206
15	0.25	1.412
20	0.25	1.676
30	0.23	2.118
40	0.24	2.441
50	0.23	2.735
60	0.23	2.921
70	0.22	3.171
80	0.23	3.418
90	0.23	3.559
100	0.22	3.712
200	0.20	4.212
300	0.19	4.409
400	0.18	4.506
500	0.17	4.605
600	0.19	4.748

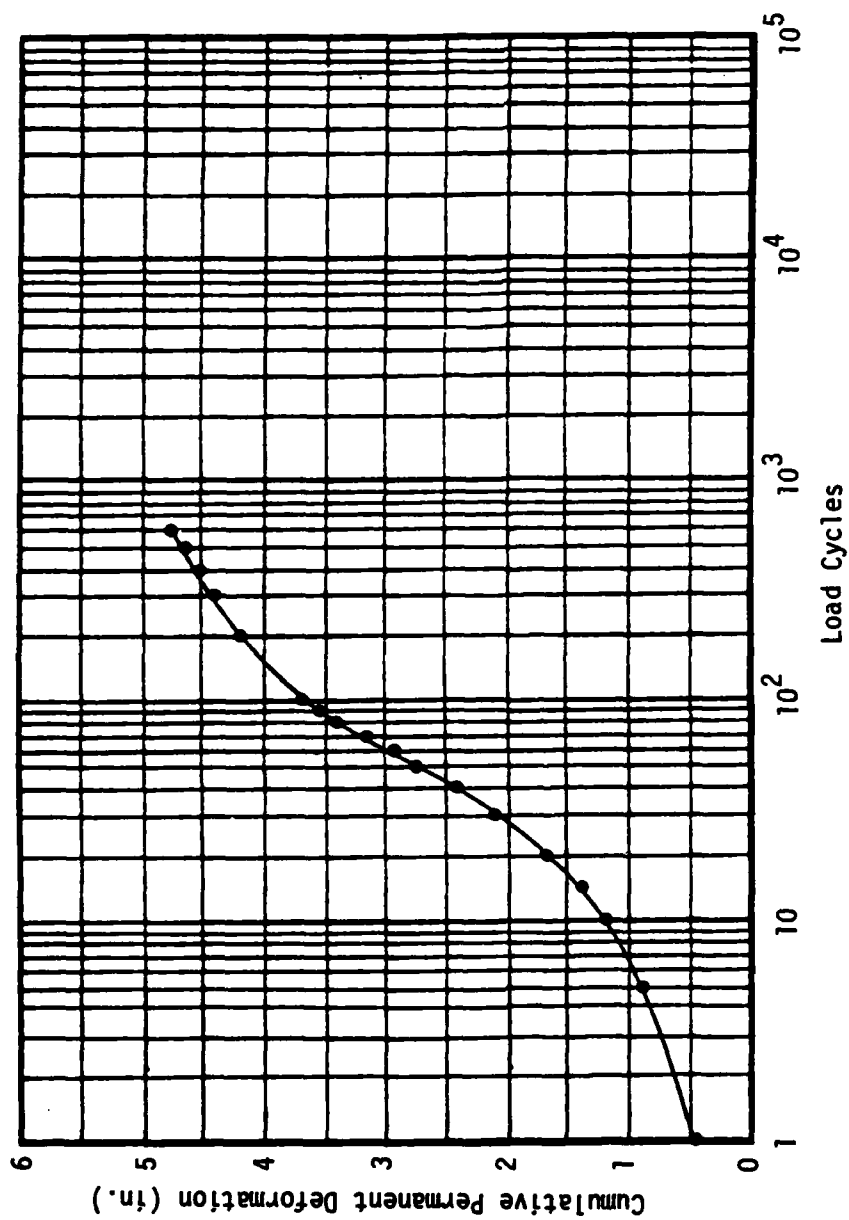


Figure E-22. Load Cycle-Cumulative Permanent Deformation Relationship, Test No. 18A (7.0 in. Stone/B-C22/Unsoaked CBR = 0.83).

Table E-23. Load Cycle-Deformation Relationships, Test No. 19A (10.0 in. Stone/None/Unsoaked CBR = 0.90).

<u>Load Cycles</u>	<u>Total Deformation Per Cycle (in.)</u>	<u>Cumulative Permanent Deformation (in.)</u>
1	--	0.295
5	0.139	0.556
10	0.128	0.632
15	0.122	0.689
20	0.124	0.761
30	0.113	0.889
40	0.109	0.964
50	0.106	1.019
60	0.100	1.068
70	0.096	1.129
80	0.096	1.155
90	0.093	1.181
100	0.091	1.202
200	0.089	1.334
300	0.091	1.502
400	0.089	1.602
500	0.085	1.676
600	0.083	1.727
700	0.078	1.773
800	0.076	1.808
900	0.072	1.836
1000	0.074	1.858
2000	0.072	2.014
3000	0.072	2.138
4000	0.074	2.205
5000	0.072	2.252
10000	0.069	2.368
15000	0.069	2.475
20000	0.065	2.566

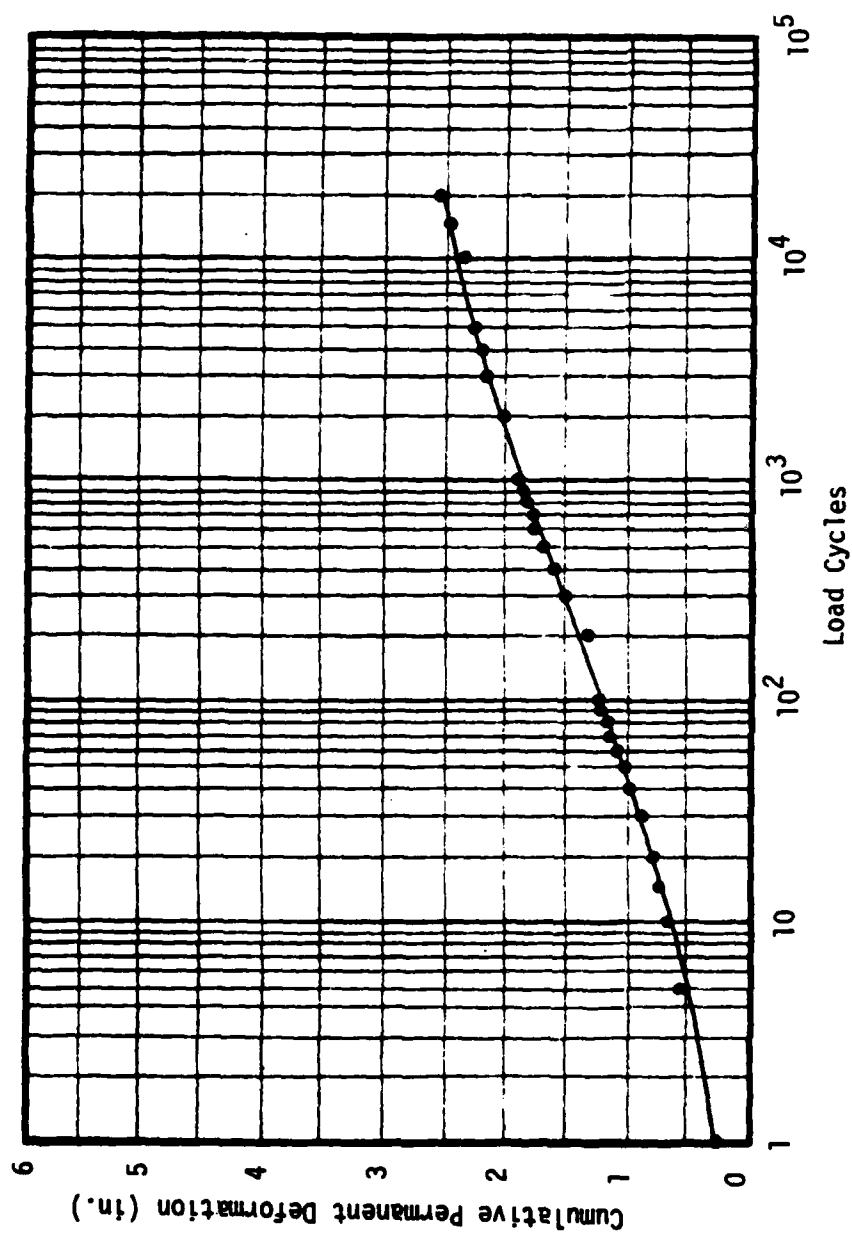


Figure E-23. Load Cycle-Cumulative Permanent Deformation Relationship, Test No. 19A (10.0 in. Stone/None/Unsoaked CBR = 0.90).

Table E-24. Load Cycle-Deformation Relationships, Test No. 19B (10.0 in. Stone/None/Unsoaked CBR = 0.93).

<u>Load Cycles</u>	<u>Total Deformation Per Cycle (in.)</u>	<u>Cumulative Permanent Deformation (in.)</u>
1	--	0.142
5	0.115	0.205
10	0.111	0.244
15	0.106	0.265
20	0.102	0.394
30	0.096	0.507
40	0.100	0.585
50	0.095	0.646
60	0.093	0.695
70	0.093	0.731
80	0.093	0.764
90	0.091	0.790
100	0.089	0.818
200	0.089	1.003
300	0.087	1.155
400	0.089	1.241
500	0.087	1.320
600	0.085	1.382
700	0.089	1.443
800	0.087	1.473
900	0.085	1.524
1000	0.083	1.611
2000	0.078	1.831
3000	0.076	2.045
4000	0.072	2.173
5000	0.069	2.229
10000	0.069	2.416
15000	0.067	2.452
20000	0.065	2.525

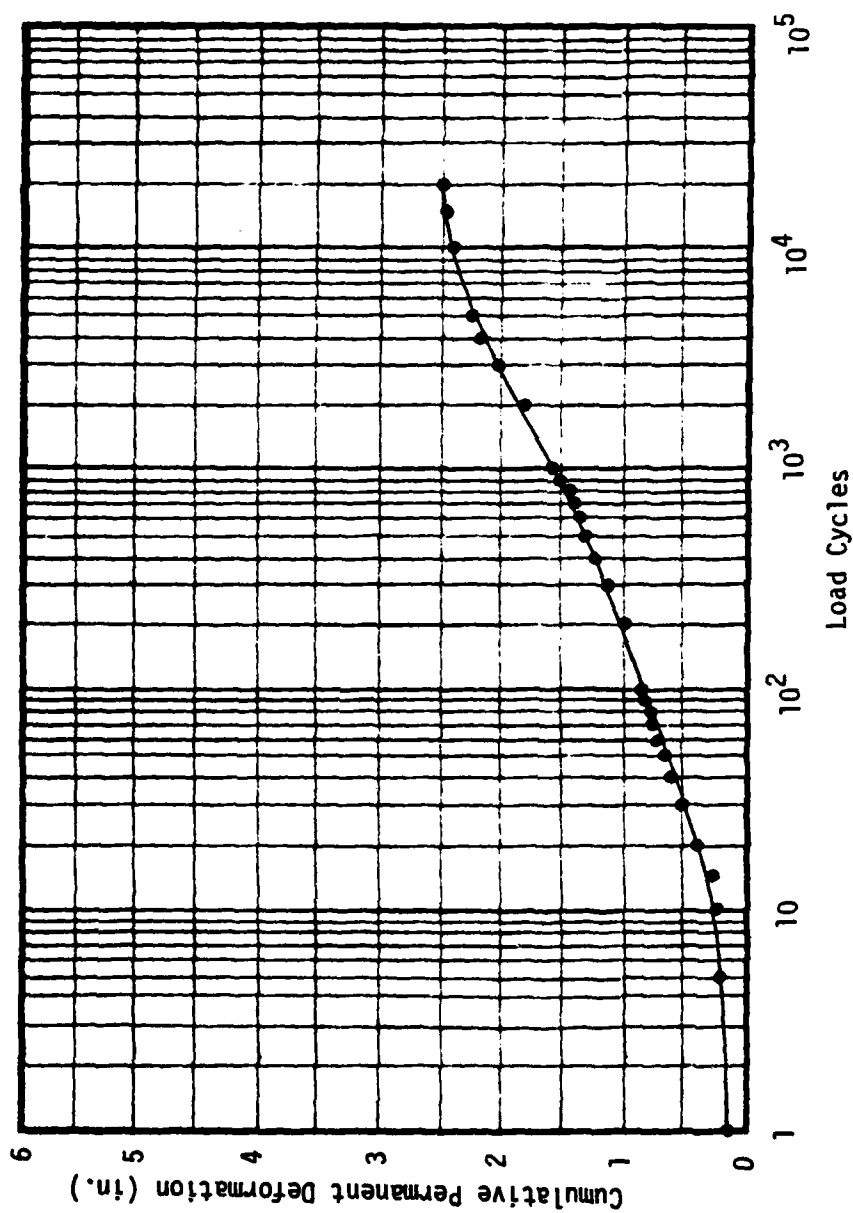


Figure E-24. Load Cycle-Cumulative Permanent Deformation Relationship, Test No. 19B (10.0 in. Stone/None/Unsoaked CBR = 0.93).

Table E-25. Load Cycle-Deformation Relationships, Test No. 20A (10.0 in. Stone/T-3401/Unsoaked CBR = 0.87).

<u>Load Cycles</u>	<u>Total Deformation Per Cycle (in.)</u>	<u>Cumulative Permanent Deformation (in.)</u>
1	--	0.206
5	0.128	0.332
10	0.118	0.429
15	0.109	0.485
20	0.106	0.573
30	0.106	0.637
40	0.102	0.705
50	0.100	0.747
60	0.096	0.799
70	0.096	0.857
80	0.096	0.909
90	0.091	0.964
100	0.093	0.991
200	0.091	1.178
300	0.089	1.242
400	0.091	1.315
500	0.089	1.401
600	0.087	1.464
700	0.083	1.499
800	0.085	1.539
900	0.085	1.566
1000	0.083	1.593
2000	0.078	1.786
3000	0.074	1.852
4000	0.076	1.898
5000	0.074	1.935
10000	0.072	2.006
15000	0.069	2.076
20000	0.069	2.150

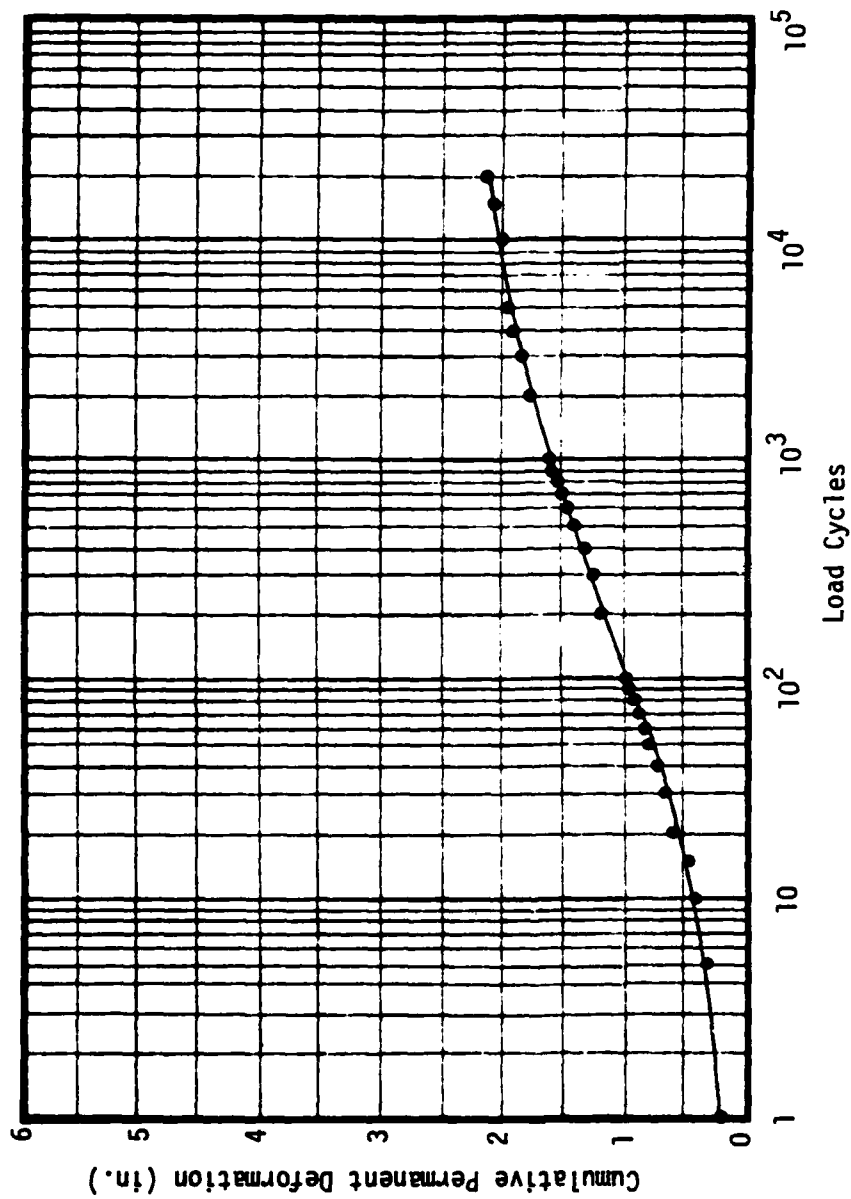


Figure E-25. Load Cycle-Cumulative Permanent Deformation Relationship, Test No. 20A (10.0 in. Stone/T-3401/Unsoaked CBR = 0.87).

Table E-26. Load Cycle-Deformation Relationships, Test No. 208 (10.0 in. Stone/T-3401/Unsoaked CBR = 0.96).

<u>Load Cycles</u>	<u>Total Deformation Per Cycle (in.)</u>	<u>Cumulative Permanent Deformation (in.)</u>
1	--	0.083
5	0.091	0.156
10	0.089	0.193
15	0.087	0.213
20	0.087	0.231
30	0.085	0.261
40	0.085	0.281
50	0.085	0.297
60	0.083	0.309
70	0.085	0.324
80	0.083	0.335
90	0.080	0.345
100	0.080	0.355
200	0.078	0.518
300	0.078	0.599
300	0.078	0.697
500	0.076	0.796
600	0.078	0.851
700	0.076	0.938
800	0.076	0.993
900	0.074	1.034
1000	0.076	1.072
2000	0.076	1.209
3000	0.074	1.397
4000	0.072	1.467
5000	0.067	1.515
10000	0.065	1.632
15000	0.063	1.663
20000	0.061	1.710

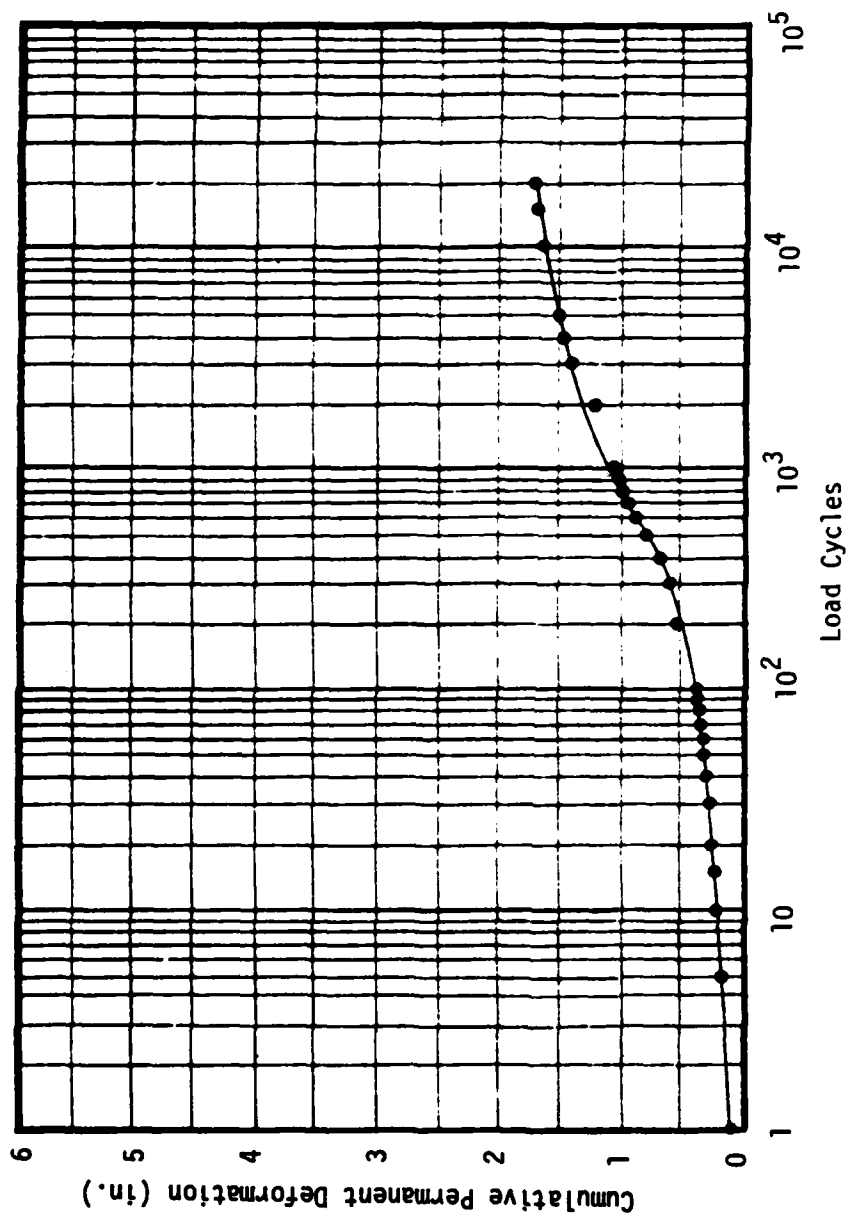


Figure E-26. Load Cycle-Cumulative Permanent Deformation Relationship, Test No. 20B (10.0 in. Stone/T-3401/Unsoaked CBR = 0.96).

Table E-27. Load Cycle-Deformation Relationships, Test No. 21A (10.0 in. Stone/T-3601/Unsoaked CBR = 0.78).

<u>Load Cycles</u>	<u>Total Deformation Per Cycle (in.)</u>	<u>Cumulative Permanent Deformation (in.)</u>
1	--	0.178
5	0.131	0.308
10	0.122	0.397
15	0.107	0.429
20	0.103	0.485
30	0.102	0.532
40	0.104	0.596
50	0.101	0.624
60	0.097	0.676
70	0.099	0.715
80	0.097	0.741
90	0.095	0.782
100	0.095	0.797
200	0.093	1.012
300	0.095	1.138
400	0.093	1.219
500	0.091	1.285
600	0.089	1.341
700	0.087	1.394
800	0.085	1.426
900	0.081	1.459
1000	0.083	1.508
2000	0.081	1.654
3000	0.079	1.751
4000	0.075	1.815
5000	0.073	1.864
10000	0.071	1.988
15000	0.069	2.035
20000	0.065	2.052

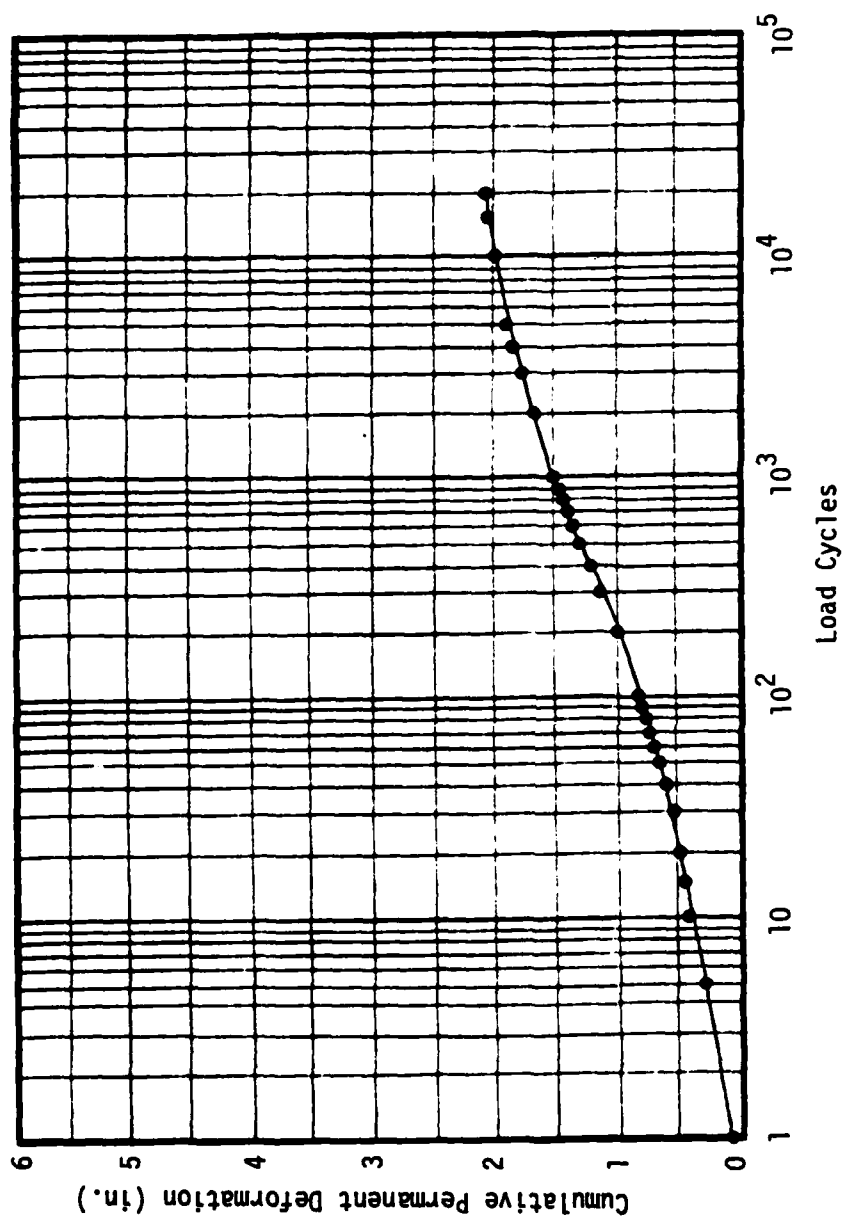


Figure E-27. Load Cycle-Cumulative Permanent Deformation Relationship, Test No. 21A (10.0 in. Stone/T-3601/Unsoaked CBR = 0.78).

Table E-28. Load Cycle-Deformation Relationships, Test No. 22A (13.0 in. Stone/None/Unsoaked CBR = 0.99).

<u>Load Cycles</u>	<u>Total Deformation Per Cycle (in.)</u>	<u>Cumulative Permanent Deformation (in.)</u>
1	--	0.184
5	0.125	0.359
10	0.106	0.460
15	0.101	0.497
20	0.098	0.522
30	0.099	0.576
40	0.094	0.649
50	0.094	0.686
60	0.086	0.715
70	0.088	0.745
80	0.086	0.767
90	0.086	0.784
100	0.082	0.807
200	0.078	0.947
300	0.076	1.036
400	0.075	1.135
500	0.071	1.184
600	0.074	1.230
700	0.074	1.267
800	0.069	1.301
900	0.068	1.331
1000	0.068	1.357
2000	0.075	1.549
3000	0.070	1.699
4000	0.068	1.787
5000	0.065	1.854
10000	0.057	2.006
15000	0.054	2.098
20000	0.049	2.143

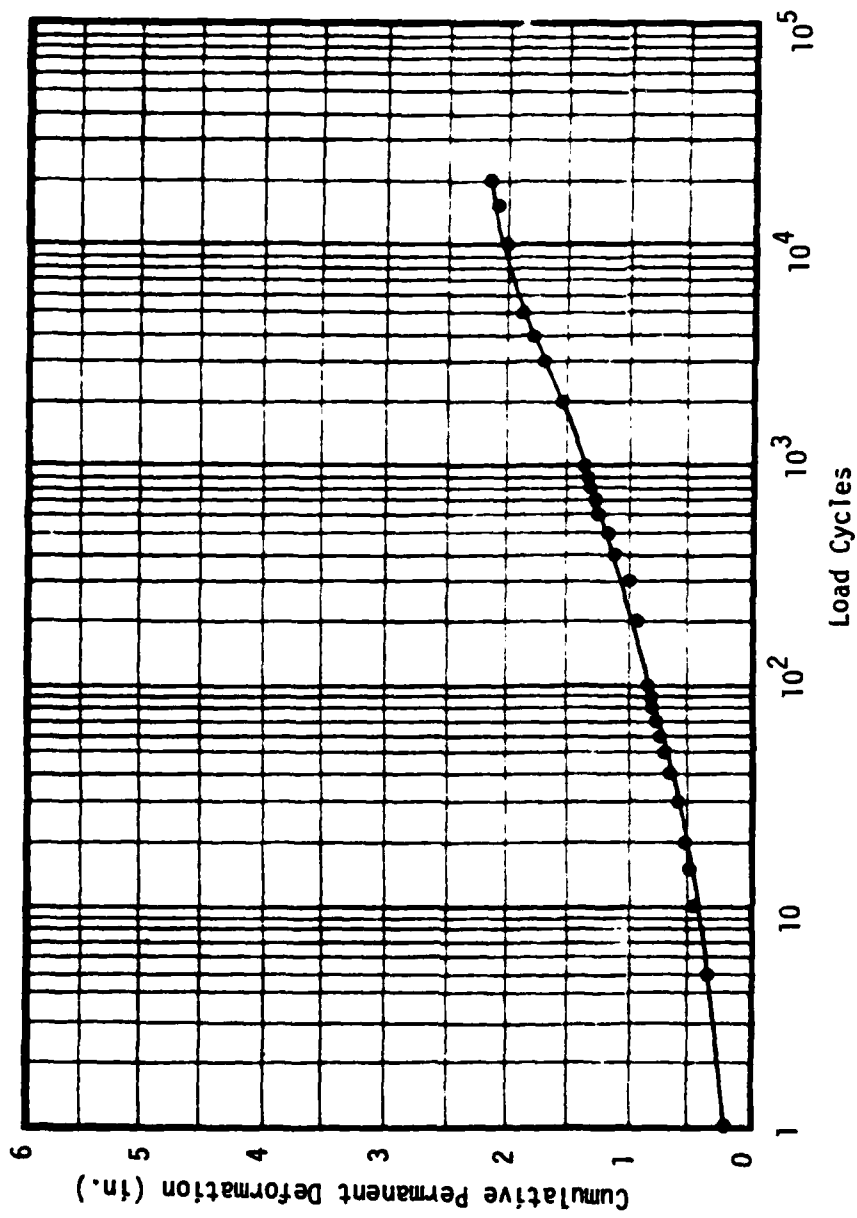


Figure E-28. Load Cycle-Cumulative Permanent Deformation Relationship, Test No. 22A (13.0 in. Stone/None/Unsoaked CBR = 0.99).

Table E-29. Load Cycle-Deformation Relationships, Test No. 23A (13.0 in. Stone/T-3401/Unsoaked CBR = 0.97).

<u>Load Cycles</u>	<u>Total Deformation Per Cycle (in.)</u>	<u>Cumulative Permanent Deformation (in.)</u>
1	--	0.142
5	0.085	0.232
10	0.086	0.284
15	0.086	0.321
20	0.088	0.339
30	0.090	0.378
40	0.087	0.443
50	0.085	0.487
60	0.086	0.531
70	0.084	0.566
80	0.082	0.589
90	0.082	0.623
100	0.083	0.639
200	0.079	0.792
300	0.076	0.869
400	0.073	0.899
500	0.069	0.994
600	0.068	1.035
700	0.065	1.073
800	0.070	1.115
900	0.066	1.146
1000	0.067	1.187
2000	0.065	1.229
3000	0.062	1.331
4000	0.062	1.377
5000	0.059	1.424
10000	0.048	1.501
15000	0.042	1.544
20000	0.039	1.589

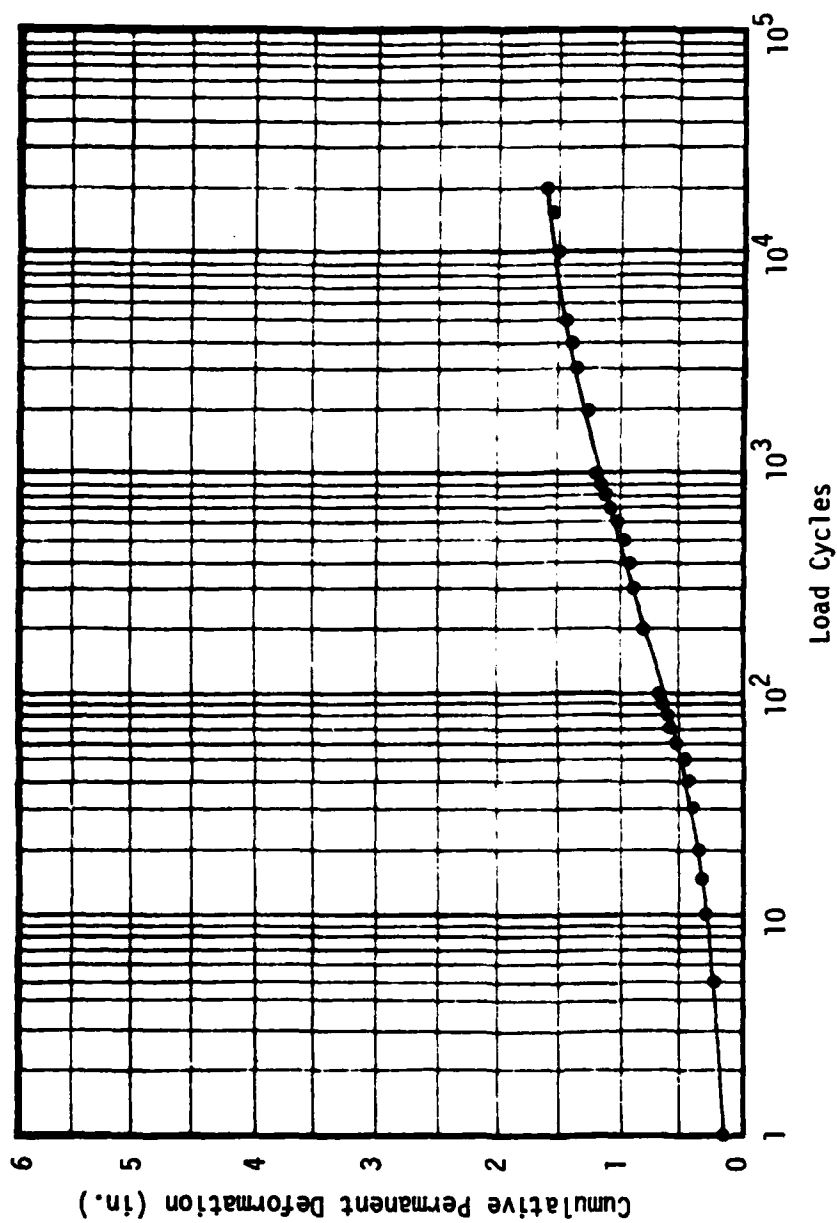


Figure E-29. Load Cycle-Cumulative Permanent Deformation Relationship, Test No. 23A (13.0 in. Stone/T-3401/Unsoaked CBR = 0.97).

Table E-30. Load Cycle-Deformation Relationships, Test No. 24A (13.0 in. Stone/M-140/Unsoaked CBR = 0.84).

<u>Load Cycles</u>	<u>Total Deformation Per Cycle (in.)</u>	<u>Cumulative Permanent Deformation (in.)</u>
1	--	0.221
5	0.112	0.416
10	0.105	0.491
15	0.099	0.536
20	0.098	0.572
30	0.101	0.626
40	0.099	0.667
50	0.098	0.702
60	0.094	0.728
70	0.095	0.751
80	0.094	0.772
90	0.091	0.791
100	0.083	0.806
200	0.076	0.936
300	0.074	0.999
400	0.072	1.052
500	0.069	1.097
600	0.068	1.128
700	0.066	1.154
800	0.063	1.175
900	0.062	1.191
1000	0.059	1.197
2000	0.064	1.336
3000	0.063	1.446
4000	0.063	1.509
5000	0.060	1.551
10000	0.058	1.681
15000	0.056	1.789
20000	0.051	1.854

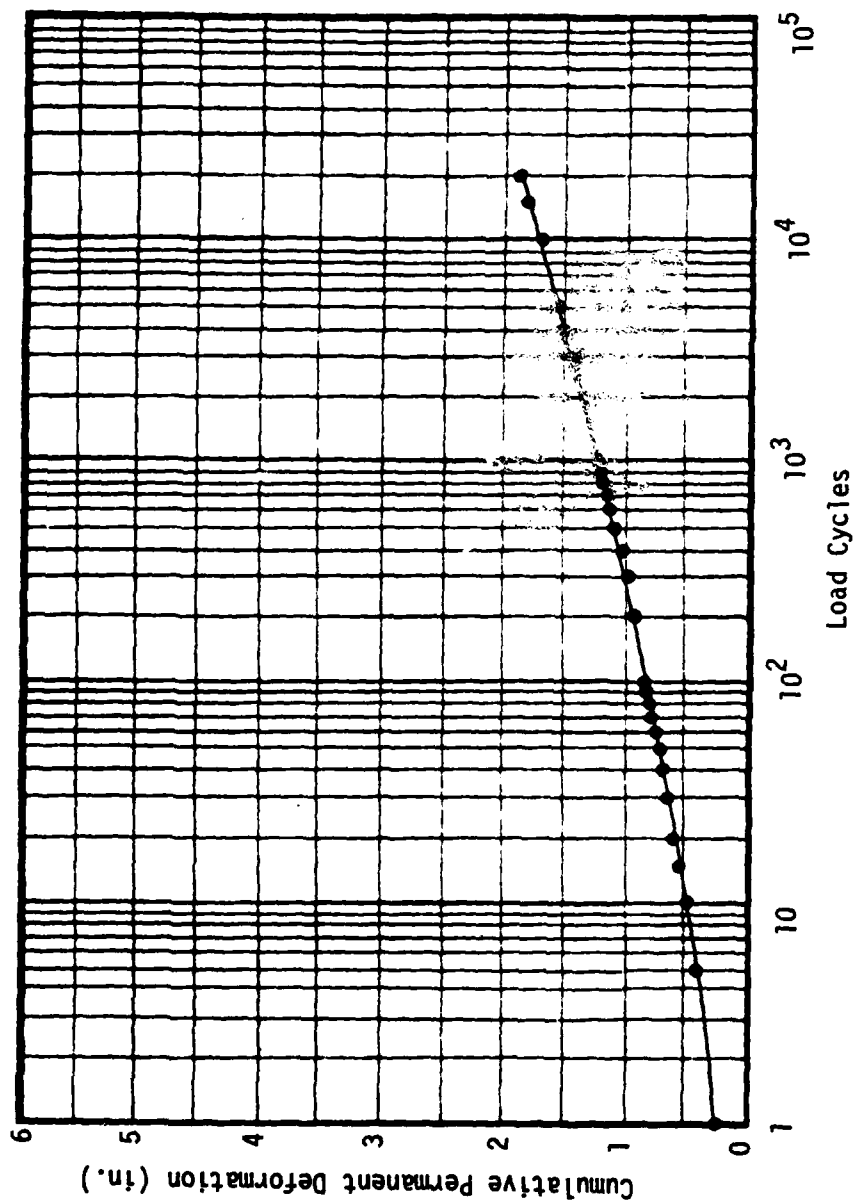


Figure E-30. Load Cycle-Cumulative Permanent Deformation Relationship, Test No. 24A (13.0 in. Stone/M-140/Unsoaked CBR = 0.84).

Table E-31. Load Cycle-Deformation Relationships, Test No. 25A (13.0 in. Stone/B-C22/Unsoaked CBR = 0.84).

<u>Load Cycles</u>	<u>Total Deformation Per Cycle (in.)</u>	<u>Cumulative Permanent Deformation (in.)</u>
1	--	0.101
5	0.116	0.202
10	0.108	0.266
15	0.102	0.301
20	0.099	0.324
30	0.099	0.358
40	0.098	0.386
50	0.095	0.408
60	0.091	0.418
70	0.087	0.436
80	0.084	0.462
90	0.086	0.477
100	0.083	0.490
200	0.079	0.604
300	0.076	0.675
400	0.074	0.714
500	0.073	0.774
600	0.071	0.822
700	0.070	0.861
800	0.067	0.897
900	0.065	0.925
1000	0.062	0.954
2000	0.061	1.118
3000	0.061	1.249
4000	0.060	1.349
5000	0.060	1.424
10000	0.057	1.597
15000	0.055	1.705
20000	0.052	1.794

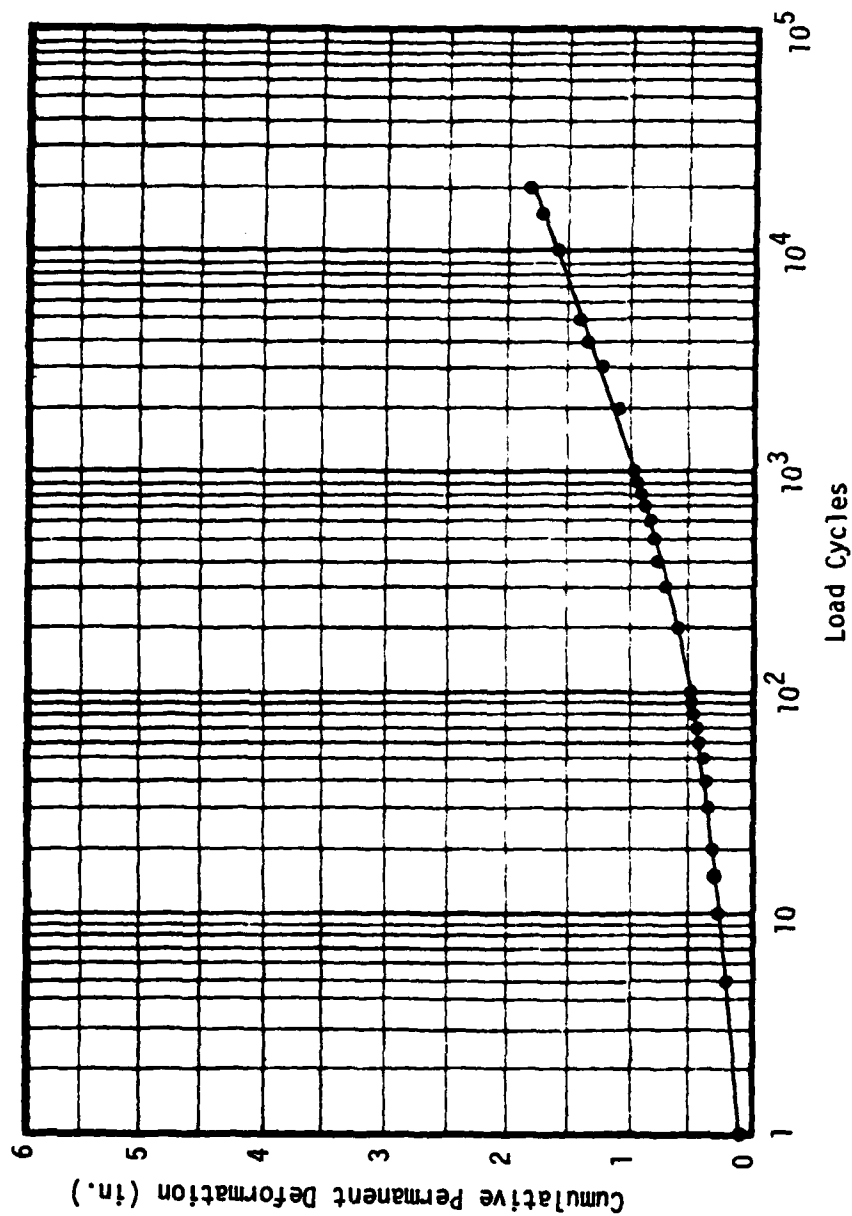


Figure E-31. Load Cycle-Cumulative Permanent Deformation Relationship, Test No. 25A (13.0 in. Stone/B-C22/Unsoaked CBR = 0.84).

Table E-32. Load Cycle-Deformation Relationships, Test No. 26B (3.0 in. Stone/None/Unsoaked CBR = 1.55).

<u>Load Cycles</u>	<u>Total Deformation Per Cycle (in.)</u>	<u>Cumulative Permanent Deformation (in.)</u>
1	--	0.526
5	--	0.997
10	--	1.571
15	--	1.924
20	--	2.353
30	--	2.983
40	--	3.553
50	--	4.012
60	--	4.147
70	--	4.556
80	--	5.040

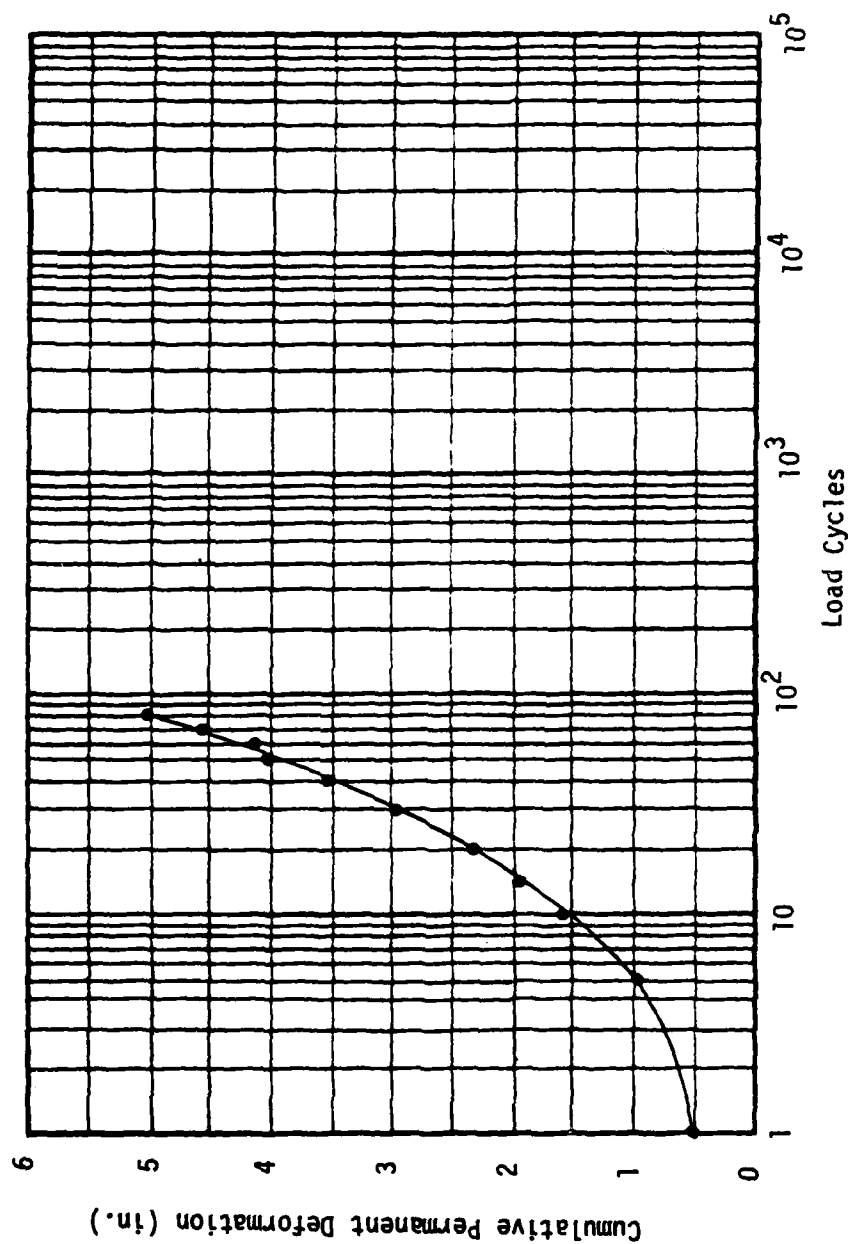


Figure E-32. Load Cycle-Cumulative Permanent Deformation Relationship, Test No. 26B (3.0 in. Stone/None/Unsoaked CBR = 1.55).

Table E-33. Load Cycle-Deformation Relationships, Test No. 27B (3.0 in. Stone/T-3401/Unsoaked CBR = 1.56).

<u>Load Cycles</u>	<u>Total Deformation Per Cycle (in.)</u>	<u>Cumulative Permanent Deformation (in.)</u>
1	--	0.225
5	0.42	0.650
10	0.38	1.044
15	0.37	1.176
20	0.35	1.282
30	0.32	1.528
40	0.32	1.594
50	0.29	1.738
60	0.32	2.051
70	0.35	2.235
80	0.37	2.367
90	0.45	2.641
100	0.57	2.964
200	0.36	4.660

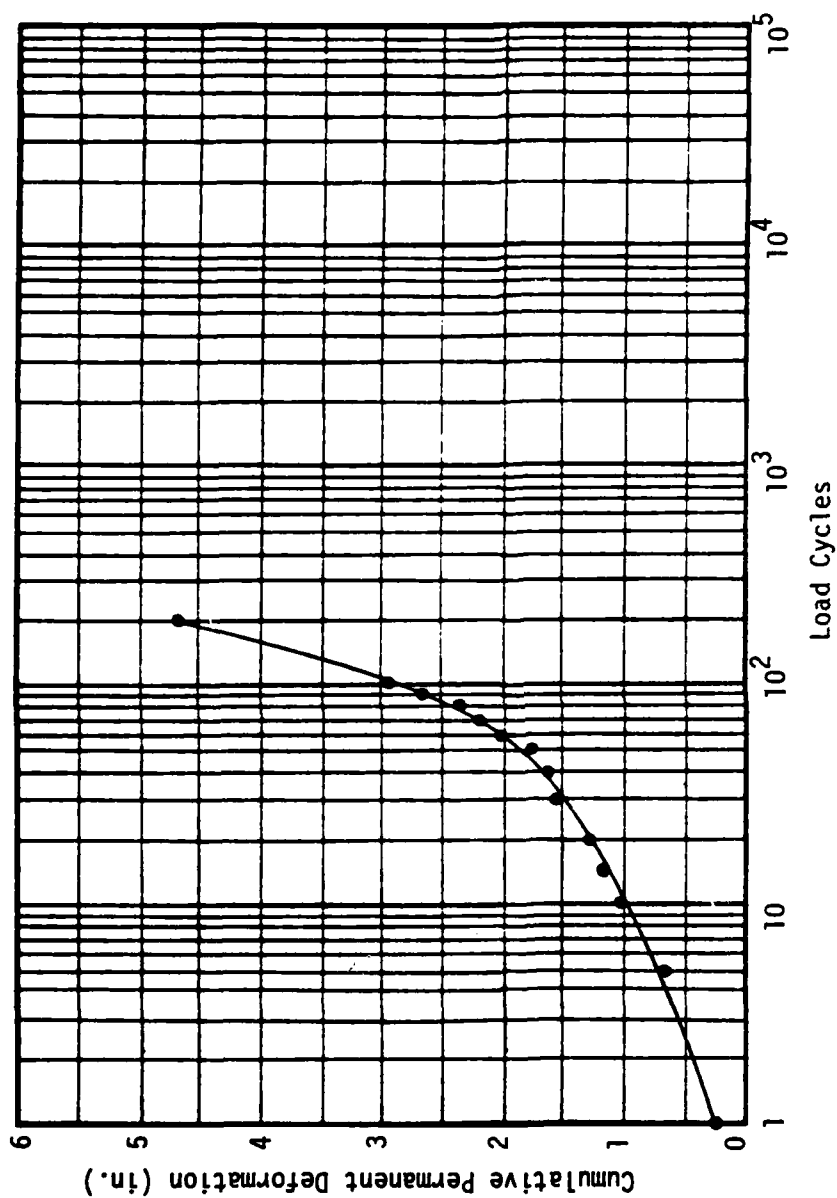


Figure E-33. Load Cycle-Cumulative Permanent Deformation Relationship, Test No. 27B (3.0 in. Stone/T-3401/Unsoaked CBR = 1.56).

Table E-34. Load Cycle-Deformation Relationships, Test No. 28B (4.5 in. Stone/None/Unsoaked CBR = 1.59).

<u>Load Cycles</u>	<u>Total Deformation Per Cycle (in.)</u>	<u>Cumulative Permanent Deformation (in.)</u>
1	--	0.282
5	0.27	0.624
10	0.25	0.876
15	0.24	0.994
20	0.24	1.106
30	0.23	1.341
40	0.22	1.541
50	0.23	1.724
60	0.22	1.882
70	0.22	2.018
80	0.23	2.171
90	0.22	2.299
100	0.24	2.398
200	0.25	3.029
300	0.26	3.723
400	0.25	4.042
500	0.27	4.412
600	0.28	4.643

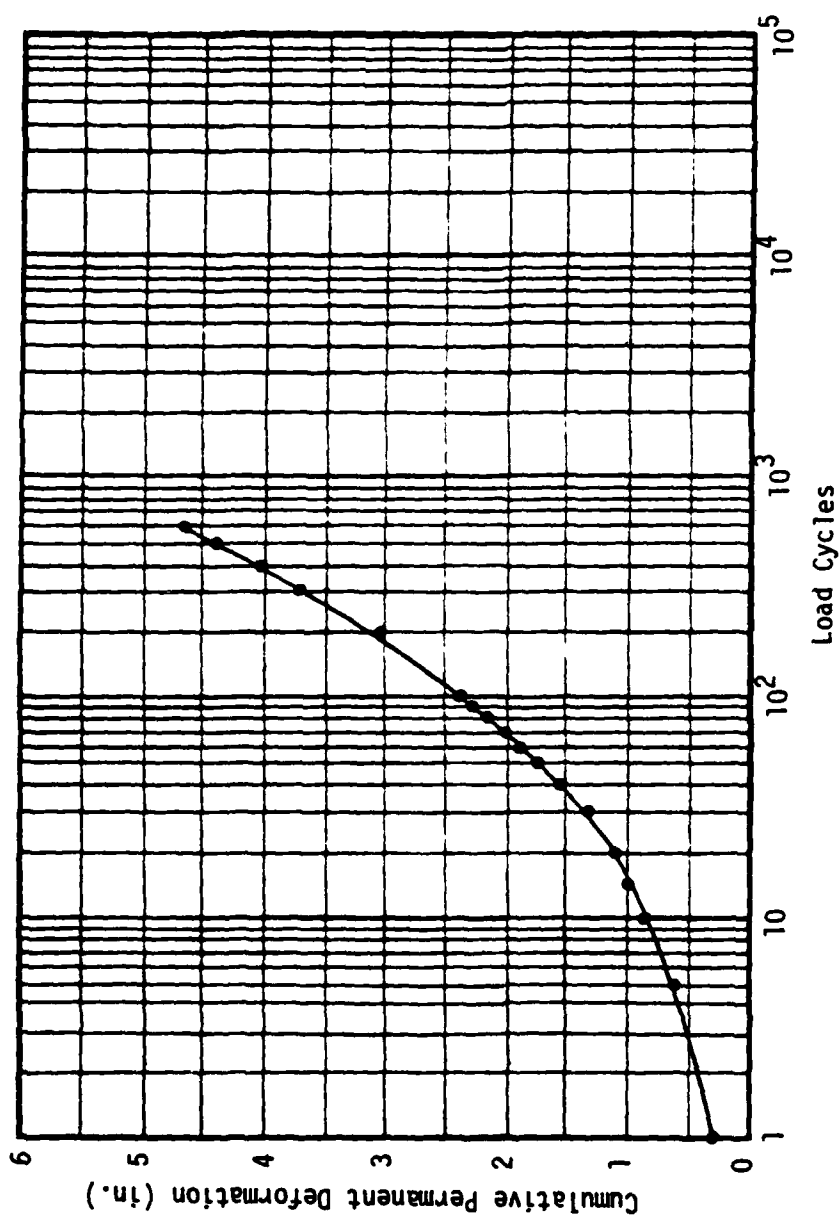


Figure E-34. Load Cycle-Cumulative Permanent Deformation Relationship, Test No. 28B (4.5 in. Stone/None/Unsoaked CBR = 1.59).

Table E-35. Load Cycle-Deformation Relationships, Test No. 29B (4.5 in. Stone/T-3401/Unsoaked CBR = 1.61).

<u>Load Cycles</u>	<u>Total Deformation Per Cycle (in.)</u>	<u>Cumulative Permanent Deformation (in.)</u>
1	--	0.139
5	0.24	0.276
10	0.23	0.384
15	0.21	0.454
20	0.23	0.531
30	0.21	0.634
40	0.23	0.719
50	0.22	0.788
60	0.22	0.888
70	0.21	0.978
80	0.21	1.041
90	0.23	1.166
100	0.23	1.245
200	0.23	1.676
300	0.21	1.891
400	0.24	2.041
500	0.24	2.263
600	0.25	2.370
700	0.22	2.477
800	0.27	2.716
900	0.28	2.876
1000	0.27	2.974
2000	0.29	3.824
3000	0.28	4.705

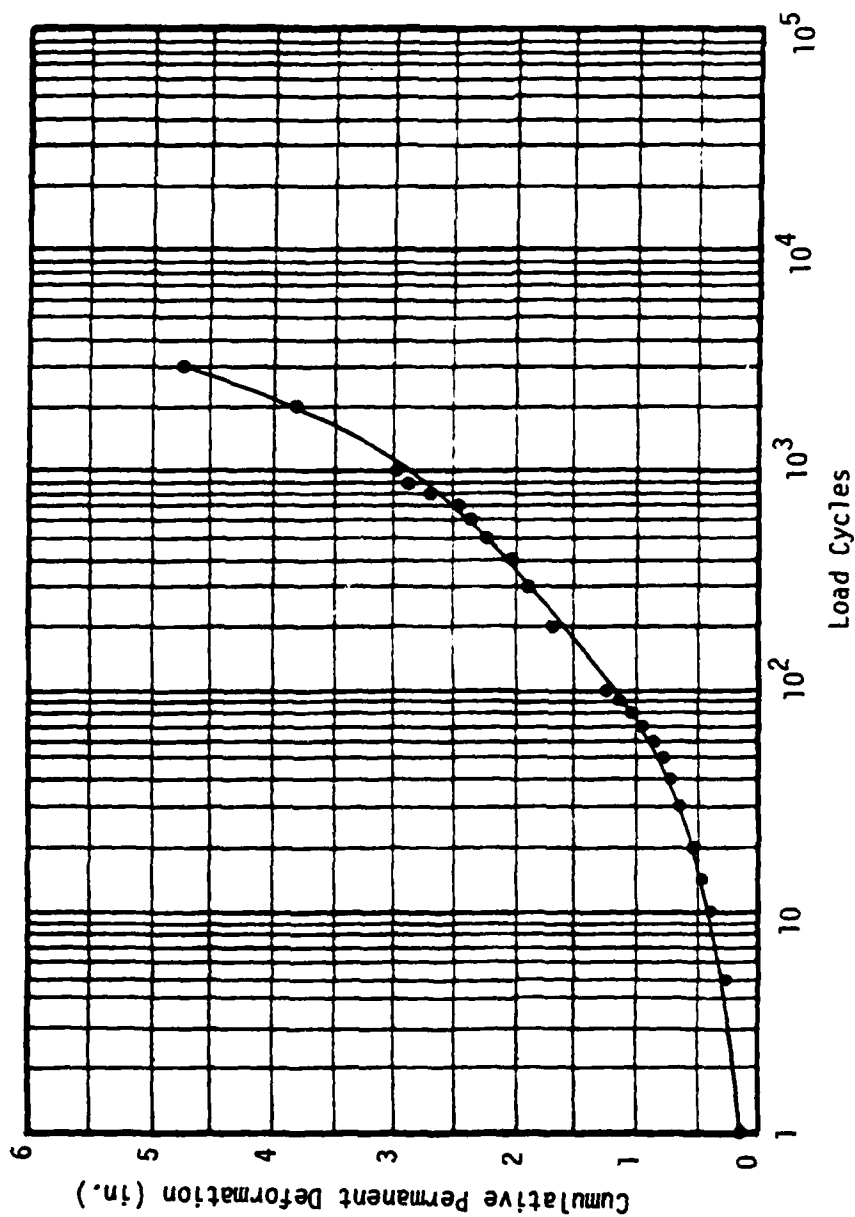


Figure E-35. Load Cycle-Cumulative Permanent Deformation Relationship, Test No. 29B (4.5 in. Stone/T-3401/Unsoaked CBR = 1.61).

Table E-36. Load Cycle-Deformation Relationships, Test No. 30B (6.0 in. Stone/None/Unsoaked CBR = 1.72).

<u>Load Cycles</u>	<u>Total Deformation Per Cycle (in.)</u>	<u>Cumulative Permanent Deformation (in.)</u>
1	--	0.152
5	0.18	0.287
10	0.18	0.419
15	0.16	0.508
20	0.16	0.572
30	0.17	0.678
40	0.17	0.759
50	0.17	0.813
60	0.16	0.919
70	0.15	1.001
80	0.15	1.076
90	0.14	1.134
100	0.14	1.185
200	0.12	1.712
300	0.12	2.107
400	0.13	2.373
500	0.12	2.548
600	0.10	2.744
700	0.11	2.882
800	0.12	2.965
900	0.12	3.128
1000	0.13	3.295
2000	0.12	3.896
3000	0.13	4.013
4000	0.13	4.294
5000	0.12	4.425
10000	0.11	4.723

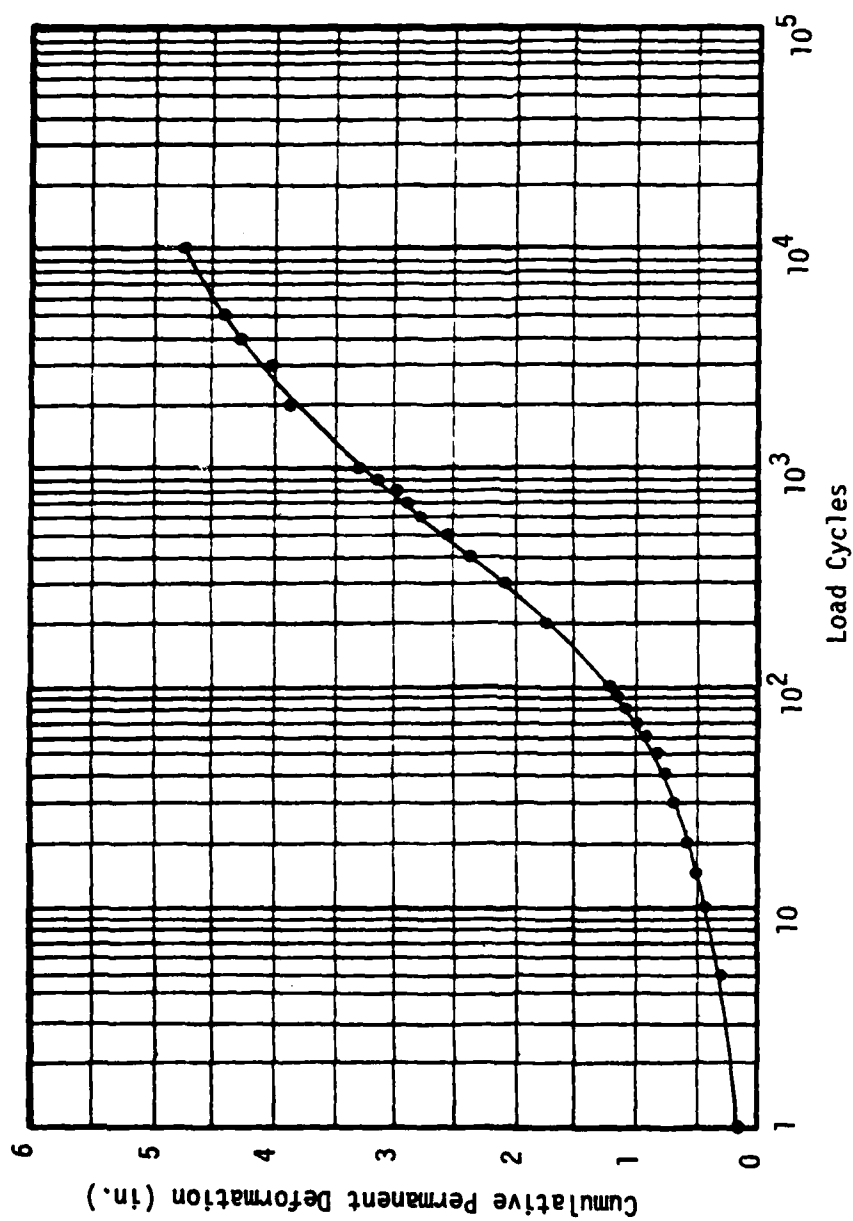


Figure E-36. Load Cycle-Cumulative Permanent Deformation Relationship, Test No. 30B (6.0 in. Stone/None/Unsoaked CBR = 1.72).

Table E-37. Load Cycle-Deformation Relationships, Test No. 31B (6.0 in. Stone/T-3401/Unsoaked CBR = 1.44).

<u>Load Cycles</u>	<u>Total Deformation Per Cycle (in.)</u>	<u>Cumulative Permanent Deformation (in.)</u>
1	--	0.198
5	0.21	0.368
10	0.21	0.533
15	0.19	0.663
20	0.18	0.791
30	0.17	0.945
40	0.19	1.145
50	0.19	1.298
60	0.20	1.386
70	0.21	1.459
80	0.19	1.519
90	0.19	1.606
100	0.18	1.668
200	0.17	2.062
300	0.16	2.420
400	0.16	2.602
500	0.17	2.837
600	0.16	2.994
700	0.15	3.088
800	0.16	3.224
900	0.15	3.322
1000	0.14	3.487
2000	0.14	3.839
3000	0.13	4.035
4000	0.14	4.353
5000	0.13	4.502
6000	0.13	4.611
7000	0.12	4.706

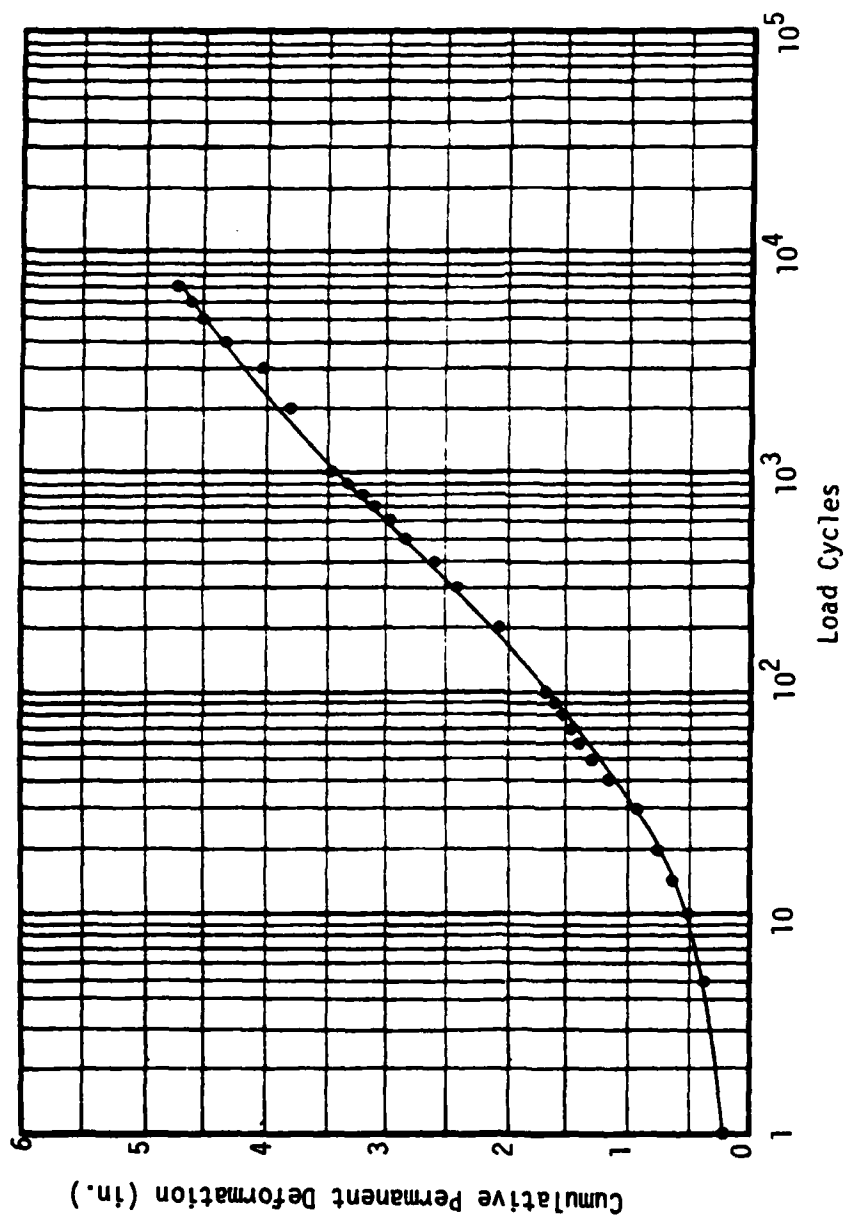


Figure E-37. Load Cycle-Cumulative Permanent Deformation Relationship, Test No. 31B (6.0 in. Stone/T-3401/Unsoaked CBR = 1.44).

Table E-38. Load Cycle-Deformation Relationships, Test No. 32B (3.0 in. Stone/None/Unsoaked CBR = 2.43).

<u>Load Cycles</u>	<u>Total Deformation Per Cycle (in.)</u>	<u>Cumulative Permanent Deformation (in.)</u>
1	--	0.404
5	0.48	0.844
10	0.39	1.253
15	0.37	1.471
20	0.39	1.815
30	0.37	2.223
40	0.36	2.487
50	0.34	2.782
60	0.36	2.979
70	0.36	3.198
80	0.37	3.406
90	0.39	3.617
100	0.41	3.718
200	0.46	4.741

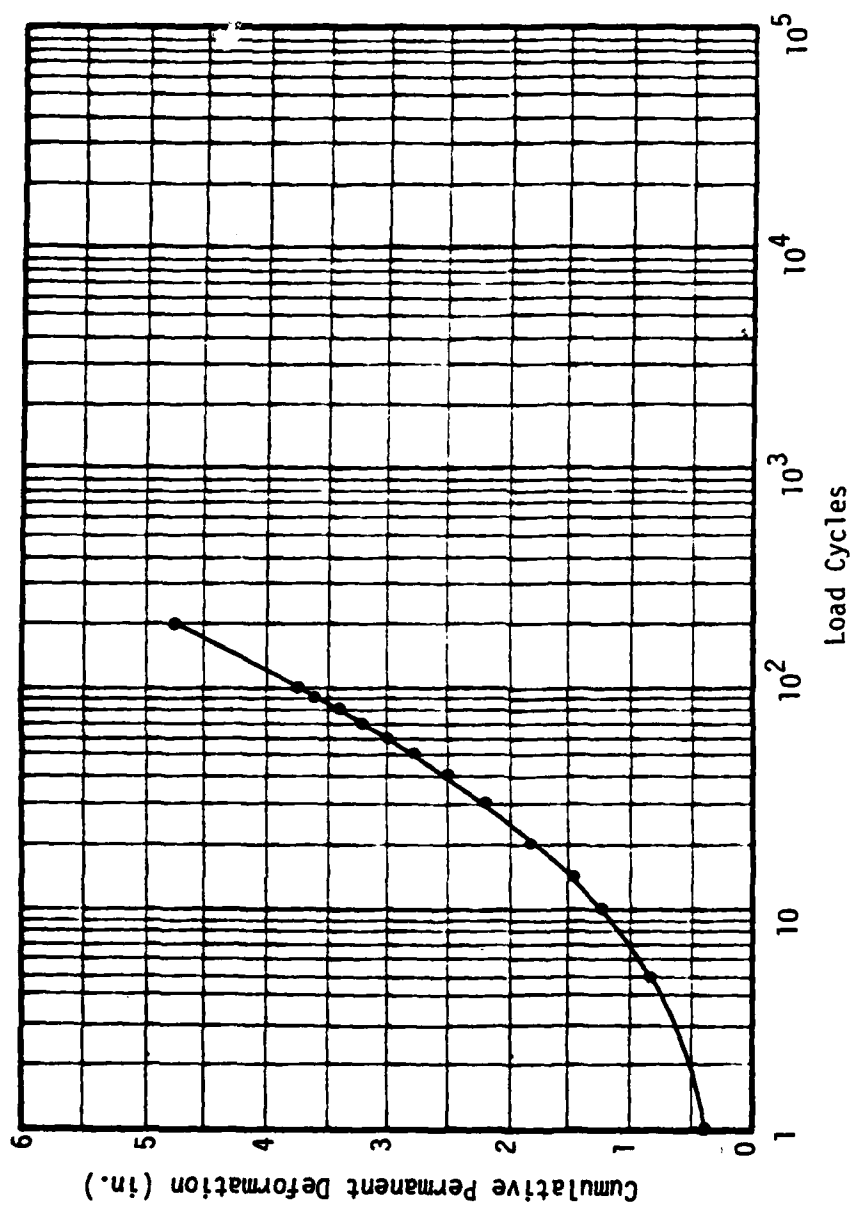


Figure E-38. Load Cycle-Cumulative Permanent Deformation Relationship, Test No. 32B (3.0 in. Stone/None/Unsoaked CBR = 2.43).

Table E-39. Load Cycle-Deformation Relationships, Test No. 33B (3.0 in. Stone/T-3401/Unsoaked CBR = 2.39).

<u>Load Cycles</u>	<u>Total Deformation Per Cycle (in.)</u>	<u>Cumulative Permanent Deformation (in.)</u>
1	--	0.254
5	0.38	0.518
10	0.35	0.765
15	0.34	0.974
20	0.32	1.121
30	0.31	1.424
40	0.30	1.665
50	0.28	1.874
60	0.29	2.043
70	0.27	2.224
80	0.27	2.365
90	0.28	2.501
100	0.30	2.626
200	0.33	3.418
300	0.36	4.191
400	0.38	4.806

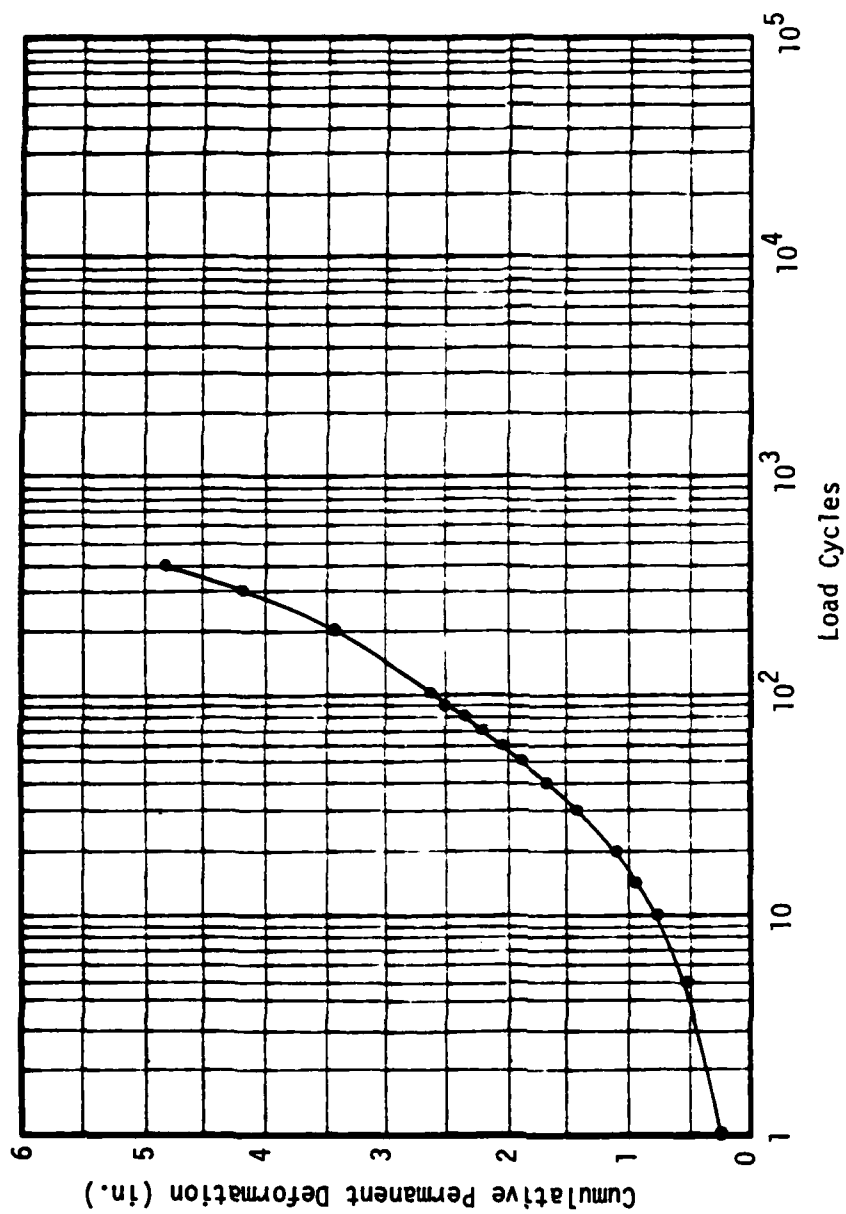


Figure E-39. Load Cycle-Cumulative Permanent Deformation Relationship, Test No. 33B (3.0 in. Stone/T-3401/Unsoaked CBR = 2.39).

APPENDIX F

MODEL TEST PROGRAM SUBGRADE SOIL SURFACE PROFILE CHANGE DATA

The initial surface profile of the subgrade soil was determined for each model test by placing a reference beam across the top of the test pit and measuring the vertical distance between this beam and the subgrade soil at intervals of two inches across the diameter of the pit. Upon completion of the test and careful removal of the crushed stone and fabric, the above procedure was utilized to determine the final surface profile along the same diameter. The change in surface profile was determined as the difference between the final and initial profile readings. The average of the profile changes at those points on the diameter having the same radial offset from the centerline was then calculated. This resulted in determination of an average subgrade profile change along any radius of the test pit. The average profile change (ΔZ) data at radial offset points (X) are presented herein. A net downward profile change (i.e., rutting) is considered positive, while a net upward profile change (i.e., heave) is considered negative. Crushed stone depth, interfacial membrane type, and the unsoaked CBR of the subgrade soil are provided with the profile data for each test. The percentages of the subgrade rut volume taken in shear and densification are also indicated for each test. These latter quantities were computed as follows:

$$(\% \text{ Shear}) = \frac{\text{Heave Volume}}{\text{Rut Volume}} \times 100\% \quad (\text{F-1})$$

and

$$(\% \text{ Densification}) = 100\% - (\% \text{ Shear}). \quad (\text{F-2})$$

The volumes were computed as:

$$V = 2\pi\bar{x}A \quad (\text{F-3})$$

where V = volume of heave or rut, in^3 .

\bar{x} = horizontal distance between footing centerline axis and centroid of average heave or rut area along any radius of the test pit, inches

A = average area of heave or rut along any radius of the test pit, in^2 .

The subgrade soil profile changes were plotted to scale and the areas of the heave and rut portions determined by use of a polar planimeter, Model 4236, manufactured by the Keuffel and Esser Company. This instrument has divisions of 0.01 inch. Each area was computed as the average of three separate determinations. The area centroids were located by graphical construction techniques.

Table F-1. Subgrade Soil Surface Profile Changes, Test Group I.

Test No.	1B	2B	3B	4B	5B	6B
Stone (in.)	6.0	6.0	7.5	7.5	9.0	9.0
Membrane	None	T-3401	None	T-3401	None	T-3401
Unsoaked CBR	0.38	0.39	0.43	0.41	0.40	0.41
X (in.)	ΔZ (in.)	ΔZ (in.)	ΔZ (in.)	ΔZ (in.)	ΔZ (in.)	ΔZ (in.)
18	-0.12	-0.18	-0.13	-0.12	-0.10	-0.10
16	-0.18	-0.22	-0.18	-0.17	-0.12	-0.15
14	-0.22	-0.25	-0.20	-0.22	-0.15	-0.14
12	-0.15	-0.18	-0.19	-0.21	-0.09	-0.07
10	-0.11	-0.15	-0.10	-0.13	-0.05	-0.03
8	-0.06	0.13	-0.04	0.13	-0.02	0.16
6	0.26	0.82	0.47	0.81	0.53	0.69
4	1.88	1.89	1.66	1.65	1.38	1.25
2	3.95	2.70	2.92	2.28	2.04	1.59
0	4.30	3.06	3.61	2.42	2.99	1.82
% Shear	58.8	57.2	61.7	62.6	47.0	41.6
% Densification	41.2	42.8	38.3	37.4	53.0	58.4

Table F-2. Subgrade Soil Surface Profile Changes, Test Group II
(Stone Thickness = 4.5 in.).

Test No.	7A	7B	8A	9A	9B	10A	11A	12A
Stone (in.)	4.5	4.5	4.5	4.5	4.5	4.5	4.5	4.5
Membrane	None	None	Sand	T-3401	T-3401	T-3601	M-140	B-C22
Unsoaked CBR	0.88	0.91	0.97	0.86	0.89	0.85	0.75	0.78
<u>X (in.)</u>	<u>ΔZ (in.)</u>	<u>ΔZ (in.)</u>	<u>ΔZ (in.)</u>	<u>ΔZ (in.)</u>	<u>ΔZ (in.)</u>	<u>ΔZ (in.)</u>	<u>ΔZ (in.)</u>	<u>ΔZ (in.)</u>
18	-0.02	-0.01	-0.03	-0.02	-0.03	-0.08	-0.06	-0.06
16	-0.04	-0.03	-0.03	-0.05	-0.06	-0.11	-0.08	-0.09
14	-0.09	-0.07	-0.11	-0.07	-0.09	-0.17	-0.09	-0.17
12	-0.18	-0.20	-0.14	-0.13	-0.15	-0.14	-0.14	-0.21
10	-0.35	-0.36	-0.16	-0.18	-0.24	-0.09	-0.18	-0.23
8	-0.27	-0.38	-0.22	-0.16	-0.15	0.08	-0.03	-0.13
6	-0.18	-0.23	0.04	0.07	0.24	0.56	0.52	0.38
4	1.48	1.59	1.18	0.98	1.03	1.58	1.87	1.88
2	3.36	3.45	3.92	2.43	2.38	2.95	3.61	3.59
0	4.00	4.03	4.24	2.99	2.96	3.47	4.12	3.92
% Shear	80.3	81.8	60.6	74.2	80.6	41.1	36.1	55.8
% Densification	19.7	18.2	39.4	25.8	19.4	58.9	63.9	44.2

Table F-3. Subgrade Soil Surface Profile Changes, Test Group 11
(Stone Thickness = 7.0 in.).

Test No.	13A	13B	14A	15A	15B	16A	17A	18A
Stone (in.)	7.0	7.0	7.0	7.0	7.0	7.0	7.0	7.0
Membrane	None	None	Sand	T-3401	T-3401	T-3601	M-140	B-C22
Unsoaked CBR	0.82	0.81	0.81	0.94	0.78	0.74	0.82	0.83
X (in.)	ΔZ (in.)	ΔZ (in.)	ΔZ (in.)	ΔZ (in.)	ΔZ (in.)	ΔZ (in.)	ΔZ (in.)	ΔZ (in.)
18	-0.02	-0.03	-0.10	-0.03	-0.06	-0.10	-0.11	-0.05
16	-0.06	-0.06	-0.15	-0.04	-0.09	-0.16	-0.10	-0.11
14	-0.15	-0.12	-0.21	-0.07	-0.08	-0.20	-0.18	-0.17
12	-0.22	-0.21	-0.16	-0.12	-0.10	-0.22	-0.23	-0.23
10	-0.19	-0.21	-0.12	-0.12	-0.08	-0.08	-0.17	-0.16
8	-0.12	-0.16	0.25	0.02	0.11	0.16	-0.13	-0.10
6	0.74	0.63	0.92	0.72	0.56	0.97	0.44	0.59
4	2.32	2.24	2.12	1.54	1.33	1.96	1.79	2.13
2	2.84	2.93	3.05	2.18	1.92	2.73	2.93	2.84
0	3.41	3.31	3.62	2.45	2.29	2.96	3.32	3.26
% Shear	45.3	45.8	43.0	34.4	31.6	48.5	74.0	61.9
% Densification	54.7	54.2	57.0	65.6	68.4	51.5	26.0	38.1

Table F-4. Subgrade Soil Surface Profile Changes, Test Group II
(Stone Thickness = 10.0 in.).

Test No.	19A	19B	20A	20B	21A
Stone (in.)	10.0	10.0	10.0	10.0	10.0
Membrane	None	None	T-3401	T-3401	T-3601
Unsoaked CBR	0.90	0.93	0.87	0.96	0.78
<u>X (in.)</u>	<u>ΔZ (in.)</u>	<u>ΔZ (in.)</u>	<u>ΔZ (in.)</u>	<u>ΔZ (in.)</u>	<u>ΔZ (in.)</u>
18	-0.06	-0.04	-0.03	-0.02	-0.03
16	-0.03	-0.06	-0.04	-0.05	-0.05
14	-0.03	-0.03	-0.05	-0.03	-0.04
12	-0.01	-0.03	-0.02	0.00	-0.02
10	0.02	0.04	0.05	0.04	0.03
8	0.09	0.12	0.14	0.12	0.11
6	0.25	0.28	0.32	0.23	0.27
4	0.42	0.47	0.57	0.39	0.41
2	0.59	0.66	0.80	0.56	0.62
0	0.82	0.88	0.90	0.64	0.78
% Shear	42.4	39.6	33.1	25.6	33.7
% Densification	57.6	60.4	66.9	74.4	66.3

Table F-5. Subgrade Soil Surface Profile Changes, Test Group II
(Stone Thickness = 13.0 in.).

Test No.	22A	23A	24A	25A
Stone (in.)	13.0	13.0	13.0	13.0
Membrane	None	T-3401	M-140	B-C22
Unsoaked CBR	0.99	0.97	0.84	0.84
<u>X (in.)</u>	<u>ΔZ (in.)</u>	<u>ΔZ (in.)</u>	<u>ΔZ (in.)</u>	<u>ΔZ (in.)</u>
18	-0.06	-0.04	-0.05	-0.04
16	-0.03	-0.02	-0.03	-0.04
14	-0.03	0.00	0.01	-0.02
12	0.03	0.03	0.04	0.02
10	0.06	0.08	0.06	0.06
8	0.12	0.15	0.12	0.11
6	0.21	0.26	0.24	0.15
4	0.35	0.40	0.38	0.18
2	0.43	0.53	0.48	0.24
0	0.49	0.59	0.53	0.30
% Shear	27.0	15.4	18.6	37.0
% Densification	73.0	84.6	81.4	63.0

Table F-6. Subgrade Soil Surface Profile Changes, Test Group III.

Test No.	26B	27B	28B	29B	30B	31B
Stone (in.)	3.0	3.0	4.5	4.5	6.0	6.0
Membrane	None	T-3401	None	T-3401	None	T-3401
Unsoaked CBR	1.55	1.56	1.59	1.61	1.72	1.44
X (in.)	ΔZ (in.)	ΔZ (in.)	ΔZ (in.)	ΔZ (in.)	ΔZ (in.)	ΔZ (in.)
18	-0.02	-0.02	-0.03	-0.02	-0.05	-0.05
16	-0.02	-0.01	-0.04	-0.02	-0.02	-0.08
14	-0.05	-0.02	-0.08	-0.03	-0.04	-0.07
12	-0.07	-0.05	-0.12	-0.07	-0.11	-0.10
10	-0.12	-0.08	-0.18	-0.12	-0.14	-0.16
8	-0.21	-0.12	-0.11	-0.17	-0.16	-0.03
6	-0.30	-0.12	0.23	-0.09	-0.01	0.44
4	0.47	0.47	1.15	0.58	0.97	1.18
2	4.29	2.63	2.86	2.45	2.07	2.01
0	4.65	3.28	3.74	2.87	3.11	2.38
% Shear	60.0	70.9	50.8	76.7	68.0	45.4
% Densification	40.0	29.1	49.2	23.3	32.0	54.6

Table F-7. Subgrade Soil Surface Profile Changes, Test Group IV.

Test No.	32B	33B
Stone (in.)	3.0	3.0
Membrane	None	T-3401
Unsoaked CBR	2.43	2.39
<u>X (in.)</u>	<u>ΔZ (in.)</u>	<u>ΔZ (in.)</u>
18	-0.04	-0.02
16	-0.06	-0.03
14	-0.12	-0.06
12	-0.16	-0.09
10	-0.21	-0.16
8	-0.24	-0.18
6	-0.18	-0.22
4	0.64	0.23
2	3.72	2.69
0	4.25	3.78
% Shear	97.2	84.2
% Densification	2.2	15.8

APPENDIX G

MODEL TEST PROGRAM STRAIN SENSOR DATA

Bison strain sensors were utilized to determine relative movements between points in the soil mass. The coils were placed at predetermined locations (Figure G-1) within the soil. A complete description of the sensors and instrument package and the procedures for coil pair calibration and operation are provided in Appendix C. The relative movements (Δ) between coil pairs, as indicated by the corresponding changes in amplitude readings during each test, are provided herein. A decrease in the sensor spacing is considered positive, while an increase in spacing is considered negative. Crushed stone depth, interfacial membrane type, and the unsoaked CBR of the subgrade soil are also provided for each test.

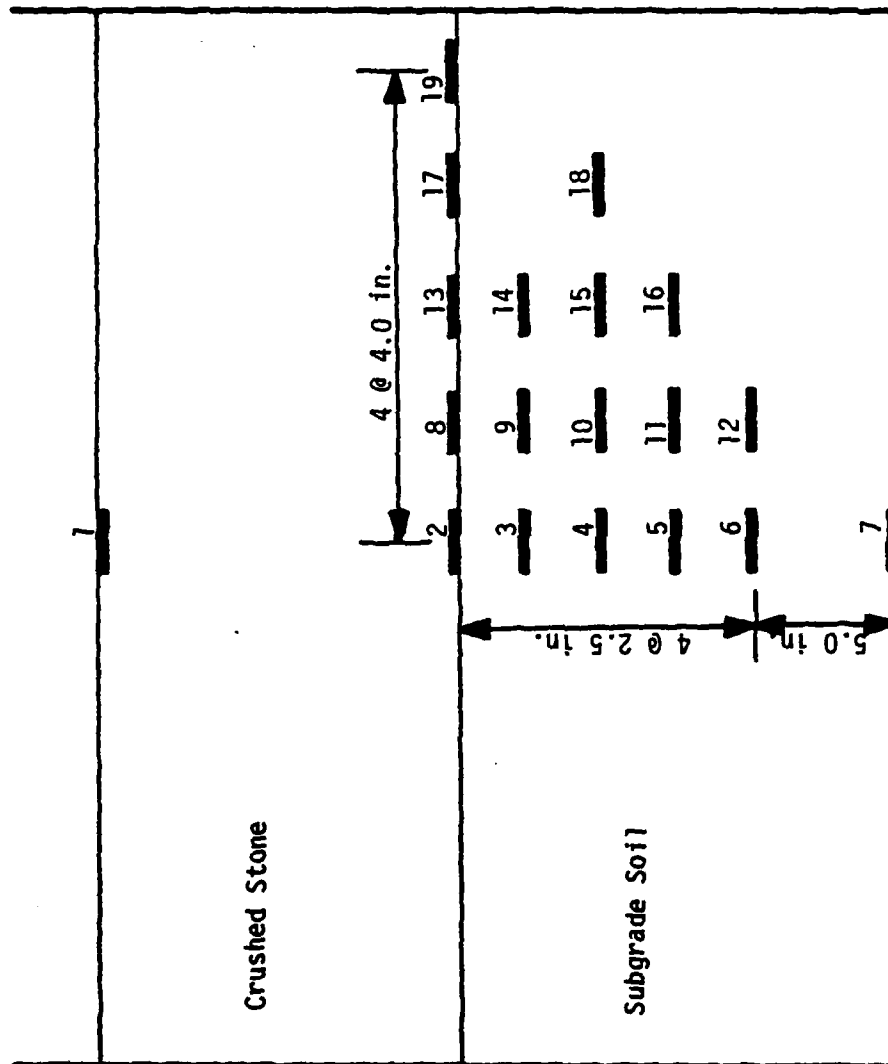


Figure G-7. Bison Coil Designations and Initial Placement Configuration.

Table G-1. Strain Sensor Relative Movements, Test Group I.

Test No.	1B	2B	3B	4B	5B	6B
Stone (in.)	6.0	6.0	6.0	6.0	6.0	6.0
Membrane	None	T-3401	None	T-3401	None	T-3401
Unsoaked CBR	0.38	0.39	0.43	0.41	0.40	0.41
Coil Pair	Δ (in.)	Δ (in.)	Δ (in.)	Δ (in.)	Δ (in.)	Δ (in.)
1-2	0.62	1.91	1.20	2.28	1.80	1.94
2-3	1.58	0.93	1.61	0.58	1.07	0.47
3-4	1.16	0.82	0.90	0.69	0.78	0.44
4-5	0.41	0.66	0.31	0.58	0.37	0.43
5-6	0.59	0.41	0.40	0.27	0.42	0.22
6-7	0.56	0.24	0.39	0.30	0.35	0.26
8-9	0.41	0.53	0.40	0.36	0.39	0.33
9-10	0.27	0.57	0.31	0.29	0.17	0.24
10-11	0.24	0.36	0.17	0.27	0.18	0.19
11-12	0.35	0.17	0.06	0.16	0.12	0.08
13-14	-0.16	-0.07	0.11	0.16	0.15	0.14
14-15	-0.08	-0.09	-0.08	-0.10	-0.06	-0.02
15-16	-0.13	-0.04	-0.06	-0.09	-0.04	-0.21
17-18	-0.17	-0.19	-0.11	-0.30	-0.13	-0.24
2-8	-1.31	-0.71	-0.98	-0.71	-0.64	-0.48
8-13	0.42	0.18	0.28	0.26	0.28	0.21
13-17	-0.12	-0.07	-0.02	0.11	0.06	0.10
17-19	0.04	0.05	0.03	0.05	0.02	0.03
3-9	-1.15	-0.59	-0.82	-0.38	-0.46	-0.33
9-14	0.31	0.22	0.41	0.29	0.27	0.18
4-10	-0.88	-0.48	-0.50	-0.31	-0.32	-0.27
10-15	0.22	0.10	0.26	0.14	0.15	0.13
15-18	0.12	0.18	-0.03	0.13	0.11	0.09
5-11	-0.25	-0.12	-0.20	-0.26	-0.22	-0.16
11-16	0.06	0.03	0.03	0.09	0.04	0.05
6-12	-0.11	-0.09	-0.12	-0.11	-0.09	-0.06

Table G-2. Strain Sensor Relative Movements, Test Group II
(Stone Thickness = 4.5 in.)

Test No.	7A	7B	8A	9A	9B	10A	11A	12A
Stone (in.)	4.5	4.5	4.5	4.5	4.5	4.5	4.5	4.5
Membrane	None	None	Sand	T-3401	T-3401	T-3601	M-140	B-C22
Unsoaked CBR	0.88	0.91	0.97	0.86	0.89	0.85	0.75	0.78
Coil Pair	Δ (in.)	Δ (in.)	Δ (in.)	Δ (in.)	Δ (in.)	Δ (in.)	Δ (in.)	Δ (in.)
1-2	0.73	0.76	0.51	2.04	2.00	1.28	0.67	0.83
2-3	1.31	1.43	1.52	0.53	0.71	1.19	1.46	1.34
3-4	0.90	0.99	1.14	1.04	0.90	0.84	0.93	0.91
4-5	0.52	0.62	0.69	0.77	0.86	0.72	0.79	0.62
5-6	0.65	0.50	0.57	0.45	0.33	0.46	0.54	0.49
6-7	0.62	0.49	0.32	0.20	0.17	0.26	0.40	0.56
8-9	0.51	0.54	0.60	0.13	0.34	0.38	0.71	0.68
9-10	0.42	0.39	0.45	0.12	0.59	0.33	0.42	0.24
10-11	0.24	0.25	0.30	0.23	0.21	0.25	0.26	0.39
11-12	0.31	0.32	0.28	0.06	0.07	0.18	0.21	0.22
13-14	-0.13	-0.05	-0.08	-0.25	-0.06	-0.06	-0.22	-0.11
14-15	-0.30	-0.55	-0.35	-0.13	-0.07	-0.16	-0.06	-0.32
15-16	-0.17	-0.11	-0.21	-0.19	-0.03	-0.09	-0.09	-0.05
17-18	-0.21	-0.18	-0.17	-0.11	-0.27	-0.19	-0.31	-0.26
2-8	-1.21	-1.13	-1.45	-0.71	-0.62	-0.88	-1.18	-1.07
8-13	0.34	0.49	0.23	0.41	0.27	0.31	0.33	0.36
13-17	0.15	0.15	0.09	0.02	-0.06	0.09	0.18	0.12
17-19	0.03	0.05	0.05	0.02	0.03	0.03	0.05	0.07
3-9	-1.30	-1.64	-1.50	-0.63	-0.83	-0.73	-1.03	-0.94
9-14	0.47	0.55	0.51	0.38	0.26	0.36	0.29	0.39
4-10	-1.03	-0.97	-1.05	-0.35	-0.55	-0.63	-0.73	-0.68
10-15	0.42	0.37	0.45	0.22	0.12	0.32	0.41	0.32
15-18	0.18	0.24	0.23	0.02	0.20	0.14	0.18	0.25
5-11	-0.18	-0.16	-0.30	-0.07	-0.04	-0.19	-0.31	-0.24
11-16	0.05	0.05	0.06	0.10	0.02	0.10	0.10	0.13
6-12	-0.15	-0.18	-0.21	-0.10	-0.08	-0.12	-0.17	-0.18

Table G-3. Strain Sensor Relative Movements, Test Group II
(Stone Thickness = 7.0 in.).

Test No.	13A	13B	14A	15A	15B	16A	17A	18A
Stone (in.)	7.0	7.0	7.0	7.0	7.0	7.0	7.0	7.0
Membrane	None	None	Sand	T-3401	T-3401	T-3601	M-140	B-C22
Unsoaked CBR	0.82	0.81	0.81	0.94	0.78	0.74	0.82	0.83
Coil Pair	Δ (in.)	Δ (in.)	Δ (in.)	Δ (in.)	Δ (in.)	Δ (in.)	Δ (in.)	Δ (in.)
1-2	1.29	1.37	1.13	2.28	2.45	1.82	1.46	1.48
2-3	1.18	1.02	1.01	0.75	0.53	0.93	0.94	1.01
3-4	0.84	0.73	0.84	0.67	0.57	0.52	0.86	0.92
4-5	0.63	0.78	0.63	0.52	0.51	0.47	0.71	0.58
5-6	0.30	0.37	0.45	0.32	0.39	0.58	0.44	0.42
6-7	0.46	0.40	0.69	0.20	0.29	0.46	0.37	0.33
8-9	0.37	0.41	0.34	0.31	0.28	0.44	0.27	0.26
9-10	0.29	0.36	0.31	0.32	0.37	0.38	0.36	0.29
10-11	0.15	0.18	0.19	0.18	0.15	0.20	0.25	0.21
11-12	0.16	0.23	0.15	0.07	0.09	0.28	0.19	0.24
13-14	-0.05	-0.06	-0.15	-0.08	-0.11	-0.22	-0.06	-0.09
14-15	-0.23	-0.37	-0.27	-0.12	-0.08	-0.10	-0.18	-0.16
15-16	-0.05	-0.03	-0.05	-0.04	-0.01	-0.05	-0.07	-0.02
17-18	-0.03	-0.06	-0.05	-0.03	-0.10	-0.18	-0.05	-0.08
2-8	-0.92	-0.82	-0.87	-0.58	-0.61	-0.79	-0.78	-0.82
8-13	0.37	0.43	0.46	0.33	0.26	0.35	0.32	0.34
13-17	0.12	0.11	0.10	0.09	0.07	0.14	0.08	0.08
17-19	0.05	0.04	0.06	0.05	0.04	0.07	0.05	0.07
3-9	-0.61	-0.53	-0.60	-0.51	-0.48	-0.55	-0.54	-0.52
9-14	0.43	0.37	0.35	0.21	0.22	0.26	0.29	0.31
4-10	-0.26	-0.22	-0.28	-0.32	-0.28	-0.29	-0.34	-0.27
10-15	0.18	0.21	0.15	0.12	0.07	0.17	0.16	0.14
15-18	0.11	0.14	0.12	0.08	0.11	0.13	0.13	0.10
5-11	-0.11	-0.10	-0.11	-0.06	-0.08	-0.13	-0.09	-0.11
11-16	0.05	0.03	0.05	0.04	0.02	0.06	0.06	0.03
6-12	-0.09	-0.06	-0.07	-0.06	-0.07	-0.08	-0.08	-0.05

Table G-4. Strain Sensor Relative Movements, Test Group II
(Stone Thickness = 10.0 in.).

Test No.	19A	19B	20A	20B	21A
Stone (in.)	10.0	10.0	10.0	10.0	10.0
Membrane	None	None	T-3401	T-3401	T-3601
Unsoaked CBR	0.90	0.93	0.87	0.96	0.78
Coil Pair	Δ (in.)	Δ (in.)	Δ (in.)	Δ (in.)	Δ (in.)
1-2	1.75	1.65	1.25	1.07	1.27
2-3	0.22	0.26	0.19	0.15	0.18
3-4	0.15	0.19	0.16	0.14	0.17
4-5	0.14	0.11	0.18	0.13	0.15
5-6	0.14	0.08	0.19	0.09	0.12
6-7	0.17	0.24	0.18	0.13	0.16
8-9	0.07	0.10	0.09	0.05	0.05
9-10	0.05	0.07	0.07	0.06	0.07
10-11	0.04	0.04	0.06	0.03	0.04
11-12	0.03	0.04	0.05	0.03	0.05
13-14	0.01	0.03	0.03	0.02	0.02
14-15	0.01	0.01	0.06	0.02	0.01
15-16	0.02	0.05	0.04	0.01	0.03
17-18	0.00	-0.03	-0.04	0.01	0.01
2-8	-0.09	-0.13	-0.15	-0.07	-0.12
8-13	0.05	-0.11	0.07	0.02	0.05
13-17	0.03	0.06	0.04	0.04	0.03
17-19	0.02	0.03	0.02	0.01	0.02
3-9	-0.07	-0.09	-0.08	-0.03	-0.07
9-14	0.01	0.01	0.02	0.00	0.03
4-10	-0.06	-0.05	-0.05	-0.02	-0.03
10-15	0.02	-0.01	0.02	0.02	0.01
15-18	0.01	-0.02	0.00	0.01	0.02
5-11	-0.03	-0.02	-0.05	-0.03	-0.05
11-16	0.01	0.01	0.02	0.02	0.02
6-12	-0.01	-0.02	-0.02	-0.02	-0.03

Table G-5. Strain Sensor Relative Movements, Test Group II
(Stone Thickness = 13.0 in.).

Test No.	22A	23A	24A	25A
Stone (in.)	13.0	13.0	13.0	13.0
Membrane	None	T-3401	M-140	B-C22
Unsoaked CBR	0.99	0.97	0.84	0.84
Coil Pair	Δ (in.)	Δ (in.)	Δ (in.)	Δ (in.)
1-2	1.65	1.00	1.32	1.49
2-3	0.12	0.25	0.18	0.10
3-4	0.10	0.10	0.11	0.07
4-5	0.10	0.05	0.10	0.05
5-6	0.09	0.07	0.07	0.05
6-7	0.08	0.12	0.07	0.03
8-9	0.06	0.18	0.10	0.11
9-10	0.04	0.13	0.09	0.07
10-11	0.03	0.05	0.05	0.02
11-12	0.02	0.07	0.04	0.02
13-14	0.04	0.13	0.09	0.02
14-15	0.02	0.06	0.08	0.01
15-16	0.01	0.03	0.01	0.01
17-18	-0.01	0.04	0.01	0.02
2-8	-0.03	-0.05	-0.12	-0.02
8-13	0.02	-0.02	0.04	0.02
13-17	0.02	0.03	0.05	0.02
17-19	0.02	0.02	0.02	0.02
3-9	-0.02	-0.03	-0.04	-0.02
9-14	0.01	0.01	0.02	0.00
4-10	-0.03	-0.02	-0.03	-0.02
10-15	0.02	0.00	0.01	0.01
15-18	0.01	0.00	0.02	0.00
5-11	-0.01	-0.02	-0.02	-0.01
11-16	0.01	-0.03	-0.01	0.00
6-12	-0.01	-0.02	-0.03	-0.02

Table G-6. Strain Sensor Relative Movements, Test Group III.

Test No.	26B	27B	28B	29B	30B	31B
Stone (in.)	3.0	3.0	4.5	4.5	6.0	6.0
Membrane	None	T-3401	None	T-3401	None	T-3401
Unsoaked CBR	1.55	1.56	1.59	1.61	1.72	1.44
Coil Pair	Δ (in.)	Δ (in.)	Δ (in.)	Δ (in.)	Δ (in.)	Δ (in.)
1-2	0.39	1.38	0.90	1.84	1.61	2.33
2-3	1.71	0.74	1.29	0.78	0.89	0.68
3-4	1.18	0.99	0.87	0.92	0.76	0.72
4-5	0.87	0.74	0.73	0.52	0.66	0.40
5-6	0.47	0.49	0.43	0.38	0.48	0.31
6-7	0.42	0.32	0.42	0.27	0.32	0.27
8-9	0.61	-0.15	0.46	0.05	0.31	0.33
9-10	0.43	-0.05	0.31	0.08	0.14	0.26
10-11	0.34	0.09	0.22	0.11	0.16	0.21
11-12	0.14	0.10	0.21	0.25	0.18	0.14
13-14	-0.09	-0.06	-0.08	-0.07	-0.11	-0.07
14-15	-0.21	-0.11	-0.27	-0.18	-0.25	-0.08
15-16	-0.09	-0.05	-0.10	-0.08	-0.08	0.03
17-18	-0.05	-0.06	-0.12	-0.07	-0.11	-0.07
2-8	-1.74	-1.01	-0.94	-0.76	-0.61	-0.55
8-13	0.38	-0.08	0.44	0.20	0.22	0.22
13-17	0.12	-0.02	0.13	0.03	0.04	0.08
17-19	0.07	0.01	0.04	0.02	0.03	0.03
3-9	-1.27	-0.71	-0.76	-0.40	-0.31	-0.41
9-14	0.20	0.28	0.38	0.31	0.28	0.23
4-10	-0.91	-0.39	-0.52	-0.28	-0.23	-0.29
10-15	0.34	0.10	0.29	0.11	0.09	0.11
15-18	0.26	0.06	0.21	0.10	0.11	0.09
5-11	-0.21	-0.10	-0.17	-0.10	-0.13	-0.09
11-16	0.04	0.06	0.04	0.05	0.03	0.05
6-12	-0.12	-0.07	-0.10	-0.04	-0.08	-0.06

Table G-7. Strain Sensor Relative Movements, Test Group IV.

Test No.	32B	33B
Stone (in.)	3.0	3.0
Membrane	None	T-3401
Unsoaked CBR	2.43	2.39
<u>Coil Pair</u>	<u>Δ (in.)</u>	<u>Δ (in.)</u>
1-2	0.49	1.03
2-3	1.73	1.59
3-4	1.04	0.85
4-5	0.71	0.66
5-6	0.46	0.32
6-7	0.31	0.36
8-9	0.33	0.18
9-10	0.35	0.27
10-11	0.16	0.05
11-12	0.11	0.08
13-14	-0.08	-0.04
14-15	-0.17	-0.08
15-16	-0.06	-0.06
17-18	-0.09	-0.04
2-8	-1.03	-0.89
8-13	0.41	0.28
13-17	0.15	0.07
17-19	0.05	0.04
3-9	-0.78	-0.65
9-14	0.26	0.27
4-10	-0.51	-0.36
10-15	0.29	0.23
15-18	0.23	0.11
5-11	-0.19	-0.25
11-16	0.07	0.06
6-12	-0.14	-0.13

APPENDIX H

MODEL TEST PROGRAM FABRIC DEFORMATION DATA

The fabric deformation was determined during all those model tests which utilized Tytar fabrics. A pattern was placed on the fabric by a silk-screen process. The pattern resembled a spider web, being composed of 24 radial lines, each connected to the adjoining two radials at intervals of one inch, proceeding outward from the center to a radial distance of 10 inches. Initial and final gage lengths were determined with a caliper along perpendicular diameters. The average gage length changes for segments along a typical radius were then computed, rounding to the nearest 0.01 inch. Metal discs were epoxied to the fabric at radial distances of 12, 14, and 16 inches. A thin rod was welded to each disc, run along the fabric surface, extended to outside the test pit through a hole drilled specifically for that purpose, and attached to a dial gage stem by setscrew. Recording the changes in dial gage readings permitted determination of the absolute movement of and relative movement between those points on the fabric to which the discs were fastened. The deformations (Δ) for radial offset segments (X) are provided herein for all appropriate tests. Elongation of the initial gage length is considered negative. Crushed stone depth, fabric grade, and the unsoaked CBR of the subgrade soil are provided with the deformation data for each test.

Table H-1. Fabric Segment Deformations, Test No. 2B
(6.0 in. Stone/T-3401/Unsoaked CBR = 0.39).

<u>X (in.)</u>	<u>Δ (in.)</u>
0-1	-0.04
1-2	-0.04
2-3	-0.03
3-4	-0.02
4-5	-0.03
5-6	-0.02
6-7	-0.02
7-8	-0.02
8-9	-0.01
9-10	-0.01
10-12	-0.013
12-14	-0.006
14-16	-0.005

Table H-2. Fabric Segment Deformations, Test No. 4B
(7.5 in. Stone/T-3401/Unsoaked CBR = 0.41).

<u>X (in.)</u>	<u>Δ (in.)</u>
0-1	-0.02
1-2	-0.03
2-3	-0.03
3-4	-0.02
4-5	-0.02
5-6	-0.02
6-7	-0.01
7-8	-0.01
8-9	-0.01
9-10	-0.01
10-12	-0.014
12-14	-0.009
14-16	-0.004

Table H-3. Fabric Segment Deformations, Test No. 6B
(9.0 in. Stone/T-3401/Unsoaked CBR = 0.41).

<u>X (in.)</u>	<u>Δ (in.)</u>
0-1	-0.02
1-2	-0.01
2-3	-0.02
3-4	-0.01
4-7	-0.02
7-10	-0.01
10-12	-0.006
12-14	-0.006
14-16	-0.009

Table H-4. Fabric Segment Deformations, Test No. 9A
(4.5 in. Stone/T-3401/Unsoaked CBR = 0.86).

<u>X (in.)</u>	<u>Δ (in.)</u>
0-1	-0.07
1-2	-0.06
2-3	-0.09
3-4	-0.07
4-5	-0.06
5-6	-0.06
6-7	-0.03
7-8	-0.03
8-9	-0.02
9-10	-0.02
10-12	-0.024
12-14	-0.008
14-16	-0.007

Table H-5. Fabric Segment Deformations, Test No. 9B
(4.5 in. Stone/T-3401/Unsoaked CBR = 0.89).

<u>X (in.)</u>	<u>Δ (in.)</u>
0-1	-0.08
1-2	-0.08
2-3	-0.08
3-4	-0.06
4-5	-0.05
5-6	-0.04
6-7	-0.04
7-8	-0.02
8-9	-0.02
9-10	-0.01
10-12	-0.019
12-14	-0.009
14-16	-0.006

Table H-6. Fabric Segment Deformations, Test No. 10A
(4.5 in. Stone/T-3601/Unsoaked CBR = 0.85).

<u>X (in.)</u>	<u>Δ (in.)</u>
0-1	-0.09
1-2	-0.07
2-3	-0.08
3-4	-0.08
4-5	-0.07
5-6	-0.06
6-7	-0.05
7-8	-0.03
8-9	-0.03
9-10	-0.02
10-12	-0.030
12-14	-0.011
14-16	-0.008

Table H-7. Fabric Segment Deformations, Test No. 15A
(7.0 in. Stone/T-3401/Unsoaked CBR = 0.94)

<u>X (in.)</u>	<u>Δ (in.)</u>
0-1	-0.04
1-2	-0.03
2-3	-0.02
3-4	-0.01
4-5	-0.01
5-6	-0.02
6-7	-0.02
7-8	-0.01
8-9	-0.01
9-10	-0.01
10-12	-0.012
12-14	-0.005
14-16	-0.002

Table H-8. Fabric Segment Deformations, Test No. 15B
(7.0 in. Stone/T-3401/Unsoaked CBR = 0.78).

<u>X (in.)</u>	<u>Δ (in.)</u>
0-1	-0.03
1-2	-0.03
2-3	-0.02
3-4	-0.01
4-5	-0.02
5-6	-0.02
6-7	-0.01
7-8	-0.01
8-9	-0.02
9-10	-0.01
10-12	-0.018
12-14	-0.005
14-16	-0.003

Table H-9. Fabric Segment Deformations, Test No. 16A
(7.0 in. Stone/T-3601/Unsoaked CBR = 0.74).

<u>X (in.)</u>	<u>Δ (in.)</u>
0-1	-0.04
1-2	-0.03
2-3	-0.03
3-4	-0.02
4-5	-0.01
5-6	-0.02
6-7	-0.02
7-8	-0.01
8-9	-0.01
9-10	-0.01
10-12	-0.013
12-14	-0.006
14-16	-0.002

Table H-10. Fabric Segment Deformations, Test No. 20A
(10.0 in. Stone/T-3401/Unsoaked CBR = 0.87).

<u>X (in.)</u>	<u>Δ (in.)</u>
0-1	-0.01
1-2	-0.01
2-4	-0.01
4-7	-0.01
7-10	-0.01
10-12	-0.005
12-14	-0.004
14-16	-0.006

Table H-11. Fabric Segment Deformations, Test No. 20B
(10.0 in. Stone/T-3401/Unsoaked CBR = 0.96).

<u>X (in.)</u>	<u>Δ (in.)</u>
0-2	-0.01
2-4	-0.01
4-7	-0.01
7-10	0.00
10-12	-0.001
12-14	-0.001
14-16	-0.002

Table H-12. Fabric Segment Deformations, Test No. 21A
(10.0 in. Stone/T-3601/Unsoaked CBR = 0.78).

<u>X (in.)</u>	<u>Δ (in.)</u>
0-1	-0.01
1-2	-0.01
2-4	-0.01
4-7	-0.01
7-10	-0.01
10-12	-0.004
12-14	-0.003
14-16	-0.001

Table H-13. Fabric Segment Deformations, Test No. 23A
(13.0 in. Stone/T-3401/Unsoaked CBR = 0.97).

<u>X (in.)</u>	<u>Δ (in.)</u>
0-5	-0.02
5-10	-0.01
10-12	-0.002
12-14	-0.003
14-16	-0.001

Table H-14. Fabric Segment Deformations, Test No. 27B
(3.0 in. Stone/T-3401/Unsoaked CBR = 1.56).

<u>X (in.)</u>	<u>Δ (in.)</u>
0-1	-0.02
1-2	-0.04
2-3	Torn
3-4	-0.02
4-5	-0.01
5-6	-0.01
6-7	-0.02
7-8	-0.01
8-9	-0.02
9-10	-0.01
10-12	-0.019
12-14	-0.008
14-16	-0.005

Table H-15. Fabric Segment Deformations, Test No. 29B
(4.5 in. Stone/T-3401/Unsoaked CBR = 1.61).

<u>X (in.)</u>	<u>Δ (in.)</u>
0-1	-0.04
1-2	-0.09 (Tearing)
2-3	-0.03
3-4	-0.04
4-5	-0.02
5-6	-0.01
6-7	-0.02
7-8	-0.01
8-9	-0.01
9-10	-0.01
10-12	-0.011
12-14	-0.002
14-16	-0.003

Table H-16. Fabric Segment Deformations, Test No. 31B
(6.0 in. Stone/T-3401/Unsoaked CBR = 1.44).

<u>X (in.)</u>	<u>Δ (in.)</u>
0-1	-0.03
1-2	-0.02
2-3	-0.03
3-4	-0.02
4-5	-0.02
5-6	-0.01
6-7	-0.02
7-8	-0.01
8-9	-0.01
9-10	-0.01
10-12	-0.012
12-14	-0.004
14-16	-0.001

Table H-17. Fabric Segment Deformations, Test No. 33B
(3.0 in. Stone/T-3401/Unsoaked CBR = 2.39).

<u>X (in.)</u>	<u>Δ (in.)</u>
0-1	-0.03
1-2	-0.02
2-3	-0.02
3-4	Torn
4-5	-0.03
5-6	-0.02
6-7	-0.01
7-8	-0.01
8-9	-0.02
9-10	-0.01
10-12	-0.018
12-14	-0.007
14-16	-0.004

APPENDIX I

MODEL TEST PROGRAM STRESS CELL DATA

Vertical pressures within the subgrade soil were monitored for all those model tests which utilized the Type B Loading (i.e., 0.2 second load pulse applied at the rate of 20 cpm). Five pressure cells were utilized, placed in a single stack, centered under the edge of the footing. These cells were designed and constructed by Intrapasart (50). Design considerations, cell details, and procedures for calibration and operation are provided in Appendix D. Output was monitored, to an appropriate scale, on a strip chart recorder. Stress cell readings were taken of each cell for a period of two to three load cycles during the beginning stages of the model test. The readings were taken beginning with the uppermost cell and proceeding in order to the lowest cell in the stack. This procedure was utilized to minimize any uncertainty concerning cell position due to cell translation and rotation under load application. For several tests, stress cell readings were also taken during the latter stages of the test. In such cases, final stress cell positions and orientations were carefully determined during excavation of the subgrade soil. Stress cell data are presented herein. Radial offset distance from the footing centerline (X), depth below the footing base (Z), and orientation with respect to a horizontal plane (θ) are provided for each cell, along with the load induced stress per cycle. The former two quantities are also provided,

expressed in terms of the footing radius (R). Crushed stone depth, interfacial membrane type, and the unsoaked CBR of the subgrade soil are provided with the stress cell data for each test.

Table I-1. Pressure Cell Readings, Test No. 1B (6.0 in. Stone/None/Unsoaked CBR = 0.38).

Cell No.	X (in.)	Z (in.)	X/R	Z/R	θ (Deg.)	Stress (psi)
1	3.0	7.4	1.00	2.47	0	10.2(a)
2	3.0	10.0	1.00	3.33	0	6.8
3	3.0	12.3	1.00	4.10	0	4.4
4	3.0	14.8	1.00	4.93	0	3.0
5	3.0	17.2	1.00	5.73	0	2.4
<hr/>						
1	3.0	4.6	1.00	1.53	51	16.0(b)
2	3.0	7.2	1.00	2.40	18	11.0
3	3.0	8.8	1.00	2.93	7	8.6
4	3.0	10.7	1.00	3.57	7	6.0
5	3.0	12.7	1.00	4.23	4	4.4

(a) Initial

(b) Final

Table I-2. Pressure Cell Readings, Test No. 2B (6.0 in. Stone/T-3401/Unsoaked CBR = 0.39).

Cell No.	X (in.)	Z (in.)	X/R	Z/R	θ (Deg.)	Stress (psi)
1	3.0	7.3	1.00	2.43	0	9.8(a)
2	3.0	9.6	1.00	3.20	0	7.2
3	3.0	12.1	1.00	4.03	0	4.0
4	3.0	14.9	1.00	4.96	0	2.8
5	3.0	17.1	1.00	5.70	0	1.6
<hr/>						
1	3.0	4.4	1.00	1.47	19	15.4(b)
2	3.0	6.4	1.00	2.13	12	10.8
3	3.0	8.2	1.00	2.73	9	8.4
4	3.0	10.6	1.00	3.53	6	6.2
5	3.0	12.3	1.00	4.10	4	4.4
<hr/>						
(a) Initial						
(b) Final						

Table I-3. Pressure Cell Readings, Test No. 3B (7.5 in. Stone/None/Unsoaked CBR = 0.43).

Cell No.	X (in.)	Z (in.)	X/R	Z/R	θ (Deg.)	Stress (psi)
1	3.0	8.6	1.00	2.87	0	8.8(a)
2	3.0	11.3	1.00	3.77	0	5.2
3	3.0	13.6	1.00	4.53	0	3.8
4	3.0	16.4	1.00	5.47	0	2.4
5	3.0	18.6	1.00	6.20	0	1.8

1	3.0	5.7	1.00	1.90	27	13.8(b)
2	3.0	7.5	1.00	2.50	14	9.8
3	3.0	9.5	1.00	3.17	8	7.6
4	3.0	12.1	1.00	4.03	9	4.8
5	3.0	14.0	1.00	4.67	5	3.4

(a) Initial

(b) Final

Table I-4. Pressure Cell Readings, Test No. 4B (7.5 in. Stone/T-3401/Unsoaked CBR = 0.41).

Cell No.	X (in.)	Z (in.)	X/R	Z/R	θ (Deg.)	Stress (psi)
1	3.0	9.0	1.00	3.00	0	7.6(a)
2	3.0	11.1	1.00	3.70	0	5.4
3	3.0	13.6	1.00	4.53	0	3.6
4	3.0	16.3	1.00	5.43	0	2.2
5	3.0	18.7	1.00	6.23	0	2.0
<hr/>						
1	3.0	5.6	1.00	1.87	13	11.6(b)
2	3.0	7.2	1.00	2.40	12	8.8
3	3.0	9.6	1.00	3.20	11	6.6
4	3.0	12.0	1.00	4.00	7	4.4
5	3.0	14.2	1.00	4.73	4	3.2

(a) Initial

(b) Final

Table I-5. Pressure Cell Readings, Test No. 5B (9.0 in. Stone/None/Unsoaked CBR = 0.40).

Cell No.	X (in.)	Z (in.)	X/R	Z/R	θ (Deg.)	Stress (psi)
1	3.0	10.3	1.00	3.43	0	6.6(a)
2	3.0	12.7	1.00	4.23	0	4.2
3	3.0	15.3	1.00	5.10	0	2.8
4	3.0	17.7	1.00	5.90	0	2.4
5	3.0	20.1	1.00	6.70	0	1.6

1	3.0	7.0	1.00	2.33	16	10.2(b)
2	3.0	9.0	1.00	3.00	11	8.6
3	3.0	10.9	1.00	3.63	8	6.2
4	3.0	13.4	1.00	4.47	4	4.0
5	3.0	15.5	1.00	5.17	2	3.2

(a) Initial

(b) Final

Table I-6. Pressure Cell Readings, Test No. 6B (9.0 in. Stone/T-3401/Unsoaked CBR = 0.41).

Cell No.	X (in.)	Z (in.)	X/R	Z/R	θ (Deg.)	Stress (psi)
1	3.0	10.5	1.00	3.50	0	6.4(a)
2	3.0	12.9	1.00	4.30	0	4.0
3	3.0	15.4	1.00	5.13	0	3.0
4	3.0	17.8	1.00	5.93	0	2.2
5	3.0	20.4	1.00	6.80	0	1.8
<hr/>						
1	3.0	7.9	1.00	2.63	9	8.6(b)
2	3.0	9.9	1.00	3.30	7	6.4
3	3.0	12.2	1.00	4.07	7	4.4
4	3.0	14.3	1.00	4.77	4	3.2
5	3.0	16.7	1.00	5.57	3	2.6

(a) Initial

(b) Final

Table I-7. Pressure Cell Readings, Test No. 7B (4.5 in. Stone/None/Unsoaked CBR = 0.91).

Cell No.	<u>X (in.)</u>	<u>Z (in.)</u>	<u>X/R</u>	<u>Z/R</u>	<u>Stress (psi)^(a)</u>
1	3.0	5.7	1.00	1.90	13.0
2	3.0	8.2	1.00	2.73	9.2
3	3.0	10.6	1.00	3.53	6.6
4	3.0	13.0	1.00	4.33	4.2
5	3.0	17.1	1.00	5.70	2.8

(a) Initial

Table I-8. Pressure Cell Readings, Test No. 9B (4.5 in. Stone/T-3401/Unsoaked CBR = 0.89).

<u>Cell No.</u>	<u>X (in.)</u>	<u>Z (in.)</u>	<u>X/R</u>	<u>Z/R</u>	<u>Stress (psi)</u> ^(a)
1	3.0	5.9	1.00	1.97	12.2
2	3.0	8.5	1.00	2.83	8.8
3	3.0	10.9	1.00	3.63	5.4
4	3.0	13.1	1.00	4.37	4.0
5	3.0	17.4	1.00	5.80	1.6

(a) Initial

Table I-9. Pressure Cell Readings, Test No. 13B (7.0 in. Stone/None/Unsoaked CBR = 0.81).

Cell No.	X (in.)	Z (in.)	X/R	Z/R	Stress (psi) ^(a)
1	3.0	8.3	1.00	2.77	8.8
2	3.0	10.7	1.00	3.57	6.2
3	3.0	13.1	1.00	4.37	4.2
4	3.0	15.7	1.00	5.23	2.8
5	3.0	18.2	1.00	6.07	2.2

(a) Initial

Table 1-10. Pressure Cell Readings, Test No. 158 (7.0 in. Stone/T-3401/Unsoaked CBR = 0.78).

Cell No.	X (in.)	Z (in.)	X/R	Z/R	Stress (psi) ^(a)
1	3.0	8.1	1.00	2.70	9.0
2	3.0	10.5	1.00	3.50	6.6
3	3.0	13.2	1.00	4.40	4.2
4	3.0	15.8	1.00	5.27	3.0
5	3.0	18.1	1.00	6.03	2.2
(a) Initial					

Table I-11. Pressure Cell Readings, Test No. 19B (10.0 in. Stone/None/Unsoaked CBR = 0.93).

<u>Cell No.</u>	<u>X (in.)</u>	<u>Z (in.)</u>	<u>X/R</u>	<u>Z/R</u>	<u>Stress (psi) (a)</u>
1	3.0	11.2	1.00	3.73	6.2
2	3.0	13.6	1.00	4.53	4.4
3	3.0	16.3	1.00	5.43	3.2
4	3.0	18.7	1.00	6.23	2.4
5	3.0	21.2	1.00	7.07	1.8

(a) Initial

Table I-12. Pressure Cell Readings, Test No. 20B (10.0 in. Stone/T-3401/Unsoaked CBR = 0.96).

Cell No.	X (in.)	Z (in.)	X/R	Z/R	Stress (psi) (a)
1	3.0	11.3	1.00	3.77	6.4
2	3.0	13.7	1.00	4.57	4.4
3	3.0	16.1	1.00	5.35	3.0
4	3.0	18.6	1.00	6.20	2.6
5	3.0	21.0	1.00	7.00	1.8

(a) Initial

Table I-13. Pressure Cell Readings, Test No. 26B (3.0 in. Stone/None/Unsoaked CBR = 1.55).

<u>Cell No.</u>	<u>X (in.)</u>	<u>Z (in.)</u>	<u>X/R</u>	<u>Z/R</u>	<u>Stress (psi)^(a)</u>
1	3.0	4.2	1.00	1.40	17.2
2	3.0	6.8	1.00	2.27	11.0
3	3.0	9.1	1.00	3.03	7.8
4	3.0	11.7	1.00	3.90	4.2
5	3.0	14.4	1.00	4.80	3.0

(a) Initial

Table I-14. Pressure Cell Readings, Test No. 27B (3.0 in. Stone/T-3401/Unsoaked CBR = 1.56).

Cell No.	<u>X (in.)</u>	<u>Z (in.)</u>	<u>X/R</u>	<u>Z/R</u>	<u>Stress (psi)^(a)</u>
1	3.0	4.4	1.00	1.47	16.4
2	3.0	6.6	1.00	2.20	11.2
3	3.0	9.3	1.00	3.10	8.2
4	3.0	11.8	1.00	3.93	4.4
5	3.0	14.2	1.00	4.73	3.2

(a) Initial

Table I-15. Pressure Cell Readings, Test No. 28B (4.5 in. Stone/None/Unsoaked CBR = 1.59).

Cell No.	<u>X (in.)</u>	<u>Z (in.)</u>	<u>X/R</u>	<u>Z/R</u>	<u>Stress (psi) (a)</u>
1	3.0	5.7	1.00	1.90	13.2
2	3.0	8.2	1.00	2.73	8.8
3	3.0	10.6	1.00	3.53	6.4
4	3.0	13.3	1.00	4.43	3.8
5	3.0	15.6	1.00	5.20	3.0

(a) Initial

Table I-16. Pressure Cell Readings, Test No. 29B (4.5 in. Stone/T-3401/Unsoaked CBR = 1.61).

Cell No.	<u>X (in.)</u>	<u>Z (in.)</u>	<u>X/R</u>	<u>Z/R</u>	<u>Stress (psi)^(a)</u>
1	3.0	5.8	1.00	1.93	13.0
2	3.0	8.1	1.00	2.70	9.2
3	3.0	10.7	1.00	3.57	6.4
4	3.0	13.2	1.00	4.40	3.6
5	3.0	15.7	1.00	5.23	2.8

(a) Initial

Table I-17. Pressure Cell Readings, Test No. 30B (6.0 in. Stone/None/Unsoaked CBR = 1.72).

Cell No.	<u>X (in.)</u>	<u>Z (in.)</u>	<u>X/R</u>	<u>Z/R</u>	<u>Stress (psi)^(a)</u>
1	3.0	7.2	1.00	2.40	10.6
2	3.0	9.7	1.00	3.23	7.2
3	3.0	12.1	1.00	4.03	4.6
4	3.0	14.6	1.00	4.86	3.2
5	3.0	17.3	1.00	5.77	2.4

(a) Initial

Table I-18. Pressure Cell Readings, Test No. 31B (6.0 in. Stone/T-3401/Unsoaked CBR = 1.44).

Cell No.	<u>X (in.)</u>	<u>Z (in.)</u>	<u>X/R</u>	<u>Z/R</u>	<u>Stress (psi)</u> ^(a)
1	3.0	7.1	1.00	2.37	10.2
2	3.0	9.6	1.00	3.20	7.0
3	3.0	12.3	1.00	4.10	4.2
4	3.0	14.7	1.00	4.90	3.0
5	3.0	17.2	1.00	5.73	1.8

(a) Initial

Table I-19. Pressure Cell Readings, Test No. 32B (3.0 in. Stone/None/Unsoaked CBR = 2.43).

Cell No.	X (in.)	Z (in.)	X/R	Z/R	θ (Deg.)	Stress (psi)
1	3.0	4.2	1.00	1.40	0	18.2(a)
2	3.0	6.8	1.00	2.27	0	10.8
3	3.0	9.1	1.00	3.03	0	8.4
4	3.0	11.7	1.00	3.90	0	4.8
5	3.0	14.1	1.00	4.70	0	3.6

1	3.0	2.1	1.00	0.70	49	33.0(b)
2	3.0	3.5	1.00	1.17	18	21.4
3	3.0	5.2	1.00	1.73	9	15.6
4	3.0	7.4	1.00	2.47	6	10.2
5	3.0	9.6	1.00	3.20	6	7.6

(a) Initial

(b) Final

AD-A110 434

AIR FORCE INST OF TECH WRIGHT-PATTERSON AFB OH
PERFORMANCE OF FABRIC REINFORCED AGGREGATE-SOIL SYSTEMS UNDER R--ETC(U)
DEC 81 W SCHAUZ
AFIT-CI-81-69D

F/G 13/2

UNCLASSIFIED

NL

6 of 6

AD-A
110 434

END

DATE

FORMED

03-82

DTIC



MICROCOPY RESOLUTION TEST CHART
NATIONAL BUREAU OF STANDARDS-1963-A

Table I-20. Pressure Cell Readings, Test No. 33B (3.0 in. Stone/T-3401/Unsoaked CBR = 2.39).

Cell No.	X (in.)	Z (in.)	X/R	Z/R	θ (Deg.)	Stress (psi)
1	3.0	4.4	1.00	1.46	0	17.8(a)
2	3.0	6.7	1.00	2.23	0	12.0
3	3.0	9.2	1.00	3.07	0	8.6
4	3.0	11.8	1.00	3.93	0	5.2
5	3.0	14.2	1.00	4.73	0	3.4

1	3.0	1.8	1.00	0.60	38	38.0(b)
2	3.0	3.1	1.00	1.03	17	27.5
3	3.0	5.0	1.00	1.67	8	17.2
4	3.0	7.3	1.00	2.43	6	10.4
5	3.0	9.6	1.00	3.20	4	7.4

(a) Initial

(b) Final

APPENDIX J

STRESS RATIO-CUMULATIVE PERMANENT DEFORMATION-LOAD CYCLE RELATIONSHIPS
FOR MODEL TEST PROGRAM

Test data were analyzed for each membrane type to determine the relationships between stress ratio (i.e., vertical stress on load center-line at subgrade soil surface computed from Boussinesq theory, divided by subgrade soil vane shear strength), cumulative permanent deformation, and load cycles. Plots of stress ratio versus rut depth after 10 , 10^2 , and 10^3 load cycles and load cycles versus stress ratio for permanent deformations of two, three, and four inches are presented herein.

Figures J-1 through J-24 deal with the Type A load tests, being comprised of four sets of six figures each. Each set includes the data for the AS and Typar 3401 reinforced AFS systems, plus the data for one of the remaining interlayers (i.e., sand in J-1 through J-6; Typar 3601 in J-7 through J-12; Mirafi 140 in J-13 through J-18; and Bidim C-22 in J-19 through J-24). Figures J-25 through J-30 deal with the Type B load tests, displaying the data for AS and Typar 3401 reinforced AFS systems. Several extrapolated data points are included in the plots. All extrapolated data points are circled. The extrapolated data points were determined by extending the load cycle-cumulative permanent deformation plots from the individual tests (Appendix E). Extension was carried a maximum of one-half log cycle on the load scale or one inch on the deformation scale. For the stress ratio-permanent deformation-load

cycle relationships presented herein, a power curve fit method was utilized to determine a best fit curve through the appropriate data points. Due to the limited number of tests conducted with each interlayer under Type A loading, curve fitting was not possible in all cases, due to lack of sufficient data points. When only two tests were conducted for a given interlayer (i.e., sand) the data points are plotted, but no curves. For the remaining interlayers, when insufficient data points (i.e., less than three) were available for fitting a power curve for any plot, a smooth curve was visually fit and drawn through the data points. The behavior of those model tests, for the interlayer being analyzed, stopped prior to achieving a given number of load cycles or a given rut depth were considered in making such plots. Visually fit curves are indicated by dashed lines. While highly subjective, these plots do provide some comparison between systems.

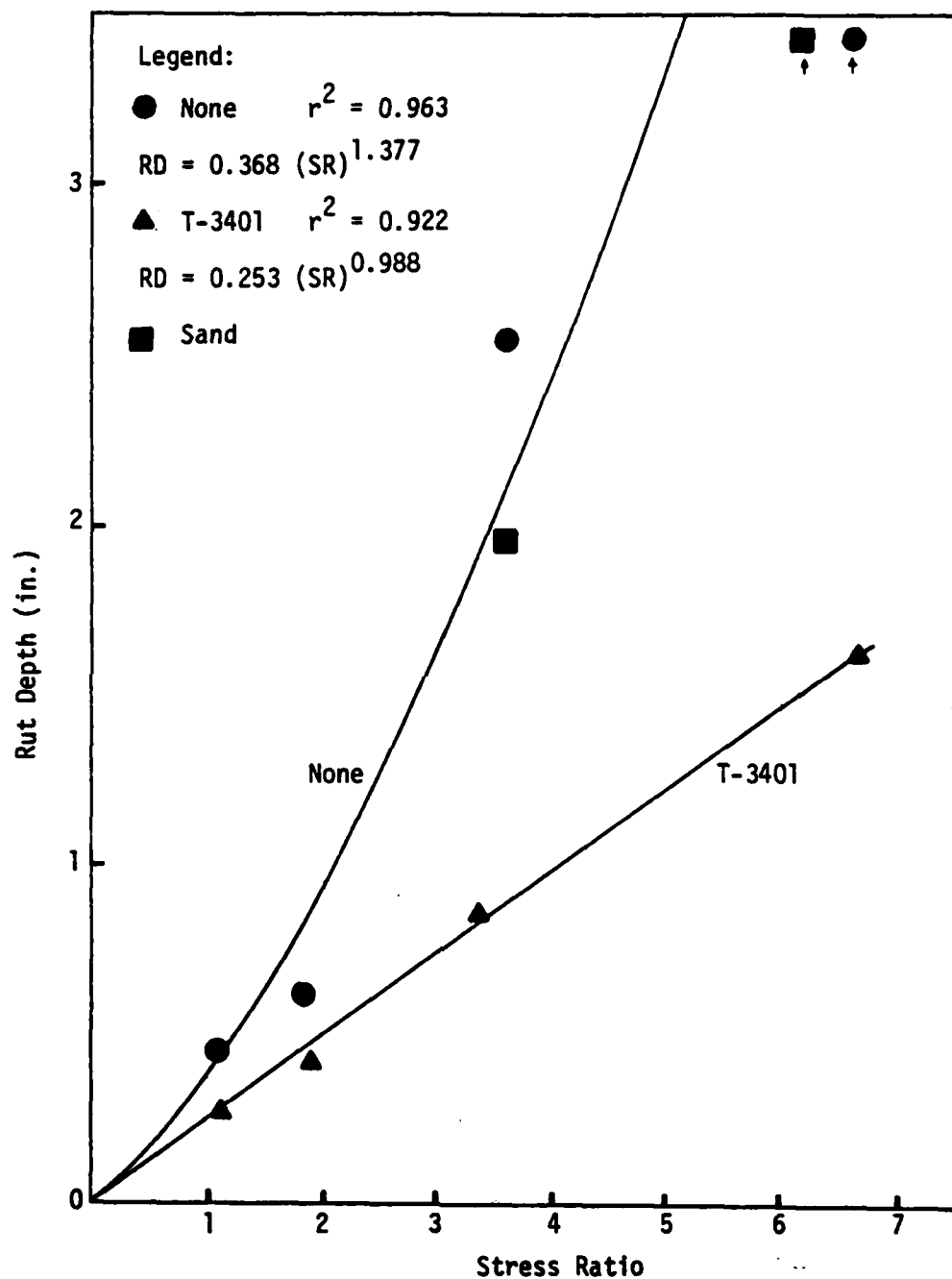


Figure J-1. Stress Ratio-Rut Depth Relationships for 10 Load Cycles, Type A Loading.

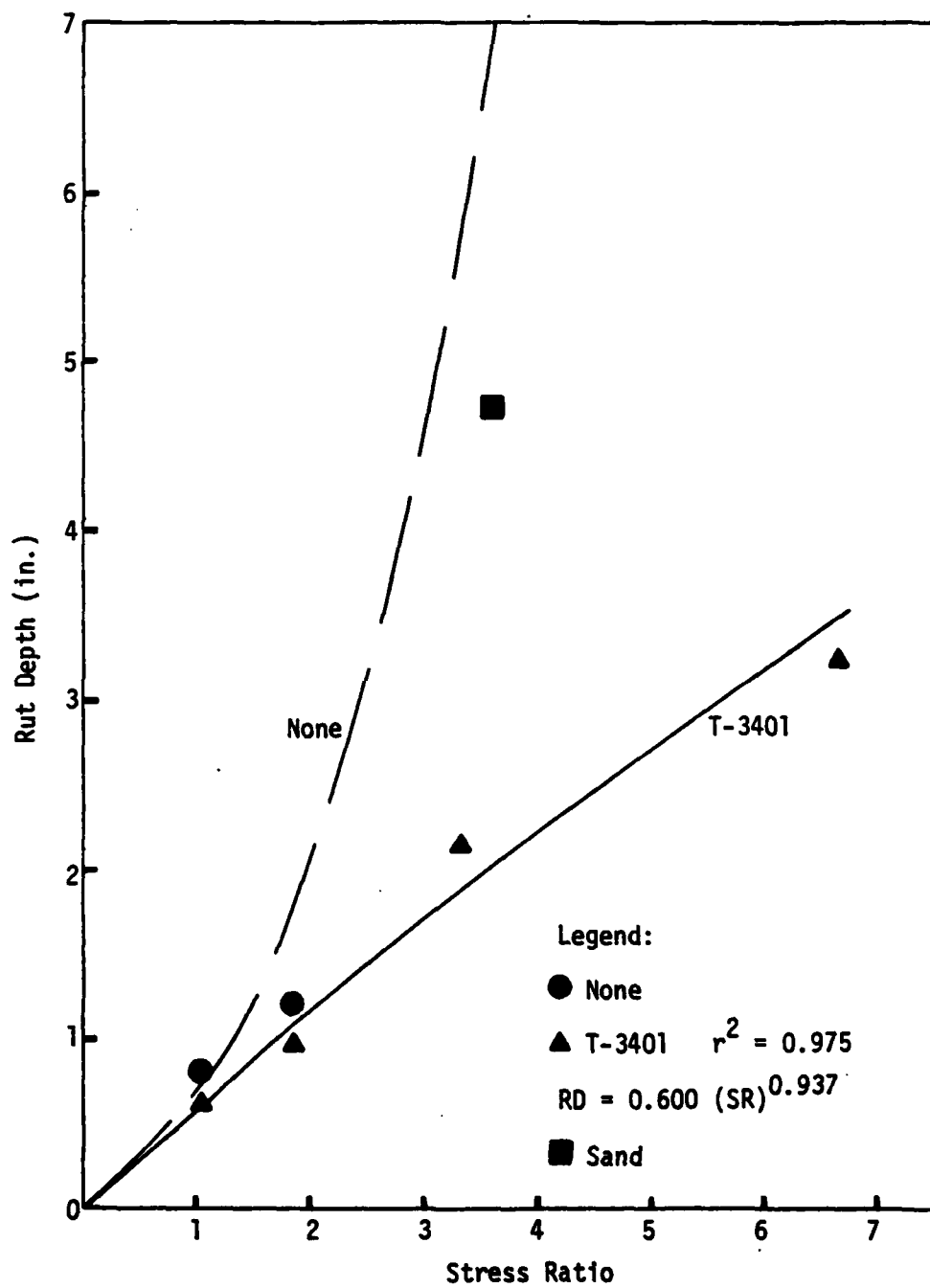


Figure J-2. Stress Ratio-Rut Depth Relationships for 100 Load Cycles, Type A Loading.

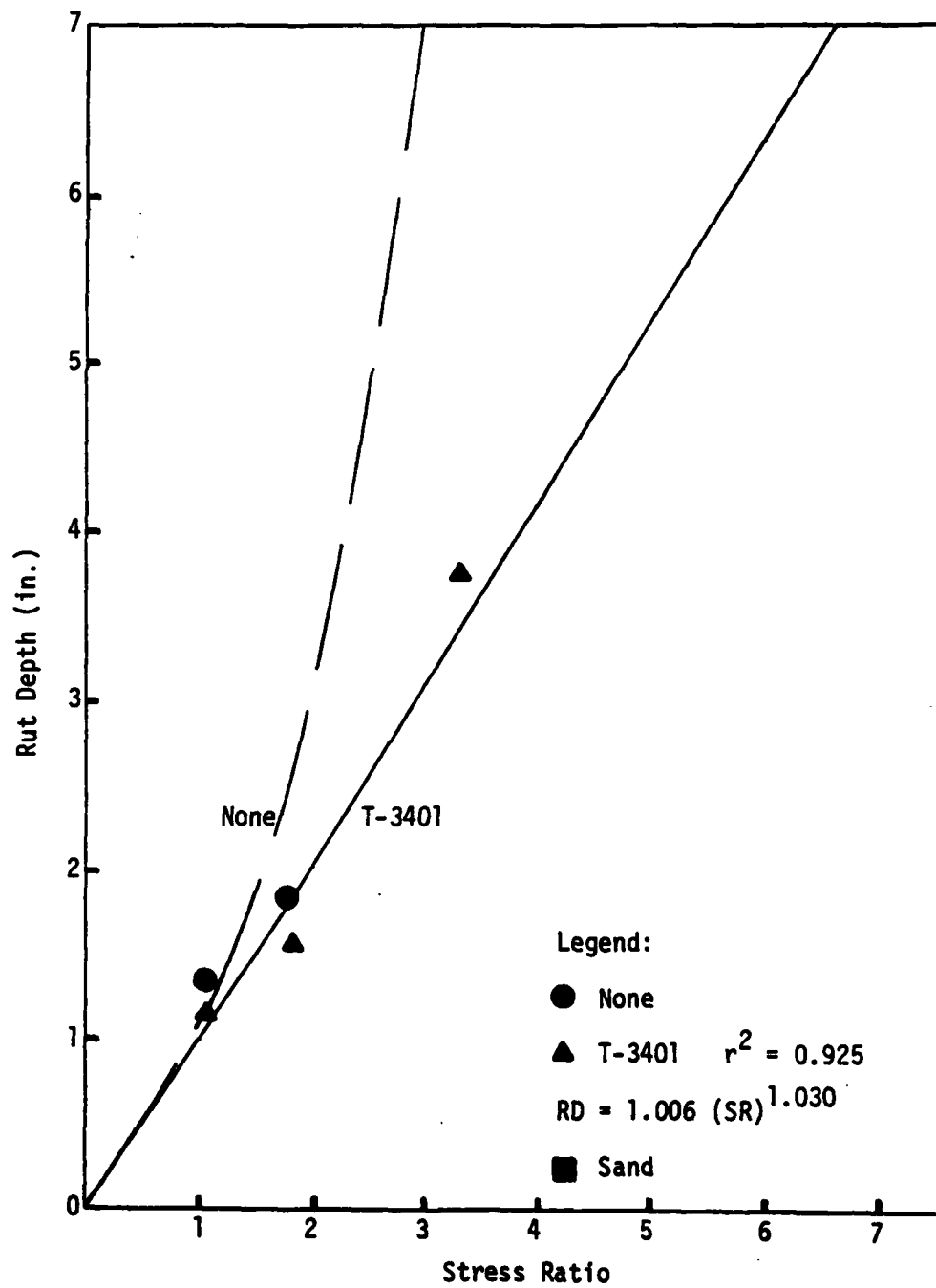


Figure J-3. Stress Ratio-Rut Depth Relationships for 1000 Load Cycles, Type A Loading.

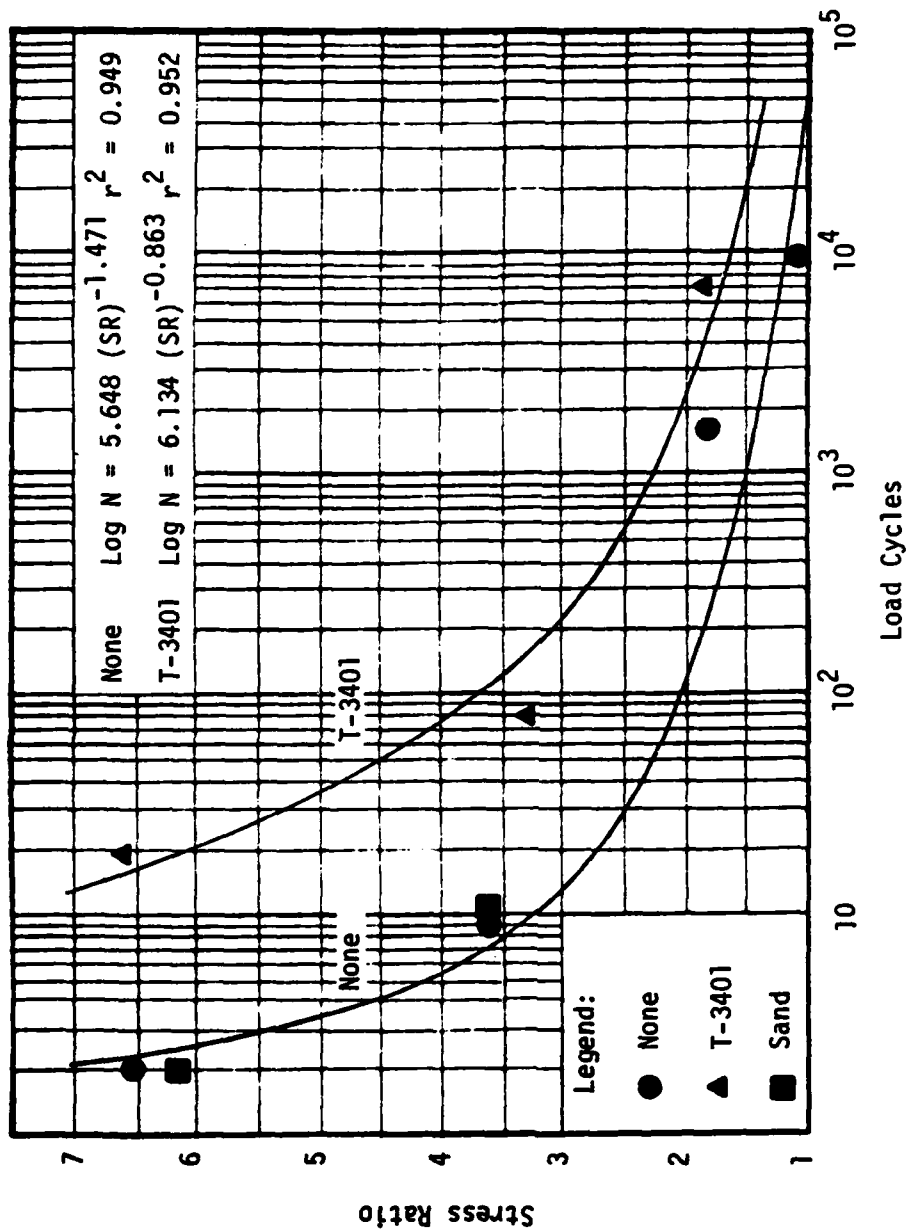


Figure J-4. Load Cycle-Stress Ratio Relationships for 2 in. Rut, Type A Loading.

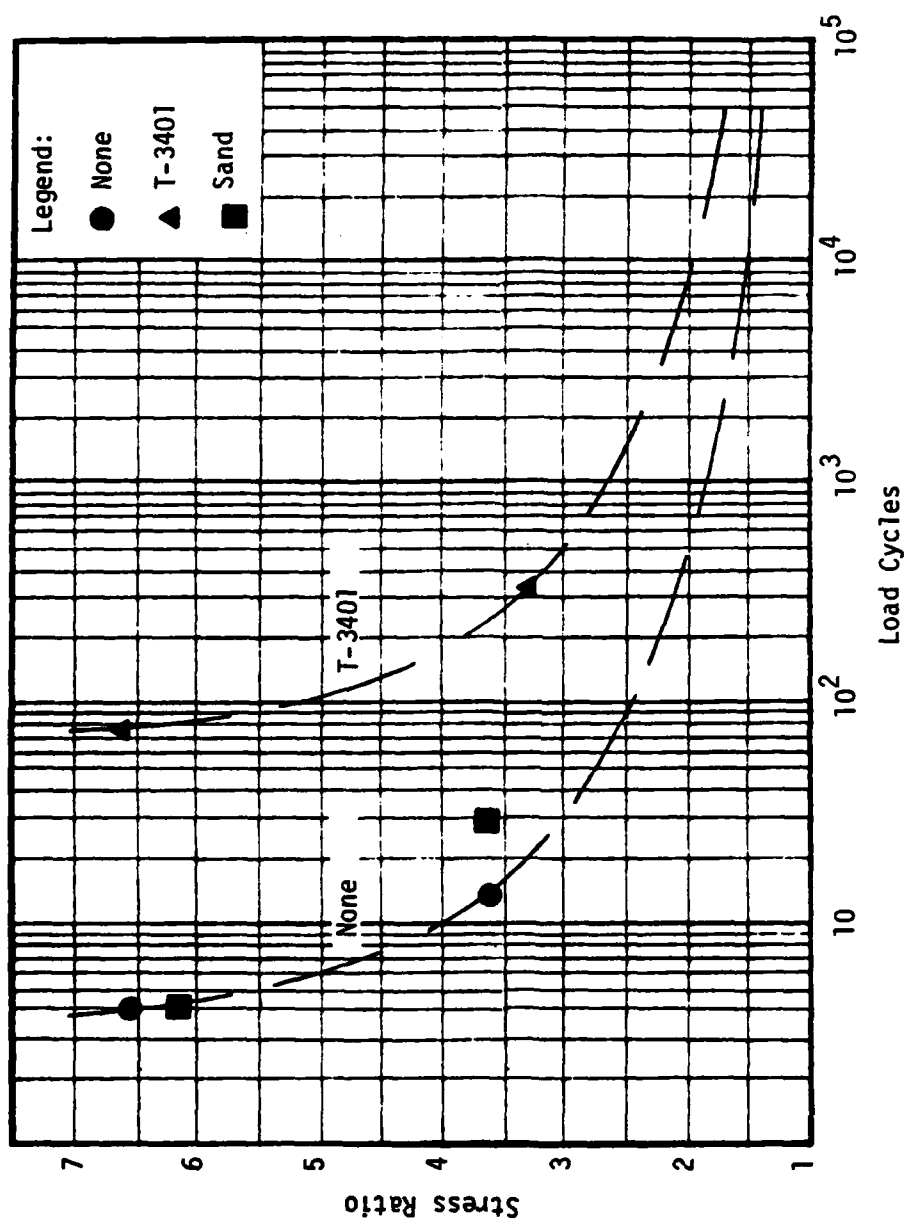


Figure J-5. Load Cycle-Stress Ratio Relationships for 3 in. Rut, Type A Loading.

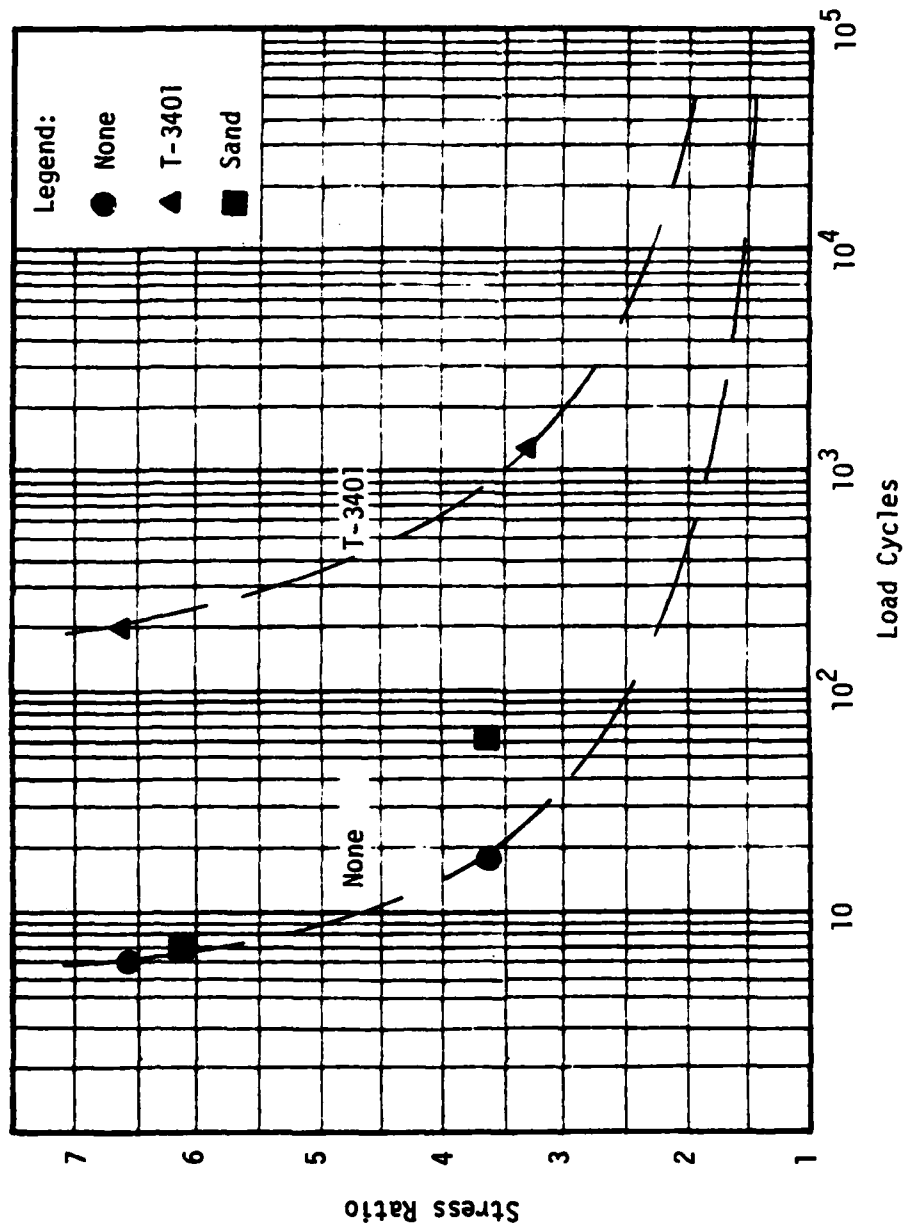


Figure J-6. Load Cycle-Stress Ratio Relationships for 4 in. Rut, Type A Loading.

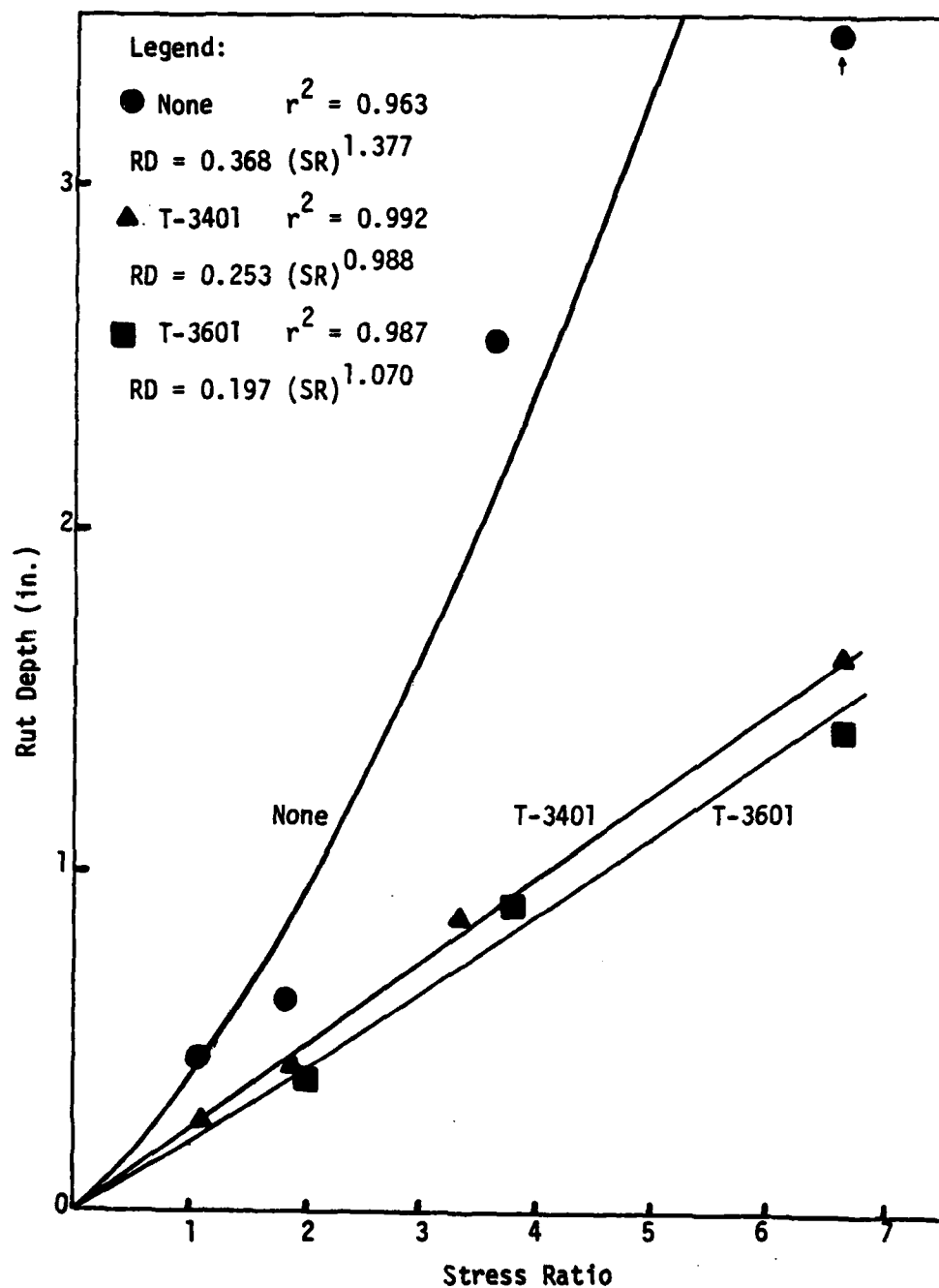


Figure J-7. Stress Ratio-Rut Depth Relationships for 10 Load Cycles, Type A Loading.

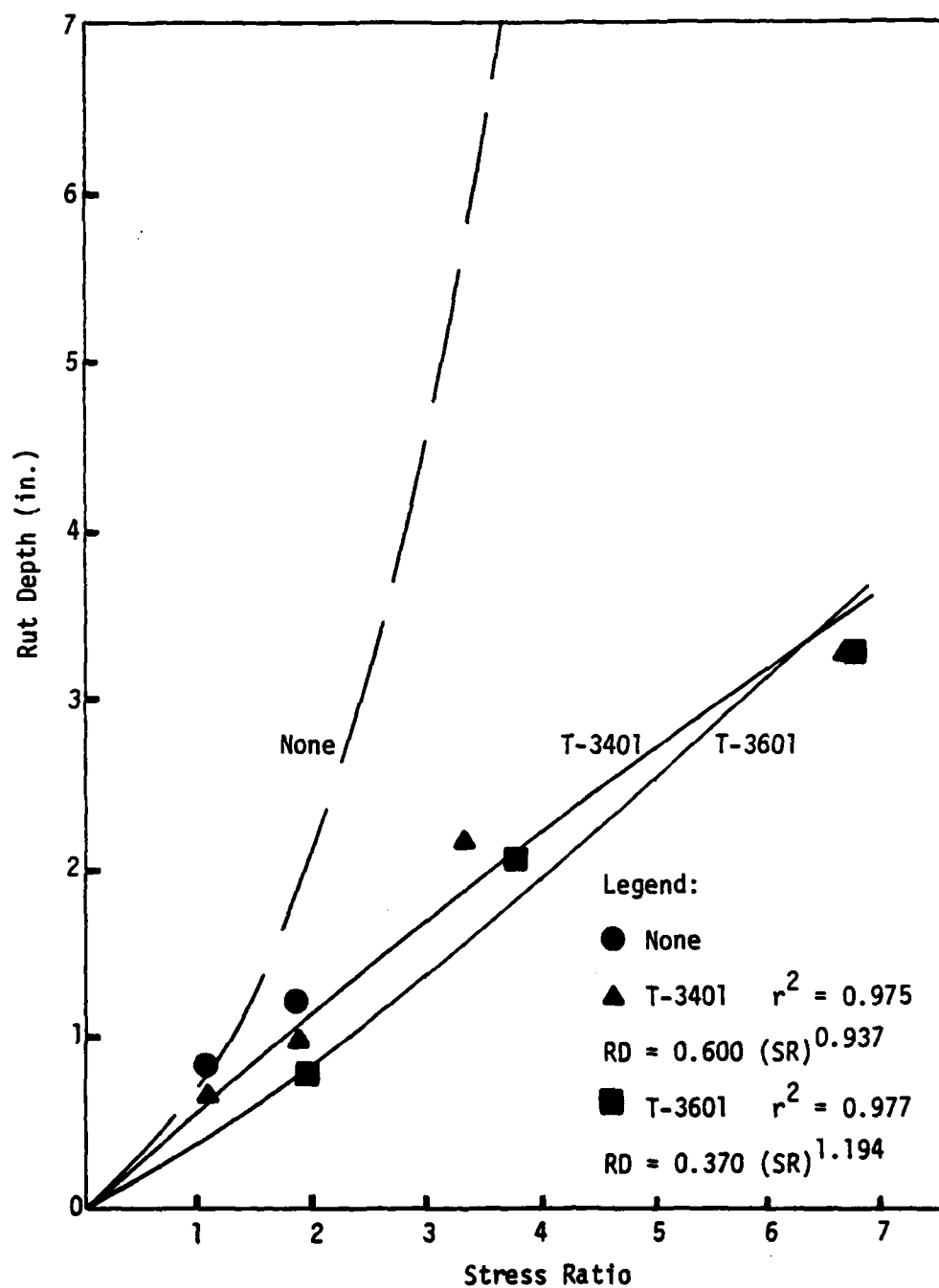


Figure J-8. Stress Ratio-Rut Depth Relationships for 100 Load Cycles, Type A Loading.

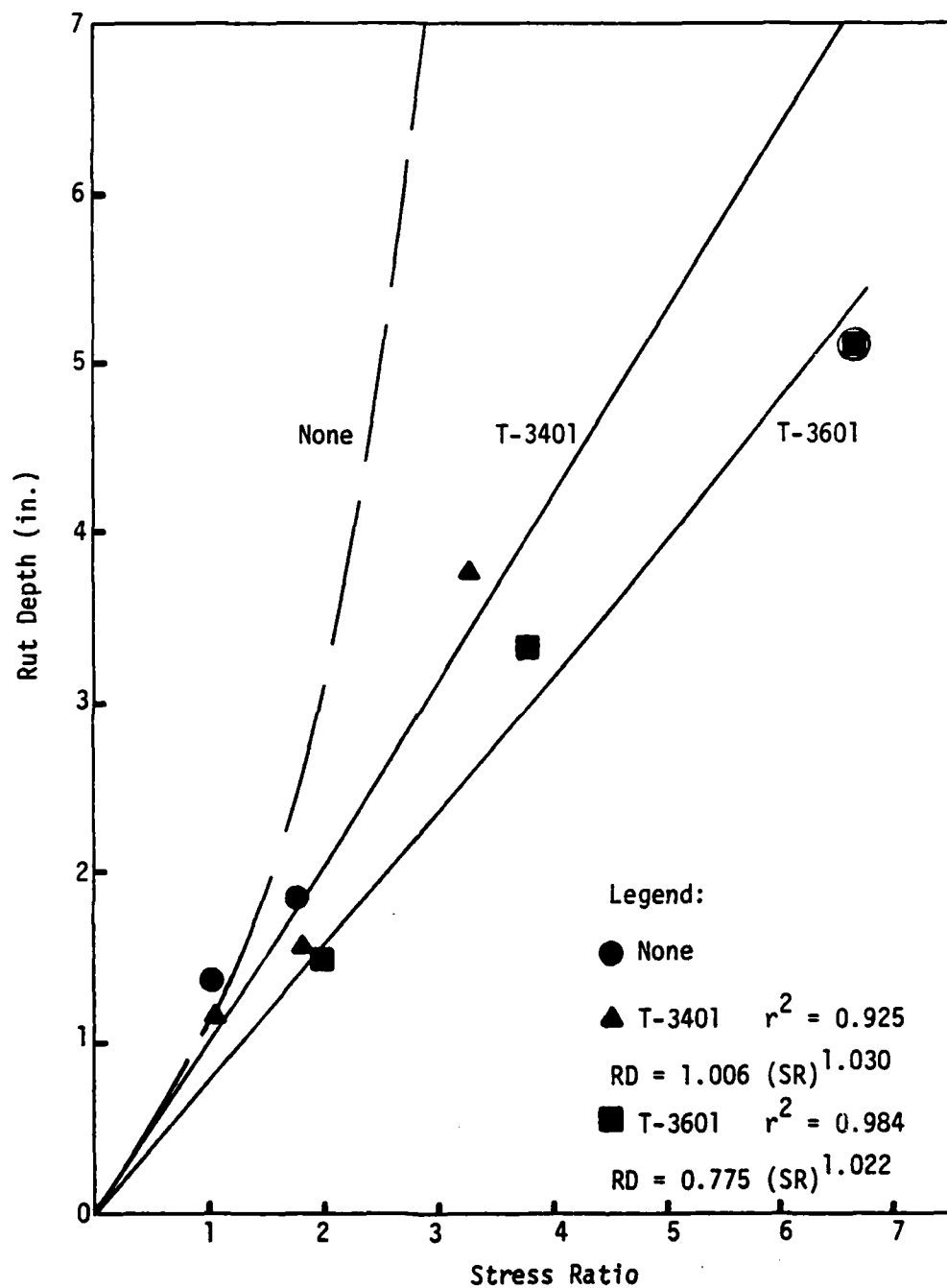


Figure J-9. Stress Ratio-Rut Depth Relationships for 1000 Load Cycles, Type A Loading.

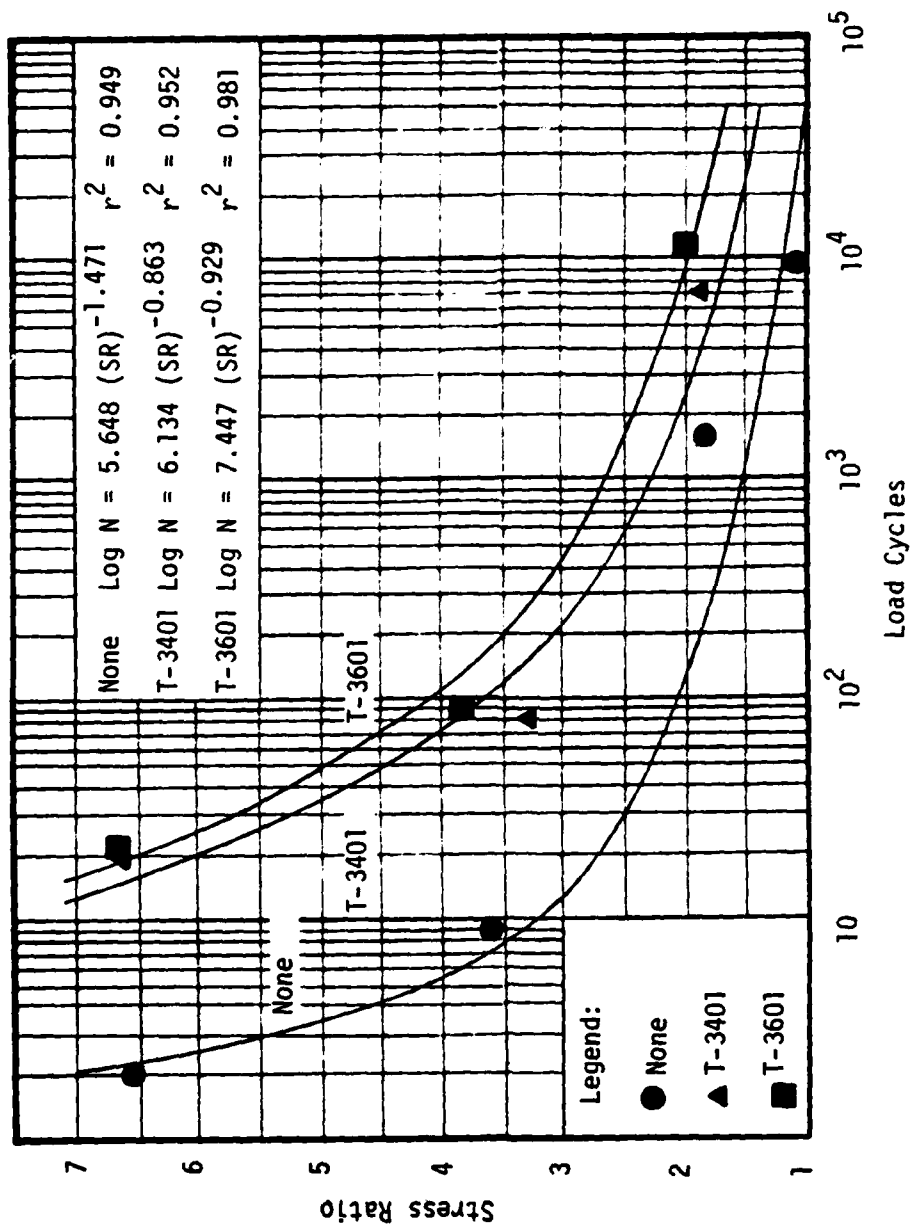


Figure J-10. Load Cycle-Stress Ratio Relationships for 2 in. Rut, Type A Loading.

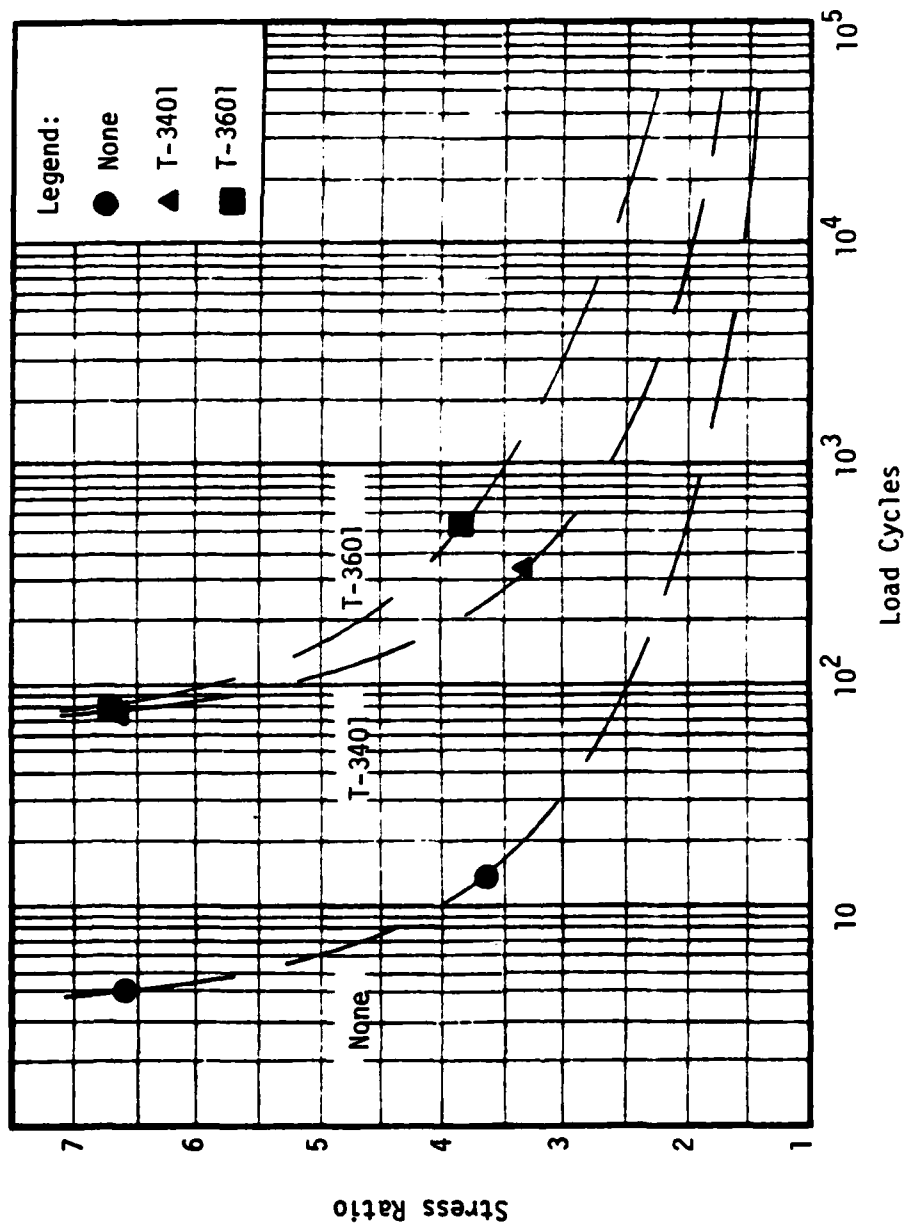


Figure J-11. Load Cycle-Stress Ratio Relationships for 3 in. Rut, Type A Loading.

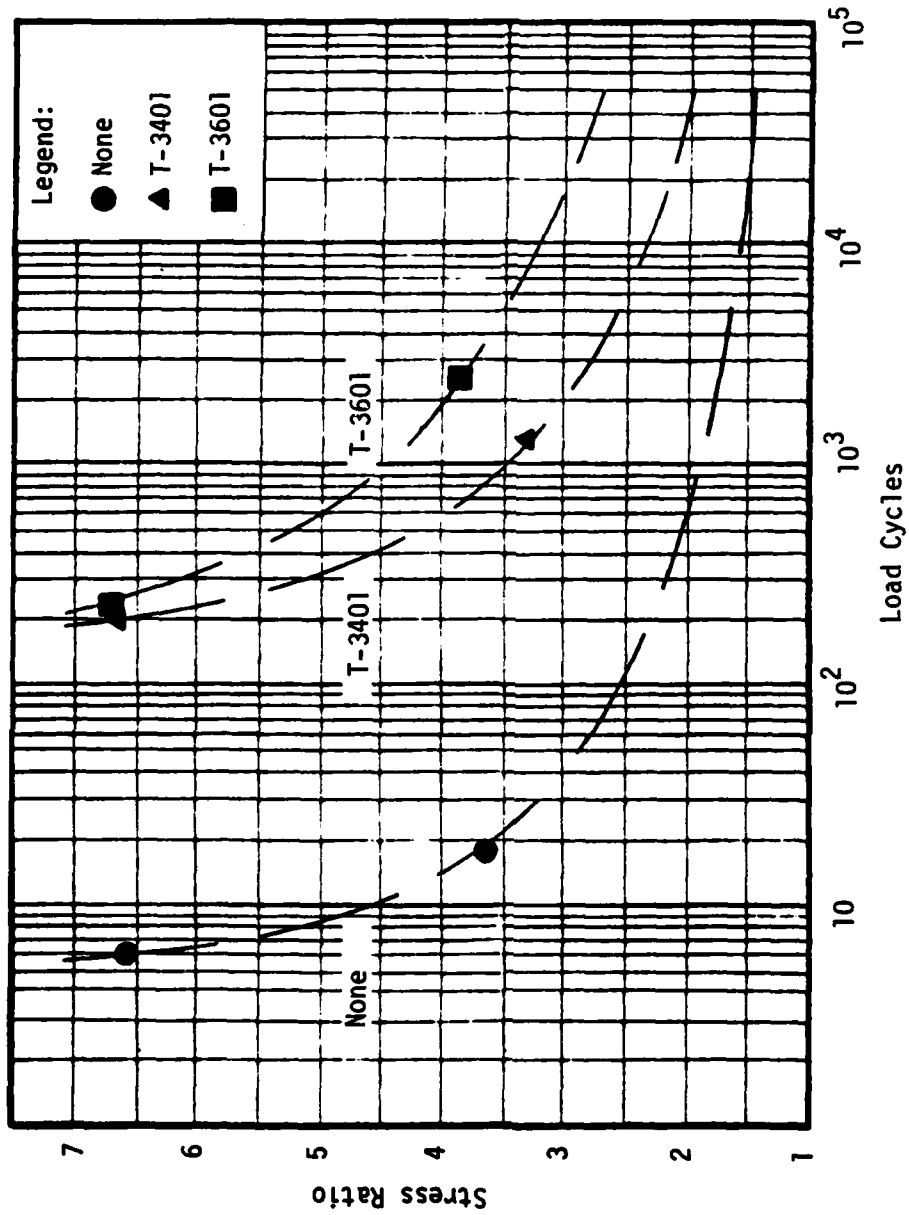


Figure J-12. Load Cycle-Stress Ratio Relationships for 4 in. Rut, Type A Loading.

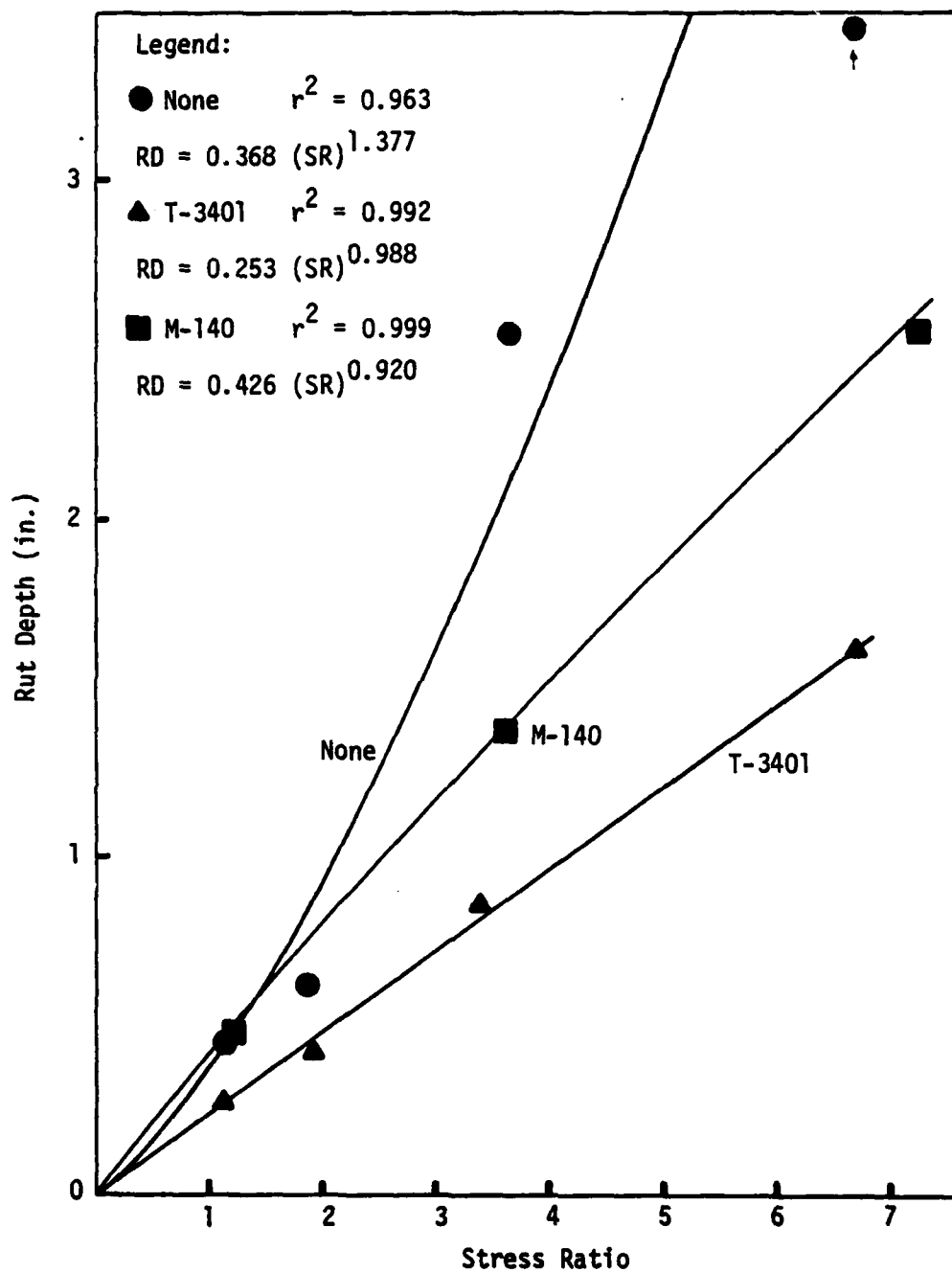


Figure J-13. Stress Ratio-Rut Depth Relationships for 10 Load Cycles, Type A Loading.

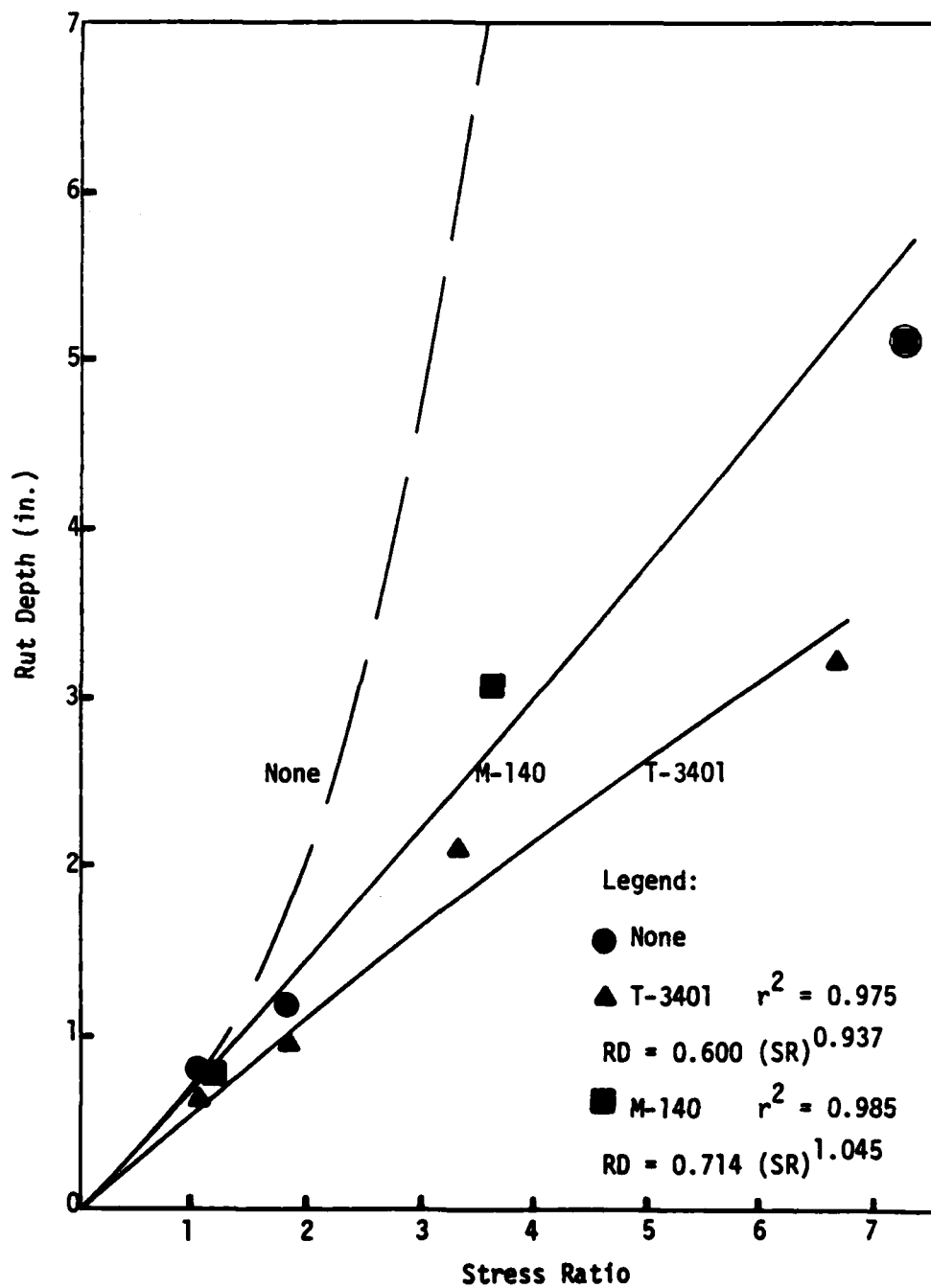


Figure J-14. Stress Ratio-Rut Depth Relationships for 100 Load Cycles, Type A Loading.

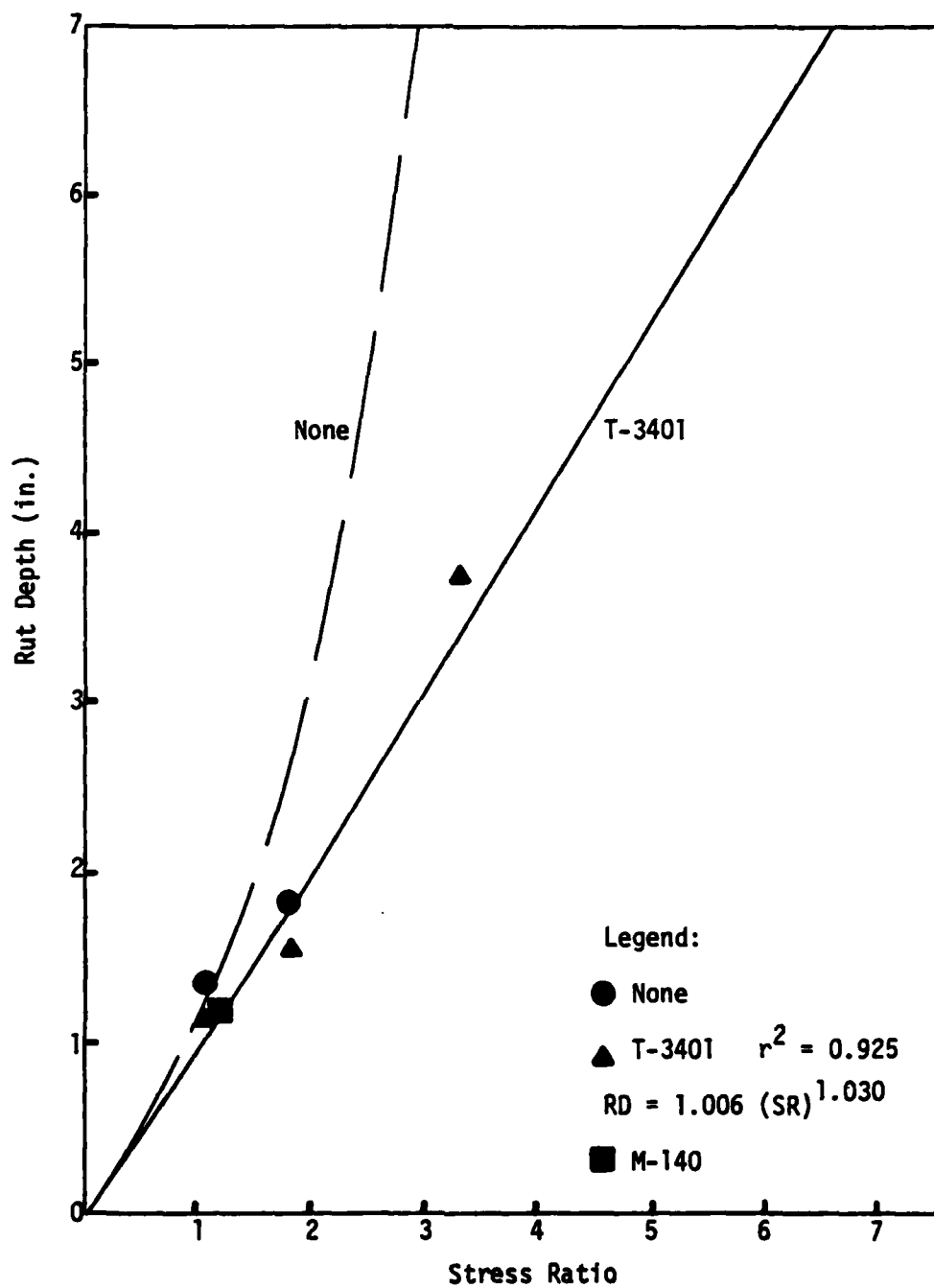


Figure J-15. Stress Ratio-Rut Depth Relationships for 1000 Load Cycles, Type A Loading.

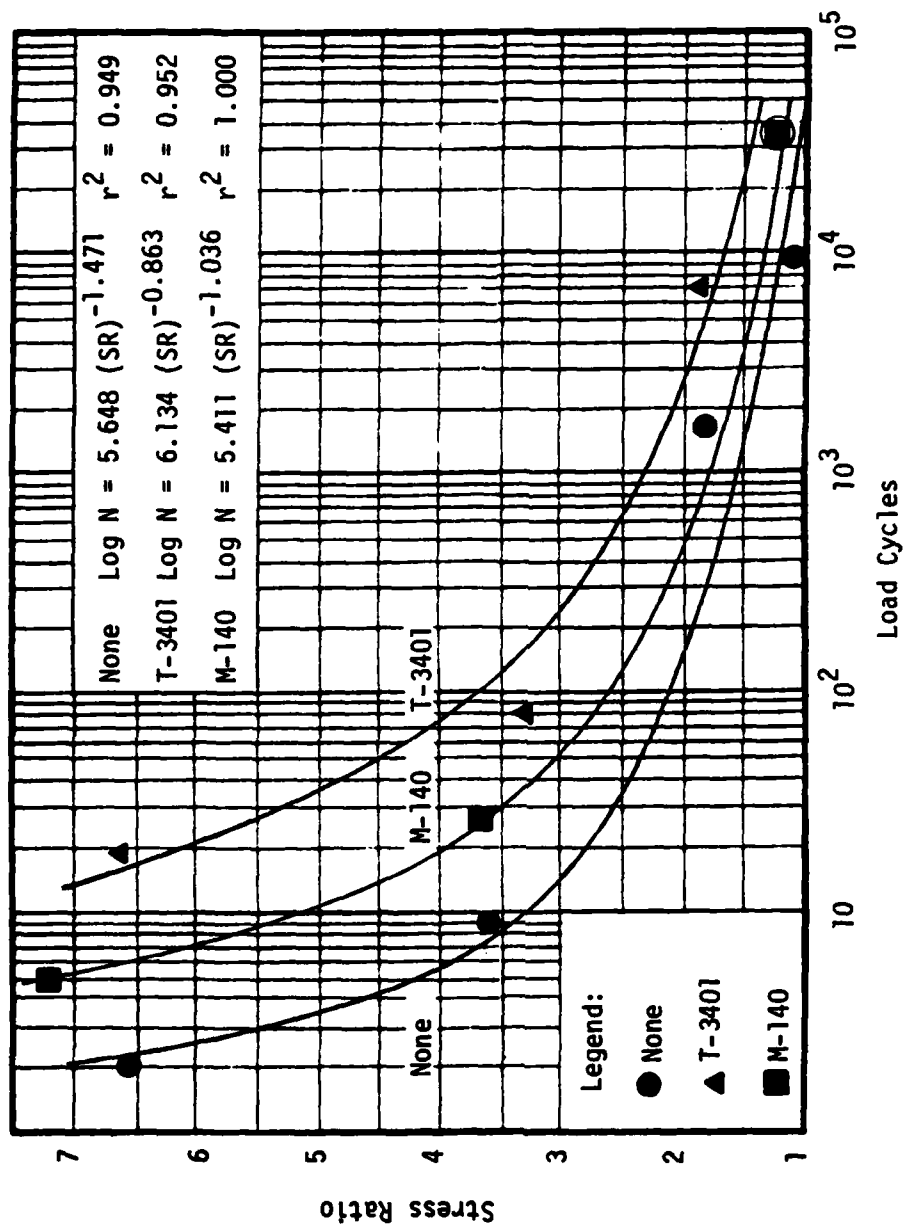


Figure J-16. Load Cycle-Stress Ratio Relationships for 2 in. Rut, Type A Loading.

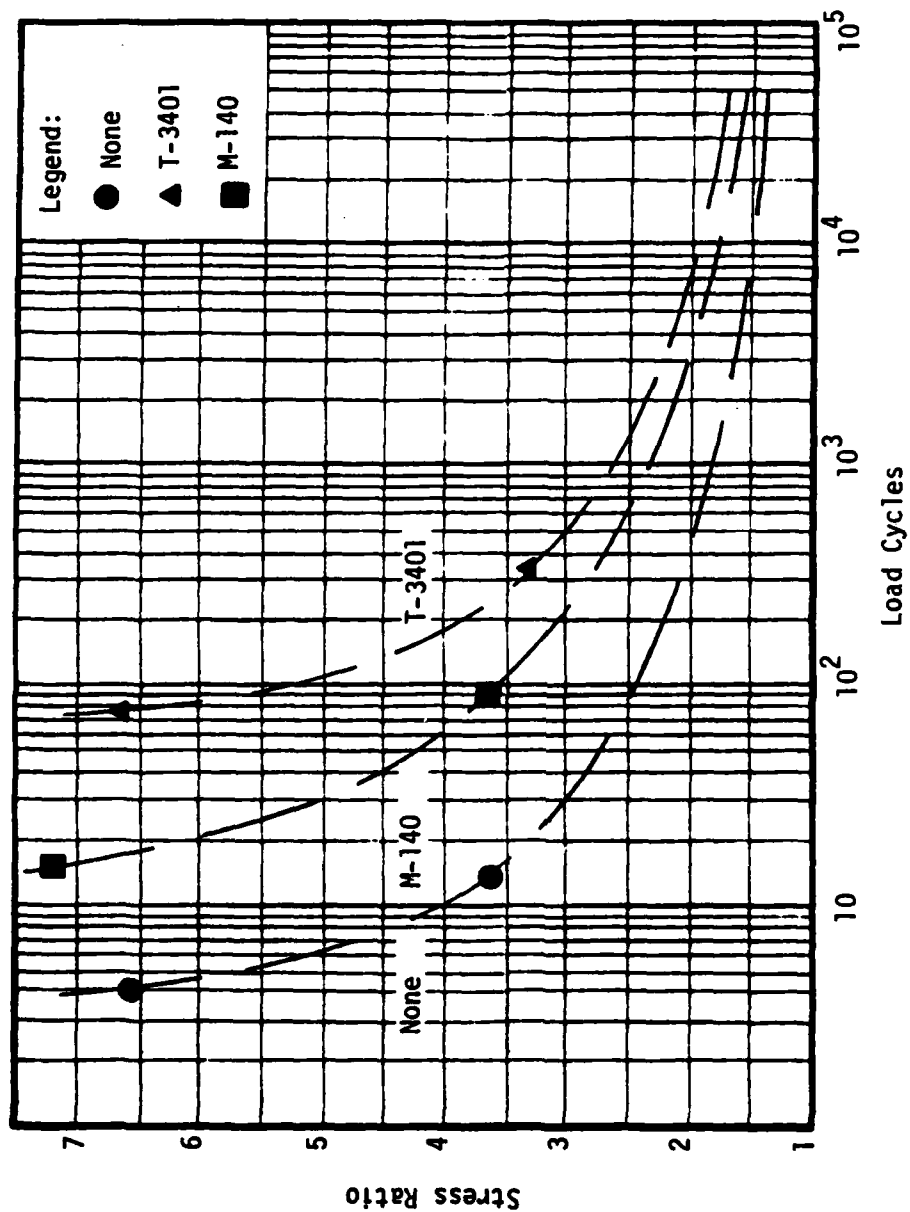


Figure J-17. Load Cycle-Stress Ratio Relationships for 3 in. Rut, Type A Loading.

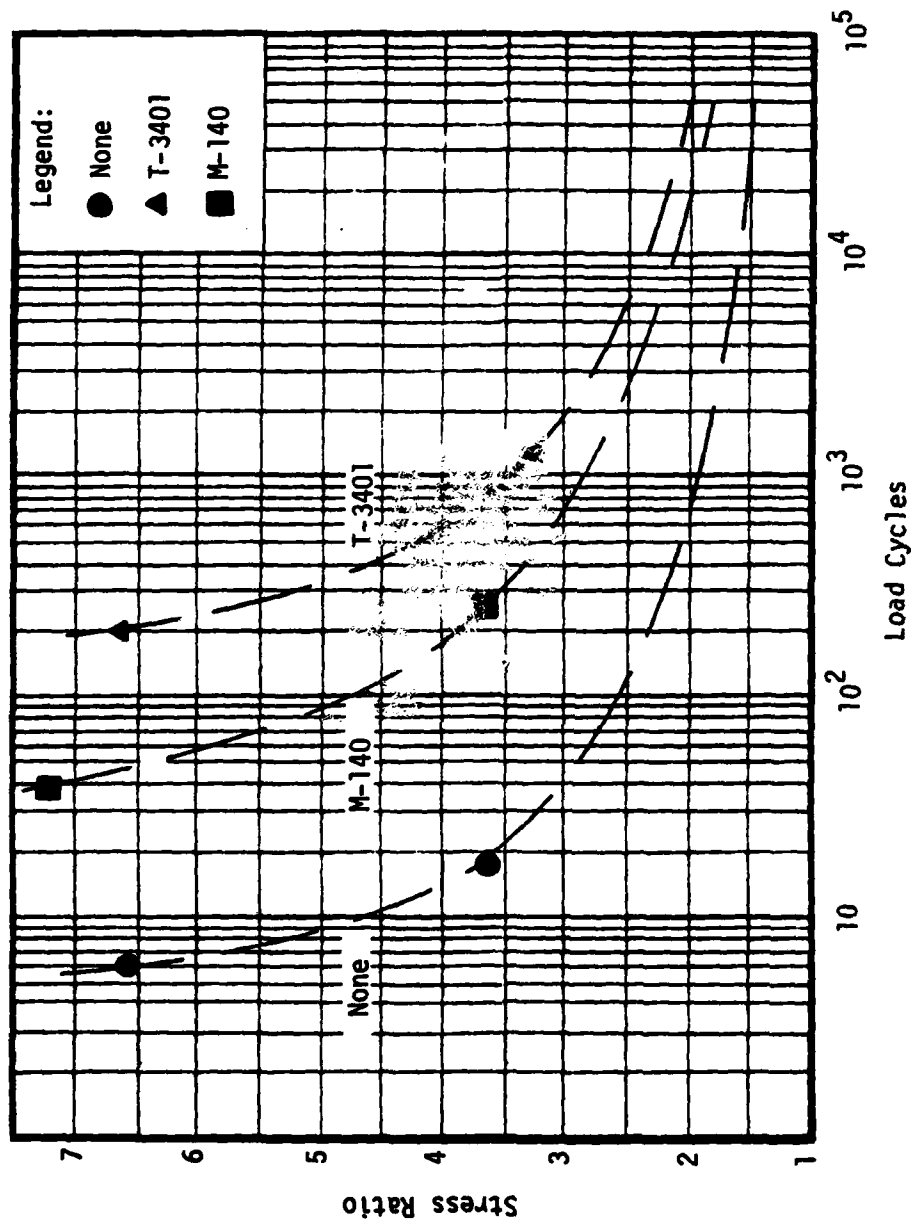


Figure J-18. Load Cycle-Stress Ratio Relationships for 4 in. Rut, Type A Loading.

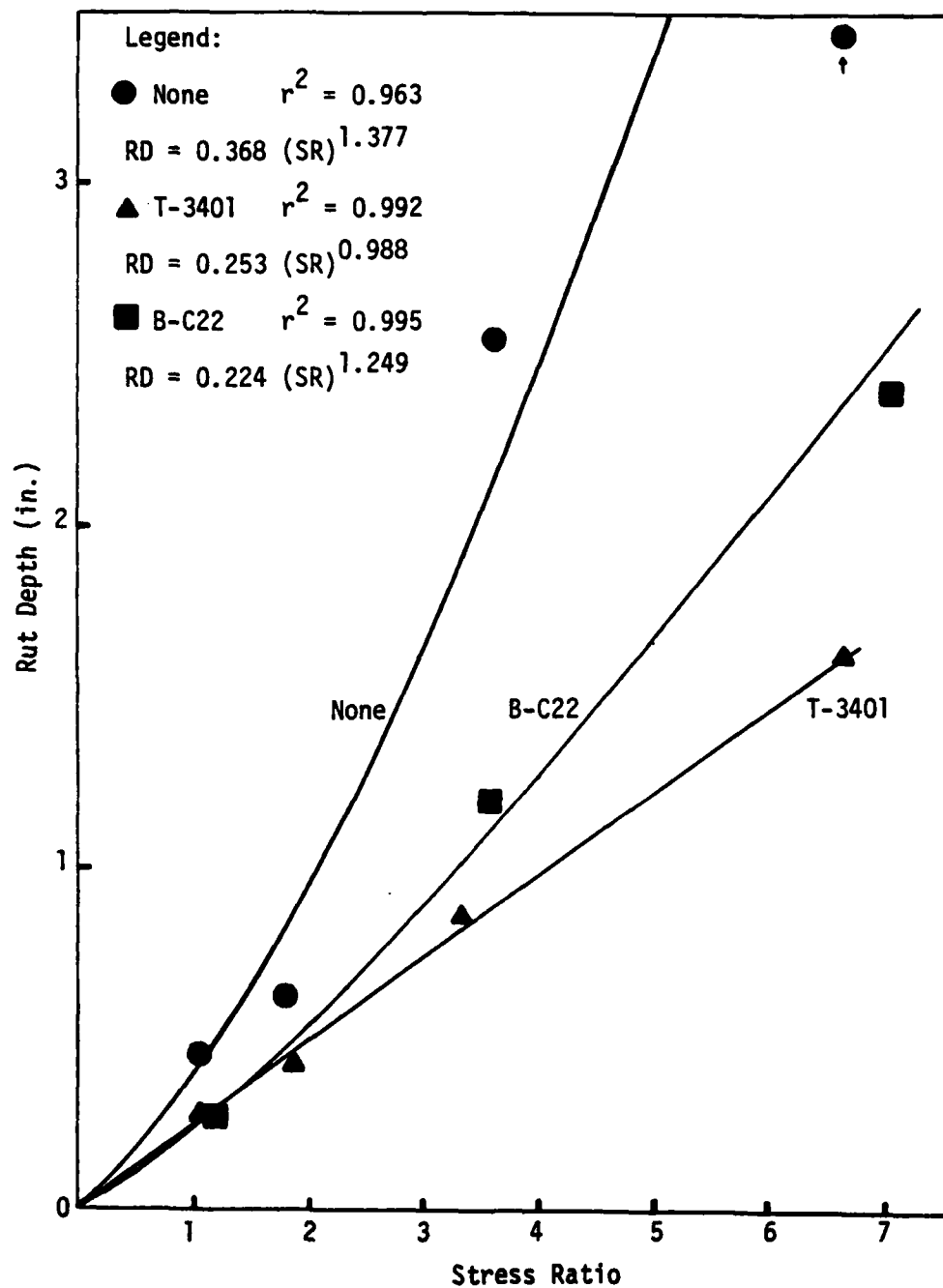


Figure J-19. Stress Ratio-Rut Depth Relationships for 10 Load Cycles, Type A Loading.

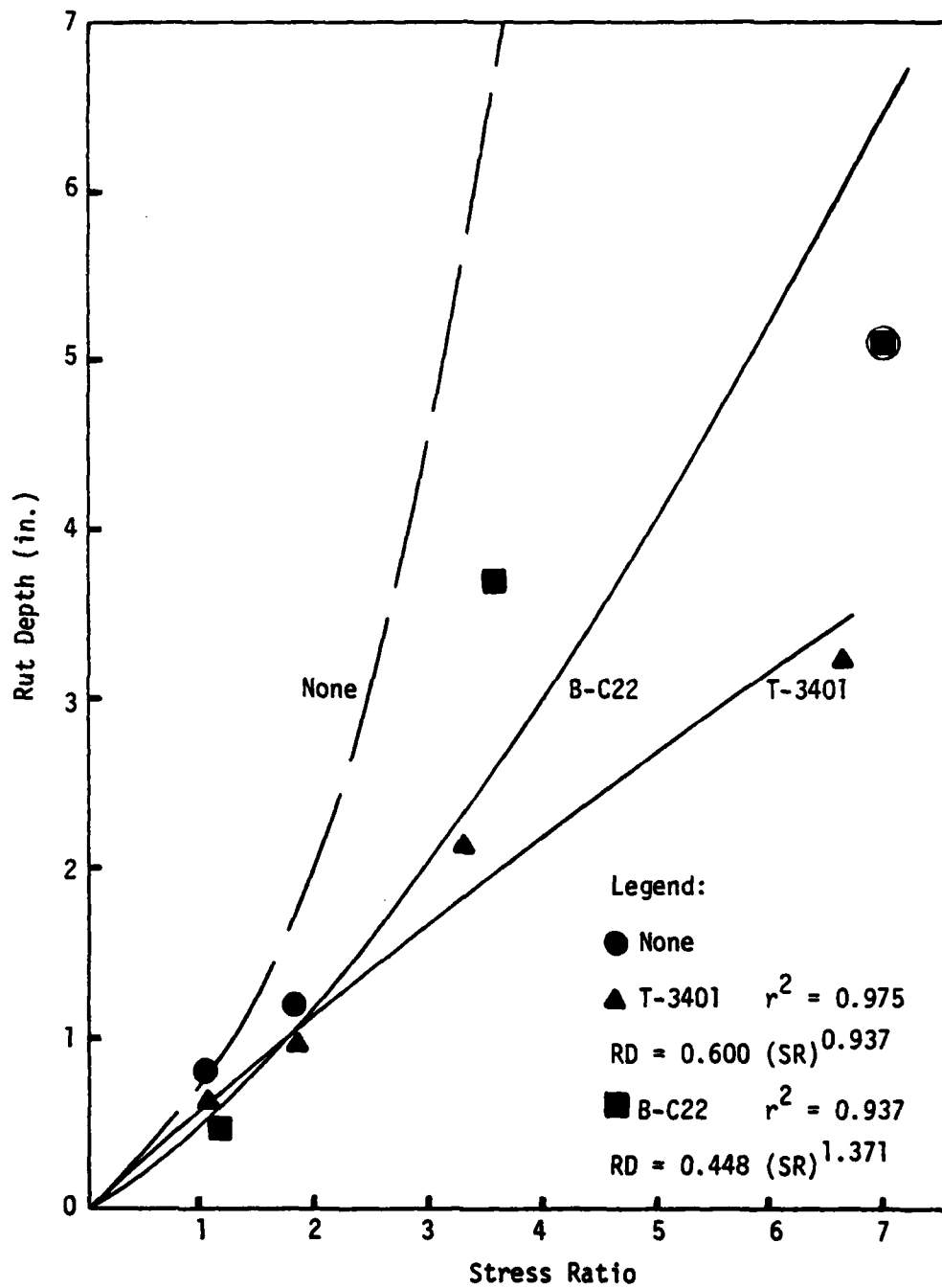


Figure J-20. Stress Ratio-Rut Depth Relationships for 100 Load Cycles, Type A Loading.

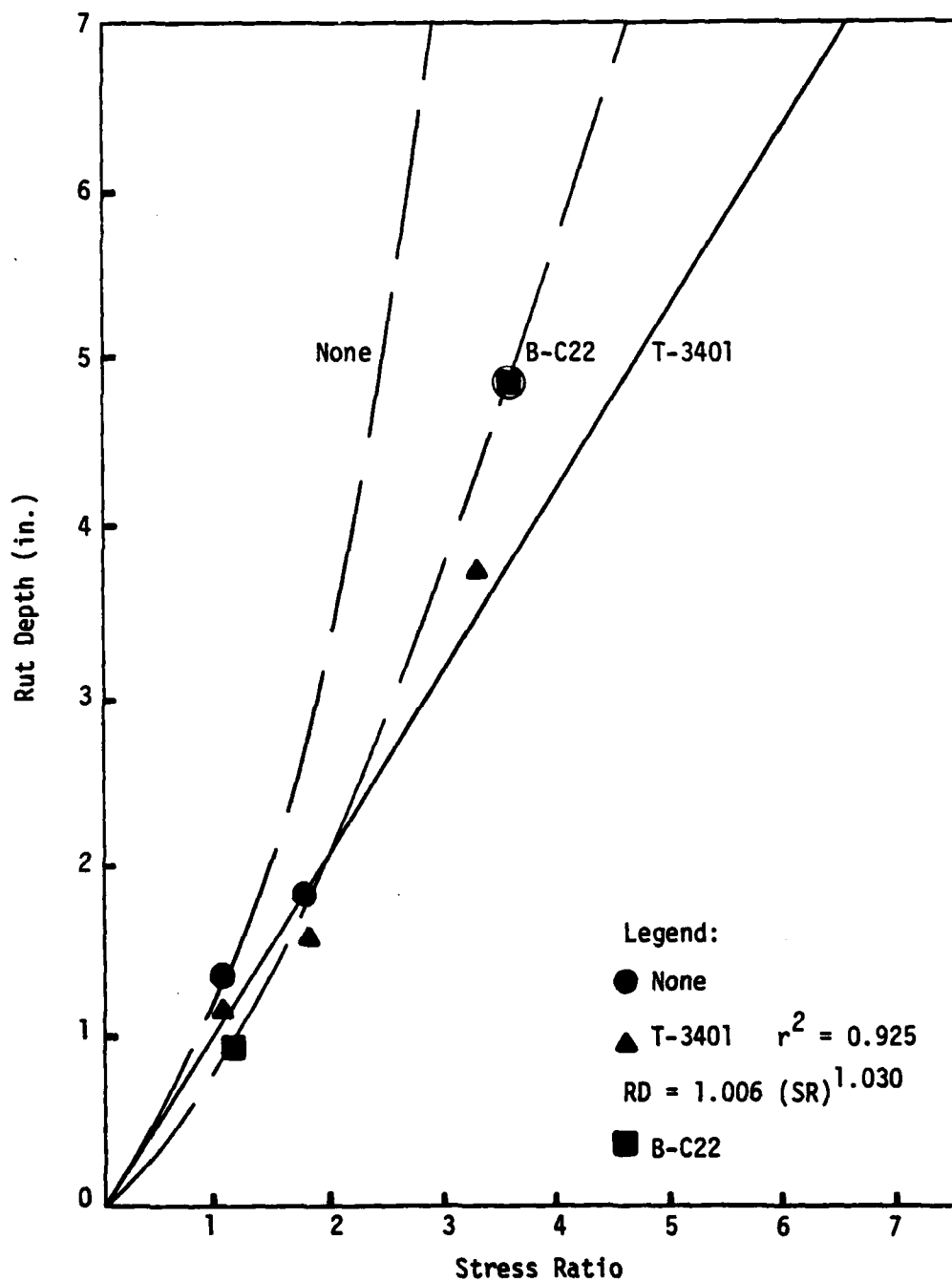


Figure J-21. Stress Ratio-Rut Depth Relationships for 1000 Load Cycles, Type A Loading.

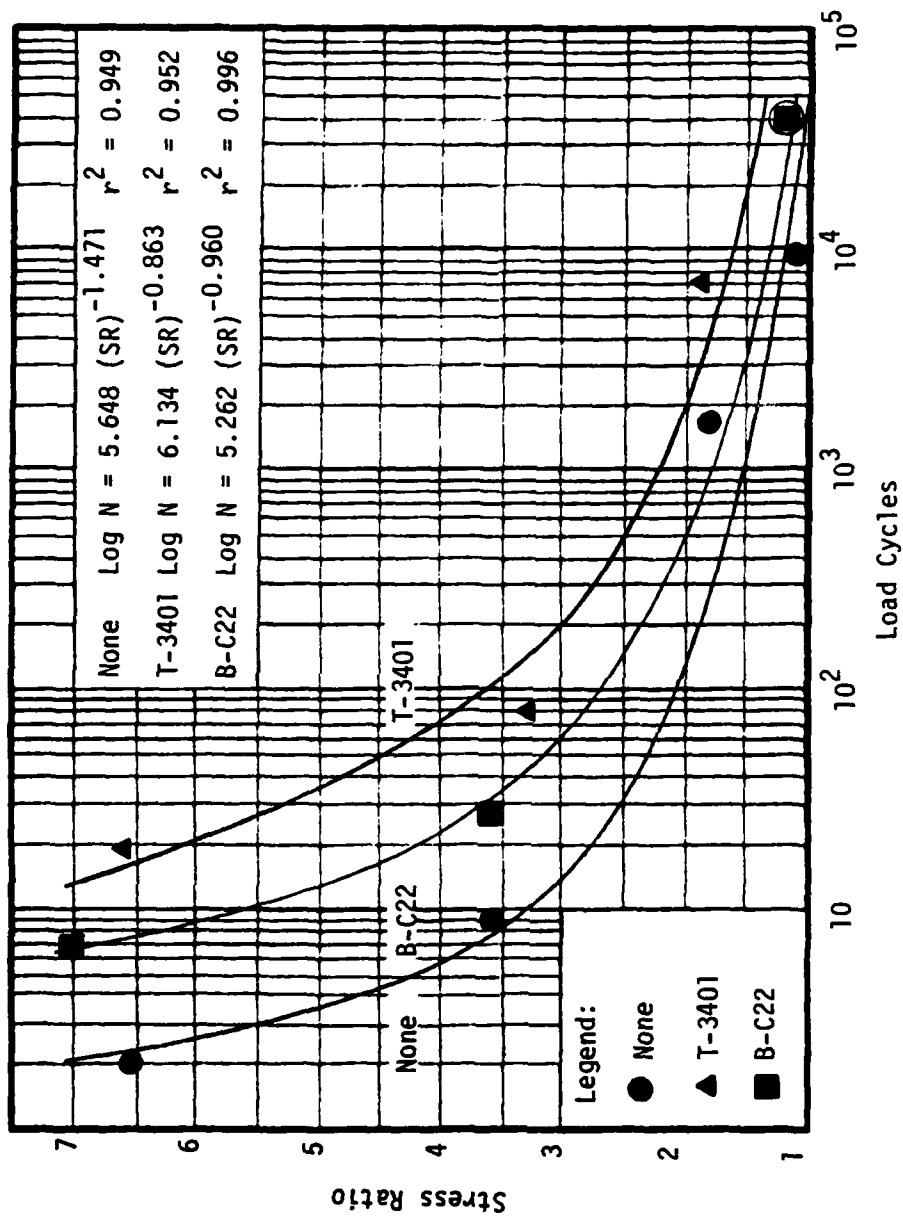


Figure J-22. Load Cycle-Stress Ratio Relationships for 2 in. Rut, Type A Loading.

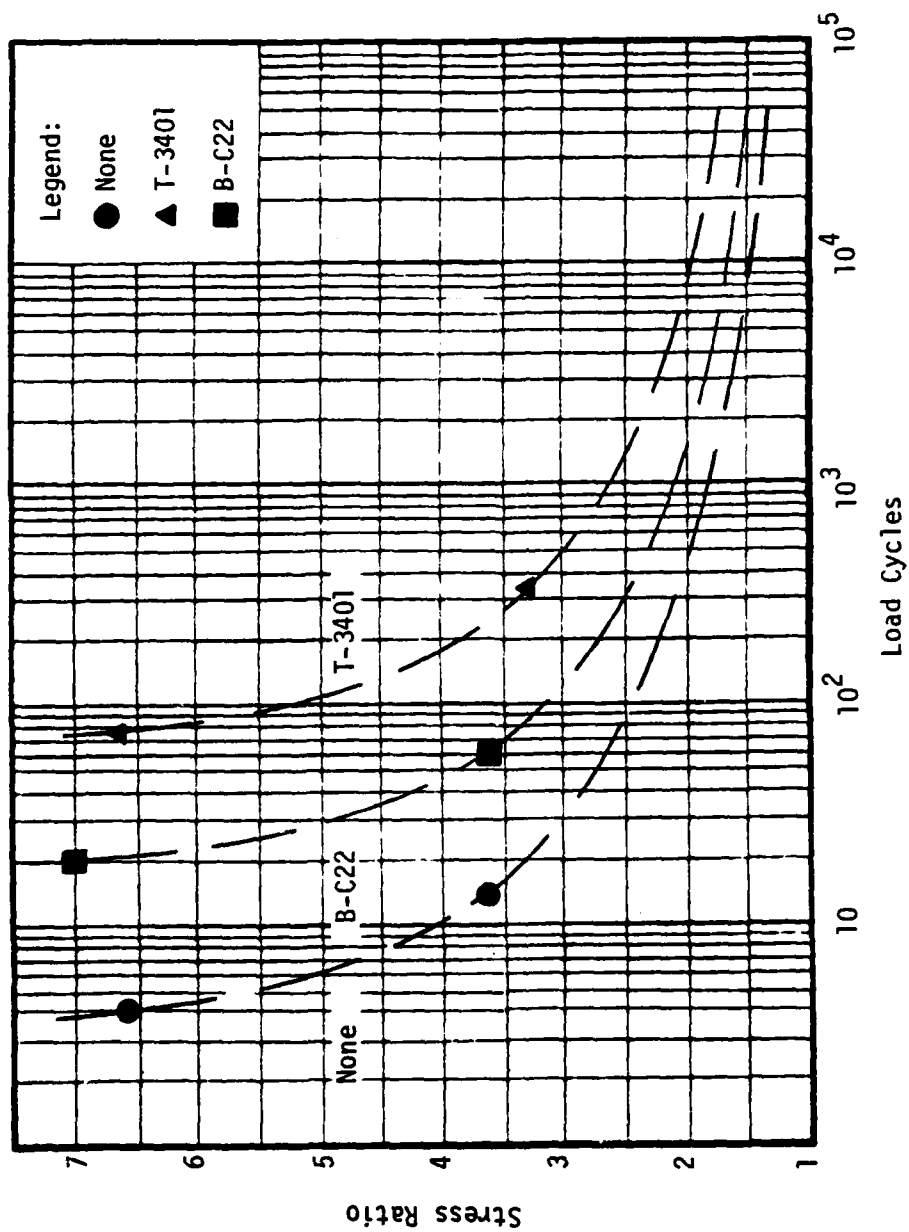


Figure J-23. Load Cycle-Stress Ratio Relationships for 3 in. Rut, Type A Loading.

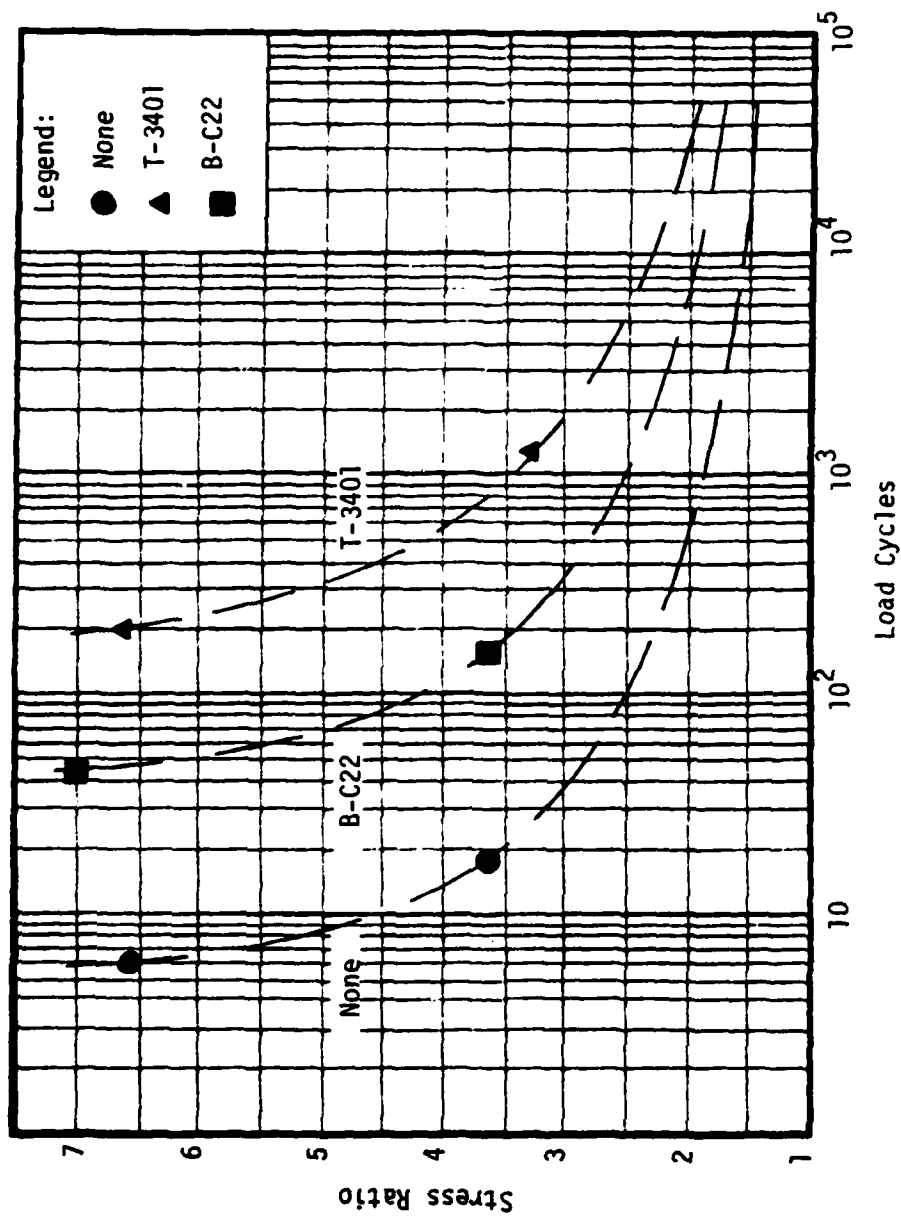


Figure J-24. Load Cycle-Stress Ratio Relationships for 4 in. Rut, Type A Loading.

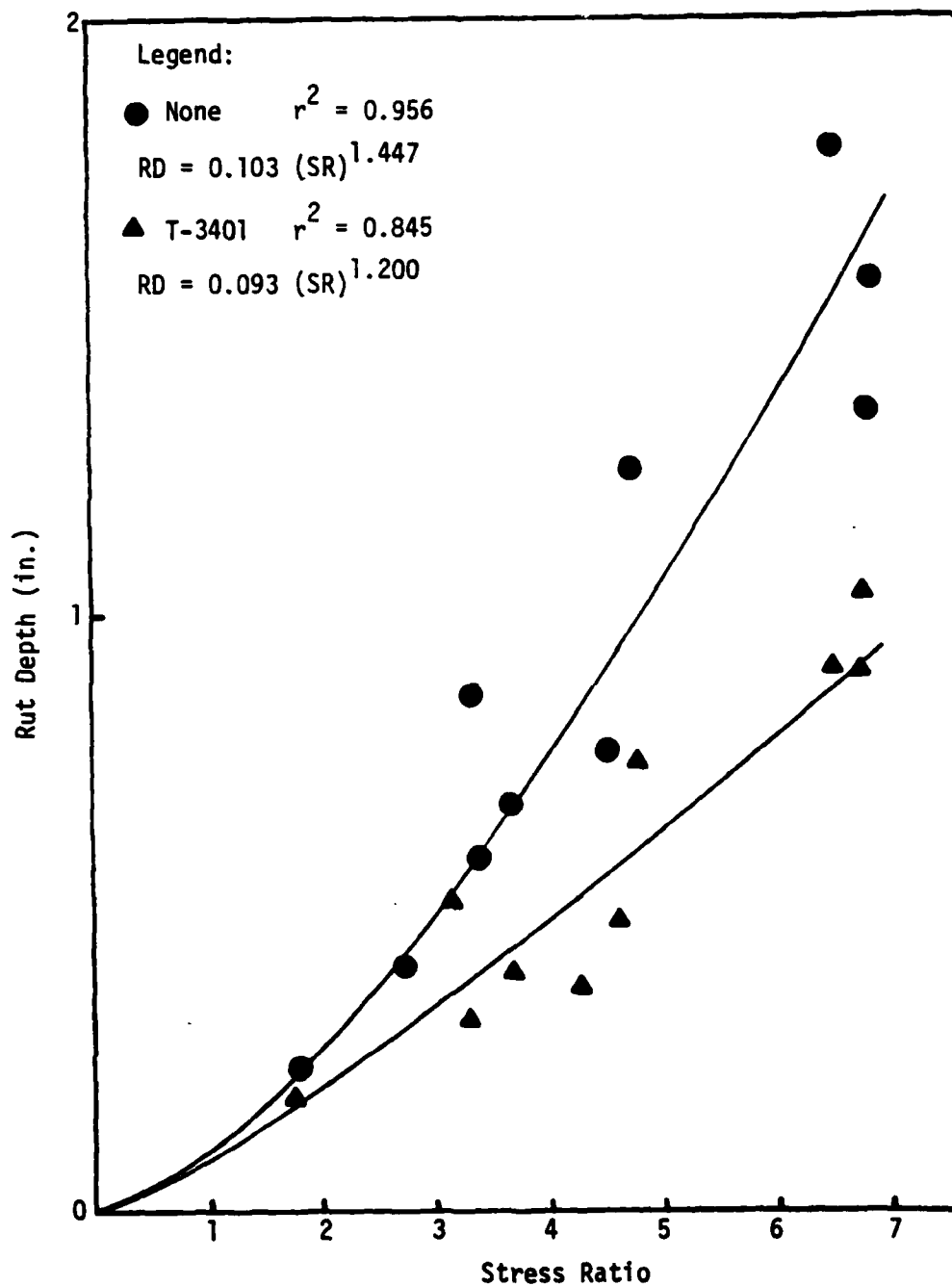


Figure J-25. Stress Ratio-Rut Depth Relationships for 10 Load Cycles, Type B Loading

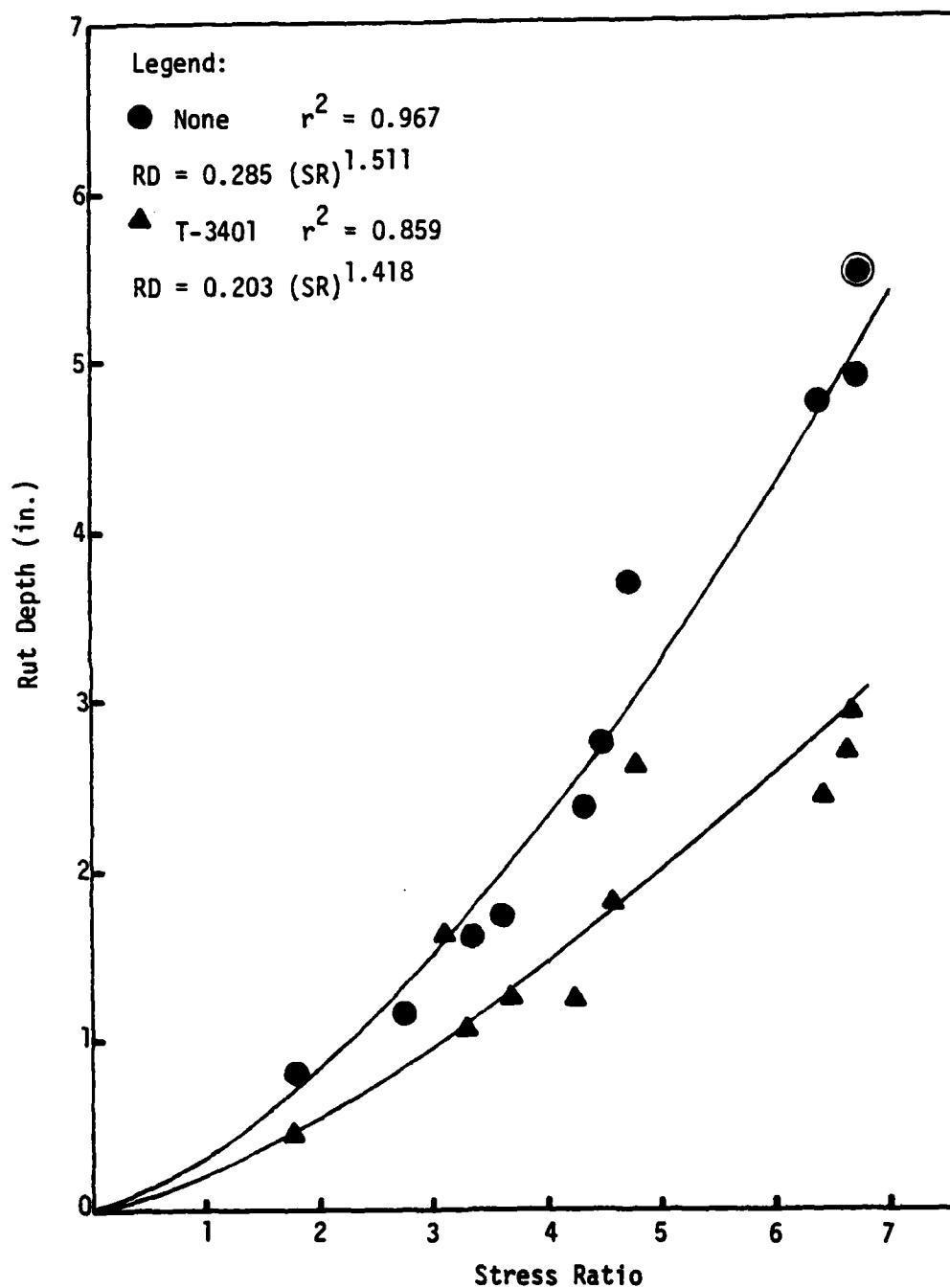


Figure J-26. Stress Ratio-Rut Depth Relationships for 100 Load Cycles, Type B Loading.

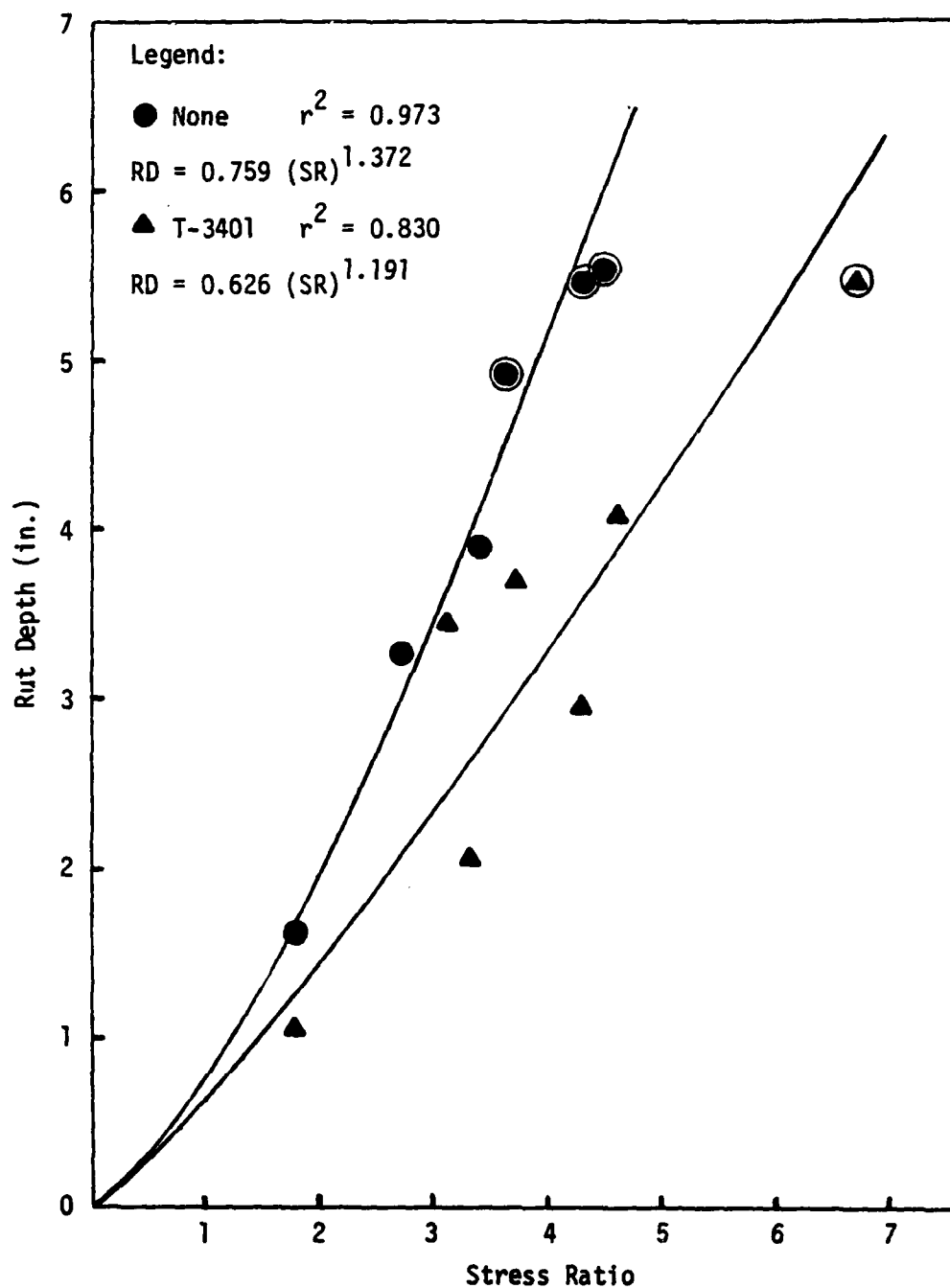


Figure J-27. Stress Ratio-Rut Depth Relationships for 1000 Load Cycles, Type B Loading.

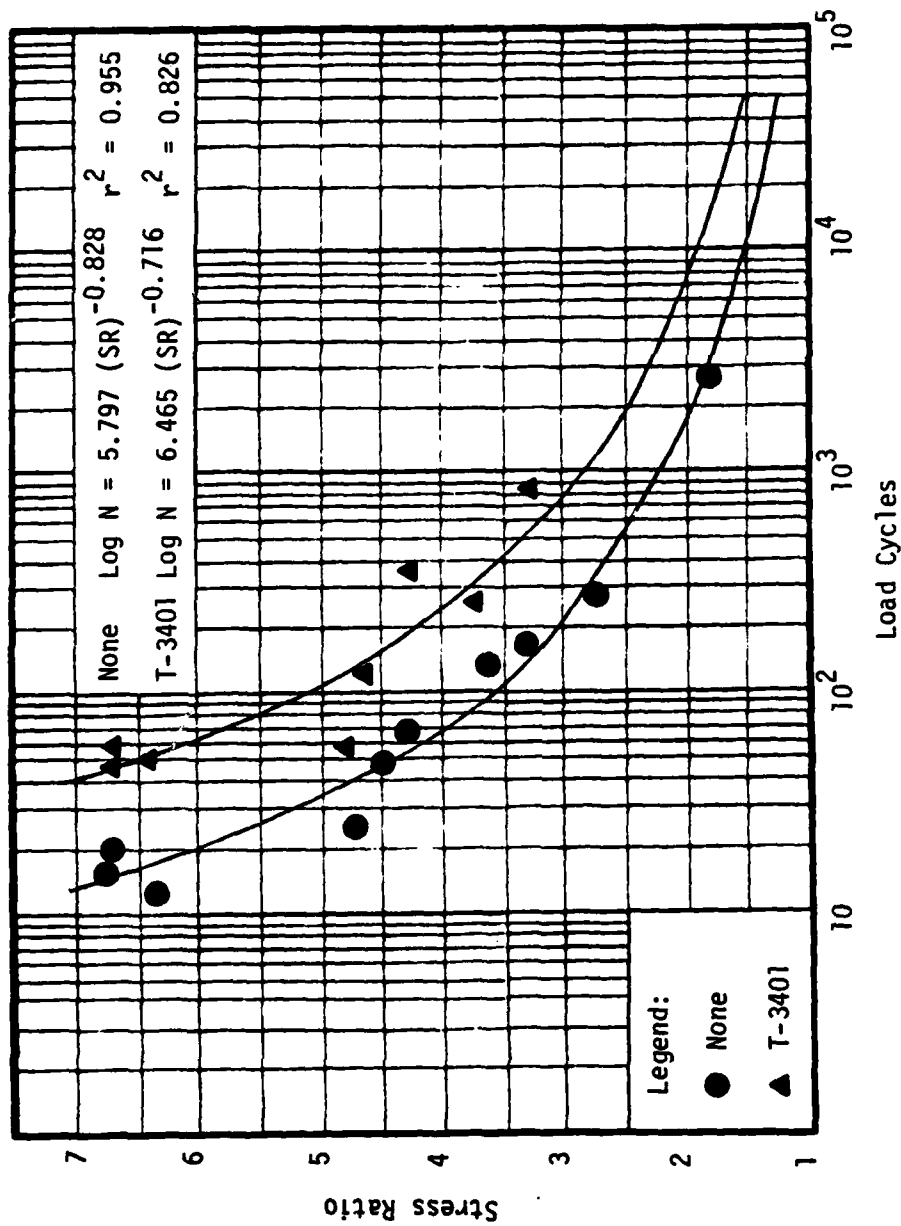


Figure J-28. Load Cycle-Stress Ratio Relationships for 2 in. Rut, Type B Loading.

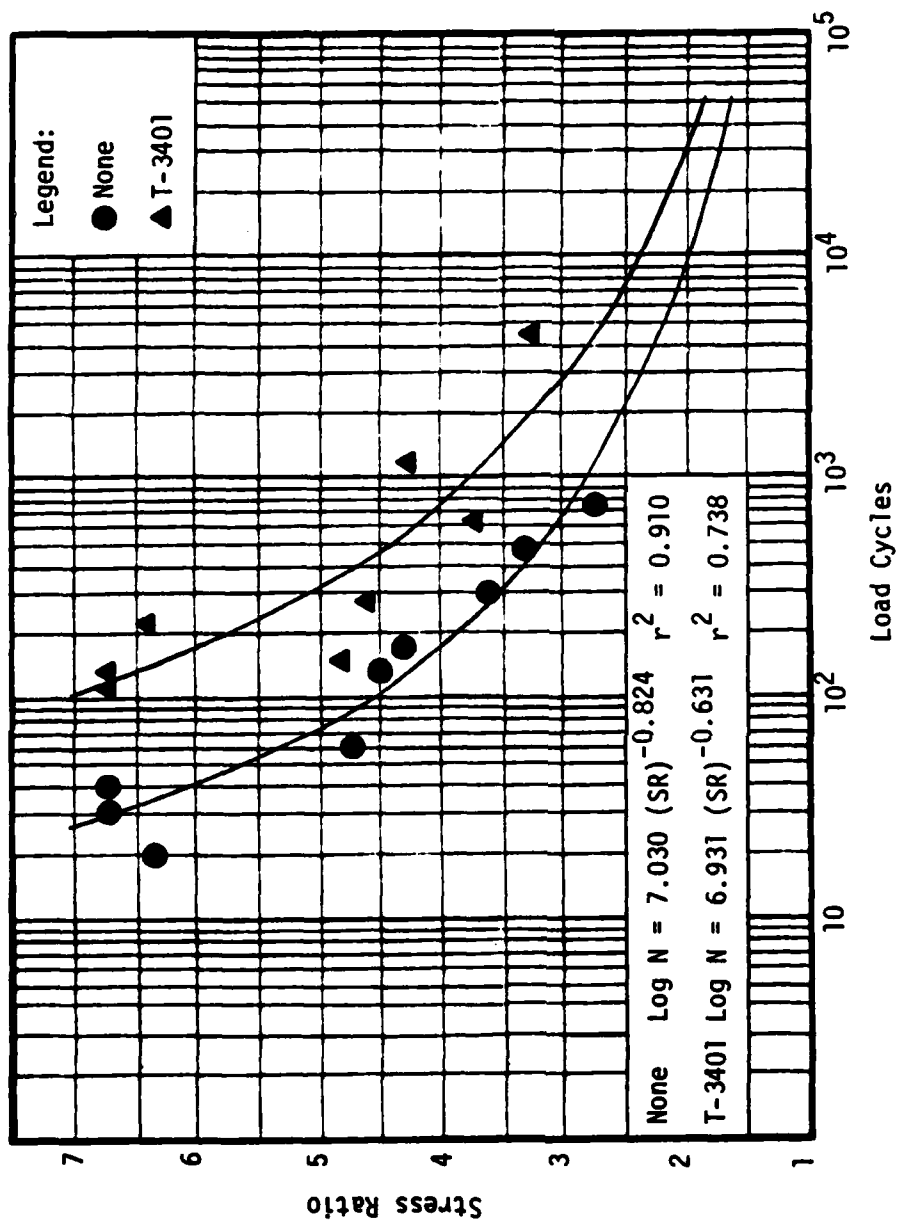


Figure J-29. Load Cycle-Stress Ratio Relationships for 3 in. Rut, Type B Loading.

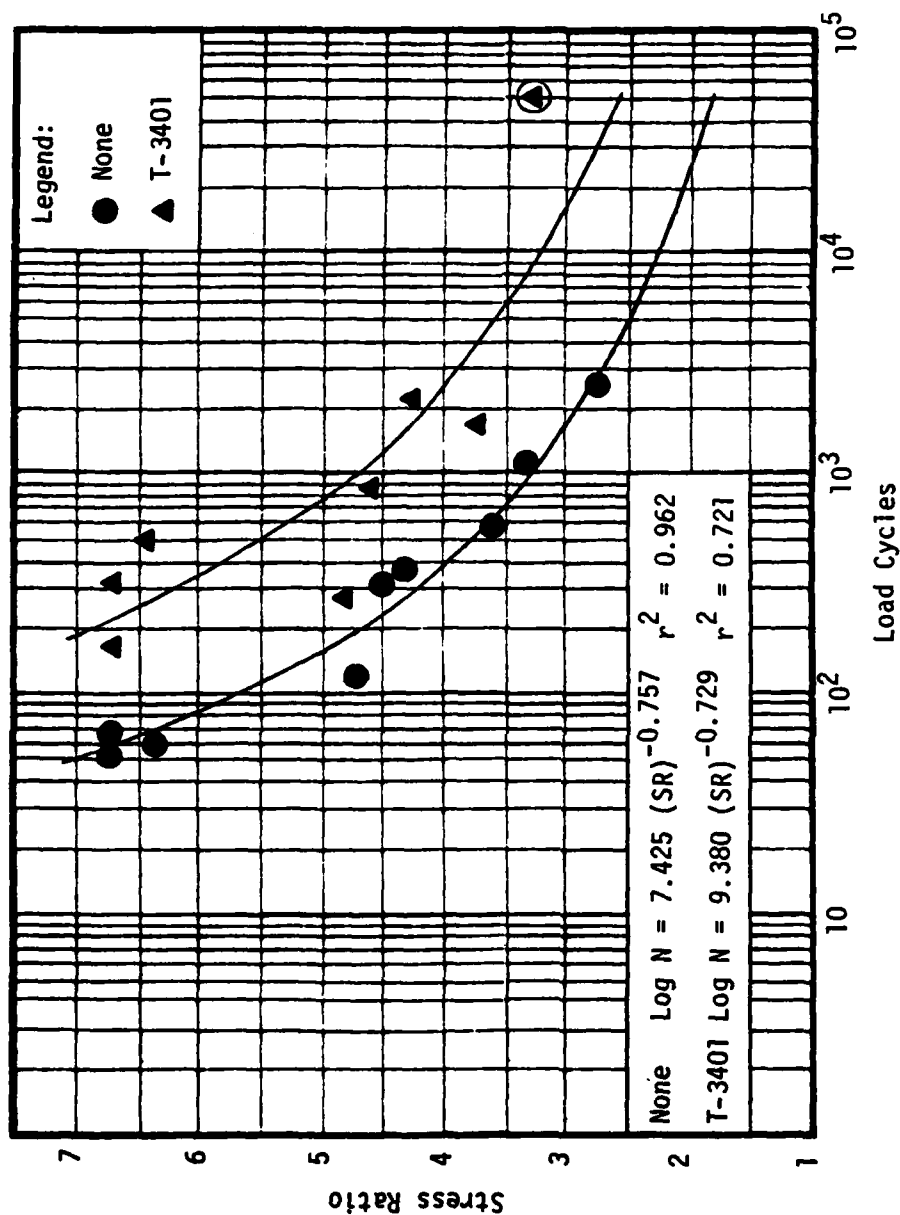


Figure J-30. Load Cycle-Stress Ratio Relationships for 4 in. Rut, Type B Loading.

APPENDIX K

BEARING CAPACITY ANALYSES

Meyerhof (68) presented techniques for analyzing the bearing capacities of layered systems comprised of either dense sand on soft clay or loose sand on stiff clay. The AS systems of this study approximated the former case and Meyerhof's approach was utilized to analyze the bearing capacities of the models and the corresponding prototypes.

When the sand layer is relatively thin, failure occurs by punching action. For a circular surface footing, the bearing capacity of the system may be computed as:

$$q_u = 1.2c N_c + \frac{2\gamma H^2 s K_s \tan \phi}{B} \quad (K-1)$$

where q_u = ultimate bearing capacity, psf

c = cohesion of clay layer, psf

N_c = 5.14 = bearing capacity factor

γ = unit weight of sand layer, pcf

H = thickness of sand layer, feet

s = shape factor (conservatively taken as equal to unity)

K_s = coefficient of punching shear resistance

ϕ = angle of internal friction of sand layer

B = footing diameter, feet.

As the thickness of the sand layer becomes relatively thick, this layer controls system response, with failure due to shearing

within this layer. This case defines the maximum bearing capacity of the system and, for a circular surface footing, may be computed as:

$$q_u = 0.3\gamma B N_\gamma \quad (K-2)$$

where q_u = ultimate bearing capacity, psf

γ = unit weight of sand layer, pcf

B = footing diameter, feet

N_γ = bearing capacity factor.

The bearing capacity values for the models of this study and the corresponding prototypes are presented in Table K-1. The bearing capacities of the prototypes average 1.43 times those of the half-scale models, with a range of 1.07-2.0. For equal contact pressures and assuming similar relationships between load and settlement (expressed as a percentage of footing diameter), deformations in the prototypes will be less than twice those in the models.

Table K-1. Bearing Capacity Values for Models and Prototypes.

$$\gamma = 132.1 \text{ pcf}$$

$$\phi = 48^\circ$$

$$K_s = 16$$

$$N_\gamma = 496$$

$c(a)$ (psi)	Model (B = 0.5 ft.)		Prototype (B = 1.0 ft.)		$\frac{q_{u-\text{Prototype}}}{q_{u-\text{Model}}}$
	H (in.)	q_u (psf)	H (in.)	q_u (psf)	
2.96	6.0	4976	12.0	7324	1.47
3.07	7.5	6395	15.0	10062	1.57
3.02	9.0	7964	18.0	13246	1.66
4.56	4.5	5371	9.0	6691	1.25
4.42	7.0	7121	14.0	10316	1.45
4.66	10.0	9828*	20.0	17180	1.75
4.88	13.0	9828*	26.0	19656*	2.00
6.72	3.0	6556	6.0	7142	1.09
6.86	4.5	7413	9.0	8734	1.1
6.80	6.0	8387	12.0	10735	1.28
9.48	3.0	9007	6.0	9594	1.07

(a) Average of Values for Corresponding AS and Typar 3401 Reinforced AFS Systems

* Maximum Bearing Capacity for Layered System (Equation K-2)

BIBLIOGRAPHY

1. Alfheim, S. L. and Sørli, A., "Testing and Classification of Fabrics for Application in Road Construction," Proceedings of the International Conference on the Use of Fabrics in Geotechnics, Ecole Nationale Des Ponts et Chaussees, Paris, April 1977, pp. 333-338.
2. Andersson, O., "The Influence of a Plastic Fabric for Pavement Protection During Frost Break," Proceedings of the International Conference on the Use of Fabrics in Geotechnics, Ecole Nationale Des Ponts et Chaussees, Paris, April 1977, pp. 143-149.
3. Asphalt Institute, "Soils Manual for Design of Asphalt Pavement Structures," MS-10, Second Edition, April 1963.
4. ASTM, "Annual Book of ASTM Standards, Part 19: Natural Building Stones; Soil and Rock; Peats, Mosses, and Humus," 1977.
5. ASTM, "Annual Book of ASTM Standards, Part 32: Textiles - Yarns, Fabrics, and General Test Methods," 1977.
6. ASTM, "Annual Book of ASTM Standards, Part 33: Textiles - Fibers and Zippers; High Modulus Fibers," 1977.
7. ASTM, "Annual Book of ASTM Standards, Part 38: Rubber Products, Industrial Specifications and Related Test Methods; Carbon Black; Gaskets; Tires," 1977.
8. Audibert, J. M. E. and Tavenas, F. A., Discussion: "Evaluation of Stress Cell Performance," Journal of the Geotechnical Engineering Division, ASCE, GT 7, Vol. 101, July 1975, pp. 705-707.
9. Barksdale, R. D. and Leonards, G. A., "Predicting Performance of Bituminous Surfaced Pavements," Proceedings of the Second International Conference for Structural Design of Asphalt Pavements, Ann Arbor, Michigan, 1967, pp. 321-340.
10. Barksdale, R. D., "Repeated Load Test Evaluation of Base Course Materials," Final Report, GHD Research Project No. 7002, Georgia Institute of Technology, May 1972.
11. Barksdale, R. D., "Evaluation of Base Course Materials to Control Rutting," Presentation to the Conference on Asphalt Pavements for South Africa (CAPSA), Durban, South Africa, 1974.

12. Barenberg, E. J., "A Structural Design Classification of Pavements Based on an Analysis of Pavement Behavior, Material Properties, and Modes of Failure," Ph.D. Thesis, University of Illinois, 1965.
13. Barenberg, E. J., "A Shear Layer Concept for Flexible Pavements," University of Illinois at Urbana-Champaign, 1967.
14. Barenberg, E. J., Dowland, J. H. and Hales, J. H., "Evaluation of Soil-Aggregate Systems with Mirafi Fabric," Final Report, No. UILU-ENG-75-2020, University of Illinois at Urbana-Champaign, August 1975.
15. Barvashov, V. A., Budenov, V. G., et al., "Deformations of Soil Foundations Reinforced with Pre-stressed Synthetic Fabrics," Proceedings of the International Conference on the Use of Fabrics in Geotechnics, Ecole Nationale Des Ponts et Chaussees, Paris, April 1977, pp. 67-69.
16. Bell, J. R., Hicks, R. G., Copeland, J., et al., "Evaluation of Test Methods and Use Criteria for Filter Fabrics," Interim Report, No. DOT-FH-11-9353, Oregon State University, September 1978.
17. Bender, D. A. and Barenberg, E. J., "Design and Behavior of Soil-Fabric-Aggregate Systems," Presentation to the 57th Annual Meeting of the Transportation Research Board, Washington, D.C., January 1978.
18. Bison Instruments, Inc., "Bison Soil Strain Gage Model 4101A," Instruction Manual, 1975.
19. Bonakdar-Hashemi, A. R., "Mechanical Properties of Geotechnical Fabrics," Special Research Problem, Georgia Institute of Technology, March, 1979.
20. Boussinesq, J., "Application des Potentials a L'Etude de L'Equilibre et du Mouvement des Solides Elastiques," Gathier-Villars, 1885.
21. Brown, S. F. and Pell, P. S., "An Experimental Investigation of the Stresses, Strains, and Deflections in a Layered Pavement Structure Subjected to Dynamic Loads," Proceedings of the Second International Conference for Structural Design of Asphalt Pavements, Ann Arbor, Michigan, 1967, pp. 487-504.
22. Brown, S. F., "The Measurement of In-Situ Stress and Strain in Soil," Proceedings of the Symposium on Field Instrumentation in Geotechnical Engineering, London, 1973, pp. 38-51.
23. Brown, S. F. and Brodrick, B. V., "The Performance of Stress and Strain Transducers for Use in Pavement Research " University of Nottingham, June 1973.

24. Brown, S. F., "State of the Art on Field Instrumentation for Pavement Experiments," Transportation Research Record, No. 640, 1977, pp. 13-28.
25. Browning, M. Y., "The Dynamic Stress-Strain Response of Four Piedmont Fine-Grained Subgrade Soils," Special Research Problem, Georgia Institute of Technology, August 1976.
26. Burmister, D. M., "The Theory of Stresses and Displacements in Layered Systems and Applications to the Design of Airport Runways," Proceedings, Highway Research Board, 1943, pp. 126-144.
27. Byrnes, L. G., "Applicability of Hyperbolic Stress-Strain Theories to Predict the Response of a Shell-Soil System," Special Research Problem, Georgia Institute of Technology, August 1977.
28. Carlson, C. A. and McDaniel, A. R., "Forecasting Trafficability of Soils," TM-3-331, Report 8, U.S. Army Waterways Experiment Station, December 1967.
29. Celanese Fibers Marketing Company, "Constructing Access Roads with Mirafi 140 Fabric," PM-6, 1975.
30. Celanese Fibers Marketing Company, "Principles of Design for Ground Stabilization Applications with Mirafi 140 Fabric," PM-4, 1976.
31. Celanese Fibers Marketing Company, "Mirafi 500X Fabric, Design Guidelines: Haul Roads and Area Stabilization," MTB-1, 1979.
32. Chou, Y. T., "An Iterative Layered Elastic Computer Program for Rational Pavement Design," TRS-76-3, U.S. Army Waterways Experiment Station, February 1976.
33. Chou, Y. T., "Analysis of Permanent Deformations of Flexible Airport Pavements," TRS-77-8, U.S. Army Waterways Experiment Station, February 1977.
34. Dallaire, G., "Filter Fabrics: Bright Future in Road and Highway Construction," Civil Engineering, ASCE, May 1976, pp. 61-65.
35. Department of the Navy, "Design Manual - Soil Mechanics, Foundations, and Earth Structures," NAVFAC DM-7, March 1971.
36. Derick, K. R., "Repeated Load Evaluation of Shell-Sand-Clay Mixtures," Special Research Problem, Georgia Institute of Technology, August 1977.
37. Dixon, W. J. and Brown, M. B., "Biomedical Computer Programs - P Series," University of California Press, 1979.

38. Duncan, J. M. and Chang, C. Y., "Nonlinear Analysis of Stress and Strain in Soils," Journal of the Soil Mechanics and Foundations Division, ASCE, SM5, Vol. 96, September 1970, pp. 1629-1653.
39. Elliot, J. F. and Moavenzadeh, F., "Analysis of Stresses and Displacements in Three Layer Viscoelastic Systems," Highway Research Record, No. 345, 1971, pp. 45-57.
40. Foster, C. R. and Ahlvin, R. G., "Stresses and Deflection Induced by a Uniform Circular Load," Proceedings, Highway Research Board, Vol. 33, pp. 467-470.
41. Giroud, J. and Noiray, L., "Design of Geotextile-Reinforced, Unpaved Roads," Research Paper of the Geotextiles and Geomembranes Group of Woodward-Clyde Consultants, 1979.
42. Griffel, W., "Handbook of Formulas for Stress and Strain," Frederick Ungar Publishing Co., 1966.
43. Hadala, P. F., "The Effect of Placement Method on the Response of Soil Stress Gages," Proceedings of the Symposium on Wave Propagation and Dynamic Properties of Earth Materials, University of New Mexico, 1967.
44. Hammitt, II, G. M., "Thickness Requirements for Unsurfaced Roads and Airfields - Bare Base Support," TRS-70-5, U.S. Army Waterways Experiment Station, July 1970.
45. Hammitt, II, G. M., "Structural Design of Unsurfaced Roadways and Airfields," Highway Research Record, No. 362, 1971, pp. 96-97.
46. Herner, R. C., "Effect of Base Course Quality on Load Transmission Through Flexible Pavements," Proceedings, Highway Research Board, 1955, pp. 224-233.
47. Holtz, R. D. and Broms, B. B., "Walls Reinforced by Fabrics," Proceedings of the International Conference on the Use of Fabrics in Geotechnics, Ecole Nationale Des Ponts et Chaussees, Paris, April 1977, pp. 113-117.
48. Hufford, W. L. and Lai, J. S., "Analysis of N-Layered Viscoelastic Pavement Systems," Final Report FHWA-RD-78-22, FHWA, January 1978.
49. Ingles, O. G. and Metcalf, J. B., "Soil Stabilization," John Wiley and Sons, Inc., 1974.
50. Intraprassart, S., "Experimental Studies and Analysis of Compacted Fills Over a Soft Subsoil," Ph.D. Thesis, Georgia Institute of Technology, December 1978.

51. Jarrett, P. M., Lee, R. A., and Ridell, D. V. B., "The Use of Fabrics in Road Pavements Constructed on Peat," Proceedings of the International Conference on the Use of Fabrics in Geotechnics, Ecole Nationale Des Ponts et Chaussees, Paris, April 1977, pp. 19-22.
52. Jessberger, H. L., "Load-Bearing Behavior of a Gravel Subbase-Non-woven Fabric-Soft Subgrade System," Proceedings of the International Conference on the Use of Fabrics in Geotechnics, Ecole Nationale Des Ponts et Chaussees, Paris, April 1977, pp. 9-14.
53. Johnson, R. D., "The Development and Preliminary Testing of a Testing Apparatus to Study the Effectiveness of Typar in Improving the Rutting Resistance of an Aggregate-Soft Subgrade System," Special Research Problem, Georgia Institute of Technology, August 1979.
54. Kallstenius, T. and Bergau, W., "Investigations of Soil Pressure Measuring by Means of Cells," Proceedings 12, Royal Swedish Geotechnical Institute, 1956.
55. Kerisel, J., "Scaling Laws in Soil Mechanics," Proceedings of the Third Pan American Conference on Soil Mechanics and Foundation Engineering, Caracas, 1967, Vol. III, pp. 69-92.
56. Kinney, T. C., "Fabric Induced Changes in High Deformation Soil-Fabric-Aggregate Systems," Ph.D. Thesis, University of Illinois at Urbana-Champaign, 1979.
57. Koerner, R. M. and Welsh, J. P., "Construction and Geotechnical Engineering Using Synthetic Fabrics," John Wiley and Sons, Inc., 1980.
58. Kondner, R. L., "Hyperbolic Stress-Strain Response: Cohesive Soils," Journal of the Soil Mechanics and Foundations Division, ASCE, SM1, Vol. 89, January 1963, pp. 115-143.
59. Lai, J. S., "VESYS G - A Computer Program for Analysis of N-Layered Flexible Pavements," Final Report FHWA-RD-77-117, FHWA, April 1977.
60. Lai, J. S., Robnett, Q. L., et al., "Use of Geotextiles in Road Construction: An Experimental Study," Presentation to the First Canadian Symposium on Geotextiles, Calgary, Canada, September 1980.
61. Lambe, T. W. and Whitman, R. V., "Soil Mechanics," John Wiley and Sons, Inc., 1970.
62. Lavin, J. G., Murray, C. G., et al., "Prospects for Spunbonded Fabrics in Civil Engineering Applications," Presentation to the Non-Woven Fabrics Conference, University of Manchester Institute of Science and Technology, June 1980.

63. Ledbetter, R. H., "Pavement Response to Aircraft Dynamic Loads," TRS-75-11, Vol. III, U.S. Army Waterways Experiment Station, June 1976.
64. List, H. J., "Investigations of Synthetic Filters Applied in Hydraulic Structures Under the Influence of Non-Stationary Flow," Mitt. Bl. Bundesanst. Wasserb. Karlsruhe, No. 35, pp. 123-147.
65. Lysmer, J. and Duncan, J. M., "Stresses and Deflections in Foundations and Pavements," Fifth Edition, University of California at Berkeley, 1972.
66. McGown, A. and Andrawes, K. Z., "The Influence of Non-Woven Fabric Inclusions on the Stress-Strain Behavior of a Soil," Proceedings of the International Conference on the Use of Fabrics in Geotechnics, Ecole Nationale Des Ponts et Chaussees, Paris, April 1977, pp. 161-166.
67. McMahon, T. F. and Yoder, E. J., "Design of a Pressure-Sensitive Cell and Model Studies of Pressure in a Flexible Pavement Subgrade," Proceedings, Highway Research Board, 1960, pp. 650-682.
68. Meyerhof, G. G., "Ultimate Bearing Capacity of Footings on Sand Layer Overlying Clay," Canadian Geotechnical Journal, Vol. II, No. 2, May 1974, pp. 223-229.
69. Michelow, J., Warren, H. and Dieckman, W. L., "Numerical Computation of Stresses and Strains in a Multiple-Layered Asphalt Pavement System," California Research Corporation, 1963.
70. Monismith, C. L., "Rutting Prediction in Asphalt Concrete Pavements," Transportation Research Record, No. 616, 1976, pp. 2-8.
71. Monsanto Textiles Company, "Bidim Engineering Fabric," 1978.
72. Morel, G., Quibel, A., Puiatti, D., and Puig, J., "The Use of Fabrics Under a Subbase Upon a Low Bearing Capacity Subgrade," Proceedings of the International Conference on the Use of Fabrics in Geotechnics, Ecole Nationale Des Ponts et Chaussees, Paris, April 1977, pp. 29-34.
73. Nieuwenhuis, J. D., "Membranes and the Bearing Capacity of Roadbases," Proceedings of the International Conference on the Use of Fabrics in Geotechnics, Ecole Nationale Des Ponts et Chaussees, Paris, April 1977, pp. 3-8.
74. Paterson, W. D. O., "Measurement of Pavement Deformation Using Inductance Coils," RRU Bulletin, No. 13, National Roads Board, Wellington, New Zealand, 1972.

75. Paute, J. L. and Segouin, M., "Determination of Strength and Deformability Characteristics of Fabrics by Dilatation of a Cylindrical Sleeve," Proceedings of the International Conference on the Use of Fabrics in Geotechnics, Ecole Nationale Des Ponts et Chaussees, Paris, April 1977, pp. 293-298.
76. Peattie, K. R. and Sparrow, R. W., "The Fundamental Action of Earth Pressure Cells," Journal of the Mechanics and Physics of Solids, Vol. 2, 1954, pp. 141-155.
77. Poulos, H. G. and Davis, E. H., "Elastic Solutions for Soil and Rock Mechanics," John Wiley and Sons, Inc., 1974.
78. Raad, L. and Figueroa, J. L., "Load Response of Transportation Support Systems," Transportation Engineering Journal of ASCE, Vol. 106, No. TE1, January 1980, pp. 111-128.
79. Roark, R. J. and Yound, W. C., "Formulas for Stress and Strain," Fifth Edition, McGraw-Hill Book Company, 1975.
80. Robnett, W. L., Thompson, M. R., Hay, W. W., et al., "Ballast and Foundation Materials Research Program," Technical Data Bases Summary Report, University of Illinois at Urbana-Champaign, July 1975.
81. Robnett, Q. L. and Lai, J. S., "Use of Geotextiles to Extend Aggregate Resources," Presentation to the ASTM Symposium on Extending Aggregate Resources, September 1980.
82. Robnett, Q. L., Private Communication - Unpublished Data, Georgia Institute of Technology, October 1980.
83. Rodin, S., "Ability of a Clay Fill to Support Construction Plant," Journal of Terramechanics, Vol. 2, No. 4, 1965, pp. 51-68.
84. Schuring, D. J. and Emori, R. I., "Soil Deforming Processes and Dimensional Analysis," Paper 897C, Presented at the SAE National Farm, Construction, and Industrial Machinery Meeting, September 1964.
85. Seed, H. B. and Chan, C. K., "Thixotropic Characteristics of Compacted Clays," Journal of the Soil Mechanics and Foundations Division, ASCE, SM4, Vol. 83, November 1957, pp. 1427-1 to 1427-25.
86. Seed, H. B., Mitry, F. G., Monismith, C. L., and Chan, C. K., "Prediction of Flexible Pavement Deflections from Laboratory Repeated Load Tests," NCHRP, Report 35, 1967.
87. Seemel, R. N., "Plastic Filter Fabrics Challenging the Conventional Granular Filter," Civil Engineering, ASCE, March 1976, pp. 57-59.

88. Selig, E. T., "A Review of Stress and Strain Measurement in Soil," Proceedings of the Symposium on Soil Structure Interaction, University of Arizona, 1964, pp. 172-186.
89. Selig, E. T. and Grangaard, O. H., "A New Technique for Soil Strain Measurement," Journal of Material Research and Standards, Vol. 10, No. 10, 1970, pp. 19-36.
90. Selig, E. T., "Soil Strain Measurement Using Inductance Coil Method," Proceedings of the Symposium on Performance Criteria and Monitoring for Geotechnical Construction, ASTM, STP 584, 1975, pp. 141-158.
91. Selig, E. T. and Sluz, A., "Ballast and Subgrade Response to Train Loads," Report to the Transportation Research Board, January 1978.
92. Sissons, C. R., "Strength Testing of Fabrics for Use in Civil Engineering," Proceedings of the International Conference on the Use of Fabrics in Geotechnics, Ecole Nationale Des Ponts et Chaussees, Paris, April 1977, pp. 287-292.
93. Smith, P. C., Johnson, A. I., Fisher, C. P., and Womack, L. M., "The Use of Nuclear Meters in Soils Investigations: A Summary of Worldwide Research and Practice," ASTM 412, 1968.
94. Soiltest International, Inc., "Subsurface Investigation," 1975.
95. Sørli, A., "The Effect of Fabrics on Pavement Strength-Plate Bearing Tests in the Laboratory," Proceedings of the International Conference on the Use of Fabrics in Geotechnics, Ecole Nationale Des Ponts et Chaussees, Paris, April 1977, pp. 15-18.
96. Sowers, G. F. and Scholtes, R. M., "Laboratory Manual for Soil Testing," Georgia Institute of Technology, 1955.
97. Sowers, G. B. and Sowers, G. F., "Introductory Soil Mechanics and Foundations," Third Edition, MacMillan Publishing Co., Inc., 1970.
98. Spiegel, M. R., "Statistics," McGraw-Hill Book Company, 1961.
99. Steele, R. G. D. and Torrie, J. H., "Principles and Procedures of Statistics," McGraw-Hill Book Company, 1960.
100. Steward, J., Williamson, R. and Mohney, J., "Guidelines for Use of Fabrics in Construction and Maintenance of Low Volume Roads," USDA, Forest Service, June 1977.
101. Stuart, E., Miyaoka, Y., Skok, E. L., and Wenck, N. C., "Field Evaluation of an Asphalt Stabilized Sand Pavement Design Using the Elastic Layered System," Proceedings of the Association of Asphalt Paving Technologists, 49th Annual Meeting, February 1974.

102. Terzaghi, K. and Peck, R. B., "Soil Mechanics in Engineering Practice," Second Edition, John Wiley and Sons, Inc., 1967.
103. Thompson, M. R., Kinney, T. C., et al., "Subgrade Stability," Final Report, No. UILU-ENG-77-2009, University of Illinois at Urbana-Champaign, June 1977.
104. Tory, A. C. and Sparrow, R. W., "The Influence of Diaphragm Flexibility on the Performance of an Earth Pressure Cell," Journal of Scientific Instruments, No. 44, 1967, pp. 781-785.
105. Townsend, F. C. and Chisolm, E. E., "Plastic and Resilient Properties of Heavy Clay Under Repetitive Loadings," TRS-76-16, U.S. Army Waterways Experiment Station, November 1976.
106. Traylor, M. L. and Thompson, M. R., "Sinkage Prediction - Subgrade Stability," Technical Report, No. UILU-ENG-77-2008, University of Illinois at Urbana-Champaign, June 1977.
107. Triandifilidis, G. E., "Soil Stress Gage Design and Evaluation," Journal of Testing and Evaluation, ASTM, Vol. 2/3, May 1974, pp. 146-158.
108. Tygar Sales Division - DuPont Company, "DuPont Tygar Support Fabric for the Construction Industry," 1978.
109. Tygar Sales Division - DuPont Company, "A Method for Constructing Aggregate Bases Using Tygar Spunbonded Polypropylene," 1979.
110. University of Illinois at Urbana-Champaign, "User's Manual - The Finite Element Program for Pavement Analysis," 1973.
111. U.S. Army Waterways Experiment Station, "Soil Pressure Cell Investigation," Technical Memorandum, No. 210-1, 1944.
112. Van Leeuwen, J. H., "New Methods of Determining the Stress-Strain Behavior of Woven and Non-Woven Fabrics in the Laboratory and in Practice," Proceedings of the International Conference on the Use of Fabrics in Geotechnics, Ecole Nationale Des Ponts et Chaussees, Paris, April 1977, pp. 299-304.
113. Vesic, A. S. and Domaschuk, L., "Theoretical Analysis of Structural Behavior of Road Test Flexible Pavements," NCHRP, Report 10, 1964.
114. Viergever, M. A., DeFeijter, J. W., and Mouw, K. A. G., "Bi-Axial Tensile Strength and Resistance to Cone Penetration of Membranes," Proceedings of the International Conference on the Use of Fabrics in Geotechnics, Ecole Nationale Des Ponts et Chaussees, Paris, April 1977, pp. 311-316.

115. Vulcan Materials Company, "Standard Sizes of Coarse Aggregate for Highway Construction," Standard Specifications Series, January 1972.
116. Webster, S. L. and Andress, R. A., "Investigation of Fabrics and Bituminous Surfaces for Use in MESL Construction," MPS-76-14, U.S. Army Waterways Experiment Station, August 1976.
117. Webster, S. L. and Watkins, J. E., "Investigation of Construction Techniques for Tactical Bridge Approach Roads Across Soft Ground," TRS-77-1, U.S. Army Waterways Experiment Station, February 1977.
118. Webster, S. L. and Alford, S. J., "Investigation of Construction Concepts for Pavements Across Soft Ground," TRS-78-6, U.S. Army Waterways Experiment Station, July 1978.
119. Westergaard, H. M., "A Problem of Elasticity Suggested by a Problem in Soil Mechanics: A Soft Material Reinforced by Numerous Strong Horizontal Sheets," Contribution, Mechanics of Solids, S. Timoshenko, 60th Anniversary Volume, The MacMillan Company, 1938.
120. Whiffin, A. C. and Lister, N. W., "The Application of Elastic Theory to Flexible Pavements," Proceedings of the First International Conference for Structural Design of Asphalt Pavements, Ann Arbor, Michigan, 1962, pp. 499-521.
121. Winterkorn, H. F. and Fang, H., "Foundation Engineering Handbook," Van Nostrand Reinhold Company, 1975.
122. Yoder, E. J. and Witczak, M. W., "Principles of Pavement Design," Second Edition, John Wiley and Sons, Inc., 1975.
123. Zeevaert, A. E., "Finite Element Formulation for the Analysis of Interfaces, Nonlinear and Large Displacement Problems in Geotechnical Engineering," Ph.D. Thesis, Georgia Institute of Technology, September 1980.

DATE
ILME